TWO-DIMENSIONAL X-RAY DIFFRACTION

TWO-DIMENSIONAL X-RAY DIFFRACTION

BOB BAOPING HE

Second Edition

WILEY

This edition first published 2018
© 2018 John Wiley & Sons, Inc.

Edition History
John Wiley & Sons, Inc. (1e, 2009)

All rights reserved. No part of this publication may be reproduced, stored in a retrieval system, or transmitted, in any form or by any means, electronic, mechanical, photocopying, recording or otherwise, except as permitted by law. Advice on how to obtain permission to reuse material from this title is available at http://www.wiley.com/go/permissions.

The right of Bob Baoping He to be identified as the author of this work has been asserted in accordance with law.

Registered Office
John Wiley & Sons, Inc., 111 River Street, Hoboken, NJ 07030, USA

Editorial Office
111 River Street, Hoboken, NJ 07030, USA

For details of our global editorial offices, customer services, and more information about Wiley products visit us at www.wiley.com.

Wiley also publishes its books in a variety of electronic formats and by print-on-demand. Some content that appears in standard print versions of this book may not be available in other formats.

Limit of Liability/Disclaimer of Warranty
In view of ongoing research, equipment modifications, changes in governmental regulations, and the constant flow of information relating to the use of experimental reagents, equipment, and devices, the reader is urged to review and evaluate the information provided in the package insert or instructions for each chemical, piece of equipment, reagent, or device for, among other things, any changes in the instructions or indication of usage and for added warnings and precautions. While the publisher and authors have used their best efforts in preparing this work, they make no representations or warranties with respect to the accuracy or completeness of the contents of this work and specifically disclaim all warranties, including without limitation any implied warranties of merchantability or fitness for a particular purpose. No warranty may be created or extended by sales representatives, written sales materials or promotional statements for this work. The fact that an organization, website, or product is referred to in this work as a citation and/or potential source of further information does not mean that the publisher and authors endorse the information or services the organization, website, or product may provide or recommendations it may make. This work is sold with the understanding that the publisher is not engaged in rendering professional services. The advice and strategies contained herein may not be suitable for your situation. You should consult with a specialist where appropriate. Further, readers should be aware that websites listed in this work may have changed or disappeared between when this work was written and when it is read. Neither the publisher nor authors shall be liable for any loss of profit or any other commercial damages, including but not limited to special, incidental, consequential, or other damages.

Library of Congress Cataloging-in-Publication Data

Names: He, Bob B., 1954- author.
Title: Two-dimensional x-ray diffraction / by Bob Baoping He.
Description: Second edition. | Hoboken, NJ : John Wiley & Sons, 2018. |
Includes bibliographical references and index. |
Identifiers: LCCN 2018001011 (print) | LCCN 2018007081 (ebook) | ISBN 9781119356066 (pdf) | ISBN 9781119356097 (epub) | ISBN 9781119356103 (cloth)
Subjects: LCSH: X-rays–Diffraction. | X-rays–Diffraction–Experiments. | X-rays–Diffraction–Industrial applications.
Classification: LCC QC482.D5 (ebook) | LCC QC482.D5 H4 2018 (print) | DDC 548/.83–dc23
LC record available at https://lccn.loc.gov/2018001011

Cover Design: Wiley
Cover Image: Image courtesy of Bob B. He

Set in 10/12pt TimesLTStd by SPi Global, Chennai, India

Printed in the United States of America

10 9 8 7 6 5 4 3 2 1

CONTENTS

Preface xiii

1. Introduction 1

1.1 X-Ray Technology, a Brief History, 1
1.2 Geometry of Crystals, 2
1.2.1 Crystal Lattice and Symmetry, 2
1.2.2 Lattice Directions and Planes, 6
1.2.3 Atomic Arrangement in Crystal Structures, 7
1.2.4 Imperfections in Crystal Structure, 10
1.3 Principles of X-Ray Diffraction, 11
1.3.1 Bragg's Law, 12
1.3.2 Diffraction Patterns, 13
1.4 Reciprocal Space and Diffraction, 13
1.4.1 Reciprocal Lattice, 14
1.4.2 The Ewald Sphere, 16
1.4.3 Diffraction Cone and Diffraction Vector Cone, 18
1.5 Two-Dimensional X-Ray Diffraction, 19
1.5.1 Diffraction Pattern Measured by Area Detector, 19
1.5.2 Materials Characterization with 2D Diffraction Pattern, 21
1.5.3 Two-Dimensional X-Ray Diffraction System and Major Components, 23
1.5.4 Summary, 24
References, 26

2. Geometry and Fundamentals 29

2.1 Introduction, 29
2.1.1 Comparison Between XRD^2 and Conventional XRD, 30
2.2 Diffraction Space and Laboratory Coordinates, 31

2.2.1 Diffraction Cones in Laboratory Coordinates, 31
2.2.2 Diffraction Vector Cones in Laboratory Coordinates, 34
2.3 Detector Space and Detector Geometry, 35
2.3.1 Ideal Detector for Diffraction Pattern in 3D Space, 35
2.3.2 Diffraction Cones and Conic Sections with Flat 2D Detectors, 36
2.3.3 Detector Position in the Laboratory System, 36
2.3.4 Pixel Position in Diffraction Space – Flat Detector, 38
2.3.5 Pixel Position in Diffraction Space – Flat Detector Out of Diffractometer Plane, 40
2.3.6 Pixel Position in Diffraction Space – Cylindrical Detector, 43
2.4 Sample Space and Goniometer Geometry, 46
2.4.1 Sample Rotations and Translations in Eulerian Geometry, 46
2.4.2 Variation of Goniometer Geometry, 48
2.5 Transformation from Diffraction Space to Sample Space, 50
2.6 Reciprocal Space, 52
2.7 Summary, 53
References, 55

3. X-Ray Source and Optics **57**

3.1 X-Ray Generation and Characteristics, 57
3.1.1 X-Ray Spectrum and Characteristic Lines, 57
3.1.2 Focal Spot and Takeoff Angle, 58
3.1.3 Focal Spot Brightness and Profile, 59
3.1.4 Absorption and Fluorescence, 61
3.1.5 Synchrotron Radiation, 62
3.2 X-Ray Optics, 63
3.2.1 Liouville's Theorem and Fundamentals, 63
3.2.2 X-Ray Optics in Conventional Diffractometer, 65
3.2.3 X-Ray Optics in a Two-Dimensional Diffractometer, 68
3.2.4 The β-Filter, 71
3.2.5 Crystal Monochromator, 73
3.2.6 Multilayer Mirrors, 75
3.2.7 Pinhole Collimator, 80
3.2.8 Capillary Optics, 82
References, 85

4. X-Ray Detectors **87**

4.1 History of X-Ray Detection Technology, 87
4.2 Point Detectors in Conventional Diffractometers, 89
4.2.1 Proportional Counters, 90
4.2.2 Scintillation Counters, 91
4.2.3 Solid State Detectors, 91
4.3 Characteristics of Point Detectors, 92
4.3.1 Counting Statistics, 92
4.3.2 Detective Quantum Efficiency and Energy Range, 94
4.3.3 Detector Linearity and Maximum Count Rate, 95
4.3.4 Energy Resolution, 97

4.3.5 Detection Limit and Dynamic Range, 99
4.4 Line Detectors, 100
4.4.1 Geometry of Line Detectors, 100
4.4.2 Types of Line Detectors, 103
4.4.3 Characteristics of Line Detectors, 104
4.5 Characteristics of Area Detectors, 107
4.5.1 Active Area and Angular Coverage, 107
4.5.2 Weight and Dimension, 111
4.5.3 Angular Coverage of Pixels, 112
4.5.4 Spatial Resolution of Area Detectors, 114
4.5.5 Pixel Number and Angular Resolution, 116
4.5.6 Angular Resolution of a 2D Diffractometer, 117
4.6 Types of Area Detectors, 119
4.6.1 Multiwire Proportional Counter, 119
4.6.2 Image Plate, 121
4.6.3 CCD Detector, 122
4.6.4 CMOS Detector, 125
4.6.5 Pixel Array Detector, 126
4.6.6 CPAD Detector, 129
4.6.7 Microgap Detector, 130
4.6.8 Comparison of Area Detectors, 135
References, 137

5. Goniometer and Sample Stages **141**

5.1 Goniometer and Sample Position, 141
5.1.1 Introduction, 141
5.1.2 Two-Circle Base Goniometer, 141
5.1.3 Sample Stages, 142
5.1.4 Sequence of the Goniometer Axes, 144
5.2 Goniometer Accuracy, 145
5.2.1 Sphere of Confusion, 145
5.2.2 Angular Accuracy and Precision, 148
5.3 Sample Alignment and Visualization Systems, 149
5.4 Environment Stages, 151
5.4.1 Domed High Temperature Stage, 151
5.4.2 Temperature Stage Calibration, 153
References, 155

6. Data Treatment **157**

6.1 Introduction, 157
6.2 Non-Uniform Response Correction, 157
6.2.1 Calibration Source, 158
6.2.2 Non-Uniform Response Correction Algorithms, 159
6.3 Spatial Correction, 161
6.3.1 Fiducial Plate and Detector Plane, 162
6.3.2 Spatial Correction Algorithms, 163
6.4 Detector Position Accuracy and Calibration, 166

6.4.1 Detector Position Tolerance, 168
6.4.2 Detector Position Calibration, 169
6.4.3 Detector Roll Calibration with Diffraction Rings, 171
6.4.4 Intersection Between Diffraction Cones, 171
6.5 Frame Integration, 177
6.5.1 Definition of Frame Integration, 177
6.5.2 Algorithm of Frame Integration – Flat Image, 180
6.5.3 Algorithm of Frame Integration – Cylindrical Image, 185
6.6 Multiple Frame Merge, 186
6.6.1 Merging Multiple Frames, 186
6.6.2 Cylinder Projection of Flat 2D Frames, 187
6.6.3 Merging of the Overlapping Region, 191
6.7 Scanning 2D Pattern, 194
6.8 Lorentz, Polarization, and Absorption Corrections, 197
6.8.1 Lorentz, 197
6.8.2 Polarization, 197
6.8.3 Air Scatter and Be-Window Absorption, 201
6.8.4 Sample Absorption, 203
6.8.5 Combined Intensity Correction, 207
References, 209

7. Phase Identification **211**

7.1 Introduction, 211
7.2 Relative Intensity, 212
7.2.1 Multiplicity Factor, 213
7.2.2 Electron and Atomic Scattering, 214
7.2.3 Structure Factor, 215
7.2.4 Attenuation Factors, 216
7.3 Geometry and Resolution, 216
7.3.1 Detector Distance and Resolution, 217
7.3.2 Defocusing Effect, 218
7.3.3 Transmission Mode Diffraction, 220
7.4 Sampling Statistics, 221
7.4.1 Effective Sampling Volume, 222
7.4.2 Angular Window, 223
7.4.3 Virtual Oscillation, 224
7.4.4 Sample Oscillation, 225
7.5 Preferred Orientation Effect, 227
7.5.1 Relative Intensity with Texture, 227
7.5.2 Intensity Correction on Fiber Texture, 229
References, 233

8. Texture Analysis **235**

8.1 Introduction, 235
8.2 Pole Density and Pole-Figure, 236
8.3 Fundamental Equations, 238
8.3.1 Pole-figure Angles, 238

8.3.2 Pole Density, 240
8.4 Data Collection Strategy, 242
8.4.1 Single φ Scan, 242
8.4.2 Multiple ϕ Scans, 243
8.4.3 Combination of φ and ω Scans, 246
8.4.4 Goniometer ϕ Rotation Direction, 247
8.4.5 Transmission Mode, 248
8.4.6 Comparison with Point Detector, 250
8.5 Texture Data Process, 251
8.5.1 2θ Integration, 251
8.5.2 Absorption Correction, 255
8.5.3 Pole-Figure Interpolation, 255
8.5.4 Pole-Figure Symmetry, 256
8.5.5 Pole-Figure Normalization, 256
8.6 Orientation Distribution Function, 256
8.6.1 Eulerian Angles and Space, 256
8.6.2 ODF Calculation, 258
8.6.3 Calculated Pole-Figures from ODF, 259
8.7 Fiber Texture, 260
8.7.1 Pole-Figures of Fiber Texture, 262
8.7.2 ODF of Fiber Texture, 262
8.8 Polymer Texture, 264
8.8.1 Data Collection Strategy for Polymers, 264
8.8.2 Pole-Figure from Polymer Film, 265
8.9 Other Advantages of XRD^2 for Texture, 268
8.9.1 Orientation Relationship, 268
8.9.2 Direct Observation of Texture, 268
References, 269

9. Stress Measurement **271**

9.1 Introduction, 271
9.1.1 Stress, 272
9.1.2 Strain, 276
9.1.3 Elasticity and Hooke's Law, 277
9.1.4 X-Ray Elasticity Constants and Anisotropy Factor, 278
9.1.5 Residual Stresses, 279
9.2 Principle of X-ray Stress Analysis, 280
9.2.1 Strain and Bragg's Law, 280
9.2.2 Strain Measurement, 282
9.2.3 Stress Measurement, 283
9.2.4 Stress Measurement Without d_o, 286
9.2.5 ψ-Tilt and Goniometer, 288
9.2.6 $\sin^2\psi$ Method with Area Detector, 291
9.3 Theory of Stress Analysis with XRD^2, 292
9.3.1 2D Fundamental Equation for Stress Measurement, 292
9.3.2 Relationship Between Conventional Theory and 2D Theory, 295
9.3.3 2D Equations for Various Stress States, 298
9.3.4 True Stress-Free Lattice d-Spacing, 300

9.3.5 Diffraction Cone Distortion Simulation, 302
9.3.6 Goniometer ϕ Rotation Direction, 306
9.4 Process of Stress Measurement with XRD^2, 307
9.4.1 Instrument Requirements and Configurations, 308
9.4.2 Data Collection Strategy, 309
9.4.3 Data Integration and Peak Evaluation, 313
9.4.4 Stress Calculation, 316
9.4.5 Effect of Texture and Large Grain, 318
9.4.6 Intensity Weighted Least Squares Regression, 318
9.4.7 Stress-Free Sample and Standard Sample, 320
9.4.8 Dynamic Sample Height Alignment, 321
9.4.9 Correction with Stress-Free Sample, 322
9.4.10 Correction with Stress Standard, 324
9.5 Experimental Examples, 325
9.5.1 Comparison Between 2D Method and Conventional Method, 325
9.5.2 Sample Oscillation and Virtual Oscillation, 327
9.5.3 Stress Mapping on Weldment, 329
9.5.4 Residual Stresses in Thin Films, 332
9.5.5 Residual Stress Measurement with Multiple {*hkl*} Rings, 335
9.5.6 Single Tilt Method, 340
9.5.7 Gage Repeatability and Reproducibility Study, 347
A9.1 Calculation of Principal Stresses from the General Stress Tensor, 349
A9.1.1 Calculate Principal Stresses, 349
A9.1.2 Calculate the direction cosines for principal stresses (Eigenvectors), 350
A9.2 Parameters for Stress Measurement, 351
References, 353

10. Small Angle X-ray Scattering 357

10.1 Introduction, 357
10.1.1 Principle of Small Angle Scattering, 357
10.1.2 General Equation and Parameters in SAXS, 358
10.1.3 X-Ray Source and Optics for SAXS, 359
10.2 2D SAXS Systems, 361
10.2.1 SAXS Attachments, 361
10.2.2 Dedicated SAXS System, 364
10.2.3 Detector Correction and System Calibration, 365
10.2.4 Data Collection and Integration, 366
10.3 Applications Examples, 367
10.3.1 Particles in Solutions, 367
10.3.2 Scanning SAXS and Transmission Measurement, 367
10.4 Some Innovations in 2D SAXS, 370
10.4.1 Simultaneous Measurements of Transmission and SAXS, 370
10.4.2 Vertical SAXS System, 372
References, 374

11. Combinatorial Screening 379

11.1 Introduction, 379
11.1.1 Combinatorial Chemistry, 379
11.1.2 High Throughput Screening, 379
11.2 XRD^2 Systems for High Throughput Screening, 380
11.2.1 Screening in Reflection Geometry, 380
11.2.2 Retractable Knife-Edge, 383
11.2.3 Screening in Transmission Geometry, 386
11.3 Combined Screening with XRD^2 and Raman, 390
References, 393

12. Miscellaneous Applications 395

12.1 Percent Crystallinity, 395
12.1.1 Introduction, 395
12.1.2 Comparison of Conventional XRD and XRD^2, 397
12.1.3 Scatter Correction, 397
12.1.4 Internal and External Methods, 398
12.1.5 Full Method, 400
12.2 Crystal Size, 402
12.2.1 Introduction, 402
12.2.2 Line Broadening for Crystallite Size, 402
12.2.3 Crystallite Size Using γ-Profile Analysis, 404
12.3 Retained Austenite, 412
12.4 Crystal Orientation, 414
12.4.1 Orientation with Respect to Sample, 414
12.4.2 Angle Between Two Crystal Planes, 416
12.4.3 Miscut Angle of Single Crystal Wafer, 416
12.5 Thin Film Analysis, 418
12.5.1 Grazing Incidence X-Ray Diffraction, 418
12.5.2 Reflectometry with 2D Detector, 423
12.5.3 Reciprocal Space Mapping, 424
References, 429

13. Innovation and Future Development 433

13.1 Introduction, 433
13.2 Scanning Line Detector for XRD^2, 434
13.2.1 Working Principle, 434
13.2.2 Advantages of Scanning Line Detector, 436
13.3 Three-Dimensional Detector, 438
13.3.1 Third Dimension of a Detector, 438
13.3.2 Geometry of Three-Dimensional Detector, 438
13.3.3 Three-Dimensional Detector and Reciprocal Space, 440
13.4 Pixel Direct Diffraction Analysis, 441

13.4.1 Concept, 441
13.4.2 Pixel Diffraction Vector and Pixel Count, 442
13.4.3 PDD Analysis in Phase-ID, Texture, and Stress, 442
13.5 High Resolution Two-Dimensional X-Ray Diffractometer, 444
13.5.1 Background, 444
13.5.2 HRXRD^2 in Reciprocal Space, 445
13.5.3 New Configuration for HRXRD^2, 447
References, 451

Appendix A. Values of Commonly Used Parameters **453**

Appendix B. Symbols **459**

Index **465**

PREFACE

Two-dimensional X-ray diffraction is the ideal non-destructive analytical method for characterizing many types of materials, such as metals, polymers, ceramics, semiconductors, thin films, coatings, paints, biomaterials, and composites. It has been widely used for material science and engineering, drug discovery and processing control, forensic analysis, archeological analysis, and many emerging applications. In the long history of powder X-ray diffraction, data collection and analysis have been based mainly on one-dimensional diffraction profiles measured with scanning point detectors or linear position-sensitive detectors. Therefore, almost all X-ray powder diffraction applications – such as phase identification, texture, residual stress, crystallite size, and percent crystallinity – are developed in accord with the one-dimensional diffraction profiles collected by conventional diffractometers. In recent years, use of two-dimensional detectors has dramatically increased due to the advances in detector technology. A two-dimensional diffraction pattern contains abundant information about the atomic arrangement, microstructure, and defects of a solid or liquid material. Because of the unique nature of the data collected with a two-dimensional detector, many algorithms and methods developed for conventional X-ray diffraction are not sufficient or accurate for interpreting and analyzing the data. New concepts and approaches are necessary for designing a two-dimensional diffractometer and for understanding and analyzing two-dimensional diffraction data. In addition, the new theory should also be consistent with conventional theory because two-dimensional X-ray diffraction is also a natural extension of conventional X-ray diffraction.

The purpose of this book is to give an introduction to two-dimensional X-ray diffraction. Chapter 1 gives a brief introduction to X-ray diffraction and its extension to two-dimensional X-ray diffraction. Discussion of the general principles of crystallography and X-ray diffraction is kept to a minimum since many books on the subjects are available. Chapter 2 describes the geometry conventions and diffraction vector analysis which establish the foundation for the subjects discussed in the following chapters. A diffraction vector approach is used for deriving many fundamental equations for various applications in the following chapters. The critical steps are included so that readers can use similar approach for any analysis not included in the book.

Chapters 3 to 6 focus on the instrumentation technologies, including X-ray source and optics, detectors, goniometers, system configurations and basic data collection, and evaluation algorithms. Chapters 7 to 12 cover the basic concepts, fundamental theory, diffractometer configurations, data collection strategy, data analysis algorithms, and experimental examples for various applications, such as phase identification, texture, stress, microstructure analysis, crystallinity, thin film analysis, and combinatorial screening. Chapter 13 presents some ideas on innovations and future development.

Since publication of the first edition of this book in 2009, there has been remarkable progress in the instrumentation and applications of two-dimensional X-ray diffraction. I have received many constructive reviews, comments, and suggestions from readers. In addition to the recent progress in instrumentation and applications, the most important improvement in the second edition is to have most figures in full color, so that different elements in illustrations and the details of diffraction patterns can be better revealed.

I would like to express my sincere appreciation to Professors Mingzhi Huang, Huijiu Zhou and Jiawen He, Charles Houska, Guoquan Lu, and Robert Hendricks for their guidance, assistance, and encouragement in my education and career development. I wish to acknowledge the support, suggestions, and contributions from my colleagues, especially from Kingsley Smith, Uwe Preckwinkel, Roger Durst, Yacouba Diawara, John Chambers, Gary Schmidt, Peter LaPuma, Lutz Brügemann, Frank Burgäzy, Martin Haase, Mark Depp, Hannes Jakob, Kurt Helmings, Arnt Kern, Geert Vanhoyland, Alexander Ulyanenkov, Jens Brechbuehl, Ekkehard Gerndt, Hitoshi Morioka, Keisuke Saito, Susan Byram, Michael Ruf, Charles Campana, Joerg Kaercher, Bruce Noll, Delaine Laski, Beth Beutler, Rob Hooft, Alexander Seyfarth, Joseph Formica, Richard Ortega, Brian Litteer, Bruce Becker, Detlef Bahr, Heiko Ress, Kurt Erlacher, Christian Maurer, Olaf Meding, Christoph Ollinger, Kai-Uwe Mettendorf, Joachim Lange, Martin Zimmermann, Hugues Guerault, Ning Yang, Hao Jiang, Jon Giencke, and Brain Jones. I would also like to thank Robert Cernik, Shepton Steve, Christian Lehmann, George Kauffman, Gary Vardon, Werner Massa, Joseph Reibenspies, and Nattamai Bhuvanesh for spending their valuable time to publish book reviews of the first edition, which encouraged and helped me to make many corrections and improvements in the second edition.

I am grateful to those who have so generously contributed their ideas, inspiration, and insights through many thoughtful discussions and communications, particularly to Thomas Blanton, Davor Balzar, Camden Hubbard, James Britten, Joseph Reibenspies, Timothy Fawcett, Scott Misture, James Kaduk, Ralph Tissot, Mark Rodriguez, Matteo Leoni, Herbert Göbel, Scott Speakman, Thomas Watkins, Jian Lu, Xun-Li Wang, John Anzelmo, Brian Toby, Ting Huang, Alejandro Navarro, Peter Zavalij, Mario Birkholz, Kewei Xu, Berthold Scholtes, Chang-Beom Eom, Gregory Stephenson, Raj Suryanarayanan, Shawn Yin, Naveen Thakral, Lian Yu, Siddhartha Das, Chris Frampton, Chris Gilmore, Keisuke Tanaka, Wulf Pfeiffer, Dierk Raabe, Robert Snyder, Jose Miguel Delgado, Winnie Wong-Ng, Xiaolong Chen, Chuanhai Jiang, Wenhai Ye, Weimin Mao, Leng Chen, Kun Tao, Erqiang Chen, Danmin Liu, Dulal Goldar, Vincent Ji, Peter Lee, Yan Gao, Lizhi Liu, Yujing Tang, Minqiao Ren, Ying Shi, Chunhua Tony Hu, Shaoliang Zheng, Ravi Ananth, Philip Conrad, Linda Sauer, Roberta Flemming, Chan Park, Dongying Ju, Milan Gembicky, Hui Zhang, Willard Schultz, Licai Jiang, Ning Gao, Fangling Needham, and John Faber. I am particularly indebted to my wife Judy for her patience, care, and understanding, and to my son Mike for his support.

Serving as a scientist and as director of R&D and business development for over 20 years for Bruker AXS, an industry leader in X-ray diffraction instrumentation and solutions, gives me the opportunity to meet many scientists, engineers, professors, and students working in the field of X-ray diffraction, and the necessary resources to put many ideas into practice. The many pictures and experimental data in this book are collected from diffractometers manufactured by Bruker

AXS Inc. This should not be construed as an endorsement of a particular vendor, but rather a convenient way to illustrate the ideas contained in this book. The approaches and algorithms suggested in the book are not necessarily the best alternatives, and some errors may exist due to my mistakes. A list of references is included in each chapter, but I apologize for missing any original and important references due to my oversight. I welcome any and all comments, suggestions, and criticisms.

Bob Baoping He

1

INTRODUCTION

1.1 X-RAY TECHNOLOGY, A BRIEF HISTORY

X-ray technology has more than a hundred years of history and its discovery and development have revolutionized many areas of modern science and technology [1]. X-rays were discovered by the German physicist Wilhelm Conrad Röntgen in 1895, who was honored with the Noble prize for physics in 1901. In many languages today X-rays are still referred to as Röntgen rays or Röntgen radiation. This mysterious light was found to be invisible to human eyes, but capable of penetrating opaque object and expose photographic films. The density contrast of the object is revealed on the developed film as a radiograph. Since then X-rays have been developed for medical imaging, such as for detection of bony structures and diseases in soft tissues like pneumonia and lung cancer. X-rays have also been used to treat disease. Radiotherapy employs high energy X-rays to generate a curative medical intervention to the cancer tissues. A recent technology, tomotherapy, combines the precision of a computerized tomography scan with the potency of radiation treatment to selectively destroy cancerous tumors while minimizing damage to surrounding tissue. Today, medical diagnoses and treatments are still the most common use of X-ray technology.

The phenomenon of X-ray diffraction by crystals was discovered in 1912 by Max von Laue. The diffraction condition in a simple mathematical form, which is now known as Bragg's law, was formulated by Lawrence Bragg in the same year. The Nobel Prize in Physics in consecutive two years (1914 and 1915) was awarded to von Laue and the elder and junior Braggs for the discovery and explanation of X-ray diffraction. X-ray diffraction techniques are based on elastic scattered X-rays from matter. Due to the wave nature of X-rays, the scattered X-rays from a sample can interfere with each other, such that the intensity distribution is determined by the wavelength and the incident angle of the X-rays and the atomic arrangement of the sample structure, particularly the long range order of crystalline structures. The expression of the space distribution of the scattered X-rays is referred to as an X-ray diffraction pattern. The atomic level structure

Two-Dimensional X-Ray Diffraction, Second Edition. Bob Baoping He.
© 2018 John Wiley & Sons, Inc. Published 2018 by John Wiley & Sons, Inc.

of the material can then be determined by analyzing the diffraction pattern. Over its hundred year history of development, X-ray diffraction techniques have evolved into many specialized areas. Each has its specialized instruments, samples of interest, theory, and practice. Single-crystal X-ray diffraction (SCD) is a technique used to solve the complete structure of crystalline materials, typically in the form of a single crystal. The technique started with simple inorganic solids and grew into complex macromolecules. Protein structures were first determined by X-ray diffraction analysis by Max Perutz and Sir John Cowdery Kendrew in 1958, and both shared the 1962 Nobel Prize in Chemistry. Today, protein crystallography is the dominant application of SCD. X-ray powder diffraction (XRPD), alternatively called powder X-ray diffraction (PXRD), got its name from the technique of collecting X-ray diffraction patterns from packed powder samples. Generally, X-ray powder diffraction involves the characterization of the crystallographic structure, crystallite size, and orientation distribution in polycrystalline samples [2–5].

X-ray diffraction (XRD), by definition, covers single crystal diffraction and powder diffraction as well as many X-ray diffraction techniques. However, it has been accepted as convention that SCD is distinguished from XRD. By this practice, XRD is commonly used to represent various X-ray diffraction applications other than SCD. These applications include phase-identification, texture analysis, stress measurement, percentage crystallinity, particle (grain) size, and thin film analysis. An analogous method to X-ray diffraction is the small angle X-ray scattering (SAXS) technique. SAXS measures scattering intensity at scattering angles within a few degrees from the incident angle. SAXS pattern reveals the material structures, typically particle size and shape, in the nanometer to micrometer range. In contrast to SAXS, other X-ray diffraction techniques are also referred to as wide angle X-ray scattering (WAXS).

1.2 GEOMETRY OF CRYSTALS

Solids can be divided into two categories: amorphous and crystalline. In an amorphous solid, glass for example, atoms are not arranged with long range order. Thus amorphous solids are also referred to as "glassy" solids. In contrast, a crystal is a solid formed by atoms, molecules, or ions stacking in three-dimensional space with a regular and repeating arrangement. The geometry and structure of a crystalline solid determines the X-ray diffraction pattern. Comprehensive knowledge of crystallography has been covered by many books [2, 5–9]. This section gives only some basics to help further discussion on X-ray diffraction.

1.2.1 Crystal Lattice and Symmetry

A crystal structure can be simply expressed by a point lattice, as shown in Figure 1.1(a). The point lattice represents the three-dimensional arrangement of the atoms in the crystal structure. It can be imagined as being comprised of three sets of planes, each set containing parallel crystal planes with equal interplane distance. Each intersection of three planes is called a lattice point and may represent the location of an atom, ion, or molecule in the crystal. A point lattice can be minimally represented by a unit cell, highlighted in bold in the bottom left corner. A complete point lattice can be formed by the translation of the unit cell in three-dimensional space. This feature is also referred to as translation symmetry. The shape and size of a unit cell can be defined by three vectors **a**, **b**, and **c**, all starting from any single lattice point as shown in Figure 1.1(b). The three vectors are called the crystallographic axes of the cell. As each vector can be defined by its length and direction, a unit cell can also be defined by the three lengths of the vectors (a, b, and c) as well as the angles between them (α, β, and γ). The six parameters (a, b, c, α, β, and γ) are referred to as the lattice constants or lattice parameters of the unit cell.

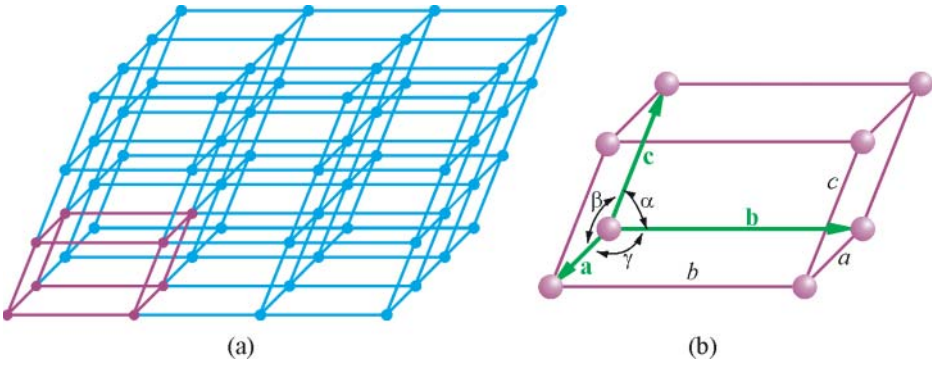


FIGURE 1.1 A point lattice (a) and its unit cell (b).

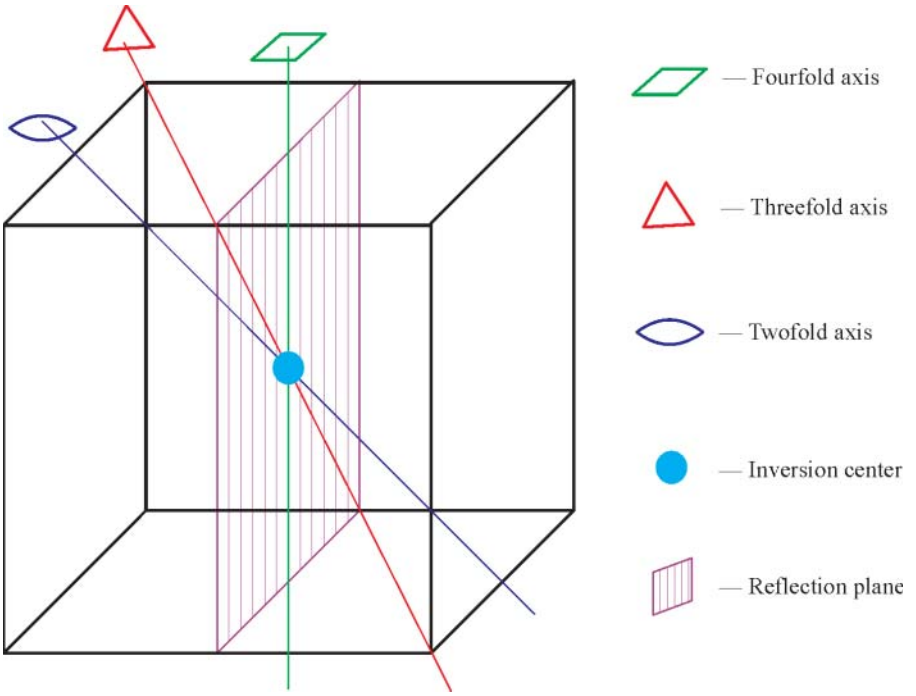


FIGURE 1.2 Symmetry elements of a cubic unit cell.

One important feature of crystals is their symmetry. In addition to the translation symmetry in point lattices, there are also four basic point symmetries: reflection, rotation, inversion, and rotation-inversion. Figure 1.2 shows all four basic point symmetries on a cubic unit cell. The reflection plane is like a mirror. The reflection plane divides the crystal into two sides. Each side of the crystal matches the mirrored position of the other side. The cubic structure has several reflection planes. The rotation axes include 2-, 3-, 4-, and 6-fold axes. A rotation of a crystal about an n-fold axis by 360°/n will bring it into self-coincidence. A cubic unit cell has several 2-, 3-, and 4-fold axes. The inversion center is like a pinhole camera, the crystal will maintain self-coincidence if every point of the crystal is inverted through the inversion center. Any straight

line passing through the inversion center intersects with the same lattice point at the same distance at both sides of the inversion center. A cubic unit cell has an inversion center in its body center. The rotation-inversion center can be considered as a combined symmetry of rotation and inversion.

The various relationships among the six lattice parameters (a, b, c, α, β, and γ) result in various crystal systems. The simplest crystal system is cubic system in which all three crystallographic vectors are equal in length and perpendicular to each other ($a = b = c$ and $\alpha = \beta = \gamma = 90°$). Seven crystal systems are sufficient to cover all possible point lattices. The French crystallographer Bravais found that there are a total of 14 possible point lattices. Seven point lattices are given by the seven crystal systems for the case that only one lattice point is in each unit cell and that the lattice point is located in the corner of the unit cell. These seven types of unit cells are called primitive cells and labeled by P or R. By adding one or more lattice points within a unit cell one can create non-primitive cells depending on the location of the additional lattice points. The location of a lattice point in the unit cell can be specified by fractional coordinates within a unit cell (u, v, w). For example, the lattice point in a primitive cell is (0, 0, 0). Therefore, we can define three types of non-primitive cells. The label I represents the body centered point lattice, which has one additional lattice point at the center of the unit cell, or can be defined by the fraction (½, ½, ½). The label F represents the face centered point lattice with additional lattice points at the center of unit cell face, or (0, ½, ½), (½, 0, ½), and (½, ½, 0). The label C represents the base centered point lattice with an additional lattice point at the center of the base face (½, ½, 0). All seven crystal systems and 14 Bravais lattices are summarized in Table 1.1. The unit cells of the 14 Bravais lattices are shown in Figure 1.3.

Table 1.1 Crystal Systems and Bravais Lattices

The seven crystal systems	Unit cell	Minimum symmetry	Bravais lattices	Lattice symbol
Cubic	$\alpha = \beta = \gamma = 90°$ $a = b = c$	Four 3-fold rotation axes at 109° 23′ to each other	Simple Body-centered Face-centered	P I F
Tetragonal	$\alpha = \beta = \gamma = 90°$ $a = b \neq c$	One 4-fold rotation axis or one 4-fold rotation-inversion axis	Simple Body-centered	P I
Hexagonal	$\alpha = \beta = 90°$ $\gamma = 120°$ $a = b \neq c$	One 6-fold rotation axis or one 6-fold rotation-inversion axis	Simple	P
Rhombohedral (Trigonal)	$\alpha = \beta = \gamma \neq 90°$ $a = b = c$	One 3-fold rotation axis	Simple	R
Orthorhombic	$\alpha = \beta = \gamma = 90°$ $a \neq b \neq c$	Any combination of three mutually perpendicular 2-fold rotation axes or planes of symmetry	Simple Body-centered Base-centered Face-centered	P I C F
Monoclinic	$\alpha = \gamma = 90°$ $\beta \neq 90°$ $a \neq b \neq c$	One 2-fold rotation axis or one 2-fold rotation-inversion axis	Simple Base-centered	P C
Triclinic	$\alpha \neq \beta \neq \gamma \neq 90°$ $a \neq b \neq c$	None	Simple	P

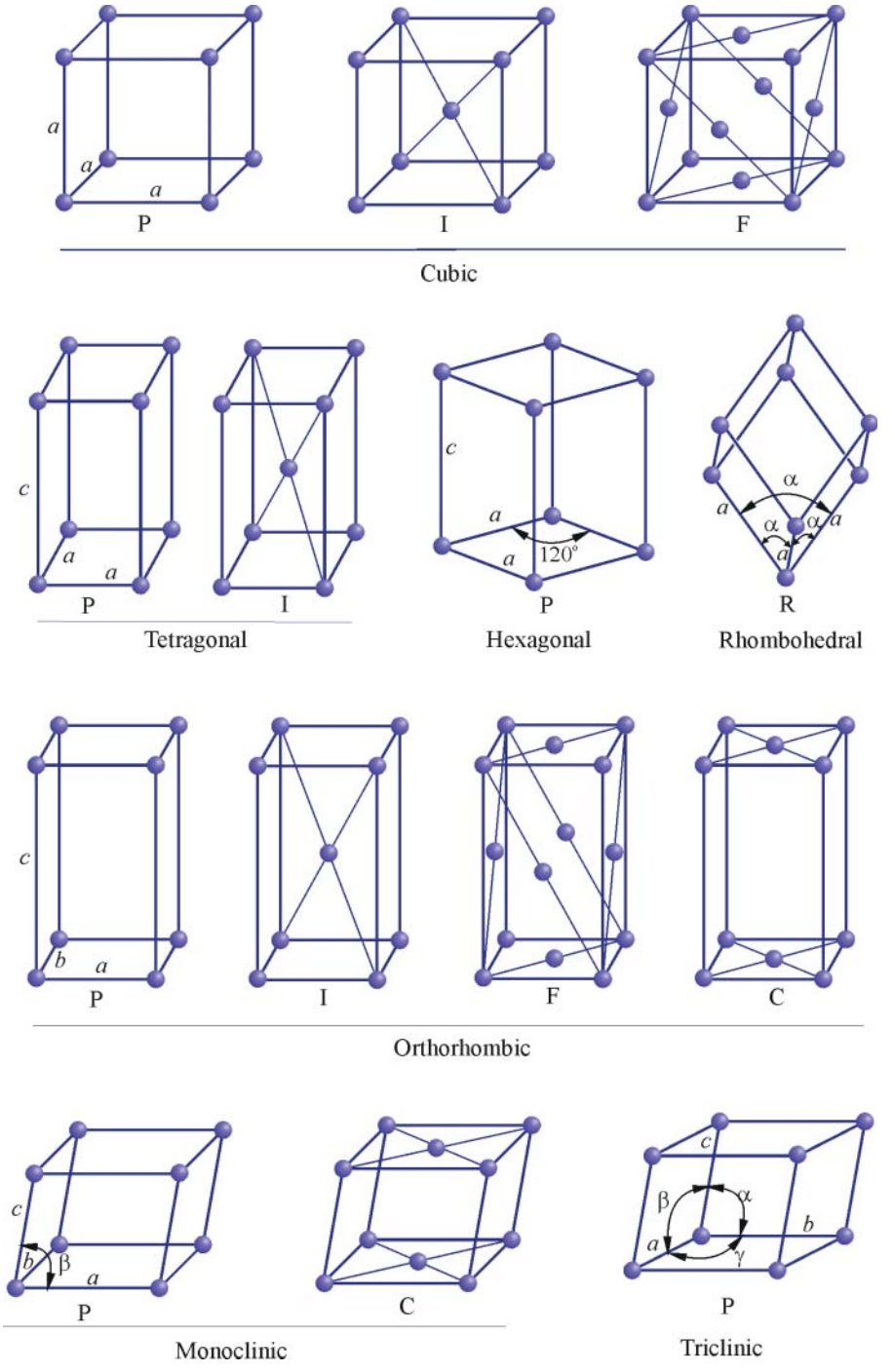


FIGURE 1.3 Unit cells of the 14 Bravais lattices.

1.2.2 Lattice Directions and Planes

The direction of any line in a crystal lattice can be specified by drawing a line starting from the unit cell origin parallel to the given line and then taking the coordinates (u', v', w') of any point on the line. The coordinates (u', v', w') are not necessarily integers. However, by conventional, (u', v', w') are multiplied by the smallest number that produces integers u, v, and w. The crystal direction is described by putting the three integers in square brackets as $[uvw]$. The $[uvw]$ are the indices of a specific crystal direction, and each of the indices can take the value of a positive or negative integer. All directions in a crystal that are symmetry equivalent to $[uvw]$ are represented by a notation with the integers in angular brackets as $<uvw>$. For example, in a cubic crystal all diagonals of the unit cell are symmetry equivalent. So all the directions [111], $[\bar{1}11]$, $[1\bar{1}1]$, $[11\bar{1}]$, $[\bar{1}\bar{1}1]$, $[\bar{1}1\bar{1}]$, $[1\bar{1}\bar{1}]$, and $[\bar{1}\bar{1}\bar{1}]$ can be represented by <111>. The bar over the number is for negative indices. Figure 1.4(a) shows some lattice directions and their indices in a unit cell.

The orientation of lattice planes can be described by using a set of three integers referred to as Miller indices. Miller indices are the reciprocal intercepts of the plane on the unit cell axes. If the crystal plane makes fractional intercepts of $1/h$, $1/k$, $1/l$ with the three crystal axes respectively, the Miller indices are (hkl). If the plane runs parallel to an axis, the intercept is at ∞, so the Miller index is 0. Miller indices describe the orientation and spacing of a family of planes. Figure 1.4(b) shows some lattice planes and their Miller indices in a unit cell. The spacing between adjacent planes in a family is referred to as the "d-spacing". The symbol $\{hkl\}$ refers to all planes that are symmetry equivalent to (hkl). This group of equivalent planes is referred to as planes of a form. For the cubic system all the planes (100), (010), (001), $(\bar{1}00)$, $(0\bar{1}0)$, and $(00\bar{1})$ belong to the form $\{100\}$. For a tetragonal crystal, a = b ≠ c, only the first two indices imply the same interception distance on the crystal axes, so the form $\{100\}$ would only include (100), (010), $(\bar{1}00)$, and $(0\bar{1}0)$.

Figure 1.5(a) shows the hexagonal unit cell and indices of some directions. It follows the same definition as other lattice types. However, lattice planes are often described by a different system of plane indexing, called Miller–Bravais indices. In hexagonal unit cells it is common to use four axis coordinates, $\mathbf{a_1}$, $\mathbf{a_2}$, $\mathbf{a_3}$, and $\mathbf{c}$, in which $\mathbf{a_1}$, $\mathbf{a_2}$, $\mathbf{a_3}$ are lying in the basal plane and $\mathbf{c}$ is perpendicular to all three axes. The indices of a plane in the hexagonal system are written as $(hkil)$. Figure 1.5(b) shows some lattice planes in a hexagonal lattice described by Miller–Bravais indices. Since $\mathbf{a_1}$, $\mathbf{a_2}$, $\mathbf{a_3}$ are symmetry equivalent and 120° apart each other, there are only two

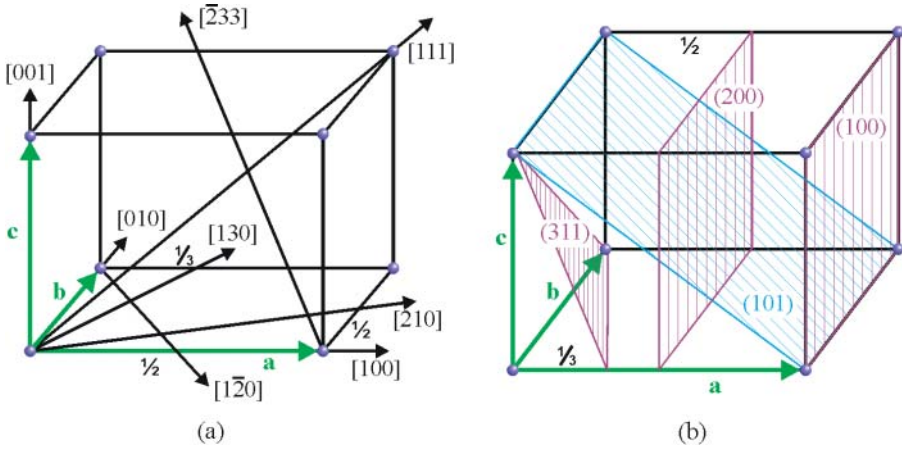


FIGURE 1.4 (a) Indices of lattice directions and (b) Miller indices of lattice planes.

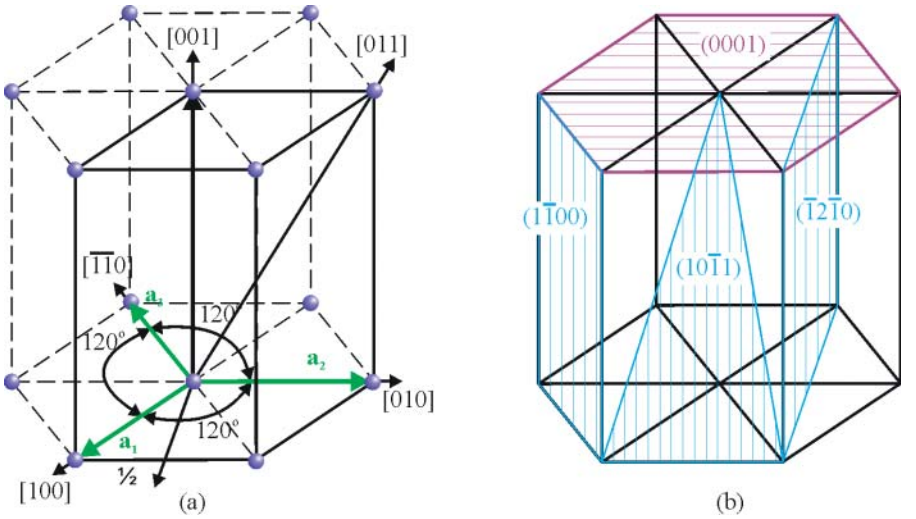


FIGURE 1.5 (a) Hexagonal unit cell (heavy lines) and indices of some lattice directions and (b) Miller–Bravais indices of some lattice planes in a hexagonal lattice.

independent axes among them. So that the first three values in the Miller–Bravais indices maintain the relation

$$h + k + l = 0 \tag{1.1}$$

Since all cyclic permutations of h, k, and i are symmetry equivalent, $(10\bar{1}0)$, $(\bar{1}100)$, $(0\bar{1}10)$ are equivalent.

A zone is defined as a set of non-parallel planes that are all parallel to one axis. This axis is called the zone axis. Miller indices for all planes in a zone obey the relationship

$$hu + kv + lv = 0 \tag{1.2}$$

where $[uvw]$ defines the zone axis and (hkl) are the Miller indices of each plane in the zone. Figure 1.6 shows some of the crystal planes in the cubic lattice that belong to the [001] zone.

The distance between two adjacent planes with the same indices is called the interplanar spacing or d-spacing, which is an important parameter in Bragg's law. The interplanar spacing d_{hkl} is a function of both the plane indices (hkl) and the lattice parameters $(a, b, c, \alpha, \beta, \gamma)$. The equations of d-spacings for all seven crystal systems are listed in Table 1.2. More equations on the unit cell volume and interplanar angles can be found in appendix 3 of ref. [2].

1.2.3 Atomic Arrangement in Crystal Structures

Actual crystal structures can be described by the Bravais lattice filled with the same or different kind of atoms. The atoms take either the exact lattice points and/or points with fixed offset to the lattice points. The three most common crystal structures of metals are body-centered cubic (BCC), face-centered cubic (FCC), and hexagonal close-packed (HCP) structures, as shown in Figure 1.7. BCC has two atoms per unit cell located at the coordinates 0 0 0 and ½ ½ ½ respectively. Many metals, such as α-iron, niobium, chromium, vanadium, and tungsten have BCC structure. FCC has four atoms per unit cell at the coordinates 0 0 0, 0 ½ ½, ½ 0 ½, and ½ ½ 0 respectively. Metals with FCC structure include γ-iron, aluminum, copper, silver, nickel, and gold. HCP contains three

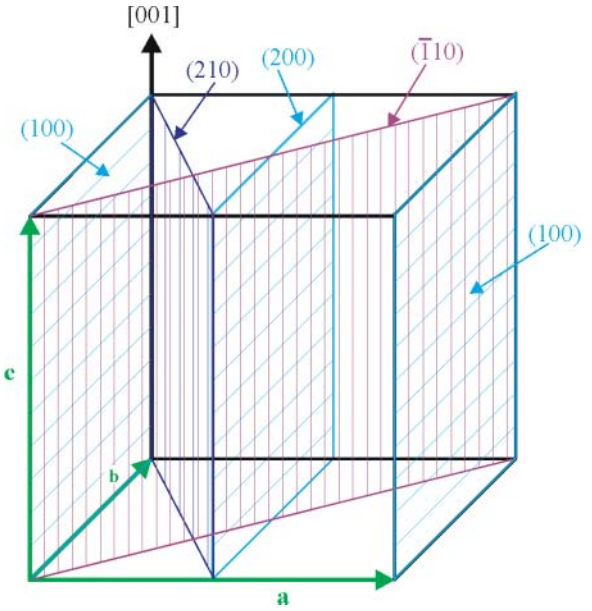


FIGURE 1.6 All shaded crystal planes belong to the [001] zone in the cubic lattice.

Table 1.2 Equation of D-Spacing for All Seven Crystal Systems

Crystal system	Equations
Cubic	$\frac{1}{d_{hkl}^2} = \frac{h^2+k^2+l^2}{a^2}$
Tetragonal	$\frac{1}{d_{hkl}^2} = \frac{h^2+k^2}{a^2} + \frac{l^2}{c^2}$
Hexagonal	$\frac{1}{d_{hkl}^2} = \frac{4}{3}\left(\frac{h^2+hk+k^2}{a^2}\right) + \frac{l^2}{c^2}$
Rhombohedral (Trigonal)	$\frac{1}{d_{hkl}^2} = \frac{(h^2+k^2+l^2)\sin^2\alpha + 2(hk+kl+hl)(\cos^2\alpha - \cos\alpha)}{a^2(1-3\cos^2\alpha+2\cos^3\alpha)}$
Orthorhombic	$\frac{1}{d_{hkl}^2} = \frac{h^2}{a^2} + \frac{k^2}{b^2} + \frac{l^2}{c^2}$
Monoclinic	$\frac{1}{d_{hkl}^2} = \frac{1}{\sin^2\beta}\left(\frac{h^2}{a^2} + \frac{k^2\sin^2\beta}{b^2} + \frac{l^2}{c^2} - \frac{2hl\cos\beta}{ac}\right)$
Triclinic	$\frac{1}{d_{hkl}^2} = (1-\cos^2\alpha-\cos^2\beta-\cos^2\gamma+2\cos\alpha\cos\beta\cos\gamma)^{-1}$ $\left(\frac{h^2}{a^2}\sin^2\alpha + \frac{k^2}{b^2}\sin^2\beta + \frac{l^2}{c^2}\sin^2\gamma + \frac{2kl}{bc}(\cos\beta\cos\gamma-\cos\alpha)\right.$ $\left. + \frac{2lh}{ca}(\cos\gamma\cos\alpha-\cos\beta) + \frac{2hk}{ab}(\cos\alpha\cos\beta-\cos\gamma)\right)$

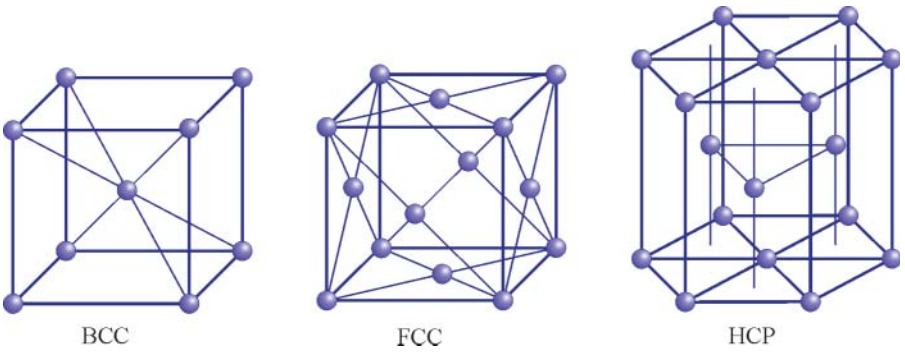


FIGURE 1.7 Atomic arrangements in three common crystal structures of metals.

equivalent hexagonal unit cells, each has two atoms at the coordinates 0 0 0 and ⅔ ⅓ ½ (or at equivalent position ⅓ ⅔ ½). Metals with HCP structure include beryllium, magnesium, zinc and α-titanium. Both FCC and HCP are close-packed arrangements. Both FCC (111) plane and HCP (0002) have the same atomic arrangement within the plane, but have different stacking sequences.

Structures of crystals formed by unlike atoms are built by a Bravais lattice with certain conditions. One is that the translation of a Bravais lattice must begin and end on the atoms of the same kind. The other is that the space arrangement of each kind of atom poses the same symmetry elements as the whole crystal. The structure of NaCl (rock salt) is shown in Figure 1.8. The unit cell of NaCl contains eight ions, located at the following coordinates:

four Na^+ ions at 0 0 0, ½ ½ 0, ½ 0 ½, and 0 ½ ½,
four Cl^- ions at ½ ½ ½, 0 0 ½, 0 ½ 0, and ½ 0 0.

It can be seen that Na^+ ions formed a FCC structure and 4 Cl^- ions form an FCC with ½ ½ ½ translation from the Na^+ "lattice". Therefore, the Bravais lattice of NaCl crystal is face-centered cubic.

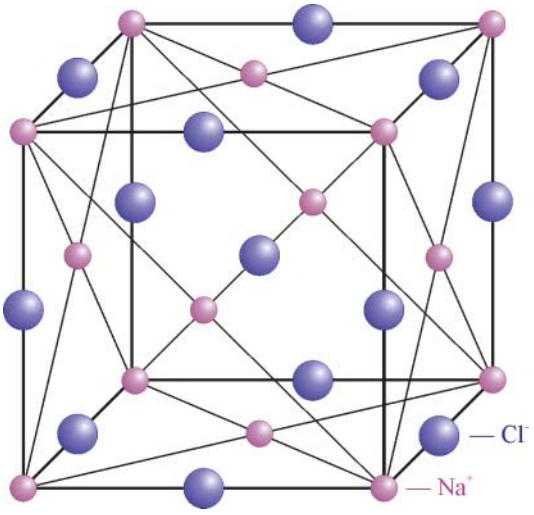


FIGURE 1.8 The structure of NaCl. Na^+ is FCC and Cl^- is FCC with ½, ½, ½ translation.

1.2.4 Imperfections in Crystal Structure

Thus far we have assumed that crystals have a very regular atomic arrangement following the crystal structure. However, most crystalline materials are not perfect. The regular pattern of atomic arrangement may be interrupted by crystal defects. There are various types of crystal defects, such as point defects, line defects, planar defects, and bulk defects.

Point defects are defects that involve randomly distributed extra or missing atoms. There is no strict definition of the size of a point defect, but generally a point defect is not extended in space in any dimension, but within a region of one or a few atoms. Vacancies are sites that should be occupied by an atom in a perfect crystal but that are unoccupied. Interstitials are extra atoms inserted between the normal atomic sites. Typically interstitials are significantly smaller atoms compared to the matrix atoms in the crystal, for example, hydrogen, carbon, boron, or nitrogen atoms in metal crystals. Crystals with interstitials are also referred to as interstitial solid solutions. A substitutional solid solution contains another type of point defects – substitutional defects. In a substitutional solid solution of B in A, B atoms replace the sites normally occupied by A atoms. In a typical substitutional solution, B atoms are randomly distributed in the crystal. Under certain conditions, B atoms may replace A atoms in a regular pattern, called long range order. The solution is then called ordered or superlattice structure. Point defects may change the lattice parameters in proportion to the concentration of the defects. Point defects play an important role in semiconductors.

Line defects are defects that extend in one dimension within a region of one or a few atoms in the other two dimensions. Crystal dislocations are line defects. There are two basic types of dislocations, the edge dislocation and the screw dislocation. An edge dislocation is caused by the termination of a plane of atoms in the middle of a crystal, or it can be thought of as the result of adding or subtracting a half crystal plane between two adjacent full crystal planes. A screw dislocation is a line defect along which the atom arrangement is distorted like a screw thread, or it can be thought of as the result of cutting partway through the crystal and displacing it parallel to the edge of the cut. Dislocations can dramatically reduce the energy barrier to shearing a crystal along a crystal plane, so that the density of dislocations in a crystal can change the resistance of the crystal to plastic deformation.

Plane defects are crystal defects that extend in two dimensions and within a region of one or a few atoms in the third dimension. Grain boundaries are interfaces between contacting crystals that have different orientations. Depending on the degree of misorientation between the two contacting crystals, grain boundaries are categorized as low angle grain boundaries and high angle grain boundaries. The difference between low angle grain boundary misorientation and high angle grain boundary misorientation varies in the range of 10–15° depending on the material. The structure and property of low angle grain boundaries have a strong dependence on the misorientation angle, while high angle grain boundaries are not dependent on the misorientation. Antiphase boundaries are another type of plane defect existing in ordered alloys. The crystals on both sides of the boundary have the same structure and orientation with the interruption of the order by removing or adding a layer of atoms. For example, if the ordering is in the sequence of ABABABAB an antiphase boundary takes the form of ABABBABA or BABAABAB. Stacking faults are another type of plane defect. Stacking faults commonly occur in close-packed structures. The {111} planes of FCC and the {0002} planes of HCP have the same close-packed atomic planes with six-fold symmetry. Any two adjacent close-packed crystal planes in FCC and HCP are stacked in an identical sequence and labeled as AB. Each atom in the B plane is directly on top of the center of triangles formed by three atoms in A plane. In an HCP structure, the atomic location in the third plane is directly above those of the first plane, so the stacking sequence continues as ABABABAB. In an FCC structure, the atoms in the third layer fall on a location not

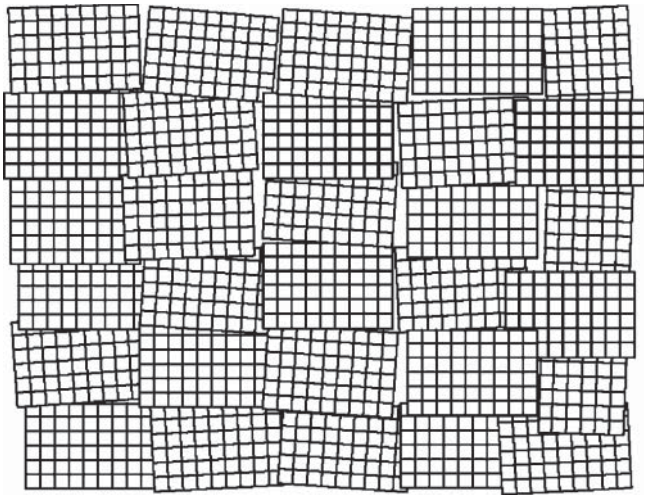


FIGURE 1.9 Illustration of crystal mosaicity.

directly above either A or B, but at a third location C. The atoms in the fourth plane are directly above those of the A plane, so the sequence continues as ABCABCABC. A stacking fault is a one or two plane deviation from the above perfect sequence. For example, ABCABCBCABCABC in FCC is a stacking fault and ABABABCABAB in HCP is a stacking fault. All plane defects disrupt the motion of dislocations through a material; so introducing the plane defects can change the mechanical properties of a material.

Bulk defects, also known as volume defects, are either clusters of the above defects or small regions of a different phase. The latter are often called precipitates. Bulk defects are obstacles to dislocation motion, so they are one of the mechanisms for strengthening materials. A crystal may contain many small regions or blocks with identical lattice structure, but separated by faults and dislocation clusters, as shown in Figure 1.9. The adjacent blocks are slightly disoriented so that the perfect crystal lattice extends only within each block. This kind of structure is referred to as a mosaic structure. The extent of the mosaic structure is also described as mosaicity. To say that a crystal has low mosaicity means that it has larger perfect crystal blocks or smaller misorientation between blocks.

1.3 PRINCIPLES OF X-RAY DIFFRACTION

X-rays are electromagnetic radiation with a wavelength in the range of 0.01 to 100 angstroms (Å). X-rays belong to a portion of the electromagnetic spectrum overlapping with gamma rays in the shorter wavelengths and with ultraviolet in the longer wavelengths. The wavelength of typical X-rays used in X-ray diffraction is in the region of 1 Å, which is comparable to the range of interatomic spacing in crystals. When a monochromatic X-ray beam hits a sample, in addition to absorption and other phenomena, it generates scattered X-rays with the same wavelength as the incident beam. This type of scattering is also known as elastic scatter or coherent scattering. The scattered X-rays from a sample are not evenly distributed in space, but are a function of the electron distribution in the sample. The atomic arrangement in the sample can be ordered as with a single crystal or disordered for glass or liquid. As such, the intensities and spatial distributions of the scattered X-rays form a specific diffraction pattern that is uniquely determined by the structure of the sample.

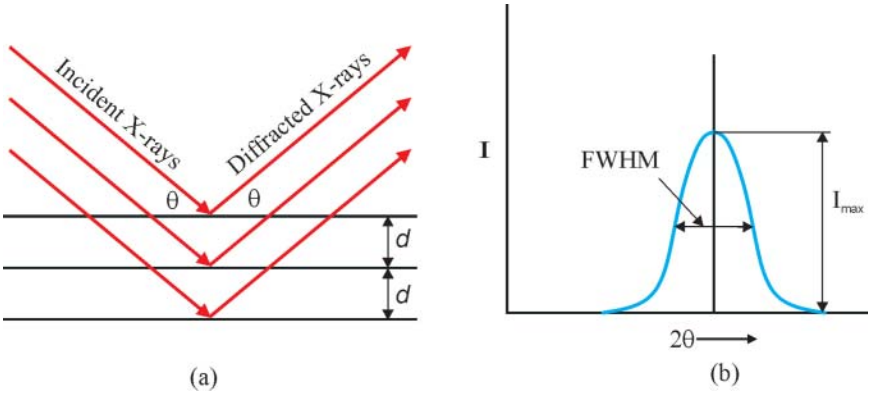


FIGURE 1.10 (a) The incident X-rays and reflected X-rays make an angle of θ symmetric to the normal of crystal plane. (b) The diffraction peak is observed at the Bragg angle θ.

1.3.1 Bragg's Law

There are many theories and equations about the relationship between the diffraction pattern and the material structure. Bragg's law is a simple way to describe the diffraction of X-rays by a crystal. In Figure 1.10(a), the incident X-rays hit the crystal planes with an incident angle θ and reflection angle θ. The diffraction peak is observed when the Bragg condition is satisfied:

$$\boxed{n\lambda = 2d\sin\theta} \tag{1.3}$$

where λ is the wavelength, d is the distance between each adjacent crystal planes (d-spacing), θ is the Bragg angle at which one observes a diffraction peak, and n is an integer, called the order of reflection. That means that the Bragg condition with the same d-spacing and 2θ angle can be satisfied by various X-ray wavelengths (energies). Or for the same wavelength and d-spacing, the Bragg condition may be satisfied by several 2θ angles. In X-ray diffraction using a single wavelength, the Bragg equation is typically expressed with $n = 1$ for the first order of diffraction because the higher order reflections can be considered as being from different lattice planes. For instance, the second order reflection from (hkl) planes is equivalent to the first order reflection from $(2h, 2k, 2l)$ planes. The diffraction peak is displayed as diffracted intensities at a range of 2θ angles. For perfect crystals with perfect instrumentation, the peak is a delta functions (the black straight vertical line) as shown in Figure 1.10(b). The intensity is denoted by **I**.

The delta function is an oversimplified model, which requires a perfect crystal without mosaic structure and a perfectly collimated monochromatic X-ray beam. A typical diffraction peak is a broadened peak displayed by the blue curved line in Figure 1.10(b). The peak broadening can be due to many different effects, including imperfect crystal conditions, such as strain, mosaic structure, and finite size; ambient conditions, such as atomic thermal vibration; and instrumental conditions, such as X-ray beam size, beam divergence, beam spectrum distribution, and detector resolution. The curved line gives a peak profile which is the diffracted intensity distribution in the vicinity of the Bragg angle. The highest point on the curve gives the maximum intensity of the peak, $\mathbf{I}_{max}$. The width of a peak is typically measured by its full width at half maximum (FWHM). The total diffracted energy of a diffracted beam for a peak can be measured by the area under the curve, which is referred to as integrated intensity. The integrated intensity is a more consistent value for measuring the diffracted intensity of a reflection since it is less affected by all the peak broadening factors. Causes of peak broadening, while increasing FWHM, typically also reduce

the maximum intensity at the same time. Therefore, overall variation of the integrated intensity is less significant compared to the variations of FWHM and $\mathbf{I}_{max}$.

1.3.2 Diffraction Patterns

This diffraction condition is based on the existence of the long periodicity of crystalline materials. In general, X-ray diffraction can provide information on the atomic arrangement in materials with long range order, short range order, or no order at all, like gases, liquids, and amorphous solids. A material may have one of the above atomic arrangement types, or a mixture of the above types. Figure 1.11 gives a schematic comparison of diffraction patterns for crystalline solids, liquid, amorphous solids, and monatomic gases as well as their mixtures. The diffraction pattern from crystals has many sharp peaks corresponding to various crystal planes based on Bragg's law. The peaks at low 2θ angles are from crystal planes of large d-spacing and vice versa at high 2θ angles. In order to satisfy the Bragg condition at all crystal planes, the crystal diffraction pattern is actually generated from polycrystalline materials or powder materials. Therefore, the diffraction pattern is also called the powder diffraction pattern. A similar diffraction pattern can be collected with a single crystal if the crystal has been rotated at various angles during data collection so that Bragg's law can be satisfied when the crystal is at the right orientation. The technique has been used in the Gandolfi camera in which the crystal is rotated above an axis tilted 45° from the camera axis. The powder-like pattern generated by rotating a single crystal sample with other types of diffractometers is also referred as a Gandolfi pattern.

Both amorphous solid and liquid materials do not have the long range order as a crystal does, but the atomic distance has a narrow distribution due to the atoms being tightly packed. In this case, the intensity of the scattered X-rays forms one or two maxima with a very broad distribution in the 2θ range. The intensity vs. 2θ distribution reflects the distribution of the atomic distances. In principle, a pattern like this should be called a scattering pattern since there is no diffraction as we have defined earlier, but we may call it a diffraction pattern for convenience. A monatomic gas has no order at all. The atoms are distributed randomly in space. The scattering curve shows no features at all except that the scattered intensity drops continuously with the increase of the 2θ angle. The scattering curve for air or gas shows a similar feature although the molecules have a preferred distance between atoms within each molecule. The diffraction pattern from a material containing both amorphous and crystalline solids has a broad background from the amorphous phase and sharp peaks from crystalline phase. For example, many polymer materials have an amorphous matrix with crystallized regions. The diffraction pattern may contain air-scattering background in addition to sharp diffraction peaks. The air-scattering can be generated from the incident beam or diffracted beam. If the air-scattering is not removed by the diffractometer, the diffraction pattern contains a high background at low 2θ angle and the background gradually decreases with increasing 2θ angle.

1.4 RECIPROCAL SPACE AND DIFFRACTION

Bragg's law gives a simple relationship between the diffraction pattern and the crystal structure. Many X-ray diffraction applications can be easily explained by Bragg's law. X-ray diffraction phenomena can also be explained in reciprocal space by the reciprocal lattice and the Ewald sphere. X-ray diffraction analysis with concepts in reciprocal space is a powerful way of understanding and solving many diffraction problems [2–5].

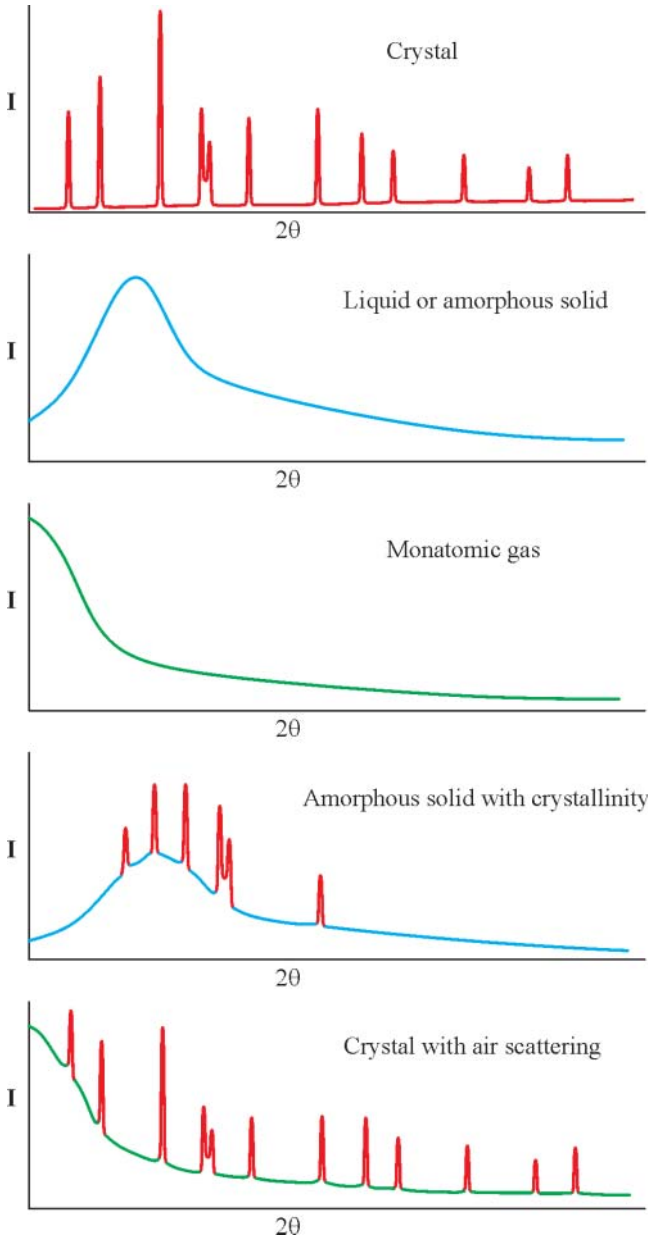


FIGURE 1.11 Diffraction patterns from crystalline solids, liquid, amorphous solid and monatomic gases as well as their mixtures.

1.4.1 Reciprocal Lattice

The reciprocal lattice is a transformation of the crystal lattice in real space to reciprocal space. The shape and size of a unit cell in real space can be defined by three vectors **a**, **b**, and **c**, all starting from any single lattice point. The unit cell of the corresponding reciprocal lattice is then give by three vectors **a***, **b***, and **c*** (also referred to as reciprocal lattice axes,

and

$$\mathbf{a}^* = \frac{1}{V}(\mathbf{b} \times \mathbf{c}),$$
$$\mathbf{b}^* = \frac{1}{V}(\mathbf{c} \times \mathbf{a}),$$
$$\mathbf{c}^* = \frac{1}{V}(\mathbf{a} \times \mathbf{b}) \tag{1.4}$$

where V is the volume of the crystal unit cell in the real space and

$$V = \mathbf{a} \cdot \mathbf{b} \times \mathbf{c} \tag{1.5}$$

Since each reciprocal lattice axis is the vector product of two lattice axes in real space, it is perpendicular to the planes defined by the two lattice axes. The original lattice axes and reciprocal lattice axes maintain the following relations:

$$\mathbf{a} \cdot \mathbf{a}^* = \mathbf{b} \cdot \mathbf{b}^* = \mathbf{c} \cdot \mathbf{c}^* = 1 \tag{1.6}$$

and

$$\mathbf{b} \cdot \mathbf{a}^* = \mathbf{c} \cdot \mathbf{a}^* = \mathbf{a} \cdot \mathbf{b}^* = \mathbf{c} \cdot \mathbf{b}^* = \mathbf{b} \cdot \mathbf{c}^* = \mathbf{a} \cdot \mathbf{c}^* = 0 \tag{1.7}$$

Figure 1.12 illustrates the relationship between the original lattice in real space and reciprocal lattice. The unit cell of the original lattice is drawn as green lines. The three reciprocal lattice axes define a unit cell of the reciprocal lattice (blue lines). The origin of the reciprocal lattice axes, denoted by O, is the origin of the reciprocal lattice. The repeat translation of the reciprocal

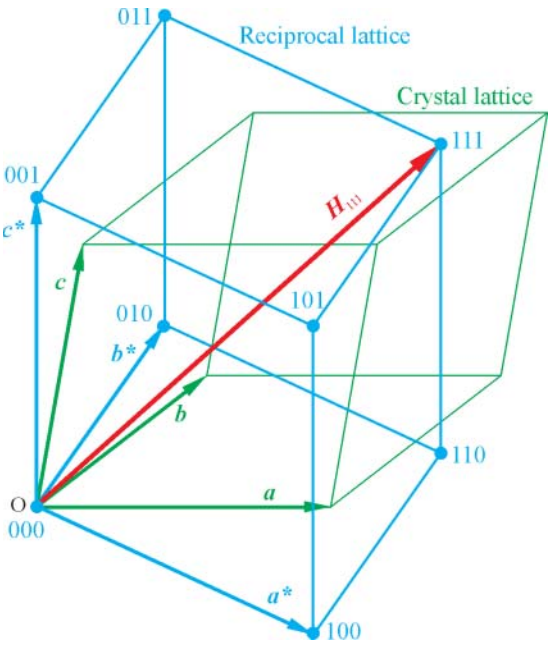


FIGURE 1.12 Relationship between the original crystal lattice in real space and reciprocal lattice.

lattice unit cell in three dimensions forms the complete reciprocal lattice. Except for the origin, each lattice point is denoted by a set of three integers (*hkl*), which are the number of translations of the three reciprocal lattice axes respectively to reach the lattice point. In other words, the vector drawn from the origin to the lattice point (*hkl*) is given by

$$\mathbf{H}_{hkl} = h\mathbf{a}^* + k\mathbf{b}^* + l\mathbf{c}^* \tag{1.8}$$

and the direction of the vector $\mathbf{H}_{hkl}$ is normal to the lattice planes (*hkl*) in real space. The magnitude of the vector $\mathbf{H}_{hkl}$ is given by the d-spacing of the (*hkl*) planes by

$$|\mathbf{H}_{hkl}| = \frac{1}{d_{hkl}} \tag{1.9}$$

Therefore, each point (*hkl*) in the reciprocal lattice represents a set of lattice planes (*hkl*) in the real space lattice. The position of the point in the reciprocal lattice defines the orientation and d-spacing of the lattice planes in the real space lattice. The further away a reciprocal lattice point is from the origin, the smaller is the d-spacing of the corresponding lattice planes. For example, the reciprocal lattice point (111) represents the (111) lattice planes in the real space lattice, and the lattice vector is given by

$$\mathbf{H}_{111} = \mathbf{a}^* + \mathbf{b}^* + \mathbf{c}^*$$

and

$$d_{111} = \frac{1}{|\mathbf{H}_{111}|} = \frac{1}{|\mathbf{a}^* + \mathbf{b}^* + \mathbf{c}^*|}$$

1.4.2 The Ewald Sphere

The relationship between the Bragg condition and the reciprocal lattice can be explained visually by the Ewald sphere, also referred to as the reflection sphere. Ewald came up with a geometrical construction to help visualize which Bragg planes are in the correct orientation to diffract. In Figure 1.13, the diffracting crystal is located in the center of the Ewald sphere, C. The radius of

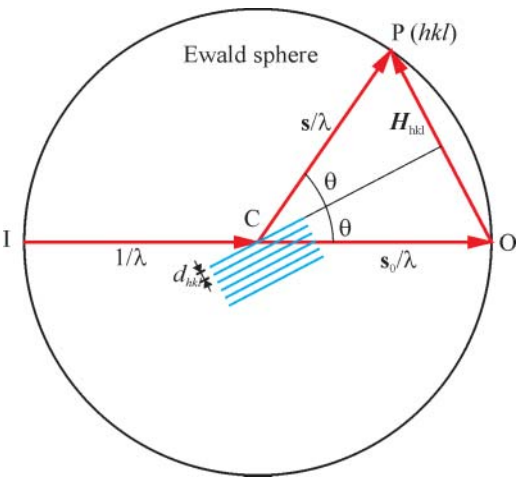


FIGURE 1.13 Ewald sphere and Bragg condition in reciprocal space.

the Ewald sphere is defined as $1/\lambda$. The incident beam can be visualized as the vector from I to C, and the diffracted beam is the vector from C to P. Both the incident beam and the diffracted beam are at an angle θ from a set of crystal planes (hkl). The d-spacing of the crystal planes is d_{hkl}. In Ewald sphere, both the incident beam vector $\mathbf{s_0}/\lambda$ and the diffracted beam vector $\mathbf{s}/\lambda$ start at the point C and end at points O and P respectively. The vector from O to P is the reciprocal lattice vector $\mathbf{H}_{hkl}$ and is perpendicular to the crystal planes. The three vectors have the relationship

$$\boxed{\frac{\mathbf{s}-\mathbf{s}_0}{\lambda} = \mathbf{H}_{hkl} = h\mathbf{a}^* + k\mathbf{b}^* + l\mathbf{c}^*} \tag{1.10}$$

and the magnitude of the vectors has the relationship based on Bragg's law:

$$\boxed{\left|\frac{\mathbf{s}-\mathbf{s}_0}{\lambda}\right| = \frac{2\sin\theta}{\lambda} = |\mathbf{H}_{hkl}| = \frac{1}{d_{hkl}}} \tag{1.11}$$

The point O is the origin of the reciprocal lattice and the point P is the reciprocal point (hkl). The Bragg condition is satisfied only when the reciprocal lattice point falls on the Ewald sphere. For a single crystal, the chance of having a reciprocal lattice point on the Ewald sphere is very small if the crystal orientation is fixed. Multiplying both ends of equation (1.10) by the three lattice axes in real space respectively, we obtain the Laue equations

$$\boxed{\begin{aligned}\mathbf{a}\cdot(\mathbf{s}-\mathbf{s}_0) &= h\lambda\\ \mathbf{b}\cdot(\mathbf{s}-\mathbf{s}_0) &= k\lambda\\ \mathbf{c}\cdot(\mathbf{s}-\mathbf{s}_0) &= l\lambda\end{aligned}} \tag{1.12}$$

The Laue equations establish that a periodic three-dimensional lattice produces diffraction maxima at specific angles depending on the incident beam direction and the wavelength. The Laue equations are suitable to describe the diffraction geometry of a single crystal. Bragg's law is more conveniently used for powder diffraction. Both the Laue equations and Bragg's law define the diffraction condition in different formats.

The distance between the origin of the reciprocal lattice (O) and the lattice point (P) is reciprocal to the d-spacing. The largest possible magnitude of the reciprocal lattice vector is given by $2/\lambda$. This means that the smallest d-spacing satisfying the Bragg condition is $\lambda/2$. In powder X-ray diffraction, the random orientation of all crystallites can take all possible orientations assuming an infinite number of crystallites in diffraction. The trace of the reciprocal lattice points from all crystallites can be considered as a series of spherical surfaces with the origin O as the center. Therefore, the condition for satisfying Bragg's law is only if the d-spacing is greater than half of the wavelength. In other words, the Bragg condition can be satisfied if a reciprocal lattice point falls in a sphere of $2/\lambda$ from the origin O. This sphere is called the limiting sphere for powder diffraction. Figure 1.14 illustrates the limiting sphere for powder diffraction in a two-dimensional cut through the origin. Only two of the three reciprocal lattice vectors **a*** and **b*** are shown in the 2D illustration. All the reciprocal lattice points within the limiting sphere are denoted by blue dots. For powder samples, all the reciprocal lattice points having the same distance from the origin form a sphere shown by a circle with a blue line. For example, the reciprocal lattice point P(hkl) would not fall on the Ewald sphere for a single crystal with fixed orientation. But for powder samples, the equivalent reciprocal lattice point from some crystallites would fall on the Ewald

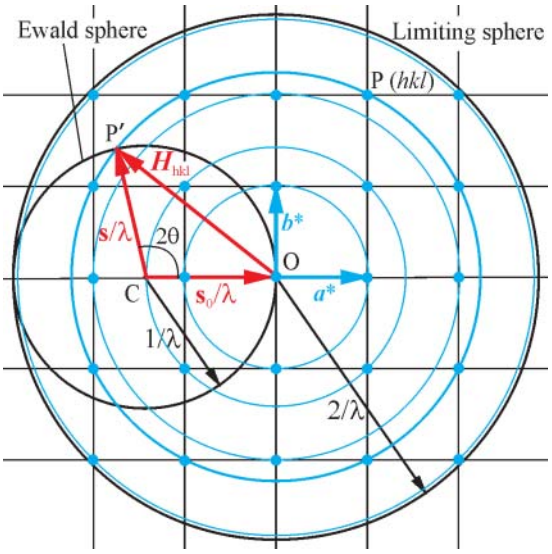


FIGURE 1.14 Limiting sphere for the powder diffraction.

sphere at point P′. The same explanation can also be given for a rotating single crystal. In this case, the reciprocal lattice point P(*hkl*) can cross with the Ewald sphere by a proper rotation. The Gandolfi camera works on this principle.

There is another set of vectors, usually in physics and related fields, which are used to describe the above diffraction condition with the following relations:

$$\mathbf{Q} = \mathbf{k} - \mathbf{k}_0 \tag{1.13}$$

and

$$|\mathbf{k} - \mathbf{k}_0| = \frac{4\pi \sin\theta}{\lambda} = |\mathbf{Q}| = \frac{2\pi}{d_{hkl}} \tag{1.14}$$

where, $\mathbf{k}$ and $\mathbf{k_0}$ are called the wave vectors for the incident and diffracted beams, and both have a magnitude of $2\pi/\lambda$. The scattering vector $\mathbf{Q}$ has a similar physical meaning of $\mathbf{H}_{hkl}$, except with a factor of 2π in magnitudes. Overall, we have the following relations between the two sets of vectors:

$$\mathbf{k}_0 = \frac{2\pi}{\lambda}\mathbf{s}_0, \quad \mathbf{k} = \frac{2\pi}{\lambda}\mathbf{s}, \quad \text{and} \quad \mathbf{Q} = 2\pi \cdot \mathbf{H} \tag{1.15}$$

in which, $\mathbf{s}$ and $\mathbf{s_0}$ can be considered as the unit vectors of $\mathbf{k}$ and $\mathbf{k_0}$ respectively. $\mathbf{H}$ is a general expression of the diffraction vector by removing the indices (*hkl*) from the subscript. For consistency, the vector set $\mathbf{s}$, $\mathbf{s_0}$, and $\mathbf{H}$ will be used in the following chapters except when the vector set $\mathbf{k}$, $\mathbf{k_0}$, and $\mathbf{Q}$ are specified.

1.4.3 Diffraction Cone and Diffraction Vector Cone

In powder diffraction, for a fixed incident X-ray vector $\mathbf{s_0}/\lambda$, the diffracted beam vector $\mathbf{s}/\lambda$ takes all directions at a 2θ angle from the incident beam direction, as shown in Figure 1.15. The end of the $\mathbf{s}/\lambda$ vector forms a circle on the Ewald sphere passing through the reciprocal lattice point P(*hkl*), P′(*hkl*) and all equivalent reciprocal lattice points. The diffracted beams form a cone with

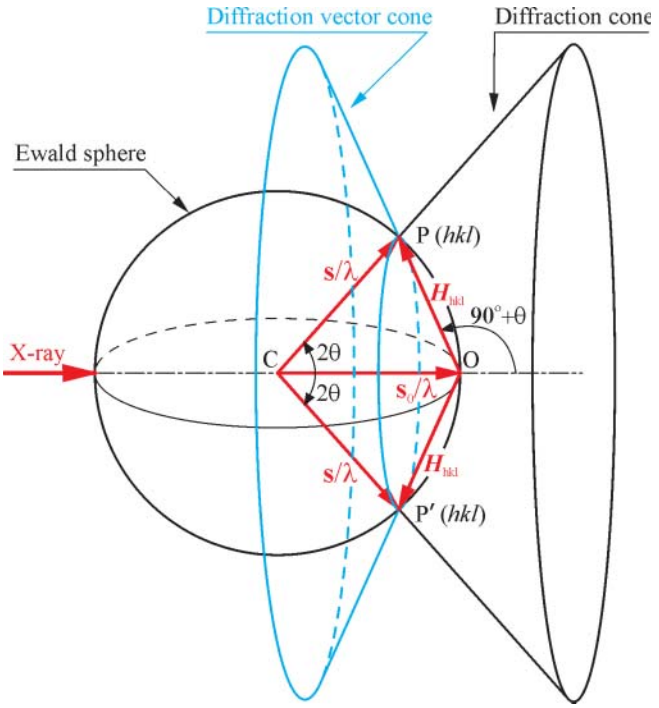


FIGURE 1.15 Diffraction cone and diffraction vector cone illustrated on the Ewald sphere.

the incident beam on the rotation axis. This cone is referred to as diffraction cone. The 2θ angle can take values from 0° to 180°, corresponding to all the directions of the diffracted beams. The diffraction vector $\boldsymbol{H}_{hkl}$, starting from the origin of the reciprocal lattice (O) to the trace circle of the lattice point P(*hkl*) and equivalents, also forms a cone, called the diffraction vector cone. The angle between the diffraction vector and the incident beam is $90° + \theta$. In the illustration of the Ewald sphere, the diffraction cone and the diffraction vector cone start from different points. In real space geometry, both the diffraction cone and the diffraction vector cone are considered as starting from the same point (the sample location or the instrument center).

1.5 TWO-DIMENSIONAL X-RAY DIFFRACTION

1.5.1 Diffraction Pattern Measured by Area Detector

The diffraction patterns shown in Figure 1.11 are displayed as diffracted intensity vs. 2θ angle assuming that the diffracted intensity is a unique function of diffraction angle. The actual diffraction pattern is distributed in the 3D space around the diffracting sample. Figure 1.16 illustrates the diffraction patterns from a single crystal and from polycrystalline samples. The diffracted beams from a single crystal point to discrete directions each correspond to a family of diffracting planes, as shown in Figure 1.16(a). Each diffracted beam is a direct reflection of the incident X-ray beam based on Bragg's law. The diffracted beams are intercepted by an area detector and the X-ray intensity distribution on the sensing area is converted to an image-like diffraction pattern, also referred to as a frame. The region representing each diffracted beam in the frame is called a diffraction spot. Figure 1.16(b) is a diffraction frame from a single crystal of the sweet

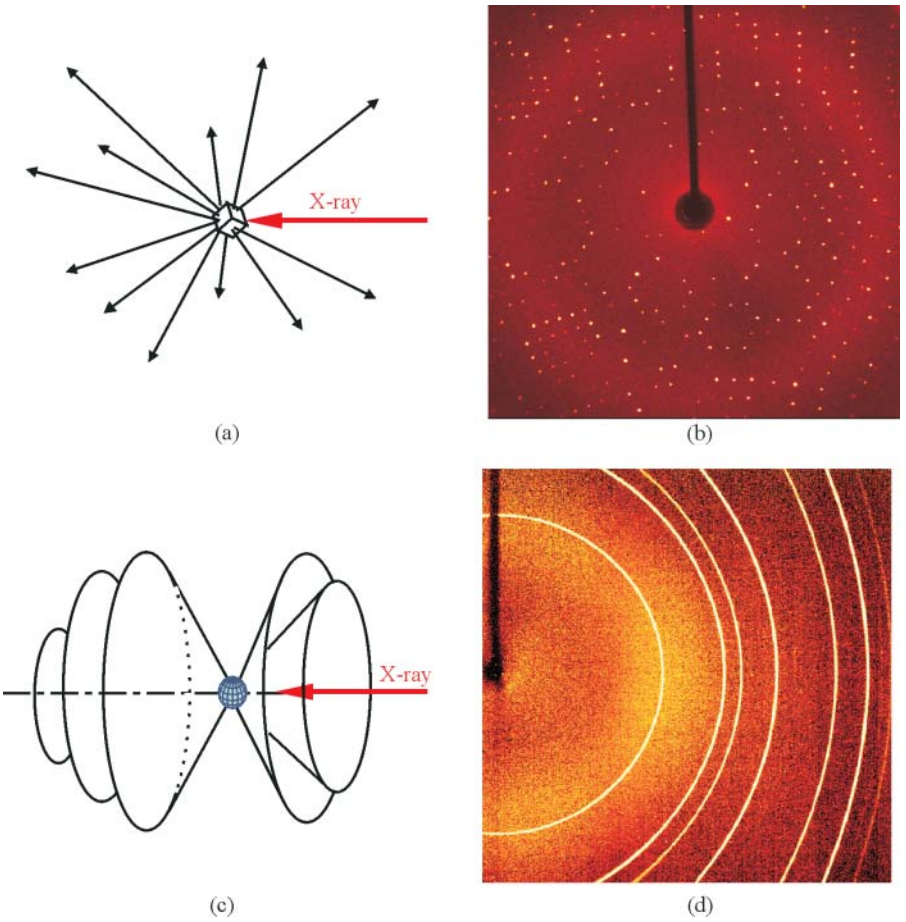


FIGURE 1.16 Patterns of diffracted X-rays: (a) from a single crystal, (b) diffraction frame from single crystal of protein thaumatin, (c) diffraction cones from a polycrystalline sample. (d) diffraction frame from corundum powder.

protein thaumatin. Due to the large and complex unit cell of this protein crystal, there are many diffraction spots in the frame. Today, in the area of single crystal diffraction, two-dimensional detectors are required to collect enough diffraction data to solve the structure of a complex crystal. Single crystal X-ray diffraction (SCD) has been covered by much literature [9–10]. This book will mainly cover diffraction from polycrystalline materials or other non-single crystal materials in the following chapters.

Polycrystalline materials consist of many crystalline domains, ranging from a few to more than a million in the incident beam. In single-phase polycrystalline materials, all these domains have the same crystal structure but various orientations. Polycrystalline materials can also be multiphase materials with more than one kind of crystal structure blended together. Polycrystalline materials can also be mixed or bonded to different materials such as thin films or coatings on single-crystal substrates. The crystalline domains can be embedded in an amorphous matrix. Most often, the sample undergoing X-ray analysis is not a randomly oriented polycrystalline material, but a combination of polycrystalline, amorphous, and single crystal contents, polycrystalline with preferred orientation or deformed due to residual stresses. The diffracted beams from

a polycrystalline (powder) sample forms a series of diffraction cones in 3D space since large numbers of crystals oriented randomly in the space are covered by the incident X-ray beam, as shown in Figure 1.16(c). Each diffraction cone corresponds to the diffraction from the same family of crystalline planes in all the participating grains. The diffraction frame from a polycrystalline sample is a cross-section of the detecting surface and the diffraction cones. Figure 1.16(d) is a diffraction frame collected from corundum powder by an area detector with flat detecting surface. The diffraction pattern collected with an area detector is typically given as a two-dimensional image frame, so the X-ray diffraction with an area detector is called two-dimensional X-ray diffraction [11]. In this book and a lot of literature, XRD^2 or 2D-XRD may be used alternatively as an abbreviation for two-dimensional X-ray diffraction.

1.5.2 Materials Characterization with 2D Diffraction Pattern

A 2D diffraction pattern can be considered as the intensity distribution of the scattered X-rays as a function of γ and 2θ angles. Figure 1.17(a) shows such a 2D pattern collected from corundum powder with a flat 2D detector. It contains several diffraction rings with various Bragg angles, denoted by 2θ. The diffraction ring closest to the trajectory of the incident beam has the smallest 2θ value. The angle along each diffraction ring can be described by γ, which defines the dimension orthogonal to the 2θ direction. In order to explain the basic concept of materials characterization with 2D diffraction patterns, the frame can be converted to an image with rectangular γ-2θ coordinates, as shown in Figure 1.17(b). This image can be referred to as a γ-2θ plot or simply a gamma plot.

A 2D diffraction pattern can be analyzed directly or by data reduction to the intensity distribution along γ or 2θ. The γ-integration can reduce the 2D pattern into a diffraction profile analogous to the conventional diffraction pattern which is the diffraction intensity distribution as a function of 2θ angles. This kind of diffraction pattern can be evaluated by most exiting software and algorithms for conventional applications, such as phase identification, structure refinement, and 2θ-profile analysis. However, the materials structure information associated with the intensity distribution along the γ direction is lost through γ-integration. In order to evaluate the material's structure associated with the intensity distribution along the γ angle, either the 2D diffraction pattern should be directly analyzed or the γ-profile generated by 2θ-integration should be used.

The relationship between the diffraction ring profile and materials characterization can be explained by the following four types of γ-2θ plots. Figure 1.18 illustrates four γ-2θ plots of a

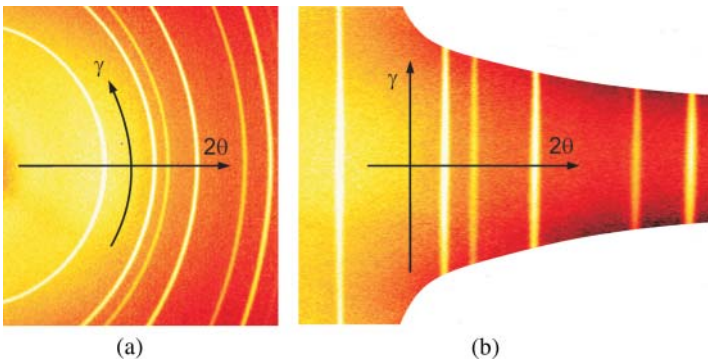


FIGURE 1.17 (a) 2D diffraction pattern from corundum powder, (b) 2D pattern displayed in rectangular γ-2θ coordinates.

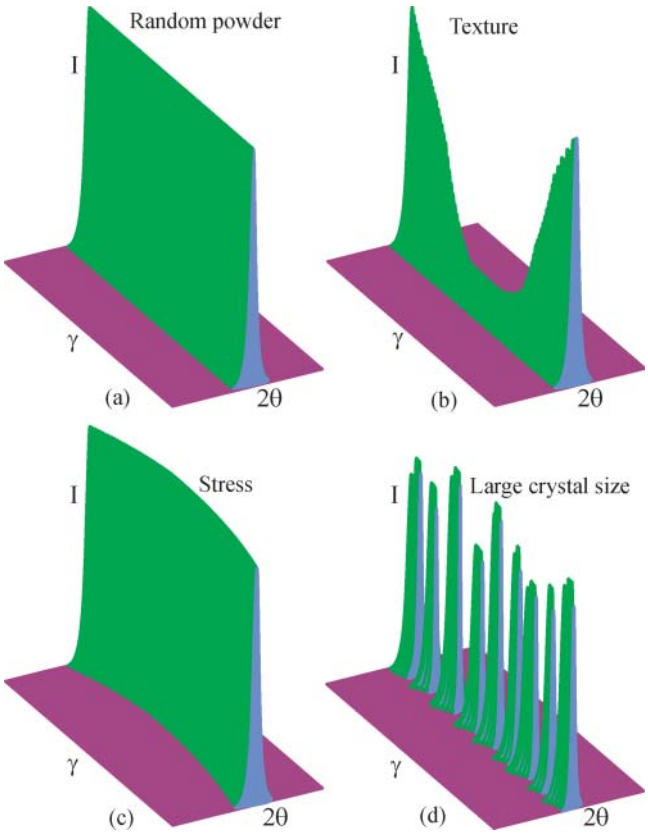


FIGURE 1.18 Illustrations of gamma plots from samples with (a) random fine powder, (b) texture, (c) stress, (d) large crystal size.

single diffraction ring in 3D view. Figure 1.18(a) shows a straight "wall" with a constant 2θ and constant intensity along γ. Due to the large amount of randomly oriented fine powder irradiated by the incident X-ray, the number of crystallites satisfying the Bragg condition is statistically the same at all γ angles. Figure 1.18(b) shows the intensity variation along γ due to the preferred orientation. The texture in the sample will change the diffraction intensity measured at a different angle, but not the 2θ value. Figure 1.18(c) illustrates the intensity distribution when the sample contains residual stress or applied stress loading. The d-spacing variation at different orientation due to stress will result in the 2θ value variation measured at different γ angles. Figure 1.18(d) shows a spotty intensity distribution along γ due to only a limited number of large crystals satisfying the Bragg condition. Apparently, the spottiness is related to the crystal size and its size distribution.

A material may contain texture, stress, and large crystal size simultaneously so the 2D diffraction pattern can be a mix of the above four models. Figure 1.19(a) is a diffraction frame collected from a proprietary multilayer battery anode with Bruker VÅNTEC-500 2D detector. Figure 1.19(b) is the same diffraction pattern displayed as a 3D plot with intensity, denoted as I, in the vertical direction. The material characterization can be observed directly from the 2D frame. For example, some diffraction rings show very strong intensity variation but smooth transition from high intensity to low intensity. These diffraction rings are produced from materials with strong preferred orientation and fine crystal grains. Some other diffraction rings are very spotty with sharp transition from high intensity to low intensity. These diffractions are produced from

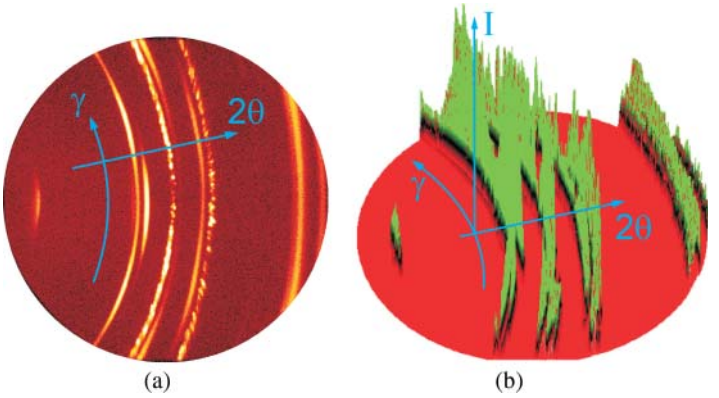


FIGURE 1.19 (a) 2D diffraction pattern from a battery anode, (b) the 2D pattern displayed in 3D plot with the intensity in vertical direction.

materials with large crystal grain size. By comparing two types of the diffraction rings, it can also be concluded that the sample contains at least two phases, because it is impossible for a sample with homogenous single phase to produce diffraction rings so dramatically different.

1.5.3 Two-Dimensional X-Ray Diffraction System and Major Components

Two-dimensional X-ray diffraction (XRD^2) systems have a variety of configurations and component options to fulfill the requirements of different samples and applications. As shown in Figure 1.20, a typical XRD^2 system normally consists of five basic components:

- X-ray source – produces X-rays with the required radiation energy, focal spot size, and intensity

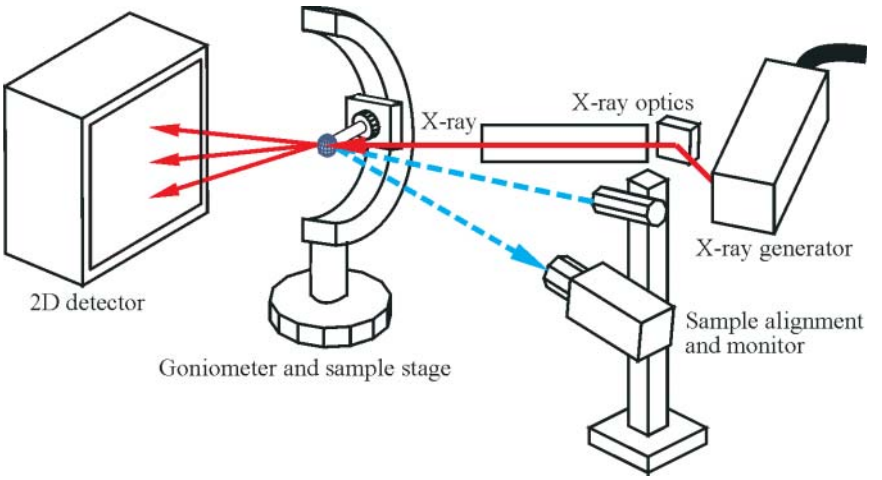


FIGURE 1.20 Five basic components in an XRD^2 system: X-ray source (sealed tube generator); X-ray optics (monochromator and collimator); goniometer and sample stage; sample alignment and monitor (laser-video); and area detector.

- X-ray optics – conditions the primary X-ray beam to the required wavelength, beam focus size, beam profile and divergence
- goniometer and sample stage – establishes and maneuvers the geometric relationship between primary beam, sample and detector
- sample alignment and monitor – assists users with positioning the sample into the instrument center and monitors the sample state and position
- area detector – intercepts and records the scattering X-rays from a sample, and saves and displays the diffraction pattern into a two-dimensional frame

Each of the basic components may have several options suitable for various applications and functions. The whole system is controlled by a computer, with software for instrument control, data acquisition, and data analysis. In addition to the five basic components, there are some other accessories, such as a low temperature stage, high temperature stage, helium or vacuum beam path for SAXS, beamstop, and alignment and calibration fixtures. The geometry conventions, X-ray source and optics, detector, goniometer, sample stage, and various configurations will be covered in the following chapters.

1.5.4 Summary

A two-dimensional diffraction frame contains far more information than a diffraction pattern measured with conventional diffraction system with a point detector or a linear position-sensitive detector. The speed of two-dimensional diffraction is typically several orders of magnitude higher than conventional diffraction. Two-dimensional X-ray diffraction analyses, commonly performed on polycrystalline materials, include phase identification, quantitative phase analysis, preferred orientation, and residual stresses.

Phase identification (phase ID) can be done by integration in the selected 2θ range along the Debye rings [12–16]. The integrated data gives better intensity and statistics for phase ID and quantitative analysis, especially for those samples with texture, large grain size, or small quantity. Then the integrated diffraction profiles can be analyzed with existing algorithms and methods, profile fitting with conventional peak shapes and fundamental parameters, quantification of phases, and lattice parameter indexing and refinement. The diffraction results can be used to search and match with the ICDD database [17–21]. The large 2D diffraction pattern collected at a single exposure can reveal many materials characteristics, which is suitable for in-situ measurement of time sensitive events, such as phase transformation, deformation, or chemical reactions [22–25].

Texture measurement with two-dimensional diffraction is extremely fast compared to measurement using a point or linear detector. The area detector collects texture data and background values simultaneously for multiple poles and multiple directions. Due to the high measurement speed, pole-figures can be measured at very fine steps, allowing detection of very sharp textures [26–28].

Stress measurement using the area detector is based on a direct relationship between the stress tensor and diffraction cone distortion. Since the whole or a part of the Debye ring is used for stress calculation, two-dimensional diffraction can measure stress with high sensitivity, high speed, and high accuracy. It is very suitable for samples with large crystals and textures. Simultaneous measurement of stress and texture is also possible since 2D data consists of both stress and texture information [29–32].

Percent crystallinity can be measured faster and more accurately with data analysis over 2D frames, especially for samples with anisotropic distribution of crystalline orientation.

The amorphous region can be defined externally within user-defined regions, or the amorphous region can be defined with the crystalline region included when the crystalline region and the amorphous region overlap.

Small angle X-ray scattering (SAXS) data can be collected at high speed. Anisotropic features from specimens, such as polymers, fibrous materials, single crystals, and biomaterials, can be analyzed and displayed in two dimensions. De-smearing correction is not necessary due to the collimated point X-ray beam. Since one exposure takes all the required SAXS information, it is easy to scan over the sample to map the structure information from small angle diffraction [33, 34].

Microdiffraction and diffraction mapping data is collected with speed and accuracy. X-ray diffraction from small sample amounts or small sample areas has always been a slow process because of limited beam intensity. The 2D detector captures whole or a large portion of the diffraction rings, so spotty, textured, or weak diffraction data can be integrated over the selected diffraction rings [35–40].

Thin film samples with a mixture of single crystal, random polycrystalline layers, and highly textured layers can be measured with all the features appearing simultaneously in diffraction frames [41–47]. The pole-figures from different layers and substrate can be overlapped to reveal the orientation relationship [48, 49]. The use of an area detector can dramatically speed up the data collection for reciprocal space mapping on an in-plane reciprocal lattice point [50].

Combinatorial screening by two-dimensional X-ray diffraction is one of the most powerful high-throughput screening techniques. Because of the penetrating power of the X-ray beam, non-destructive to samples, and fast data collection and abundant information about the materials atomic structure, two-dimensional X-ray diffraction can be used to screen a material library with high speed and high accuracy [51–53]. In addition to high-throughput screening, two-dimensional X-ray diffraction systems have been widely used in pharmaceuticals and biomaterials research [54–57].

Forensics and archeology have benefitted from two-dimensional X-ray diffraction for identifying materials and structures from small amounts or small areas of samples, which is often the case in these fields. It is non-destructive and does not require special sample treatment, so the original evidence or sample can be preserved. Two-dimensional diffraction patterns contain abundant information and are easy to observe and explain in the courtroom. All the techniques discussed in this book can be used for forensics and archeological analysis. Experimental examples and case studies can be found in many references [36, 58–62].

In summary, two-dimensional X-ray diffraction refers to X-ray diffraction applications with a two-dimensional detector and corresponding data reduction and analysis. Two-dimensional X-ray diffraction is the ideal, non-destructive, analytical method for examining samples of all kinds, such as metals, polymers, ceramics, semiconductors, thin films, coatings, paints, biomaterials, and composites for material science research, molecular structure determination and polymorphism study for drug discovery and processing, for samples with micro volume or micro area for forensic analysis, and archeological analysis. A two-dimensional diffraction pattern contains abundant information about the atomic arrangement, microstructure, and defects of solid or liquid materials. In recent years, the use of two-dimensional diffractometers has dramatically increased in academic researches and various industries. This book covers the basic concept and recent progress in two-dimensional X-ray diffraction theory and technologies, including geometry conventions, X-ray source and optics, two-dimensional detectors, diffraction data interpretation, and configurations for various applications, such as phase identification, texture, stress, microstructure analysis, crystallinity, thin film analysis, and combinatorial screening.

REFERENCES

1. A. Michette and S. Pfauntsch, *X-ray: The First Hundred Years*, John Wiley & Sons, New York, 1996.
2. B. D. Cullity, *Elements of X-ray Diffraction*, 2nd ed., Addison-Wesley, Reading, MA, 1978.
3. B. E. Warren, *X-ray Diffraction*, Dover Publications, New York, 1990.
4. R. Jenkins and R. L. Snyder, *Introduction to X-ray Powder Diffractometry*, John Wiley & Sons, New York, 1996.
5. A. J. C. Wilson, *International Tables for Crystallography*, Kluwer Academic, Boston, 1995.
6. F. D. Bloss, Crystallography and Crystal Chemistry, Holt, Rinehart, and Winston, New York, 1971.
7. F. C. Phillips, *An Introduction to Crystallography*, Wiley, New York, 1972.
8. T. C. W. Mak and G-D. Zhou, Crystallography in Modern Chemistry, Wiley, New York, 1997.
9. C. Giacovazzo et al., *Fundamentals of Crystallography*, IUCR and Oxford University Press, New York, 1992.
10. D. E. McRee, *Practical Protein Crystallography*, Academic Press, San Diego, 1993, pp. 84–86.
11. P. R. Rudolf and B. G. Landes, Two-dimensional X-ray diffraction and scattering of microcrystalline and polymeric materials, *Spectroscopy*, **9**(6), pp. 22–33, July/August 1994.
12. J. Filik, et al., Processing two-dimensional X-ray diffraction and small-angle scattering data in DAWN 2, *J. Appl. Cryst.* (2017). **50**, 959–966.
13. A. P. Hammersley, FIT2D: a multipurpose data reduction, analysis and visualization program, *J. Appl. Cryst.* (2016). **49**, 646–652.
14. A. B. Rodríguez-Navarro, XRD2DScan: New software for polycrystalline materials characterization using two-dimensional X-ray diffraction, *J. Appl. Cryst.* (2006). **39**, 905–909.
15. K. C. Rossa, J. A. Petrusa, A. M. McDonald, An empirical assessment of the accuracy and precision of 2D Debye-Scherrer-type data collapsed into a 1D diffractogram, *Powder Diffraction*, (2014). **29** (4), 337–345.
16. X. Yang, P. Juhásb, and S. J. L. Billinge, On the estimation of statistical uncertainties on powder diffraction and small-angle scattering data from two-dimensional X-ray detectors, *J. Appl. Cryst.* (2014). **47**, 1273–1283.
17. J. Formica, X-ray diffraction, *Handbook of Instrumental Techniques for Analytical Chemistry*, edited by F. Settle, Prentice-Hall, New Jersey, 1997.
18. N. F. M. Henry, H. Lipson, and W. A. Wooster, *The Interpretation of X-ray Diffraction Photographs*, St. Martin's Press, New York, 1960.
19. H. Lipson and H. Steeple, *Interpretation of X-ray Powder Diffraction Patterns*, St. Martin's Press, New York, 1970.
20. S. N. Sulyanov, A. N. Popov and D. M. Kheiker, Using a Two-dimensional Detector for X-ray Powder Diffractometry, *J. Appl. Cryst.* 1994, **27**, 934–942.
21. Bob B. He, Introduction to two-dimensional X-ray diffraction, *Powder Diffraction*, 2003, **18** (2) 71–85.
22. G. Geandier, et al., In situ monitoring of X-ray strain pole-figures of a biaxially deformed ultra-thin film on a flexible substrate, *J. Appl. Cryst.* (2014). **47**, 181–187.
23. R. Blondé, et al., Position-dependent shear-induced austenite–martensite transformation in double-notched TRIP and dual-phase steel samples, *J. Appl. Cryst.* (2014). **47**, 956–964.
24. M. B. Dickerson, et al., Applications of 2D detectors in X-ray analysis, *Advances in X-ray Analysis*, 2002, **45**, 338–344.
25. J. J. M. Griego, M. A. Rodriguez, and D. E. Wesolowski, Phase transition behavior of a processed thermal battery, *Adv. in X-ray Anal*, (2013) **56**, 1–9.
26. H. J. Bunge and H. Klein, Determination of quantitative, high-resolution pole-figures with the area detector, *Z. Metallkd.* 1996, **87**(6), 465–475.

27. K. L. Smith and R. B. Ortega, Use of a two-dimensional, position sensitive detector for collecting pole-figures, *Advances in X-ray Analysis*, **36**, 641–647, Plenum, New York, 1993.
28. C. Mocuta, et al., Fast pole figure acquisition using area detectors at the DiffAbs beamline – Synchrotron SOLEIL, *J. Appl. Cryst.* (2013). **46**, 1842–1853.
29. B. B. He and K. L. Smith, strain and stress measurement with two-dimensional detector, *Advances in X-ray Analysis*, **41**, 501–508, 1997.
30. B. B. He and K. L. Smith, Fundamental Equation of Strain and Stress Measurement Using 2D Detectors, *Proceedings of 1998 SEM Spring Conference on Experimental and Applied Mechanics*, Houston, Texas, USA, 1998.
31. B. B. He, U. Preckwinkel and K. L. Smith, Advantages of Using 2D Detectors for Residual Stress Measurement, *Advances in X-ray Analysis*, **42**, 429–438, 1998.
32. T. Miyazaki and T. Sasaki, A comparison of X-ray stress measurement methods based on the fundamental equation, *J. Appl. Cryst.* (2016). **49**, 426–432
33. R. W. Hendricks, The ORNL 10-meter small-angle X-ray scattering camera. *J. Appl. Cryst.* (1978). **11**, 15–30.
34. T. Furuno, H. Sasabe, and A. Ikegami, A small-angle X-ray camera using a two-dimensional multiwire proportional chamber, *J. Appl. Cryst.* (1987). **20**, 16–22.
35. R. G. Tissot, Microdiffraction applications utilizing a two-dimensional detector, *Powder Diffraction*, 2003, **18** (2) 86–90.
36. N. S. P. Bhuvanesh and J. H. Reibenspies, A novel approach to micro-sample X-ray powder diffraction using nylon loops, *J. Appl. Cryst.* (2003). **36**, 1480–1481.
37. B. B. He, Microdiffraction using two-dimensional detectors, *Powder Diffraction*, 2004, **19** (2) 110–118.
38. R. L Flemming, Micro X-ray diffraction (μXRD): a versatile technique for characterization of earth and planetary materials, *Can. J. Earth Sci.* (2007) **44**, 1333–1346.
39. M. Allahkarami and J. C. Hanan, X-ray diffraction mapping on a curved surface, *J. Appl. Cryst.* (2011). **44**, 1211–1216.
40. F. Friedel, et al., Material analysis with X-ray microdiffraction, *Cryst. Res. Technol.* (2005) **40**, No. 1/2, 182–187.
41. J. Stein, U. Welzel, W. Huegel, S. Blatt, and E. J. Mittemeijer, Aging-time-resolved in situ microstructural investigation of tin films electroplated on copper substrates, applying two-dimensional-detector X-ray diffraction, *J. Appl. Cryst.* (2013). **46**, 1645–1653.
42. L. Deng, K. Wang, C. X. Zhao, H. Yan, J. F. Britten, and G. Xu, Phase and texture of solution-processed copper phthalocyanine thin films investigated by two-dimensional grazing incidence X-ray diffraction, *Crystals* (2011), **1**, 112–119.
43. K. J. Choi, et al., Enhancement of ferroelectricity in strained BaTiO3 thin films, *Science* (2004) **306**, 1005.
44. S. H. Baek, et al., Giant piezoelectricity on Si for hyperactive MEMS, *Science* (2011) **334**, 958.
45. P. Wadley, et al., Obtaining the structure factors for an epitaxial film using Cu X-ray radiation, *J. Appl. Cryst.* (2013). **46**, 1749–1754.
46. S. Jin, et al., Detailed analysis of gyroid structures in diblock copolymer thin films with synchrotron grazing incidence X-ray scattering, *J. Appl. Cryst.* (2007). **40**, 950–958.
47. G. Geandier, et al., Benefits of two-dimensional detectors for synchrotron X-ray diffraction studies of thin film mechanical behavior, *J. Appl. Cryst.* (2008). **41**, 1076–1088.
48. B. He, K. Xu, F. Wang, and P. Huang, Two-dimensional X-ray diffraction for structure and stress analysis, *ICRS-7 Proceeding*, *Mat. Sci. Forum*, **490–491**, 1–6, 2005.
49. B. B. He, Measurement of residual stresses in thin films by two-dimensional XRD, *Proceedings of the 7th European Conference on Residual Stresses,* September 13–15, 2006 Berlin, Germany.
50. M. Schmidbauer et al., A novel multi-detection technique for three-dimensional reciprocal-space mapping in grazing-incidence X-ray diffraction, *J. Synchrotron Rad.* (2008). **15**, 549–557.

51. J. Klein, C. W. Lehmann, H-W. Schmidt, and W. F. Maier, Combinatorial material libraries on the microgram scale with an example of hydrothermal synthesis, *Angew. Chem., Int. Ed. Engl.* 1998, **37** (24), 3369–3372.
52. B. B. He et al., XRD rapid screening system for combinatorial chemistry, *Advances in X-ray Analysis*, 2001, **44**, 1–5.
53. S. Roncallo, et al., An approach to high-throughput X-ray diffraction analysis of combinatorial polycrystalline thin film libraries, *J. Appl. Cryst.* (2009). **42**, 174–178.
54. N. K. Thakral, S. Mohapatra, G. A. Stephenson, and R. Suryanarayanan, Compression-induced crystallization of amorphous indomethacin in tablets: characterization of spatial heterogeneity by two-dimensional X-ray diffractometry, *Mol. Pharmaceutics*, 2014, **12** (1), 253–263.
55. N. K. Thakral, H. Yamada, G. A. Stephenson, R. Suryanarayanan, Spatial distribution of trehalose dihydrate crystallization in tablets by X-ray diffractometry, *Mol. Pharmaceutics*, 2015, **12** (10), pp. 3766–3775.
56. S. Thakral, M. W. Terban, N. K. Thakral, R. Suryanarayanan, Recent advances in the characterization of amorphous pharmaceuticals by X-ray diffractometry, *Adv. Drug Deliv. Rev.* (2015), http://dx.doi.org/10.1016/j.addr.2015.12.013.
57. Q. Jiang, C. Hu, and M. D. Ward, Stereochemical control of polymorph transitions in nanoscale reactors, *J. Am. Chem. Soc.* 2013, **135**, 2144−2147.
58. W. Kugler, X-ray diffraction analysis in the forensic science: the last resort in many criminal cases, *Advances in X-ray Analysis*, 2003, **46**, 1–16.
59. W. Kugler, Application of X-ray diffraction in the forensic science institute of the Landeskriminalamt Baden-Wuerttemberg, Germany, handout to a workshop at NYPD Crime Laboratory, New York, May 25, 2004.
60. L. Bertrand, et al., Microbeam synchrotron imaging of hairs from Ancient Egyptian mummies, *J. Synchrotron Rad.* (2003). **10**, 387–392.
61. W. Wagermaier, et al., Scanning texture analysis of lamellar bone using microbeam synchrotron X-ray radiation, *J. Appl. Cryst.* (2007). **40**, 115–120.
62. D. Berger, Artificial patination in early iron age europe: an analytical case study of a unique bronze artefact, *Journal of Archaeological Science*, (2015). **57**, 130–141.

2

GEOMETRY AND FUNDAMENTALS

2.1 INTRODUCTION

Two-dimensional X-ray diffraction (XRD^2) is a relatively new technique in the field of X-ray diffraction. XRD^2 is not simply a diffractometer with a two-dimensional (2D) detector. In addition to 2D detector technology, it involves 2D image processing, 2D diffraction pattern evaluation, and interpretation. Because of the unique nature of the data collected with a 2D detector, new concepts and new approaches are necessary to configure an XRD^2 system and to understand and analyze 2D diffraction data. In addition, new theories should also be consistent with conventional theory, so that the 2D data can also be used for conventional applications.

The geometry of a two-dimensional X-ray diffraction system can be explained by three distinguishable and interrelated geometry spaces, each defined by a set of parameters [1]. The three geometry spaces are the diffraction space, detector space, and sample space. The laboratory coordinate system, $\mathbf{X_L Y_L Z_L}$ is the basis of all three spaces. Although the three spaces are interrelated, the definitions and corresponding parameters should not be confused. The geometry of a typical two-dimensional diffractometer is similar to the geometry of the conventional four-circle diffractometer in which one circle is used for the detector position and the other three circles in Eulerian geometry are for sample orientation. Except for a few parameters introduced specifically for XRD^2, many of these parameters have been used in conventional X-ray diffraction systems. Therefore, the same definitions are maintained for consistency. All the algorithms for data interpretation and evaluation in this book are based on the four-circle diffractometer with Eulerian geometry. Similar algorithms can be developed for the geometries of other types by following the same approach. Detailed discussion on Eulerian geometry and various other geometries can be found in the literature [2–13].

Two-Dimensional X-Ray Diffraction, Second Edition. Bob Baoping He.
© 2018 John Wiley & Sons, Inc. Published 2018 by John Wiley & Sons, Inc.

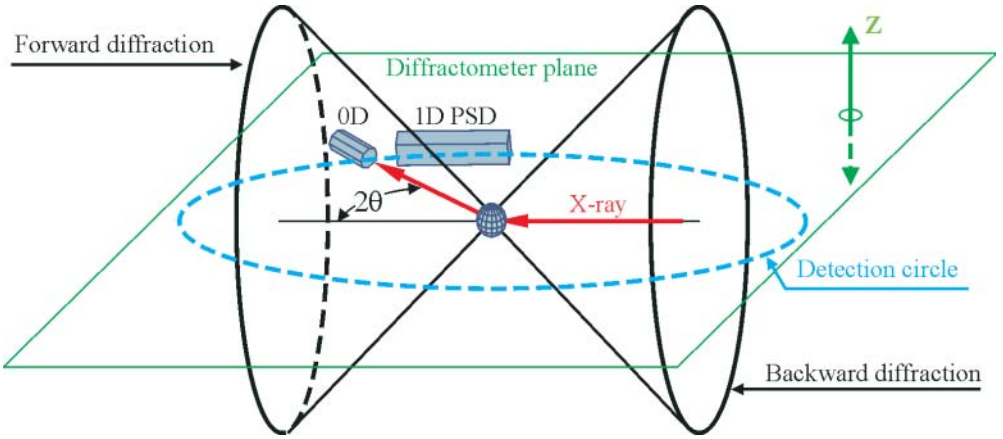


FIGURE 2.1 Diffraction patterns in 3D space from a powder sample and the diffractometer plane.

2.1.1 Comparison Between XRD^2 and Conventional XRD

First, we compare conventional X-ray diffraction and two-dimensional X-ray diffraction. Figure 2.1 is a schematic of X-ray diffraction from a powder (polycrystalline) sample. For simplicity, it shows only two diffraction cones: one represents forward diffraction ($2\theta \leq 90°$) and one for backward diffraction ($2\theta > 90°$). The diffraction measurement in the conventional diffractometer is confined within a plane, here referred to as the diffractometer plane. A point (0D) detector makes a 2θ scan along a detection circle. If a one-dimensional (1D) position sensitive detector (PSD) is used in the diffractometer, it will be mounted on the detection circle. Since the variation of diffraction pattern in the direction (Z) perpendicular to the diffractometer plane is not considered in the conventional diffractometer, the X-ray beam is normally extended in the Z direction (line focus) with solar slits. The actual diffraction pattern measured by a conventional diffractometer can be considered as superposition diffraction patterns collected at several layers of diffractometer planes in parallel. The number of layers is determined by the beam size in the Z direction and the solar slits. Since the diffraction data out of the diffractometer plane is not detected, the material structures represented by the missing diffraction data will either be ignored, or extra sample rotation and time are needed to complete the measurement.

With a two-dimensional detector, the diffraction measurement is no longer limited to the diffractometer plane. Depending on the detector size, distance to the sample and detector position, the whole or a large portion of the diffraction rings can be measured simultaneously. Figure 2.2 shows the diffraction pattern of corundum collected with a two-dimensional detector compared with the diffraction measurement range of a point (0D) detector or a line (1D) detector. The 2D diffraction pattern covers the information in both the 2θ direction and the vertical (Z) direction. Figure 2.2(a) shows a comparison with a point detector. By scanning the detector within the diffractometer plane, a point detector can collect the diffraction pattern in a range of 2θ. Figure 2.2(b) shows a line detector, which when mounted in the diffractometer plane can measure the diffraction pattern in a range of 2θ simultaneously. However, neither can give the diffraction information in the vertical (Z) direction.

The diffraction pattern out of the diffractometer plane has long been recorded by the Debye–Scherrer camera, so that the diffraction cone has been referred to as a Debye cone or Debye diffraction cone and the diffraction ring as a Debye diffraction ring or a Debye ring. However, when a Debye–Scherrer camera is used, the diffraction pattern is typically regarded as

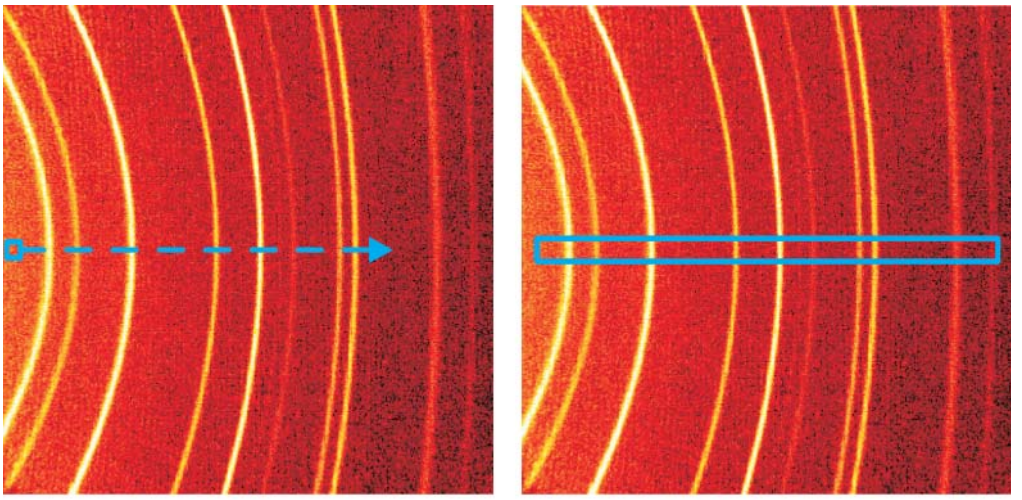


FIGURE 2.2 Coverage comparison: point, line, and area detectors.

"isotropic" and only the position of the arches in the 2θ direction and their relative intensities are used for powder diffraction analysis. The intensity distributions along the Debye rings are mostly ignored in data evaluation. To be more specific, a typical diffraction pattern collected with a Debye–Scherrer camera is the cross-section between diffraction cones and a cylindrical film with very limited dimension out of the diffractometer plane. The diffraction patterns collected with a 2D detector extend further in the "vertical" direction due to the large detection area of 2D detectors. Therefore, "diffraction cone" and "diffraction ring" will be mostly used in this book as an alternative to Debye cone and Debye ring.

2.2 DIFFRACTION SPACE AND LABORATORY COORDINATES

2.2.1 Diffraction Cones in Laboratory Coordinates

Figure 2.3 describes the geometric definition of diffraction cones in the laboratory coordinate system, $\mathbf{X_L Y_L Z_L}$. The laboratory coordinate system is a Cartesian coordinate system. Analogous to the conventional three-circle and four-circle goniometer, the direct X-ray beam propagates along the $\mathbf{X_L}$ axis, $\mathbf{Z_L}$ is up, and $\mathbf{Y_L}$ makes up a right-handed rectangular coordinate system. The diffraction sample is located at the origin of the laboratory coordinates, which is also referred to as the goniometer center, instrument center, or diffractometer center. Since the axis $\mathbf{X_L}$ is always coincident with the incident X-ray beam, it is also the rotation axis of the diffraction cones. The apex angles of the cones are determined by the 2θ values given by the Bragg equation. The apex angles are twice the 2θ values for forward reflection ($2\theta \leq 90°$) and twice the value of $180° - 2\theta$ for backward reflection ($2\theta > 90°$).

In order to describe the variation of the diffraction pattern along the circumferential direction of diffraction rings, the γ angle is introduced. The γ angle is the azimuthal angle from the origin at the 6 o'clock direction ($-\mathbf{Z_L}$ direction) with a right-handed rotation axis along the opposite direction of incident beam ($-\mathbf{X_L}$ direction). In many publications, χ is used to denote this azimuthal angle for 2D diffraction patterns. Since χ has also been used to denote one of the goniometer angles in

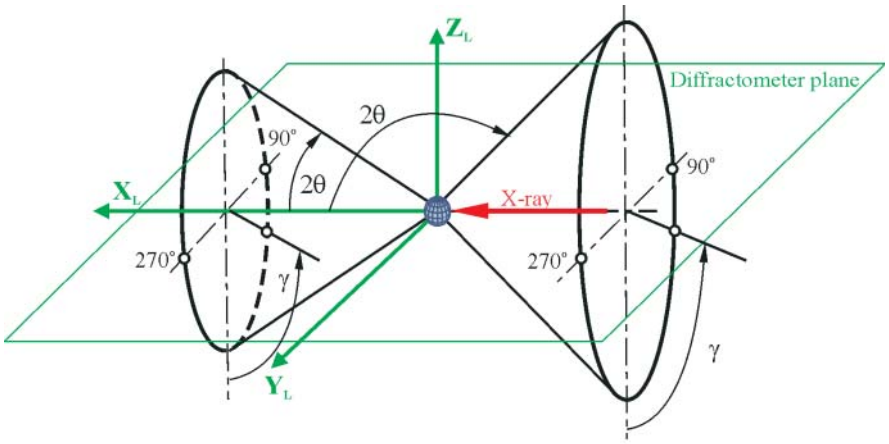


FIGURE 2.3 Geometric definition of diffraction rings in laboratory axes.

the four-circle convention, to avoid any confusion, γ will be used hereafter to represent this angle. The γ angle actually defines a half plane with the $\mathbf{X_L}$ axis as the edge, and it will be referred to as γ plane hereafter. Intersections of any diffraction cones with a γ plane have the same γ value. The conventional diffractometer plane consists of two γ planes with one $\gamma = 90°$ plane in the negative $\mathbf{Y_L}$ side and one $\gamma = 270°$ plane in the positive $\mathbf{Y_L}$ side. Therefore many equations developed for XRD^2 in this book should also apply to conventional XRD if the γ angle is set at 90° or 270°.

A pair of γ and 2θ values represents the direction of a diffracted beam. A 2D diffraction pattern is the diffraction intensity distribution over a part of the diffraction space: $\mathbf{I}(\gamma, 2\theta)$. The γ angle takes a value of 0 to 360° for a complete diffraction ring, and 2θ takes a value from 0 to 180°. For simplicity of many equations, the γ angle may take a value in the range of −180° to 180°. Complete γ and 2θ angles form a kind of spherical coordinate system which covers all the directions from the goniometer center. The γ-2θ system is fixed in the laboratory systems $\mathbf{X_L Y_L Z_L}$, which is independent of the sample orientation and detector position in the goniometer. This is a very important concept in XRD^2 data collection and analysis. In the laboratory coordinate system $\mathbf{X_L Y_L Z_L}$, the surface plane of a diffraction cone can be mathematically expressed as

$$y_L{}^2 + z_L{}^2 = x_L{}^2 \tan^2 2\theta \tag{2.1}$$

with $x_L \geq 0$ or $2\theta \leq 90°$ for forward diffraction cones and $x_L < 0$ or $2\theta > 90°$ for backward diffraction cones.

Each diffraction cone is formed by the diffracted beams from the same family of crystalline planes in all the participating grains which satisfy the Bragg condition. Bragg's law can be expressed in vector form as shown in Figure 2.4, in which $\mathbf{s_0}$ is the unit vector representing the incident X-ray beam and $\mathbf{s}$ is the unit vector representing the diffracted X-ray beam. When vectors $\mathbf{s_0}/\lambda$ and $\mathbf{s}/\lambda$ make angles θ with diffracting planes (hkl), the Laue equation is then given by

$$\frac{\mathbf{s} - \mathbf{s}_0}{\lambda} = \mathbf{H}_{hkl} \tag{2.2}$$

where $\mathbf{H}_{hkl}$ is the reciprocal lattice vector, also referred to as the diffraction vector. We'll use the diffraction vector in most parts of this book. $\mathbf{H}_{hkl}$ is normal to the (hkl) crystal planes and its

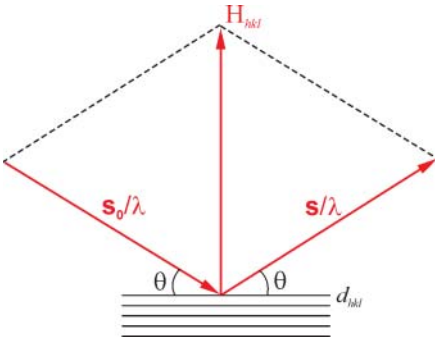


FIGURE 2.4 Diffraction vector satisfying Bragg's law.

magnitude is given as

$$\left|\frac{\mathbf{s}-\mathbf{s}_0}{\lambda}\right| = \frac{2\sin\theta}{\lambda} = |\mathbf{H}_{hkl}| = \frac{1}{d_{hkl}} \tag{2.3}$$

in which d_{hkl} is the d-spacing of crystal planes (hkl). It can be easily seen that it is Bragg's law in a different form.

The incident beam is in the direction of the $\mathbf{X_L}$ axis in the laboratory coordinates so that the unit vector of the incident beam is given by

$$\mathbf{s_0} = \begin{bmatrix} s_{0x} \\ s_{0y} \\ s_{0z} \end{bmatrix} = \begin{bmatrix} 1 \\ 0 \\ 0 \end{bmatrix} \tag{2.4}$$

Each diffraction cone can be expressed as the trace of all diffracted beams from a crystal plane family. In the laboratory system it can be represented by the unit vector of diffracted beam $\mathbf{s}$ as

$$\mathbf{s} = \begin{bmatrix} s_x \\ s_y \\ s_z \end{bmatrix} = \begin{bmatrix} \cos 2\theta \\ -\sin 2\theta \sin\gamma \\ -\sin 2\theta \cos\gamma \end{bmatrix} \tag{2.5}$$

where the three components in the bracket are the projections of the unit vector on the three axes of the laboratory coordinates respectively. Both 2θ and γ are parameters defined in the diffraction space. If γ takes all values from 0 to 360° at a given Bragg angle 2θ, the trace of diffracted beams forms a diffraction cone. The trace of the unit vector of diffracted beams for all possible 2θ and γ values forms a unit sphere. If γ takes only the values within the diffractometer plane, i.e. $\gamma = 90°$ in the negative $\mathbf{Y_L}$ side and $\gamma = 270°$ in the positive $\mathbf{Y_L}$ side, the diffracted beams stay within the diffractometer plane. This is the case in the conventional diffractometer. There has been much confusion on the definition of the diffraction plane; some literature names the crystalline planes satisfying the Bragg condition as diffraction planes, some call the plane containing the incident beam and diffracted beam the diffraction plane. In order to keep consistency, the diffraction plane in this book always refers to the plane containing the incident beam and the diffracted beam, therefore the diffraction vector too. In the conventional diffractometer, the diffraction plane is also the diffractometer plane. In the two-dimensional X-ray diffraction system, there are various diffraction planes for various γ angles. The crystalline planes that satisfy the Bragg condition will be referred to as crystal planes, (hkl) planes, reflection planes, or diffracting planes.

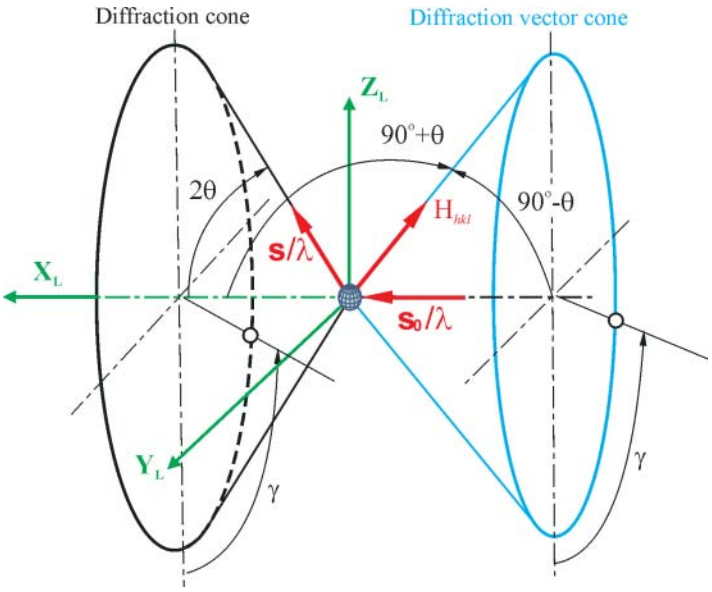


FIGURE 2.5 Relation between the diffraction cone and the corresponding diffraction vector cone.

2.2.2 Diffraction Vector Cones in Laboratory Coordinates

Since the direction of a diffraction vector is a bisector of the angle between the incident and diffracted beams, corresponding to each diffraction cone, the trace of the diffraction vectors forms a cone as shown in Figure 2.5. This cone is referred to as the diffraction vector cone or vector cone. The angle between the diffraction vector and the incident X-ray beam is $90^\circ + \theta$ and the apex angle of a vector cone is $90^\circ - \theta$. It is apparent that diffraction vector cones can only exists in the $-\mathbf{X_L}$ side of the diffraction space.

A 2D diffraction pattern can be considered as the intensity distribution of the scattered X-rays as a function of γ and 2θ angles. In order to describe the diffraction vector corresponding to all the scattering directions covered in the continuous 2D diffraction pattern, we introduce a more general expression for the diffraction vector by removing the indices (*hkl*) from the subscript. The diffraction vector is given in laboratory coordinates by

$$\boldsymbol{H} = \frac{\boldsymbol{s} - \boldsymbol{s}_0}{\lambda} == \frac{1}{\lambda}\begin{bmatrix} s_x - s_{0x} \\ s_y - s_{0y} \\ s_z - s_{0z} \end{bmatrix} = \frac{1}{\lambda}\begin{bmatrix} \cos 2\theta - 1 \\ -\sin 2\theta \sin\gamma \\ -\sin 2\theta \cos\gamma \end{bmatrix} \tag{2.6}$$

The direction of a diffraction vector can be represented by its unit vector given by

$$\mathbf{h_L} = \frac{\mathbf{H}}{|\mathbf{H}|} = \begin{bmatrix} h_x \\ h_y \\ h_z \end{bmatrix} = \begin{bmatrix} -\sin\theta \\ -\cos\theta \sin\gamma \\ -\cos\theta \cos\gamma \end{bmatrix} \tag{2.7}$$

where $\boldsymbol{h}_\mathbf{L}$ is a unit vector expressed in laboratory coordinates and the three components in the bracket are the projection of the unit vector on the three axes of laboratory coordinates respectively. As a unit vector, the three components are bounded by $h_x^2 + h_y^2 + h_z^2 = 1$, and there are

only two independent components to specify a unit diffraction vector. But for convenience and simplicity, we will use all three components explicitly when necessary. If γ takes all values from 0 to 360°, at a given Bragg angle 2θ, the trace of the diffraction vector forms a diffraction vector cone. Since the possible values of θ are within 0 to 90°, the trace of the unit vector of the diffraction vectors for all possible θ and γ values forms a hemisphere with radius 1. It can also be seen from equation (2.7) that h_x takes only negative values. If γ takes only the values within the diffractometer plane, i.e. $\gamma = 90°$ in the negative $\mathbf{Y_L}$ side and $\gamma = 270°$ in the positive $\mathbf{Y_L}$ side, the diffraction vectors stay within the diffractometer plane. This is the case in the conventional diffractometer and $h_Z = 0$. Since a diffraction vector is always perpendicular to the corresponding crystal planes, the unit diffraction vector expressed in the laboratory coordinates can be used for analyzing diffraction data with respect to the incident X-ray beam, and the orientation relationship between diffraction features regardless of the sample orientation.

The diffraction vector has been defined based on the Bragg condition. Therefore, a diffraction vector should be normal to the lattice planes with a given d-spacing. In order to analyze all the X-rays measured by an area detector, we extend the concept to all scattered X-rays from a sample, regardless of the Bragg condition. In general physics, the diffraction vector, also referred to as scattering vector, is defined as the difference between the wave vectors of the scattered wave and the incident wave. Although there seems to be preferences in different fields between the terms diffraction vector and scattering vector, we will use diffraction vector or scattering vector alternatively. We can simply describe a diffraction vector as a vector that takes the direction bisecting the incident beam and the scattered beam, and has a dimension of an inverse length given by $2\sin\theta/\lambda$. Here 2θ is the scattering angle from the incident beam. When the Bragg condition is satisfied, the diffraction vector is normal to the diffracting lattice planes and its magnitude is reciprocal to the d-spacing of the lattice planes. In this case the diffraction vector is equivalent to the reciprocal lattice vector. Each pixel in an area detector measures scattered X-rays in a given direction with respect to the incident beam. We can calculate a diffraction vector for any pixel, even if the pixel is not measuring Bragg scattering. The "diffracted beam", hereafter in this book, does not necessarily imply that it is from Bragg scattering.

2.3 DETECTOR SPACE AND DETECTOR GEOMETRY

2.3.1 Ideal Detector for Diffraction Pattern in 3D Space

An ideal detector is defined as a detector with the detecting surface covering the complete diffraction space. Figure 2.6 shows an ideal detector of a spherical shape with the sample at the center of the sphere. The incident X-ray beam points to the center of the sphere through the detector at $2\theta = 180°$. The direction of a diffracted beam is defined by γ (longitude) and 2θ (latitude). Since the detector surface covers the whole spherical surface, i.e. 4π in solid angle, the ideal detector is sometimes also referred to as a 4π detector. In addition to the geometry definition, an ideal detector should also have many desired physical properties, such as large dynamic range, small pixel size, and narrow point spread function, as well as many other ideal properties. In practice, such an ideal detector does not exist. There are many 2D detector technologies available, including photographic film, charge coupled device (CCD), image plate (IP), multiwire proportional counter (MWPC), microgap detector, and pixel detector. Each technique has advantages over the others. A typical 2D detector has a limited detection surface and the detection surface can be a spherical, cylindrical, or flat. The spherical and cylindrical detectors are normally designed for a fixed sample-to-detector distance, while a flat detector has the flexibility to be used at different

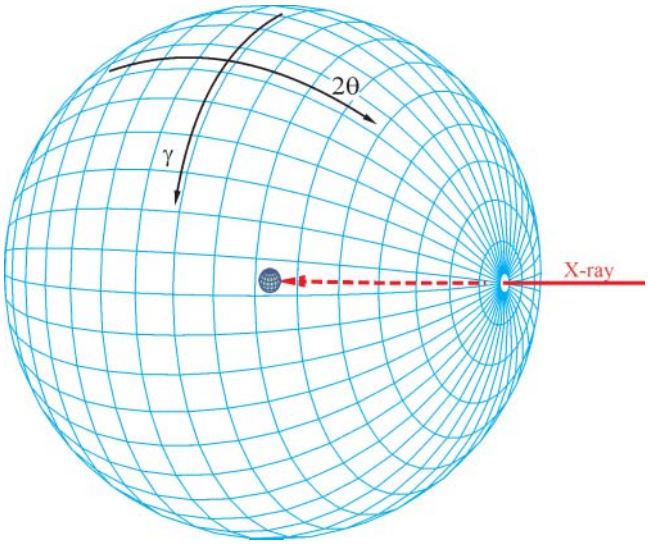


FIGURE 2.6 Schematics of an ideal detector covering 4π solid angle.

sample-to-detector distances so as to choose either high resolution at large distance or large angular coverage at short distance. The following discussion on XRD^2 geometry will focus mainly on flat 2D detectors.

2.3.2 Diffraction Cones and Conic Sections with Flat 2D Detectors

Figure 2.7 shows the geometry of a diffraction cone. The incident X-ray beam always lies along the rotation axis of the diffraction cone. The whole apex angle of the cone is twice the 2θ value given by Bragg's law. For a flat 2D detector, the detection surface can be considered as a plane that intersects the diffraction cone to form a conic section. D is the distance between the sample and the detector; it will be referred as sample-to-detector distance or simply detector distance hereafter. In some literature, the sample parameter may be called the camera length. The angle between the incident X-ray beam and the line connecting detector center and the instrument center is the detector swing angle α. The conic section takes different shapes for different α angles. When imaged on-axis ($\alpha = 0°$) the conic sections appear as circles. When the detector is at an off-axis position ($\alpha \neq 0°$), the conic section may be an ellipse, parabola, or hyperbola. For convenience, all kinds of conic sections will be referred to as diffraction rings or Debye rings without referring to their specific shapes. The 2D diffraction image collected in a single exposure will be referred to as a frame. The frame is normally stored as X-ray intensity values on 2D pixels. The determination of the diffracted beam direction involves the conversion of pixel information into the γ-2θ coordinates. In an XRD^2 system, γ and 2θ values at each pixel position are given according to the detector position. The diffraction rings can be displayed in terms of γ and 2θ coordinates, regardless of the actual shape of the diffraction ring.

2.3.3 Detector Position in the Laboratory System

The position of a flat detector is defined by the sample-to-detector distance D and the detector swing angle α. Both D and α are referred to as the detector space parameters. D is the perpendicular distance from the goniometer center to the detection plane and α is a right-handed rotation

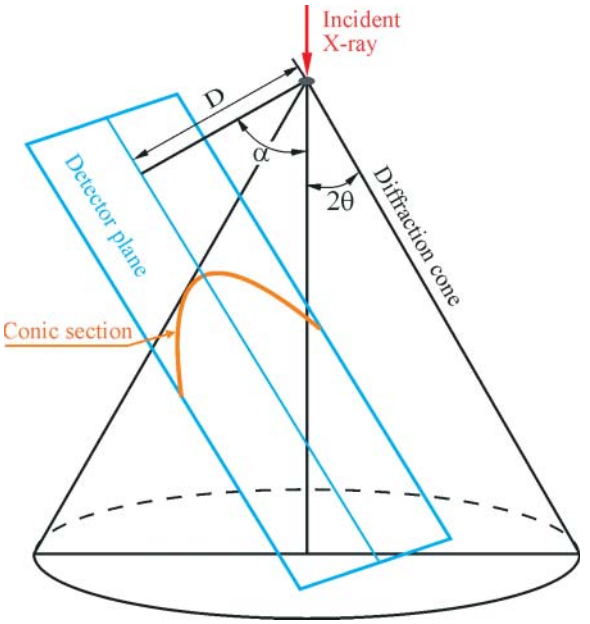


FIGURE 2.7 A diffraction cone and the conic section by a 2D detector plane.

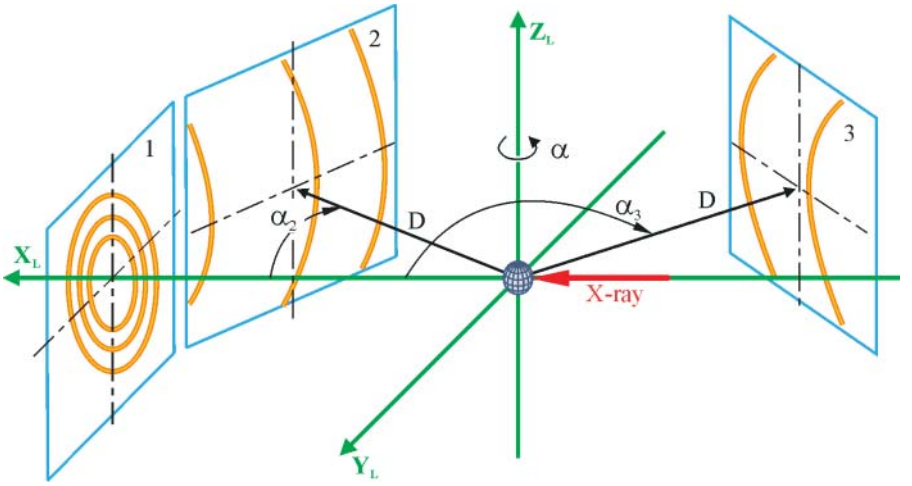


FIGURE 2.8 Detector position in the laboratory system $\mathbf{X_L Y_L Z_L}$: D is the sample-to-detector distance; α is the swing angle of the detector.

angle above the $\mathbf{Z_L}$ axis. In the laboratory coordinates $\mathbf{X_L Y_L Z_L}$, detectors at different positions are as shown in Figure 2.8 The center of detector 1 is right on the positive side of $\mathbf{X_L}$ axis (on-axis), $\alpha = 0$. Both detectors 2 and 3 are rotated away from $\mathbf{X_L}$ axis with negative swing angles ($\alpha_2 < 0$ and $\alpha_3 < 0$). Inherited from the conventional diffractometer, the swing angle may be denoted as detector 2θ angle, or simply $2\theta_D$. It is very important to distinguish between the 2θ angle and the detector swing angle α. In a conventional diffractometer, measuring the 2θ angle is uniquely

determined by the angular position of the point detector. In an XRD^2 system, however, a range of 2θ values can be measured at a given α angle. It is acceptable to use 2θ to describe the detector position for convenience, but α is used in all equations to avoid confusion.

2.3.4 Pixel Position in Diffraction Space – Flat Detector

To analyze XRD^2 diffraction data it is necessary to find the diffraction space coordinates $(2\theta, \gamma)$ of each pixel in the 2D detector. The calculation is based on the detector space parameters and the pixel position in the detector. Figure 2.9 shows the relationship of a pixel P(x,y) to the laboratory coordinates, $\mathbf{X_L Y_L Z_L}$. The detector with a flat detection plane is located at the sample-to-detector distance D with the swing angle α. The center of the detector is the intersection of the detector plane with the $\mathbf{X_L}$ axis when $\alpha = 0$. The position of a pixel in the detector is defined by the (x,y) coordinates, where the detector center is defined as $x = y = 0$. The detector center and accurate coordinates for each pixel are determined by specific detector design, calibration, and spatial correction. The pixel coordinates may be defined differently in a specific detector, or the calibrated beam center is not at the origin of the pixel coordinates. In these cases, a conversion is necessary so the pixel coordinates used in the following equations follow the definition here. The diffraction space coordinates $(2\theta,\gamma)$ for a pixel at P(x,y) are given by

$$2\theta = \arccos \frac{x \sin\alpha + D\cos\alpha}{\sqrt{D^2 + x^2 + y^2}}, \quad (0 < 2\theta < \pi) \tag{2.8}$$

$$\gamma = \frac{x\cos\alpha - D\sin\alpha}{|x\cos\alpha - D\sin\alpha|} \arccos \frac{-y}{\sqrt{y^2 + (x\cos\alpha - D\sin\alpha)^2}}, \quad (-\pi < \gamma \le \pi) \tag{2.9}$$

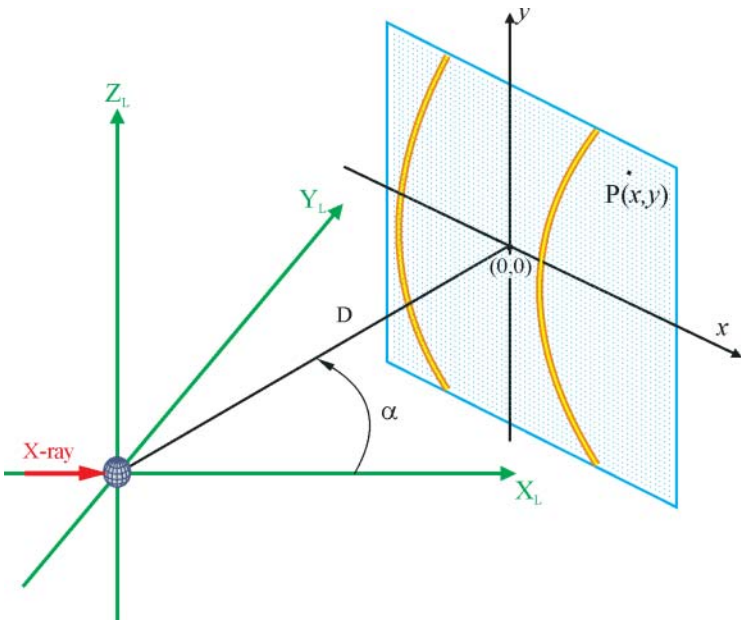


FIGURE 2.9 Relationship between a pixel P and detector position in the laboratory coordinates, $\mathbf{X_L Y_L Z_L}$.

When $x\cos\alpha - D\sin\alpha = 0$ in equation 2.9, the division by zero may cause the computer calculation to terminate or return an error value. This happens when the detection plane intersects the $\mathbf{X_L Z_L}$ plane. The intersection is a vertical line with a constant x value. On this intersection line and $y = 0$, the incident X-ray strikes the detector if not blocked by the sample or a beamstop. The pixel position P(x,0) is the point representing the location of direct beam on the detector at this particular swing angle. At this point $2\theta = 0$ and γ takes any arbitrary value or no definition. The γ values for all the pixels on this intersection line, except at $y = 0$, is given by

$$\gamma = \begin{cases} 0 & \text{if} \quad x\cos\alpha = D\sin\alpha \quad \text{and} \quad y < 0 \\ \pi & \text{if} \quad x\cos\alpha = D\sin\alpha \quad \text{and} \quad y > 0 \end{cases} \tag{2.10}$$

To analyze the shapes of the conic sections on a flat 2D detector, equation 2.8 can be written in quadratic form as

$$ax^2 + bxy + cy^2 + dx + ey + f = 0 \tag{2.11}$$

in which

$$\begin{aligned} a &= \cos^2 2\theta - \sin^2\alpha \\ b &= 0 \\ c &= \cos^2 2\theta \\ d &= -2D\sin\alpha\cos\alpha \\ e &= 0 \\ f &= D^2(\cos^2 2\theta - \cos^2\alpha) \end{aligned}$$

Simple tests for forward diffraction ($2\theta < 90°$ and $\alpha < 90°$) are shown in Table 2.1; the same is true for other quadrants.

In the first edition of this book and some previous publications, we have given the following inverse functions of equation 2.8 and 2.9, to calculate (x,y) coordinates from the diffraction space coordinates (2θ,γ):

$$x = \frac{\cos\alpha\tan 2\theta\sin\gamma + \sin\alpha}{\cos\alpha - \sin\alpha\tan 2\theta\sin\gamma} D, \quad (-\pi \le \alpha \le \pi, \quad 0 \le 2\theta < \pi) \tag{2.12}$$

$$y = -(x\sin\alpha + D\cos\alpha)\tan 2\theta\cos\gamma \quad (-\pi \le \alpha \le \pi, \quad 0 \le 2\theta < \pi) \tag{2.13}$$

Both equations contain a term tan2θ and it becomes infinitive when $2\theta = 90°$. The x value has to be calculated first before calculating the y value from the second equation. In practice, it is not likely to have a diffraction cone exactly at $2\theta = 90°$. But since the 2D image are processed as a continuous distribution of intensity over 2θ and γ ranges, some pixels or subpixels may fall at the

Table 2.1 Simple Tests for Forward Diffraction

$\alpha = 0$	$x^2 + y^2 = D^2\tan^2 2\theta$	circle
$2\theta + \alpha < 90°$	$b^2 - 4ac < 0$	ellipse
$2\theta + \alpha = 90°$	$b^2 - 4ac = 0$	parabola
$2\theta + \alpha > 90°$	$b^2 - 4ac > 0$	hyperbola

position of $2\theta = 90°$, so the above singularity issues may crash the evaluation software. In order to avoid the singularity of the tangent function at $2\theta = 90°$ and the dependence of the second equation to the x value from the first equation, the following equations are derived to replace equations 2.12 and 2.13 in the rest of this book and future publications for converting 2θ and γ into x and y:

$$x = \frac{\cos\alpha \sin 2\theta \sin\gamma + \sin\alpha \cos 2\theta}{\cos\alpha \cos 2\theta - \sin\alpha \sin 2\theta \sin\gamma} D, \quad \left(-\pi \le \alpha \le \pi,\ 0 \le 2\theta < \pi\right) \tag{2.14}$$

$$y = \frac{-\sin 2\theta \cos\gamma}{\cos\alpha \cos 2\theta - \sin\alpha \sin 2\theta \sin\gamma} D, \quad \left(-\pi \le \alpha \le \pi,\ 0 \le 2\theta < \pi\right) \tag{2.15}$$

These two equations can be used to calculate the cross point of any scattered X-ray with a flat detector. For example, a conic line can be drawn on the 2D frame with variable γ at a given 2θ. But the equations must be used within proper boundary conditions to avoid singularity and erroneous results. For instance, singularity appears when $\cos\alpha \cos 2\theta - \sin\alpha \sin 2\theta \sin\gamma = 0$.

Erroneous results may be obtained if the γ and 2θ are calculated out of the boundary given by the detector size, distance, and swing angle. Mathematically, the conic section is the intersection of the detector plane with a "double cone", in which two cones are placed apex to apex. For instance, for a diffraction cone of $2\theta = 45°$, if the detector swing angle is set at $\alpha \ge 135°$, there should be no intersection between the detector plane and the diffraction cone, no matter how large the detector is. However, due to the double cone, a set of (what appear to be reasonable) x and y values can be obtained from the above two equations. Therefore, some boundary conditions should be applied to proper use the above two equations. The γ and 2θ values should be within ranges determined by the detector size, distance, and swing angle. For detector at on-axis position or at a swing angle that $\mathbf{X_L}$ axis crosses with the detector active area, γ values should be within the following ranges:

$$\begin{array}{lll} 0 \le \gamma \le \pi & \text{if} & x \ge D\tan\alpha \\ -\pi < \gamma < 0 & \text{if} & \mathrm{x} < D\tan\alpha \end{array} \quad \text{and} \quad -\frac{\pi}{2} < \alpha < \frac{\pi}{2} \tag{2.16}$$

For detector at a swing angle that no part of the detector active area crosses with the $\mathbf{X_L}$ axis, γ values should be within the following ranges:

$$\begin{aligned} 0 < \gamma < \pi \quad &\text{if} \quad -\pi < \alpha < 0 \\ -\pi < \gamma < 0 \quad &\text{if} \quad 0 < \alpha < \pi \end{aligned} \tag{2.17}$$

2.3.5 Pixel Position in Diffraction Space – Flat Detector Out of Diffractometer Plane

The 2θ range covered by a flat 2D detector can be changed by the detector swing angle α. The detector center stays within the diffractometer plane ($\mathbf{X_L Y_L}$ plane) when moving detector position by the swing angle. The detector center may move out of the diffractometer plane to cover a different part of the diffraction space or γ range. If the detector moves up or down within the same detection plane, the equations to convert between the pixel position (x,y) and the diffraction space (2θ,γ) are the same except an offset to the y value. In other words, the origin of the detector coordinates (x,y) should always be defined as the point on the detector plane that crosses with the $\mathbf{X_L}$ axis if the detector swings to $\alpha = 0$.

In order to follow the trace of the diffraction rings, a reasonable way to move the detector out of the diffractometer plane is the azimuthal rotation about the incident X-ray beam ($\mathbf{X_L}$ axis) in addition to the swing angle. Figure 2.10(a) illustrates such a rotation. The swing angle α is a right-hand rotation about $\mathbf{Z_L}$ axis. The detector position 1 is at positive swing angle α_1 and the detector position 2 is at negative swing angle α_2. The centers of the detector and the detector axis x of both detector positions 1 and 2 are within the diffractometer plane. The detector azimuthal angle β is a right-hand rotation about the $\mathbf{X_L}$ axis. The detector position 3 is at positive azimuthal rotation angle β_1 from the detector position 1, and the detector position 4 is at positive azimuthal rotation angle β_2 from the detector position 2. The diffraction space coordinates $(2\theta,\gamma)$ for a pixel at P(x,y) for the detector position 3 and 4 are given by

$$\begin{aligned} 2\theta &= \arccos\frac{x\sin\alpha + D\cos\alpha}{\sqrt{D^2+x^2+y^2}}, \quad (0<2\theta<\pi) \\ \gamma &= \frac{x\cos\alpha - D\sin\alpha}{|x\cos\alpha - D\sin\alpha|}\arccos\frac{-y}{\sqrt{y^2+(x\cos\alpha - D\sin\alpha)^2}} - \beta \end{aligned} \tag{2.18}$$

where the equation for 2θ is identical to the equation for the detector position with α swing only, because the β rotation does not change the angular relation between any part of the detector and the incident X-ray beam. The β rotation only adds an offset to the γ value. If taking the $\mathbf{X_L}$ as the pole, the trace of the detector center with β rotation forms a circle of latitude. A flat 2D detector can cover the complete 4π diffraction space with a combination of α rotation $(-\pi<\alpha<\pi)$ and β rotation $(-\pi/2<\beta<\pi/2)$ if such a mechanism is implemented. The information in the 2D patterns collected by this mechanism can be projected to the sphere (given by 2θ and γ as in Figure 2.6) with equations 2.18.

Moving the detector out of the diffractometer plane by β (about the $\mathbf{X_L}$ axis) is a preferred way to cover more diffraction space because the detector motion follows the diffraction rings. However, it is hard to achieve this motion mechanically. Another alternative way to move the detector out of the diffractometer plane is illustrated in Figure 2.10(b). In addition to the swing angle within diffractometer plane (α), the detector moves with another swing angle out of the diffractometer plane (η) about the instrument center and towards the $\mathbf{Z_L}$ axis. Or in other words, 90° η rotation at any α will put the detector center onto the $\mathbf{Z_L}$ axis. If considering the $\mathbf{Z_L}$ as the pole, the trace of the detector center with η swing is a line of longitude. In this geometry, the diffraction space coordinates $(2\theta,\gamma)$ for a pixel at P(x,y) for the detector position α and η are given by

$$\begin{aligned} 2\theta &= \arccos\frac{x\sin\alpha + (D\cos\eta - y\sin\eta)\cos\alpha}{\sqrt{D^2+x^2+y^2}}, \quad (0<2\theta<\pi) \\ \gamma &= \pm\arccos\frac{-y\cos\eta - D\sin\eta}{\sqrt{(y\cos\eta + D\sin\eta)^2 + [x\cos\alpha - (D\cos\eta - y\sin\eta)\sin\alpha]^2}} \\ \text{with} \quad & \begin{array}{ll} 0\le\gamma\le\pi & \text{if } x\cos\alpha - (D\cos\eta - y\sin\eta)\sin\alpha \ge 0 \\ -\pi<\gamma<0 & \text{if } x\cos\alpha - (D\cos\eta - y\sin\eta)\sin\alpha < 0 \end{array} \end{aligned} \tag{2.19}$$

The information in the 2D patterns can be projected onto the diffraction space by equations 2.19. Although the detector motion out of the diffractometer plane does not follow the diffraction ring, A flat 2D detector can cover a large or even complete 4π diffraction space with a combination of α rotation $(-\pi<\alpha<\pi)$ and η rotation $(-\pi/2<\eta<\pi/2)$.

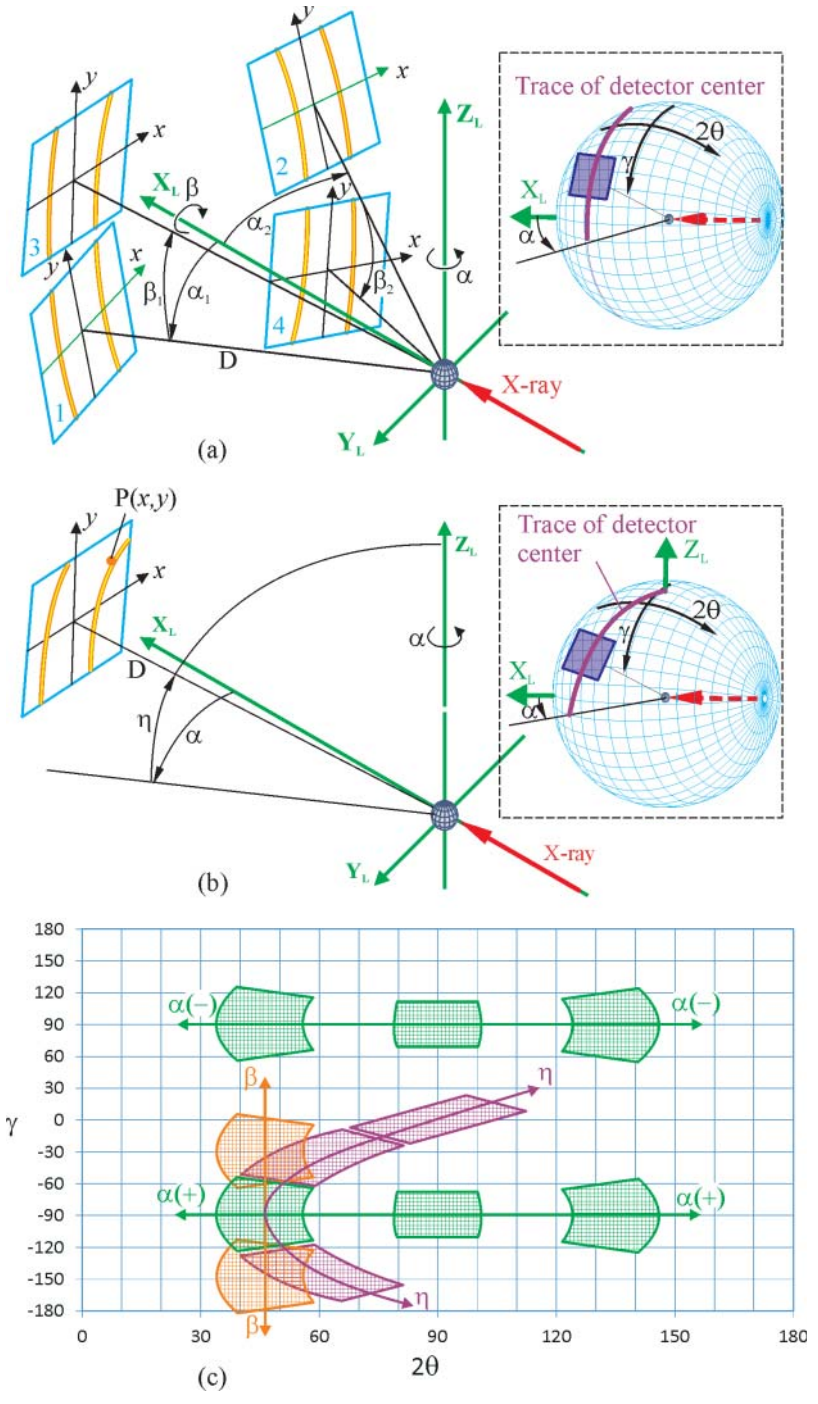


FIGURE 2.10 Detector motion out of diffractometer plane: (a) azimuthal rotation of the detector about the $\mathbf{X_L}$ axis, (b) detector swing angle (η) about the instrument center and towards the $\mathbf{Z_L}$ axis, (c) diffraction space coverage of various detector motions.

Figure 2.10(c) is a comparison of the diffraction space coverage of various detector motions for an EIGER2 detector (H = 77.2 mm and L = 38.6 mm) in γ-optimized mode. The coverages with swing angles within the diffractometer plane for positive swing $\alpha(+)$ angles 45°, 90°, and 135° and negative swing $\alpha(-)$ angles −45°, −90°, and −135° are displayed as green boxes. In the γ-optimized mode, the detector has more angular coverage in the γ direction. But 2θ and γ are not displayed at the same scale, so the coverage box looks shrunk in the γ direction. At $\alpha = 45°$, the coverages at out-of-diffractometer-plane rotation angle $\beta = \pm 60°$ are given by the orange boxes. The β rotation changes γ coverage with the same 2θ coverage. At $\alpha = 45°$, the coverages at out-of-diffractometer-plane rotation $\eta = 45°$, −45°, and −90° are given by the purple boxes. The η rotation changes both γ and 2θ coverages.

2.3.6 Pixel Position in Diffraction Space – Cylindrical Detector

The conic sections of the diffraction cones with the detection surface of a curved detector cannot be expressed by quadratic functions. The forms of the functions are dependent on the shape of the detector. The most common curved detectors are cylinder shaped detectors. Some cylinder shaped detectors, such as image plates, may be flattened during the diffraction image readout. Some curved detectors may be read out in the same curved shape as during the data collection. In either case, the diffraction frame measured by a cylindrical detector can be displayed as a flat frame, typically a rectangle. Once the diffraction space coordinates $(2\theta,\gamma)$ of each pixel in the curved 2D detector are determined, most data analysis algorithms developed for the flat detectors are applicable to the curved detector as well. A cylindrical detector may be positioned in the laboratory coordinates in two orientations, one is to align the rotation axis of the cylinder in the vertical direction and overlapping with $\mathbf{Z_L}$, the other is to align the rotation axis in the horizontal direction and overlapping with $\mathbf{X_L}$. The other possibility is to align the rotation axis to $\mathbf{Y_L}$, but this is equivalent to the orientation aligned with $\mathbf{Z_L}$ in terms of conic sections.

Figure 2.11(a) shows a cylindrical detector in the vertical direction and the corresponding laboratory coordinates, $\mathbf{X_L Y_L Z_L}$. The sample is located at the origin of the laboratory coordinates

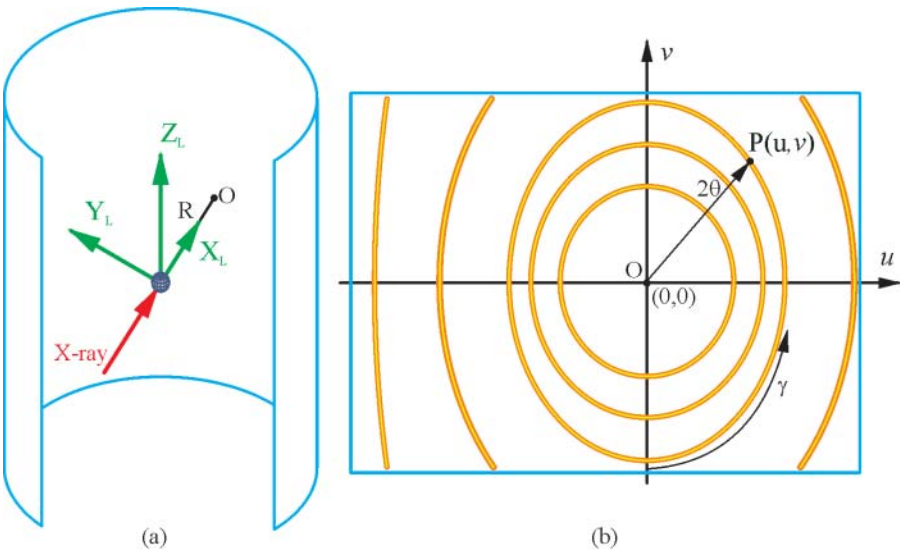


FIGURE 2.11 Cylinder-shaped detector in vertical direction: (a) detector position in the laboratory coordinates, $\mathbf{X_L Y_L Z_L}$, (b) pixel position in the flattened image.

inside the cylinder. The incident X-rays strike the detector at a point O if there is no sample or beamstop to block the direct beam. The radius of the cylinder is R. For a cylindrical detector, R is a constant. Figure 2.11(b) illustrates the 2D diffraction image collected with the cylindrical detector. The pixel position in the flattened image is given by the coordinates u and v. We take the point O as the origin of the pixel position (0,0). The diffraction space coordinates $(2\theta,\gamma)$ for a pixel at P(u,v) are given by

$$2\theta = \arccos \frac{R\cos\left(\frac{u}{R}\right)}{\sqrt{R^2+v^2}} \qquad (0 < 2\theta < \pi) \tag{2.20}$$

$$\gamma = \frac{u}{|u|}\arccos \frac{-v}{\sqrt{v^2+R^2\sin^2\left(\frac{u}{R}\right)}} \qquad (-\pi < \gamma \leq \pi) \tag{2.21}$$

When $u = 0$ in equation 2.21, the division by zero may cause the computer calculation to terminate or return an error value. This happens when the cylindrical detection surface intersects the $\mathbf{X_L Z_L}$ plane. The intersection is a vertical line on the v axis. At the pixel position (0,0), $2\theta = 0$ and γ takes any arbitrary value or no definition. The γ values for all the pixels on this intersection line, except at $v = 0$, are given by

$$\gamma = \begin{cases} 0 & \text{if } v < 0 \\ \pi & \text{if } v > 0 \end{cases} \tag{2.22}$$

We can also obtain the inverse functions of equations (2.20) and (2.21), so that (u,v) coordinates on the cylindrical 2D image can be calculated from the diffraction space coordinates $(2\theta,\gamma)$:

$$v = \frac{-R\sin 2\theta \cdot \cos\gamma}{\sqrt{1-\sin^2 2\theta \cdot \cos^2\gamma}} \tag{2.23}$$

$$u = \frac{\sin\gamma}{|\sin\gamma|} R \cdot \arccos\left(\frac{\sqrt{R^2+v^2}}{R}\cos 2\theta\right) \tag{2.24}$$

The line curve representing a diffraction ring can be drawn on the cylindrical 2D image with variable γ at a given 2θ.

Figure 2.12(a) shows a cylindrical detector in the horizontal direction and the corresponding laboratory coordinates, $\mathbf{X_L Y_L Z_L}$. The sample is located at the origin of the laboratory coordinates inside the cylinder. The incident X-ray beam overlaps with the rotation axis of the cylinder. The negative side of the $\mathbf{Y_L}$ axis crosses the detector at a point O. The radius of the cylinder is a constant R. The cylinder is cut open to reveal the laboratory coordinates. The actual detector may cover the complete azimuthal angles. Figure 2.12(b) illustrates the 2D diffraction image collected by the horizontal cylindrical detector. The 2D image is displayed as if the cylindrical surface is cut split by a half plane defined by $\mathbf{X_L}$ and $+\mathbf{Y_L}$ (a half plane with $\gamma = -90°$) and then to be flattened into a plane. All the diffraction rings appear as straight vertical lines. The azimuthal angle γ has a linear relation with the pixel coordinate y, and the 2θ angle direction is parallel to the pixel coordinate x. We take the point O as the origin of the pixel position (0,0). The diffraction space coordinates $(2\theta,\gamma)$ for a pixel at P(u,v) are given by

$$2\theta = \frac{\pi}{2} + \arctan\frac{u}{R} \tag{2.25}$$

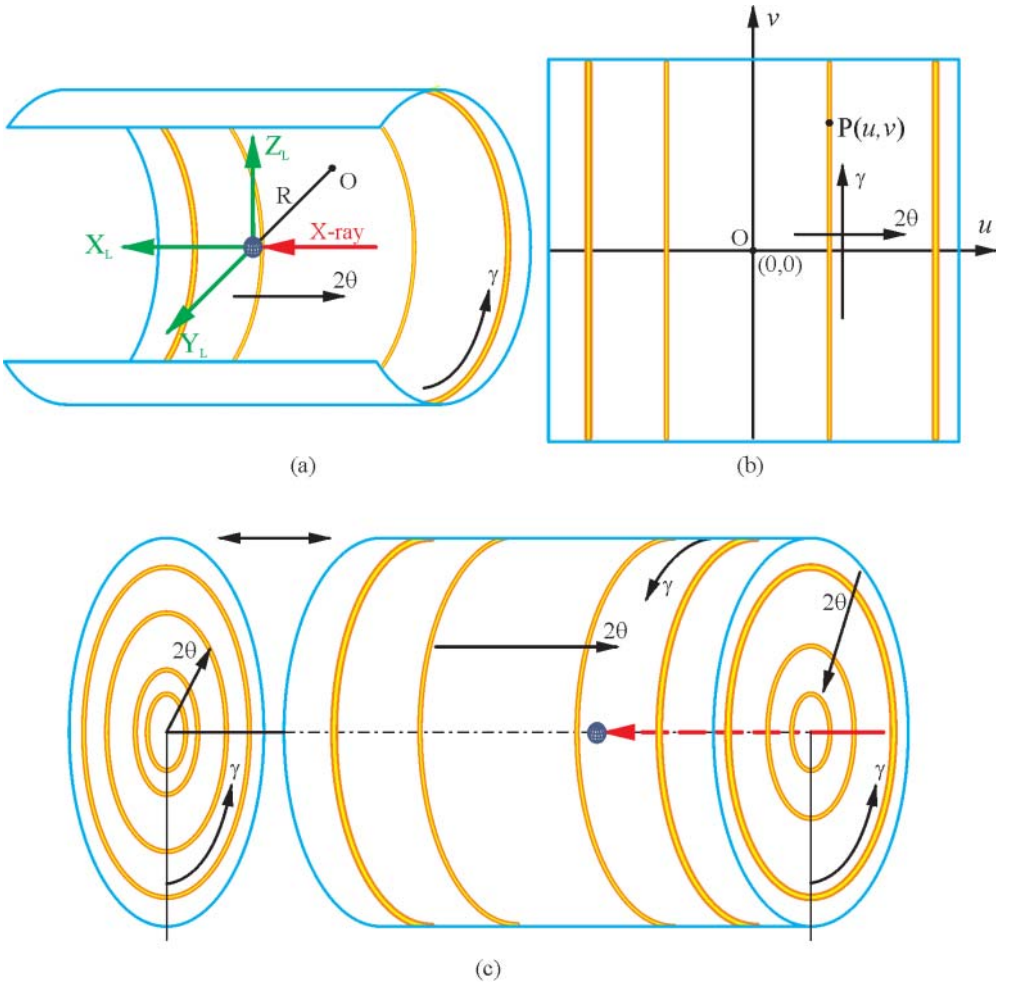


FIGURE 2.12 Cylinder shaped detector in horizontal direction: (a) detector position in the laboratory coordinates, $\mathbf{X_L Y_L Z_L}$, (b) pixel position in the flattened image, (c) two flat detector and a cylinder detector combined to cover the complete diffraction space.

$$\gamma = \frac{\pi}{2} + \frac{v}{R} \tag{2.26}$$

The (u,v) coordinates on the flattened image from such a horizontal cylindrical detector can be calculated from the diffraction space coordinates $(2\theta,\gamma)$:

$$u = -R\cot 2\theta \tag{2.27}$$

$$v = R\left(\gamma - \frac{\pi}{2}\right) \qquad \left(-\frac{\pi}{2} < \gamma < \frac{3\pi}{2}\right) \tag{2.28}$$

In equation (2.28), γ has a boundary condition based on the fact that the cylindrical surface is cut split at $\gamma = -90°$, as illustrated in Figure 2.12(b). A different boundary condition should be used if the cylindrical surface is cut and flattened at a different γ value. At a given 2θ, u is a constant. The vertical lines representing a diffraction ring can be drawn on the 2D image with variable

γ at a given 2θ. It can be seen from the above equations that the horizontal detector is not suitable for collecting diffraction rings at small 2θ and high 2θ angles. For instance, if the horizontal detector size is twice the radius R, the measurable 2θ range is between 45° and 135°. Doubling the horizontal detector size to $4R$ can only increase the 2θ range of 18.4° at both the low and high angles (26.6°~153.4°). One possibility is to use flat detectors for the low and high 2θ angles and a cylinder detector for the intermediate 2θ ranges. Figure 2.12(c) illustrates a concept of covering the whole diffraction space with two flat detectors and one horizontal cylinder detector. The flat detector for low 2θ angles is separated from the cylinder detector in the illustration to show the diffraction rings. The algorithms to calculate the diffraction space coordinates $(2\theta,\gamma)$ for a pixel are the same equations given previously in this section for flat detectors. The algorithms can be simplified by letting the swing angle take values of 0 and π for the low angle flat (forward) detector and high angle flat (backward) detector respectively. These combined detectors have similar functionality to the spherical ideal (4π) detector, while being a technically feasible solution.

2.4 SAMPLE SPACE AND GONIOMETER GEOMETRY

2.4.1 Sample Rotations and Translations in Eulerian Geometry

In an XRD^2 system, three rotation angles are necessary to define the orientation of a sample in the diffractometer. These three rotation angles can be achieved either by a Eulerian geometry, a kappa (κ) geometry or other kind of geometry. The three angles in Eulerian geometry are ω (omega), ψ (psi), and ϕ (phi). In a typical four-circle diffractometer with Eulerian geometry there is also a 2θ circle for point detectors. In an XRD^2 system, the fourth circle should be the detector swing angle α instead. The detector swing angle α belongs to the detector space and it is independent of the sample orientation. Figure 2.13(a) shows the relationship between rotation axes (ω,ψ,ϕ) in the laboratory system $\mathbf{X_L Y_L Z_L}$. The ω angle is defined as a right-handed rotation about the $\mathbf{Z_L}$ axis. The ω axis is fixed on the laboratory coordinates. The ψ angle is a right-handed rotation about a horizontal axis. The ψ axis makes an angle of ω with the $\mathbf{X_L}$ axis in the $\mathbf{X_L Y_L}$ plane. The ψ axis lies on $\mathbf{X_L}$ when ω is set at zero. The ϕ angle defines a left-handed rotation about an

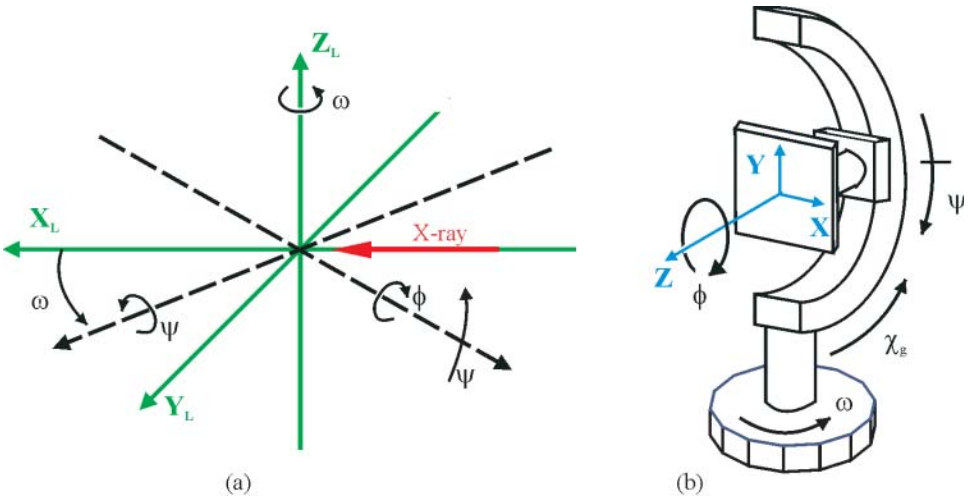


FIGURE 2.13 Sample rotation and translation: (a) three rotation axes in $\mathbf{X_L Y_L Z_L}$ coordinates, (b) rotation axes $(\omega,\chi_g,\psi,\varphi)$ and translation axes **XYZ**.

axis on the sample, typically the normal of a flat sample. The ϕ axis lies on the $\mathbf{Y_L}$ axis when $\omega = \psi = 0$. In an aligned diffraction system, all three rotation axes and the primary X-ray beam cross at the origin of the $\mathbf{X_L Y_L Z_L}$ coordinates. This cross point is also known as the goniometer center or instrument center.

Figure 2.13(b) shows the relationship and stacking sequence between all the rotation axes ($\omega, \chi_g, \psi, \phi$) and the sample translation axes **XYZ**. ω is the base rotation; all other rotations and translations are on top of this rotation. The next rotation above ω is the ψ rotation. χ_g is also a rotation about a horizontal axis. Since the χ symbol has also been used for the azimuthal angle on the diffraction cones in some publications and software, a subscript g indicates that the angle is a goniometer angle. ψ and χ_g have the same axis but different starting positions and rotation directions, and $\chi_g = 90° - \psi$. Therefore, χ_g is also the angle between the ϕ axis and $\mathbf{Z_L}$. For consistency and clarity ψ will be used hereafter whenever possible in this book. The next rotation above ω and ψ is ϕ rotation. Due to the above stacking sequence, the ω axis is always on the $\mathbf{Z_L}$ axis. The ψ axis is on $\mathbf{X_L}$ at $\omega = 0$ and on $\mathbf{Y_L}$ at $\omega = 90°$. The direction of the ϕ axis in $\mathbf{X_L Y_L Z_L}$ at special ω and ψ values are given in Table 2.2.

The sample translation coordinates **XYZ** are so defined that, when $\omega = \psi = \phi = 0$, the relationship to the laboratory axes becomes $\mathbf{X} = -\mathbf{X_L}$, $\mathbf{Y} = \mathbf{Z_L}$, and $\mathbf{Z} = \mathbf{Y_L}$ assuming the origins of the two coordinates are overlapping. The ϕ rotation axis is always on the **Z** axis, which is typically normal to the sample surface in reflection mode diffraction. In the later part of this chapter, X-ray diffraction in reflection mode is assumed if not specified otherwise. Therefore, the **XY** plane is parallel to the sample surface. In the preferred embodiment, **XYZ** translations are above all the rotations so that the translations will not move any rotation axis away from the goniometer center. Instead, the **XYZ** translations bring different parts of the sample into the goniometer center. For example, in Figure 2.14, a sample translation of $+\Delta x$ and $+\Delta y$ will bring the sample spot $\mathbf{P}(-\Delta x, -\Delta y)$ into the instrument center. Therefore, the origin of **XYZ** is not fixed on the sample but on the instrument. In practice, the ϕ axis may be built above the **Z** axis. Since both axes are parallel, **Z** translation will not move the ϕ axis away from the instrument center.

Table 2.2 The Direction of the ϕ axis in $\mathbf{X_L Y_L Z_L}$ at Special ω and ψ

ω	ψ	ϕ axis on
0	0	$\mathbf{Y_L}$
90°	0	$-\mathbf{X_L}$
any value	90°	$\mathbf{Z_L}$

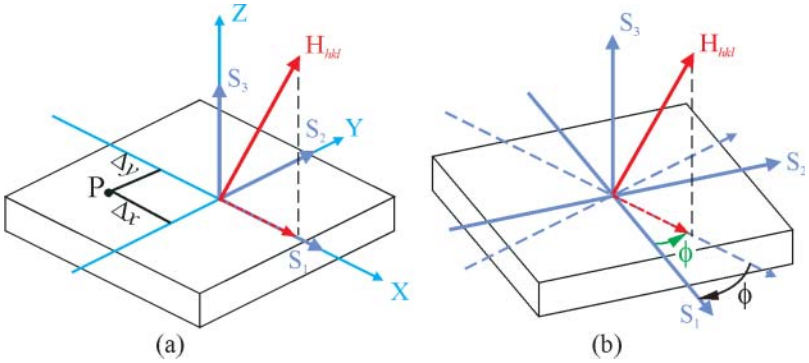


FIGURE 2.14 Sample translation axes **XYZ** and the sample coordinates $\mathbf{S_1 S_2 S_3}$.

In order to analyze the diffraction results relative to the sample orientation, it is necessary to define the sample coordinates $\mathbf{S_1}$, $\mathbf{S_2}$, and $\mathbf{S_3}$. Typically, the sample coordinates $\mathbf{S_1}$, $\mathbf{S_2}$, and $\mathbf{S_3}$ have the same directions as the sample translation coordinates **X**, **Y**, and **Z** respectively. However, the origin of the sample coordinates is considered as on the sample spot which is measured by X-ray diffraction. In other words, the sample coordinates $\mathbf{S_1S_2S_3}$ and the laboratory coordinates $\mathbf{X_L Y_L Z_L}$ have the same origin, which is the instrument center. The $\mathbf{S_1S_2}$ plane is the sample surface plane, and $\mathbf{S_3}$ is the sample surface normal. In principle, it is important to carefully note the distinction between the two sets of coordinates. The **XYZ** translation coordinates indicate the relative sample position. For example, samples are moved to multiple locations by an **XY** translation stage to collect diffraction mapping data sets, while **Z** translation is used to align the sample height at each mapping spot. The $\mathbf{S_1S_2S_3}$ coordinates are fixed on the sample with origin at the measurement spot. The $\mathbf{S_1S_2S_3}$ coordinates are mainly used to establish the relationship between the sample orientation and diffraction pattern.

The ϕ rotation in the goniometer is intentionally chosen as a left-handed rotation so that the diffraction vectors will make a right-hand rotation observed in the sample coordinates $\mathbf{S_1S_2S_3}$. Figure 2.14(a) shows a diffraction vector $\mathbf{H}_{hkl}$ and its projection on the $\mathbf{S_1}$ axis. In Figure 2.14(b) the sample made a left-hand rotation of ϕ. The projection of the same diffraction vector on the sample rotates away from the $\mathbf{S_1}$ axis in a right-hand rotation of ϕ. In other words, the left-hand sample ϕ rotation results in the right-hand rotation of $\mathbf{H}_{hkl}$ when observed in the sample coordinates. The corresponding rotations in the two-dimensional polar coordinate system, three-dimensional cylindrical coordinate system, and spherical coordinate system are all right-hand rotations. Therefore it is imperative to give the sample ϕ a left-hand rotation so that orientation-sensitive diffraction results can be properly mapped into the sample space by mathematical operations. In summary, there are a total of six parameters in the sample space, including three independent rotations (ω,ψ,ϕ) and three orthogonal translations (**X,Y,Z**). The position of a sample in the laboratory coordinates can be uniquely determined by the six parameters. For diffraction data analysis on each particular sample spot, only the three Eulerian angles (ω,ψ,ϕ) are necessary to determine the sample orientation.

2.4.2 Variation of Goniometer Geometry

Many variations of goniometer geometry exist, for historical reasons and because of preferences for various applications. A diffractometer may not have every rotation and translation axis described in the above sections. That means that some of the axes need to be assigned as constants. The diffractometer may be set in a horizontal or vertical orientation relative to the ground level. The ω angle may be achieved by rotating the sample against a stationary primary X-ray beam, or by rotating the primary X-ray beam against the sample. The diffractometer may also be categorized with a left-hand or right-hand goniometer depending on the relative position of the primary beam, the goniometer, and the operator.

Figure 2.15 shows two typical diffractometer configurations. Figure 2.15(a) is the configuration of a horizontal diffractometer with left-hand goniometer and the θ-2θ configuration. As observed by the operator, the goniometer is mounted in the left side of the X-ray tube and primary optics, so the system is categorized as a left-hand system. The diffractometer plane, determined by the primary X-ray beam ($\mathbf{X_L}$ axis) and the rotation plane of ω and α, is in the horizontal position, so the diffractometer is also referred to as a horizontal diffractometer. In this diffractometer, the primary X-ray beam ($\mathbf{X_L}$ axis) is fixed. The ω angle is achieved by sample rotation and the α angle is achieved independently by detector rotation. Following the naming scheme of the Bragg–Brentano geometry, we call this a θ-2θ configuration.

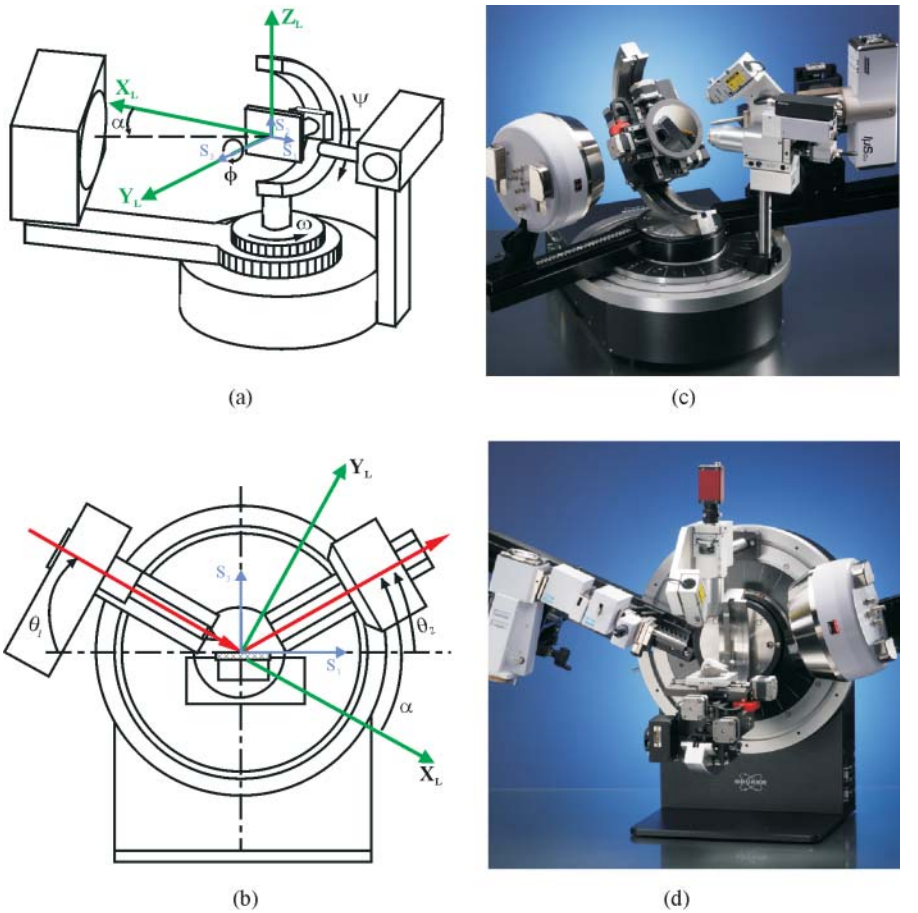


FIGURE 2.15 Typical XRD[2] diffractometer configurations: (a) horizontal θ-2θ, (b) vertical θ-θ, (c) and (d) diffractometers in horizontal and vertical configurations (Bruker D8 Discover™).

Figure 2.15(b) shows the configuration of a vertical diffractometer with the θ-θ configuration. The diffractometer plane ($\mathbf{X_L Y_L}$ plane) is in the vertical position, so the diffractometer is also referred to as a vertical diffractometer. In this diffractometer, the sample is fixed with the surface in the horizontal plane when $\psi = 0$. The ω angle and the α angle are determined by the primary X-ray beam incident angle θ_1 and the detector angle from the horizontal plane θ_2. In this configuration the laboratory coordinates $\mathbf{X_L Y_L Z_L}$ are not actually fixed to the "laboratory". This sounds unreasonable, but it is essential to make all the configurations consistent in physics and mathematics. A better way to explain this is that the diffraction space is determined by the primary X-ray beam and the instrument center. Since the primary beam direction varies, so does the diffraction space. Following the Bragg–Brentano geometry, we call this the vertical θ-θ configuration. In order to make the θ-θ configuration consistent with the previous definitions of the diffraction space and the detector space, we have $\omega = \theta_1$ and $\alpha = \theta_1 + \theta_2$. The other parameters keep the same definitions. In a commercial diffractometer for XRD[2], these conversions are typically done automatically by the software. Figure 2.15(c) and (d) are pictures of two Bruker AXS D8 Discover™ diffractometers in horizontal and vertical configurations respectively. The other configurations are not discussed here, but the same approaches should be followed.

2.5 TRANSFORMATION FROM DIFFRACTION SPACE TO SAMPLE SPACE

In two-dimensional diffraction data analysis, it is crucial to know the diffraction vector distribution in terms of the sample coordinates $\mathbf{S_1S_2S_3}$. However, the diffraction vector distribution corresponding to the measured 2D data is always given in terms of the laboratory coordinates $\mathbf{X_L Y_L Z_L}$ because the diffraction space is fixed to the laboratory coordinates. Figure 2.16 shows the unit vector of a diffraction vector in both (a) the laboratory coordinates $\mathbf{X_L Y_L Z_L}$ and (b) the sample coordinates $\mathbf{S_1S_2S_3}$. In Figure 2.16(a) the unit vector $\boldsymbol{h}_\mathbf{L}$ is projected to the $\mathbf{X_L}$, $\mathbf{Y_L}$, and $\mathbf{Z_L}$ axes as h_x, h_y, and h_z respectively. The three components are given by equation 2.7. In order to analyze the diffraction results respective to the sample orientation, it is necessary to transform the unit vector to the sample coordinates $\mathbf{S_1S_2S_3}$. Figure 2.16(b) shows the same unit vector in the sample coordinates, denoted by $\boldsymbol{h}_\mathbf{s}$ projected to $\mathbf{S_1}$, $\mathbf{S_2}$, and $\mathbf{S_3}$ as h_1, h_2 and h_3, respectively.

The angular relationships between the laboratory coordinates $\mathbf{X_L Y_L Z_L}$ and the sample coordinates $\mathbf{S_1S_2S_3}$ are

	X_L	Y_L	Z_L
S_1	a_{11}	a_{12}	a_{13}
S_2	a_{21}	a_{22}	a_{23}
S_3	a_{31}	a_{32}	a_{33}

(2.29)

Based on the Eulerian geometry defined above, the transformation matrix from the laboratory coordinates $\mathbf{X_L Y_L Z_L}$ to the sample coordinates $\mathbf{S_1S_2S_3}$ is

$$\boldsymbol{A} = \begin{bmatrix} a_{11} & a_{12} & a_{13} \\ a_{21} & a_{22} & a_{23} \\ a_{31} & a_{32} & a_{33} \end{bmatrix} = \begin{bmatrix} -\sin\omega\sin\psi\sin\phi & \cos\omega\sin\psi\sin\phi & -\cos\psi\sin\phi \\ -\cos\omega\cos\phi & -\sin\omega\cos\phi & \\ \sin\omega\sin\psi\cos\phi & -\cos\omega\sin\psi\cos\phi & \cos\psi\cos\phi \\ -\cos\omega\sin\phi & -\sin\omega\sin\phi & \\ -\sin\omega\cos\psi & \cos\omega\cos\psi & \sin\psi \end{bmatrix} \tag{2.30}$$

The unit vector $\boldsymbol{h}_s$ of the diffraction vector expressed in the sample coordinates $\mathbf{S_1S_2S_3}$ is then given by the transformation

$$\boldsymbol{h}_s = \boldsymbol{A}\boldsymbol{h}_L \tag{2.31}$$

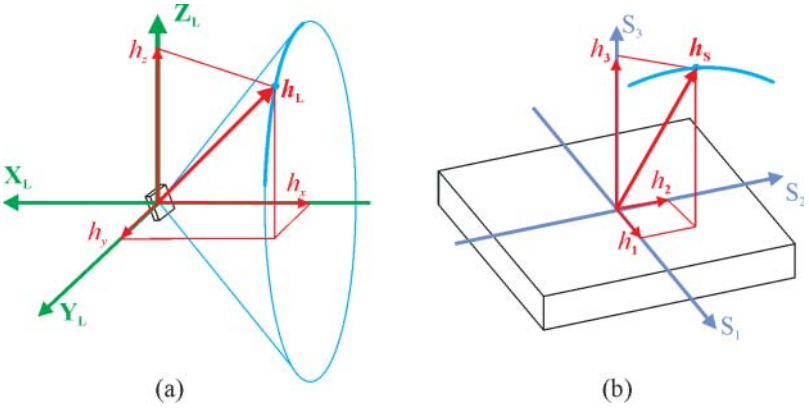


FIGURE 2.16 Unit vector of diffraction vector in (a) the laboratory coordinates $\mathbf{X_L Y_L Z_L}$ and (b) the sample coordinates $\mathbf{S_1S_2S_3}$.

In matrix form, we have

$$\begin{bmatrix} h_1 \\ h_2 \\ h_3 \end{bmatrix} = \begin{bmatrix} a_{11} & a_{12} & a_{13} \\ a_{21} & a_{22} & a_{23} \\ a_{31} & a_{32} & a_{33} \end{bmatrix} \begin{bmatrix} h_x \\ h_y \\ h_z \end{bmatrix}$$

$$= \begin{bmatrix} -\sin\omega\sin\psi\sin\phi & \cos\omega\sin\psi\sin\phi & -\cos\psi\sin\phi \\ -\cos\omega\cos\phi & -\sin\omega\cos\phi & \\ \sin\omega\sin\psi\cos\phi & -\cos\omega\sin\psi\cos\phi & \cos\psi\cos\phi \\ -\cos\omega\sin\phi & -\sin\omega\sin\phi & \\ -\sin\omega\cos\psi & \cos\omega\cos\psi & \sin\psi \end{bmatrix} \begin{bmatrix} -\sin\theta \\ -\cos\theta\sin\gamma \\ -\cos\theta\cos\gamma \end{bmatrix} \tag{2.32}$$

Or in expanded form

$$\begin{aligned} h_1 &= \sin\theta(\sin\phi\sin\psi\sin\omega + \cos\phi\cos\omega) + \cos\theta\cos\gamma\sin\phi\cos\psi \\ &\quad - \cos\theta\sin\gamma(\sin\phi\sin\psi\cos\omega - \cos\phi\sin\omega) \\ h_2 &= -\sin\theta(\cos\phi\sin\psi\sin\omega - \sin\phi\cos\omega) - \cos\theta\cos\gamma\cos\phi\cos\psi \\ &\quad + \cos\theta\sin\gamma(\cos\phi\sin\psi\cos\omega + \sin\phi\sin\omega) \\ h_3 &= \sin\theta\cos\psi\sin\omega - \cos\theta\sin\gamma\cos\psi\cos\omega - \cos\theta\cos\gamma\sin\psi \end{aligned} \tag{2.33}$$

As three components of the unit diffraction vector, we also have the condition

$$h_1^2 + h_2^2 + h_3^2 = 1 \tag{2.34}$$

Therefore, there are only two independent components to specify a unit diffraction vector. But for convenience and simplicity we will use all three components explicitly when necessary. In addition to the diffraction intensity and Bragg angle corresponding to each data point on the diffraction ring, the unit vector $\mathbf{h_s}\{h_1, h_2, h_3\}$ provides orientation information in the sample space. Since a diffraction vector is always perpendicular to the corresponding crystal planes, the unit diffraction vector and its expression in the sample coordinates is mostly used for analyzing orientation-sensitive diffraction data, texture, or stress for instance. It should be noted that in the above transformation equations, while θ is always a positive value, all other variables (γ, ω, ψ, and ϕ) may take positive or negative values. These variables appear as both sine function, which is an odd function, and cosine function, which is even. The unit vector components $\{h_1, h_2, h_3\}$ equations contain both odd and even functions. That means that if any of the above variables is given in a wrong sign, the resulting unit vector components will neither be symmetric nor identical to the correct results. Therefore, the rotation direction of goniometer angles (ω, ψ, and ϕ) cannot be mistakenly reversed. This will be further explored later in the book, in stress and texture analysis. The transformation matrix of any other goniometer geometry, such as kappa geometry [3, 4, 8, 11, 13], can be introduced into equation 2.31 so that the unit vector $\mathbf{h_s}\{h_1, h_2, h_3\}$ can be expressed in terms of the specified geometry. All equations using the unit vector $\mathbf{h_s}\{h_1, h_2, h_3\}$ in the following chapters, such as data treatment, texture analysis, and stress measurement, are applicable to all goniometer geometries provided that the unit vector components are generated from the corresponding transformation matrix from diffraction space to the sample space.

2.6 RECIPROCAL SPACE

The diffraction patterns displayed in reciprocal space have been frequently used to visualize or analyze samples with highly oriented structures, diffuse scattering from crystal defects, and thin films [14–17]. The equations of the unit vector calculation given above can also be used to transform the diffraction intensity from the diffraction space to the reciprocal space with respect to the sample coordinates. The direction of the scattering vector is given by the unit vector $\mathbf{h}_s\{h_1, h_2, h_3\}$ and the magnitude of the scattering vector is given by $2\sin\theta/\lambda$ so that the scattering vector corresponding to a pixel is given by

$$\boldsymbol{H} = \frac{2\sin\theta}{\lambda}\boldsymbol{h}_s \tag{2.35}$$

The three-dimensional reciprocal space mapping can be obtained by applying the pixel intensities to the corresponding reciprocal points. With various sample orientations, all pixels on the detector and all possible 2θ angles from 0 to π, the reciprocal space mapping can cover the three-dimensional reciprocal space within a sphere of maximum radius of $2/\lambda$ (limiting sphere).

Figure 2.17(a) shows the coverage of a 2D detector on the Ewald sphere. For an arbitrary spot P within the coverage, both incident beam vector $\mathbf{s}_0/\lambda$ and diffracted beam vector $\mathbf{s}/\lambda$ start at point C, but end at points O and P respectively. The angle between the incident beam and diffracted beam is 2θ. The vector from O to P is the diffraction vector $\boldsymbol{H}$. The diffracted beam vector and the diffraction vector meet at the point P on the surface of the Ewald sphere. Considering the diffraction vectors corresponding to all the pixels of the 2D detector, the coverage of the 2D diffraction can be mapped on the surface of the Ewald sphere. For simplicity, the areas are marked within the angular ranges of $\Delta 2\theta$ and $\Delta\gamma$. The actual coverage depends on the size and shape of the detector, but it is not likely to have such a simple boundary, taking the γ-2θ plot in Figure 1.17(b) from Chapter 1 as an example. Figure 2.17(b) illustrates the coverage of three diffraction frames with the incident X-ray in different orientations relative to the sample orientation. The different orientation can be achieved by changing any one or a combination of the Eulerian angles

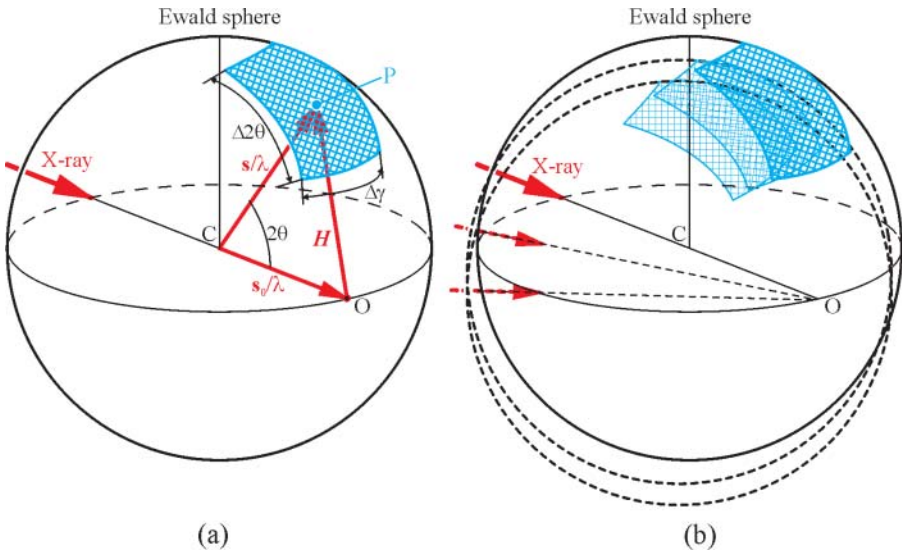


FIGURE 2.17 Two-dimensional detector coverage on Ewald sphere: (a) single frame covers a surface area on Ewald sphere, (b) multiple frames at various sample orientation cover a volume in reciprocal space.

(ω, ψ, ϕ). A three-dimensional mapping can be obtained in the reciprocal space from multiple frames collected by scanning the above angles.

2.7 SUMMARY

The definitions, parameters, and relationship between the three spaces are displayed in Figure 2.18. The laboratory coordinate system is the basis of all three spaces. The laboratory coordinates are determined by the primary X-ray beam and the main axes of the goniometer. The diffraction space is fixed in the laboratory coordinates. The diffraction pattern is distributed in the diffraction space, which is mainly defined by the sample crystal structure, material microstructure, and X-ray beam wavelength. The detector space is the angular coverage, resolution, and location of a detector in the laboratory coordinates. For a flat 2D, the detector space is determined by the detector size, pixel resolution, distance, swing angle, and possibly azimuthal angle. The sample space is defined by the sample location and orientation. Selection of detector space parameters should be based on the diffraction space. Changing the detector space parameters changes the part of the diffraction space to be measured and the measurement resolution, but not the diffraction space itself. For an ideal powder (polycrystalline) sample without stress and preferred orientation, the diffraction pattern is independent of the sample orientation and the measurement location on the sample. Changing the sample space parameters for a sample with texture, stress, or inhomogeneous microstructure will affect the intensity distribution of the diffraction pattern, but not the diffraction space parameter. It is very important to note that the detector space and sample space are two independent spaces and cannot be mutually replaced. For instance, no motion of the detector can change the angular relationship between the sample

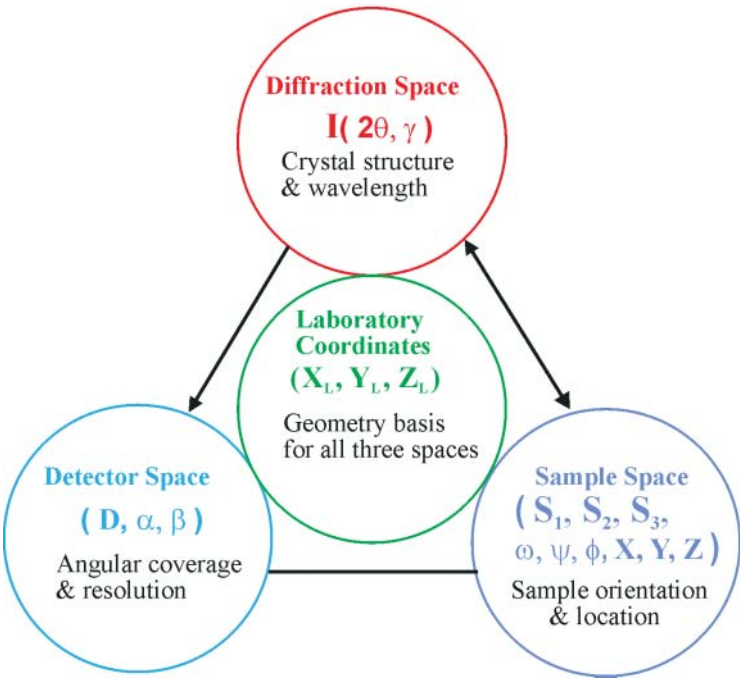


FIGURE 2.18 Relationship between the three spaces and the laboratory coordinates.

orientation and the incident X-ray beam. It is still necessary to rotate the sample for a particular diffraction condition even with a complete coverage of the 4π diffraction space.

Figure 2.19 illustrates the relationship between the fundamental equations. The diffraction condition in vector form in the green circle can be considered as the basis of all the other equations. Laue equations, expressed with three lattice axes **a**, **b**, and **c** in the top left blue circle, are suitable to describe the diffraction geometry of a single crystal. Bragg's Law, derived from the magnitude of the diffraction vector equation, defines the relationship between the crystal d-spacing, 2θ angle, and wavelength. Bragg's law is more conveniently used for powder diffraction with large amounts of randomly oriented fine crystallites. A 2D diffraction pattern contains the intensity distribution as a function of both 2θ and γ, so that the diffraction condition in the vector form

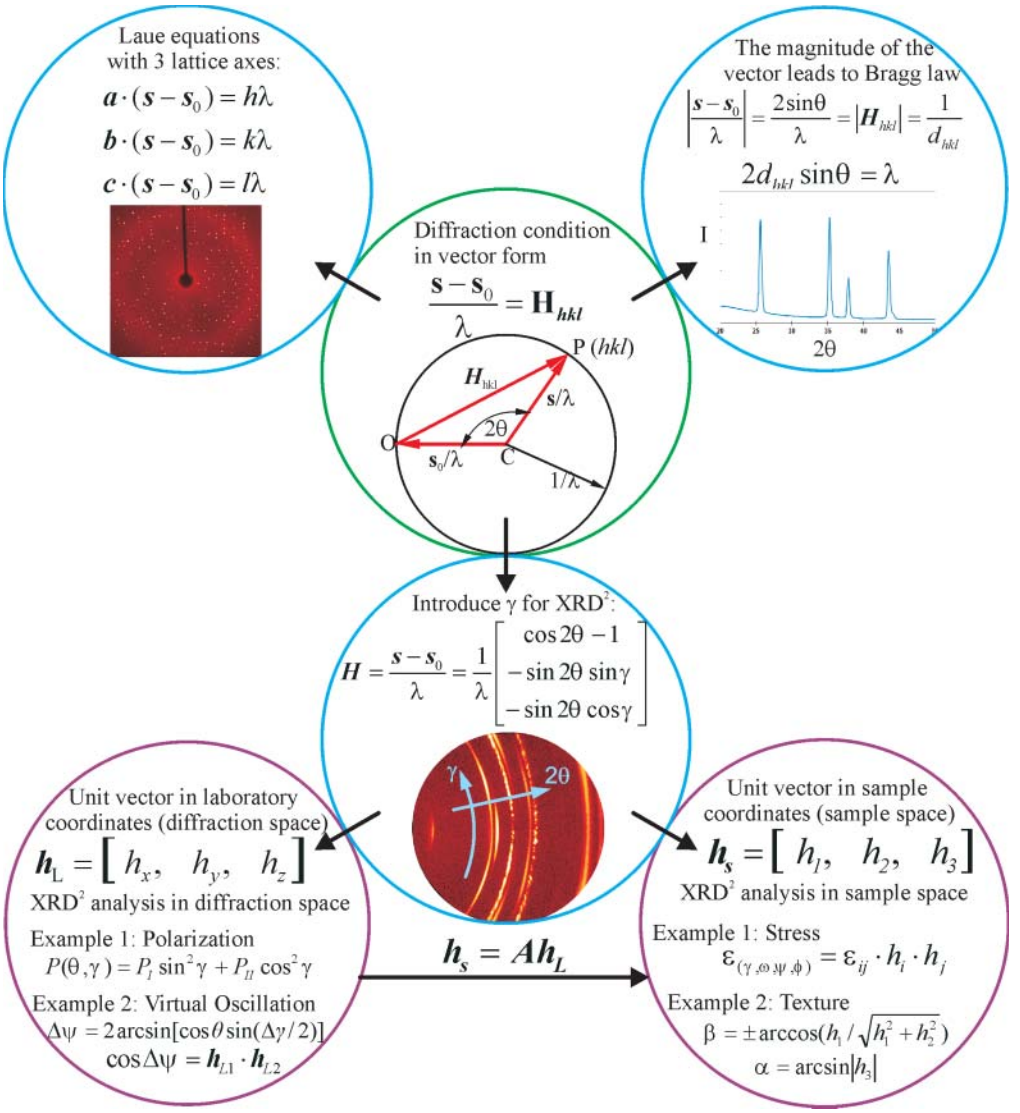


FIGURE 2.19 Relationship between the fundamental equations.

can be expressed as a function of both 2θ and γ (blue circle in the center). This expression serves as a fundamental relationship for two-dimensional diffraction. In the left bottom purple circle, the two-dimensional diffraction vector can be further reduced to the unit diffraction vector in the laboratory coordinates ($\boldsymbol{h}_{\mathbf{L}}$). The unit vector $\boldsymbol{h}_{\mathbf{L}}$ does not contain the sample orientation information. Therefore, it can be used to derive data evaluation equations not directly related to the sample orientation. Derivations of the polarization equation and virtual oscillation equation are two examples. In the right bottom purple circle, the unit diffraction vector $\boldsymbol{h}_{\mathbf{L}}$ is transformed into the unit vector in the sample coordinates ($\boldsymbol{h}_{\mathbf{S}}$). The unit vector $\boldsymbol{h}_{\mathbf{S}}$ contains the sample orientation information. Therefore, it can be used to derive fundamental equations for applications directly related to the sample orientation, stress, texture, and reciprocal space mapping, for instance. The details of the description and the steps for each application are further explored in the following chapters.

REFERENCES

1. B. B. He, Introduction to two-dimensional X-ray diffraction, *Powder Diffraction*, **18** (2), June 2003, 71–85.
2. W. Busing and H. A. Levy, Angle calculations for 3- and 4-circle X-ray and neutron diffractometers, *Acta Cryst.* (1967). **22**, 457–464.
3. W. R. Massey Jr. and P. C. Manor, A four-circle single crystal diffractometer with a rotating anode source, *J. Appl. Cryst.* (1976). **9**, 119–125.
4. D. J. Thomas, Modern equations of diffractometry. Goniometry, *Acta Cryst.* (1990). **A46**, 321–343.
5. D. J. Thomas, Modern equations of diffractometry. Diffraction geometry, *Acta Cryst.* (1992). **A48**, 134–158.
6. M. Lohmeier and E. Vlieg, Angle calculations for a six-circle surface X-ray diffractometer, *J. Appl. Cryst.* (1993). **26**, 706–716.
7. E. Vlieg, Integrated intensities using a six-circle surface X-ray diffractometer, *J. Appl. Cryst.* (1997). **30**, 532–543.
8. P. Dera and A. Katrusiak, Towards general diffractometry. I. Normal-beam equatorial geometry, *Acta Cryst*. (1998). **A54**, 653–660.
9. H. You, Angle calculations for a '4S + 2D' six-circle diffractometer, *J. Appl. Cryst.* (1999). **32**, 614–623.
10. P. Dera and A. Katrusiak, Towards general diffractometry. II. Unrestricted normal-beam equatorial geometry, *J. Appl. Cryst*. (1999). **32**, 193–196.
11. G. Thorkildsen, R. H. Mathiesen, and H. B. Larsen, Angle calculations for a six-circle κ diffractometer, *J. Appl. Cryst.* (1999). **32**, 943–950.
12. P. Dera and A. Katrusiak, Towards general diffractometry. III. Beyond the normal-beam geometry, *J. Appl. Cryst.* (2001). **34**, 27–32
13. G. Thorkildsen, H. B. Larsen, and J. A. Beukes, Angle calculations for a three-circle goniostat, *J. Appl. Cryst.* (2006). **39**, 151–157.
14. S. Hanna and A. H. Windle, A novel polymer fibre diffractometer, based on a scanning X-ray-sensitive charge-coupled device, *J. Appl. Cryst.* (1995). **28**, 673–689.
15. M. Schmidbauer et al., A novel multidetection technique for three-dimensional reciprocal-space mapping in grazing-incidence X-ray diffraction, *J. Synchrotron Rad.* (2008). **15**, 549–557.
16. D.-M. Smilgies and D. R. Blasini, Indexation scheme for oriented molecular thin films studied with grazing-incidence reciprocal-space mapping, *J. Appl. Cryst.* (2007). **40**, 716–718.
17. S. T. Mudie et al., Collection of reciprocal space maps using imaging plates at the Australian National Beamline Facility at the Photon Factory, *J. Synchrotron Rad.* (2004). **11**, 406–413.

3

X-RAY SOURCE AND OPTICS

3.1 X-RAY GENERATION AND CHARACTERISTICS

A variety of X-ray sources, from sealed X-ray tubes and rotating anode generators to synchrotron radiation can be used in X-ray diffraction. The sealed tube generator and rotating anode generator (RAG) produce X-ray radiation using the same physical principle. Electrons are emitted from the cathode, and accelerated by high voltages between the cathode and the anode. The anode is made of a selected metal, so it is also called a metal target. When the electron beam hits the target, X-rays are produced and radiate in all directions. This section will give a brief introduction to X-ray sources and X-ray optics related to two-dimensional X-ray diffraction. The history and principles of X-ray generation can be found in many sources [1, 2].

3.1.1 X-Ray Spectrum and Characteristic Lines

X-rays generated by sealed tube or rotating anode generators have a spectrum (intensity vs. wavelength) as shown in Figure 3.1 The polychromatic radiation consists of continuous radiation and a number of discrete characteristic lines. The continuous radiation is also called white radiation or *bremsstrahlung*. The shortest wavelength (highest energy) in the bremsstrahlung is called the short wavelength limit λ_{SWL}, which is given by

$$\lambda_{SWL} = \frac{12400}{V} \tag{3.1}$$

where V is the voltage applied to the X-ray generator. With increasing generator voltage, the intensity of the whole spectrum increases and the white radiation also extends to shorter wavelengths. For X-ray diffraction, the three most important characteristic lines are $K_{\alpha 1}$, $K_{\alpha 2}$ and K_{β}. The $K_{\alpha 1}$ and $K_{\alpha 2}$ lines are so close in wavelength that they are also called the K_{α} doublet. The $K_{\alpha 1}$ line is about twice the intensity of $K_{\alpha 2}$. When the $K_{\alpha 1}$ and $K_{\alpha 2}$ lines cannot be resolved,

Two-Dimensional X-Ray Diffraction, Second Edition. Bob Baoping He.
© 2018 John Wiley & Sons, Inc. Published 2018 by John Wiley & Sons, Inc.

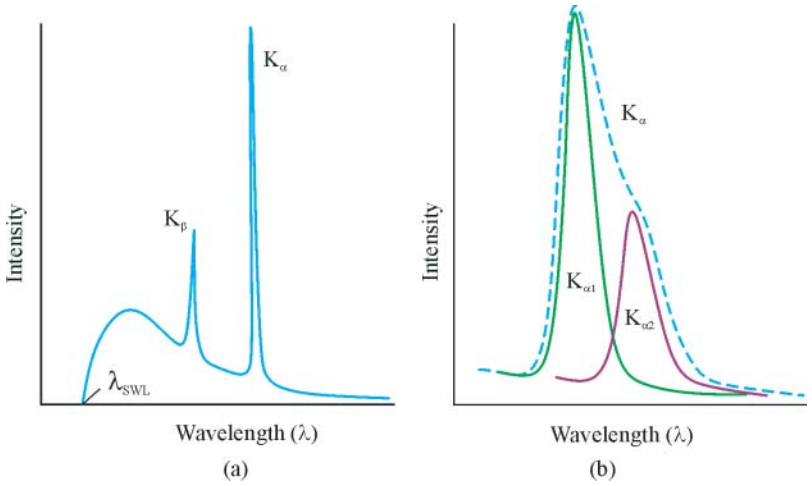


FIGURE 3.1 X-ray spectrum generated by a sealed X-ray tube or rotating anode generator: (a) spectrum consisting of continuous (white) radiation and characteristic radiation lines K_α and K_β, (b) K_α line as a combination of two lines $K_{\alpha1}$ and $K_{\alpha2}$.

Table 3.1 Wavelengths of Characteristic Lines of Common Anode Elements

	Energy (K_α)	Wavelength (Å = 10^{-1} nm)			
Anode	keV	K_α	$K_{\alpha1}$	$K_{\alpha2}$	K_β
Ag	22.11	0.560868	0.5594075	0.563789	0.497069
Mo	17.44	0.710730	0.709300	0.713590	0.632288
Cu	8.04	1.541838	1.540562	1.544390	1.392218
Co	6.93	1.790260	1.788965	1.792850	1.62079
Fe	6.40	1.937355	1.936042	1.939980	1.75661
Cr	5.41	2.29100	2.28970	2.293606	2.08487

they are simply referred to as the K_α line. The wavelengths of characteristic lines are determined by the target (anode) material of the X-ray generator. Table 3.1 gives a list of common anode materials, their average photon energy corresponding to the K_α line, and their wavelengths. Since the K_α line is the most intense characteristic line, the tube anode is typically chosen based on the wavelength of the K_α line. The longer the wavelength is, the larger the separation between diffraction peaks. Therefore fewer diffraction peaks can be measured within the limited 2θ range. The opposite is true with shorter wavelengths. The Cu-K_α radiation with a wavelength of 1.54 Å is the most frequently used in X-ray diffraction since the wavelength is suitable for applications of most polycrystalline materials. The other considerations include penetration and fluorescence. For example, the Ag-K_α and Mo-K_α radiations are used when the application demands deep penetration through the sample. The Co-K_α and Cr-K_α radiations are used for ferrous alloys (steels) to avoid Fe fluorescence. The longer wavelength of Cr-K_α radiation also gives better 2θ angular resolution in residual stress measurements.

3.1.2 Focal Spot and Takeoff Angle

In sealed tube and rotating anode generators, X-rays are produced by the bombardment of the anode with electrons generated from the filament (cathode). The schematic of a sealed X-ray tube

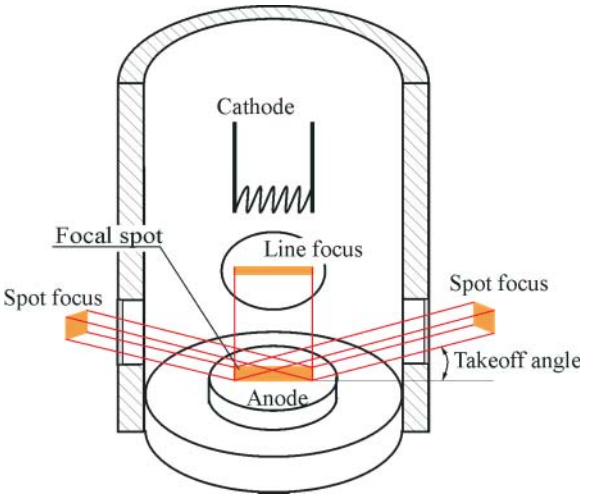


FIGURE 3.2 Schematic of a sealed X-ray tube showing filament (cathode), anode, focal spot on anode, takeoff angle, line focus projection, and spot focus projection.

Table 3.2 Focal Spot Size, Line Focus Size, and Spot Focus Size of Some Typical X-ray Tubes

Tube type	Focal spot size	Line focus size	Spot focus size
Normal focus	1 mm × 10 mm	0.1 mm × 10 mm	1 mm × 1 mm
Fine focus	0.4 mm × 8 mm	0.04 mm × 8 mm	0.4 mm × 0.8 mm
Long fine focus	0.4 mm × 12 mm	0.04 mm × 12 mm	0.4 mm × 1.2 mm
Microfocus	0.15 mm × 8 mm	0.015 mm × 8 mm	0.15 mm × 0.8 mm

is shown in Figure 3.2. The area on the anode bombarded by electrons is called the focal spot. The size and shape of the focal spot is one of the most important features for an X-ray generator. The focal spot is typically extended in one direction along the filament direction. The projection along the length at a takeoff angle from the anode surface is the spot focus, also called square focus or point focus. The projection of the focal spot perpendicular to the length is the line focus. The line focus and spot focus are separated by 90° around the tube cylinder. Sealed X-ray tubes normally have 2 to 4 beryllium windows to emit X-rays. The line focus is commonly used for a conventional diffractometer with point or line detectors. A two-dimensional X-ray diffraction (XRD^2) system typically uses the spot focus. The takeoff angle can be set from 3° to 7°, with 6° for most systems. Table 3.2 lists focal spot size, line focus size, and spot focus size at 6° takeoff angle for some typical sealed X-ray tubes.

3.1.3 Focal Spot Brightness and Profile

The X-ray beam intensity depends on X-ray optics, focal spot brightness, and focal spot profile. X-ray optics will be discussed in the next section. X-ray generation in sealed tube and rotation anode is very inefficient. Only about 0.1% of power applied to the generator is converted to X-rays, with the rest transformed to heat. Therefore, cooling water circulation is typically provided to the generator to avoid the meltdown of the anode. Depending on the cooling efficiency, only limited power can be applied to an X-ray generator. The total amount of X-rays generated is proportional to the total power load on the anode. The focal spot brilliance is determined by

Table 3.3 Focal Spot Brilliance for Sealed Tubes, Rotating Anode Generators, and Microsources with Cu Anode and Metal Jet with Ga Anode

Source	Focal spot (mm^2)	Max. load (kW)	Specific loading (kW/mm^2)
Sealed tube: normal focus	1 × 10	2.0	0.2
Sealed tube: fine focus	0.4 × 8	1.5	0.5
Sealed tube: long fine focus	0.4 × 12	2.2	0.5
Sealed tube: microfocus	0.15 × 8	0.8	0.7
Rotating anode generator	0.5 × 10	18.0	3.6
	0.3 × 3	5.4	6.0
	0.2 × 2	3.0	7.5
	0.1 × 1	1.2	12.0
Microsource	0.01~0.05	<0.05	5~50
Liquid metal jet	0.005~0.040	<0.3	300~2500

the maximum target loading per unit area of the focal spot, also referred to as the specific loading. Table 3.3 gives the maximum target loading and specific loading (relative brilliance) for some typical sealed tubes, rotating anode sources, and microsource with a Cu target. It can be seen that microfocus sealed tubes have the brightest focal spot among all sealed tubes. Rotating anode generators, with more efficient cooling, have very high brilliance compared with sealed tubes.

The intensity over the focal spot is not evenly distributed. The focal spot profile is eventually translated to the beam profile. The beam profile is sometimes very important to the diffraction result. The focal spot profile across the beam from fine focus and long fine focus sealed tubes are typically saddled in the center with the maximum near the edge. The intensity at the center can be as low as 50% of the maximum. The focal spot profile for RAG is normally more evenly distributed, like a flat-topped Gaussian distribution. The focal profile from a fine focus or long fine focus sealed tube can satisfy most XRD[2] applications.

The latest type of microfocus sealed tubes, also called microsources, have been introduced to the XRD field thanks to several technical innovations [3–5]. The microsource tube has a very small focal spot size in the range of 10 to 50 μm. The tube is typically air cooled because the X-ray generator power is less than 50 W. The brilliance of a microsource can be as much as one to two orders of magnitude higher than a conventional fine focus sealed tube. The X-ray optics for a microsource, either multilayer or polycapillary, are typically mounted very close to the focal spot so as to maximize the gain on the capture angle.

The most powerful laboratory X-ray source is based on liquid metal jet anode [6, 7]. The brilliance of an X-ray generator is proportional to the specific power loading on the anode. For an X-ray generator with a solid anode, the power loading is limited by the surface temperature of the anode which must be well below the melting point in order to avoid damage. The liquid-metal-jet anode does not have such a limitation due to the target material already being in the liquid state. In order to reach different X-ray emission lines, different metal alloys are used. Gallium (Ga) rich alloy and indium (In) rich alloy are typically used as anode materials since both alloys are in liquid state at, near or below room temperature. The Ga rich alloy has K_α emission of 9.2 keV, which is suitable for applications normally using the copper (Cu) K_α radiation at 8.0 keV. The In rich alloy has K_α emission of 24.2 keV which is close to the silver (Ag) K_α emission line at 22.1 keV. The focal spot size in diameter, maximum target loading and specific loading (relative brilliance) for liquid metal jet with Ga alloy anode are added to the Table 3.3 for comparison. The combination of high brilliance and fine focus makes the liquid metal jet source the most powerful

X-ray source for X-ray image and X-ray diffraction with small single crystal, small sample area, and small quantity.

Correct and careful operation of an X-ray generator is critical for satisfactory performance of a diffractometer. All X-ray tubes have a maximum power rating which defines the highest power input to the tube. A cathode current vs. anode voltage chart (or table) is normally supplied for a sealed tube or RAG. The tube filament current is also given by the tube vendors. The following practices should be adapted in order to increase the lift time of a generator. The cooling system should be checked for the specified temperature, pressure, and flow rate before powering up the generator. When increasing the generator power manually, always increase voltage first and increase current afterward. When reducing the generator power, always reduce the current first and then the voltage. In order to increase the lifetime of X-ray tubes, run the generator at full power only if it is necessary, and set the generator to standby mode if the generator is not in use for an extended time.

3.1.4 Absorption and Fluorescence

When X-rays pass through matter of any form, whether gas, liquid, or solid, only part of the X-rays are transmitted; the other part of the X-rays are absorbed. The intensity of the transmitted X-rays from a homogenous substance is given as

$$\boxed{I = I_0 e^{-\mu t}} \tag{3.2}$$

where I_0 is the intensity of the incident X-ray beam, I is the intensity of the transmitted beam, μ is the linear absorption coefficient, and t is the thickness of the substance. The value of the linear absorption coefficient depends also on the density of the substance. A more consistent parameter for a specific element is called the mass absorption coefficient, which is equivalent to the linear absorption coefficient normalized by the density, and expressed as (μ/ρ). Here ρ is the density of the absorption substance. Equation (3.2) can then be written as

$$I = I_0 e^{-(\mu/\rho)\rho t} \tag{3.3}$$

Since the intensity of the transmitted X-ray beam is always less than that of the incident X-ray beam, the X-ray is attenuated by the material. Therefore the linear and mass absorption coefficients are also called the linear attenuation coefficient and the mass attenuation coefficient, respectively. The mass absorption coefficient of an element is dependent on the wavelength of the X-rays. The mass absorption coefficients (μ/ρ) of most elements for the four most commonly used X-rays (Mo-K_α, Mo-K_α, Mo-K_α, and Mo-K_α) can be found in Appendix A. The mass absorption coefficient of a material containing multiple elements is given by

$$\frac{\mu}{\rho} = \sum_{i=1}^{n} w_i \left(\frac{\mu}{\rho}\right)_i \tag{3.4}$$

where n is the total number of elements, w_i is the weight fractions, and $(\mu/\rho)_i$ is the mass absorption coefficient of the i-th element.

The loss of intensity of an X-ray beam transmitted through materials is due to many physical processes, including the emission of photoelectrons, Auger electrons, Compton recoil electrons, coherent scattered X-rays in the same wavelength, and incoherent scattered X-rays, also known as Compton scattering, which has a slightly longer wavelength than the incident X-rays. A substantial amount of absorption occurs when the energy of the X-ray photons is high enough to eject electrons from one of the electron shells. The fluorescent radiation is emitted when the

outer electrons fall into the vacancies of electron shells. If the mass absorption coefficient of an element is plotted against the wavelength, the mass absorption coefficient generally decreases with decreasing wavelength except at certain wavelengths where the mass absorption coefficient increases dramatically. These sharp discontinuities in the absorption are called critical absorption edges of the material. The most relevant absorption edge is the K absorption edge, which is at a wavelength slightly shorter than the K_β line. If the X-rays used for diffraction have a wavelength slightly shorter than the K absorption edge of the sample, it produces a significant amount of fluorescent radiation, which spreads over the diffraction pattern as a high background. The wavelength values of the K absorption edge for most elements can be found in Appendix A.

In order to avoid intensive fluorescence, the wavelength of the X-ray tube K_α line should either be longer than the K absorption edge of the sample or far away from the K absorption edge. For example, Cu-K_α should not be used for samples containing significant amount of iron or cobalt elements. Since the K_α line of an element cannot excite fluorescence of the same element, it is also safe to use the anode of the same metallic element as the sample if the X-ray tube is available, for instance Co-K_α for Co samples. In general, intensive fluorescence is produced when the atomic number of the anode material is 2, 3, or 4 larger than the sample elements. The effect is reduced when the atomic number difference increases. The fluorescence from Ag-K_α and Mo-K_α is not a big concern, but Mo-K_α excites Pb-L_1 fluorescence. Cu-K_α should avoid Co, Fe, and Mn, Co-K_α should avoid Mn, Cr, and V, and Cr-K_α should avoid Ti, Sc, and Ca.

3.1.5 Synchrotron Radiation

Synchrotron radiation is the electromagnetic radiation emitted when charged particles, such as electrons, are forced to travel in a curved path by a magnetic field. Synchrotron X-ray sources have many advantages over laboratory X-ray sources, including high intensity, tunable wavelength, and high collimation. The researchers in synchrotron radiation labs have pioneered the use of the 2D detector for XRD, and many ideas and devices were first developed in synchrotron radiation labs. Therefore, most theory, instrumentation, and applications discussed in this book apply to synchrotron sources. But it is worth mentioning some properties of synchrotron X-ray beams and their impact on two-dimensional X-ray diffraction.

Synchrotron sources have a broad spectrum, from microwaves to hard X-rays. Unlike the laboratory sources, which have limited number of wavelengths from the characteristic radiation of the metal target, a synchrotron beam can be tuned to a desired wavelength for the experiment by using crystal monochromators or multilayer mirrors. White radiation with a broad spectrum can be used for collecting Laue diffraction patterns. By tuning the beam energy (wavelength) through a given range, a three-dimensional reciprocal-space mapping can be constructed.

Synchrotron sources have high brightness and high intensity, many orders of magnitude higher than a typical laboratory X-ray source. Therefore, the 2D detectors used for synchrotron radiation should have high count rate. This allows much faster data collection, especially for in-situ or time-resolved studies. The high brightness, combined with high photon energy, means high penetration, so the synchrotron beam is the best choice for diffraction of materials inside an environmental stage, or under high pressure, such as in a diamond anvil cell. A small beam size in microns or at a submicron level with high photon flux is ideal for microdiffraction and diffraction mapping with high spatial resolution. The 2D detector used for synchrotron radiation should also have high radiation hardness to prevent detector damage or malfunction.

Because of the high brilliance, synchrotron X-rays can be collimated into a parallel beam with extremely small divergence. This is especially beneficial for high resolution powder diffraction, small angle X-ray scattering (SAXS), grazing-incidence small angle X-ray scattering (GISAXS), and ultra-small angle X-ray scattering (USAXS).

A synchrotron X-ray beam is highly polarized. The planar acceleration geometry makes the radiation linearly polarized when observed in the horizontal plane (orbital plane), and circularly polarized when observed at a small angle to that plane. The correction for polarization given in this book is based on laboratory sources. Caution must be given when the polarization correction is necessary for the data collected with a synchrotron beam. The instrument configuration may also need to be designed for a synchrotron beam, for example, a vertical θ-2θ configuration with the detector swing perpendicular to the horizontal plane.

A synchrotron X-ray beam is delivered in a fixed horizontal direction. The incident angle to the sample and the diffraction pattern coverage are established by sample rotation, 2D detector size, and position (distance and swing angle). Vertical θ-θ configuration and vertical transmission configuration cannot be achieved with a synchrotron beam.

3.2 X-RAY OPTICS

3.2.1 Liouville's Theorem and Fundamentals

The function of X-ray optics in X-ray diffraction is to condition the X-ray beam into a desired spectrum purity, intensity, divergence, cross-section size, and shape. The spectrum purity for a laboratory source is typically defined as the percentage of the X-rays within a given energy window in the vicinity of a K_α line or $K_{\alpha 1}$ line over the total amount of X-rays, including the bremsstrahlung and all characteristic lines. The intensity ratio of K_α line to K_β may also be used sometimes as a measurement of spectrum purity. The X-ray intensity should be defined within a specified bandwidth of wavelength ($\Delta\lambda$). For most laboratory sources, a given characteristic line implies a specific bandwidth. Therefore, it is not necessary to specify the value of $\Delta\lambda$. There are many parameters or definitions for describing the intensity of an X-ray beam. Four parameters are commonly used to describe the intensity of X-ray beams within a given bandwidth ($\Delta\lambda$). They are flux, fluence, brightness, and brilliance.

Flux is defined as the total number of X-ray photons passing a plane crossing the X-ray beam per unit time. The typical unit for flux is *photons/second* or *pps*. The flux is sometimes also referred to as the integrated intensity of the X-ray beam, or simply beam intensity.

Fluence is defined as the number of X-ray photons passing a unit area of the beam crossing plane per unit time. The typical unit is *photons/second·mm*^{2} or *pps/mm*^{2} An alternative, perhaps more popular, terminology for fluence is flux density. Fluence is also an appropriate parameter for measuring the local counting rate of area detectors.

Brightness is defined as the number of photons passing through a surface having unit solid angle. The typical unit is *photons/second·milliradian*^{2} or *pps/mrad*^{2}. Since no linear dimension is defined in brightness, it is more appropriate to be used for measuring the strength of X-ray emission from a point source. Brightness is an appropriate parameter to compare two sources of the same focal spot size.

Brilliance is defined as the number of photons passing through a unit area of surface within a unit solid angle. The typical unit is *photons/second·mm*^{2}*·milliradian*^{2} or *pps/mm*^{2}*·mrad*^{2}. Two X-ray beams may have the same fluence, but different brilliance if the two beams have different beam divergence. Brilliance is an appropriate parameter to compare two sources of different focal spot sizes. In many publications, there are no clear distinctions between brightness and brilliance, but the exact definitions and units should be recognized to avoid misleading conclusions.

The units of all the above four parameters contains photons per second (pps). An alternative unit, count per second (cps), may be used instead of pps. Although most publications do not

have a clear distinction between the two units, it must be noted that counts per second is not necessarily equivalent to photons per second unless the measurement counts are calibrated to one count per photon.

Liouville's theorem is the key theorem in describing the nature of the X-ray source, X-ray optics, and the coupling of the source and optics. Figure 3.3 shows the relationship between X-ray source, optics, and X-ray image on the sample as expressed by Liouville's theorem. This theorem states that the phase space distribution function is constant with time along the trajectories of the system. Liouville's theorem can be given in a variety of ways, but for X-ray optics, the most well-known form is [8]

$$S_1\alpha = S_2\beta \tag{3.5}$$

where S_1 is the effective size of the X-ray source, α is the capture angle, which is determined by the effective size of the X-ray optics and the distance between the source and optics, f_1. S_2 is the size of the image focus. β is the convergence angle of the X-ray beam from the optics, which is also determined by the effective size of the X-ray optics and the distance between the optics and the image focus, f_2. The β angle is also called the crossfire of the X-ray beam. The above parameters and equation (3.5) describe the condition within one plane along the X-ray beam and horizontal direction $\boldsymbol{x}$. The condition on another orthogonal plane along the X-ray beam and vertical direction $\boldsymbol{y}$ can be described by another set of parameters in the same or different values with the same equation. Considering the two-dimensional effect of the X-ray optics, the capture angle and crossfire can be expressed in solid angles given by the two planar angles in x and y directions

$$\Theta = \alpha_x\alpha_y \text{ and } \Phi = \beta_x\beta_y \tag{3.6}$$

Liouville's theorem can then be given as

$$A_1\Theta = A_2\Phi \tag{3.7}$$

where A_1 is the effective focal spot area of the X-ray source, Θ is the capture solid angle determined by the effective area of the X-ray optics and the distance between the source and optics, f_1. A_2 is the area of the image focus. Φ is the convergence solid angle of the X-ray beam from the optics, which is also determined by the effective area of the X-ray optics and the distance between the optics and the image focus, f_2.

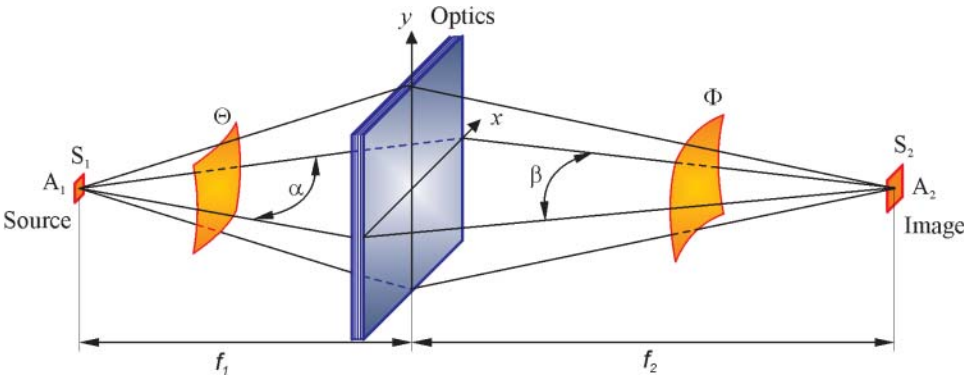


FIGURE 3.3 Schematics of X-ray source, optics, and X-ray image on the sample and their relationship expressed by Liouville's theorem.

S_2 and β are typically determined by experimental requirements such as beam size and divergence. Therefore, the product $S_1\alpha$ is also determined by experimental conditions. In another expression of Liouville's theorem, the density of states in phase space cannot increase. An increase in density is equivalent to an increase in the entropy of the system, which violates the second law of thermodynamics. Applying the expression in X-ray optics implies that the space volume containing the X-ray photons cannot be reduced with time along the trajectories of the system. Therefore, the brilliance of an X-ray source cannot be increased by optics, but may be reduced due to the loss of X-ray photons passing the optics. In practice, no optics can have 100% reflectivity or transmission. Considering this, Liouville's theorem given in equation (3.5) should be expressed as

$$S_1\alpha \leq S_2\beta \tag{3.8}$$

Similarly

$$A_1\Theta \leq A_2\Phi \tag{3.9}$$

This implies that the product of divergence and image size can be equal to or greater than the product of capture angle and source size. If the X-ray source is a point with zero area, the focus image from the focusing optics or the cross-section of a parallel beam can be any chosen size. For focusing optics, the source size must be considerably smaller than the output beam size in order to achieve a gain in flux. In this case the flux gain is from the increased capture angle. For parallel optics, the divergence angle β is infinitely small by definition, so that it is necessary to use an X-ray source as small as possible to achieve a parallel beam. Focusing optics have an advantage over parallel optics in terms of beam flux. Using an X-ray beam with a divergence much smaller than the mosaicity of the specimen crystal does not improve the resolution, but it does sacrifice the diffraction intensity. For many X-ray diffraction applications with polycrystalline materials, a large crossfire is acceptable as long as the concerned diffraction peaks can be resolved. The improved peak profile and counting statistics can most often compensate for the peak broadening due to large crossfire.

3.2.2 X-Ray Optics in Conventional Diffractometer

Most conventional X-ray diffractometers have the Bragg–Brentano parafocusing geometry [2, 9] as is shown in Figure 3.4. In the Bragg–Brentano geometry, the sample surface normal is always a bisector between the incident beam and the diffracted beam. In another word, the incident beam and diffracted beam are symmetric to the sample surface normal. This angular relationship can be achieved by scanning the θ_1 and θ_2 at the same speed in the θ-θ configuration or scanning 2θ at twice the speed of ω in the θ-2θ configuration. Figure 3.4(a) shows the X-ray beam path and components projected to the diffractometer plane. A divergent beam from the X-ray tube passes first through the soller slits 1 and the divergent slit, then hits the sample surface with an incident angle θ. The incident X-rays spread over the sample surface with various incident angles in the vicinity of θ. The area of the irradiated region depends on the incident angle θ and the beam divergence. The diffracted X-rays from the irradiated area leave the sample at an angle 2θ from the corresponding incident X-rays, pass through the antiscatter slit and soller slits 2, and focus at the receiving slit. A point X-ray detector can be mounted at the position right after the receiving slit or after a crystal monochromator. It can be seen that the beam-spread over the sample varies with the incident angle θ, but the diffracted beam is focused back to the receiving slit as long as the axis of the X-ray source line focus and the receiving slit are at the same distance from the instrument center (goniometer main axis). This distance, R, is referred to as the goniometer circle radius. There is another circle denoted by the dotted line passing through the source, the

sample surface, and the receiving slit. This circle is referred as the focusing circle. The radius of the focusing circle r_f varies with the 2θ angle in the following relation to the goniometer circle, R:

$$r_f = \frac{R}{2\sin\theta} \tag{3.10}$$

In order to have the divergent beam from the source perfectly focused back to the receiving slit, the sample surface should be a curved surface matching the focusing circle, but this is impossible since the focusing curve varies with 2θ. A typical flat sample will introduce an error depending on the 2θ angle, slit opening, and goniometer circle radius. This error is also referred to as the flat specimen aberration. This error can be controlled by proper selection of the divergence slit. A smaller aperture of the divergence slit is used for higher 2θ resolution and a larger aperture for fast data collection. Air scattering from the primary beam and diffracted beam may contribute to a high background in the diffraction pattern. The antiscatter slit prevents most air scattered X-rays from reaching the receiving slit.

The function of the soller slits can be better explained with the cross-section view of the diffractometer plane shown in Figure 3.4(b). The soller slits are made of equally spaced tantalum or molybdenum foils. The soller slits 1 on the primary beam side control the beam divergence in the goniometer axial direction. Due to the narrow spacing between the metal foils, the X-rays from the line focus source with high divergence in axial direction are blocked. The primary line beam sliced by the soller slits 1 can also be considered an array of point beams in parallel diffractometer planes. Each of these point beams will produce a diffraction cone from the sample. The diffraction cone extends out from the diffractometer plane. The aperture of the receiving slit in the goniometer axial direction is typically the same size as the line focus source. If the diffraction cone in the range of the receiving slit is measured, the overlap of all the diffraction cones will create a smeared diffraction peak. The diffracted beam along the diffraction cone makes an angle with the diffractometer plane, except for the part of the cone near the diffractometer plane. The soller slits 2 in the receiving side allow only those diffracted beams nearly parallel to the diffractometer plane to pass through, so the smearing effect is eliminated.

The radiation spectrum from the X-ray tube contains white radiation and several characteristic radiations. If there is no monochromator on the primary side, all wavelengths of the spectrum will diffract from the sample when Bragg's law is satisfied. In order to collect a diffraction pattern from a single wavelength, for instance from the K_α line, a crystal monochromator is installed before the detector. This monochromator is also called a diffracted-beam monochromator. The receiving slit, monochromator crystal, and detector are so positioned that only the K_α line or the $K_{\alpha 1}$ line satisfy the Bragg law. The diffracted X-rays from other wavelengths are blocked by the monochromator. Another important function of the diffracted-beam monochromator is to block the fluorescence radiation from the sample since the wavelength of the fluorescence is different from the K_α line.

Figure 3.5 shows a diffractometer with a point detector in the parallel beam geometry. A single parabolic bent Göbel mirror transforms the divergent primary beam from the source into a parallel beam. The Göbel mirror is a multilayer mirror that serves also as a monochromator, so that the incident parallel beam is a single wavelength X-ray beam. The incident X-rays spread over the sample surface with the same incident angle θ. The surface of the irradiated region can either be flat or uneven, but only the diffracted X-rays in the direction of 2θ defined by the soller slits can reach the point detector. It is noticeable that the soller slits have an orientation different from the soller slits in the Bragg–Brentano geometry. In the Bragg–Brentano geometry, the foils in the soller slits are parallel to the diffractometer plane, while in the parallel beam geometry the foils are perpendicular to the diffractometer plane and are aligned in the direction between the instrument

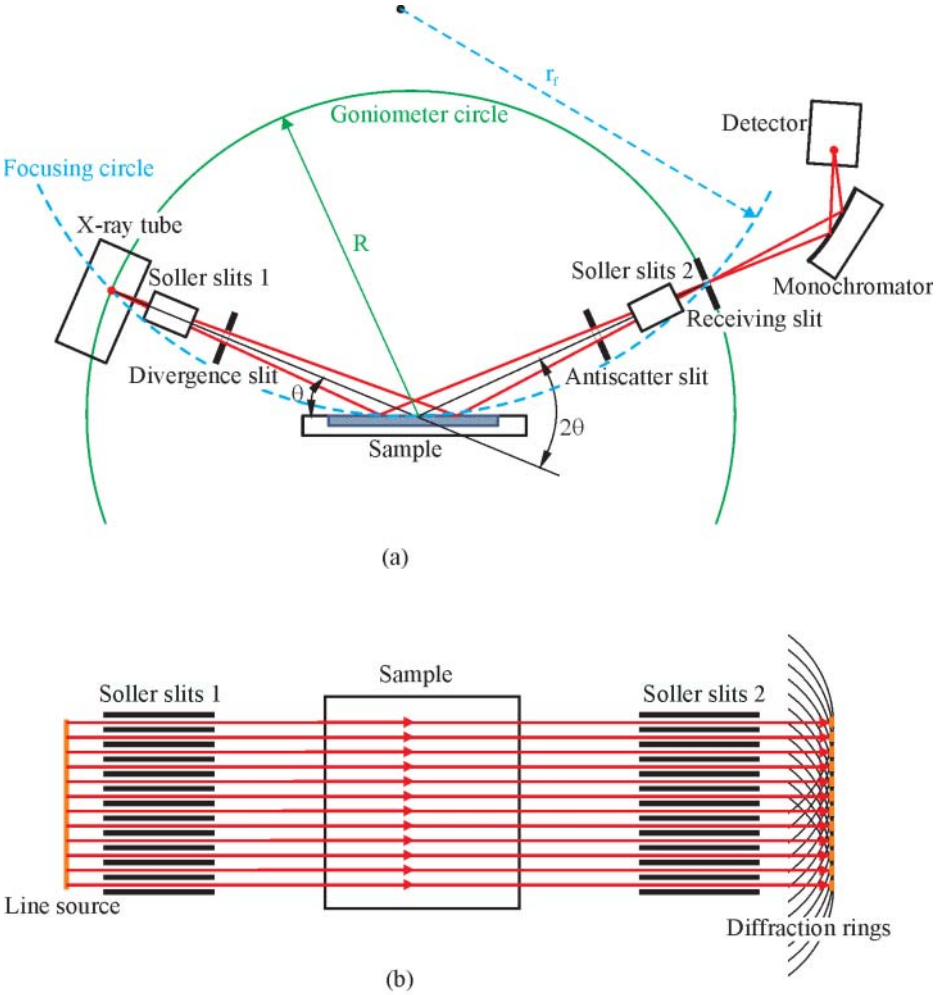


FIGURE 3.4 Conventional diffractometer in the Bragg–Brentano geometry: (a) Components arrangement projected in the diffractometer plane, (b) Axial divergence controlled by the soller slits.

center and the detector. The soller slits here also cover the entire active area of the detector so that only the X-rays of the same direction can reach the detector. Therefore, the diffractometer with parallel beam geometry is not sensitive to the surface roughness of the sample. This is especially beneficial when collecting diffraction data from samples with a rough, uncertain, or variable sample surface enclosed in an environment chamber. The goniometer circle in the parallel geometry is not restricted to a particular definition. It may be referenced only for practical reasons. There is actually no focusing circle in the parallel geometry. The source and detector do not have to be the same distance from the sample in the parallel geometry. The Göbel mirror can only collimate the beam in planes parallel to the diffractometer plane. In order to remove the axial divergence, soller slits in either or both the incident and diffracted beam side may be used in the same way as in the Bragg–Brentano geometry. The soller slits in the incident beam can be mounted right after the mirror as shown by the dotted-line box. For parallel geometry, no specific goniometer circle radius has to be maintained.

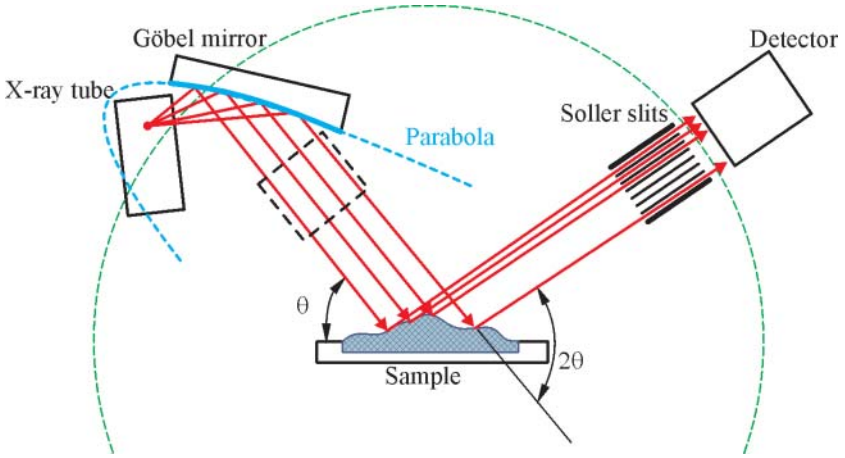


FIGURE 3.5 Conventional diffractometer in parallel beam geometry.

3.2.3 X-Ray Optics in a Two-Dimensional Diffractometer

In a two-dimensional X-ray diffraction (XRD^2) system the whole or a large portion of the diffraction rings are measured simultaneously. Therefore, the requirements for X-ray optics are different from the conventional diffractometer in many respects. In an XRD^2 system, the diffracted X-rays are measured simultaneously in a two-dimensional range so that neither the Bragg–Brentano geometry nor the parallel geometry with detector soller slits can be used. The beam-spread over the sample surface cannot be focused back to the detector, so most of the time a collimated point beam is used. Therefore, X-ray optics for XRD^2 systems have different requirements in terms of the beam spectrum purity, divergence, and beam cross-section profile. Figure 3.6 shows the X-ray optics in an XRD^2 system with the θ-θ configuration. The X-ray tube, monochromator, and collimator assembly are mounted on one of the two main axes. In a conventional diffraction system, the monochromator can be used on either the source side or the detector side, or both sides, while it is only possible to have a monochromator on the source side for an XRD^2 system.

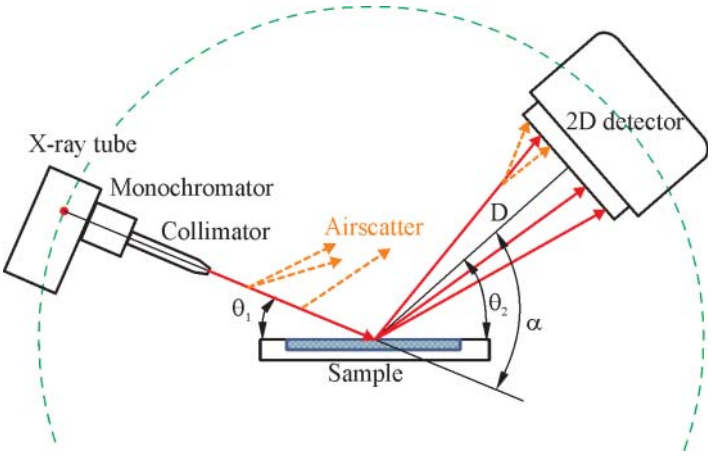


FIGURE 3.6 X-ray optics in an XRD^2 system.

The incident beam from the assembly rotates about the instrument center and makes an incident angle θ_1 from the sample surface. The first main axis is also called the θ_1 axis. The diffracted beams travel in all directions and some are intercepted by a 2D detector. The detector is mounted on the other main axis, θ_2. The detector position is determined by the sample-to-detector distance D and the detector swing angle α ($= \theta_1 + \theta_2$). In most XRD^2 diffractometers, the source-to-the sample and the sample-to-detector distance can be changed manually or automatically, therefore no particular goniometer circle radius is specified.

All the components and space between the focal spot of the X-ray tube and the sample are collectively referred to as the primary beam path. The primary beam path in an XRD^2 system is typically sheltered by optical components except between the exit of the collimator and the sample. The X-rays traveling through this open incident beam path are scattered by the air with two adverse effects. One is the attenuation of the primary beam intensity. The more harmful effect is that the scattered X-rays travel in all directions and some reach the detector, as is shown by the dotted lines with arrows. This air scatter introduces a background over the diffraction pattern. Weak diffraction patterns may be buried under the background. Obviously, the air scatter from the incident beam is significantly stronger than that from diffracted X-rays. The intensity of the air scatter from the incident beam is proportional to the length of the open incident beam path. The effect of air scatter also depends on the wavelength of the X-rays. The longer the wavelength, the more severe is the air scatter effect. The secondary beam path is the space between the sample and the 2D detector. The diffracted X-rays are also scattered by air so that the diffraction pattern is both attenuated and blurred by the air scattering. In the conventional diffractometer, one can use an antiscatter slit, diffracted beam monochromator or detector soller slits to remove most air scatter not traveling in the diffracted beam direction. These measures cannot be used for an XRD^2 system, which requires an open space between the sample and the 2D detector. Therefore, the open incident beam path should be kept as small as possible. In order to reduce the air attenuation and air scatter of the incident beam, a helium purged beam path or a vacuum beam path are sometimes used in a diffractometer. The air scatter from the diffracted X-rays is relatively weak and the effect depends on sample-to-detector distance. It is typically not necessary to take measures to remove air scatter from the diffracted X-rays between the sample and 2D detector if the sample-to-detector distance is 30 cm or less with Cu-K_α radiation. However, if the sample-to-detector distance is larger than 30 cm or a longer wavelength, such as Co-K_α or Cr-K_α radiations, is used, it is then necessary to use a He beam-path or vacuum beam-path to reduce the air scatter.

Radiation fluorescence is another source of intensity background in XRD^2, especially when the X-ray energy of the incident beam is slightly higher than the absorption edge of the sample elements, for example, when Cu-K_α radiation is used for iron or ferrous alloys. In a conventional diffractometer, fluorescence can be removed by a diffracted beam monochromator, or an energy discrimination device. However, most two-dimensional detectors have a very limited energy resolution and it is impossible to add a diffracted beam monochromator in front of the 2D detector. The best way to avoid fluorescence is to choose a tube anode having K_α energy lower than the absorption edge of the sample materials. For example, Cr-K_α can be used for ferrous alloys.

Since the secondary beam-path in an XRD^2 system is an open space, almost all X-ray optics components are on the primary side. The function of the X-ray optics is to condition the primary X-ray beam into the required wavelength, beam focus size, beam profile, and divergence. The X-ray optics components commonly used for XRD^2 systems are a monochromator, pinhole collimator, cross-coupled multilayer mirrors, polycapillaries, and monocapillaries. Figure 3.7 shows a sketch of an X-ray optics assembly used in an XRD^2 system (GADDS™ – from Bruker AXS), which includes an X-ray tube, tube mount, monochromator, labyrinth, collimator, collimator mount, and beamstop. It also shows the instrument center, which is the rotation center of the goniometer and also the location of the sample. The tube mount provides the necessary rotation

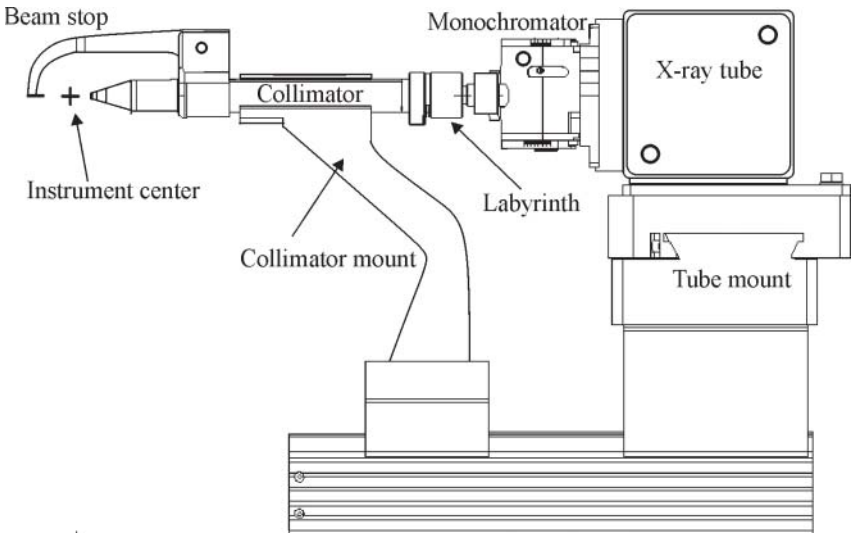


FIGURE 3.7 Typical X-ray optics in standard GADDS (courtesy of Bruker AXS) includes X-ray tube, monochromator, collimator, and beamstop .

and translation so that the X-ray tube can be aligned to an appropriate position and takeoff angle. The monochromator eliminates the white radiation and K_β line and allows only the K_α line to pass through the prealigned collimator and reach the instrument center. The labyrinth provides a flexible connection between monochromator and collimator so that the X-ray tube and monochromator can be adjusted without affecting the prealigned collimator. The labyrinth traps the X-ray radiation inside the beam path to prevent radiation leakage from the gap between the coupling optics. The collimator alignment is maintained by the prealigned collimator mount so that collimators of various pinhole sizes can be exchanged without losing the alignment. The collimator pinhole size is selected based on the sample condition and application. A large pinhole collimator can deliver a large X-ray beam size, i.e. higher X-ray flux, which is good for fast data collection and better sampling statistics. The smaller pinhole collimation enables small samples to be examined (microdiffraction) or small regions on a large sample (selected-area diffraction or diffraction mapping). The beamstop is used in transmission mode to prevent the direct beam from striking the detector. This configuration enables crystallographic phase, texture, and residual stress to be measured from precise locations on irregularly shaped parts, including curved surfaces.

In principle, the cross-sectional shape of the X-ray beam used in a two-dimensional diffraction system should be small and round. In data analysis algorithms, the beam size is typically considered a point. In practice, the beam cross-section can be either round, square, or other shape in limited size. If the beam shape is not round or square, the beam size measured at two extremes should be close enough so that the beam can be approximated as a point without introducing significant error or smearing effect. Such an X-ray beam is typically collimated or conditioned by the X-ray optics in two perpendicular directions, so that the X-ray optics used for the point beam is often call two-dimensional X-ray optics. In a conventional diffraction system, a line focus beam is typically used since the diffraction variation perpendicular to the diffractometer plane is not considered. However, if a line focus beam is used in a two-dimensional diffraction system, the smearing effect will dramatically increase the peak width, especially at γ angles away from the diffractometer plane ($\gamma = 90°$ and $\gamma = 270°$). Figure 3.8(a) shows a diffraction frame of corundum, collected with a line-shaped beam. The diffraction rings are broadened at the portion away from

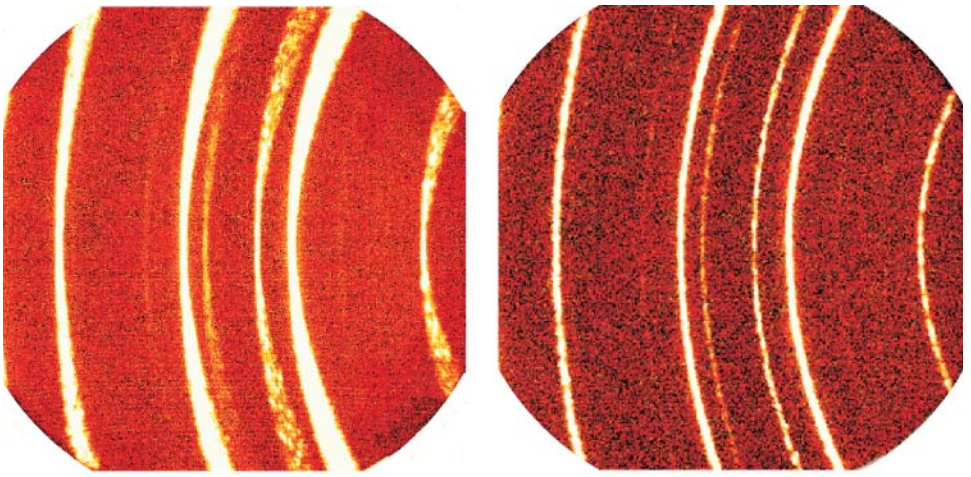


FIGURE 3.8 Diffraction frame from corundum powder: (a) smearing effect from line beam, (b) diffraction rings from point beam.

the diffractometer plane. As a comparison, Figure 3.8(b) shows the diffraction frame collected with a point beam; no smearing effect is observed and so all of the diffraction rings can be used for data analysis. Therefore, in an XRD^2 system the spot focus of the X-ray tube or rotating anode generator should be used. The X-ray optics and collimator should condition the X-ray beam in two dimensions perpendicular to the beam direction.

3.2.4 The β-Filter

As mentioned earlier, X-rays generated from a sealed X-ray tube or rotating anode generator consist of white radiation and characteristic radiation lines, typically a strong K_α line and a relatively weak K_β line. For most X-ray diffraction applications, only one specific characteristic line, typically K_α, is needed. The K_β line produces extra diffraction peaks (rings) in the diffraction pattern. The relative intensity of the K_α line to the K_β line can be enhanced by adding a material with absorption edge between the wavelengths of the K_α and K_β lines. The material inserted in the beam path with the given absorption edge is called a β-filter. Figure 3.9 shows the effect of a β-filter. The dashed line is the mass absorption coefficient of the β-filter. Figure 3.9(a) is the original spectrum in the vicinity of K_α and K_β lines. Although the K_α line is significantly stronger than the K_β line, the K_β line is still substantial. For example, the intensity ratio of the K_α line to the K_β line from a Cu anode is about 7.5. The diffraction pattern from the K_β line is still strong enough to confuse the diffraction pattern from the K_α line. Figure 3.9(b) is the spectrum in the same wavelength range after transmission through the β-filter. The intensity of the K_α line is attenuated by the β-filter, but the K_β line is more significantly attenuated. Typically, a β-filter with a thickness causing 50% reduction of the K_α line can change the intensity ratio of the K_α line to the K_β line from 7.5 to 500. Table 3.4 gives the β-filters and their parameters for typical anode materials.

In Table 3.4, $I_0(K_\alpha)/I_0(K_\beta)$ is the initial intensity ratio of K_α to K_β radiated from the anode, $(\mu/\rho)_\alpha$ and $(\mu/\rho)_\beta$ are the mass absorption coefficients of the β-filter to the X-rays of K_α to K_β respectively. For a β-filter with a thickness t, the intensity ratio of K_α to K_β in the transmitted

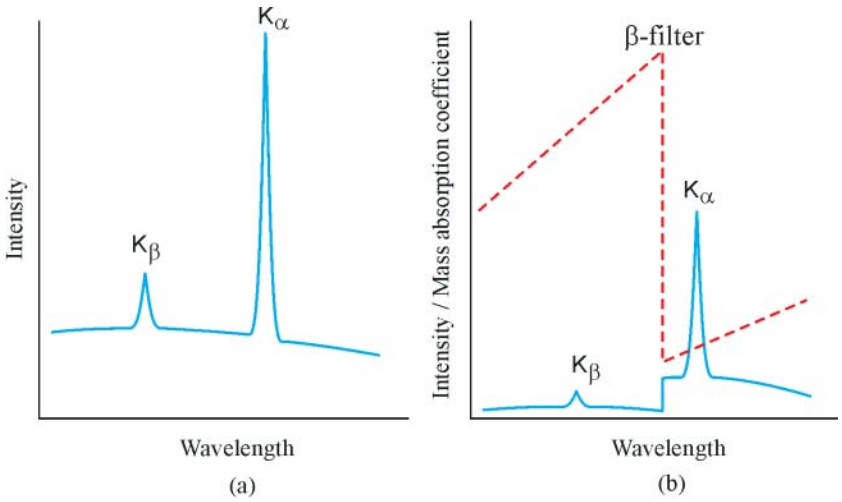


FIGURE 3.9 Effect of β-filter: (a) spectrum in the vicinity of the K_α line and K_β line, (b) spectrum after transmission from the β-filter. The dashed line is the mass absorption coefficient of the β-filter.

Table 3.4 The β-Filter for Common Target Elements

Target material	$\frac{I_0(K_\alpha)}{I_0(K_\beta)}$	β-filter material	$(\mu/\rho)_\alpha$ (cm^2/gm)	$(\mu/\rho)_\beta$ (cm^2/gm)	ρ(gm/cm^3)	t(μm)	$\frac{I_t(K_\alpha)}{I_t(K_\beta)}$	$\frac{I_t(K_\alpha)}{I_0(K_\alpha)}$
Ag		Pd	12.30	57.50	12.00	75	339	0.33
		Rh	11.50	5.20	12.42	75	340	0.34
Mo	5.4	Nb	16.96	81.32	8.58	75	340	0.34
		Zr	16.10	75.20	6.51	100	253	0.35
Cu	7.5	Ni	48.83	282.8	8.91	20	485	0.42
Co	9.4	Fe	56.25	345.5	7.87	15	286	0.51
Fe	9.0	Mn	57.20	395.0	7.47	15	396	0.53
Cr	8.5	V	75.06	501.0	6.09	15	416	0.50

X-ray beam is

$$\frac{I_t(K_\alpha)}{I_t(K_\beta)} = \frac{I_0(K_\alpha)}{I_0(K_\beta)} \exp\left\{\left[\left(\frac{\mu}{\rho}\right)_\beta - \left(\frac{\mu}{\rho}\right)_\alpha\right]\rho t\right\} \tag{3.11}$$

The intensity ratio of K_α to K_β is significantly enhanced due to the difference between the two mass absorption coefficients. This enhancement effect follows an exponential function of the thickness. Therefore, a slight increment in the β-filter thickness can increase the ratio significantly. However, the intensity of K_α decreases with increasing β-filter thickness. The ratio of the transmitted K_α line to the original K_α line is given by

$$\frac{I_t(K_\alpha)}{I_0(K_\alpha)} = \exp\left[-\left(\frac{\mu}{\rho}\right)_\alpha\right]\rho t \tag{3.12}$$

The thickness of the β-filter should be so selected that the thickness is sufficient to cut down the K_β line to a negligible intensity level without sacrificing too much K_α line intensity. The

commercial availability of the corresponding metal foil should also be a consideration. Table 3.4 gives the recommended β-filter for common X-ray tube target materials, their mass absorption coefficients at the corresponding K_α and K_β lines, density, and the recommended thickness that yield an intensity ratio of K_α to K_β between 200 to 500, and at least 30% K_α line intensity. The actual thickness and the effect of the β-filter can be calculated from equations (3.11) and (3.12). Not all the recommended β-filters are available in metal foils. In this case, the β-filter can be prepared from other compounds, typically oxides, by mixing the powder with wax or glue. Mn β-filters may be produced by electrolytic deposition on aluminum foil. The thickness of β-filters not made with metal foil should be adjusted based on the actual density. While reducing the K_β line intensity, the incident X-rays are scattered by the filter, and fluorescence radiation is generated. In order to avoid the scattering and fluorescence from the β-filter reaching a 2D detector, the β-filter should be installed in the primary beam path and before the collimator.

Installing the β-filter in front of a 2D detector may reduce the effects of the K_β line, but there are some adverse effects too. In this case, a large piece of homogenous β-filter foil is required and the scattering and fluorescence cause high background. Since the K_β line photon energy is always higher than the K absorption edge of the β-filter, fluorescence will be generated from the β-filter material. However, if the primary beam is mainly K_α radiation, the β-filter on a 2D detector can remove the fluorescence from the sample because the absorption for the fluorescence of longer wavelengths is always higher than the absorption of K_α radiation. For example, Cu-K_α has a wavelength of 1.54 Å, the mass absorption coefficient of Ni at this wavelength is 48.8 (cm^2/gm). Cu-K_α radiation produces significant fluorescence on a Fe sample. The mass absorption coefficient of Ni to the Fe-K_α fluorescence line is 93.1(cm^2/gm), which is approximately twice as much. A Ni foil of 17 μm in thickness cuts the diffracted intensity by half, but absorbs three-quarters of the Fe-K_α fluorescent radiations. A similar effect can be achieved by using aluminum foil since its absorption coefficient is always smaller for the target K_α than for the sample fluorescence. For instance, a 55 μm thick Al foil can achieve almost the same effect as a 17 μm Ni foil for Fe-K fluorescence from Cu-K_α radiation. Overall, adding a filter in front of a 2D detector for either purpose should only be used as a last resort. The filter foil compromises the sensitivity of the detector, and the scattering and diffraction from the foil contributes to a high background in the collected diffraction pattern. In some cases, a strong diffracted beam from single crystal can produce a weak diffraction ring around the strong spot.

3.2.5 Crystal Monochromator

In a two-dimensional X-ray diffraction system, the incident beam crystal monochromator is one of the best ways to obtain an X-ray beam with the desired spectrum purity. For most X-ray diffraction applications only one specific characteristic line, normally K_α or $K_{\alpha 1}$, is needed – both the white radiation and the unwanted characteristic lines should all be eliminated. A crystal monochromator allows only a selected characteristic line to pass through. A crystal monochromator is illustrated in Figure 3.10 The single crystal has a d-spacing d. The wavelength of the X-rays diffracted by the crystal is given by the Bragg law, $\lambda = 2d \sin\theta_M$. We can set the monochromator crystal to a diffraction condition that only allows the selected characteristic line, for instance K_α, satisfying the Bragg law. X-rays of other wavelengths are filtered out by the monochromator. It can be seen that X-rays also have to be in the right direction to satisfy the diffraction condition. For a "perfect" crystal, the reflected beam from the monochromator is also a parallel X-ray beam. X-rays in the bremsstrahlung with wavelength of λ/n, such as $\lambda/2$, $\lambda/3$ (i.e. 2 or 3 times the fundamental photon energy), may also be diffracted by the monochromator at the same 2θ angle. These X-rays with half or one-third of the K_α wavelength may introduce extra lines in the diffraction pattern.

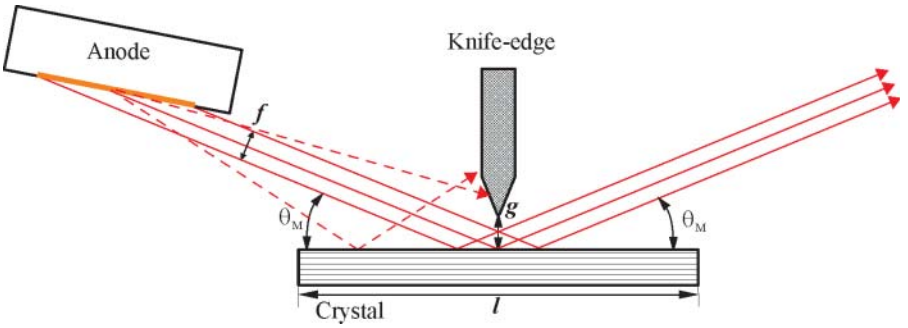


FIGURE 3.10 Illustration of a crystal monochromator. Monochromatic X-rays are obtained by diffraction from a single crystal plate.

Therefore, the X-ray generation voltage should not be set too high such that strong bremsstrahlung is produced. A detector with moderate energy resolution can also avoid harmonic patterns.

The monochromator may include a knife-edge to control the incident and diffracted beams on the crystal. It prevents the direct beam from shining through the monochromator. It cuts down the divergence of the incident beam and diffracted beam on the crystal so as to block the white radiation not in the vicinity of the selected characteristic line. As is shown by the broken lines, the white radiation with the shorter wavelength cannot reach the far side of the crystal to satisfy their Bragg conditions, while the diffracted beams from the longer wavelength white radiation is blocked by the knife-edge. In practice, the knife-edge is also helpful in aligning the monochromator by making it easy to distinguish the K_α line and K_β line on a fluorescent screen. The gap between the knife edge and crystal, g, should be carefully determined such that it blocks the unwanted X-rays but does not decrease the intensity of the desired X-ray beam. The maximum gap is determined by the Bragg angle and the size of the crystal. The knife-edge should control the gap so that all X-rays satisfying the Bragg conditions are confined within the crystal and that no direct X-rays shine through the monochromator. The maximum gap is given by

$$g_{\max} = \tfrac{1}{2} l \tan \theta_M \tag{3.13}$$

where $\boldsymbol{l}$ is the size of the crystal. The minimum gap should allow all parallel characteristic X-rays from the focal spot to pass through the monochromator. The minimum gap is given by

$$g_{\min} = \frac{f}{2 \cos \theta_M} \tag{3.14}$$

where f is the size of the spot focus. The most common crystal monochromator uses a flat graphite crystal. The graphite crystal gives the strongest beam intensity among many crystals. Table 3.5 lists Bragg angles for graphite crystal (002) plane for various anode materials. The graphite crystal cannot resolve $K_{\alpha 1}$ and $K_{\alpha 2}$ lines, so the wavelength of K_α line is given. The $2\theta_M$ value is also required for polarization correction. The maximum and minimum knife-edge gaps are given as an example for a monochromator with 10 mm graphite crystal and 0.4 mm spot focus. It is common practice to use one monochromator adjustable for several tube target types. It can be seen that a knife-edge gap between 0.3 to 0.4 mm would satisfy all targets from Ag to Cr.

In practice, the reflected beam from a monochromator is not strictly monochromatic, but with a certain bandwidth depending on the mosaic of the crystal. The mosaicity of a crystal is measured by the FWHM of the rocking curve. The FWHM of graphite crystals is typically around 0.4°.

Table 3.5 Bragg Angles of Graphite Crystal (002) Plane for Various Target Materials and the Knife-Edge Gap for 10 mm Crystal and 0.4 mm Spot Focus

Target	λ-K_α (Å)	$2\theta_M$	g_{max} (mm)	g_{min} (mm)
Ag	0.560868	9.58	0.419	0.201
Mo	0.710730	12.14	0.532	0.201
Cu	1.541838	26.53	1.177	0.205
Co	1.790260	30.90	1.382	0.207
Fe	1.937355	33.51	1.505	0.209
Cr	2.29100	39.87	1.815	0.213

The crystal type in a monochromator has to be chosen based on the performance requirement in terms of intensity and resolution. The crystals, such as Si, Ge and quartz, have narrow rocking curves, accompanying high resolution and low intensity, while graphite and LiF crystals have high intensity and low resolution due to large mosaic spreads. The spectrum purity and parallelism of an X-ray beam can be further improved by using multiple crystals or channel cut crystals in which the X-ray beam is bounced several times by crystals. This is typically associated with high resolution X-ray diffraction and covered by various references [10–12]. The monochromator crystal shape also varies from flat, bent, or cut to curve. A flat crystal is used for parallel beams and a curved crystal for focus geometry. It is important to have an appropriate monochromator matching the characteristics of the source, specimen, and instrument geometry. In the current state of the art, graphite monochromators can satisfy most applications of XRD[2] [13, 14]. In the near future, with the improvement of area detector resolution, high resolution monochromators tuned to the $K_{\alpha 1}$ line will become necessary.

3.2.6 Multilayer Mirrors

Advances in materials processing technology make it possible to produce another type of X-ray optics categorized as multilayer mirrors [15]. A multilayer mirror consists of alternating layers of heavy materials, such as tungsten or nickel, as a reflection layer, and light materials, such as carbon or carbide, as a spacer layer. A multilayer mirror works on the same principle as Bragg diffraction from a natural crystal, so in essence a multilayer mirror is a monochromator with an artificial crystal. Each pair of reflection layer and spacer layer is referred to as bi-layer. A bi-layer functions like an atomic plane in a natural crystal, and the thickness of each bi-layer is the d-spacing. In contrast to a natural crystal, a multilayer mirror typically has a larger d-spacing such that the incident angle and diffracted angle are typically only a few degrees. The number of layers, the d-spacing of the layers, and the distribution of the layer thickness can also be varied to achieve different levels of performances.

The performance of a multilayer mirror can be simply described by its rocking curve. The intensity of the rocking curve represents the reflectivity of the mirror and the FWHM represents the mirror's bandpass in terms of either the range of wavelengths or the incident angle. A multilayer mirror has much broader rocking curve compared to Si single crystal optics – its FWHM is typically about one order of magnitude wider than that of Si single crystals. Therefore, a multilayer mirror can remove bremsstrahlung and most of the K_β line, but not the $K_{\alpha 2}$ from the K_α doublet. The reflectivity of multilayer mirrors is also higher than most crystal monochromators. The high peak reflectivity is always beneficial, while different bandpasses are preferred for different X-ray sources and applications. For example, with an X-ray tube having a small focal spot and applications involving small crystal and microarea diffraction, the preferred multilayer mirror

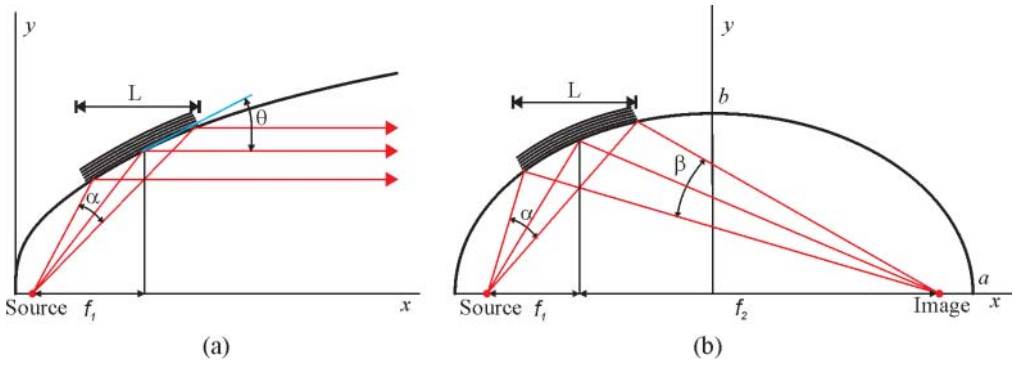


FIGURE 3.11 (a) Geometry of a parabolic mirror, (b) Geometry of an elliptical mirror.

should have a narrow rocking curve but the highest possible reflectivity. However, with a large focal spot X-ray source and applications requiring a high flux of X-rays, a combination of wide bandpass and high reflectivity should be a better choice.

The multilayer mirror can also be made into different shapes to optimize its performance in a system. One method of achieving the various mirror shapes is deposition of multilayer films on prefigured substrates. The reflecting surface of a mirror can be flat, spherical, parabolic, or elliptical. A flat multilayer mirror can be used as a monochromator, but not be able to collimate or focus X-ray beams. Multilayer mirrors with a spherical reflecting surface are relative easy to make, but astigmatism and spherical aberration diminishes their performance. The most commonly used mirror shapes are parabolic and elliptical, as shown in Figure 3.11. In order to illustrate the geometric relationships, the y axis is considerably scaled up. Figure 3.11(a) illustrates the geometry of a parabolic mirror. The X-ray source is at the focal point of the parabolic curve. The parabolic shaped multilayer mirror reflects X-rays from the source and forms a parallel X-ray beam. Since the incident angle from source to mirror varies along the length of the mirror, the d-spacing of the multilayer, and the corresponding Bragg angle θ, varies accordingly. The angle α is the capture angle determined by the length of the mirror, L, and the distance between the mirror center and the source, f_1. The capture angle determines the total flux collected by the mirror, so it is also referred to as the collection angle. The total flux or capture angle can be increased either by increasing the mirror length or by placing the mirror closer to the source.

Figure 3.11(b) illustrates the geometry of an elliptical mirror. The mirror is shaped as an ellipse with major axis in the x direction and minor axis in the y direction. The lengths of the major and minor axes are $2a$ and $2b$ respectively. The actual ellipse is much elongated in the x direction, with the b/a ratio typically being a few tens to hundreds. The X-ray source is placed at one focus of the ellipse and the source is imaged at the other focus, called the image focus. Since the incident angle from source to mirror varies along the length of the mirror, the d-spacing of the multilayer also varies accordingly. The angle α is the capture angle determined by the length of the mirror, L, and the distance between the mirror center and the source, f_1. Just as in a parabolic mirror, the capture angle determines the total flux collected by the mirror. The angle β is the convergence angle of the X-ray beam from the mirror, which is also determined by the mirror length and the distance between the mirror center and the image focus, f_2. A multilayer mirror, either parabolic or elliptical, is typically designed for a particular wavelength due to the d-spacing distribution along the mirror being designed specifically for one wavelength.

In both the parabolic and elliptical mirror geometries, the X-ray source is assumed to be a point. The actual focus size from an X-ray source has extended dimensions. The so-called spot

focus is not a true spot either, but rather a projection from an elongated focal spot on the anode. For example, the standard fine focus sealed tube has a focal spot 0.4 mm × 8 mm on the anode, the projected spot focus is 0.4 mm × 0.8 mm and the line focus is 0.04 mm × 8 mm at 6° takeoff angle. Rotating anode generators (RAG) and microfocus X-ray tubes may have smaller source size. Depending on the type of multilayer mirror, only a limited sized source spot can satisfy the Bragg conditions of the mirror. This is the effective source size of the mirror. The actual source size should match the effective source size for the best performance. The effective source size of a mirror depends on many factors, including the mirror material type, the capture angle and d-spacing of the multilayer [16–18]. For a given example, the Bragg peak width is approximately 1 mrad for W/C multilayers, and approximately 0.5 mrad for Ni/C multilayers. The Bragg peak width defines a solid angle covering X-rays effectively reflected by the mirror. At a source to mirror distance of 120 mm, the W/C mirror has an effective source size of 120 μm and only 60 μm for the Ni/C mirror. Reducing the d-spacing of the multilayers can also reduce the effective source size. One way to increase the capture angle to increase the flux is to increase the *b* axis, but due to the corresponding decrease in d-spacing, the effort may be diminished by the smaller effective source size unless a smaller and brighter source is used at the same time.

In another expression of Liouville's theorem, the X-ray beam size at the focus (image size) is determined by a magnification ratio given by

$$M = \frac{f_2}{f_1} = \frac{\alpha}{\beta} = \frac{S_2}{S_1} \tag{3.15}$$

where M is the magnification ratio, S_1 is the effective source size and S_2 is the image size. For the above example with W/C multilayers, $S_1 = 120\,\mu m$, $f_1 = 120\,mm$ and $f_2 = 380\,mm$, and the magnification $M = 3.2$, then we can obtain the image size $S_2 = 384\,\mu m$ and the convergence angle $\beta = 3.8$ mrad. In the above relation, the image size and convergence angle are the two parameters most important to X-ray diffraction applications. An intensive small image size is suitable for microdiffraction. A small divergence is good for resolution, while a large divergence is good for sampling statistics.

Figure 3.12 shows three arrangements of multilayer mirrors used in X-ray diffraction. The multilayer mirror can be used either as a single mirror or combined in a mirror group. A single mirror curved in one direction is typically used for conditioning a line focus beam. Figure 3.12(a) illustrates a single mirror, a graded multilayer X-ray mirror, known as a Göbel mirror [19]. The Göbel mirror is parabolic, which causes a divergent beam striking the mirror at different locations and angles to yield an intense and highly parallel beam. In contrast to conventional monochromator crystals, mirrors are manufactured so that the d-spacing between the layers varies in a controlled manner. The appropriate gradient in the d-spacing depends on factors which include wavelength, the location of the mirror with respect to the source, and the application for which the mirror is designed. With Bragg diffraction, the radiation is monochromatized to K_α, while K_β and bremsstrahlung are suppressed. The single Göbel mirror collimates the X-ray beam only in the directions parallel to the diffractometer plane. The X-ray beam conditioned by the mirror is a parallel beam only at the projection on the diffractometer plane. The divergence in the vertical direction or axial direction still exists. For a conventional diffractometer with line focus source, the axial divergence can be controlled by soller slits in the same way as in the Bragg–Brentano geometry. A channel cut monochromator may be coupled to the Göbel mirror to further improve X-ray beam parallelism and spectrum purity. The line focus X-ray bean from a single Göbel mirror is not suitable for XRD^2, so it is necessary to add a pinhole collimator after the mirror to obtain a point beam. This is especially convenient when the configuration of an X-ray diffractometer is frequently switched between a conventional one-dimensional diffractometer and a two-dimensional diffractometer.

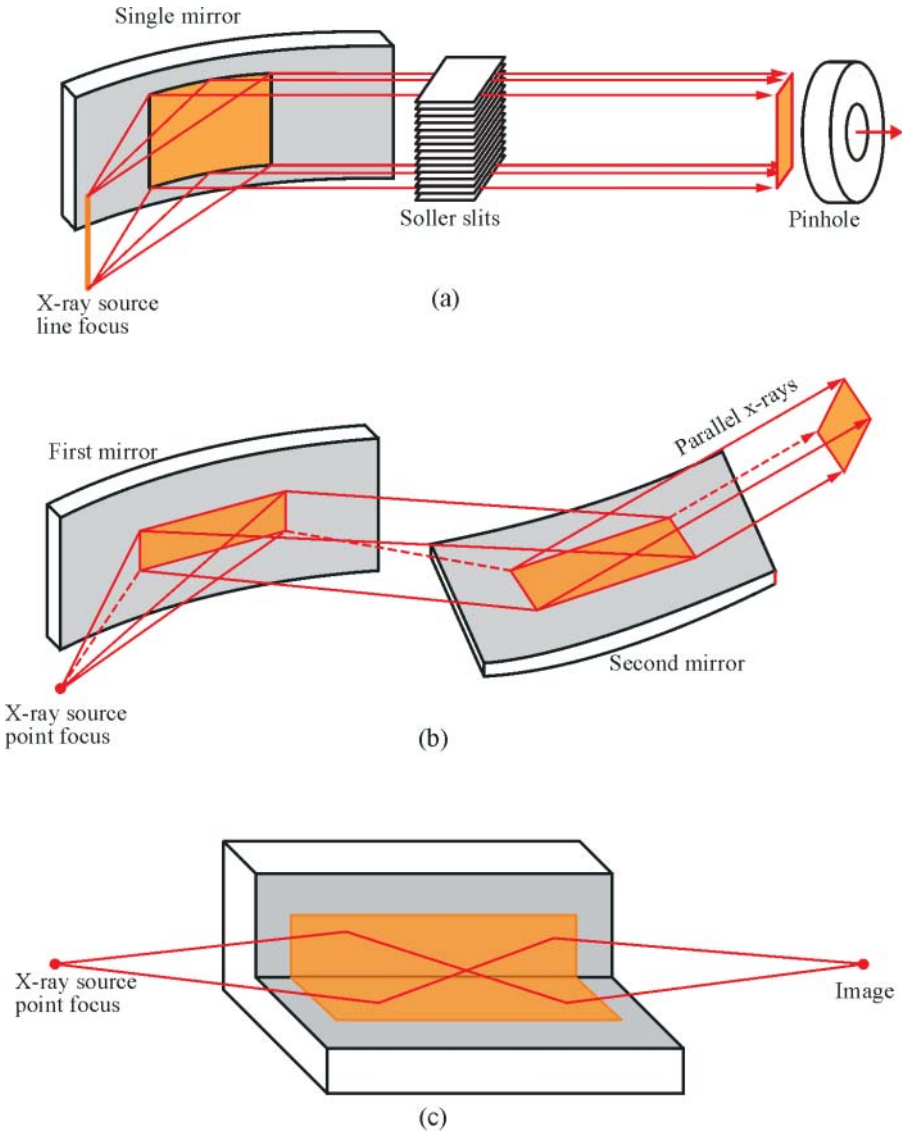


FIGURE 3.12 (a) A single parabolic mirror produces a parallel beam, (b) cross-coupled Göbel mirrors produce a parallel point beam, (c) side-by-side mirror produces a convergence beam.

Two mirrors arranged in such a way that the X-ray beam is first reflected by the first mirror and then reflected by the second mirror positioned in an orthogonal direction was suggested by Kirkpatric and Beaz [20]. Therefore, this arrangement is called the Kirkpatric–Beaz (K-B) scheme. Alternatively, the two mirror assembly is also referred to as cross-coupled mirrors. Figure 3.12(b) illustrates a set of cross-coupled Göbel mirrors used as an X-ray source with point focus, in which a second Göbel mirror, turned 90° from the first mirror, collimates the beam in the direction perpendicular to the first mirror. A crossed-coupled arrangement of two mirrors provides a highly parallel beam which is much more intense than can be obtained with a graphite monochromator for small beam size. For applications such as microdiffraction where a small spot size is desired, a

set of cross-coupled Göbel mirrors can offer upwards of an order of magnitude more intensity than conventional optics. The low divergence of the beam incident on the sample from Göbel mirrors also decreases the width of crystalline peaks, improving the resolution of an XRD^2 system. For all applications requiring strong collimation of the beam, Göbel mirrors provide considerable intensity gains. Figure 3.13 shows the relative beam intensity from a set of cross-coupled Göbel mirrors coupled with collimator of various pinhole sizes compared with a graphite monochromator [14]. Both the computer simulation and the experimental results show that the smaller the beam size, the stronger is the intensity gain from cross-coupled Göbel mirrors compared to a monochromator. The intensity break-even point for Göbel mirrors versus a graphite monochromator is approximately at the pinhole collimation size of 0.3 to 0.4 mm. In other words, for applications such as texture or phase identification from a bulk powdered specimen, which ordinarily employ collimators larger than 0.4 mm, there is no benefit to using Göbel mirrors. In fact, the low divergence of the resulting beam can cause poor statistical grain sampling in such cases. Therefore, the cross-coupled Göbel mirrors are preferred for microdiffraction and small angle X-ray scattering.

Figure 3.12(c) illustrates two multilayer mirrors arranged at the same distance from the source, and side-by-side, at an angle of 90°. This configuration was first suggested by Montel for an X-ray microscope with two spherical total reflection mirrors [21]. Therefore, this arrangement is also called the Montel scheme. In this configuration, one trace of X-rays from the point source is reflected by one of the two mirror first and then by the other mirror. Due to the symmetric design of the mirrors, both mirrors function as the first mirror and the second mirror. The passage of the X-rays can be represented by the two traces as shown in the figure. The mirror shape for side-by-side configuration can either be parabolic or elliptical, but most often two elliptical mirrors of the same focal length are used. The elliptical curves of both mirrors are so designed that all the doubly reflected X-rays meet at the image focus. The relationship defined in equation (3.15) also applies to the side-by-side elliptical mirrors with the approximation that f_1 is defined as the

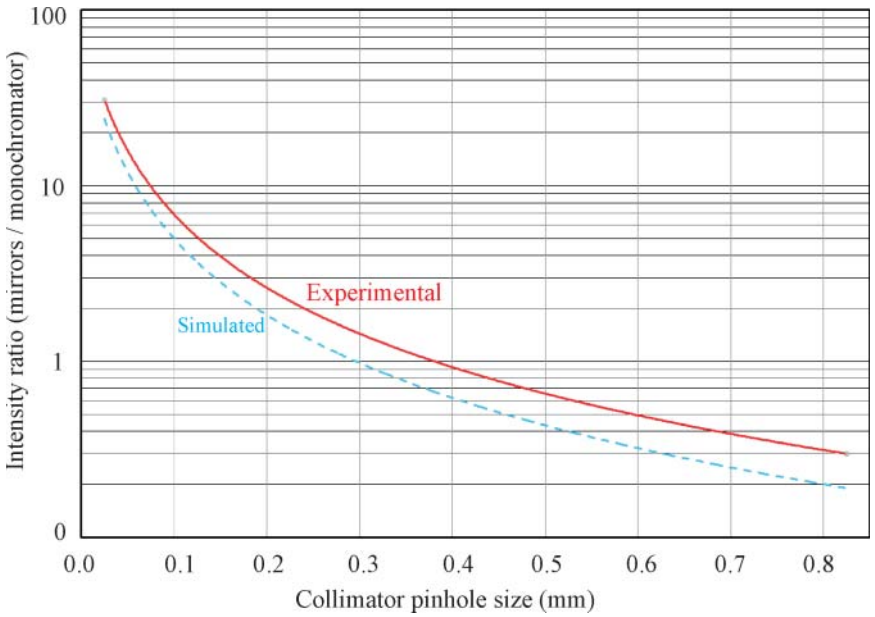


FIGURE 3.13 Comparison of X-ray intensity between cross-coupled Göbel mirrors and monochromator with various collimator pinhole size.

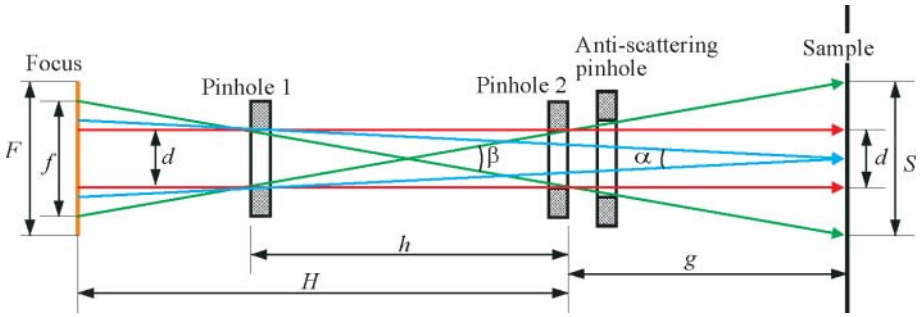


FIGURE 3.14 Schematic of the X-ray beam path in a pinhole collimator, showing the parallel, divergent and convergent X-rays and beam spot on the sample surface.

distance between the mirror center and the source and f_2 as the distance between the mirror center and the image focus. The total flux entering the mirrors is determined by the capture angle α, which is determined by the mirror length, L, and primary focusing distance, f_1. The angle β is the convergence angle of the X-ray beam from the mirror, which is also determined by the mirror length and the distance between the mirror center and the image focus, f_2. Since all X-rays are doubly reflected by both mirrors in the side-by-side scheme, only half of the mirror length is used for the primary reflection and the other half for the secondary reflection. Therefore, the capture angle α of a set of side-by-side mirrors is approximately half that of a single mirror for the same mirror length L. The same is true for the convergence angle β.

3.2.7 Pinhole Collimator

The pinhole collimator is normally used to control the beam size and divergence. In XRD^2 systems, the pinhole collimator is normally coupled with other optics such as a crystal monochromator or multilayer mirrors. Figure 3.14 shows the X-ray beam path in a pinhole collimator consisting of two pinholes apertures of the same diameter d separated by a distance h. F is the source size of the X-ray tube or beam focus image from other optics, such as a monochromator or a set of mirrors. The distance between the source and the second pinhole is H. The distance from the second pinhole to the sample surface is g. The X-ray beam exiting from the collimator consists of three components: parallel, divergent, and convergent X-rays. The parallel part of the beam has a size of d all the way from focus to sample. The antiscattering pinhole is used to block the X-ray scattering from the second pinhole. The size of the antiscattering pinhole is so chosen that it has no exposure to direct rays from the focus. The maximum divergence angle β is given by

$$\beta = \frac{2d}{h} \tag{3.16}$$

For the same pinhole size, the beam divergence is inversely proportional to the distance between the two pinholes. The maximum angle of convergence α is given by

$$\alpha = \frac{d}{h+g} \tag{3.17}$$

which is the maximum angle that X-rays, exiting a focusing optic or source, can focus on the sample surface. It is determined by the first pinhole size and its distance to the sample. As can be seen from the equation, the divergence angle β is always great than α, so that β determines

the maximum crossfire of the X-ray beam from a collimator. The maximum beam spot S on a flat sample facing the X-ray source is given by

$$S = d\left(1 + \frac{2g}{h}\right) \tag{3.18}$$

It can be seen from this equation that the shorter the distance between the second pinhole and the sample or the longer the distance between the two pinholes, the smaller the beam spot on the sample. The effective source size f is determined by the pinhole distance h and the distance between the X-ray source and the pinholes.

$$f = d\left(\frac{2H}{h} - 1\right) \tag{3.19}$$

If the actual X-ray source F is larger than the effective source size f, the difference between F and f represents the wasted X-ray energy. This is the reason that a microfocus tube is recommended when a small beam size is used. The actual beam divergence is also determined by the monochromator and the mirrors advancing the collimator in the beam path. For example, when cross-coupled Göbel mirrors are used, the X-ray beam is almost a parallel beam, the divergence of the beam is smaller than the value calculated from equation (3.16). When the actual source size f' is smaller than f, we have the following equations to calculate the maximum divergence (β'), convergence (α'), and beam spot size on sample (S'):

$$\beta' = \frac{d + f'}{H} \tag{3.20}$$

$$\alpha' = \frac{f'}{H + g} \tag{3.21}$$

$$S' = \beta'(H + g) - f' \tag{3.22}$$

Taking the collimator shown in Figure 3.7 as an example, Table 3.6 lists the values of beam divergence, convergence and the maximum beam spot on a sample surface for a variety of collimator sizes coupled with a graphite monochromator or cross-coupled Göbel mirrors. In addition to the different pinhole sizes, the other dimensions are: $H = 280$ mm, $h = 140$ mm, $g = 30$ mm, and $F = 0.8$ mm for the 0.4 mm × 0.8 mm fine focus tube. A collimator may determine the maximum divergence of an X-ray beam passing through it or reduce the divergence by cutting off the high divergent X-rays, but it can never increase the divergence from the optics coupled preceding it. The graphite monochromator has a rocking curve of 0.4°, and cross-coupled Göbel mirrors of 0.06°. The beam divergence and convergence angles should not be above these values even if the collimator may allow a more divergent beam to pass. For the same pinhole size, if the focal spot is larger than the pinhole size, the beam divergence is inversely proportional to the distance between two pinholes. If the focal spot size is smaller than the pinhole size, the beam divergence is inversely proportional to the distance between the source and the second pinhole. In every case, the lower divergence is typically associated with a long beam path. At the same time, the beam flux is inversely proportional to the square of the distance between the source and the sample. There are mainly two factors determining the length of primary beam path: the required distance for collimating the beam into the required divergence; and the space required for primary X-ray optics, sample stage, and detector. On the condition that the above two factors are satisfied, the primary X-ray beam path should be kept as short as possible.

Table 3.6 X-ray Beam Divergence Angle (β), Convergence Angle (α), and Beam Spot Size on Sample (S) for a 0.8 mm Point Focus Tube with Graphite Monochromator or Cross-Coupled Göbel Mirrors

Pinhole	Graphite Monochromator				Göbel Mirrors		
d (mm)	β (°)	α (°)	S (mm)	f (mm)	β (°)	α (°)	S (mm)
0.05	0.041	0.017	0.07	0.15	0.041	0.017	0.07
0.10	0.082	0.034	0.14	0.30	0.060	0.034	0.13
0.20	0.164	0.067	0.29	0.60	0.060	0.060	0.23
0.30	0.246	0.101	0.42	0.80	0.060	0.060	0.33
0.50	0.266	0.148	0.64	0.80	0.060	0.060	0.53
0.80	0.327	0.148	0.97	0.80	0.060	0.060	0.83

Table 3.7 Comparison between Single Pinhole Collimator and Double Pinhole Collimator in Terms of Intensity Gain, Beam Divergence Angle (β), and Beam Spot Size on Sample (S)

Collimator Size	Intensity Gain	Single Pinhole		Double Pinhole	
d (mm)	Single/Double	β (°)	S (mm)	β (°)	S (mm)
0.05	>20	0.174	0.14	0.041	0.07
0.10	16	0.184	0.20	0.082	0.14
0.20	4	0.205	0.31	0.164	0.29
0.30	2.4	0.225	0.42	0.225	0.42
0.50	1.2	0.266	0.64	0.266	0.64
0.80	1.0	0.327	0.97	0.327	0.97

Table 3.6 also shows that the beam divergence decreases continuously with decreasing pinhole size for the combination of double pinhole collimator and monochromator. In cases where the application requires a small beam size but not necessarily a small divergence, it is advisable to remove pinhole 1 from the collimator tube to achieve higher beam intensity. Table 3.7 gives the comparison between double pinhole collimators and single pinhole collimators in terms of intensity gain (the approximate ratio of single to double pinhole), beam divergence, and beam spot size on the sample.

The 50 μm and 100 μm collimators are preferred for microdiffraction and 0.5 mm or 0.8 mm collimators are typically used for quantitative analysis, texture, or percentage crystallinity measurements. In the case of quantitative analysis and texture measurements, using too small a collimator can actually be a detriment, causing poor statistical grain sampling. In such cases, the statistics can be improved by oscillating the sample. The choice of collimator size is often a trade-off between intensity and the ability to illuminate small regions or resolve closely spaced lines. The smaller the collimator, the lower the photon flux striking the sample and the longer the count time to acquire statistically significant data.

3.2.8 Capillary Optics

Capillary X-ray optics are based on the concept of total external reflection. X-rays can be reflected by a smooth surface when the angle of incidence is smaller than the critical angle for total reflection θ_c. The critical angle is a function of the wavelength and materials; the shorter the wavelength, the lower the critical angle. When X-rays are reflected by the inner surface of a capillary at a grazing angle smaller than the critical angle of the capillary materials, X-rays are reflected with

Table 3.8 Intensity Gain (Calculation and Experimental) and Beam Spot Size Containing 90% Beam Intensity for Monocapillaries Compared with Double Pinhole Collimators

	Cu-K_α-radiation (8.0 keV)			Mo-K_α-radiation (17.4 keV)			Collimator
Capillary/pinhole size: *d* (mm)	Gain-cal	Gain-exp	Spot (90%)	Gain-cal	Gain-exp	Spot (90%)	Spot (90%)
0.10	110	66	0.18	39	40	0.14	0.10
0.30	15	10	0.34	5.6	5.9	0.31	0.31
0.50	7.4	6.0	0.50	2.6	3.0	0.49	0.50
1.00	3.4	4.2	0.89	1.2	1.5	0.97	0.98

little energy loss. It can produce significant intensity gain on the sample relative to the pinhole collimators. The transmission efficiency depends upon the X-ray energy, the capillary materials, the reflection surface smoothness, the capillary inner diameter, and the incident beam divergence. The K_β radiation, having higher energy than K_α, has less transmission efficiency. For a typical capillary material, the critical angle is about 0.2° for Cu-K_α radiation.

The monocapillary is a cylindrical tube with a smooth inner surface. The monocapillary can collimate the beam spatially to a variety of beam sizes for different applications. The typical choice of monocapillary sizes is from 1.0 mm down to 0.01 mm. The exit beam divergence is controlled by the capillary dimensions (diameter and length) and the critical angle of total reflection. It can produce significant intensity gain on the sample relative to pinhole collimators. For the X-ray optics system shown in Figure 3.7, the monocapillary is mounted inside a steel tube. The tube is of the same design as that used for the pinhole collimator, so it is easy to switch between the pinhole collimator and a monocapillary. Table 3.8 lists the intensity gain (calculated and experimental) and beam spot size containing 90% beam intensity for monocapillaries compared with double pinhole collimators of the same size.

Table 3.8 shows that 0.1 to 1.0 mm capillaries give practically the same spot sizes on the sample as the corresponding double-pinhole collimators. The capillaries produce large intensity gain relative to the corresponding double-pinhole collimators. In the case of small beam size a special combination of capillaries and pinhole collimators may be favorable. Capillaries of slightly larger diameter capture more radiation near the source and transport it with less intensity loss. The pinhole with the smaller diameter defines the final beam size. The combination can obtain more uniformly distributed radiation energy on the sample. A tapered monocapillary is another alternative to achieve a small beam size in which the larger capture angle gives much better intensity gain while focusing X-rays into a small beam size. For instance, the gain provided by a 20 μm tapered monocapillary can produce an intensity gain of 6 to 25 compared to a pinhole collimator with the same beam size [22]. Although monocapillaries can reduce the weight of high energy X-rays in the spectrum due to lower critical angles for higher energy X-rays, it cannot remove the K_β line and the bremsstrahlung. Therefore, the monocapillary is mostly coupled with a graphite monochromator in a diffractometer. The mosaicity of a graphite crystal is slightly larger than the critical angle of the total external reflection angle in a monocapillary. This is a good match. The results given in Table 3.8 are based on the coupling of a monocapillary with a graphite monochromator.

Polycapillary optics, consisting of thousands to millions of capillaries bundled into designed shapes, can collect X-rays from the source and redirect the X-rays to form desired beam profiles [23, 24]. Polycapillary optics are also very often referred to as a polycapillary lens. Advances in the production of polycapillaries have led to a new technology based on polycapillary fibers. Each fiber contains hundreds to thousands of glass capillary channels. The diameter of each channel is typically 2 to 25 μm and varies along the length of the lens to achieve the optimum transmission

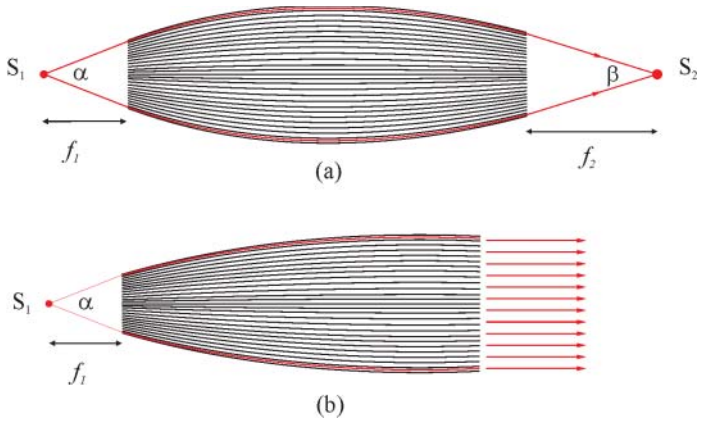


FIGURE 3.15 Schematic of polycapillary optics: (a) focusing polycapillary, (b) parallel polycapillary.

efficiency. A polycapillary lens is made of thousands of such fibers. Figure 3.15 shows two typical polycapillary optics, (a) a focusing polycapillary and (b) a parallel polycapillary. For both optics, S_1 is the size of the X-ray source, α is the capture angle and f_1 is the input focal distance or access distance. X-rays within a large capture angle can be collected by the polycapillary optics. The X-rays collected in each capillary are transferred efficiently by total external reflection at the inner surfaces of capillaries. The X-rays leaving a focusing polycapillary form a focused beam with divergence angle β, output focal distance f_2, and focus image size S_2. The capillaries at the exit of a parallel polycapillary optics are almost parallel to each other, so the X-ray beam delivered by parallel polycapillary optics has a very small divergence angle.

For focusing polycapillary optics, Liouville's theorem requires that the source size S_1 must be considerably smaller than the output beam size S_2 in order to achieve a gain in flux by a large capture angle α. For a given beam divergence β and beam size S_2, the polycapillary lens should be located as close as possible to the X-ray source if a large capture angle is required. The intensity gain of a focusing polycapillary compared to a pinhole collimator is significant, typically greater by two orders of magnitude. The total flux of the beam increases with larger divergence and smaller source size. For many X-ray diffraction applications with polycrystalline materials, a primary beam with a large divergence is acceptable or even beneficial as long as the concerned diffraction peaks can be resolved. The high flux and divergence can improve the counting statistics and sampling statistics if the angular resolution is not critical. A polycapillary lens can also focus the beam into a very small irradiated spot on the sample, which is desirable for microdiffraction.

A parallel polycapillary lens, also referred to as collimating polycapillary lens, can convert a highly divergent beam from a point source into a near parallel beam with a divergence angle β as small as 0.06°. Based on Liouville's theorem, it is necessary to use an X-ray source as small as possible to achieve a parallel beam. For an ideal point source, the focal spot is infinitely small, so the beam could be collimated by a polycapillary into any chosen cross-section. However, a real X-ray source has a finite size and there is a limitation to the divergence and cross-section of the output beam. The parallel beam from a polycapillary typically has a large cross-section, from several millimeters to centimeters. This kind of parallel optics can be used in the conventional diffractometer in the parallel beam geometry as shown in Figure 3.5. The flux gain from a polycapillary is mostly determined by the acceptance angle, so a parallel polycapillary can also have a flux gain two orders of magnitude greater than a pinhole collimator. For a two-dimensional

X-ray diffraction system, a parallel beam with a small cross-section is desired. In this case, a small X-ray source and short access distance are necessary. Another option is to use a slightly convergent polycapillary lens, which gives a short access distance and long output focal distance so that the output beam from the lens focus to the sample has a low divergence.

Just like monocapillaries, polycapillaries can reduce the weight of high energy X-rays in the spectrum due to lower critical angles for higher energy X-rays, but cannot remove the K_β line and the bremsstrahlung. Due to the large capture angle, polycapillary optics cannot be coupled with a crystal monochromator, therefore a β-filter is typically used with polycapillaries. Although the spectrum purity is not as good as with a crystal monochromator or multilayer mirror, one advantage is that a polycapillary lens can be used for various wavelengths. For instance, a diffractometer with a sealed Cu X-ray tube can use a polycapillary to condition the primary X-ray beam. When it is necessary to switch to a Cr X-ray tube, the same polycapillary can be used. Alignment of the system may also be avoided if the focal spot position of the X-ray tubes is reproducible. It is necessary only to replace the Ni filter by a V-filter. This kind of system is very convenient for stress and texture analysis, where spectrum purity is not very critical, but the high flux beam from the polycapillary can improve data quality and reduce the data collection time.

REFERENCES

1. H. P. Klug and L. E. Alexander, *X-ray Diffraction Procedures for Polycrystalline and Amorphous Materials*, John Wiley & Son, New York, 1974, 58–119.
2. B. D. Cullity, *Elements of X-ray Diffraction*, 2nd ed., Addison-Wesley, Reading, MA, 1978.
3. A. C. Bloomer and U. W. Arndt, Experiences and expectations of a novel X-ray microsource with focusing mirror. *I, Acta Cryst.* (1999). **D55**, 1672–1680.
4. J. Wiesmann, J. Graf, C. Hoffmann, and C. Michaelsen, New possibilities for X-ray diffractometry, *Physics meets Industry*, edited by J. Gegner and F. Haider, 2007 Expert Verlag, ISBN 978-3-8169-2740-2.
5. U. W. Arndt et al., Focusing mirrors for use with microfocus X-ray tubes, *J. Appl. Cryst.* (1998). **31**, 733–741.
6. O. Hemberg, M. Otendal, and H. M. Hertz, Liquid-metal-jet anode electron-impact X-ray source, *Applied Physics Letters*, (2003), Vol. **83**, No. 7, 1483–1485.
7. Excillum brochure: Redefining the X-ray tube – metal jet X-ray sources, (2012), VAT# SE556734144001.
8. U. W. Arndt, Focusing optics for laboratory sources in X-ray crystallography, *J. Appl. Cryst.* (1990) **23**, 161–168.
9. R. Jenkins and R. L. Snyder, *Introduction to X-ray Powder Diffractometry*, John Wiley & Sons, New York, 1996.
10. C. Giannini and L. Tapfer, A high-resolution multiple-crystal monochromator for X-ray diffraction studies, *J. Appl. Cryst.* (1996). **29**, 230–235.
11. M. Servidori, X-ray monochromator combining high resolution with high intensity, *J. Appl. Cryst.* (2002). **35**, 41–48.
12. H. Stöcker, K. K. Reuter and D. C. Meyer, Si(511) channel cut for monochromatization and linear polarization of X-rays, *J. Appl. Cryst.* (2007). **40**, 635–636.
13. B. B. He, Microdiffraction using two-dimensional detectors, *Powder Diffraction*, **19** (2), June 2004.
14. B. B. He and U. Preckwinkel, X-ray optics for two-dimensional X-ray diffraction, *Advances in X-ray Analysis*, **45**, 332–337, 2002.
15. L. Jiang, Z. Al-Mosheky, and N. Grupido, Basic principles and performance characteristics of multilayer beam conditioning optics, *Powder Diffraction*, **17** (2), June 2002.

16. C. Michaelsen, J. Wiesmann, C. Hoffmann, A. Oehr, A. B. Storm, and L. J. Seijbel, Optimized performance of graded multilayer optics for X-ray single-crystal diffraction, *Proceedings of SPIE* Vol. **5193**, pp. 211–219 (2004).
17. A. B. Storm, C. Michaelsen, A. Oehr, and C. Hoffmann, Multilayer optics for Mo-radiation-based crystallography, *Proceedings of SPIE* Vol. **5537**, p. 177–181 (2004).
18. C. Michaelsen, J. Wiesmann, K. Wulf, L. Brügemann, A. Storm, Recent developments of multilayer x-ray optics for laboratory x-ray instrumentation, *Proceedings of SPIE* Vol. **4782**, pp. 143–151 (2002).
19. M. Schuster and H. Göbel, Graded-spacing Multilayers for X-ray diffraction applications, *Advances in X-ray Analysis*, **39**, 57–71, 1996.
20. P. Kirkpatrick and A. V. Baez, Formation of optical images by X-rays, *J. Opt. Sci., Am.* **38**, 766 (1948).
21. M. Montel, *The X-ray microscope with catamegonic roof-shaped objective, X-ray microscope and microradiography* (Elsevier, Amsterdam, 1953), p. 177.
22. P. J. Schields, I. Y. Ponomarev, N. Gao, and R. B. Ortega, Comparison of diffraction intensity using a monocapillary optic and pinhole collimators in a microdiffractometer with a curved image-plate, *Powder Diffraction*, *Vol.* **17***, No 2*, June 2002.
23. C. A. MacDonald, S. M. Owens, and W. M. Gibson, Polycapillary X-ray optics for microdiffraction, *J. Appl. Cryst.* (1999). **32**, 160–167.
24. P. J. Schields, D. M. Gibson, W. M. Gibson, N. Gao, H. Huang, and I. Y. Ponomarev, Overview of polycapillary X-ray optics, *Powder Diffraction*, *Vol.* **17***, No 2*, June 2002.

4

X-RAY DETECTORS

4.1 HISTORY OF X-RAY DETECTION TECHNOLOGY

The development of X-ray detection technology is an important part of the development of X-ray technology. The X-ray was first observed by Röntgen on fluorescent screens in a darkened room in November 1895. A month later he published a paper announcing his discovery with an X-ray radiograph of his wife's hand which was collected with a photographic plate. In this exciting story of discovery, both the fluorescent screens and photographic plates played important roles in the discovery of X-rays. X-ray photographic plates and films are actually the first generation of X-ray detectors. It so happens that they were actually the first generation of two-dimensional X-ray detectors [1]. A photographic X-ray film is typically made of a flexible base and photosensitive layer. The photosensitive layer contains silver halides, which can record a latent image when exposed to X-rays. The later development process makes the image visible. In the X-ray diffraction field, many diffraction techniques are based on photographic plates or films. In 1912, Max von Laue and his two assistants, Walter Friedrich and Paul Knipping published a diffraction pattern of single crystal ZnS collected with a photographic plate using the whole spectrum of X-rays produced from an X-ray tube. This experiment gave a proof that X-rays are electromagnetic waves and could be diffracted by crystals. This was the beginning of X-ray diffraction. Since then diffraction patterns of single crystals collected with polychromatic X-rays are mostly referred to as Laue patterns. Diffraction apparatus based on X-ray photographic plates and films is generally referred to as a diffraction camera. In a diffraction camera, the whole diffraction pattern is recorded simultaneously by an exposure.

Laue cameras are the most simple X-ray diffraction apparatus [2]. The camera uses a flat photographic plate or film, oriented perpendicular to an X-ray beam. The white radiation from a sealed X-ray tube with heavy metal target, tungsten for instance, is typically used. The specimen used in the Laue method is a single crystal. There are two configurations of Laue cameras: transmission and back-reflection. In the transmission configuration, the X-ray source and the plate or film are

Two-Dimensional X-Ray Diffraction, Second Edition. Bob Baoping He.
© 2018 John Wiley & Sons, Inc. Published 2018 by John Wiley & Sons, Inc.

located on opposite sides of the crystal. A collimated X-ray beam hits a crystal and the diffracted X-rays reach a photographic plate at 2θ angles considerably smaller than 90°. A beamstop is typically used to prevent the transmitted direct beam from striking the photographic plate. In the back-reflection configuration, there is a hole in the center of the film or plate. The X-ray source is located behind the X-ray plate or film. The collimated X-ray beam passes through the hole on the plate first and then hits the crystal. The backward diffracted X-rays with 2θ angles considerably larger than 90° are collected by the plate. The transmission configuration requires that the crystal size matches the size of the X-ray beam and is not so large that the crystal will block the beam transmission and forward diffracted X-rays. The back-reflection configuration can use the same crystal size as in the transmission configuration, but it is also possible to deal with very large crystals. For instance, the back-reflection Laue camera can be used to characterize or determine the orientation of the lattice planes in a variety of crystal materials such as silicon wafers and turbine blades [3]. At present, the Laue camera and configurations are still used in industrial and academic laboratories. However, the photographic plates and films are mostly replaced by modern X-ray detectors, and the Laue patterns are stored and analyzed with computers.

Another type of X-ray camera based on X-ray photographic films is the Debye–Scherrer camera [2]. Figure 4.1 shows a picture of a Debye–Scherrer camera and an illustration of the diffraction lines on the film. The Debye–Scherrer camera consists of a cylinder shaped camera chamber with a beam entry collimator and a beamstop. The collimator controls the beam size



FIGURE 4.1 Debye–Scherrer camera (a) and the diffraction lines on the film (b).

and divergence. The beamstop has a trap tube to cover the transmitted direct beam and extend the secondary beam path beyond the cylinder chamber. The beamstop consists of a fluorescent screen and a thick piece of lead glass so that the exposure can be monitored. Both the collimator and beamstop tubes are extended as close as possible to the sample to reduce the air scatter from the direct beam. The exit end of the collimator is extended near the sample so as to reduce the air scatter from the primary beam. A very small amount of powdered material is used as the specimen. There are many methods for loading the powder sample; for instance, the powder can be sealed into a fine capillary tube made from glass that does not diffract X-rays. The specimen is mounted on a rotating stage and accurately aligned to the center of the camera. The rotation axis is also the axis of the cylinder chamber. The film used for the camera is a long narrow strip, matching the inside surface of the cylinder chamber. Two holes are punched on the film to adapt to the collimator and the beamstop tube. After exposure, the film is removed from the camera, flattened and chemically processed. Figure 4.1(b) illustrates the diffraction pattern on the developed film. It shows the diffraction lines and the entry hole for the incident beam and exit hole for the transmitted beam. The powder specimen diffracts the X-rays in accordance with Bragg's law to produce cones of diffracted beams. These cones intersect with the film located in the cylindrical camera to generate so-called Debye diffraction rings on the film. The 2θ angle is measured from the center of the beam exit hole, and the center of the entry hole represents $2\theta = 180°$. The 2θ resolution depends on the size of the incident X-ray beam and the length of the film strip, which is determined by the radius of the cylinder chamber. The Debye–Scherrer camera was at one time one of the most widely used diffraction cameras for powder diffraction. Many concepts and theories developed in the application of the camera are still applicable to modern diffractometers.

In addition to the Laue camera and Debye–Scherrer camera, there are many other X-ray diffraction cameras developed to achieve various improved functions [2, 4]. The Seemann–Bohlin focusing camera uses a focusing beam and with a large powder loaded along the camera circle. It can achieve twice the resolution of a Debye–Scherrer camera of the same radius. Due to the large irradiated area, the exposure time can be significantly shorter. However, the total 2θ range on the film is limited. The back-reflection focusing camera employs the same focusing principle as the Seemann–Bohlin camera, but is designed for measuring the back-reflected high 2θ lines. The Guinier camera is a combination of a focusing monochromator and a focusing camera. The low angle reflections are measured in transmission mode. The monochromatic beam passes through the thin specimen and the diffracted beams focus on the film loaded along the cylinder chamber. The high angle reflections are measured in a similar geometry to the Seemann–Bohlin camera. Compared with a Debye–Scherrer camera of the same radius, a Guinier camera can achieve twice the resolution and clearer patterns due to the spectrum purity from the monochromator. Just as in a Seemann–Bohlin camera, the total 2θ range measured by a Guinier camera is limited. The Gandolfi camera [5, 6] adds another rotation axis at a tilt angle of 45° from the original rotation axis of the Debye–Scherrer camera. Both axes rotate during an exposure to provide the randomization in large angular ranges, so the Gandolfi camera can obtain a powder diffraction pattern from a single crystal or a specimen with a few large crystal particles.

4.2 POINT DETECTORS IN CONVENTIONAL DIFFRACTOMETERS

The above diffraction techniques are based on X-ray photographic plates or films, so the apparatuses are normally referred to as X-ray diffraction cameras. The diffraction systems, based on various electronic radiation counters, are usually referred to as X-ray diffractometers. The counters used in conventional diffractometers, such as a diffractometer in Bragg–Brentano

geometry, are point detectors, or zero-dimensional (0D) detectors. Regardless of the actual size of the active area, a point detector can only measure the diffraction intensity from a single 2θ position at a time. The measurement at each 2θ position contributes a data point on the diffraction pattern. The diffraction pattern is measured by scanning the detector over a given 2θ range. An X-ray detector contains at least two basic parts: the transducer and the counting electronics. The transducer converts the incoming X-ray photons into electronic signals. The transducer itself is most often referred to as a detector regardless of the counting electronics. Three types of point detectors are most commonly used in a diffractometer: gas proportional counters or simply proportional counters, scintillation counters, and semiconductor counters [2, 4, 5].

4.2.1 Proportional Counters

A proportional counter is one kind of gaseous ionization detector. It consists of a cylindrical metal shell as a cathode and a thin metal wire as an anode. The cylindrical metal shell is filled with a gas mixture containing mainly inert gas, such as argon. An electric field is applied between the anode and cathode. One end of the cylinder is sealed with an X-ray transparent window. The performance of the detector is then determined by the potential difference of this field. The operating voltage in the proportional counter is set in a range, such as 1000 to 1500 volts. A phenomenon, called multiple ionization or gas amplification occurs when an incoming X-ray photon ionizes the inert gas atoms. Each ionized atom produces an electron and positively charged atom, commonly known as an ion pair. As the charged particle travels through the chamber to the anode wire, it accelerates rapidly under the influence of the applied electric field. The electrons gain enough energy over a mean free path to ionize more gas atoms. The electrons created in these new events also drift toward the anode and generate more ion pairs themselves. In this manner, a cascade of ion pairs can be created, known as a Townsend avalanche. In this multiplication process, a single X-ray photon can generate as many as 10^3 to 10^5 ion pairs. Each avalanche of electrons hits the anode wire and generates a detectable pulse signal which is picked up by the counting electronics. This process of charge amplification can improve the signal-to-noise ratio and also reduce the amount of amplification required from the counting electronics. If the operating voltage is properly chosen, the pulse generated by each avalanche can be distinguished by the electronics as a count. At a given operating voltage, the intensity of the pulse, represented by the total charge between the cathode and anode, is proportional to the energy of the X-ray photon. By measuring the time integral of the electric current of each pulse, we can distinguish the photon energy (wavelength) of the incoming X-rays. Therefore, the detector is named a proportional counter. This proportionality between the photon energy of the incoming X-rays and the pulse intensity makes proportional counters useful for X-ray diffractometers requiring energy discrimination. However, the energy resolution of the proportional counter is not sufficient to be used for energy dispersive X-ray diffraction.

If the voltage is below a range of the proportional counter, the electrons do not gain sufficient energy to create the avalanche, so the detector operates as an ionization chamber. An ionization chamber is not suitable as a detector in an X-ray diffractometer. However, it has been used to monitor the incident beam in X-ray diffraction experiments [7]. If the voltage is too high, the degree of charge amplification reaches a maximum value, and all pulses from the chamber have the same amplitude regardless of the X-ray photon energy, so the detector operates as a Geiger–Müller counter, commonly called a Geiger counter. Geiger counters lose the proportionality to X-ray photon energy, but it has such a high charge amplification that a particle or photon of radiation can temporarily make the gas conductive. The Geiger counter is one of the classic radiation detectors used for radiation survey for safety purposes.

4.2.2 Scintillation Counters

Scintillation counters detect X-rays and other radiation by making use of the phenomenon that certain solid or liquid substances can emit light when struck by X-ray photons or any other ionizing radiation. A typical scintillation counter consists of two main components: a sheet of scintillator (phosphors), which is a type of crystal that fluoresces visible light after excitation by X-ray photons, and a photomultiplier which converts the light flash into electrons and produces a voltage pulse with a large degree of amplification. There are two main types of scintillators: inorganic (such as sodium iodide) and organic (such as a plastic like polystyrene). For X-ray detection, sodium iodide doped with thallium is typically used as the scintillator, denoted as NaI(Tl). The photomultiplier consists of an evacuated envelope with a photocathode at one end. The photocathode is typically made of a photosensitive material, such as a cesium-antimony intermetallic compound. The photocathode is maintained at a large negative potential. The light photons generate electrons when passing through the cathode. The electrons are accelerated towards a dynode maintained at a positive potential, about 100 volts above the photocathode, and excite more electrons. This process continues down the dynode chain, each maintained at a higher voltage than the preceding one. After more than 10 dynodes, the multiplication factor reaches the order of 10^7, so that a large signal is collected at the anode.

The height of the pulses produced in a scintillation counter is proportional to the photon energy of X-rays, but the scintillation counters have much poorer energy resolution than proportional counters. However, scintillation counters are very stable and with quantum efficiency approaching 100%. Scintillation counters are the most widely used point detectors in conventional powder diffractometers. Scintillation counters typically have a very good time resolution. In high-energy physics experiments, a pair of scintillation counters placed some distance apart can be used to measure the time of flight of the particles.

4.2.3 Solid State Detectors

Solid state detectors are made of semiconductor materials as the detecting medium. Therefore, the solid state detector may be referred to as a semiconductor counter or a semiconductor detector. The most commonly used solid state detectors for conventional diffractometers are manufactured from silicon or germanium single crystals doped with lithium, specified as Si(Li) or Ge(Li) detectors. These detectors work in principle much like a solid state diode with a reverse bias. The absorption of an X-ray photon by the semiconductor crystal results in the creation of a cloud of electron–hole pairs, analogous to the electron–ion pairs in a proportional counter. Both the electron and the hole, as negatively and positively charge carriers, are free to move, in opposite directions, under the influence of the bias. This photon-induced current is then preamplified by a field effect transistor to generate an input signal to the main amplifier, and then processed by the counting electronics. The number of electron–hole pairs created by an X-ray photon is proportional to the energy of the X-ray photon divided by the energy required to produce an electron–hole pair. Consequently, the charge collected from each incoming X-ray photon is proportional to the energy of the photon. For example, the energy required to generate an electron–hole pair for an Si(Li) detector is approximately 3.8 eV at an operating temperature of 77 K. An X-ray photon of Cu-K_α radiation has the photon energy of 8041 eV. The total number of electron–hole pairs produced by a single X-ray photon is more than 2000. Compared to proportional counters, solid state detectors have a much higher energy resolution. The energy window for an Si(Li) detector can be set to a value smaller than 200 eV. This energy resolution allows an Si(Li) detector to be used in a diffractometer without a monochromator, since the detector and its counting electronics can eliminate K_β radiation and most white radiation [8–10]. The detector can also effectively discriminate fluorescent radiation from the sample.

One disadvantage of the solid-state detector, particularly the Si(Li) detector, is that the detector needs to be kept at a very low temperature, typically at the liquid nitrogen temperature of 77 K. The low operating temperature is necessary to reduce the detection noise and to prevent the migration of the doping elements, such as Li in Si(Li) detector. It is very common to see a diffractometer with a liquid nitrogen Dewar mounted on top of the solid state detector. Thermoelectric (Peltier) cooling is an alternative way to cool the detector and has been used for most recent solid state detectors.

The most recent development in solid state detectors has introduced more detector types using a variety of different materials – for instance, cadmium telluride, mercuric iodide, and cadmium zinc telluride. The best detector for a given application depends on many factors. For instance, germanium detectors have a high quantum efficiency at shorter wavelength compared to a silicon detector, but it can be easily damaged by accidentally operating at room temperature. Detectors made of high Z semiconductor materials, such as cadmium telluride, mercuric iodide, and cadmium zinc telluride, can operate at room temperature with high efficiency.

4.3 CHARACTERISTICS OF POINT DETECTORS

There are a number of parameters that characterize the performance of a point (0D) detector. The most important are the detective quantum efficiency, count rate, linearity, and energy resolution. The selection of a point detector for X-ray diffraction should be based on the combination and optimization of those parameters.

4.3.1 Counting Statistics

These three types of detectors, proportional counters, scintillation counters, and solid state detectors, are categorized as photon-counting detectors. In a photon-counting detector, each X-ray photon is absorbed and converted to an electronic pulse. The number of pulses counted per unit time is proportional to the incident X-ray flux. Photon-counting detectors typically have a high counting efficiency, approaching 100% at low count rate. Other detectors are integrating detectors, in which a collection of X-ray photons is converted into an analog electrical signal and the size of the signal is proportional to the intensity of incident X-rays. Since the three most commonly used point detectors are all photon-counting detectors, the integrating detectors will be discussed later with two-dimensional detectors.

Assuming that the incident X-rays have a constant flux, the total number of incident X-ray photons at a specified time, t, should be a constant N_0. Because X-ray emission and detection are randomly occurring events, the counts measured in the same time period on the same X-ray beam will not be exactly the same due to variable spacing between counting pulses. The statistics of the process can be explained by a Poisson distribution function [5]:

$$P(N) = \frac{N_0}{N!}\exp(-N_0) \tag{4.1}$$

where N is the total number of X-ray counts measured at the given time t. If the measurement is repeated a large number of times and the values of N are averaged, the average value of N approaches the true value N_0, as the number of repeated measurements approaches infinity. For a large number of counts the Poisson distribution can be expressed approximately as a Gaussian (normal) distribution so that the standard deviation of the measured counts is given as

$$\sigma = \sqrt{N} = \sqrt{Rt} \tag{4.2}$$

where R is the count rate. The probability that the true counts N_0 is between $N\pm\sigma$ is 68.3%, between $N\pm2\sigma$ is 95.4%, and between $N\pm3\sigma$ is 99.7% as shown in Figure 4.2(a). A more revealing expression of the measurement precision can be obtained by multiplying the relative standard deviation, σ/N, by 100% to give the percentage standard deviation as

$$\sigma\% = 100\frac{\sqrt{N}}{N}\% = \frac{100}{\sqrt{N}}\% = \frac{100}{\sqrt{Rt}}\% \tag{4.3}$$

Clearly, a larger number of counts or a larger count rate results in a better precision, based on equations (4.2) and (4.3).

Figure 4.2(b) shows how the percentage standard deviation improves as the number of counts increases. At $N=1$, $\sigma\%=100\%$; at $N=100$, $\sigma\%=10\%$; at $N=10{,}000$, $\sigma\%=1\%$; and at $N=1{,}000{,}000$, $\sigma\%=0.1\%$.

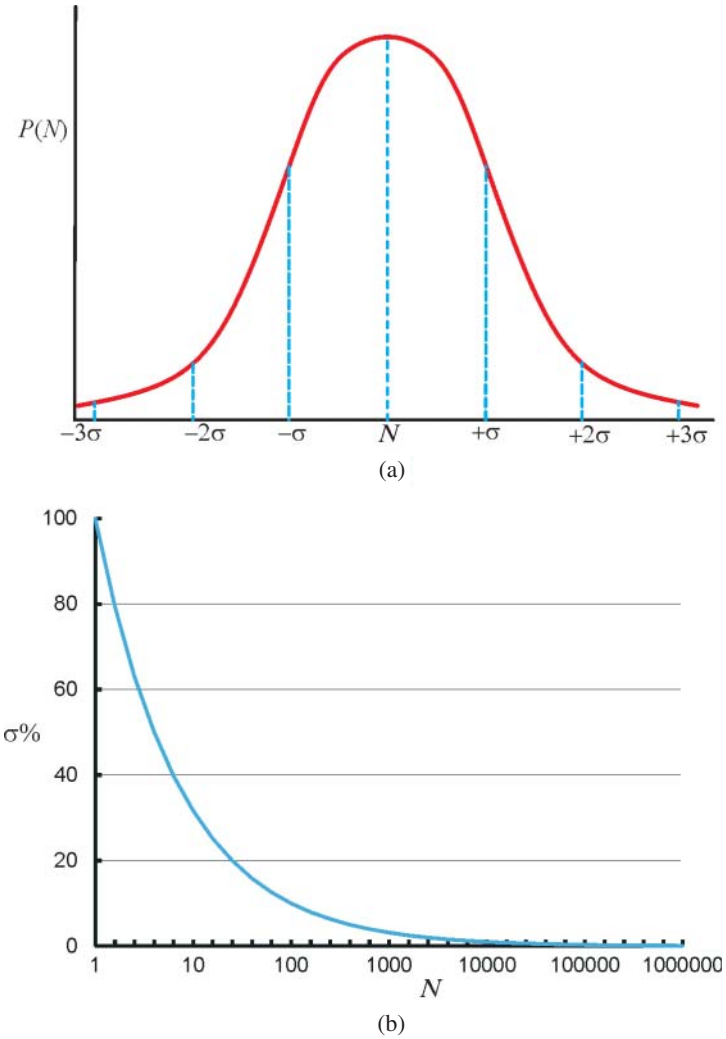


FIGURE 4.2 Description of counting statistics: (a) Gaussian distribution and standard deviation, (b) the relative standard deviation vs. the counts.

The equations (4.2) and (4.3) assume no background in the number of counts. Since the probable error of the counts above the background is a combination of the probable errors of both the total counts and the backgrounds counts, the standard deviation of counts with background is given by

$$\sigma = \sqrt{N_p + N_b} \tag{4.4}$$

where N_p is the total number of counts (including background counts) and N_b is the background counts. The relative standard deviation of the counts above the background is given by

$$\sigma\% = 100\frac{\sqrt{N_p + N_b}}{N_p - N_b}\% \tag{4.5}$$

This equation can be used to calculate the uncertainty of the integrated intensity counts with background correction. However, care must be taken that an appropriate 2θ range is selected. A wide 2θ range may unrealistically increase the contribution of the background counts so as to overestimate the standard deviation. A 2θ range of twice the FWHM can have 98% peak counts covered assuming the peak has Gaussian distribution.

Counting statistics should not be confused with sampling statistics, which will be discussed in Chapter 7 of this book. Both are related and important for the diffraction data quality, but can be influenced by different factors. For instance, increasing the brilliance of the X-ray source will improve the counting statistics, but not the sampling statistics, assuming the incident beam profile and size are the same. This is especially true in transmission mode when the effective diffraction volume is not affected by the penetration depth of the incident X-rays. Sample oscillation may improve the sampling statistics, but not necessarily the counting statistics. For the same diffraction condition with the same sample, the peak from the crystalline planes with high multiplicity will have better counting statistics and sampling statistics. Increasing the data collecting time and detector sensitivity will improve the counting statistics, but not necessarily the sampling statistics. Increasing the beam size will normally improve both the counting statistics and sampling statistics.

4.3.2 Detective Quantum Efficiency and Energy Range

The detective quantum efficiency (DQE), alternatively referred to as the detector quantum efficiency or quantum counting efficiency, is measured by the percentage of incident photons that are converted by the detector into electrons that constitute a measurable signal. For an ideal detector, in which every X-ray photon is converted to a detectable signal without additional noise added, the DQE = 100%. The DQE of a real detector is less than 100% because not every incident X-ray photon is detected, and because there is always some detector noise. The DQE is a parameter defined as the square of the ratio of the output and input signal-to-noise ratios (SNR) [11, 12].

$$DQE = \left(\frac{(S/N)_{out}}{(S/N)_{in}}\right)^2 \tag{4.6}$$

A detector's DQE is affected by many variables – for example, X-ray wavelength, transmission of the detector window, geometric design, the choice of the filling gas, the gas pressure for a gas detector, the doping level of the semiconductor, and the detection active area, etc. The dependence of the DQE on the wavelength, or X-ray photon energy, defines the energy range of a detector. The DQE drops significantly if a detector is used out of its energy range. Figure 4.3 is a schematic

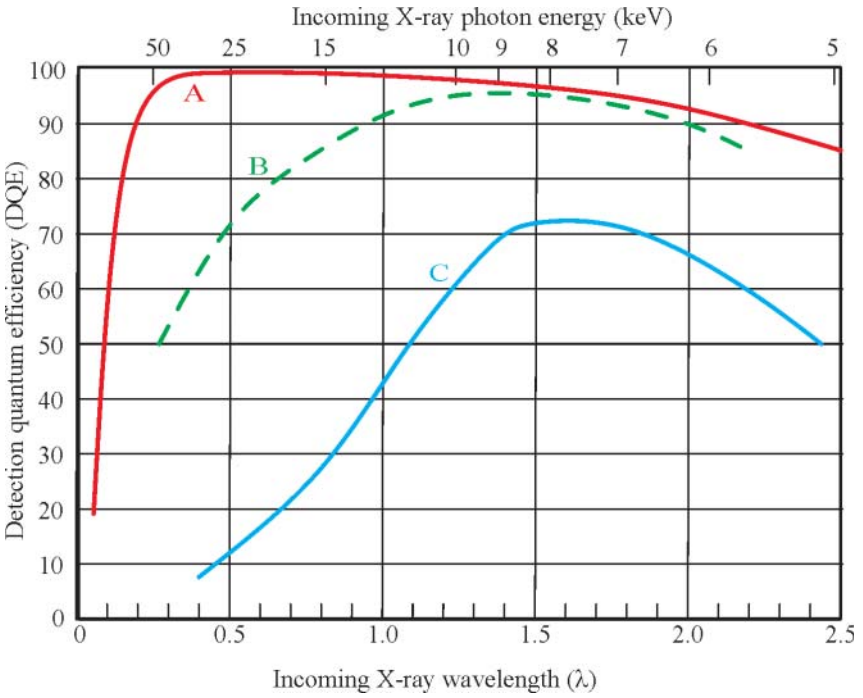


FIGURE 4.3 Detector quantum efficiency (DQE) as a function of wavelength for three typical point detectors: A – scintillation counter, B – Si(Li) solid state detector and C – xenon filled proportional counter. (Schematic comparison based on data from references [2, 4, 5].)

comparison of DQE as a function of wavelength for three typical point detectors. A scintillation counter can have a DQE greater than 80% within the range of 5 to 30 keV. A proportional counter can only achieve a DQE 50% or better within the energy range of 5 to 12 keV and the DQE decreases dramatically with increasing X-ray photon energy in the range of 12 to 20 keV. An Si(Li) solid state detector can have a DQE above 80% from 6 to 20 keV. These are just examples extracted from several references [2, 4, 5]. The specific DQE vs. energy curve of an actual detector varies depending on many factors.

4.3.3 Detector Linearity and Maximum Count Rate

The linearity of a detector determines the accuracy of the intensity measurement in a diffractometer. Figure 4.4 illustrates the detector counting curves of several detectors. The horizontal coordinate is the incoming X-ray flux to the detector, or intensity of the diffracted X-ray beam reaching the detector. The vertical coordinate is the observed count rate produced by the detector. The broken line A represents an ideal detector with 100% DQE and perfect linearity. The dotted line B represents a detector with less than 100% DQE but perfect linearity. The relative intensity measured by this detector reflects the true relative intensity of the diffracted X-rays. This is very close to the counting curve of a proportional counter in which the observed count rate is proportional to the incoming X-ray flux. However, there is a limit on the count rate proportionality, due to the counting losses of the detector. During a short period of time after each count the detector cannot collect another count. This period of time is called dead time. The dead time of a detection can be caused by either the physical characteristics of the detector – for example, the drift time

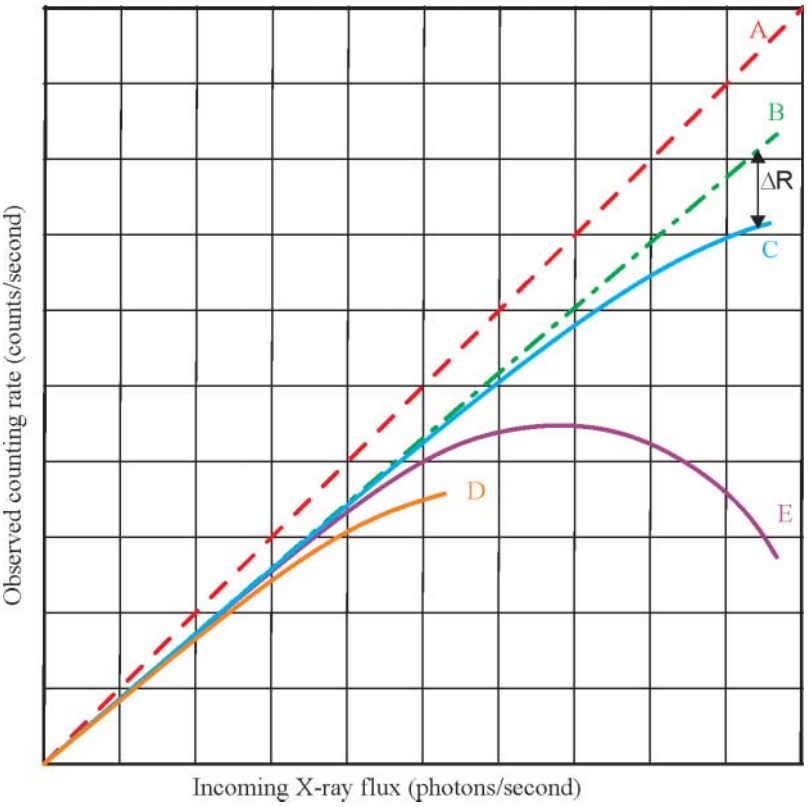


FIGURE 4.4 Illustration of the detector counting curves from: A – an ideal detector with 100% DQE; B – a detector ideal linearity; C – a detector with non-paralyzable dead time; D – a detector with paralyzable dead time; E – a detector with semi-paralyzable dead time.

in a gaseous ionization detector – or the saturation of the counting electronics, for example the shaping time of the amplifier. As a result, the measured count rate is always somewhat below the true value. The discrepancy increases with increasing count rates when the dead time becomes a more significant part of the average time separation between true counts. With the lost counts during the dead time τ, the measured count rate R_m will always be lower than the proportional count rate R with the following approximate relationship

$$R = \frac{R_m}{1 - R_m\tau} \tag{4.7}$$

The counting curve C in Figure 4.4 represents the measured count rate R_m given by the above equation. This equation is reasonably accurate for corrections less than 10%, which means that the term $R_m\tau$ should be less than 0.1. The counting loss ΔR is then given by

$$\Delta R = R - R_m = \frac{R_m^2\tau}{1 - R_m\tau} \tag{4.8}$$

The percentage counting loss is given by

$$\frac{\Delta R}{R} = R_m\tau \tag{4.9}$$

A detector can be categorized as having either non-paralyzable dead time or paralyzable dead time. The counting curve C represents the behavior of a detector with non-paralyzable dead time. That means the detector is dead for a fixed time after each count, but not influenced by the counts occurring during the dead time. The counting loss increases with increasing count rate, but the true count rate of a detector with non-paralyzable dead time can always be estimated by equation (4.7) until the true count rate reaches infinity, when the maximum observed count rate is equal to the inverse of the dead time. In a paralyzable detector, as shown by counting curve D, a second count after each observed count will not be collected except after an time interval at least equal to the dead time. Any event that occurs during the elapsed time will extend the dead time further for an additional dead time. With increasing count rate the counting loss increases so dramatically that the detector will reach a maximum count rate (saturation point) where it will be incapable of collecting any counts at all. At this saturation point the true count rate reaches the inverse of the dead time

$$R = \frac{1}{\tau} \tag{4.10}$$

The observed count rate at the saturation point based on Poisson distribution is then given by

$$R_m = \frac{1}{e\tau} \tag{4.11}$$

The counting curve E represents the behavior of a detector with semi-paralyzable dead time. When the count rate approaches saturation, the observed count rate decreases with increasing incoming flux. In practice, the maximum count rate of a detector may be defined as the count rate at a specified counting loss, 5% for instance.

4.3.4 Energy Resolution

The energy resolution of a detector is its ability to resolve X-ray photons of different energy (or wavelength). The transducer and the electronics, as well as its specific setting in a detector, can be considered as having an energy window or multiple energy windows if a multichannel analyzer (MCA) is used. The energy window allows only the signals generated from X-ray photons within a specific energy range to be counted. The energy resolution of a detector can be expressed in many formats with a variety of definitions. One is given by the size of the energy window, ΔE, in eV. The energy window is determined by the full width at half maximum (FWHM) of the detector efficiency curve as a function of energy with the detector and counting electronics set to a specific wavelength, K_α, for example. Figure 4.5 is a comparison of detector energy resolutions of scintillation counters, proportional counters, and solid state detectors with respect to the characteristic lines of copper. The energy of the characteristic lines of copper are $\boldsymbol{E}(K_{\alpha 1}) = 8.047\,\text{keV}$, $\boldsymbol{E}(K_{\alpha 2}) = 8.027\,\text{keV}$, and $\boldsymbol{E}(K_\beta) = 8.905\,\text{keV}$. The scintillation counter has the poorest resolution of the three detectors. The energy resolution (FWHM of the detector efficiency curve) ΔE is approximately 3 keV. The energy difference between $K_{\alpha 1}$ and K_β is about 900 eV. The scintillation counter does not have sufficient resolution to eliminate the K_β line. The proportional counter has better resolution, with $\Delta E \approx 1$ keV, but is still not sufficient to fully discriminate the K_β line. The Si(Li) solid state detector has significantly better resolution with $\Delta E \approx 200$ eV. This resolution is sufficient to eliminate the K_β line. The energy difference between $K_{\alpha 1}$ and $K_{\alpha 2}$ is only 20 eV. Therefore, an Si(Li) detector cannot eliminate the $K_{\alpha 2}$ line.

The energy resolution of a detector can also be expressed as the ratio of the energy window ΔE to the energy of the monochromatic X-ray beam, E, expressed as $\Delta E/E(\%)$. The $\Delta E/E(\%)$ of the above three detectors are around 37%, 12%, and 2.5% for the scintillation counter, proportional counter, and Si(Li) detector, respectively.

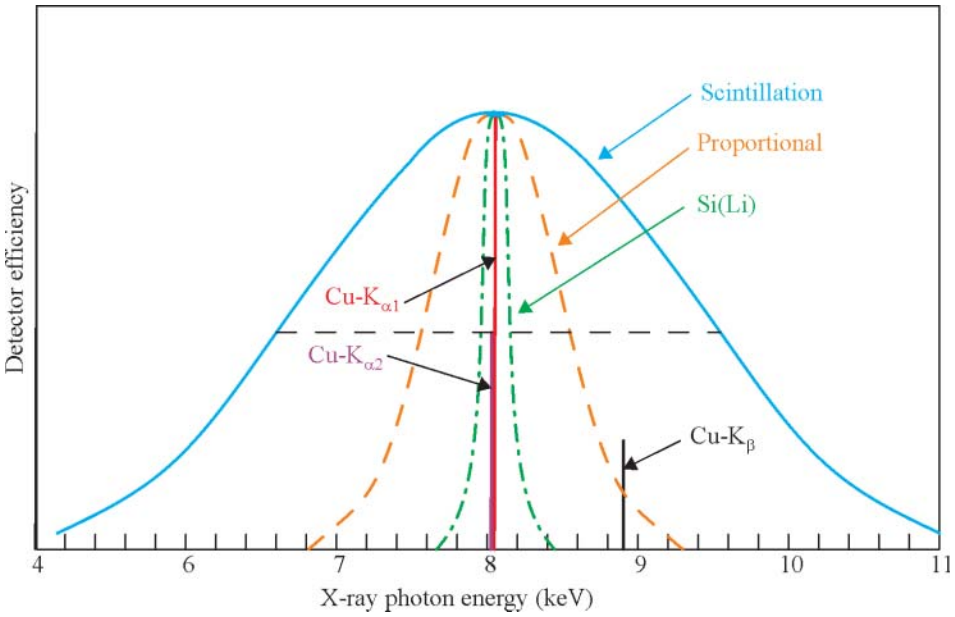


FIGURE 4.5 Comparison of detector energy resolution of scintillation counter, proportional counter, and solid state detector with the characteristic lines of copper.

Combined with an MCA, an Si(Li) detector becomes an energy-dispersive (EDS) detector, which can collect a spectrum of X-rays with an energy resolution as small as 125 eV. This leads to two X-ray analytical technologies: energy dispersive X-ray diffraction (EDXRD) [8] and energy dispersive X-ray fluorescence (EDXRF).

The principle of EDXRD can be explained by the Bragg equation:

$$\lambda = 2d \sin\theta \tag{4.12}$$

where λ is the wavelength, d is the distance between adjacent crystal planes (d-spacing), θ is the Bragg angle at which a diffraction peak is observed when the incident X-rays hit the crystal planes at an angle θ, also with a reflection angle of θ. In a conventional diffractometer, the wavelength λ is a constant. The Bragg condition is satisfied for each d-spacing at a given θ angle. The diffraction pattern is displayed as diffracted intensities at a range of 2θ angles with various peaks corresponding to each d-spacing. In EDXRD, the Bragg angle θ is a constant. The Bragg condition is satisfied for various d-spacing at various wavelengths. A polychromatic X-ray beam is required to provide the λ range. The diffraction pattern is displayed as diffracted intensities at a range of wavelengths with various peaks corresponding to each d-spacing.

The d-spacing resolution of the energy dispersive X-ray diffraction is limited by current detector technology. The d-spacing resolution of a conventional 2θ dispersive diffractometer can easily be a few orders of magnitude better. However, the entire range of EDXRD patterns can be collected simultaneously and without mechanically moving components. With a strong X-ray source, an EDXRD pattern can be collected in a very short time. The measurement unit can also be made in a small size and operated in a harsh environment. For example, the technology has been used as a detection tool for explosives hidden within luggage and packages [9]. It is also used to detect counterfeit drugs and check the quality of other consumer products. An EDXRD pattern can be collected in a constant 2θ angle and it also typically uses X-rays in the high energy

range, which gives this technique high penetration power. This has made the EDXRD a suitable technology for studying samples in pressure cells, such as a sample in a diamond anvil cell (DAC).

Another application of the solid state detector is the energy dispersive X-ray fluorescence (EDXRF). X-ray fluorescence is the phenomenon that when X-ray photons of high energy strike the sample, they produce X-ray fluorescence emissions from the sample target. The spectrum of the fluorescence is unique to the composition of the sample. An energy dispersive detector can collect this spectrum and convert it to electrical counts at various energy levels. Since each element emits a different and identifiable spectrum, EDXRF can determine the presence and concentration of the elements in the sample. Most laboratory EDXRF instruments use liquid nitrogen or Peltier cooled Si(Li) detectors, while some portable devices use other detectors such as mercuric iodide, CdTe, and CdZnTe.

4.3.5 Detection Limit and Dynamic Range

The detection limit is the lowest number of counts that can be distinguished from the absence of true counts within a specified confidence level. The detection limit is estimated from the mean of the noise, the standard deviation of the noise, and some confidence factor. Due to different choices of the confidence factors, there are many different definitions and terminologies that are commonly used. Even when the same terminology is used, there might be differences in the definition of the confidence factor and noise contribution. In order to have the incoming X-ray photons counted with a reasonable statistical certainty, the counts produced by the X-ray photons should be above the detector background noise counts. The detection limit is typically determined as the minimum number of counts that has more than a 95% probability to be truly present in the peak. For a zero noise background photon counter, a single count is the minimum detectable count. The detection limit with 95% confidence is 3 counts [13]. The detection limit when background noise is present is determined by using the standard deviation of the noise count. Assume that the noise background has a Gaussian probability distribution and the standard deviation is given by

$$\sigma_B = \sqrt{N_B} = \sqrt{R_B t} \tag{4.13}$$

where N_B is the background counts, R_B is the noise count rate, and t is the time of the data collection. The background noise counts N_B is assumed to be large enough that Gaussian probability distribution is applicable. The detection limit with 95% confidence is then given as

$$N_{CL95\%} = N_B + 1.65\sqrt{N_B} = R_B t + 1.65\sqrt{R_B t} \tag{4.14}$$

If the detection limit is expressed in the form of count rate, the above equation becomes

$$R_{CL95\%} = R_B + 1.65\sqrt{\frac{R_B}{t}} \tag{4.15}$$

It can be seen that the detection limit in the count rate approaches the noise rate with increasing counting time. In a more restrictive choice of the confidence level, the detection limit with better than 99% confidence is given as

$$N_{CL99\%} = N_B + 3\sqrt{N_B} = R_B t + 3\sqrt{R_B t} \tag{4.16}$$

In this case, the detection limit is defined as three times the standard deviation above the background count and a count measured at or above this limit has a 99.87% probability of not belonging to the background noise count.

The dynamic range of a point detector is defined as the range extending from the detection limit to the maximum count measured in the same length of counting time. The linear dynamic range is the dynamic range within which the maximum counts are collected within the specified linearity. For X-ray detectors, most often the dynamic range refers to linear dynamic range, since only the diffraction pattern collected within the linear dynamic range can be correctly interpreted and analyzed. Dynamic range is given as

$$DR = \frac{N_{\max}}{N_{DL}} = \frac{R_{\max}}{R_{DL}} \tag{4.17}$$

where $N_{\max}$ is the maximum count, N_{DL} is the detection limit, $R_{\max}$ is the maximum count rate at saturation or a specified linearity if linear dynamic range is calculated. As given by equation (4.15), when the detection limit in count rate approaches the noise rate at extended counting time, the dynamic range can be approximated by the ratio of maximum count rate to the noise rate. Therefore, the dynamic range can be approximated by

$$DR \approx \frac{R_{\max}}{R_B} \tag{4.18}$$

Dynamic range is very often confused with the maximum count rate, but must be distinguished. Based on equation (4.18), the dynamic range is equivalent to the maximum linear rate only if the noise rate is 1/s. With a low noise rate, a detector can achieve a dynamic range much higher than its count rate. For example, if a detector has a maximum linear count rate of 10^5/s with a noise rate of 10^{-3}/s. The dynamic range can approach 10^8 for an extended measurement time. The dynamic range for a line (1D) detector or area (2D) detector may be defined differently since the highest count and lowest count may be collected simultaneously at different pixels. This will be discussed later.

4.4 LINE DETECTORS

An X-ray line detector contains an array of detection elements that have identical shape, size and characteristics. The detection elements are called pixels, or sometimes, channels. Line detectors are also referred to as one-dimensional (1D) detectors. Another terminology often used is linear position sensitive detectors (LPSD) or position sensitive detector (PSD). PSD has also been used specifically for a type of line detector based on the technology of gas proportional counters. Position sensitive detector may also refer to an area detector. A line detector can simultaneously measure a one-dimensional distribution of diffracted X-rays. Therefore, a line detector can collect a diffraction pattern in a given 2θ range much faster than a point detector scanning over the same 2θ range. Each pixel of a line detector can be treated as a point detector with a limited active area. All the characteristics of point detectors discussed in the previous section applies to line detectors. There are additional characteristics associated with line detectors which will be discussed in the following sections.

4.4.1 Geometry of Line Detectors

The pixel array in a line detector can be arranged in a straight line or a curved line. Figure 4.6 illustrates the two shapes of line detectors. Figure 4.6(a) is a straight line detector. The distance between the sample S and the detector is D. The detector is located at a swing angle of α away from the incident X-ray beam. The 2θ angle corresponding to the pixel $P(x)$ is given by

$$2\theta = \alpha + \arctan\frac{x}{D} \tag{4.19}$$

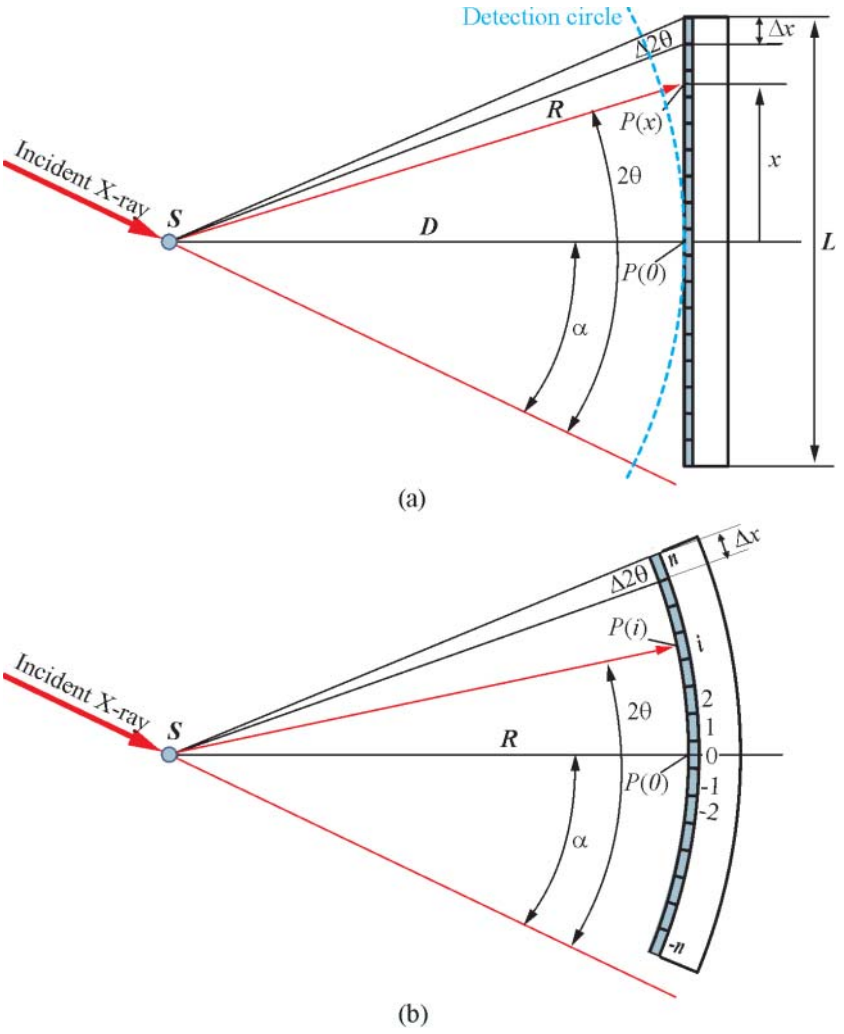


FIGURE 4.6 Illustration of line detectors: (a) straight line, (b) curved line.

where x is the distance between the pixel $P(x)$ and the center pixel $P(0)$. The total 2θ coverage by a straight line detector is then given by

$$2\theta_{coverage} = 2 \arctan \frac{L}{2D} \tag{4.20}$$

where L is the length of the detection area. It can be seen that the total 2θ coverage is dependent on the sample to detector distance – the longer the distance the less the total coverage. It is assumed that the line detector is filled by pixels along the array and that the pixel size, Δx, is the same as the distance between the centers of two adjacent pixels. The 2θ range corresponding to the pixel size for the pixel $P(x)$ is given by the first derivative of equation (4.19) as

$$\Delta(2\theta) = \frac{D}{D^2 + x^2}\Delta x = \frac{D}{R^2}\Delta x \tag{4.21}$$

where R is the distance between the sample and the pixel $P(x)$. It can be observed from this equation that, in general, the 2θ resolution improves with increasing sample-to-detector distance. Considering the effects given by both equations (4.20) and (4.21), a straight line detector has an advantage in that it can be located at short distance for a large 2θ coverage or long distance for a better 2θ resolution.

Equation (4.21) also shows that the 2θ range covered by a pixel varies depending on the location of the pixel on the detector, x. A pixel covers less 2θ range the farther it is away from the center pixel. In another words, the $\Delta 2\theta$ value of a pixel is inversely proportional to the square of the sample-to-pixel distance, or $1/R^2$ fall off. There are several adverse effects associated with this nature. First, each pixel is exposed to a different dosage of X-ray photons even if a point X-ray source located at the sample position emits homogeneous radiation. The intensity measured by the pixels at both ends of the detector would be lower than the intensity measured by the pixel in the center of the detector. In order to have equal intensity gain on all pixels, normalization on the intensity is necessary. Secondly, the straight line detector may have some geometric problems when it is used in a diffractometer with parafocusing geometry [14]. As is shown in Figure 4.6(a), when a straight line detector is located tangential to the detection circle, only the center pixel is right on the detection circle, while aberrations due to defocusing gradually increase with pixels farther away from the center. The third adverse effect happens when the line detector is used in a continuously scanning mode. A line detector may collect a diffraction pattern by scanning it along the diffraction circle over the entire 2θ range, which may be much larger than the detector angular range [15]. In the scanning mode the counts collected at a 2θ position by all the pixels passing that 2θ position are added up to get the total counts at that 2θ position. The non-linear $\Delta 2\theta$ distribution along the detector results in a 2θ mismatch among different pixels. Therefore, either a mathematical correction is required or only a limited 2θ range of the detector is used in scanning mode to reduce the effect.

A curved line detector can overcome all the above problems, since all pixels have the same distance to the sample [16, 17]. Figure 4.6(b) illustrates a curved line detector. The detector pixels are arranged along a circle of radius R with the sample in the center of the circle. The detector is located at a swing angle of α away from the incident X-ray beam. The pixel in the center of the detector is $P(0)$. The 2θ angle corresponding to the i-th pixel $P(i)$ is given by

$$2\theta = \alpha + i\frac{\Delta x}{R} \tag{4.22}$$

where Δx is the pixel size. The angular resolution corresponding to each pixel is

$$\Delta(2\theta) = \frac{\Delta x}{R} \tag{4.23}$$

The $\Delta 2\theta$ value is identical for all pixels since the radius of the detector, R, is fixed, and all pixels have the same size. If the maximum pixel number above $P(0)$ is n and below $P(0)$ is $-n$, then the total number of pixel is $N\ (=2n+1)$. The total 2θ coverage by the curved line detector is then given by

$$2\theta_{coverage} = (2n+1)\frac{\Delta x}{R} = N \cdot \Delta(2\theta) \tag{4.24}$$

It can be seen that the total 2θ coverage is determined by the number of pixels and the radius R. A curved detector does not have the flexibility to select a detector distance for a trade-off between 2θ coverage and 2θ resolution. However, there are more advantages with a curved detector. Since the 2θ distribution along the detector is linear, it is not necessary to give special consideration to pixels away from the center of the detector as has to be done with a straight line detector. The

intensity gains on all pixels are identical if all pixels have the same characteristics. The detector pixels match the diffractometer focusing circle so that all pixels are correctly focused. When used in a scanning mode, there is no 2θ mismatch between different pixels. A curved detector is also typically made for a large 2θ coverage when used in stationary mode.

When a line detector, either a straight or curved detector, is used in scanning mode, ramping-up and ramping-down periods should be added to both ends of the desired diffraction pattern. The accumulated data collection time is identical at all 2θ values only within the 2θ range between the ramping up and ramping down. The ramping-up or ramping-down period equals the 2θ range of the detector. Therefore, a line detector with smaller 2θ range may be more suitable for scanning mode. One alternative is to use the full active length of the detector in stationary mode and use only the center region of the active area in scanning mode.

4.4.2 Types of Line Detectors

The position sensitive proportional chamber has been the most popular line detectors for the past 30 years [14–19]. Although a linear position sensitive detector (LPSD) may refer to any type of line detector in general, most often a PSD implies a linear position sensitive proportional chamber. The working principle of a position sensitive proportional chamber is similar to a gas proportional counter except with a long anode wire extended along the line direction. The anode wire was initially made of a quartz fiber coated with a thin layer of carbon, but metal wire, such as tungsten or molybdenum, was introduced later [18]. The detector chamber is filled with a gas mixture similar to a proportional counter. An electric field is applied between the anode wire and the cathode. One side of the chamber parallel to the anode wire is sealed with an extended X-ray transparent window (typically made of Be foil). The operating voltage is set at the same level as in a proportional counter. An incoming X-ray photon strikes the gas atoms to produce ion pairs which consist of electrons and positive ions. The electrons accelerate rapidly toward the anode wire under the influence of the applied electric field. More electrons are created in the path of the electrons to form an avalanche. Each avalanche of electrons hits the anode wire at the location with the shortest distance to the initial ionization. The avalanche generates a detectable pulse signal. Unlike a proportional counter in which the pulse signal is picked up at one end of the wire, a PSD proportional chamber reads the signal from both ends of the anode wire. Since the time required for a pulse signal to reach the ends is very short, the readout electronics can distinguish one count from another. The difference between the readout times at the two ends is determined by the location on the wire where the signal pulse was generated. Therefore, both the X-ray photon counts and the location of each count can be measured by a PSD system. A linear proportional chamber can also be made into a cylindrical shape with the anode wire and the X-ray window curved into an arc along the diffractometer focusing circle so a large 2θ range can be covered by the detector [16, 17].

In addition to the position sensitive proportional chamber, there are many other technologies used for line and area detectors [20]. Image plates (IP) are mostly used as two-dimensional detectors, but an image plate can also be used as a one-dimensional detector [19] for its large dynamic range and flexible geometry and good spatial resolution. The silicon strip detectors (SSD) is another type of line detector. The detector is made of a semiconductor sensor with an array of n-p diodes on an Si substrate in the form of strips. Compared with a position sensitive proportional chamber, an SSD detector has a higher dynamic range. For X-ray diffractometers, two such detectors, X'Celerator™ and LynxEye™, are commercially available, offered by Panalytical and Bruker respectively. The SSD has many advantages for XRD applications, including high spatial resolution typically with 60–100 μm strip pitch, large count rate up to about 500,000 cps per strip, and high efficiency, even with Mo radiation. A diffractometer

with an SSD can increase the data acquisition rate by a factor of about 100 compared with a conventional point detector diffractometer.

The most recent development in the line detector is the mikrogap™ technology introduced in 2003 by Bruker AXS. The mikrogap™ technology has been developed for both one-dimensional and two-dimensional detectors [21, 22]. It consists of a parallel plate avalanche chamber with a resistive anode separated from the readout electrode by an insulator. The resistive anode significantly reduces the number of sparks and the damaging effect of the spark discharges. The technology details will be discussed in the section on two-dimensional detectors. An example of the line detector based on the mikrogap technology is Våntec-1™ offered by Bruker AXS. It has a large active area of 50×16 mm. The quantum efficiency is greater than 90%. It can be operated with a wide range of photon energies (5–17 keV) with energy resolution of <25%. Due to the high count rate (>10^6 cps) and low background (<0.01 cps/mm^2), it can achieve a dynamic range of 10^8. The separation of the readout electrode from the anode by an insulator of a proper thickness reduces the signal spatial distribution, hence it improves the spatial resolution significantly compared to the position sensitive proportional chamber. Figure 4.7(a) shows a diffractometer equipped with a Våntec-1 detector. Figure 4.7(b) shows the results of an in-situ phase transition investigation of NH_4NO_3, with 58 snapshots of one second each and temperature step of 3°C [23, 24]. The detector measures the diffraction pattern in a 2θ range of 8° in this case.

4.4.3 Characteristics of Line Detectors

Most characteristics of point detectors apply to line detectors with similar definitions. The detective quantum efficiency (DQE), the energy range, and the energy resolution follow the same definition. The detector linearity as defined with point detectors can be used to describe pixel linearity when each pixel is treated like a point detector. The maximum count rate for point detectors is not sufficient to describe a line detector. There are three types of count rates with a line detector and so it must be clearly defined when comparing line detectors. The pixel count rate is the maximum count rate of a pixel in the detector if the single pixel is treated like a point detector. The unit of pixel count rate is counts per second per pixel (cps/pixel). The local count rate is defined as the maximum count rate per unit area on the detector. The typical unit is counts per second per square millimeter (cps/mm^2). Since the pixel in a line detector may have various sizes in the direction perpendicular to the detection line, the parameter of the local count rate based on per unit area is more applicable to an area detector. The global count rate is the maximum count rate when the counts from all pixels or the whole active area of the detector are measured. In an ideal situation the count rate of each pixel or a local area is not affected by incoming X-ray flux of adjacent pixels or areas, and the global count rate R_{global} is a sum of the pixel count rate R_{pixel} or local count rate R_{local}

$$R_{global} = NR_{pixel} = AR_{local} \tag{4.25}$$

where N is the total number of pixels and A is the total detection area of the detector. In practice, the global count rate of most detectors is much less that the sum of the pixel count rate or local count rate

$$R_{global} \ll NR_{pixel} \text{ and } R_{global} \ll AR_{local} \tag{4.26}$$

Similar to dead time in point detectors, line detectors also have dead time for the same reason. Although each pixel in a line detector may be treated as a point detector, the dead time of a line detector has to be considered for all the pixels collectively. For example, the counts collected at a different location of the anode wire of a PSD proportional chamber have to be read at both ends

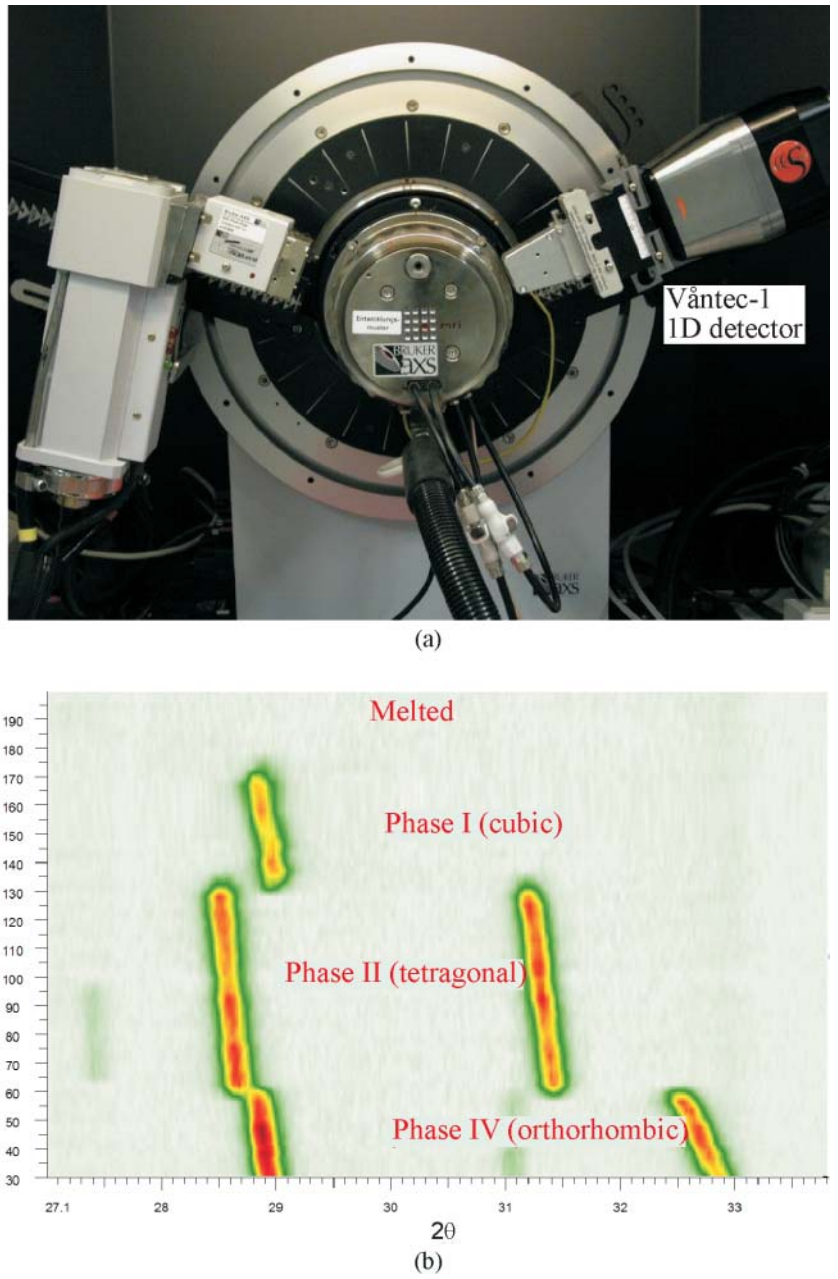


FIGURE 4.7 (a) Våntec-1 detector mounted on a diffractometer (Courtesy of Bruker AXS). (b) In-situ phase transition investigation of NH_4NO_3 with a Våntec-1 detector.

of the anode wire. Both the local count rate and the global count rate are limited by the same counting electronics, assuming that the counting electronics are the bottleneck. The local count rate measured with all the incoming X-ray flux concentrated at a few pixels would be very close to the global count rate if the incoming flux is diffused over the whole detection range. For example, both the local count rate and the global count rate of the Våntec-1 detector are 10^6 cps. In this

case, actual achievable local count rates for multiple sharp high intensity spots are limited by the global count rate.

The detection limit of a line detector is based on each individual pixel with the same definition as for point detectors, that is, the lowest counts that can be distinguished from the absence of the true counts within a specified confidence level. The dynamic range for a line detector has the same definition as with a point detector except that with a line detector the whole dynamic range extending from the detection limit to the maximum count can be observed from different pixels simultaneously.

There are several additional characteristic parameters that apply to line detectors. One is the pixel size. The pixel size of a line detector can be either the actual feature size in the structure of the detector – for instance, the size of the n-p diodes in a silicon strip detector (SSD) – or be artificially determined by the readout electronics. For example, the pixel size of a gas PSD is determined by the readout electronics and may be set at various values. The pixel size of a line detector determines the space between two adjacent pixels and also the 2θ steps in the diffraction data. Therefore the pixel size is also referred to as pixel resolution. However, the pixel sizes do not necessarily represent the spatial resolution or angular resolution of the detector. The true spatial resolution of a line detector is determined by the line spread function (LSF) or the point spread function (PSF) [25]. The LSF can be measured with a sharp line beam from a narrow slit. The FWHM of the intensity profile along the direction orthogonal to the line beam is typically used as a measurement of the LSF. The PSF is measured from a sharp point beam from a small pinhole. The FWHM of the intensity profile along any direction crossing the center of the pinhole image can be used as a measurement of the PSF. Both LSF and PSF are also an important parameter for area detectors and will be discussed in detail in the following section on area detectors.

The detector gain of each pixel is defined as the ratio of the measured counts by the pixel to the incoming photons at the pixel over the same time period. The definition is related to the detective quantum efficiency (DQE) without considering the noise. The precise relation between the gain and the DQE will be further discussed in the following section. The gain of each pixel along a line detector may vary due to the imperfections of the detector. This means that the intensity measured by the detector does not have a flat distribution even if the detector is exposed to a perfectly homogeneous source. For example, non-uniformity in the anode wire may cause a region of depressed efficiency in a PSD proportional chamber, or delay line attenuation may cause an efficiency drop along the range of the detector [16]. In order to get a correct intensity profile of the diffraction pattern, a flood field correction is necessary. There are many algorithms used for flood field correction. The simplest is to normalize all the pixel intensities by a calibration map generated from a flood field profile. The flood field profile is collected from a homogeneous source. The flood field correction is not necessary when a line detector is used in scanning mode: since all the pixels have participated in the measurement of each data point, the gain variation along the detector is averaged out.

Geometrical distortion may also appear with a line detector in which the pixel size or pixel-to-pixel spacing varies along the detector. In this case a spatial correction is necessary, by applying the inverse distortion field to the raw data. The geometrical distortion is also referred to as the linear response of the detector or detector linearity in 2θ [16]. The spatial linearity should not be confused with the linearity of the counting curve of the detector or a pixel. The relationship between 2θ position and channels may be generated by a least-square fitting of a set of calibration data including a series of known 2θ peaks and their corresponding channels. Then the accurate 2θ angles corresponding to each channel can be calculated from this linear response function.

4.5 CHARACTERISTICS OF AREA DETECTORS

Area detectors (2D detectors) are the core of two-dimensional X-ray diffraction systems. The advances in area detector technologies have inspired applications both in X-ray imaging and X-ray diffraction. An area detector contains a two-dimensional array of detection elements which typically have identical shape, size, and characteristics. The detection elements are called pixels. The term positional sensitive detector (PSD) is most often used for line detectors but may also refer to an area detector if the two-dimensional feature is specified. An area detector can simultaneously measure two-dimensional distribution of the diffracted X-rays. Therefore, an area detector may also be referred to as an X-ray camera or imager. There are many detector technologies for area detectors [26–28]. X-ray photographic plates and films are the first generation of two-dimensional X-ray detectors. Three decades ago, photographic film was the most commonly used X-ray detection medium, offering large active area and good spatial resolution with low material costs. However, they became obsolete in the field of X-ray diffraction due to many drawbacks, such as low dynamic range, deformation caused by chemical processing, and tedious digitization processing with a microdensitometer. Today, the most commonly used area detectors include multiwire proportional counters (MWPC), image plates (IP), charge coupled devices (CCD), and microgap detectors [21, 22]. A number of new 2D detector technologies have been developed in recent years, of which, CMOS detectors and pixel array detectors (PAD) are two good examples. Each detector type has its advantages over the other types. In order to make the right choice of area detector for a two-dimensional X-ray diffraction system and applications, it is necessary to characterize area detectors with consistent and comparable parameters. Each of the commonly used detector technologies is then introduced and the parameters describing the characteristics of these area detectors are then summarized in the end of this section.

Most characteristics of point detectors and line detectors apply to area detectors with similar definitions. The detective quantum efficiency (DQE), the energy range and the energy resolution follow the same definition. The detector linearity as defined with point detectors can be used to describe pixel linearity when each pixel is treated as a point detector. As with line detectors, the maximum count rate for point detectors is not sufficient to describe an area detector. There are three types of count rate with an area detector and each must be clearly defined when comparing area detectors. The three types of count rate defined for line detectors – local, pixel, and global count rates – apply to area detectors too. The detection limit of an area detector is based on each individual pixel with the same definition for point detectors: the lowest count that can be distinguished from the absence of the true counts within a specified confidence level. The dynamic range for an area detector has the same definition as with a point detector, except that with an area detector, the whole dynamic range extending from the detection limit to the maximum count can be observed from different pixels simultaneously. In order to record the entire two-dimensional diffraction pattern, it is necessary for the dynamic range of the detector to be at least the dynamic range of the diffraction pattern, which is typically in the range of 10^2 to 10^6 for most applications. If the range of reflection intensities exceeds the dynamic range of the detector, then the detector will either saturate or have low intensity patterns truncated. Therefore, it is desirable that the detector have as large a dynamic range as possible.

4.5.1 Active Area and Angular Coverage

As discussed in Chapter 2, an ideal detector is defined as a detector with a detecting surface covering the complete diffraction space of 4π solid angle. A real area detector has a limited

detection surface and the detection surface can be spherical, cylindrical, or flat. The spherical or cylindrical detectors are normally designed for a fixed sample-to-detector distance, while a flat detector has the flexibility to be used at different sample-to-detector distances, with either high resolution at large distance or large angular coverage at short distance. The detection surface shape is also determined by detector techniques. For example, a CCD detector is made of a large semiconductor wafer so that only flat CCDs are available, while an image plate is flexible so that it is easily bent to a cylindrical shape. Microgap detectors are considered to have a flat detection surface, although it is possible to make the proprietary grid into a curved shape.

The area of the detection surface is also referred to as the active area. The active area is one of the most important parameters of 2D detectors. The larger the active area of a detector, the larger the solid angle that can be covered at the same sample-to-detector distance. This is especially important when the instrumentation or sample size precludes a short sample-to-detector distance. For instance, the data collection for in-situ characterization must be able to capture the diffraction pattern corresponding to a particular stage of the phase transformation, deformation, or chemical reaction. Scanning a smaller 2D detector to cover the desired diffraction pattern can be misleading due to the fact that a different part of the diffraction pattern may represent a different stage of the material transition. The sample environment chamber or special stage, such as heating stage and loading stage, precludes a short sample-to-detector distance.

The active area is limited by the detector technology. For instance, the active area of a CCD detector is limited by the semiconductor wafer size and fabrication facility. A large active area can be achieved by using a large demagnification optical lens or fiber optical lens. Stacking several CCD chips or detector modules side by side to build a so-called mosaic detector is another way to achieve large active area. The gaseous detectors, such as multiwire and microgap detectors, can be made with relative large active area.

The angular coverage of a 2D detector is determined by the detector size and the sample-to-detector distance. Figure 4.8 illustrates the angular coverage of three 2D detectors with the active area of 14×14 mm^2, 28×28 mm^2, and 140×140 mm^2. At 150 mm detector distance (D), the angular coverages for the three detectors are 5.3°, 10.7°, and 50° respectively.

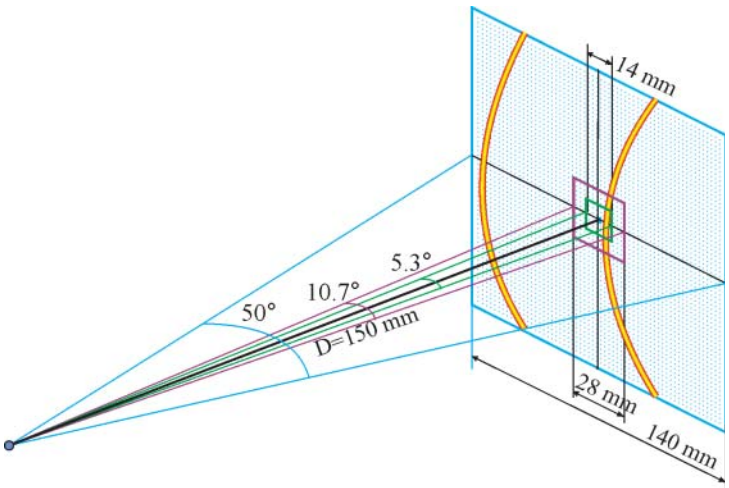


FIGURE 4.8 Angular coverage of 2D detectors of three different active areas.

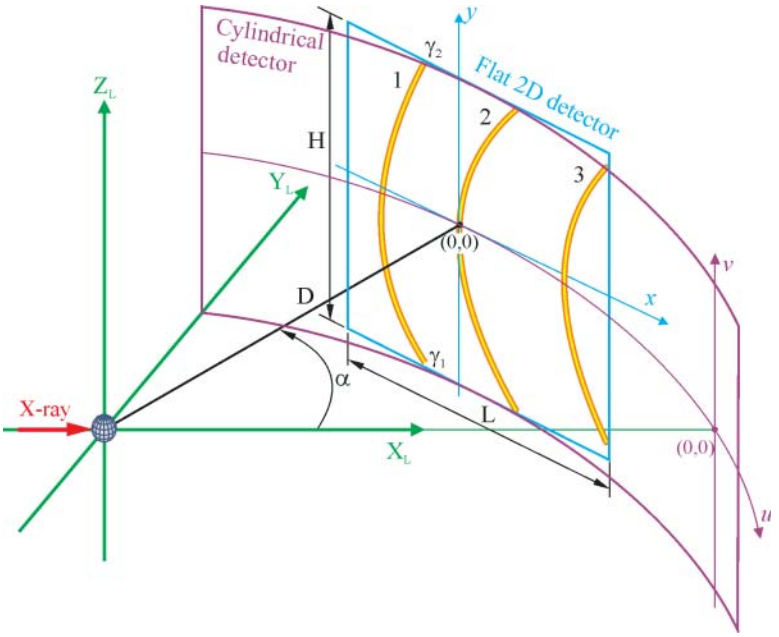


FIGURE 4.9 The γ angular coverage of rectangular flat 2D detector and cylindrical detector.

The angular coverage of a 2D detector can also be evaluated in the diffraction space as 2θ coverage and γ coverage. Figure 4.9 illustrates a rectangular 2D detector in laboratory coordinates. L is the detector width (dimension within the diffractometer plane) and H is the detector height (dimension perpendicular to the diffractometer plane). The 2θ coverage ($\Delta 2\theta$) on the diffractometer plane is given by

$$\Delta 2\theta = 2 \arctan\left(\frac{L}{2D}\right) \tag{4.27}$$

The γ coverage ($\Delta\gamma$) is more complicated and is determined by the detector distance D, detector size H and L, Bragg angle 2θ, and swing angle α. For an arbitrary diffraction ring 1, the diffraction ring ends at the top and bottom edges of the detector. In order to get $\Delta\gamma$ coverage for a flat detector, the γ_1 and γ_2 are first calculated from the following implicit equation respectively for the + and – signs:

$$H = \pm \frac{2D \sin 2\theta \cos\gamma}{\cos\alpha \cos 2\theta - \sin\alpha \sin 2\theta \sin\gamma} \begin{cases} 0 \le \gamma < \pi & \text{if} \quad \alpha \le 0 \\ -\pi < \gamma < 0 & \text{if} \quad \alpha > 0 \end{cases} \tag{4.28}$$

Or we can rewrite it as two implicit equations for γ_1 and γ_2 respectively:

$$H(\cos\alpha \cos 2\theta - \sin\alpha \sin 2\theta \sin\gamma_1) + 2D \sin 2\theta \cos\gamma_1 = 0 \tag{4.29}$$

$$H(\cos\alpha \cos 2\theta - \sin\alpha \sin 2\theta \sin\gamma_2) - 2D \sin 2\theta \cos\gamma_2 = 0 \tag{4.30}$$

Then, we have:

$$\Delta\gamma = |\gamma_2 - \gamma_1| \tag{4.31}$$

For a cylindrical detector (illustrated in purple) of the same height H, the γ_1 and γ_2 can be given by the following two explicit equations:

$$\gamma_1 = \frac{u}{|u|} \arccos \frac{H}{\sin 2\theta \sqrt{4D^2 + H^2}} \tag{4.32}$$

$$\gamma_2 = \frac{u}{|u|} \arccos \frac{-H}{\sin 2\theta \sqrt{4D^2 + H^2}} \tag{4.33}$$

where D is used for the radius of the cylindrical detector because it is equivalent to the sample-to-detector distance for a flat detector. The location of a pixel or point in the flattened cylindrical image is given by the coordinate u and v. Then we have

$$\Delta\gamma = |\gamma_2| - |\gamma_1| = \arccos \frac{-H}{\sin 2\theta \sqrt{4D^2 + H^2}} - \arccos \frac{H}{\sin 2\theta \sqrt{4D^2 + H^2}} \tag{4.34}$$

Considering that γ_1 and γ_2 are symmetric about 90°, the above equation can be simplified to

$$\Delta\gamma = 2 \arcsin \frac{H}{\sin 2\theta \sqrt{4D^2 + H^2}} \tag{4.35}$$

In a typical measurement configuration with a flat 2D detector, the swing angle, either positive or negative, is set at the vicinity of 2θ, the diffraction ring 2 ($|\alpha| = 2\theta$) for example, so that the aberration between the flat detector and cylindrical detector is small, especially when detector size H is smaller than D. In this case, $\Delta\gamma$ for the flat detector can be approximated by the above equation with negligible error. The $\Delta\gamma$ calculated from the cylindrical equation represents the maximum value for a flat detector when the diffraction ring cutoff appears at the y axis of the detector.

As shown by the diffraction ring 3, the measured γ range may be limited by the detector width L if diffraction ring is cut off at the side edge of the detector, especially for low 2θ rings and small aspect ratio ($L < H$). When the γ range is limited by the detector width, $\Delta\gamma$ is given by

$$\Delta\gamma = 2 \arccos \frac{\cos 2\theta (2D \sin\alpha + L \cos\alpha)}{\sin 2\theta (L \sin\alpha - 2D \cos\alpha)} \tag{4.36}$$

For a detector with small width L as a limit factor, the $\Delta\gamma$ coverage can be increased by using a swing angle smaller than 2θ within the range of

$$2\theta - \arctan \frac{L}{2D} < |\alpha| < 2\theta \tag{4.37}$$

In order to maximize the 2θ or γ coverage, a rectangular detector may be mounted in the system in two different orientations. When the longer dimension is used in parallel to the diffractometer plane, it is referred to as 2θ-optimized mode. When the longer dimension is used perpendicular to the diffractometer plane, it is referred to as γ-optimized mode. Figure 4.10 shows the γ range as a function of 2θ for the Eiger 2R 500k™ detector with active area about 77.2 mm × 38.6 mm at various detector distance and orientation. The purple plot is the $\Delta\gamma$ as a function of 2θ, calculated from the implicit equations for the detector in γ-optimized mode, 100 mm detector distance, and $2\theta = |\alpha|$. The blue plot is approximated from the explicit equation for cylindrical detector. Both the plots are almost overlapping in the most part of the 2θ range, except at the 2θ angle below 25° and above 155°, where the cylindrical detector collects a complete diffraction

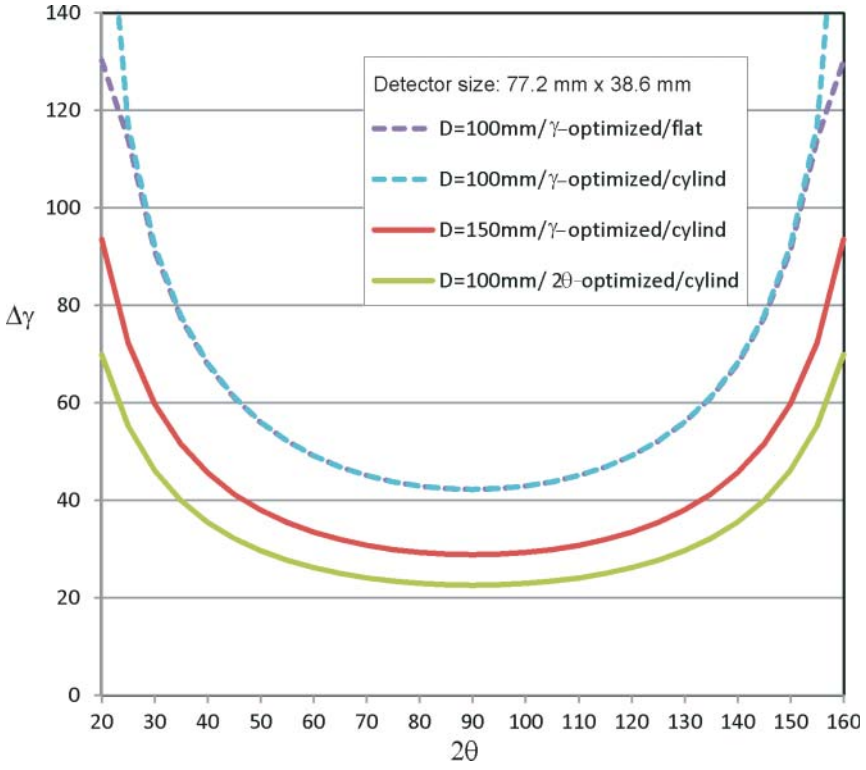


FIGURE 4.10 The γ range as a function of 2θ at various detector distances and orientations.

ring and the flat detector has a cutoff at the side edge of the detector. For the detector distance at D = 150 mm for γ optimized mode and D = 100 mm for 2θ optimized mode, the $\Delta\gamma$ vs. 2θ plot can be calculated by equation for cylindrical detector with negligible error. In general, the angular coverage $\Delta\gamma$ is minimum at $2\theta = 90°$ and increases toward both the low 2θ and high 2θ angles.

4.5.2 Weight and Dimension

In addition to the active area, the overall weight and dimensions are also very important to the performance of an area detector. The weight of the detector has to be supported by the goniometer, so a heavy detector means high demands on the size and power of the goniometer. In a vertical configuration, a heavy detector also requires a heavy counterweight to balance the driving gear. The overall dimensions of an area detector include the height, width, and depth. Those dimensions determine the maneuverability of the detector within a diffractometer, especially when a diffractometer is loaded with many accessories, such as a video microscope and sample loading mechanism. Another important parameter of an area detector that tends to be ignored by most users is the blank margin surrounding the active area of the detector. Figure 4.11 shows the relationship between the maximum measurable 2θ angle and the detector blank margin. For high 2θ angle measurement, the detector swing angle is set so that the incident X-ray optics is as closely as possible in touch with the detector. At this point, the maximum detector swing angle is α_{max} and the maximum measurable angle is $2\theta_{max}$. The unmeasurable blank angle is determined by the detector blank margin m and the optics blank margin h, the

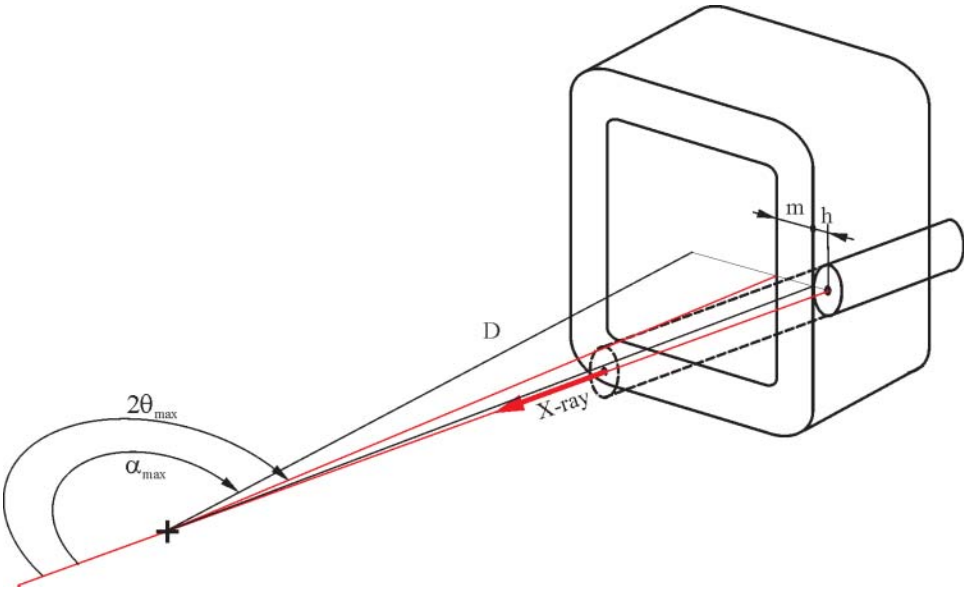


FIGURE 4.11 Detector dimensions and maximum measurable 2θ.

dimension from the incident X-ray beam to the outer surface of the X-ray optics, including collimator or beam path. The maximum measurable angle is given by

$$2\theta_{\max} = \pi - \frac{m+h}{D} \tag{4.38}$$

It can be seen that reducing either the detector blank margin or optics blank margin can increase the maximum measurable angle. For the same detector and optics, it is possible to increase the maximum measurable angle by increasing the sample-to-detector distance, but this sacrifices the detector angular coverage.

4.5.3 Angular Coverage of Pixels

The distance from the sample to a pixel in a flat detector is dependent on the location of the pixel in the detector. Therefore, the solid angle corresponding to each pixel also varies as a function of the pixel location in the detector. Figure 4.12 Illustrates the relationship between the solid angle covered by each pixel and its location in a flat area detector. The symbol S may represents a sample or a calibration source in the instrument center. The distance between the sample S and the detector is D. We first look at a pixel $P(0,y)$ located on the y axis with a distance y from the center pixel $P(0,0)$. The pixel size is Δx and Δy ($\Delta x = \Delta y$). The distance between the sample S and the pixel is R'. The angle range covered by this pixel in the y axis direction, $\Delta\beta$, can be given in an equation similar to equation (4.21) as

$$\Delta\beta = \frac{D}{D^2 + y^2}\Delta y = \frac{D}{R'^2}\Delta y \tag{4.39}$$

The angular range covered by this pixel in the x axis direction, $\Delta\alpha$ can be simply given as

$$\Delta\alpha = \frac{\Delta x}{R'} \tag{4.40}$$

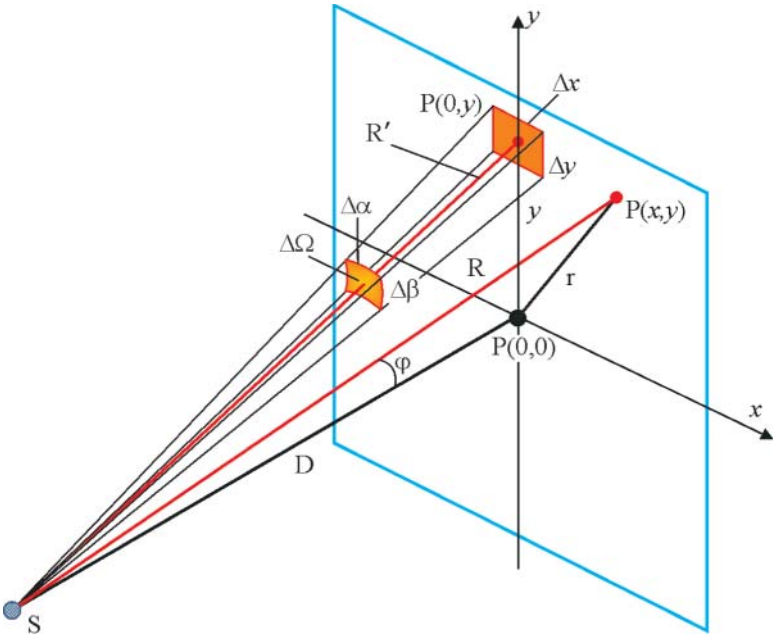


FIGURE 4.12 Illustration of a flat area detector showing the relationship between the solid angle covered by each pixel and its location on the detector.

The solid angle covered by this pixel, $\Delta\Omega$, is then given as

$$\Delta\Omega = \Delta\alpha \cdot \Delta\beta = \frac{D}{R'^3}\Delta y \cdot \Delta x = \frac{D}{R'^3}\Delta A \tag{4.41}$$

where $\Delta A = \Delta x \cdot \Delta y$ is the area of the pixel. It can be proven that this equation can apply to any pixel in an arbitrary position $P(x,y)$. The only difference is that the distance between the pixel and the sample R' is replaced by R and

$$R = \sqrt{D^2 + x^2 + y^2} = \sqrt{D^2 + r^2} \tag{4.42}$$

When a homogeneous calibration source is used, the flux to a pixel at $P(x,y)$ is given as

$$F(x,y) = \Delta\Omega B = \frac{\Delta A D B}{R^3} = \frac{\Delta A D B}{(D^2 + x^2 + y^2)^{3/2}} \tag{4.43}$$

where $F(x,y)$ is the flux (photons/second) intercepted by the pixel and B is the brightness of the source (photons/second·milliradian^2). The ratio of the flux in pixel $P(x,y)$ to the center pixel $P(0,0)$ is then given as

$$\frac{F(x,y)}{F(0,0)} = \frac{D^3}{R^3} = \frac{D^3}{(D^2 + x^2 + y^2)^{3/2}} = \cos^3\varphi \tag{4.44}$$

where φ is the angle between the X-rays to the pixel $P(x,y)$ and the X-rays to the pixel at detector center $P(0,0)$. The factor $\cos^3\varphi$ represents the pixel intensity fall-off with respect to the pixel intensity at the center of the detector. It can be seen that the greater the sample-to-detector distance, the smaller the difference between the center pixel and the edge pixel in terms of the flux

from the homogeneous source. This is the major reason that the data frame collected at short sample-to-detector distance has a higher contrast between the edge and the center.

Geometric distortion may also appear with an area detector in which the detector gain varies from pixel to pixel or a pixel position deviates from the specified pixel position (spatial distortion). The detector gain variation can be corrected by a flood field correction with a homogeneous radiation source. The flood field algorithm is dependent on the type of detector. After the flood field correction, all pixels should have the same counts when exposed to same radiation. The spatial distortion can be corrected by applying the inverse distortion field to the raw data frame. Geometric distortion is also referred to as the spatial linearity, which should not be confused with the linearity of the counting curve of the detector or a pixel. The relationship between measured pixel position and the true pixel position can be determined by measuring the centroid position of all pinholes on a fiducial plate to generate a look-up tables so that the accurate position of each pixel can be calculated. More details on the flood field correction and spatial correction will be covered in Chapter 6 on data treatment.

4.5.4 Spatial Resolution of Area Detectors

The spatial resolution of an area detector is determined by two parameters. One is the pixel size. A pixel is a single point information element in a digital graphic image. The term "pixel" is an abbreviation from picture element ("pix" and "el"). In principle, each pixel is not really a dot, or a square, but an abstract sample point. For example, in a picture image, a pixel is determined by its position in the image and the content of the pixel can be a single variable, such as the brightness in a black-white image, or three variables, such as red, green, and blue in a color image. In a two-dimensional X-ray diffraction frame, which is equivalent to a picture image, each pixel contains the X-ray intensity collected by the detector corresponding to the pixel element. The pixel size of an area detector can be determined or related to the actual feature sizes of the detector structure or artificially determined by the readout electronics or data acquisition software. Many detector techniques allow multiple settings for variable pixel size. In the diffraction frame, the pixel size is given by the actual detector active area and the number of pixels in the frame. For example, when a Hi-Star™ (MWPC) detector of 10.5 cm diameter is used to collect a diffraction frame of $1k \times 1k$ (1024×1024 pixels), the pixel size is approximately $100\,\mu m \times 100\,\mu m$. The same detector can be used to collect a frame size of 512×512 pixels, in which case the pixel size is $200\,\mu m \times 200\,\mu m$. The pixel size of an area detector determines the space between two adjacent pixels and also the minimum angular steps in the diffraction data, therefore the pixel size is also referred to as pixel resolution.

However, the pixel sizes do not necessarily represent true spatial resolution or the angular resolution of the detector. The resolving power of an area detector is its ability to measure the angular separation of the points in a diffraction frame. The resolving power of an area detector is ultimately limited by its point spread function (PSF) [29]. The PSF is the two-dimensional response of an area detector to a parallel point beam smaller than one pixel. When the sharp parallel point beam strikes the detector, not only do the pixels directly covered by the beam record counts, but the surrounding pixels also records counts to a certain extent. The phenomenon is observed as if the point beam has spread over the region directly struck by the beam. In other words, the PSF gives a mapping of the probability density that an X-ray photon is recorded by a pixel in the vicinity of the point where the direct beam hits the detector. Therefore, the PSF is also referred to as the spatial redistribution function. Figure 4.13(a) shows the PSF produced from a parallel point beam. The plane at the half maximum intensity has a cross-sectional region with the PSF. The FWHM can be measured at any direction crossing the centroid of the cross-section. Generally, the PSF is isotropic, so the FWHM should be the same measured in all directions.

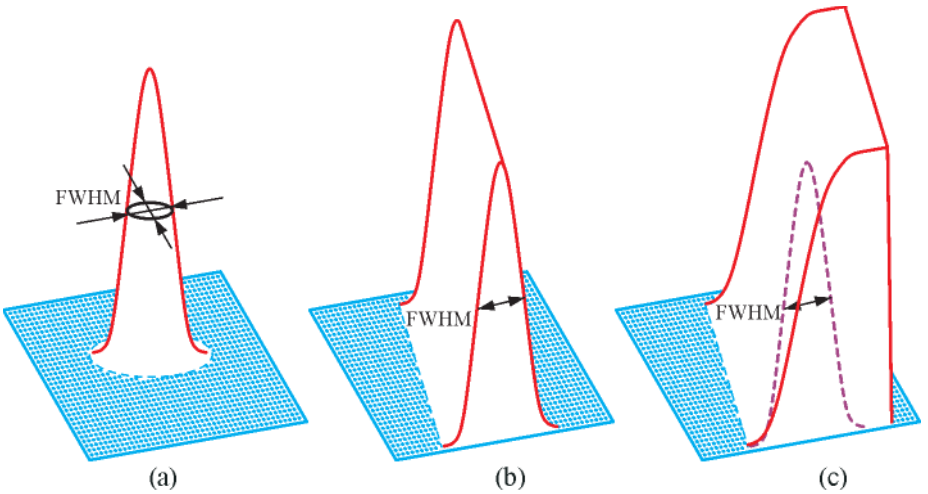


FIGURE 4.13 (a) Point spread function (PSF) from a parallel point beam, (b) line spread function (LSF) from a sharp line beam, (c) first derivative of the integrated intensity curve (broken line) from the image of a razor blade.

Measuring the PSF directly by using a small parallel point beam is difficult because the small PSF spot covers a few pixels and is hard to distinguish from hot pixels or other detector defects. Instead, the line spread function (LSF) can be measured with a sharp line beam from a narrow slit [25]. Figure 4.13(b) is the intensity profile of the image from the sharp line beam. The LSF can be obtained by integrating the image from the line beam along the direction of the line. The FWHM of the integrated profile can be used to describe the LSP. Theoretically, LSF and PSF profiles are not equivalent, but in practice they are not distinguished and may be referenced by the detector specification alternately. Since the integration is over many pixels, the measurement is less likely to be affected by hot pixels or other detector defects. When the line beam is aligned perfectly to an array of detector pixels, there are only a few pixels along the LSF profile. For accurate LSF measurement, the line beam is intentionally positioned with a tilt angle from the orthogonal direction of the pixel array so that the LSF can have smaller steps in the integrated profile [30]. Figure 4.13(c) shows an alternative method of measuring the PSF. A strong isotropic scatter or source is placed at the sample position and the X-ray frame is collected with a razor blade placed in front of the detector. An integrated intensity profile is obtained by integrating the collected intensity perpendicular to the shadow. The PSF and its FWHM are measured from the first derivation (dotted line) of the integrated intensity profile. The FWHM of the PSF obtained by the above three methods are not necessarily identical, so it is imperative to specify the measurement method when the FWHM of a PSF is referred.

The RMS (root mean square) is another parameter often used to describe the PSF. The normal distribution, also called the Gaussian distribution, is the most common shape of the PSF. The RMS of a Gaussian distribution is its standard deviation, σ. Therefore, the FWHM and RMS have the following relation assuming the PSF is a Gaussian distribution:

$$\text{FWHM} = 2\sqrt{-2\ln(1/2)} \cdot \text{RMS} = 2.3548 \cdot \text{RMS} \tag{4.45}$$

The values of the FWHM and RMS are significantly different, so it is important to be precise about which parameter is used when the value is given for a PSF.

Some recent solid-state based 2D detectors can achieve point spread functions as narrow as one pixel. For many 2D detectors with continuous detection area, such as MWPC and microgap detectors, the pixel size is artificially determined by the readout electronics or data acquisition software. In order to fully utilize the resolving power of this type of 2D detector, the pixel size should be smaller than the FWHM of the PSF. The pixel size should be small enough that at least the 50% drop from the center of the PSF can be observed by the pixel adjacent to the center pixel. In practice, the FWHM of 3 to 6 times the pixel size is a reasonable choice if a smaller pixel does not have other detrimental effects. Further reduction in pixel size does not necessarily improve resolution.

4.5.5 Pixel Number and Angular Resolution

Corresponding to the large active area, the total number of pixels is also critical. The same concept as a typical digital camera, the "megapixel" is the most important spec for a 2D X-ray detector. There are many arguments about how one can use a 2D detector for high resolution at large sample-to-detector distance or large angular coverage at short distance. However, the large distance results in a smaller angular coverage, while short distance means poor angular resolution. The best possible optimization with a 2D detector is determined by its megapixel – the number of pixels in the diffraction frame. Figure 4.14 shows the same three 2D detectors as in Figure 4.8. The large 2D detector has a pixel format of 2048×2048 with pixel size of 68 μm. The total number pixel is 4.2 megapixel (MP). At $D = 150$ mm, the angular resolution per pixel is 0.026°. The two small 2D detectors have the pixel format of 256×256 (=0.66 MP) and 512×512 (0.26 MP) for 14 mm and 28 mm respectively. To achieve the same angular coverage, the 14 mm detector has to be located at 15 mm and the 28 mm detector at 30 mm. Although both the smaller detectors have smaller pixel size of 55 μm, the angular resolution per pixel is 0.21° and 0.11° respectively. For the same angular coverage, both the small 2D detectors have much poorer angular resolution. In addition to the poor angular resolution, it is also not practical to put a detector so close to the sample because either goniometer, sample holder, or environment chamber need certain space to operate.

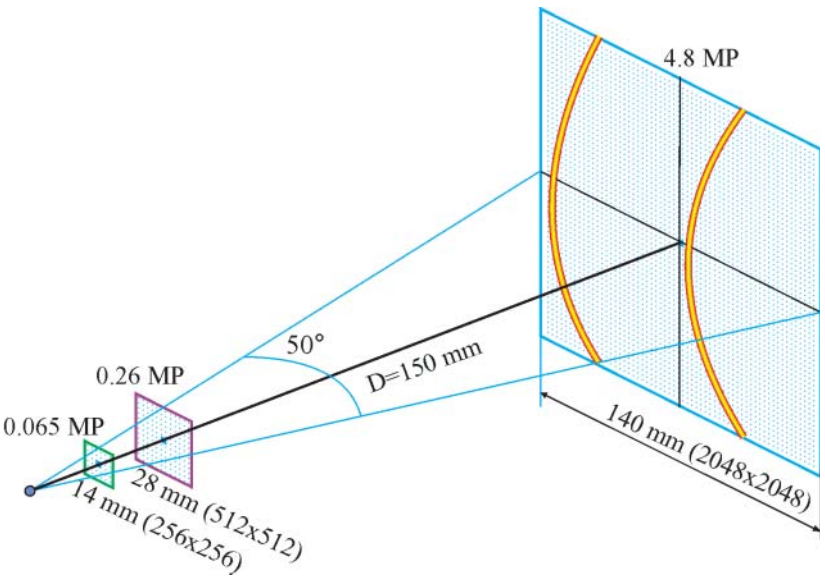


FIGURE 4.14 Total number of pixels (megapixel or MP) of 2D detectors with three different active areas.

4.5.6 Angular Resolution of a 2D Diffractometer

The angular resolution of a 2D diffractometer is not only determined by the pixel size and the PSF of the 2D detector, but also many other factors, such as the instrument broadening contributed by the X-ray optics, including beam size, beam profile, and divergence. The angular resolution represents the resolving power for both 2θ and γ. Since the angular coverage and resolution along the x axis of the detector (on the diffractometer plane) have more consistent relation to the detector size and pixel size, we analyze the angular resolution based on the 2θ resolution. The 2θ resolution is also one of the most critical characteristics of a diffractometer. If the PSF and the other broadening effects by optics are given by Gaussian function as shown in Figure 4.15(a), the overall spatial resolution is a convolution of both functions:

$$FWHM^2_{\text{Overall}} = FWHM^2_{PSF} + FWHM^2_{Optics} \tag{4.46}$$

The term $FWHM_{PSF}$ may be replaced by the pixel size if the detector has a PSF of one pixel. The relation between the overall resolution, PSF and optics can be simply given by Pythagorus, as illustrated by the right-angle triangle in Figure 4.15(b). Therefore, reducing the FWHM of the PSF may not significantly improve the resolution if the FWHM of the instrument's optics dominate the overall resolution. The 2θ resolution is determined by the overall spatial resolution and the sample-to-detector distance. The minimum angle (in radians) between two adjacent reflections which can be detected and separated is:

$$\Delta 2\theta = FWHM_{\text{Overall}}/D = \sqrt{FWHM^2_{PSF} + FWHM^2_{Optics}}/D \tag{4.47}$$

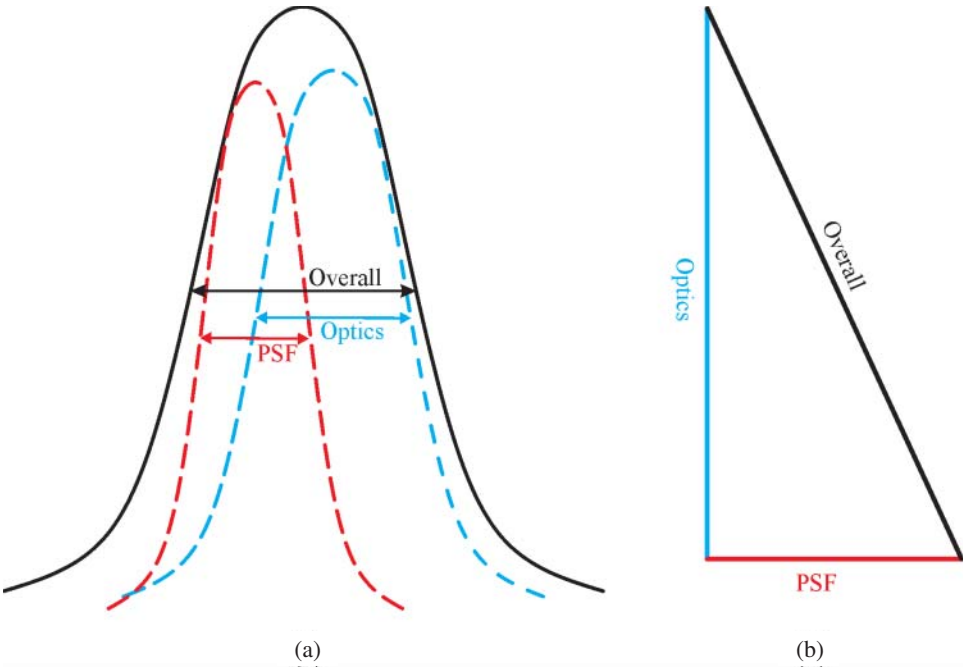


FIGURE 4.15 Point spread function (PSF) and 2θ resolution: (a) FWHM of PSF, optics, and overall instrument broadening, (b) resolution triangle.

If $FWHM_{Optics}$ varies with the detector distance, for example with a non-parallel incident X-ray beam, the optics broadening at the specific distance $FWHM_{Optics}(D)$ has to be used. If the only optics broadening is the size of the parallel beam, $FWHM_{Optics}$ can be considered as a constant regardless of the detector distance. For instance, a diffractometer with optics broadening solely from a parallel beam size of 500 μm and detector PSF 200 μm, the $FWHM_{Overall}$ is 538.5 μm. With the detector distance of 150 mm, the 2θ resolution is from 0.205°. By replacing it with a detector with PSF 50 μm, the $FWHM_{2\theta}$ becomes 502.5 μm, the 2θ resolution becomes 0.192°. The 2θ resolution benefit by improving PSF from 200 μm to 50 μm is from 0.205° to 0.192°, not significant as one would expect. However, the 2θ resolution can be significantly improved with a long detector distance. If increasing the detector distance to $D = 600$ mm for the same $FWHM_{Overall} = 538.5$ μm, the 2θ resolution becomes 0.051°. The above equations give the 2θ resolution evaluated at the center of the detector. Because the pixel-to-sample distance increases for the pixels away from the center, the angular resolution improves further towards the edge of the detector. The difference between the pixels at the center and edge of the detector diminishes with a long detector distance. The 2θ resolution given by the above two equations can be considered as the lower bounds of the angular resolution for a particular setup. Practically, with all other conditions the same, a long detector distance with large 2D detector is typically a preferred approach for achieving high angular resolution. This is the case for most two-dimensional small angle X-ray scattering (SAXS) systems.

It seems that reducing both the incident X-ray beam size and PSF will achieve high resolution, but this is only feasible for fine powder or polycrystalline materials with homogenous and randomly oriented crystallites. The effective sampling volume is significantly reduced with a smaller beam size, which results in a poor sampling statistics, and also reduced X-ray counts if the incident beam has the same flux density. Figure 4.16 illustrates the relationship between incident beam size and effective diffraction volume for two systems (a) and (b). The beam size, detector size, and pixel size (or PSF) in system (a) are proportionally twice as much as in the system (b). Both systems would achieve the same angular resolution, but the effective diffraction volume of (b) is only a quarter of system (a). In other words, the number of crystal grains in the irradiated volume of system (a) is four times that of system (b). For most applications, system (a) is preferred due to the significantly better sampling statistics.

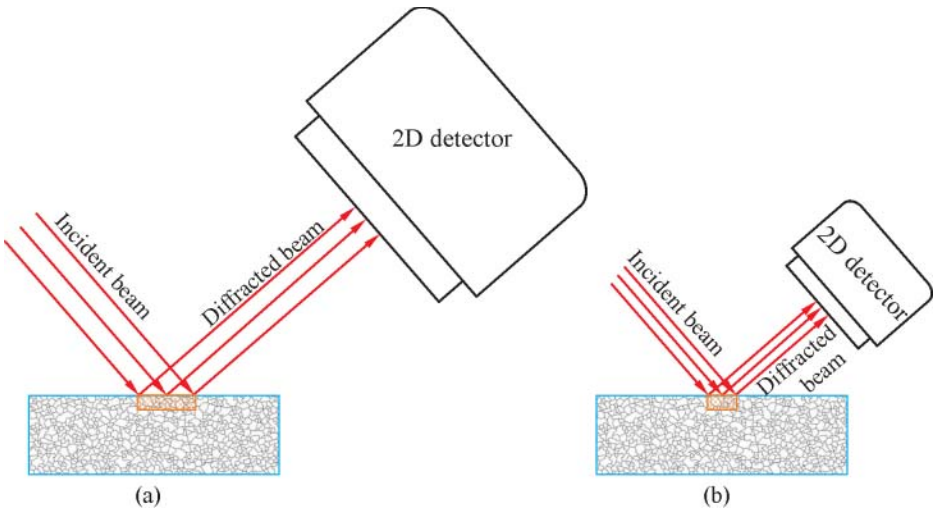


FIGURE 4.16 Effective diffraction volume for: (a) large beam size, PSF, detector size, (b) beam size, PSF, detector size, and detector distance reduced by half.

With advances in detector technology, the pixel size and PSF can be further reduced along with the improvement of other properties. But there is a limit determined by the nature of the sample microstructure. For most laboratory systems, the incident X-ray beam size is 50 to 1000 μm, therefore the pixel size or PSF in the range of 50 to 200 μm is reasonable. Except for some special applications, further reducing the pixel size or PSF below 50 μm is not necessary. For instance, a large beam size and long detector distance with a large 2D detector are typically preferred for small angle X-ray scattering (SAXS) system. For the same active area, a small pixel size also means large data files to transfer, store, and process, which might be counterproductive. Some detectors allow smaller pixels to be binned into larger pixels so as to reduce the frame file size.

4.6 TYPES OF AREA DETECTORS

Area detectors, like point and line detectors, can be classified into two broad categories: photon-counting detectors and integrating detectors [31]. Photon-counting area detectors – also referred to as digital X-ray imagers – can detect a single X-ray photon entering the active area. In a photon-counting detector, each X-ray photon is absorbed and converted to an electric pulse. The number of pulses counted per unit time is proportional to the incident X-ray flux. Photon-counting detectors typically have high counting efficiency approaching 100% at low count rate. The most commonly used photon-counting area detectors include multiwire proportional counter (MWPC), pixel arrays (PAD), and microgap detectors. Integrating area detectors, also referred to as analog X-ray imagers, can record X-ray intensity by measuring the analogue electrical signals converted from the X-ray flux. The signal size of each pixel is proportional to the fluence of incident X-rays. The most commonly used integrating area detectors include image plates (IP), charge coupled devices (CCD), and charge-integrating pixel detector (CPAD). This section gives a brief description of the working principles and performance of several of the most commonly used detector technologies.

4.6.1 Multiwire Proportional Counter

The multiwire proportional counter (MWPC) – also referred to as a two-dimensional position-sensitive proportional counter – was developed more than 40 years ago [31–35]. The MWPC is a gaseous photon-counting detector consisting of an X-ray proportional chamber, with a two-dimensional multiwire grid, a preamplifier, and decoding electronics. Figure 4.17 shows a cutaway view of a MWPC detector (Bruker Hi-Star™). The working principle of the MWPC is similar to a gas proportional counter except with the anode and cathode in a two-dimensional multiwire grid. The grid is composed of three parallel planar electrodes made of an array of parallel metal wires. The three planar electrodes consist of an anode layer sandwiched between two layers of cathodes. One layer of cathode wires is in the horizontal direction (x-cathode) and another layer in the vertical direction (y-cathode). The chamber is filled with ionization gas pressurized from one to several atmospheres. The Hi-Star uses a Xe/methane gas mixture pressurized to approximately 4 atmospheres. The Be window attenuation is the only loss of detector efficiency at low count rate. The Be window of the Hi-Star is 80% transparent to 8 keV (Cu-K_α) radiation and permits pressurized operation. When an X-ray photon enters the detector it interacts with the xenon near the front window, ionizing the gas and creating a small region of 1 to 2 μm containing primary electrons. The number of electrons in this region is proportional to the energy of the incident X-rays. The electric field accelerates these electrons from the near-window region through a drift region to reach the anode. The electrons gained enough energy over a mean free path to ionize more gas atoms. The electrons created in these new events also drift toward the anode and generate more ion pairs themselves. In this process, an avalanche of secondary electrons can produce a gain of 10^3 to 10^4. Each avalanche of electrons

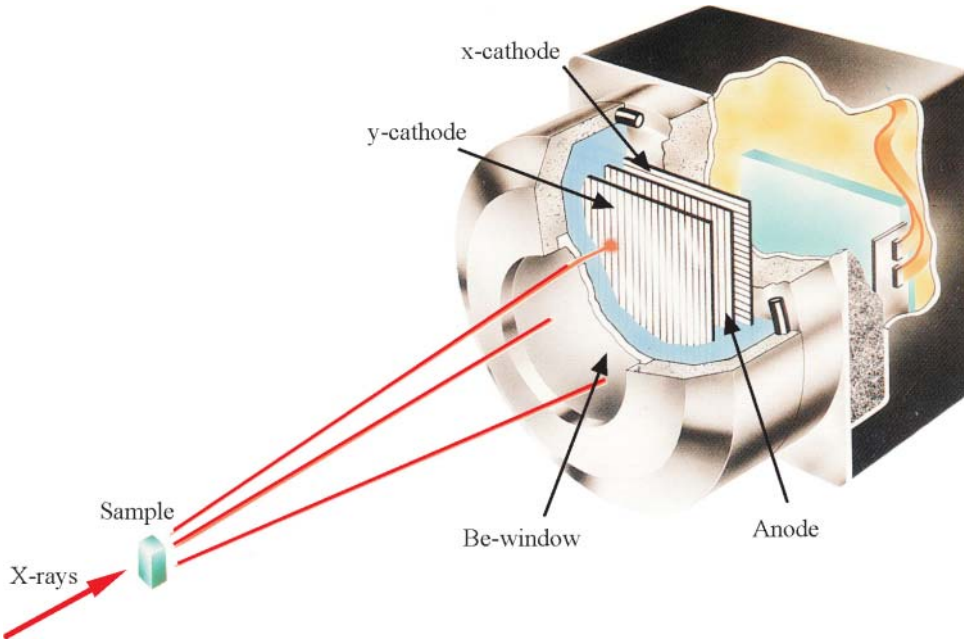


FIGURE 4.17 Cutaway view of a MWPC detector (Bruker Hi-Star™).

hits the anode wires and generates a detectable pulse signal, which is picked up by the counting electronics. The Hi-Star detection grid consists of an anode wire plane of fine wires located between two cathode planes of very fine-pitched wires. The electron cloud passes through the first cathode and is amplified by a factor of 2000 as it is collected at the anode wire surface. The charge burst is sufficient to produce a measurable pulse on the cathode wires on both sides of the anode and distributed over several wires. The centroid position of this avalanche can be calculated from the horizontal and vertical wires with accuracy significantly better than the wire spacing.

Similar to the conventional proportional counter, MWPC has limited local and global count rates. The local space charge is created during the avalanche process near the anode wires. The charge is neutralized by a drift of the charge cloud to the cathode, which takes a few microseconds. Therefore, the local counting rate is limited by this ion collection time. Reducing the spacing between wires within the cathode and anode layers, and the spacing between cathode and anode layers, can improve the local count rate, but it is very difficult to achieve more than 10^4 cps/mm^2. The local count rate of a typical MWPC is 10^3 cps/mm^2. The readout process of each count also takes time, typically a few microseconds. This is a dead time for the entire detector. The global count rate is limited due to this dead time. The global count rate can be improved by setting up parallel processes of several electronically isolated subassemblies of the detector, as if the detector were divided into an array of independent detectors. Similar to the conventional proportional counter, the dead time limits not only the global count rate, but also the linearity of a MWPC. Due to the counting losses at high count rate, the DQE of MWPC decreases with increasing count rate at high count rate.

For those X-ray diffraction applications not demanding high count rate, MWPC detectors have many advantages, including a large active area, high DQE, single photon sensitivity, real time readout, insensitivity to magnetic fields, good spatial resolution, high dynamic range, and low noise. The combination of these characteristics makes the MWPC very suitable for

a laboratory system with sealed tubes or rotation anode X-ray generators. The MWPC is also the detector of choice for microdiffraction and high-throughput XRD screening when high sensitivity and speed are critical. As an example, the Hi-Star™ area detector produced by Bruker AXS has a large imaging area (10.5 cm diameter) for X-ray detection. It is sensitive to X-ray wavelengths corresponding to the 3–15 keV energy range and is a true photon-counting device, with a detective quantum efficiency of about 80%. The near 20% loss is caused by the absorption of the Be window. It can collect a data frame of 1024×1024 (or 512×512) pixels with a pixel size of 100 μm (or 200 μm for 512×512 frames). The analog signal processing electronics located directly behind the detector produces very low noise signals, permitting high spatial resolution (200 μm) to be achieved at low charge gains of 2000. The position decoding circuit (PDC) converts the analog signals from the detector into digital values representing the *xy* position of each X-ray photon. Data from the PDC transfers to the frame buffer computer over a 32 bit wide parallel data link, allowing the frame to be displayed in real time or stored as 512×512 or 1024×1024 pixels frame, with 16 bits of data for each pixel. Because the detector is sealed, the xenon tube remains stable for years, and adjustments to its circuitry are not usually necessary. Adjustment of the detector bias is, however, required for use with different X-ray energies. Two preset bias settings are available, normally one for the given X-ray source and one for the calibration source. Two settings can be selected automatically or manually.

4.6.2 Image Plate

The imaging plate (IP) is a two-dimensional detector developed first by the Fuji Company for X-ray radiography, and then found many applications in X-ray diffraction [36–40]. Image plates, in many ways, resemble photographic films, except that no darkroom processing is necessary to reveal the recorded X-ray image. A typical image plate consists of a storage phosphor and image reader. The storage phosphor is embedded in an organic binder to form a flexible plate. The plate can be loaded in an X-ray diffraction system in the same way as a photographic film. When the plate is exposed to X-rays, the image is stored in the phosphor coating as a latent image. The image is then recovered from the phosphor by scanning an He-Ne laser beam across the plate. When the laser beam strikes an element of storage phosphor a phenomenon known as photostimulated luminescence produces light with a specified wavelength. The intensity of the light is proportional to the dosage of the original exposed X-rays by the element of storage phosphor. The luminescence is then read by a photodetector. A digitized X-ray image is then produced after the completion of the readout scan. The latent image in the plate can be erased by exposing the plate to visible light and the image plate can then be reused.

Compared to conventional X-ray films, X-ray image plates have large dynamic range ($10^5 \sim 10^6$) and high sensitivity. The large active area with a relatively low cost is the most important advantage of IP over other types of area detectors. The flexible IP makes it possible to produce a curved detection surface, for instance, in a cylindrical shape [39]. About 10 to 15 years ago, the IP has been broadly used in single crystal diffractometers for protein crystals. However, there are several drawbacks preventing the IP from being broadly used in X-ray diffraction with polycrystalline materials. The IP requires a significantly longer readout time compared to other types of area detectors. During the readout process, the film has to rotate at a high speed and the laser/reader probe has to move with great accuracy over the film. The IP has to be erased after a readout to get rid of the remaining imaging, since the readout is not 100% efficient. For very strong signals, the erasure may not be complete, leaving a ghost image for the next exposure. Considering the conversion processes from X-ray photons to latent image, from latent image to photostimulated luminescence, and photostimulated luminescence to photoelectrons, the DQE of a typical IP is 10–20% [40]. Since the overall noise level of IP is not proportional to the count

rate, the DQE at low count rate is even lower. Therefore IP is not suitable for applications with weak diffraction intensity, as the diffraction signal may be buried in the background noise [31]. The latent image in the storage phosphor decays over time if it is not read out immediately. The intensity of photostimulated luminescence reduces to one half of the value approximately ten hours after the exposure. This decay may introduce distortion in relative intensity if an application needs long exposure with weak diffraction signals.

4.6.3 CCD Detector

The charge coupled device (CCD) is another type of area detector, first introduced for X-ray imaging [41] and then introduced for X-ray diffraction [42, 43]. A CCD consists of an array of light-sensitive metal-oxide-semiconductor (MOS) capacitors. The array of potential wells is formed by transparent and conductive polysilicon gates, which are made of highly doped polycrystalline silicon electrodes. CCD detectors can detect X-ray photons directly or indirectly. Figure 4.18 shows the direct detection method. An X-ray photon passes through the polysilicon gate and oxide insulator, reaching the depletion region. The X-ray photon is absorbed within the silicon of the CCD and is converted to electron–hole pairs. If this absorption occurs within the depletion region of the CCD, the electrons and holes are separated by the internal electric field, the electrons are stored in the potential wells at each pixel site, and then are read out by applying appropriately phased voltages to the gate electrodes on the CCD.

The photoelectrons generated outside the depletion region will not contribute to the signal. The internal gain, or ideal quantum yield, is defined as the number of photoelectrons produced by each absorbed X-ray photon. It is related to the energy of the absorbed photon, for Si:

$$N_e = \frac{E}{3.65} \tag{4.48}$$

where E is the energy (in eV) of the incident X-rays. N_e is the ideal quantum yield. For example, a single X-ray photon from Cu-K_α radiation (8 keV) can produce more than 2000 electron–hole pairs. This high internal gain in the direct method may be an advantage in detecting a few photons or low energy photons, while for an integrating detector, the limited capacitance of each potential well can easily be saturated. Therefore the direct method has a low dynamic range – for instance,

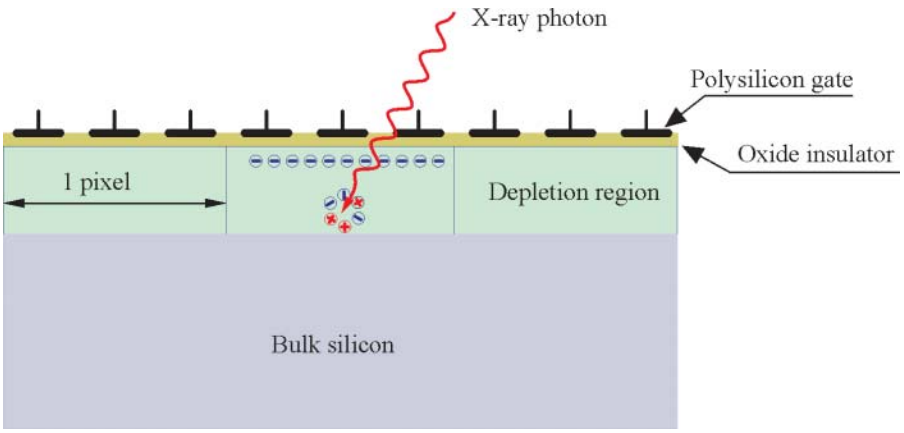


FIGURE 4.18 Schematic showing the side section of three pixels and the direct detection of an X-ray photon in a front illuminated CCD.

less than 200 for Cu-K_α with a 16-bit device. The direct detection CCD detector offers excellent spatial resolution due to its narrow PSF. The high internal gain can compensate for background noise, so device cooling may not be necessary.

The CCD in Figure 4.18 is front-illuminated, in which the X-ray photons enter the depletion region through the electrode structure on the top surface of the device. This structure attenuates low energy X-ray photons, so the DQE is reduced with soft X-ray photons. One way to achieve a high DQE over the entire energy range of interest is to use a back illuminated (or back thinned) CCD, in which the X-ray photons enter the depletion region through the reverse side of the CCD chip. The thickness of the bulk Si on the reverse side is also reduced (back thinned) to reduce the attenuation of incoming X-rays.

Most CCD X-ray detectors work by the indirect detection method. The incoming X-ray photons are first converted to visible light photons by a layer of material, known as a phosphor or scintillator. The visible photons are then detected by the CCD. There is no fundamental difference in the wavelength conversion mechanism between phosphors or scintillators. The two words are very often used interchangeably when distinction is not necessary. The differences between the two materials are in the way they are made and their microstructures. Phosphors are made of a powder-based material with thick film processing techniques and scintillators are made by vapor deposition with some degree of crystal texture. The materials for either are selected for high conversion efficiency and linearity from X-ray photons to visible light photons, high X-ray absorption or stopping power, high spatial resolution, and no memory effects. The most popularly used material with the above characteristics is terbium-doped gadolinium oxysulphide (Gd_2O_2S:Tb) often referred as GADOX or P43. This phosphor absorbs X-ray photons and emits visible photons predominately at 545 nm (2.28 eV), with approximately 15% conversion efficiency. Therefore the number of visible photons, N, emitted per absorbed X-ray photon of energy E (eV) can be calculated as

$$N = \frac{E \times 0.15}{2.28} \tag{4.49}$$

A single X-ray photon from Cu-K_α radiation (8 keV) can produce more than 500 visible light photons. The visible light photons are emitted in all directions in the 4π solid angle and only a fraction of them reaches the detector. Therefore, the conversion in the phosphor adds noise to the detection process and broadens the PSF of the CCD. In addition, the CCD detects visible light photons with an internal gain different from direct detection. Each absorbed visible photon produces only one photoelectron. The detector spatial resolution and quantum efficiency are largely dependent on the characteristics of the phosphor, such as layer thickness, particle size, and the type of phosphor material. Most phosphors, such as GADOX, are developed for medical X-ray imaging. Since medical images are collected at higher energy levels (typically >50 keV), these phosphors are not optimal for X-ray diffraction, which typically requires energy levels in the range 5–18 keV. Some proprietary phosphor screens optimized for X-ray diffraction have been developed by some detector vendors [44, 45].

Detector performance is also dependent on the coupling of the phosphor or scintillator to the CCD. Direct coupling between the phosphor and CCD will allow some incident X-ray photons to pass through the phosphor and be detected directly by the CCD as noise. One way to prevent this from happening is to couple the phosphor output to the CCD through a fiber optic taper [43]. Figure 4.19(a) shows a schematic of a typical CCD detector used in X-ray diffraction. The incoming X-rays diffracted from the sample reach a phosphor screen through an X-ray transparent window. The X-ray window is made of materials transparent to X-rays, but opaque to ambient light, such as beryllium or aluminum. X-rays excite the phosphor screen, producing visible photons which are focused onto a CCD chip by a fiber optic taper. Fiberoptic

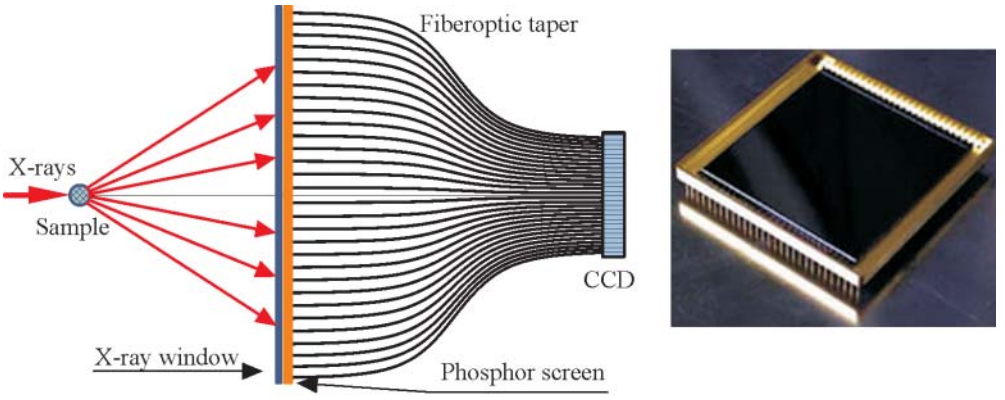


FIGURE 4.19 CCD detector: (a) schematic showing phosphor, fiberoptic taper, and CCD chip, (b) a picture of a Fairchild 486 CCD chip.

demagnification is used to increase the effective active area. Therefore, the detector has an imaging area larger than the active area of a CCD chip. The demagnification can also be achieved by a high quality lens system. However, transmission efficiencies of typical lenses are smaller than that of fiberoptic tapers in typical demagnification [12]. The number of electrons created by a single X-ray photon depends on the energy of the X-ray, the efficiency of the phosphor, demagnification, and the characteristics of the CCD chip. The CCD detector is an integral detector. The X-ray image is stored during exposure until the chip is read out. The readout time is on the order of seconds. Figure 4.19(b) shows a picture of Fairchild CCD486 chip which has an active area of $62\text{mm} \times 62\text{mm}$. The CCD can be used in 512×512, 1024×1024 (1k), 2048×2048 (2k) and 4196×4196 (4k) pixel formats. The pixel size is 15 μm in the 4k mode.

The fiberoptic taper can increase the effective active area. However, this demagnification results in a loss of sensitivity, degradation of spatial resolution, and also introduces distortions into the image. The reduced sensitivity and broadened PSF can be interpreted by the well-known Liouville's theorem [44]. Thus, a detector with a demagnification of 2 to 1 will have four times lower sensitivity assuming no loss of light photons in the optic fibers. In order to have a large active area without sacrificing too much sensitivity, the largest CCD available should be used, which requires less or no demagnification. Figure 4.20(a) shows a CCD detector (Bruker APEX II™) which is made of a very large wafer-scale CCD sensor that does not require any fiber optic demagnification. This allows the APEX II detector to achieve superior sensitivity, dynamic range, and spatial resolution. Figure 4.20(b) shows a schematic of the APEX II CCD detector. The phosphor screen is coupled with the CCD chip through a fiberoptic faceplate without demagnification. The thin fiberoptic faceplate can significantly reduce a type of noise called a zinger. These are localized noise spikes caused by the scintillation of radioactive impurities in the glass fibers. The rate of zinger production is proportional to the total volume of glass. The thin fiberoptic faceplate reduces the zinger rate by about 40 times compared to the conventional CCD detector using a fiberoptic taper. All these features result in higher sensitivity, better spatial resolution, and no spatial distortions with the APEX II detector.

The indirect detection method has many advantages over the direct detection method. The increase in the dynamic range is the most important. Due to fewer photoelectrons being produced by each X-ray photon, particularly at higher energies, the potential well in a pixel can store photoelectrons from more X-ray photons. For example, with a linear full-well capacity of over

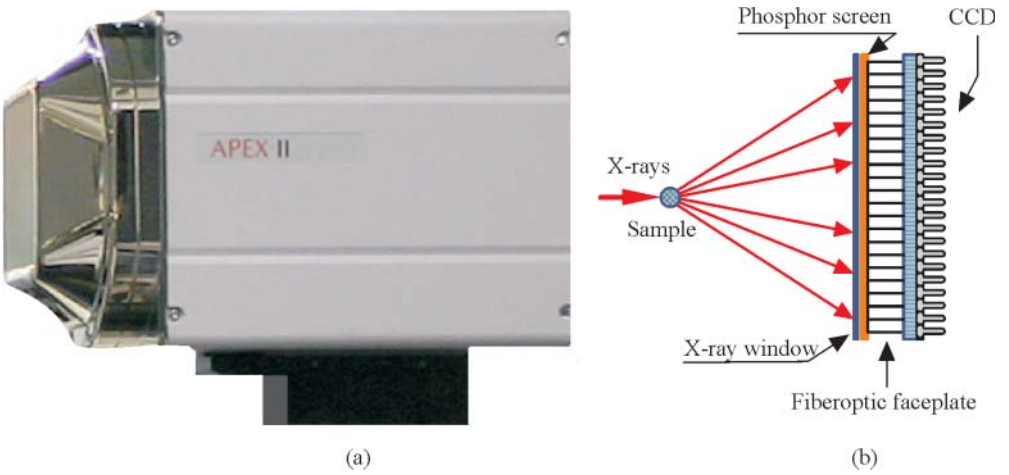


FIGURE 4.20 (a) Bruker APEX II™ CCD detector, (b) schematic showing phosphor screen, fiberoptic faceplate, and CCD chip.

700,000 electrons in 512×512 binning mode, the APEX II detector can achieve a dynamic range of over 5×10^4. The phosphor screen can also be tailored to suit the different X-ray energies, so the indirect detection method can offer wider photon energy coverage. Another important advantage of indirect detection over direct detection is the phosphor screen, and the coupling fiberoptic prevents X-ray photons from reaching the CCD sensor and protects the CCD from X-ray damage.

There are several disadvantages associated with indirect detection methods, in addition to zinger noise and spatial distortion caused by fiberoptic taper. The detector may have poorer spatial resolution due to the scattering in the phosphor screen and scattering of light in the fiberoptic taper or faceplate. A single detected photon could produce a spot of light with a diameter of approximately 100 μm in the phosphor. Reducing the thickness of the phosphor layer may improve the resolution. A certain percentage (typically 50–90%) of light is lost in the fiberoptic taper due to optical detrapping. In order to absorb the lost light, black glass fibers are inserted between the imaging fibers in the fiberoptic taper. However, the absorption is not complete and remaining scattered light in the fiberoptic taper reaches the CCD and results in a loss in spatial resolution. The reduced sensitivity is another drawback with indirect detection, since visible photons produced by the X-ray event may be spread over several pixels of the detector, resulting in signal levels approaching noise levels.

The CCD chip needs to be cooled to reduce the dark current noise. Dark current is due to thermally produced electron hole pairs which accumulate in the potential well with time. The dark current noise is the dominant noise source for long exposures. Dark current can be decreased by cooling the detector. Typical cooling temperatures for CCD detectors used for X-ray diffraction are −40 to −60°C. With every 5–6°C drop in temperature, the dark current can be reduced by a factor of 2. For example, the dark current noise of a CCD at −60°C is about one order of magnitude lower than the noise of a detector cooled only to −40°C.

4.6.4 CMOS Detector

With the advancement of CMOS (complementary metal oxide semiconductor) technology, over a period of time, CCD detectors have been superseded by CMOS detectors, especially for single crystal diffractometers. CMOS technology allows manufacturing of very large image sensors,

which is unachievable with CCD technology. The optical demagnification, such as fiber optic taper used to create a larger active area for CCD detectors, is no longer necessary for CMOS detectors. Accordingly, the CMOS detector can avoid the significant loss of signal, image smearing, and distortion, associated with the demagnification taper. Since low power consumption of CMOS sensor, the detector is air cooled for low maintenance. The CMOS detector does not suffer from blooming or streaking, which can happen for a CCD detector when a strong reflection saturates a pixel and causes a vertical streak. Due to a unique combination of sensitivity, speed, dynamic range, resolution, and detector size, the CMOS detector was designed and mainly used for single crystal diffractometer. One example is the Bruker Photon 100™ CMOS detector which has a large active area of 10 cm × 10 cm, 1024 × 1024 pixel formats and 96 μm pixel size [46].

4.6.5 Pixel Array Detector

Pixel array detector (PAD) technology has gained much attention and development in recent years, especially for applications in X-ray diffraction [47–51]. One type of PAD detector, also known as the hybrid pixel-array detector (HPAD), consists of a detection layer and readout layer, connected pixel by pixel with solder connecting bumps as shown in Figure 4.21. The top layer contains an array of pixels on high-resistivity silicon. Each pixel converts incoming X-rays to electric charge by the same process as described in the previous section on the solid state detector. The charge produced in each pixel of the detection layer is individually transferred to the corresponding pixel of the readout layer for processing and readout. The readout layer is an application-specific integrated circuit (ASIC), typically made of CMOS technology. In general, each pixel behaves like an independent point detector.

Based on the same concept of PAD technology, there are many types of detectors available, and each type is manufactured to a combination of particular features for its applications. PAD detectors can have good spatial resolution with small pixel size and narrow point spread function, high counting rate and high dynamic range, high sensitivity over a broad spectrum range, and homogenous pixel-to-pixel performance. PAD detectors can be configured to operate in either photon counting mode or charge integration mode. Some detectors are switchable between the two modes. The PAD detectors configured to operate in single photon counting mode is also referred

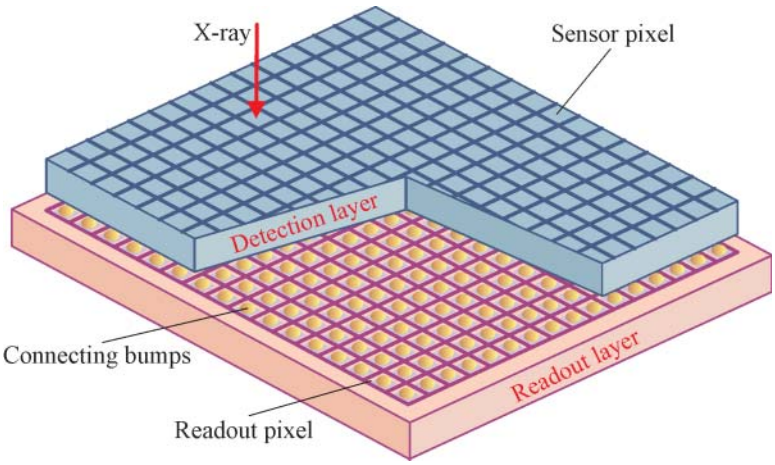


FIGURE 4.21 Illustration of a PAD detector with detection layer and readout layer connected pixel by pixel with connecting bumps.

to as a hybrid photon counting (HPC) pixel detector. HPC detectors can have high sensitivity, high readout speed, low noise, sharp point spread function (PSF) of single pixel, and energy discrimination by applying a threshold to the signals from the sensor pixels. In integration mode, the charge from sensor pixel is integrated within a given time period and then readout at the end of the integration. A PAD at integrating mode can achieve high count rate, single-photon sensitivity and avoid the count loss from charge sharing [52–55].

A PAD can achieve good spatial resolution by having small pixel size. But there is a limit mainly due to charge sharing. The charge produced by an incoming X-ray photon may spread into adjacent pixels, especially when the X-ray photon is intercepted near a pixel boundary. In order to eliminate noise, a threshold is applied to the signal pulse from the sensor pixel. If the signal pulse height is reduced, due to the charge sharing, to a value below the threshold, the count is lost. The threshold can also prevent duplicate or multiple counts from the charge sharing. Typically, the threshold is set at 50% of average pulse height so each photon cannot be counted more than once. Since the charge sharing happens when the X-ray hits the edge or corner of pixel, the smaller the pixel size, the more severe the charge sharing. For instance, 20% of pixel area is affected by charge sharing for 172 μm pixels, 43% for 75 μm pixels, and 100% for 25 μm pixels. The charge sharing becomes much worse when the threshold is increased, for instance, in order to suppress fluorescence. With increase of the threshold value, the efficiency (DQE) drops. This effect is worse for smaller pixels.

The impact of charge sharing on DQE depends on the feature size in the diffraction pattern, for example the size of a diffraction spot (reflection) from a single crystal. If reflections are large compared to the pixel size, the DQE is not strongly affected. However, reflections smaller than the pixel size are significantly affected. This might be a big problem for single crystal diffraction, but for most XRD^2 applications, charge sharing is not a significant concern, since most likely the data is integrated over features that are large compared to the pixel size. The charge sharing may cause only a small decrease in efficiency but it does not cause a significant loss of DQE since the loss of efficiency is uniformly distributed in space in normal operation with the threshold set to 50% of average pulse height. Figure 4.22 gives a good illustration on the relation

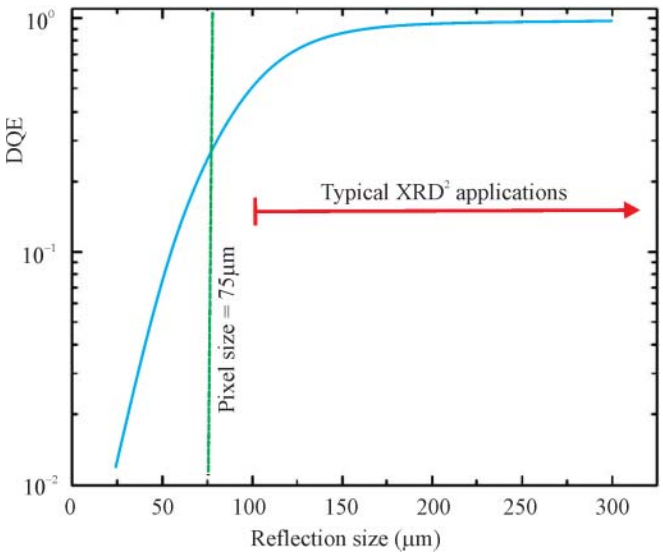


FIGURE 4.22 Relation between DQE and reflection size for a HPC detector with 75 μm pixel size.

between DQE and reflection size for a HPC detector with 75 μm × 75 μm pixel size [56]. For most laboratory XRD^2 applications, the beam size is from 50 μm to 1000 μm, plus the broadening effect from the sample, so the reflection size is typically 100 μm or above, which falls in the high DQE region.

HPC detectors also suffer counting loss due to count rate saturation, especially at high count rate. It takes time for the charge cloud to drift through the sensor. This time is called dead time, typically a few microseconds for HPCs. If two or more X-ray photons hit a sensor pixel within the dead time, the overlapping pulses will not be counted. Count rate saturation causes non-linearity at count rates above about 10^5 cps/pixel [57]. The count rate loss reaches 10% at about 10^6 cps/pixel. The count loss can partially be corrected with software if the incident count rate is constant during the data collection. Fabricated with semiconductor technology, pixel position accuracy of HPC detectors is significantly better than the mechanically produced fiducial plate. Spatial correction is normally not necessary for a laboratory instrument. The detector position is still critical and may need calibration and correction [58].

The Eiger 2R 500k™ detector (hereafter called Eiger2), manufactured by Dectris and specifically configured and integrated into laboratory X-ray diffractometers by Bruker AXS, is a good example of HPC detectors. Eiger2 can detect individual photons from 0 up to 2.6×10^6 counts per second per pixel (cpspp), which is ideal for analysis of samples consisting of weak or strong-scattering phases. Due to the direct conversion of X-ray photons to electric signals, the position of the incoming photon is accurately measured with the PSF as narrow as one pixel. The optimized pixel size (75 μm) and single pixel point-spread function allows collection of 2D data in high resolution with high quantum efficiency. The fast conversion also allows for high count rates and dynamic range, which makes the detector suitable for data collection with the most intensive lab X-ray sources on applications with strong diffraction signal, such as reflectivity and analysis of thin films with single crystal substrate. The broad energy-range covers most laboratory X-ray sources (Cr, Co, Cu, Ga, Mo, and Ag) so users can select the most suitable X-ray wavelength for the specific application and materials, and avoid fluorescence from the sample. Single photon counting without readout noise or dark current has extended the detection limit for microdiffraction on samples with small area or small quantity. Due to the extremely accurate pixel position and homogenous pixel-to-pixel sensitivity, flood filed and spatial correction are not needed.

Figure 4.23 shows the Eiger2 detector (a) and a diffractometer with the detector (b). The active area of the Eiger2 is about 77×39 mm^2, covered by 529420 pixels of 75×75 μm^2. As a 2D detector, the active area of Eiger2 is not as big as the most popular XRD^2 detectors such as Hi-Star™ and Våntec-500™, but the combination of many excellent characteristics and the high level integration to the X-ray diffractometer, makes it suitable for a large variety of XRD and XRD^2 applications. The detector dimension and weight are optimized for quick and accurate detector motion in a typical laboratory diffractometer in either horizontal θ-2θ or vertical θ-θ configurations. Within the integrated system, the detector is switchable between 0D/1D/2D mode for multipurpose XRD solutions, for example, Bragg–Brentano geometry, reflectometry, and GIXRD. The rectangular active area can be oriented in either 2θ-optimized mode or γ-optimized mode. The 2θ-optimized mode can be used for large 2θ coverage with single 2D frame for phase ID, high-throughput screening or in-situ measurement. The γ-optimized mode for large γ coverage is suitable to γ-profile-related applications such as, stress, texture, and grain size analysis. The 2θ coverage can be extended by either multiple frame merge or running the data collection in continuous scanning mode.



(a) (b)

FIGURE 4.23 The Eiger2 detector (a) and a diffractometer with the detector (b).

4.6.6 CPAD Detector

As discussed in the previous section, HPAD or HPC detectors offer many highly desirable characteristics, especially beneficial to powder diffraction. However, there are some drawbacks, such as count rate saturation, charge-sharing, and low DQE for high energy X-rays (Mo-K_α and Ag-K_α). The low absorption efficiency of silicon means that, at higher energies, some X-rays pass through the sensor without being detected, even for the thickest available sensors (e.g. 1 mm). This will result in low DQE and parallax effect.

A new type of detector, referred to as a charge-integrating pixel detector (CPAD) can preserve some of the desirable characteristics of HPAD (e.g. fast frame rates and single-photon sensitivity), but eliminate count rate saturation and charge-sharing problems. In a CPAD, each pixel contains its own preamplifier, stored in a local capacitor, and then read out after a finite exposure time. By measuring the integrated charge, CPAD can detect X-rays with extremely high count rates with high accuracy. Since the signals are not filtered by a threshold in CPADs, there is no charge-sharing noise, and X-ray counts are measured without charge-sharing loss. The CPADs can be designed either with a semiconductor sensor or with a scintillation converter. CPADs with a high-density scintillator layer can improve DQE and reduce the parallax effect for high-energy radiation. The CPAD detector has excellent sensitivity over a wide energy range of the wavelength suitable for lab X-ray sources from Cu-K_α to In-K_α radiation. It has no parallax effect, i.e. no distortion of the diffraction pattern near the edge of the active area even at short detector distance.

One example of the CPAD detector using high X-ray absorption scintillation layer is the Bruker Photon II™ detector. The Photon II CPAD has a large single chip sensor with an active area of 139 mm × 104 mm, high detector quantum efficiency, high speed, and high dynamic range. The detector is designed mainly for single crystal diffractometer, but many features, such as the

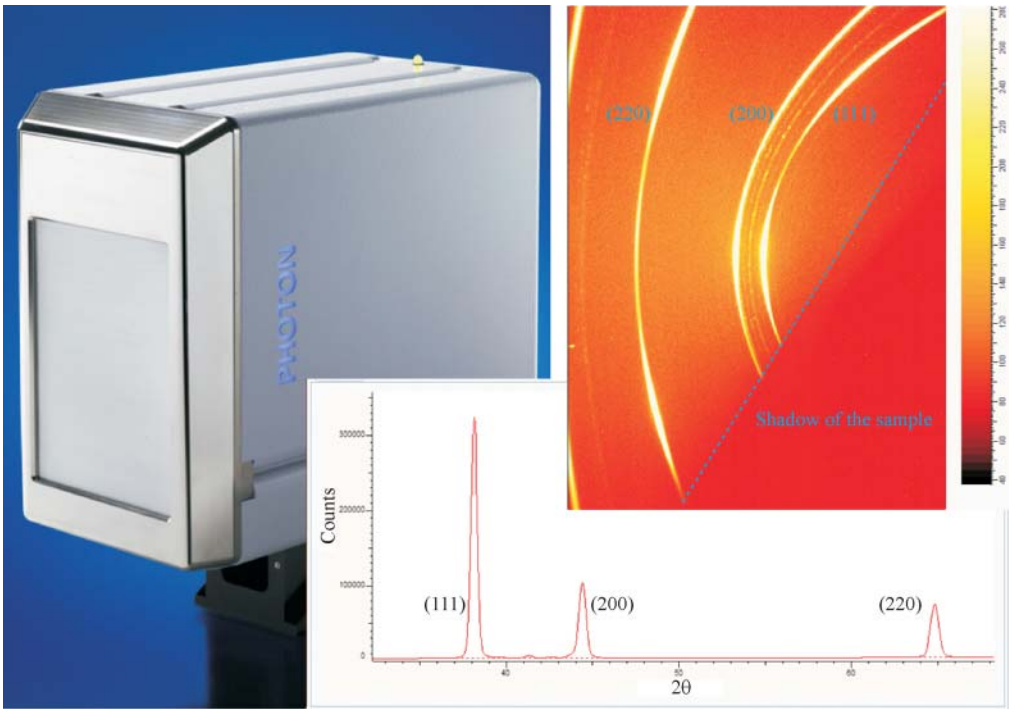


FIGURE 4.24 Bruker Photon II™ detector, 2D frame and integrated profile from Al foil.

ultra-low parallax, zero dead area, and uniformity in pixel size, make it a possible detector choice for XRD[2] applications too. Figure 4.24 shows a Bruker Photon II CPAD detector, a 2D diffraction frame collected with the detector and integrated diffraction profile. The Photon II detector has a large rectangular active area of 10 cm × 14 cm, 768 × 1024 pixel format, and 135 μm pixel size. The detector was designed for single crystal diffractometer, but also suitable for powder applications, such as phase identification, stress, and texture [59]. The frame was collected with D8 Venture with IμS Cu microsource and Photon II detector, from an Al foil at the detector distance $D = 60$ mm for 60 seconds. The frame shows three diffraction rings: (111), (200), and (220) and the area below the blue dashed line is the area blocked by the sample at $\psi = 30°$ for reflection mode diffraction. Below the frame is the integrated profile showing the three peaks at 2θ angles of 38.5°, 44.7°, and 65.1° respectively. The maximum counts for all three peaks are very high (80k to 320k), therefore, the data collection time can be significantly reduced if necessary.

4.6.7 Microgap Detector

Efforts to improve the local count rate of MWPC led to the introduction of several detectors categorized as "microgap" detectors, including the GEM [60], the MSGC [61], the MGC [62], the CAT [63], and the Micromegas [64] detectors. With reduced cathode-to-anode spacing and increased average electric field intensity, so as to reduce the ion collection time, microgap detectors can achieve count rates several order of magnitude higher than the MWPC. However, the above microgap detectors suffer a common limitation in that the maximum gain, spatial resolution, and energy resolution are reduced at high count rates due to electrical sparks and discharge. A new type of microgap detector with a resistive-anode was introduced by Bruker AXS, named the mikrogap™ detector [21, 22]. Mikrogap™ technology has been used for both

one-dimensional and two-dimensional detectors. It consists of a parallel plate avalanche chamber with a resistive anode separated from the readout electrode by an insulator. The resistive anode significantly reduces the number of sparks and the damaging effects of the spark discharges. In the rest of this chapter, "mikrogap" will be used to distinguish the microgap detector with a resistive anode from other types of microgap detectors.

Figure 4.25 shows the cross-section and working principle of a two-dimensional mikrogap detector [22]. Figure 4.25(a) shows that the grid, anode, and delay lines are contained in a sealed

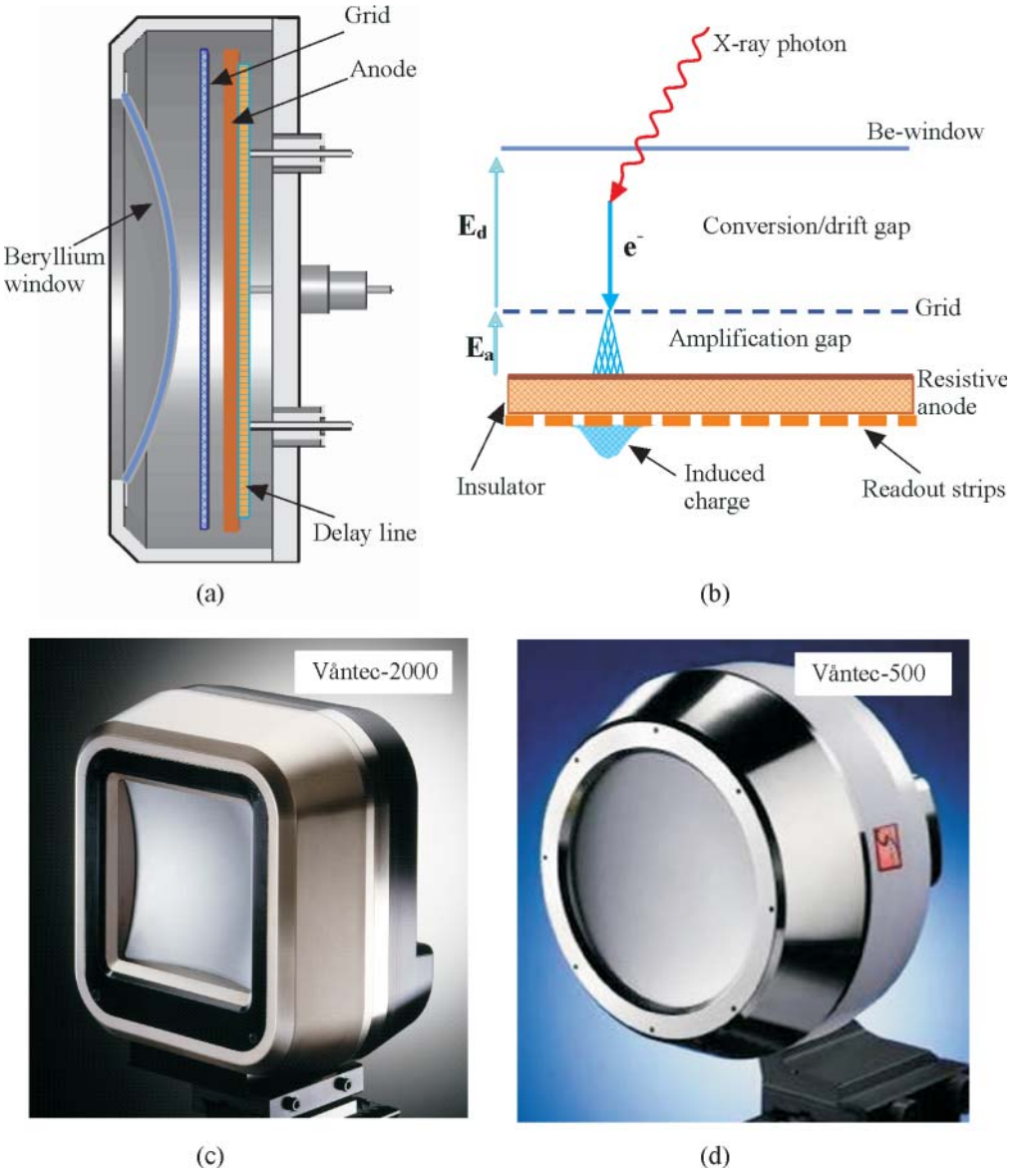


FIGURE 4.25 Two-dimensional mikrogap detector: (a) cross-section of the detector showing the beryllium window, grid, anode, and delay line, (b) schematic of the parallel-plate resistive-anode chamber with the readout electrode separated from the anode, (c) Våntec-2000™ and (d) Våntec-500™ (Courtesy of Bruker AXS).

vessel with a beryllium entrance window. The window has a spherical shape to reduce parallax effects. The radius of curvature is designed to match the most often used sample-to-detector distance to minimize the parallax effect. The actual operational sample-to-detector distance can be less or greater than the window's radius of curvature. The parallax effect is more severe at a distance far shorter than the window's radius of curvature, but less severe at a distance far greater than the radius. An appropriate window curvature is also necessary to withstand the gas pressure. Less curvature (i.e. larger radius) requires a thinner window to stand the same pressure, so the curvature has to be optimized for less parallax and good sensitivity. The vessel and the window are designed to contain up to 6 atm of gas pressure. The grid is made of a photochemical perforated metal mesh separating the conversion/drift and the amplification gaps. The distance between the grid and window is about 10 mm in the center and up to 50 mm at the edge. The amplification gap width is about 1–2 mm. The anode is made of a resistive layer deposited on a ceramic substrate. The resistivity is chosen so that it is high enough to limit discharges and low enough to allow high count rates, typically in the range of 10^5–10^7 Ω/area. A set of two-dimensional readout strips is attached to the substrate backplane. The strips are connected to two (X and Y) 150 Ω impedance delay lines (DL). The total delay time for each of the lines is ∼100 ns. The detector is filled with an Xe/CO_2 (90/10) gas mixture at the absolute pressure of 2–3 atm. Figure 4.25(b) is a schematic of the parallel-plate resistive-anode chamber with the readout electrode separated from the anode. In the conversion region with the electric field $\mathbf{E_d}$, the incoming X-ray photons produce primary electrons by gas ionization. These electrons drift towards the anode under the electric field $\mathbf{E_a}$. The number of electrons is multiplied in the amplification gap. The thin amplification gap greatly reduces the volume charge effect that limits the local count rate in wire chambers. It has been shown that the count rate can reach as high as 10^7 cps/mm^2 at a fairly high gas gain ($>10^4$) [65]. The tests on the above two-dimensional mikrogap detector have demonstrated a maximum local count rate of 5×10^5 cps/mm^2 within the linear range [22]. The pulse has about a 5 ns rise time and the amplitude distribution is good enough for detection of a single photon. The resistive anode significantly reduces the number of sparks and the damaging effect of the spark discharges, which provides stable detector operation at gas gains as high as 10^5–10^6, depending on the gas mixture. The separation of the readout electrode from the anode by an insulator of a proper thickness allows optimization of the induced signal spatial distribution for avalanche centroid measurements. Figure 4.25(c) and (d) are pictures of Bruker Våntec-2000™ and Våntec-500™ detectors based on the mikrogap™ technology with a square active area of 14cm × 14cm and round active area of 14cm in diameter respectively.

In addition to the high local count rate, the mikrogap detector has achieved significant improvements in many characteristics compared to the MWPC. The detector global count rate reaches up to 10^6 cps. The spatial resolution is about two to three times better than MWPC. The PSF for the two-dimensional detector is around 200 μm FWHM. By increasing gas pressure and internal gain, a spatial resolution of 120 μm FWHM has been obtained in the one-dimensional version Våntec-1 detector. Figure 4.26 shows a diffraction frame collected from a NIST 1976 standard corundum plate with Våntec-2000 detector. The integrated profile shows the $K_{\alpha 1}$-$K_{\alpha 2}$ split in a peak (104) at 2θ as low as 35.2°. Considering a wavelength difference of $\Delta\lambda\ (K_{\alpha 2}\text{-}K_{\alpha 1}) = 0.00383$Å and corresponding $\Delta 2\theta = 0.09°$, the peak separation on the detector at 20 cm is 313 mm. The FWHM of the PSF must be smaller than this peak separation to detect the $K_{\alpha 1}$-$K_{\alpha 2}$ split. The $K_{\alpha 1}$-$K_{\alpha 2}$ split for the same peak cannot be distinguished on a diffraction frame collected with the MWPC under the same conditions.

The dynamic range of a point detector is defined as the range extending from the detection limit to the maximum count measured in the same length of the counting time. The linear dynamic range is the dynamic range within which the maximum counts are collected within the specified linearity. For X-ray detectors, most often dynamic range refers to linear dynamic range since only

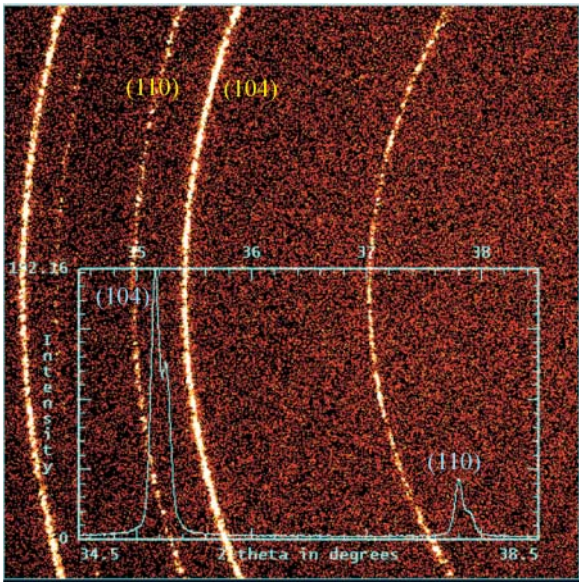


FIGURE 4.26 Diffraction frame of NIST 1976 standard corundum plate measured with Våntec-2000 showing the $K_{\alpha 1}$-$K_{\alpha 2}$ split in a peak at a 2θ of 35.2°.

the diffraction pattern collected within the linear dynamic range can be correctly interpreted and analyzed. The dynamic range for area detectors has a similar definition except that with an area detector the whole dynamic range extending from the detection limit to the maximum count can be observed from different pixels simultaneously. For integrating detectors, the dynamic range is determined by the counting capacity of each pixel and the noise counts per pixel including readout noise. For photon-counting detectors, the pixel counts are transferred and stored in real time and can be accumulated in computer storage as desired. The only limiting factor on the dynamic range is that background noise is also added to the pixel counts. Therefore, the dynamic range of a photon counting detector is given as

$$DR = \frac{R_{\max}}{R_B} \tag{4.50}$$

where $R_{\max}$ is the maximum count rate at saturation or a specified linearity if the linear dynamic range is calculated, and R_B is the noise rate. With a low noise rate, a detector can achieve a dynamic range much higher than its count rate. The mikrogap detector has a very low noise background without incoming X-rays. These background counts are caused by cosmic rays and surrounding natural radioactivity and depend on the environment as well as on the signal selection criteria. A test on the above two-dimensional detector shows a global background of 10 cps over the total area of approximately 200 cm^2. The corresponding local background rate is 5×10^{-4} cps/mm^2. Given that the maximum local count rate is 5×10^5 cps/mm^2, we have a dynamic range of 1×10^9.

In the X-ray images of the MWPC, stripes imitating the trace of the wires can be observed due to the inhomogeneous electric field produced by the wire grids. The stripes are aligned in the wire (vertical and horizontal) directions as a periodic intensity variation. Figure 4.27(a) is an X-ray image from a homogeneous X-ray source collected with a MWPC (Hi-Star detector) showing the stripes. The homogeneous X-ray source was produced by fluorescence generated from an amorphous (glassy) iron foil irradiated by a point beam of Cu-K_α radiation. The detector was set

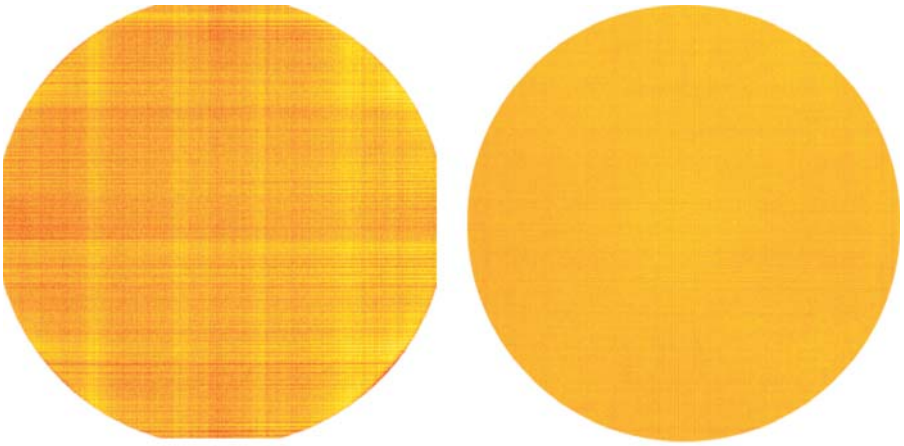


FIGURE 4.27 X-ray image from a homogeneous X-ray source: (a) MWPC (Hi-Star™) image showing stripes in horizontal and vertical directions, (b) mikrogap detector (Våntec-500™) image showing homogeneous intensity distribution.

at a 40° swing angle to avoid the penetrated direct beam. The foil plane should be parallel to the detector plane for homogenous radiation to the detector. In order to make the stripes more visible, total global counts of 350 million (390/pixel at 1024×1024 format) were collected on this frame. For most applications, the stripes are either corrected for or immersed into the background when X-ray diffraction patterns are present. But in some applications requiring high dynamic range and with critical weak signals, such as small angle X-ray scattering, the stripes can be detrimental to the correct interpretation of the detailed scattering features. Flood field correction with a homogeneous X-ray source can cosmetically reduce but not totally eliminate the stripes. The diffraction frames collected with the mikrogap detector do not have this kind of stripes due to its rather homogeneous electric field. Figure 4.27(b) is an X-ray image from a homogeneous X-ray source collected by a mikrogap detector (Våntec-500) showing a homogeneous intensity distribution with the total global counts of more than 300 million (115/pixel at 2048×2048 format). This advantage, along with high count rate and low noise, makes mikrogap detectors so far the best choice for X-ray diffraction and small angle X-ray scattering requiring high dynamic range and detailed diffraction pattern analysis.

Radiation hardness is defined as the maximum strength of radiation that a detector can withstand without permanent damage. The mikrogap detector has excellent radiation hardness compared to the MWPC. A test with the detector exposed to a narrow 100 μm X-ray beam at the count rate of 8×10^5 cps/mm^2 has shown that no variation of the detector performance is observed until the accumulated dose reaches 8×10^{11} counts/mm^2. After this dosage level, a small drop (<10%) of gas gain was detected in the irradiated area, but had no effect on the counting efficiency and spatial resolution. That means the mikrogap detector is not likely to be damaged by accidental exposure to a high intensity direct beam. One practical issue with sealed gaseous detector in many X-ray laboratories is the periodic re-gassing of the detectors. For example, a typical MWPC detector needs to be re-gassed after every 3–5 years of normal use. The accelerated out-gassing test shows that the mikrogap detector can be used for up to 10 years without gas-refilling. Since there are no dangling wires inside the detector gas chamber, the mikrogap detectors are not as sensitive to mechanical shock and vibration as the MWPC.

Similar to other gaseous detectors, the FWHM of the PSF of a mikrogap detector at the edge of the detector is broader than at the center of the detector due to electric field distortion. Parallax distortions occur when the electric field line in the conversion volume is not parallel to the X-ray photon direction. Therefore, the parallax effect depends on the beam angle and position at the entrance window. The window curvature and electric field should be optimized based on the sample-to-detector distance to minimize the parallax effect.

4.6.8 Comparison of Area Detectors

Selection of area detectors is dependent on the X-ray diffraction application, sample condition, and X-ray beam intensity. In addition to geometry features, such as the active area and pixel format, the most important performance characteristics of a detector are its sensitivity, dynamic range, spatial resolution, and background noise. The detector category, either photon-counting detectors or integrating detectors, also makes important differences in performance. Photon-counting detectors typically have high counting efficiency at low count rate, while integrating detectors have high count rate, but are not so efficient at low count rate due to the relatively high noise background.

Figure 4.28 gives a comparison of six types of detectors (MWPC, IP, CCD, Mikrogap, HCP and CPAD) in terms of their effective DQE as a function of incoming X-ray fluence. The plots are not produced from comparison tests with strictly controlled conditions, but generated approximately from values reported in various references [56, 66]. A detector from a specific vendor may deviate from the plot. However, the relative characteristics of the six types of detectors should give a reasonable comparison. The plots for the two integrating detectors, IP and CCD, are based on 30 seconds of integrating time. The MWPC has high DQE of about 0.8 when exposed to incoming local fluence from a single photon up to almost 10^3 photons/second·mm^2. The diffracted X-ray intensities from a polycrystalline or powder sample with a typical laboratory X-ray source fall into

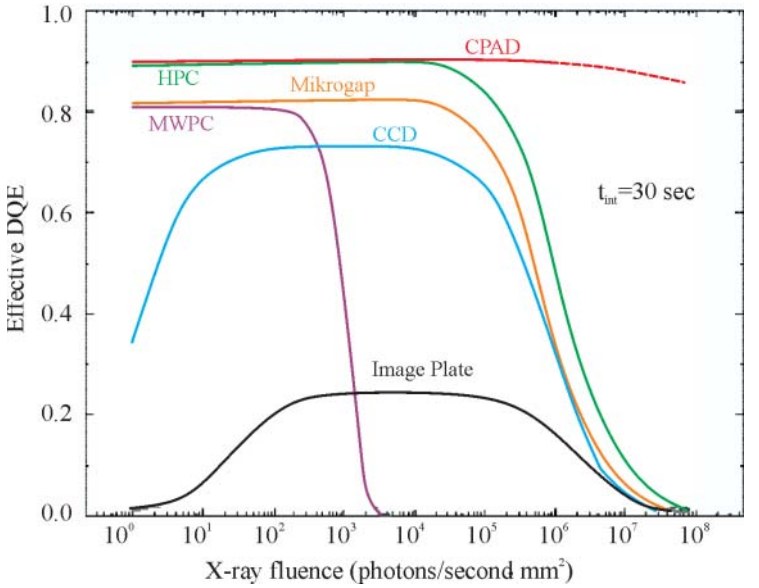


FIGURE 4.28 Comparison of six types of detectors (MWPC, IP, CCD, Mikrogap, HCP and CPAD) in terms of their effective DQE as a function of incoming X-ray fluence.

Table 4.1 **Specifications of Typical MWPC, CCD, CPAD, Mikrogap and HPC Detectors (Values on the Similar Detector Technologies are Given in Parentheses)**

Detector specifications	MWPC	CCD	CPAD	Mikrogap	HPC
Reference product (vendor)	Hi-Star™ (Bruker)	Apex II™ (Bruker)	Photon II™ (Bruker)	Våntec-500™ (Bruker)	Eiger2R500k™ (Dectris)
Detection Active area	105 mm round	62×62 mm^2	104×139 mm^2	140 mm round	77.2×38.6 mm^2
Demagnification	N/A	1:1	N/A	N/A	N/A
Pixel format	512×512, 1024×1024	512×512, 1024×1024 2048×2048 4096×4096	768×1024	512×512, 1024×1024 2048×2048	1030×514
Pixel size at maximum pixel format	103 µm	15 µm	135 µm	68 µm	75 µm
Point spread function (FWHM)	460 µm (35~1000 µm)	75 µm (30~120 µm)	1 pixel (110 µm phosphor)	230 µm (70~300 µm)	1 pixel
Detective quantum efficiency (DQE)	0.80 at 8.04 keV	0.74 at 17.4 keV	>0.90 5~24 keV	0.80 at 8.04 keV	>0.90 at 8.04 keV
Dynamic range	$>10^6$	5×10^4	>200,000	$>10^8$	$>10^9$
Maximum count /pixel	n/a	5×10^4	No count rate saturation	n/a	2.6×10^6
Global count rate:	(1×10^6 cps)	n/a			
Maximum	4.2×10^4 cps			1.6×10^6 cps	
Linear (10% deviation)	3.5×10^4 cps			9×10^5 cps	
Local count rate:	(5×10^5 cps/mm^2)	n/a			
Maximum	1.3×10^4 cps/mm^2			9×10^5 cps/mm^2	3.6×10^8
Linear (10% deviation)	1×10^4 cps/mm^2		10^6 cps/pixel (0% deviation)	5×10^5 cps/mm^2	
Background noise	5×10^{-4} cps/mm^2	Dark current: <0.05 e^-/pixel-s	<0.17 photon rms	5×10^{-4} cps/mm^2	
Read noise	none	8 e^- rms	20 e^- rms	none	none
Readout time	<0.2 sec	<1 sec at 1k mode	0.014 sec	<0.2 sec	Continuous, 4µs dead time
Energy range	3–15 keV	n/a	5–30 keV	3–15 keV	5.4–36 keV
Energy resolution $\Delta E/E$	20% @ 8 keV	n/a	n/a	20% @ 8 keV	
Operating gas	Xe-CH_4	none	none	Xe-CO_2	none
Cooling temperature	n/a	−60°C	Air cooled	n/a	Air cooled
Maintenance	Re-gas in 3–5 years	none	none	none	none
Weight	8.5 kg	8 kg	8.9 kg	9 kg	1.7 kg

this fluence range. This is especially true with microdiffraction, where high sensitivity and low noise are crucial to reveal the weak diffraction pattern. Due to the counting losses at a high count rate, the DQE of the MWPC decreases with increasing count rate and quickly saturates above 10^3 photons/second·mm^2. Therefore, the MWPC is not suitable for collecting strong diffraction patterns or to be used with high intensity sources, such as synchrotron X-rays. The image plate can be used in a large fluence range from 10 and up with a DQE of 0.2 or lower. The upper limit of X-ray fluence is 10^6 photons/second·mm^2 if the data is collected for 30 seconds. Since the IP is an integrating detector, it is not limited to instantaneous X-ray fluence. The IP can handle X-ray fluence much larger than 10^6 photons/second·mm^2 if the integration time is proportionately reduced. The IP is suitable for strong diffractions from a single crystal with high intensity X-ray sources, such as a rotating anode generator or synchrotron X-ray source. With weak diffraction signals, the image plate cannot resolve the diffraction data near the noise floor. The CCD detector can also be used in a large X-ray fluence range from 10 to very high fluence with a much higher DQE of 0.7 or higher. The upper limit of X-ray fluence is 10^6 photons/second·mm^2 if the data is collected for 30 seconds. The CCD can also handle X-ray fluence much larger than 10^6 photons/second·mm^2 if the integration time is proportionately reduced. It is suitable for collecting diffractions of medium to strong intensities from single crystal or polycrystalline samples. Due to the relative high sensitivity and high local count rate, CCDs can be used in systems with either sealed tube X-ray sources, rotating anode generators, or synchrotron X-ray sources. With a low DQE at low fluence and the presence of dark current noise, the CCD is not a good choice for applications with weak diffraction signals.

The mikrogap detector has the best combination of high DQE, low noise, and high count rate. It has a DQE of about 0.8 at X-ray fluence from single photons up to near 10^5 photons/second·mm^2. It is suitable for microdiffraction when high sensitivity and low noise are crucial to reveal weak diffraction patterns. It can also handle high X-ray fluence from strong diffraction patterns or be used with high intensity sources, such as rotating anode generators or synchrotron X-ray sources. Therefore, the microgap detector is the best choice for most applications of two-dimensional X-ray diffraction. Both HPC and CPAD detectors show high sensitivity over a large range of count rates and CPAD essentially has no count rate limitation.

The above comparison is only based on the relation between DQE and count rate. Table 4.1 lists the comprehensive characteristics of five detector technologies based on published performance data from users or vendors. Values reported from various references on similar detector technologies are given in parentheses.

REFERENCES

1. T. N. Blanton, “X-ray films as a two-dimensional detector for X-ray diffraction analysis”, *Powder Diffraction*, *Vol.* **18***, No 2*, June 2003.
2. H. P. Klug and L. E. Alexander, *X-ray Diffraction Procedures for Polycrystalline and Amorphous Materials*, John Wiley & Son, New York, 1974.
3. H. Johns, Aerospace: the aircraft gas turbine industry, *Industrial Applications of X-ray Diffraction*, edited by F. H. Chung and D. K. Smith, Marcel Dekker, New York, 2000, 129–178.
4. B. D. Cullity, *Elements of X-ray Diffraction*, 2nd ed., Addison-Wesley, Reading, MA, 1978.
5. Ron Jenkins and Robert L. Snyder, *Introduction to X-ray Powder Diffractometry*, John Wiley & Sons, New York, 1996.
6. G. Gandolfi, Discussion upon methods to obtain X-ray powder patterns from a single crystal, *Mineral. Petrog. Acta.*, Vol. **13**, 67–74, 1967.

7. R. W. Hendricks, An incident-beam ionization chamber and charge integration system for stabilization of X-ray diffraction experiments, *J. Appl Cryst.* (1972). **6**, 129.
8. M. Manther and W. Parrish, Energy dispersive X-ray diffractometry, in *Advances in X-ray Analysis*, Vol. **20**, 1–186. (1976).
9. R. D. Luggar, M. J. Farquharson, J. A. Horrocks, and R. J. Lacey, Multivariate analysis of statistically poor EDXRD spectra for the detection of concealed explosives, *X-ray Spectrometry,* Vol. **27**(2), Pages 87–94, 1998.
10. D. L. Bish and S. J. Chipera, Comparison of a solid-state Si detector to a conventional scintillation detector-monochromator system in X-ray diffraction analysis, *Powder Diffraction*, Vol. **4**, No 3, September 1989.
11. M. Stanton et al., The detective quantum efficiency of CCD and vidicon-based detectors for X-ray crystallographic applications, *J. Appl. Cryst.* (1992). **25**, 638–645.
12. N. M. Allinson, Development of non-intensified charge-coupled device area X-ray detectors, *J. Synchrotron Rad.* **1**, 54–62 (1994).
13. D. A. Gedcke, How counting statistics controls detection limits and peak precision, ORTEC Application Note AN59, 2001.
14. M. R. James and J. B. Cohen, Geometrical problems with a position-sensitive detector employed on a diffractometer, including its use in the measurement of stress, *J. Appl. Cryst.* (1979). **12**, 339–345.
15. H. E. Göbel, The use and accuracy of continuously scanning position-sensitive detector data in X-ray powder diffraction, *Advances in X-ray Analysis*, **24**, 123–138, 1980.
16. S. K. Byram, et al., A novel X-ray powder diffractometer detector system, *Advances in X-ray Analysis*, **20**, 529–545, 1976.
17. E. R. Wolfel, A novel curved position-sensitive proportional counter for X-ray diffractometry, *J. Appl. Cryst.* (1983). **16**, 341–348.
18. L. Castex, J. L. Lebrun, and S. Bras, A new model of X-ray position sensitive detector developed in France, *Advances in X-ray Analysis*, **24**, 139–141, 1980.
19. A. Kinne et al., Image plates as one-dimensional detectors in high resolution X-ray diffraction, *J. Appl. Cryst.* (1998). **31**, 446–452.
20. U. W. Arndt, X-ray position-sensitive detectors, *J. Appl. Cryst.* (1986). **19**, 145–163.
21. R. Durst et al., Readout structure and technique for electron cloud avalanche detectors, US Patent No. 6,340,819, Jan. 22, 2002.
22. D. M. Khazins, B. L. Becker, Y. Diawara, R. D. Durst, B. B. He, S. A. Medved, V. Sedov, and T. A. Thorson, A parallel-plate resistive-anode gaseous detector for X-ray imaging, *IEEE Trans. Nucl. Sci.*, **51**, (3), 943–947, June 2004.
23. L. Brügemann et al., New detector technology for super speed X-ray diffraction, The 3rd Symposium on Pharmaceutical Powder X-ray Diffraction, ICDD, Feb. 2000.
24. L. Brügemann et al., Vantec-1 hot humidity studies in parallel beam geometry, Bruker AXS Lab Report XRD53, 2004.
25. C. Ponchut, Characterization of X-ray area detectors for synchrotron beamlines, *J. Synchrotron Rad.* (2006). **13**, 195–203.
26. E. M. Westbrook, Performance characteristics needed for protein crystal diffraction X-ray detectors, *Proc. SPIE,* **3774**, 2–16 (1999).
27. M. O. Eatough, et al., A comparison of detectors used for microdiffraction applications, *Advances in X-ray Analysis*, **41**, 319–326, 1997.
28. A. C. Thompson, et al., X-ray data booklet, 2nd Edition, Center for X-ray Optics, Advanced Light Source, Jan. 2001.
29. D. Bourgeois, J. P. Moy, S. O. Svensson and A. Kvick, The point-spread function of X-ray image-intensifiers/CCD-camera and imaging-plate systems in crystallography: assessment and consequences for the dynamic range, *J. Appl. Cryst.* (1994). **27**, 868–877.

30. H. Fujita et al., A simple method for determining the modulation transfer function indigital radiography, *IEEE Trans. Med. Imag.* (1992). **11**, 34–39.
31. R. Lewis, Multiwire gas proportional counters: decrepit antiques or classic performers, *J. Synchrotron Rad.* (1994). **1**, 43–53.
32. R. W. Hendricks, The ORNL 10-meter small-angle X-ray scattering camera, *J. Appl. Cryst.* (1978). **11**, 15–30.
33. R. Hamlin et al., Characteristics of a flat multiwire area detector for protein crystallography, *J. Appl. Cryst.* (1981). **14**, 85–93.
34. C. R. Desper, An area-imaging proportional counter for X-ray diffraction, *Advances in X-ray Analysis*, **24**, 161–166 (1980).
35. Z. Derewenda and J. R. Helliwell, Calibration tests and use of a Nicolet/Xentronics imaging proportional chamber mounted on a conventional source for protein crystallography, *J. Appl. Cryst.* (1989). **22**, 123–137.
36. I. Tanaka et al., An automatic diffraction data collection system with an imaging plate, *J. Appl. Cryst.* (1990). **23**, 334–339.
37. H. Iwasaki et al., Time-resolved two-dimensional observation of the change in X-ray diffuse scattering from an alloy single crystal using an imaging plate on a synchrotron-radiation source, *J. Appl. Cryst.* (1990). **23**, 509–514.
38. K. Krause, Experience with commercial area detectors: a buyer's perspective, *J. Appl. Cryst.* (1992). **25**, 146–154.
39. N. Kamiya and H. Iwasaki, Development of a new imaging-plate diffractometer (IPD-WAS) for time-resolved crystallography with a laboratory X-ray source, *J. Appl. Cryst.* (1995). **28**, 745–752.
40. M. Thoms et al., An improved X-ray image plate detector for diffractometry, *Mat. Sci. Forum*, (1996). **228–231**, 107–112.
41. R. W. Ryon, et al., X-ray imaging: status and trends, *Advances in X-ray Analysis*, **31**, 35–52 (1987).
42. T. N. Blanton, X-ray diffraction orientation studies using two-dimensional detectors, *Advances in X-ray Analysis*, **37**, 367–373 (1993).
43. M. W. Tate, et al., A large-format high resolution area X-ray detector based on a fiber-optically bonded charge-coupled device (CCD), *J. Appl. Cryst.* **28**, 196–205 (1995).
44. Roger Durst, The design and characterization of CCD-based X-ray detectors for crystallography, Bruker AXS Technical Note SCD 5, DOC-T86-EXS005, (2008).
45. V. Valdna, R. D. Durst, High efficiency polycrystalline phosphors and method of making same, US Patent number 6254806 (2001).
46. Bruker AXS Technical Note SC-XRD 10, CMOS detectors unique performance benefits of the Photon 100 CMOS active pixel sensor, DOC-T86-EXS010, (2011).
47. Bruker AXS Technical Note SC-XRD 12, New Developments in Pixel Array Technology: Hybrid Photon Counting and Charge-Integrating Pixel Detectors, DOC-T86-EXS012, (2016).
48. E. F. Eikenberry, et al., A pixel-array detector for time-resolved x-ray diffraction, *J. Synchrotron Rad.* (1998). **5**, 252–255.
49. S. Basolo, et al., Application of a hybrid pixel detector to powder diffraction, *J. Synchrotron Rad.* (2007). **14**, 151–157.
50. C. Broennimann, et al., The Pilatus 1M detector, *J. Synchrotron Rad.* (2006). **13**, 120–130.
51. A. Ercan, et al., Analog pixel array detector, *J. Synchrotron Rad.* (2006). **13**, 110–119.
52. K. S. Shanks, Development of low-noise direct-conversion x-ray area detectors for protein microcrystallography, PhD dissertation, Cornell University, (2014).
53. A. Bergamaschi, et al., Beyond single photon counting X-ray detectors, *Nucl. Instr. And Meth.* A (2010), doi:10.1016/j.nima.2010.06.326.
54. K. Mathieson, et al., Charge sharing in silicon pixel detectors, *Nucl. Instr. And Meth.* A (2010) **487**, 113-122.

55. P. Maj, et al., Comparison of the charge sharing effect in two hybrid pixel detectors of different thickness, the 16th International Workshop on Radiation Imaging Detectors, June 22–26, 2014, Trieste, Italy.
56. R. Durst, Pixel array detectors: counting and integrating, http://www.cdifx.univ-rennes1.fr/RECIPROCS/ANF2016_Frejus/pdf/RECIPROCS2016_R_Durst_CPAD.pdf.
57. P. Kraft et al., Performance of single-photon-counting Pilatus detector modules, *J. Synchrotron Rad.* (2009), **16** (pt3), 368–375.
58. C. Le Bourlot, et al., Synchrotron X-ray diffraction experiments with a prototype hybrid pixel detector, *J. Appl. Cryst.* (2012). **45**, 38–47.
59. B. He, B. Noll and C. Campana, 2-D powder XRD applications with single crystal diffractometers – invited presentation, the 66th American Crystallography Association Annual Meeting, Denver, Co, July 22–26, (2016).
60. F. Sauli, GEM: A new concept for electron amplification in gas detectors, *Nucl. Instr. and Meth.* **A386**, p. 531, (1997).
61. A. Oed, Position sensitive detector with microstrip anode for electron multiplication with gases, *Nucl. Instr. and Meth.* **A263**, p. 351, (1988).
62. F. Aangelini, et al., The microgap chamber, *Nucl. Instr. and Meth.* **A335**, p. 69, (1993).
63. F. Bartol, et al., The CAT. Pixel proportional gas counter detector, *J. Phys. III France*, vol. **6**, p. 337, (1996).
64. Y. Giomatartis, Development and prospects of the new gaseous detector "Micromegas", *Nucl. Instr. and Meth.* **A419**, p. 239, (1998).
65. Y. Diawara, et al., Novel, photon counting detectors for X-ray diffraction applications, *Proc. SPIE,* **4784,** 358–364, (2002).
66. R. D. Durst, C. Campana, B. He, and J. Phillips, The use of CCD detectors for X-ray diffraction – invited, The 47th Annual Denver X-ray Conference, Colorado Springs, CO, August 3–7, (1998).

5

GONIOMETER AND SAMPLE STAGES

5.1 GONIOMETER AND SAMPLE POSITION

5.1.1 Introduction

The function of the goniometer and sample positioning stages is to establish and control the geometric relationship between incident beam, sample, and detector. The goniometer is also the supporting base to many components, such as the X-ray sources, X-ray optics, sample environment stages, and sample aligning microscopes. The goniometer used for two-dimensional diffraction is fundamentally the same as for a conventional diffractometer. The geometry convention discussed in Chapter 2 for XRD^2 is inherited from conventional X-ray diffraction. Therefore, most concepts and definitions from the conventional diffractometer apply to XRD^2. In an XRD^2 system, at least three rotation axes are necessary to cover all the possible orientations of a sample in the diffractometer. These three rotation angles can be achieved either by a Eulerian geometry, a kappa (κ) geometry, or other geometries [1–7]. The three angles in Eulerian geometry are ω (omega), ψ (psi), and ϕ (phi). A typical four-circle diffractometer with either Eulerian geometry or kappa geometry includes an axis for the detector swing angle α in addition to the three sample rotation axes. The diffractometer may include three translation axes (X,Y,Z) for sample positioning. Many variations of goniometer geometry exist for historical reasons and preferences for various applications. Not all diffractometers have the complete six axes. The range of each axis may also be limited due to application requirements and mechanical limitations. That means the rotation angles or coordinates of some axes should be assigned as constants or zero.

5.1.2 Two-Circle Base Goniometer

The base goniometer typically consists of two axes in parallel directions and overlapping through the instrument center. The two axes may be used for different axes with different configurations. The most common configurations are θ-2θ and θ-θ. In the θ-2θ configuration, the incident beam

Two-Dimensional X-Ray Diffraction, Second Edition. Bob Baoping He.
© 2018 John Wiley & Sons, Inc. Published 2018 by John Wiley & Sons, Inc.



FIGURE 5.1 D8™ goniometer with two main axes in vertical orientation (Bruker AXS).

has a fixed direction, one axis is used for sample rotation (ω) and the other is used for the detector (2θ or swing angle α for 2D detectors). In the θ-θ configuration, one axis is used for the incident beam angle (θ_1), which supports and moves the source and optics, and the other is used for detector (θ_2). The two axes are referred to as the main axes of a goniometer since Bragg angle precision and accuracy are mostly determined by these two angles. The two axes are perpendicular to the diffractometer plane X_L-Y_L as defined in the laboratory coordinates. The base goniometer orientation is defined by the diffractometer plane. A goniometer or diffractometer is referred to as horizontal if the diffractometer plane is parallel to the laboratory ground plane, and referred to as vertical if the diffractometer plane is perpendicular to the ground. Figure 5.1 shows a base goniometer in vertical orientation (D8™ goniometer produced by Bruker AXS). The D8-goniometer is a high-precision, two-circle goniometer with independent stepper motors and optical encoders for θ and 2θ circles. The selectable driving step size can be as small as 0.0001°. The goniometer reproducibility is ±0.0001°. The D8-goniometer can be used in horizontal θ-2θ, vertical θ-2θ, and vertical θ-θ geometry. The two axes are mechanically arranged as the inner circle and outer circle. Either circle can be used as θ_1 or θ_2 in the θ-θ geometry, but the inner circle is typically used for the sample holder or as a base for more axes in the θ-2θ geometry.

In an XRD^2 diffractometer, the two-circle goniometer can set the X-ray beam incident angle and detector swing angle. In the θ-2θ configuration, the incident angle is set by the ω angle. In order to make the θ-θ configuration consistent with the previous definitions of the diffraction space and detector space, we have $\omega = \theta_1$ and $\alpha = \theta_1 + \theta_2$. The other parameters have the same definitions.

5.1.3 Sample Stages

Additional rotation axes and translation axes may be provided by sample stages to the base goniometer to enhance the sample orientation capability and positioning of a diffractometer. The sample stages used for the sample orientation and positioning are also regarded as part of the goniometer. In a three-circle goniometer, for instance, the third axis is typically used for sample rotation. Figure 5.2 shows 3D drawings of four different sample stages used for XRD^2 systems

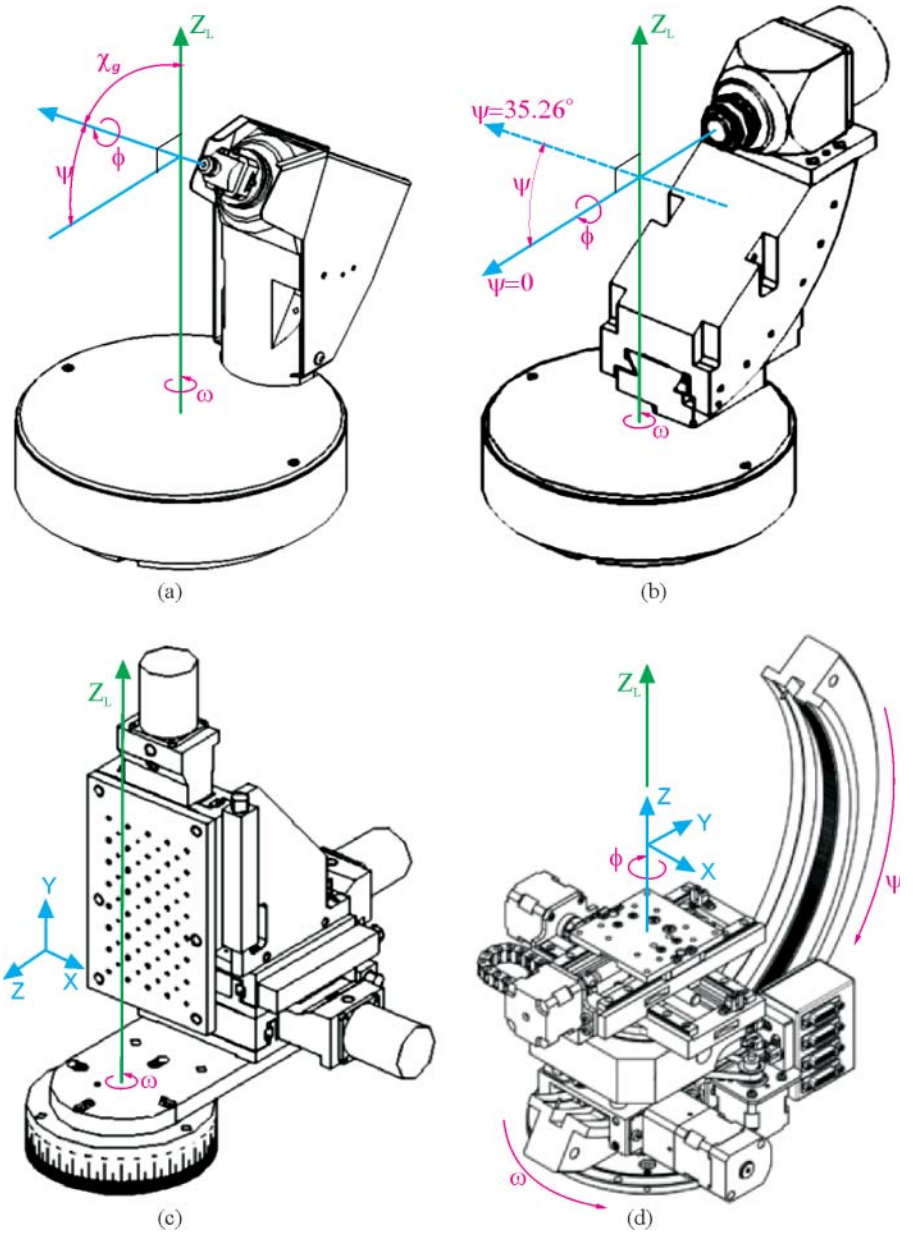


FIGURE 5.2 Various sample stages (Bruker AXS): (a) Fixed-chi, (b) two-position chi, (c) XYZ, (d) quarter-circle Eulerian cradle.

in the Bruker D8-Discover GADDS™ (general area detector diffraction system). Figure 5.2(a) is the fixed chi stage, which has a ϕ rotation axis tilted in a fixed χ_g ($=54.74°$) away from the main axes. It is typically mounted to the inner circle (ω) of the base goniometer in the θ-2θ configuration to form a three-circle goniometer. In order to achieve the most orientation completeness while achieving the full range of ω rotation and pass underneath the collimator, the fixed chi angle is chosen as the angle between the [111] and [100] directions in the cubic crystal ($\cos \chi_g = 1/\sqrt{3}$). The fixed-chi stage was first developed for, and still often used in, single crystal diffraction (SCD).

In the XRD^2 geometry convention, the tilt angle away from the diffractometer plane (ψ) is used, where $\psi = 90 - \chi_g = 35.26°$ as shown in Figure 5.2(a). The fixed-chi stage is typically used together with a goniometer head which provides small range XYZ adjustments to align a small sample into the instrument center. The fixed-chi stage is suitable to texture, stress, and phase-ID with small samples [8]. The combination of ω and ϕ rotations can generate the powder diffraction pattern from a single crystal as a simulation to the Gandolfi camera [9]. Figure 5.2(b) shows the two-position chi stage with the ϕ axis within the diffractometer plane, where $\psi = 0(\chi_g = 90°)$. The ϕ axis can also be manually moved to a tilt angle at $\psi = 35.26°(\chi_g = 54.74°)$. In addition to the functions similar to a fixed-chi stage, the $\psi = 0$ position is preferred for biaxial stress tensor measurement.

Figure 5.2(c) shows a heavy-duty XYZ stage. The stage can handle large samples or multiple samples. Motorized XYZ travel can be used for automatic sample alignment and diffraction mapping. Figure 5.2(d) is a quarter-circle Eulerian cradle. It is typically mounted to the inner circle (ω) of the base goniometer in the θ-2θ configuration to form a four-circle goniometer with all three rotation axes (ω, ψ, ϕ) and translation axes (X,Y,Z). The quarter-circle Eulerian cradle has the most functions of all the above three sample stages. Table 5.1 gives a comparison of the four sample stages. More sample stages are available for XRD^2 systems and their specs are available from their vendors.

5.1.4 Sequence of the Goniometer Axes

In order to move a sample spot into the instrument center, the six axes in the Eulerian geometry must follow a particular stacking sequence. The two main axes are the base of the goniometer and the diffractometer plane is determined by the main axes. They have the same order in the sequence. The ψ axis is a right-handed rotation about a horizontal axis within the diffractometer plane. The orientation of the ψ axis is determined by the ω angle; therefore it is mounted directly on the ω circle. The orientation of the ϕ axis is determined by both ψ and ω; therefore it is mounted on top of the ψ circle. The ϕ axis is always perpendicular to the ψ axis. All three rotation axes cross at the instrument center. The three translations should only bring a different part of the sample into

Table 5.1 Specifications and Applications of Sample Stages

Stage	Fixed-chi	Two-position-chi	XYZ stage	Quarter-circle cradle
Specifications:				
ω		$-180° \sim +180°$ (from the base goniometer)		
ψ	35.26°	0 and 35.26°	0	$-7°$~101°
ϕ	360° continue	360° continue	0	360° continue
X	n/a	n/a	−50 mm~+50 mm	−40 mm~+40 mm
Y	n/a	n/a	−50 mm~+50 mm	−40 mm~+40 mm
Z	n/a	n/a	−50 mm~+50 mm	−1 mm~+2 mm
Applications:				
Phase ID	yes, capillary	yes, capillary	Yes	yes
Stress	yes	yes (biaxial)	Yes	yes (biaxial)
Texture	yes	yes	yes (limited)	yes (best)
Mapping	no	no	Yes	yes
Microdiffraction	yes	yes	Yes	yes
Sample size	small	small	large	medium
Sample number	single	single	multiple	multiple
Auto alignment	no	no	Yes	yes

the instrument center, but not move any axis away from the instrument center. By definition, the orientation of the sample coordinates varies with any rotation axis, so the XYZ stage should be mounted last in the stacking sequence, i.e. on top of the ϕ axis. Since the Z axis overlaps with the ϕ axis, it is possible to build the ϕ axis above the Z axis. The X and Y axes must be built on top of the ϕ axis. Therefore, the acceptable axis sequence from the base goniometer to the sample can either be $\omega \rightarrow \psi \rightarrow \phi \rightarrow$(X,Y,Z) or $\omega \rightarrow \psi \rightarrow$Z$\rightarrow \phi \rightarrow$(X,Y). The axes in parentheses have the same sequence order and can be stacked in any relative order mechanically.

Any axis in the sequence can be absent. For example, in the XYZ stage shown in Figure 5.2(c), the XYZ axes are directly mounted on the ω circle, and ψ and ϕ are absent and considered to be zero. In rare cases, the above sequence is not followed, which will result in a different behavior of the goniometer. For instance, if the ϕ axis is stacked above the X and/or Y axes, the X or Y translation will offset the ϕ axis from the instrument center. In this case the ϕ rotation will bring a different part of the sample into the instrument center. The X-ray irradiated area will be a circular trace on the sample instead of a spot. This type of mechanism can be used only when the purpose of ϕ rotation is to oscillate the sample to improve sampling statistics.

5.2 GONIOMETER ACCURACY

In a diffractometer, the accuracy of the sample orientation and location are imperative for accurate data collection and analysis. The accuracy of the sample orientation and location is mainly determined by the goniometer accuracy. The most important factors affecting the sample orientation and location accuracy are the sphere of confusion, angular accuracy, and precision [10].

5.2.1 Sphere of Confusion

The sphere of confusion (SoC) is defined as the minimum spherical volume covering all possible locations of an infinitely small object at all possible goniometer orientations. The SoC is referred to as the sphere error in some literature. The minimum spherical volume means that the infinitely small sample or object has been mounted or moved to the goniometer center with the best effort. In other words, the deviation of the observed object from the instrument center is not due to errors in XYZ translations. There are many causes of the SoC, such as the mechanical tolerance of the rotation axes, off-centering of axes, or misshaped arcs or circles. The mass of the sample, goniometer components, detector, and X-ray source and optics may contribute to the SoC. Thermoexpansion mismatches between goniometer components due to environment temperature variation may also contribute to the SoC. The SoC is numerically measured by its diameter, but the radius of the sphere is also used in some literature or by some vendors. In the statistical approach, the distance of the object to the instrument center at all possible goniometer angles is considered to have a normal distribution. In this case the SoC is defined by the standard deviation, σ, from the instrument center (mean). For example, the measuring object has a 99.7% probability of falling into the SoC diameter defined by 3σ, and 95.4% by 2σ. Caution must be taken when comparing the SoC from different references and vendors.

The SoC of a goniometer is a superposition of all axes and can be measured at different levels of the stacking sequence. Taking the quarter-circle Eulerian cradle, for example, the SoC can be observed by following the typical alignment procedures. Figure 5.3 illustrates the alignment processes of each axis. The ϕ axis is first aligned and the SoC can be determined independent of other axes because it is the last in the stacking sequence of all the rotation axes. As shown in Figure 5.3(a–c), the alignment object is mounted on the ϕ axis with $\psi = 90°$ and observed in the horizontal direction. The location of the object is measured at the center of the object. The

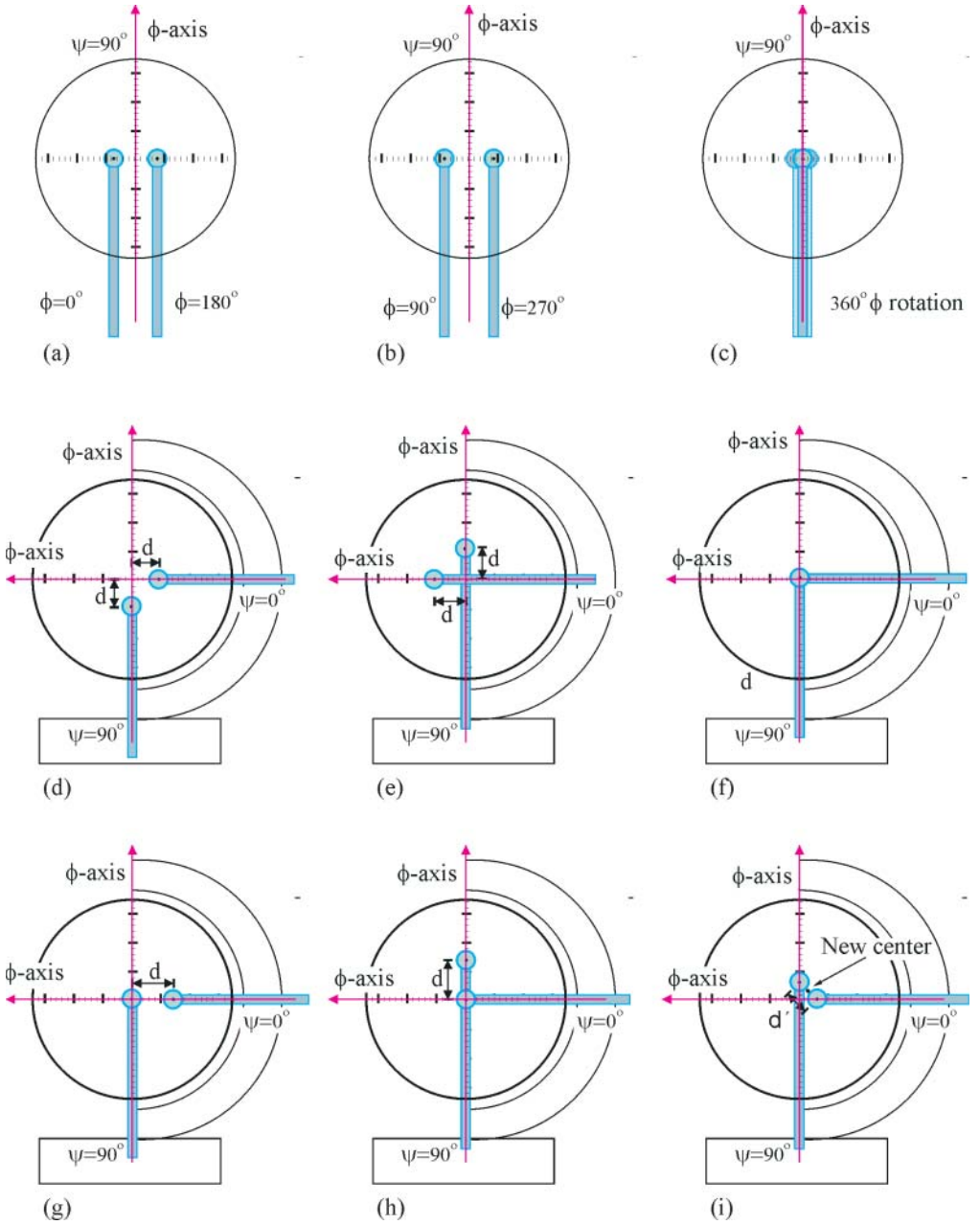


FIGURE 5.3 Sphere of confusion (SoC) from the contributions of ϕ axis and ψ axis in a quarter-circle Eulerian cradle.

deviation of the alignment object in one direction – X for instance – can be observed by rotation between 0° and 180°, and the deviation in the perpendicular direction – Y for instance – can be observed by rotation between 90° and 270°. The object can be aligned to the ϕ axis by adjusting the X and Y translation until the object stays in the same position or has minimum deviation when rotating the ϕ axis for a full 360°. The minimum deviation, as shown in Figure 5.3(c), is the ϕ

axis contribution to the SoC. The height of the object along the ϕ axis cannot be determined at this step and will be determined later by the ψ rotation center.

In further alignment, the deviation caused by ϕ rotation can be neglected and the object can be treated as a point on the ϕ axis. In principle, the center of the ψ circle should be the mean of the object locations at all ψ angles. For simplicity, we assume that only the height (Z) of the object varies with the ψ rotation. If the deviation (d) in the ϕ axis (Z) direction is the same at both $\psi = 0°$ and $\psi = 90°$ as shown in Figure 5.3(d,e). The center of the ψ circle is simply the cross point of the ϕ axis between $\psi = 0°$ and $\psi = 90°$ and the object can be aligned to the center by adjusting the object in the Z direction as shown in Figure 5.3(f). When the deviation (d) in the Z direction is not the same at both $\psi = 0°$ and $\psi = 90°$ orientations as shown in Figure 5.3(g,h), the center of the ψ circle is determined by the Z translation which results in the least deviation (d') between two object locations at $\psi = 0°$ and $\psi = 90°$ respectively. As shown in Figure 5.3(i), the ψ circle center in this case is the midpoint between the two object locations.

The above description of the SoC contribution of the ψ circle is an oversimplified model. The ψ circle is achieved by moving along a quarter-circle open cradle, which tends to have more distortions compared to a true rotation axis supported by a bearing. As is shown in Figure 5.4, the deviation due to ψ rotation includes three components: the axial deviation (1) in the ψ rotation axis direction (also the X direction when $\phi = 0$), radial deviation (2) in the Z direction, and (3) tangential deviation in the Y direction. In order to measure the "true" sphere of confusion, the object should be monitored in all three directions. This is typically achieved by rotating between two ω positions separated by 90° relative to the alignment microscope. The goniometry center of the quarter-circle Eulerian cradle is then the center of the minimum sphere covering the object locations at all possible ϕ and ω angles. This center is further aligned to the rotation center of the ω circle, and the total SoC should include the deviations caused by the ω rotation. The ω axis is one of the main axes that are supported by a high precision full bearings so the deviation is relatively small. Therefore, the overall SoC of the goniometer with a quarter-circle Eulerian cradle is mainly determined by the deviations of the ψ circle. The goniometer center of all three axes is then used to establish the instrument center during the system integration.

The specification of the SoC is dependent on the X-ray beam size, sample size, and applications [11–13]. The SoC of the goniometer, X-ray beam, and sample visualization system must converge at the instrument center to a region smaller than the sample and beam size to avoid the sample being misplaced or driven out of the X-ray beam. In order to get satisfactory diffraction data from the sample, the SoC should be a small fraction of the beam size or sample, whichever is

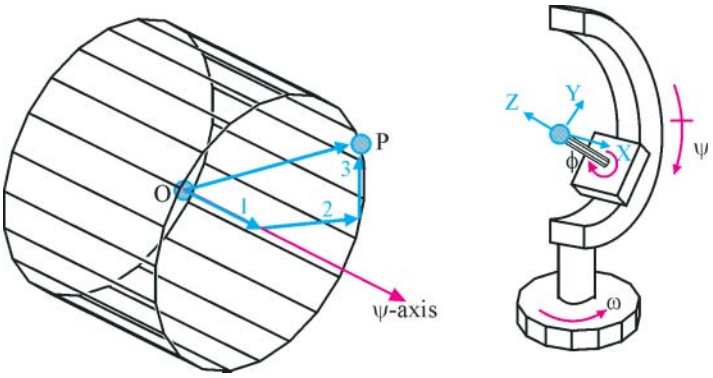


FIGURE 5.4 The sphere of confusion (SoC) from the contributions of ψ axis in a quarter-circle Eulerian cradle has three components.

smaller. For a large homogeneous sample, the SoC of the goniometer is not so critical for phase ID as long as the sample height (Z) is aligned to the instrument center. For texture measurement with a large homogeneous flat sample, the deviation of the goniometer center will shift the diffraction pattern in 2θ, but have less or no impact on the integrated intensity, so the relatively larger SoC can be tolerated. Stress measurement is very sensitive to 2θ shift, therefore the SoC of the goniometer is very critical and should be kept as small as possible. Microdiffraction typically requires a small SoC. For instance, for a 10 μm sample and 10 μm beam, the SoC of the goniometer, X-ray beam, and sample visualization system should converge within 2 μm [11]. The SoC may be better observed in a 3D plot, and the overall shape of the error point cloud or a volume containing the error points can be highly anisotropic, rather than a sphere [14]. The actual shape of the error volume can be used to optimize the operation of the goniometer.

The weights of the sample and diffractometer components have a strong impact on the SoC. More restrictive SoC requirements should also specify the sample weight limit. A goniometer axis may have different SoC contributions at different orientations due to the weight balance. For example, the bearings of the main axes in the base goniometer have relatively even loads in all radial directions in a horizontal diffractometer. But in the vertical goniometer, the loads on the bearings of the main axes can increase the SoC dramatically. The heavy 2D detector is typically attached to one of the main axes, which may also make the SoC more severe, especially as the SoC varies with the detector distance. The loading specifications of a goniometer may be specified in two or more values, typically a load limit for a specified SoC and maximum load. Within the specified load limit, the specified SoC can be maintained. While no permanent damage may occur to the goniometer under maximum load, the specified SoC cannot be maintained under the load.

5.2.2 Angular Accuracy and Precision

Accuracy and precision have been described and defined in many ways in the fields of science, engineering, industry, and statistics. The accuracy and precision of a diffractometer can be established by repeatedly measuring some stable standard reference materials (SRMs) [15]. A goniometer is both accurate and precise if the sample orientation, incident beam, and detector position can be driven to the intended values repeatedly. Figure 5.5 illustrates the definition and relationship of angular accuracy and precision in Eulerian geometry. The thick blue spot denotes the targeted sample orientation in terms of the three angles (ω, ψ, ϕ). The goniometer is repeatedly driven to the targeted orientation, and the achieved sample orientation at each attempt is denoted by the light blue spots. The achieved angular positions (light spots) form a cluster due to the variation between all the attempts. The deviation of the center (mean value) of the cluster from the targeted value is the measurement of the angular accuracy and the size of the cluster (variation) is the measurement of the angular precision. More precisely, the standard deviation of all attempts to the mean value is the measurement of the angular precision.

The angular accuracy is determined by a combination of two types of errors, one is the contributions of each individual axis, and the other is the contribution from the angular errors between various axes. For example, in Eulerian geometry, the angles between the ω and ψ axes and between the ψ and ϕ axes should be 90°. The squareness in the mechanical connections between these axes affects the angular accuracy. The squareness between the axes is typically determined by the mechanical accuracy and is adjusted during goniometer manufacturing. For a motorized goniometer axis, the accuracy and precision are determined by the design and quality of the bearing, the gear, the stepping motor, the controller, the encoders, and the homing references. For example, the optical encoders and homing references, with proper manufacturing settings, determine mainly the angular accuracy, while the step intervals of the stepping motor, the fineness of the driving gear, and the resolution of the encoders are critical to precision. The different axes of

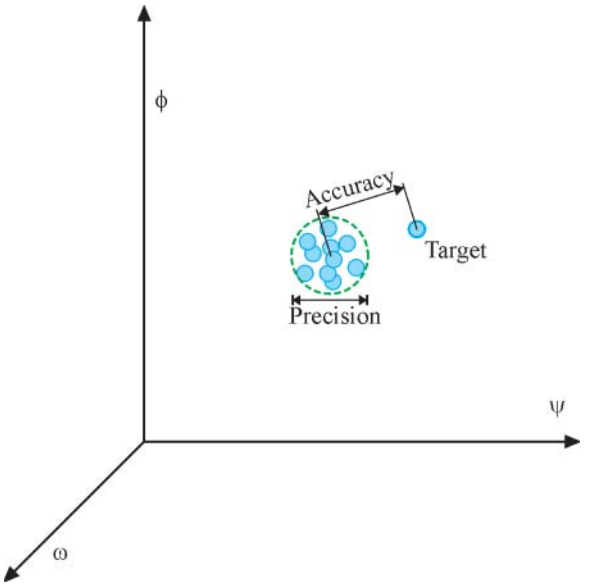


FIGURE 5.5 Angular accuracy and precision in Eulerian geometry.

a goniometer may demand different angular accuracy and precision. For example, the two main axes in the base goniometer determine the accuracy of Bragg angle measurement. The angular accuracy and precision are as good as 0.001° and angular intervals can be as fine as 0.0001°. The ψ and ϕ axes are mostly used for sample orientation, so the typical angular accuracy and precision are in the range of 0.01°.

Backlash is another factor affecting the goniometer accuracy [10]. Backlash is the discrepancy of the angular accuracy between two opposite driving directions. It is due to the gap in the gear pair and elastic deformation of the gear. Mechanical backlash can be eliminated by various approaches, such as spring-loading of the gears, a consistent driving direction during data scan, or closed loop servo motor control with optical encoders. A counterbalance can effectively reduce the gear loading, backlash, and SoC due to the stable moment loading on the bearings. Figure 5.6 shows the counterbalance for the inner and outer circles of a Bruker AXS D8™ goniometer in the vertical θ-θ configuration. The counterweights (gray parts) are located in the positions that match the weights and locations of the X-ray source and detector. The track for the X-ray source and optics (θ_1) and the track for the detector (θ_2) in the front of the goniometer are coupled to the counterweight at the back of the goniometer through connecting rods. The connecting rods limit the range to drive both the tracks down to negative angles. This is not a problem for the θ-θ reflection mode but prohibits driving the X-ray source or detector to the bottom for a vertical transmission system with horizontal sample plates. In this case, a special counterbalance is designed to couple the weight and counterweight through the inner circle of the goniometer. The design allows the system to be converted automatically between transmission mode and reflection mode [16].

5.3 SAMPLE ALIGNMENT AND VISUALIZATION SYSTEMS

Sample alignment systems are used to assist users in accurately positioning the sample into the instrument center and monitoring the sample state and position before and during the data

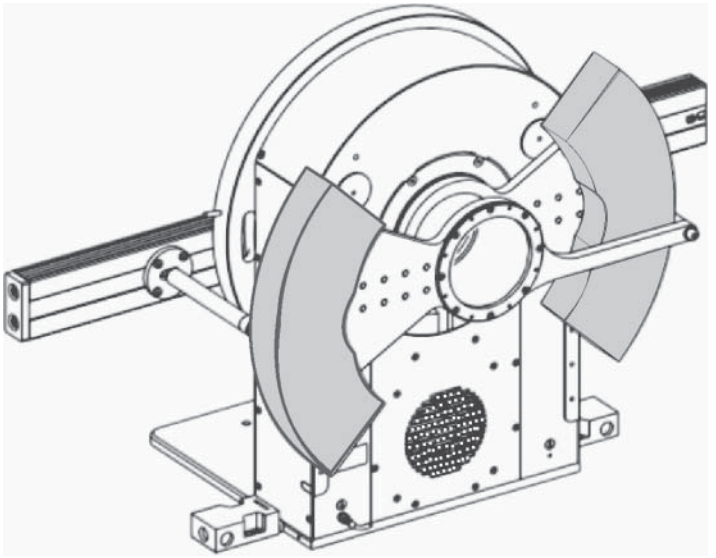


FIGURE 5.6 Counterbalance for the inner and outer circles of a vertical θ-θ goniometer (Bruker AXS).

collection. Either optical microscopes or video microscopes can be used for sample alignment and visualization. The optical microscope allows the user to directly observe the sample as a magnified image with a crosshair to determine the sample position. However, optical microscopes are obsolescent and have been gradually replaced by video microscope in recent years. The video microscope system includes a microscope head, CCD camera, and frame grabber to capture the image. Since the video image can be captured with the X-ray safety enclosure closed, the video microscope can monitor the sample state and position during data collection. The most important specifications of a microscope are the working distance, magnification, field of view, and resolution. The working distance is the distance between the viewing object and the object lens, which should be sufficient for the maneuvering of the goniometer and samples. The magnification should be sufficient to observe the smallest object for the system and sample alignment. The magnification of a video microscope consists of the optical magnification of the microscope head and video magnification. The microscope head may include an optical zoom for variable magnification, and the zoom can be either manually adjustable or motorized for automatic adjustment. The video magnification is determined by the ratio of the display size and the CCD size. The field of view is defined as the area on the object which can be observed by a video microscope. For the same video display size the field of view is reciprocal to the magnification. Therefore, one of the most important functions of the zoom adjustment is to get the best field of view at low magnification and better sample observation and alignment at high magnification. The resolution determines how much detail on the sample can be observed. The resolution of a video microscope is mostly determined by the pixel resolution of the video camera.

Figure 5.7 shows a sample alignment system consisting of a video microscope with zoom and laser beam in the Bruker GADDS™ microdiffraction system. The cross point of the laser beam and the optical axis of the zoom video are prealigned to the instrument center, as shown in Figure 5.7(a). Figure 5.7(b) is an image of the gold connection pad in an IC chip. The laser image spot falls on the center of the crosshair when the sample surface is positioned at the instrument center. Figure 5.7(c) is a picture of the laser-video alignment system. The system has a working distance of 78 mm, optical magnification with a zoom of 1× to 7×, overall magnification of

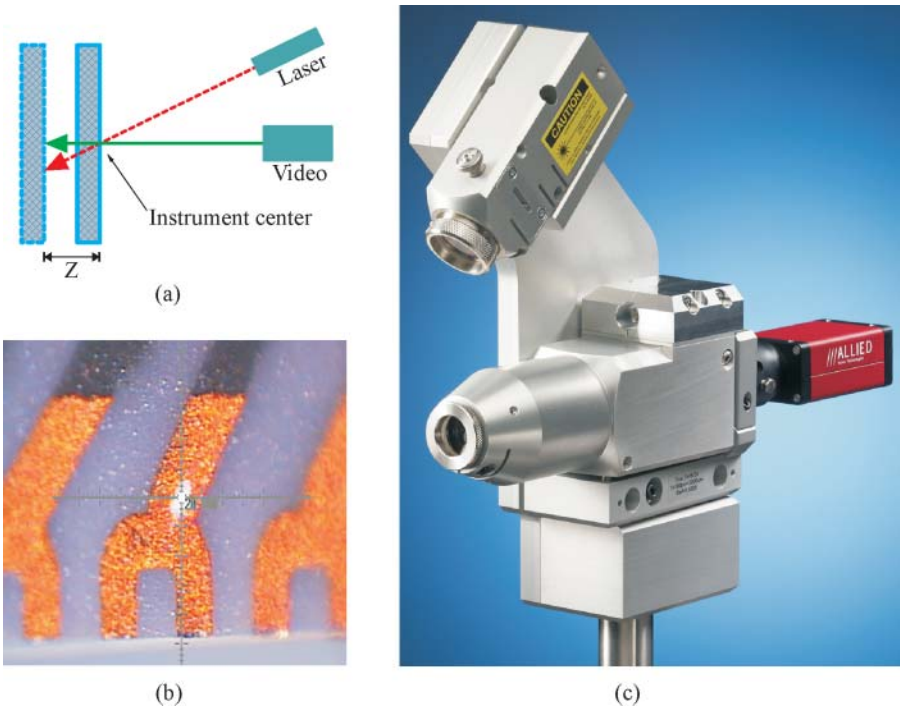


FIGURE 5.7 Laser video sample alignment system: (a) the working principle of laser-video alignment system, (b) image of laser spot and crosshair on a gold connection pad, (c) picture of the laser video system (Bruker AXS).

40× to 280× with 13″ display, field of view of 6–0.9 mm and pixel resolution of 768H × 494V. Integrated with motorized XYZ stage and controlled by the software, the system can also automatically align the sampling area into the instrument center [17]. This is essential for multitarget microdiffraction or diffraction mapping.

5.4 ENVIRONMENT STAGES

X-ray diffraction under controlled environmental and temperature conditions can reveal many materials characteristics that cannot be measured at ambient conditions. Therefore, the technique is also referred to as non-ambient X-ray diffraction. Non-ambient X-ray diffraction can be used for measuring phase transition, lattice thermal expansion, chemical reaction, lattice defects, orientation distribution, and stress variation with temperature [18, 19]. Non-ambient conditions can include humidity, vacuum, gas environment, low temperature, or high temperature. The most commonly used non-ambient sample stage is a high temperature stage.

5.4.1 Domed High Temperature Stage

Two-dimensional X-ray diffraction has special advantages in non-ambient study, such as high speed and large angular coverage [20]. Since the complete diffraction pattern can be measured simultaneously with a single exposure, it is very suitable for in-situ or time-resolved applications.

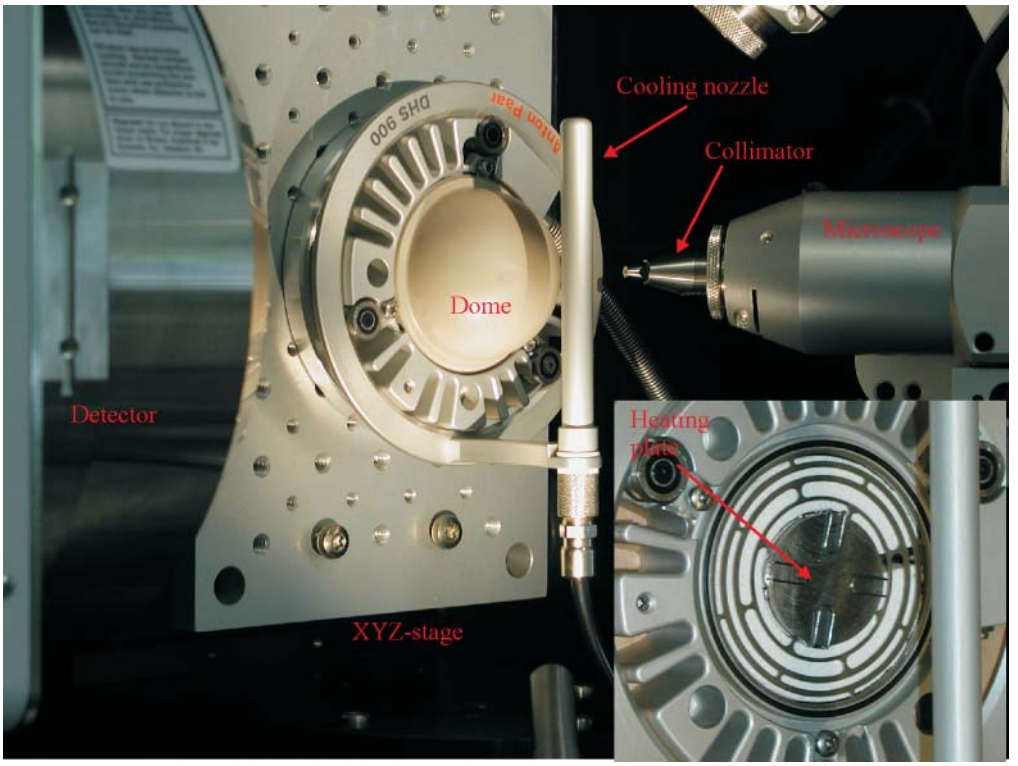


FIGURE 5.8 Domed hot stage (Anton Paar DHS 900™) mounted on the diffractometer (Bruker AXS D8 Discover GADDS™).

Accordingly, the environment stages used for XRD^2 should also have a large angular window for the incident beam and diffracted X-rays. An environment stage used for the conventional diffractometers typically has a limited window opening, which may be used with a linear detector [21], but may not be able to take the advantage of the large solid angle with the area detector. Ideal environment stages for XRD^2 should have a window opening covering all possible orientations of the sample surface. For reflection mode diffraction, the opening should have a solid angle of 2π (one hemisphere).

Figure 5.8 shows a hot stage (Anton Paar DHS 900™) with domed window mounted on the XYZ stage of a two-dimensional diffractometer (Bruker AXS D8 Discover GADDS™ with Hi-Star™ detector) [22, 23]. The domed hot stage has a light and compact design, suitable to be mounted on the quarter-circle Eulerian cradle or XYZ stage. The heating plate is made of a nickel-chromium alloy with good oxidation resistance at high temperature. The heating plate contains Ni (72%), Cr (14–17%), Fe (6–10%), and Mn (<1%), hence caution must be taken that the heating plate is not exposed to the direct beam, which may produce fluorescence radiation when Cu or Co tubes are used. The stage can be operated at temperatures up to 1173 K. The temperature is measured by a Ni-Cr sheath thermocouple. The thermocouple is mounted below the sample mounting surface at the center of the heating plate. The dome is made of PEEK, a high-performance polymer with a unique combination of mechanical properties, temperature resistance, chemical resistance, and high X-ray transmission. The sample chamber inside the dome can be kept in vacuum, with air, or with another gas environment. The sample chamber can be filled with inert gas to avoid any chemical reactions of the sample at elevated temperatures. Since the glass transition temperature of PEEK is around 170°C, the dome is blasted by cooling

gas (preferably clean, compressed air) from a nozzle when the stage is used at an operation temperature above 200°C. The dome can be made of beryllium for direct sample heating up to 1200°C in high vacuum [24].

5.4.2 Temperature Stage Calibration

The heat flowing from the heating unit to the sample and from the sample to the chamber surface or cooling units produces an inhomogeneous temperature distribution inside the chamber and the sample. The temperature measured by the thermocouple integrated to the heating stage may not be the true temperature of the sample. The temperature gradient exists between the sample surface in direct contact with the heating unit and the sample surface exposed to the X-ray beam. The extent of this temperature gradient depends on the thermal resistance of the contacting surface between the sample and heating unit, the thermal conductivity through the sample, and the heat insulation surrounding the sample.

In order to minimize the temperature error at the sample, the thermocouple should be mounted as close as possible to the sample location, a good thermal contact between the sample and heating units should be maintained, the distance between the diffraction sampling area and the heating contact should be kept minimum, and the heat flow from the sample to the surrounding environment should be reduced by good insulation, such as a vacuum.

The high temperature stage may be calibrated by using the known phase transformation temperature of a substance. Table 5.2 lists some substances which have been used for high temperature stage calibration and the corresponding phase transition [19, 25, 26].

The temperature stage may also be calibrated by a direct measurement with a thermocouple mounted in the sample location or embedded in the sample. The calibration with a thermocouple embedded in or attached to the sample gives a more accurate temperature reading, especially for samples with low heat conductivity. The calibration is typically done before the diffraction data collection and the thermocouple is then removed for the data collection at the same sample position. In cases where attaching or embedding a thermocouple to the sample is impractical, the calibration can be done with the thermocouple mounted at the intended sample position, assuming that the heating condition with the real sample is the same. Figure 5.9 shows the calibration

Table 5.2 Substances for High Temperature Stage Calibration [19, 25, 26]

Substance	Temperature (°C)	Phase transition
NH_4NO_3	84	orth.-tet.
NH_4NO_3	125	tet.-cubic
KNO_3	129	tr.-trig.
KNO_3	334	melting
CuCl	430	melting
$PbTiO_3$	490	tet.-cubic
SiO_2 (quartz)	573	α-β
K_2SO_4	586	ortho.-hex.
NaCl	801	melting
Bi_2O_3	820	melting
Ag	962	melting
Au	1064	melting
K_2SO_4	1076	melting
CaF_2	1360	melting

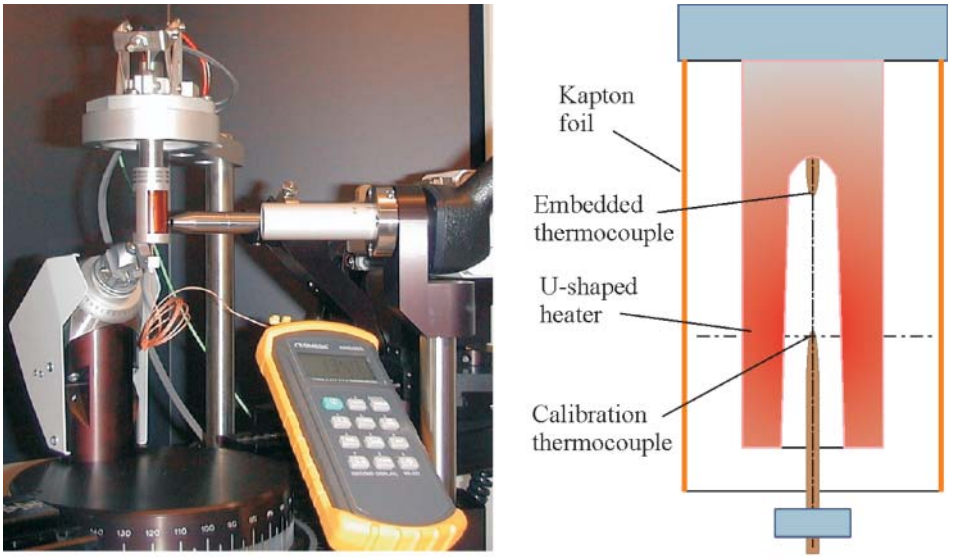


FIGURE 5.9 Hot stage calibration: (a) the hot stage (Huber™) mounted on the diffractometer (Bruker AXS D8 Discover GADDS™) with a thermocouple mounted in the sample position, (b) schematic showing the positions of the calibration thermocouple.

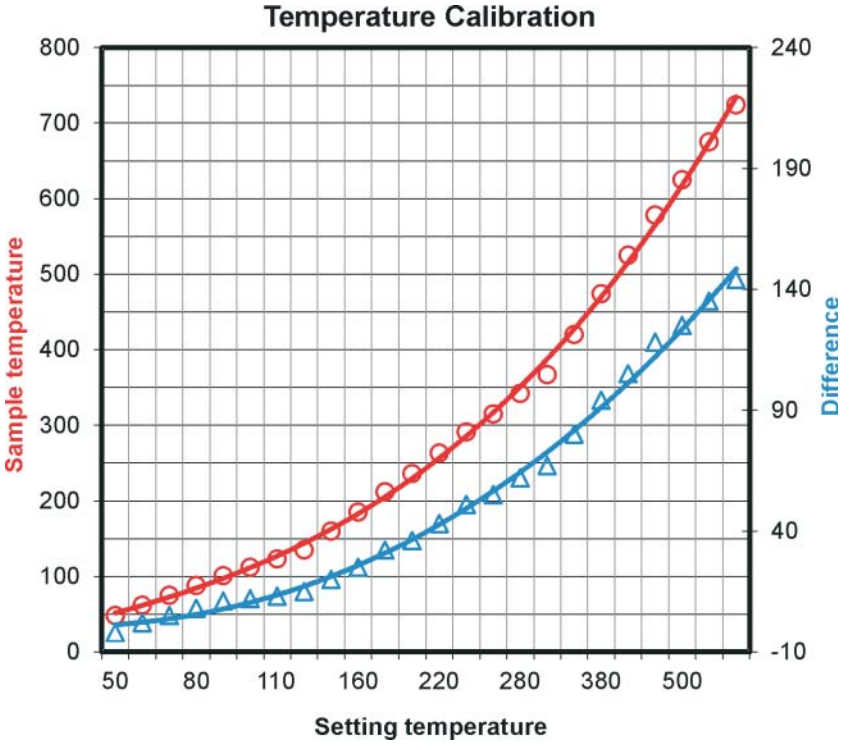


FIGURE 5.10 Temperature calibration: temperature plot and the difference.

setup with a Huber™ hot stage mounted on a GADDS™ (Bruker AXS) diffractometer [27]. As shown in Figure 5.9(b), the hot stage has a U-shaped heater with an embedded thermocouple for temperature measurement and control. The environment is enclosed in a kapton window. The sample position at the instrument center has a distance from the embedded thermocouple, therefore, a temperature difference is expected between the sample and the thermocouple. The actual temperature at the sample position is measured with an Omega HH506R digital thermometer with K-type thermocouple. The measuring tip of the thermocouple is mounted at the instrument center, where a sample is normally mounted. The heater is adjusted to various setting temperatures with control software from 50°C to 580°C. The reading temperature from the calibration thermocouple becomes stable after about 45 seconds with a fluctuation of less than ±1°. A temperature calibration plot showing the relation between the setting temperature and the actual sample temperature (circles) is shown in Figure 5.10. The difference between the setting and the actual temperatures (triangles) is shown on the right vertical scale. In this particular setup, the actual temperature is higher than the setting temperature since the embedded thermocouple is farther away from the instrument center and heating source.

REFERENCES

1. W. Busing and H. A. Levy, Angle calculations for 3- and 4-circle X-ray and neutron diffractometers, *Acta Cryst.* (1967). **22**, 457–464.
2. W. R. Massey Jr and P. C. Manor, A four-circle single crystal diffractometer with a rotating anode source, *J. Appl. Cryst.* (1976). **9**, 119–125.
3. D. J. Thomas, Modern equations of diffractometry. Goniometry, *Acta Cryst.* (1990). **A46**, 321–343.
4. M. Lohmeier and E. Vlieg, Angle calculations for a six-circle surface X-ray diffractometer, *J. Appl. Cryst.* (1993). **26**, 706–716.
5. E. Vlieg, Integrated intensities using a six-circle surface X-ray diffractometer, *J. Appl. Cryst.* (1997). **30**, 532–543.
6. P. Dera and A. Katrusiak, Towards general diffractometry. I. Normal-beam equatorial geometry, *Acta Cryst.* (1998). **A54**, 653–660.
7. G. Thorkildsen, H. B. Larsen and J. A. Beukes, Angle calculations for a three-circle goniostat, *J. Appl. Cryst.* (2006). **39**, 151–157.
8. N. S. P. Bhuvanesh and J. H. Reibenspies, A novel approach to microsample X-ray powder diffraction using nylon loops, *J. Appl. Cryst.* (2003). **36**, 1480–1481.
9. S. Guggenheim, Simulations of Debye–Scherrer and Gandolfi patterns using a Bruker Smart Apex diffractometer system, Bruker AXS Application Note 373 (2005).
10. M. F. Davis, C. Groter and H. F. Kay, On choosing off-line automatic X-ray diffractometers, *J. Appl. Cryst.* (1968). **1**, 209–217.
11. R. Sanishvili, A 7 mm mini-beam improves diffraction data from small or imperfect crystals of macromolecules, *Acta Cryst.* (2008). **D64**, 425–435.
12. I. C. Noyan et al., A cost-effective method for minimizing the sphere-of-confusion error of X-ray diffractometers, *Rev. Sci. Instrum.,* (1999). **70**, 1300–1304.
13. R. Moukhametzianov st. al., Protein crystallography with a micrometre-sized synchrotron-radiation beam, *Acta Cryst.* (2008). **D64**, 158–166.
14. P. Noiré et al., Sphere of confusion of a goniometer: measurements, techniques and results, *Diamond Light Source Proceedings*, (2010). **1**, e28, 1–4.
15. J. P. Cline, NIST standard reference materials for characterization of instrument performance, *Industrial Applications of X-ray Diffraction*, edited by F. H. Chung and D. K. Smith, Marcel Dekker, New York, (2000) 903–917.

16. B. B. He and R. C. Bollig, X-ray diffraction screening system convertible between reflection and transmission modes, US Patent No. 7,242,745, July 10, 2007.
17. J. Fink et al., X-ray micro diffractometer sample positioner, US Patent No. 5,359,640, Oct. 25, 1994.
18. S. T. Misture, E. A. Payzant, and C. R. Hubbard, Handout of high temperature XRD workshop, The 47th Annual Denver X-ray Conference, August 4, 1998.
19. M. Rodriguez, High-temperature and non-ambient X-ray diffraction, *Industrial Applications of X-ray Diffraction*, edited by F. H. Chung and D. K. Smith, Marcel Dekker, New York, (2000) 891–902.
20. L. J. Farrugia, P. Macchi, and A. Sironi, Reversible displacive phase transition in $[Ni(en)_3]^{2+}(NO_3^-)_2$: a potential temperature calibrant for area-detector diffractometers, *J. Appl. Cryst.* (2003). **36**, 141–145.
21. L. Brügemann et al., VANTEC-1 hot humidity studies in parallel beam geometry, Bruker AXS Lab Report XRD53, 2004.
22. R. Resel, A heating stage up to 1173 K for X-ray diffraction studies in the whole orientation space, *J. Appl. Cryst.* (2003). **36**, 80–85.
23. L. Brügemann, High temperature investigations with the D8 Discover using the DHS 900, Bruker AXS Inc., Lab Report XRD 40 (2001).
24. STC-Eulerian cradle – special temperature chamber with hemispherical beryllium-window for direct sample heating up to 1200°C in high vacuum, Materials Research Instruments (MRI), www.mri-gmbh.de, June 2002.
25. L. F. Connell, Jr. and J. H. Gammel, Hysteresis ranges of polymorphic transitions of some crystals, *Acta Cryst.* (1950). **3**, 75.
26. W. Ostertag and G. Fischer, Temperature measurements with metal ribbon high temperature X-ray furnaces, *Rev. Sci. Instrum.*, **39**, 888 (1968)
27. High-temperature attachment installation manual, Bruker AXS Inc., Doc#269-021902, 2001.

6

DATA TREATMENT

6.1 INTRODUCTION

Two-dimensional X-ray diffraction patterns contain abundant information for various applications. In order to accurately interpret and analyze 2D patterns it is necessary to apply some data treatment processes [1–4]. Most data treatment processes can be categorized into one of the following purposes. Some data treatments are to eliminate or reduce errors caused by detector defects, such as corrections for non-uniform detector efficiency and corrections for geometrical distortion. Some data treatments are to remove undesirable effects of instrument and sample geometry, such as corrections for polarization, sample geometry, and absorption. In order to analyze the 2D diffraction pattern for applications that were long established before area detectors were available, sometimes it is necessary to transfer the 2D frame into a format such that the data can be presented or further analyzed by conventional means and software. For example, when 2D frames are used for phase identification, the first step is to integrate the frames into one-dimensional diffraction profiles. Then the diffraction profiles can be used to search and match with the ICDD PDF database [5–10]. Some treatments, such as frame smoothing, are done for cosmetic reasons and mainly used for reports and publications. In order to extend the limited 2θ angular coverage of a 2D detector, multiple frames collected at various swing angles can be merged, or a 2D image with extended 2θ range can be collected by scanning the 2D detector.

6.2 NON-UNIFORM RESPONSE CORRECTION

An area detector can be considered an array of point detectors. Each pixel has its own detector counting curve. The detector counting curve represents the quantum efficiency, linearity, count rate, and saturation of the pixel. An ideal area detector should have identical pixels with 100% quantum efficiency and linearity. An area detector is considered to be uniform if all pixels have the

Two-Dimensional X-Ray Diffraction, Second Edition. Bob Baoping He.
© 2018 John Wiley & Sons, Inc. Published 2018 by John Wiley & Sons, Inc.

same counting curve (or the same intensity response). Unfortunately, most area detectors exhibit some non-uniformity distribution in intensity measurement when exposed to an isotropic source. The non-uniformity response can be caused by manufacturing defects, inadequate design, or limitations of the detector technology. For instance, a non-uniform phosphor screen or coupling fiber optic for a CCD detector may cause non-uniformity in quantum efficiency [11]. A gaseous detector may have a different intensity response between the detector edge and the center due to the variation in the electric field from center to edge. A thorough correction to the non-uniformity of the intensity response can be performed if the detector counting curves of all pixels are given. In practice, this is extremely difficulty or impossible because there is no independent counting curve for each pixel. The behavior of a pixel is affected by the condition of the adjacent pixels and the whole detector. The practical way to correct the non-uniformity of the intensity response is to collect an X-ray image from an isotropic point source at the instrument center and use the image data frame to generate a correction table for the future diffraction frames. The frame collected with the isotropic source is commonly referred to as a flood-field frame or a flat-field image [12], and the correction is also called flood-field correction or flat-field correction. Another type of correction for a non-uniform response is background correction, which is made by subtracting a background frame from the data frame. The background frame is collected without X-ray exposure. Integrating detectors, such as image plates or CCDs, have a strong background, which must be considered in non-uniform response correction. Photon counting detectors, such as the MWPC and mikrogap detectors, have negligible background. Background correction is not necessary.

6.2.1 Calibration Source

The calibration X-ray source for flood-field correction should be a uniform spherically radiating point source. Identical brightness (in photons/second·milliradian^2) should be observed from any pixel on the detector. The radiation strength of the source should match the medium of the expected dynamic range so as to minimize the error caused by the non-linearity of intensity response. The photon energy of the source should be the same as, or close to, the X-ray beam used for diffraction data collection so that the detector behaves the same during calibration and data collection.

There are many choices of calibration sources, from X-ray tubes, radioactive sources, diffuse scattering or X-ray fluorescence. Radioactive sources include ^{55}Fe, ^{63}Ni, ^{109}Cd, and ^{241}Am [12, 13]. Fe-55 (^{55}Fe) is the most commonly used calibration source for a diffraction system due to its photon energy levels. The emission is caused by the inner electron of the Fe-55 isotope being captured by the nucleus, transforming it into manganese. The Fe-55 source emits X-rays at three energies: Mn-K_α photons with an energy of 5.9 keV (80%), Mn-K_β photons with an energy of 6.2 keV (20%), and very weak K_α-escape with an energy of 4.12 keV. Fe-55 has a half-life of 2.741 years and decays to manganese. One favorable feature of an Fe-55 source is the absence of the continuum or bremsstrahlung X-rays. Calibrating area detectors using an Fe-55 source is very convenient because it can be easily mounted on the sample stage of a diffractometer with accurate reproducibility to the actual sample position. However, an Fe-55 source does not necessarily have the desired photon energy and its X-ray flux can only match the low end of the dynamic range in a diffraction data collection. Although typical research quantities of Fe-55 do not present a significant external exposure hazard, due to the low photon energy, Fe-55 is considered a radioactive material, which may require an appropriate authorization and safety handling procedures.

X-ray fluorescence is an alternative to a radioactive source. By placing a fluorescent material into the X-ray beam, fluorescence emission is generated. Fluorescence radiation is an isotropic point source if the irradiated area is a small point-like area. The fluorescent material is selected so that its K absorption edge is slightly longer than the wavelength of the X-rays used for diffraction.

For example, Cu-K_α can produce intensive fluorescence from materials containing significant amounts of iron or cobalt, and Mo-K_α from yttrium. In general, intensive fluorescence is produced when the atomic number of the X-ray tube anode material is 2, 3, or 4 times larger than the sample elements. In order to avoid a high localized intensity contribution from X-ray diffraction, the fluorescent material should be in an amorphous state. The amorphous state can be achieved by supercooling an alloy from the liquid state to form a metal glass foil. One example is the glassy iron foil which contains 79%Fe, 16%B, and 5%Si. The glassy Fe is stable at room temperature and the high content of B and Si prevent it from crystallization. The glassy metal foil is a very good choice for an isotropic source. Since the foil can be put in the exact same place as the diffraction sample, the calibration is done at a very accurate distance and position. However, glassy alloy foils are available for only a limited number of transition metals (Fe, Ni, Co, Mo). An alternative to the glassy alloy foil is amorphous lithium borate glass doped with the selected fluorescent element up to a 10% concentration [13].

When exposed to a Cu-K_α X-ray beam, the glassy iron foil emits X-rays of mainly Fe-K_α photons with an energy of 6.4 keV. The transmitted Cu-K_α X-rays are mostly within the transmitted direct beam, and elastically scattered Cu-K_α X-rays are negligible compared to the fluorescence. A glassy iron foil of 25 μm has been tested with the Bruker Hi-Star detector [14]. The results show that the flood-field image of the fluorescence from glassy iron has an identical intensity distribution as from Fe-55. The fluorescence generated from the glassy iron foil is much brighter than Fe-55 from a typical beam size (0.3∼0.5 mm) from a sealed X-ray beam tube. Compared to a typical Fe-55 source, using the glassy iron foil can reduce the calibration time by one or two orders of magnitude, depending on the X-ray beam size and power setting. The iron foil must be loaded at the normal sample position. Using Fe calibration foil may reduce the alignment error caused by the discrepancy between calibration source and samples. Any X-ray beam size can be used for the calibration, but different calibration times are needed due to different radiation flux levels. In order to get sufficient counting statistics, the total count of a flood-field frame should be at least 10^7 for a 1024×1024 frame format. It is recommended to use the same optics and beam size for calibration and data collection. In order to put the detector at the most homogeneous part of the radiation, the glassy iron foil should face the detector, i.e. the foil plane is parallel to the detector plane. The detector must be positioned away from the direct beam transmitted through the foil. An appropriate X-ray generator power setting is required to avoid detector saturation. Table 6.1 lists the recommended detector swing angle (the iron foil rotates the same angle from the initial position, which is perpendicular to direct beam) and the recommended power setting with a 0.5 mm beam and Hi-Star MWPC. The similar detector distance and swing angle can also be used for Våntec-2000™ and Våntec-500™ detectors. Since the flood field and diffraction pattern are collected with different energies, the detector high voltage bias setting is also changed between the two operations.

6.2.2 Non-Uniform Response Correction Algorithms

There are many algorithms available for flood-field correction, depending on the nature of the area detector. The correction is based on the flood-field frame collected from the calibration source. The simplest flood-field correction is to normalize the counts of all pixels to the same level, assuming that all pixels have the same response curve. The normalization factors for all pixels form a correction table and the table can be used to correct the data frames. The normalization factor for a pixel P_i is given as

$$N_i = \frac{M \cdot \Delta\Omega_i}{p_i \cdot \Omega} \tag{6.1}$$

Table 6.1 The Recommended Angle and Generator Power for Hi-Star Calibration with Iron Foil

Sample-to-detector distance	Detector and Fe foil assembly rotation angle	Generator power for 0.5 mm collimator
6 cm	50°	40 kV / 5 mA
10 cm	50°	40 kV / 10 mA
15 cm	45°	40 kV / 10 mA
20 cm	40°	40 kV / 15 mA
25 cm	30°	40 kV / 20 mA
30 cm	20°	40 kV / 20 mA
>35 cm	15°	40 kV / 25 mA

where M is the total counts of all pixels in the flood-field image, Ω is the solid angle of the whole detector area, p_i is the count measured by the pixel P_i in the flood-field image. $\Delta\Omega_i$ is the corresponding solid angle. Based on the equations in Chapter 4,

$$\Delta\Omega_i = \frac{(\Delta x)^2 D}{(D^2 + x_i^2 + y_i^2)^{3/2}} \tag{6.2}$$

where D is the sample-to-detector distance, Δx is the pixel size, and x_i, y_i are the position of the pixel P_i relative to the detector center. The solid angle of each pixel is considered in the normalization factor, so the count variation due to $\cos^3\varphi$ falloff as described in Chapter 4 is not normalized. The corrected frame from an isotropic source is not flat, but rather has a $\cos^3\varphi$ falloff effect. This is the result of a flat detector with identical intensity response from all pixels. The $\cos^3\varphi$ falloff effect will be considered later in the frame integration. The correction table contains normalization factors for all pixels. The corrected counts of each pixel can then be calculated from

$$p_i^c = N_i \cdot p_i^m \tag{6.3}$$

where p_i^c is the corrected count of the pixel P_i in the data frame and p_i^m is the measured pixel count of the pixel P_i. In the above simple normalization method, we assume that the response of each pixel is a linear function of incoming photons with zero background and no time-dependent changes. Furthermore, the intensity response of each pixel is independent of the X-ray exposures to other pixels.

For gaseous detectors – the MWPC for example – pixel intensity response is not independent, but affected by X-ray exposure to surrounding pixels and the whole detector. Flood-field correction is not done by applying a normalization factor to each pixel, but rather by a "rubber-sheet" stretching and shrinking in regions along the x and y detector axes to slightly alter the positions of counted photons. The total number of counts remains the same after the correction but is redistributed throughout the pixels so that the image from an isotropic source is uniformly distributed across the detector. This is mainly a cosmetic correction, which makes the images look smoother. Each pixel is first split into subpixels or bins. The bins are redistributed between neighboring pixels so that "weak" pixels cover more subpixels and "strong" pixels cover fewer subpixels. The newly formed pixels have approximately identical intensity response over the detector. Take the Hi-Star™ (Bruker AXS) MWPC as an example: the full detector is considered an array of 16376×16376 bins. In the uncorrected frames each pixel is formed by 32×32 bins in the 512×512 mode or by 16×16 bins in the 1024×1024 mode. The flood-field correction

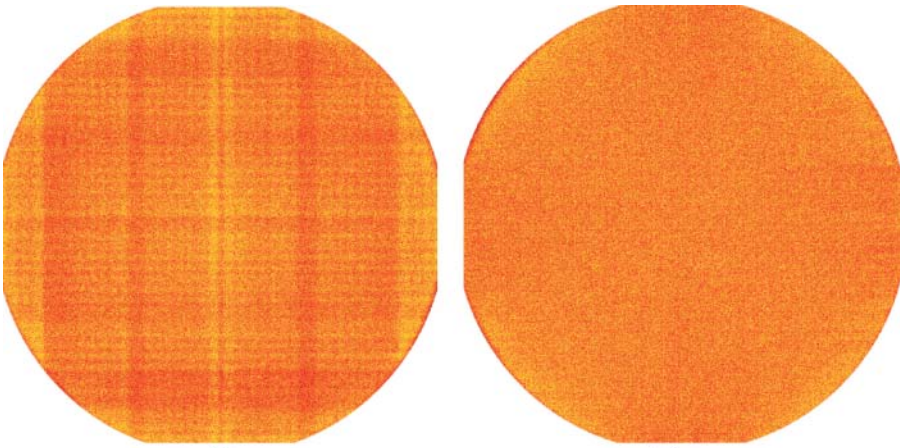


FIGURE 6.1 X-ray image from isotropic source: (a) raw image used for flood-field correction, (b) image collected with flood-field correction (Bruker Hi-Star™ MWPC).

table is a projection array which determines the detector bins to be projected to each pixel. The correction table is then used to map the detector bins to pixels during data collection so the corrected image is directly stored as a 512×512 frame or a 1024×1024 frame. Figure 6.1 shows two frames collected with the Bruker Hi-Star™ MWPC with the fluorescence radiation of glassy iron foil irradiated by a 0.5 mm point beam at a 15 cm sample-to-detector distance. Figure 6.1(a) is a raw image used for flood-field correction. The non-uniform response can be seen on this frame. Since this frame is from an isotropic source, a flood-field correction projection file can be generated from this frame. Figure 6.1(b) is an image collected under the same conditions with flood-field correction, i.e. with the projection file loaded during the data collection. This image shows a homogeneous intensity distribution. The flood-field calibration must be done with the same sample-detector distance for the diffraction data collection. However, it is possible to collect several spatial calibration files at different distances and then use them as needed.

6.3 SPATIAL CORRECTION

In an ideal flat area detector, each pixel not only has the same intensity response, but also gives an accurate position. The pixels are aligned in the x, y direction with equal spacing. In most cases we assume the detective area is completely filled by pixels, so the distance between two neighboring pixels in the x or y directions is equivalent to the pixel size. The deviation from this perfect pixel array is called spatial distortion. In reality, an area detector may exhibit spatial distortions to some extent due to the imperfection in the components, design, or manufacturing. The extent of spatial distortion is dependent on the nature and limitation of the detector technology. A CCD detector with 1:1 demagnification may have a negligible spatial distortion, but the barrel distortion in the coupling fiber optic taper can introduce substantial spatial distortion [11]. An image plate system may have spatial distortion caused by imperfections in the scanning system [15]. Gaseous detectors typically exhibit more severe spatial distortion due to the window curvature and the imperfect wire anode [16]. Spatial correction is necessary to get a diffraction image with accurate pixel positions so as to get the correct 2θ and γ values for data analysis and integration.

6.3.1 Fiducial Plate and Detector Plane

Spatial correction computation requires knowledge of the spatial distortion. The spatial distortion is measured from the X-ray images collected with a reasonably uniformly radiating point source positioned at the instrument center and a fiducial plate fastened to the front surface of the detector. The calibration sources for flood field and spatial correction have different requirements. The point source for a flood field should have isotropic brightness, but the size and location are not very critical. The source for spatial correction should have a very accurate position, point-like shape, and small size. In practice, the same point source is used for both flood field and spatial correction. Figure 6.2 illustrates the spatial correction geometry for a mikrogap detector (Bruker Våntec-2000). A fiducial plate is mounted to the front surface of the detector. The fiducial plate is made of brass with accurately distributed pinholes in the x and y direction. The flat side of the fiducial plate rests against the detector face. The diameter of the pinholes in the flat side controls the X-rays entering the detector. The side with the countersunk holes faces the calibration source. The calibration source must be placed at the exact same location as the sample position for data collection, which is the instrument center if the calibration is done on a goniometer. The X-ray image collected with this setup contains sharp peaks corresponding to the pinhole pattern of the fiducial plate. Since accurate positions of the peaks are given by the fiducial plate, the spatially corrected image is a projection of the collected image to this plane. Therefore the detector plane is defined as the contacting plane between the fiducial plate and the detector front face. The sample-to-detector distance, D, is defined as the distance between the instrument center and the detector plane. The region in which X-ray photons are converted to electrons or visible light is behind the detection plane. The region is associated with a physical component of the detector. One example is the phosphor screen in a CCD detector. Due to the flat window, the gap between the detector plane and the phosphor can be very small. In gaseous

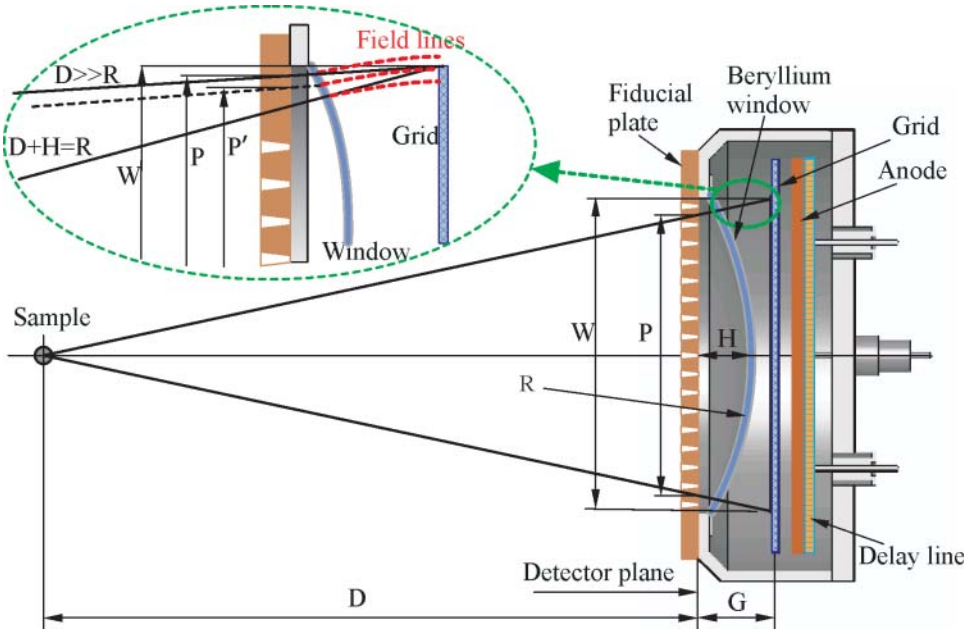


FIGURE 6.2 Geometry of the spatial correction for a mikrogap detector (Bruker VånteC-2000).

detectors – the Våntec-2000 for example – the detection region is the grid. The gap between the detector plane and the grid is much larger, which is denoted as G in the figure. The active area of gaseous area detector is determined by the active area of the grid size and the window size. The grid size is typically slightly larger than the window opening or in a different shape but covers the window opening – for example, a square grid for a circular window. Therefore, the active area is normally specified as the window opening size, provided the grid is of the same or greater size. The size of the detector active area is W in the figure. The size of the projected image on the detector plane, P, is a variable depending on the sample-to-detector distance.

$$P = \frac{WD}{D+G} \tag{6.4}$$

The projected image size approaches the size of the active area at infinite sample-to-detector distance. Since the electric field lines in the gas chamber are not straight, especially near the edge of the detector, the actual relationship is more complicated. The window is designed with a spherical curvature to reduce the parallax effect. The radius of the curvature, R, is designed to match the most often used sample-to-detector distance to minimize the parallax effect. H is the gap between the detector plane and the center of the Be-window. The least parallax effect can be achieved when $D+H=R$. The actual operational sample-to-detector distance can be less than or greater than the radius of window curvature. The parallax effect is more severe when $D+H$ is much less than R and less severe when $D+H$ is greater than R. The magnified part of the schematic shows the curved field-line. The electrons generated by ionization drift along the field lines. It shows that when $D+H=R$ or less, the curved field lines are within the active area, so the measured image size can be given by equation (6.4). When D is significantly larger than R ($D \gg R$), the field line corresponding to the extreme X-rays extend to the outside of the active area. The field line reaching the edge of the grid represents a modified projected size P' ($P' < P$). Therefore, the measured image size may be slightly smaller than the value given by equation (6.4).

6.3.2 Spatial Correction Algorithms

Spatial correction restores the spatial distorted diffraction frame into a frame with correct pixel position. A raw frame is considered to be warped by the spatial distortion, so the spatial correction is also referred to as an un-warping process [17]. Many algorithms have been suggested for spatial correction [11, 12, 15]. In the spatially corrected frame each pixel is generated by computing the pixel count from the corresponding pixels based on a spatial correction look-up table. Figure 6.3 illustrates the process of spatial correction. Figure 6.3(a) shows the pinhole pattern of the fiducial plate fastened to the detector. The pinhole size should be small enough to get a sharp image, but with sufficient size to pass enough flux to the detector. The distance between the centers of neighboring pinholes in the x and y directions should be small enough to capture short range spatial distortions, but large enough to distinguish the adjacent spots and to be able to be machined out accurately. An image containing the spots from the fiducial plate is collected. The distortion of the image is revealed by the fiducial spots as in Figure 6.3(b). The centroid positions of the spots are first computed based on a given threshold which distinguishes a pinhole spot from the background. The rows and columns of all fiducial spots are indexed. Then, the spots in each row and column are connected by smooth curves generated by spline interpolation of a polynomial function with the fiducial spots as control points. In most cases a second order polynomial is sufficient to generate piece-by-piece smooth curves. Based on the known positions of the corresponding pinholes in the fiducial plate the dislocation of each fiducial spot can be determined. The region surrounded by the four fiducial spots and connecting curves, shown as a shaded area,

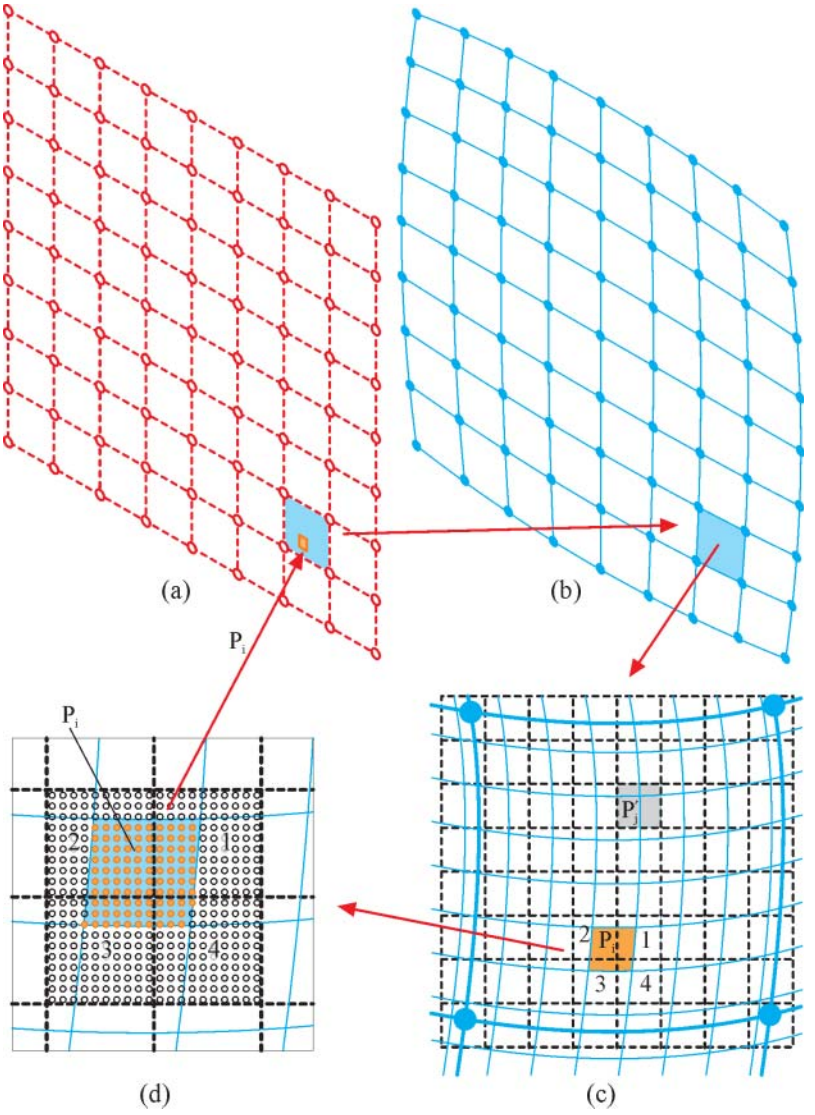


FIGURE 6.3 Process of spatial correction: (a) pinhole pattern in a fiducial plane (projected detector plane), (b) image with fiducial spots and spline curves showing the distortion, (c) interpolated curves defining the area of pixel projection, (d) subpixels in the contributing pixels.

can be considered a distorted projection of the shaded square area in Figure 6.3(a). On the other hand, the shaded square region in Figure 6.3(a) can be considered a corrected image of the shaded area in Figure 6.3(b). Therefore, the correction can be done by generating the intensities of all the pixels in the corrected image from the distorted image. The curves defining the projection of each undistorted pixel to the distorted image can be interpolated from the dislocation of the surrounding fiducial spots as shown in Figure 6.3(c). In Figure 6.3(c), P'_j is a pixel in the distorted image, which can be represented by the shaded square. The shaded area surrounded by four curves is the projection of the area of pixel P_i from the corrected image to the distorted image. This area may have overlapping areas with several pixels in the distorted image. In this case, the intensity of

pixel P_i contains the contributions from four pixels, labeled 1, 2, 3, and 4. In general, the intensity of pixel P_i is given as

$$p_i = \sum_{j=k}^{l} p'_j r_{ij} \tag{6.5}$$

where k is the number of the first contributing pixel in the distorted image to P_i and l is the number of the last contributing pixel. p'_j is the intensity of the contributing pixel p'_j and r_{ij} is the ratio of the contributing area to the whole pixel area. p_i is the intensity of the pixel P_i. The r_{ij} values for all pixels can be calculated from the spatial correction look-up table. Assuming the detector behaves the same in the real diffraction frame data collection, the look-up table generated from the fiducial image can then apply to the real diffraction frames. Calculating the contributing area for each pixel is not a programmer friendly approach. The pixels in the undistorted image may be mapped to rectangular pixels in the distorted image [12]. The curve edged pixels are approximated by the rectangular pixels. For a given pixel in the undistorted image, the projected position of the center of each edge is calculated. A rectangular region can be defined by these four points in the distorted image. The r_{ij} values can then be determined from the contributing pixels in rectangular shaped overlap regions. The intensities of the corrected pixels can then be calculated with equation (6.5). This algorithm may reduce programming effort and computing time, but also introduce errors, since the actual edges are typically curved.

An alternative approach is to redistribute the counts of each pixel into a set of identical subpixels as shown in Figure 6.3(d). The subpixels are discrete points evenly distributed inside the pixel area marked by the small circles. The total number of subpixels within each pixel is M. The contributing subpixels are those that fall into the gray area and labeled by the color-filled small circles. The number of contributing subpixels in pixels 1, 2, 3, and 4 are the m_{i1}, m_{i2}, m_{i3}, and m_{i4} respectively. In general, the intensity of pixel P_i is given as

$$p_i = \sum_{j=k}^{l} p'_j \frac{m_{ij}}{M} = \frac{1}{M} \sum_{j=k}^{l} p'_j m_{ij} \tag{6.6}$$

The m_{ij} values for all pixels can be calculated from the spatial correction look-up table.

The spatial calibration must be done at the same sample-detector distance as the diffraction data collection. A common practice is to collect several spatial calibration files at different distances and then use them as needed. Figure 6.4(a) is a raw frame used for spatial correction. It is collected with a fiducial plate fastened to a Bruker Hi-Star™ MWPC with the fluorescence radiation of glassy iron foil irradiated by a 0.5 mm point beam at a 15 cm sample-to-detector distance. The spatial distortion can be seen from the dislocation of the fiducial spot. Figure 6.4(b) displays the indexed fiducial spot positions in which all fiducial spots are properly indexed on this frame. Figure 6.4(c) displays the spatial correction table used to transform pixel x and y coordinates from raw to corrected values. Figure 6.4(d) displays the spatial correction table used to transform pixel x and y coordinates from corrected to raw values. Figure 6.4(e) shows the fiducial spots in the corrected frame. The rows and columns are aligned in a square array. Figure 6.5(a) is a fiducial frame collected with a Bruker Våntec-2000™ mikrogap area detector with the fluorescence radiation of glassy iron foil irradiated by a 0.5 mm point beam at a 20 cm sample-to-detector distance. The spatial distortion can be barely seen from the dislocation of the fiducial spot. Figure 6.5(b) displays the indexed fiducial spot positions in which all fiducial spots are properly indexed on this frame. Figure 6.5(c) displays the spatial correction table used to transform pixel x and y coordinates from raw to corrected values. Figure 6.5(d) displays the spatial correction table used to transform pixel x and y coordinates from corrected to raw values. Figure 6.5(e) shows the fiducial spots in the

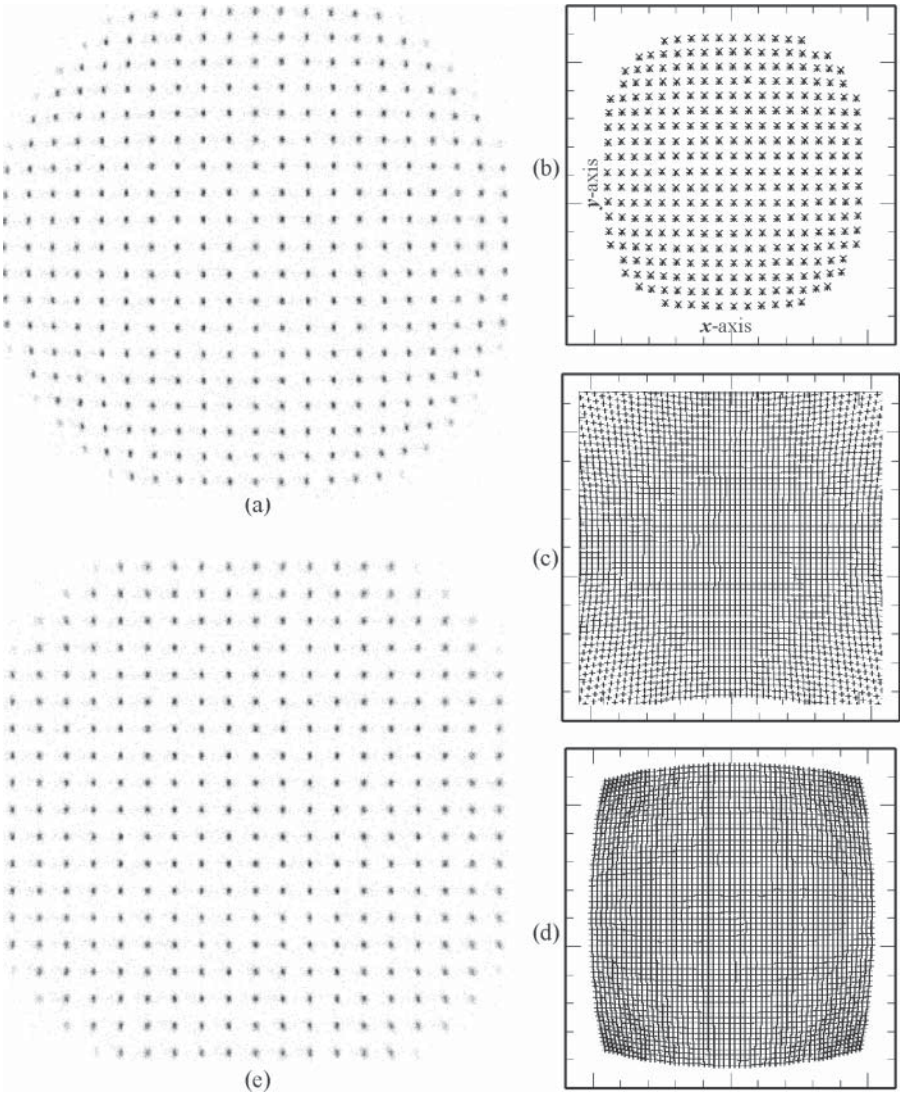


FIGURE 6.4 Spatial correction of a MWPC (Bruker Hi-Star™): (a) raw frame with distorted array of fiducial spots, (b) indexed fiducial spot, (c) correction table transforming pixel x and y coordinates from raw to corrected values, (d) correction table transforming pixel x and y coordinates from corrected to raw values, (e) fiducial spots in the corrected frame.

corrected frame aligned perfectly in a square array. The overall distortion of the Våntec-2000™ detector at 20 cm is much smaller than the Hi-Star™ at 15 cm sample-to-detector distance.

6.4 DETECTOR POSITION ACCURACY AND CALIBRATION

The flood-field correction and spatial correction ensure that all pixels in the detector have the same response to the intensity of incoming X-rays and correct positions within a detector. The detector position in the laboratory coordinates must also be determined in order to analyze the diffraction

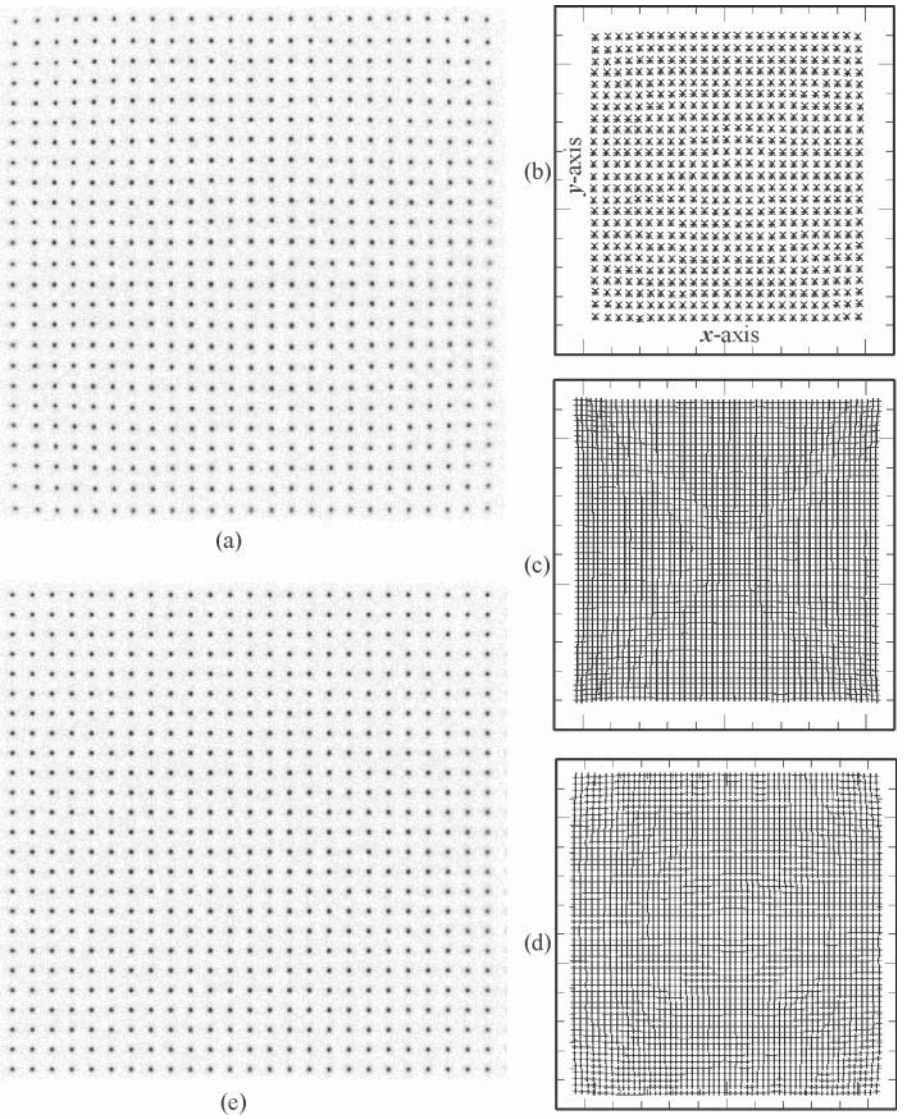


FIGURE 6.5 Spatial correction of a mikrogap area detector (Bruker Våntec-2000™): (a) raw frame with distorted array of fiducial spots, (b) indexed fiducial spot, (c) correction table transforming pixel x and y coordinates from raw to corrected values, (d) correction table transforming pixel x and y coordinates from corrected to raw values, (e) fiducial spots in the corrected frame.

pattern with accuracy. The position of a flat detector is defined by the sample-to-detector distance D and the detector swing angle α. D is the perpendicular distance from the goniometer center to the detection plane and α is a rotation angle away from the direct X-ray beam within the diffractometer plane. The beam center is defined as the intersection of the detector plane with the direct X-ray beam when $\alpha = 0$. The beam center is given by the x and y coordinates in the detector plane as x_c and y_c. The detector distance (D), swing angle (α), and beam center (x_c, y_c) must be determined to permit accurate 2θ and γ values from data reduction. In a diffractometer, D can be changed manually or automatically with a motorized stage and α can be changed automatically

by the goniometer. Since a typical goniometer has very high precision and accuracy, an accurate α is guaranteed by the goniometer, no additional attention is needed from users. However, accurate values of the sample-to-detector distance D and beam center (x_c, y_c) must be calibrated at each nominal distance D.

6.4.1 Detector Position Tolerance

An accurate detector position in a diffractometer is first determined by the mechanical mount, adjustment, and motorized driving stages. Figure 6.6 shows the position of a detector in the laboratory coordinates, $\mathbf{X_L Y_L Z_L}$. The direct X-ray beam propagates along the $\mathbf{X_L}$ axis, $\mathbf{Z_L}$ is up, and $\mathbf{Y_L}$ makes up a right-handed rectangular coordinate system. The $\mathbf{X_L}$ and $\mathbf{Y_L}$ axes define the diffractometer plane. The detector is set at on-axis position ($\alpha = 0$). The intersection of the detector plane with the $\mathbf{X_L}$ axis is the beam center on the detector. New coordinates **XYZ** can be created with a parallel translation of $\mathbf{X_L Y_L Z_L}$ in the $\mathbf{X_L}$ direction by the sample-to-detector distance D. The **Y** and **Z** axes fall in the detector plane. In order to maintain consistency within this book, the detector pixel position within the detector is given by the x, y coordinates. At this particular detector position ($\alpha = 0$), the x, y coordinates are parallel to the **Y** and **Z** axes respectively. The origin of the **XYZ** coordinates is at the beam center (x_c, y_c). The accuracy of the detector position is determined by six tolerance parameters in three translations (**X**,**Y**,**Z**) and three rotations ($\mathbf{R_X}$,$\mathbf{R_Y}$,$\mathbf{R_Z}$). The rotations, $\mathbf{R_X}$, $\mathbf{R_Y}$, and $\mathbf{R_Z}$ are the rotations about the three axes, **X**, **Y**, and **Z**, and also referred to as roll, pitch, and yaw respectively. The errors in the six axes project on the detector plane as a shift of the measured diffraction spots. The criterion of the tolerance is the amount of pixel shift produced by errors of each axis. The error in **X** corresponds to the sample-to-detector distance. The errors in **Y** and **Z** produce the same amount of pixel shifts within the detector plane. The pixel shift by errors of the three rotations varies within the detector plane. The amount of shift is a function of the rotation and the distance between the pixel and the detector center, r. The maximum shift occurs at the pixels farthest from the detector center. The pixel shift on the detector plane due to error in **X** depends on the sample-to-detector distance D and the spot to center distance r.

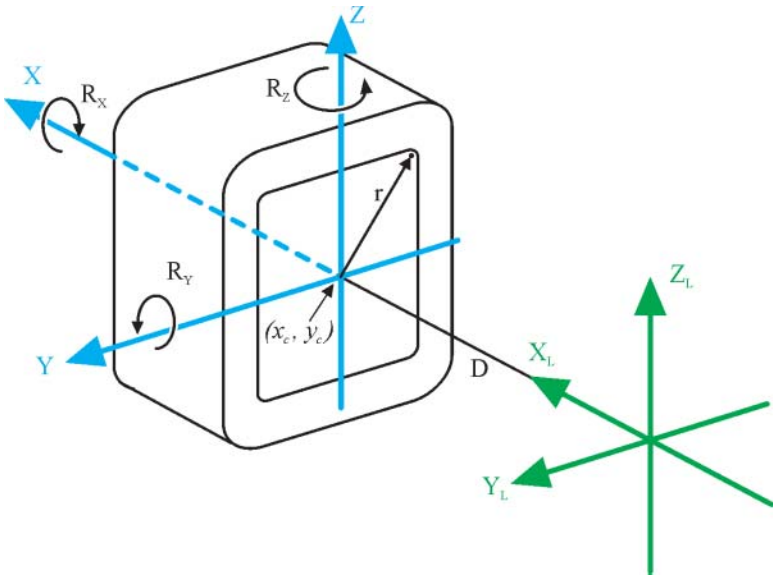


FIGURE 6.6 Detector position in the laboratory coordinates and the six parameters determining the tolerance of the detector position.

Table 6.2 Detector Position Tolerance and Reproducibility

Axis	Description	Equation for shift in detector plane	$D_{min} = 60$mm, $r_{max} = 55$mm, pixel size = 0.11mm	
			Tolerance 0.35 mm	Reproducibility0.11 mm
X	detector distance	$(r/D)\cdot\Delta\mathbf{X}$	0.38 mm	0.12 mm
Y	horizontal	$\Delta\mathbf{Y}$	0.35 mm	0.11 mm
Z	vertical	$\Delta\mathbf{Z}$	0.35 mm	0.11 mm
$\mathbf{R_x}$	roll	$r\cdot\sin(\Delta\mathbf{R_x})$	0.37°	0.12°
$\mathbf{R_y}$	pitch	$(r^2/D)\cdot\sin(\Delta\mathbf{R_y})$	0.40°	0.13°
$\mathbf{R_z}$	yaw	$(r^2/D)\cdot\sin(\Delta\mathbf{R_z})$	0.40°	0.13°

The descriptions of the six tolerance parameters and the corresponding equations for calculating the pixel shift from the errors are summarized in Table 6.2. The errors corresponding to the axes **X**, **Y**, **Z**, $\mathbf{R_X}$, $\mathbf{R_Y}$, and $\mathbf{R_Z}$ are denoted as $\Delta\mathbf{X}$, $\Delta\mathbf{Y}$, $\Delta\mathbf{Z}$, $\Delta\mathbf{R_X}$, $\Delta\mathbf{R_Y}$, and $\Delta\mathbf{R_Z}$ respectively. The shift tolerance can be as large as several pixels since the errors can be corrected by detector calibration. The errors $\Delta\mathbf{X}$, $\Delta\mathbf{Y}$ and $\Delta\mathbf{Z}$ can be corrected by the calibration of the detector distance and beam center, so the tolerance can be relatively large. The errors $\Delta\mathbf{R_X}$, $\Delta\mathbf{R_Y}$, and $\Delta\mathbf{R_Z}$ can only be partially compensated by correction and calibration, so the tolerance should be more critical. Various detector distances are used for different applications. The shift caused by the errors $\Delta\mathbf{X}$, $\Delta\mathbf{R_X}$, $\Delta\mathbf{R_Y}$, and $\Delta\mathbf{R_Z}$ increase with increasing r and decreasing D, so the tolerance must be given for the largest pixel-to-center distance (r_{max}) and shortest detector distance (D_{min}). The detector correction and calibration files at several detector distances are normally collected and saved. The files are reloaded when the corresponding detector distance is used. Therefore, the pixel shift caused by the reproducibility errors cannot be further corrected, so they must be kept to the minimum. The tolerance and reproducibility should be decided based on the detector type and the application requirements. Table 6.2 gives the equations for calculating the pixel shift caused by each error and examples of the tolerance and reproducibility for an 11 cm round detector. The tolerance is given based on a pixel shift of approximately three pixels and the reproducibility is based on a pixel shift of one pixel.

6.4.2 Detector Position Calibration

The detector position calibration determines the detector distance (D), swing angle (α), and beam center (x_c, y_c). The appropriate calibration permits accurate calculation of 2θ and γ values of pixels and diffraction features. The precise detector distance, swing angle and beam center are determined by taking diffraction frames of a known standard and comparing the measured diffraction rings with the calculated rings from the known peak 2θ positions and detector position. Any polycrystalline or powder exhibiting high stability and sharp diffraction lines can be used as calibration standard – for instance, corundum, quartz, or silicon. The calibration can be done manually by overlapping the calculated rings over the measured diffraction frame. By adjusting the values of detector distance, swing angle, and beam center, the calibrated values are found when the best overlapping occurs. Figure 6.7 shows the diffraction frame collected from a corundum (NIST SRM 676 α-Al_2O_3) powder sample with a two-dimensional diffraction system-Bruker GADDS™ (general area detector diffraction system). The software displays the diffraction frame and the calculated diffraction rings (white lines) based on the standard d/I file (PDF card 46-1212). The detector distance, swing angle, and beam center can be adjusted interactively by mouse or arrow keys until all the calculated rings precisely center over the collected diffraction rings in the data frame. In a short 2θ range the positions of the same sets of calculated rings may be moved by changing either the swing angle or the beam center (particularly x_c) to generate almost the same effect. In this case, the error in swing angle may be compensated by an error in beam center. This

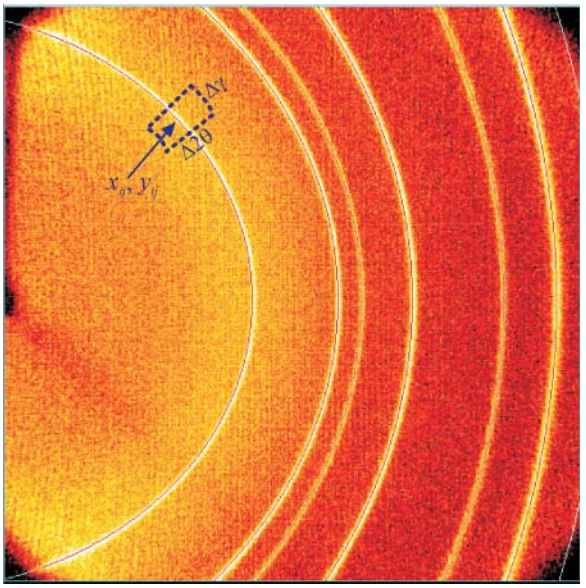


FIGURE 6.7 Detector calibration with diffraction pattern of corundum with the calculated rings (purple lines) on top of the measured diffraction rings.

is referred to as the coupling effect between the detector position parameters. In order to get a precise calibration and overcome the coupling effect, it is desirable to collect several frames at different swing angles. The sensitivity of the calibration to each parameter varies with the swing angle. For example, the diffraction frames collected at a low swing angle or on-axis position have better sensitivity to the beam center, while the frames collected at a large swing angle are more sensitive to the detector distance. The swing angle and beam center calibration can be decoupled if the frames are collected at both positive and negative swing angles.

The swing angle (α) may be determined independently by collecting a direct beam image with appropriate attenuation at more than two detector distances, preferably at the shortest and longest detector distances. The swing angle $\alpha = 0$ is determined when the direct beam images are within a small vicinity of the detector center and the measured beam center (x_c, y_c) are consistent at all detector distances. The swing angles at other values are guaranteed by the goniometer, which typically has accuracy better than 0.01° and reproducibility better than 0.001°. In this case, only the detector distance and the beam center need to be calibrated using the predetermined swing angle.

The calibration can also be done automatically by a computer program. The locations of the diffraction rings in the calibration frames are first determined in each section as shown in Figure 6.7 as the dotted line box. The $\Delta 2\theta$ and $\Delta\gamma$ are first determined based on an initial approximation of detector distance, swing angle, and beam center. The intensity gravity center of the section is then calculated as x_{ij} and y_{ij}. For the sharp peaks and negligible preferred orientation from the calibration sample, the coordinates x_{ij} and y_{ij} represents the i-th point on the j-th diffraction ring. The residual for this point on the diffraction ring is given as

$$r_{ij} = 2\theta_j - \cos^{-1}\frac{(x_{ij} - x_c)\sin\alpha + D\cos\alpha}{\sqrt{D^2 + (x_{ij} - x_c)^2 + (y_{ij} - y_c)^2}} \tag{6.7}$$

where $2\theta_j$ is the Bragg angle of the j-th diffraction ring from the standard reference material. The summed square of residuals is given as

$$S = \sum_{j=1}^{n}\sum_{i=1}^{m_j} r_{ij}^2 = \sum_{j=1}^{n}\sum_{i=1}^{m_j}\left(2\theta_j - \cos^{-1}\frac{(x_{ij}-x_c)\sin\alpha + D\cos\alpha}{\sqrt{D^2+(x_{ij}-x_c)^2+(y_{ij}-y_c)^2}}\right)^2 \tag{6.8}$$

where m_j is the number of data points on the j-th diffraction ring and n is the total number of diffraction rings used for calibration from all frames. Three parameters, detector distance (D), swing angle (α), and beam center (x_c,y_c) are determined by a non-linear least squares regression. There are many non-linear least squares routines available to use. The typical regression step is to start with the initial estimated values and then adjust the parameters in a given region by iterations with gradually reduced steps until the summed square of residuals reaches a minimum. It must be noted that in order to determine the calibrated beam center, arbitrary x, y origin coordinates are assumed, the calibrated beam center is given as x_c, y_c. In most of this book, we assume $x_c = y_c = 0$, so that x, y can be used directly to give the distances of a pixel to the beam center.

6.4.3 Detector Roll Calibration with Diffraction Rings

If diffraction angle $2\theta = 90°$, the diffraction cone becomes a plane perpendicular to the incident X-ray beams as shown in Figure 6.8. The diffraction ring collected by a flat 2D detector becomes a vertical straight line. If there is no "roll" error, the straight diffraction ring should be parallel to the y direction of the detector. Therefore, scattered X-rays along this ring will be detected by the pixels of the same x coordinates independent of y. By comparing the scattered intensity distribution and pixel array, the "roll" angle can be measured. In practice, the 2θ of the ring does not have to be exactly 90°, but within the reasonable vicinity of 90°. Figure 6.9 shows two frames collected from corundum at 2θ near 90°. The left is collected with a detector that has little or no roll error, the simulated diffraction ring is almost parallel to the diffraction ring as pointed by the arrow. The right frame is collected with a detector with significant roll error. The simulated ring forms an angle to the real diffraction ring. The roll angle can be evaluated from the angle between the simulated ring and the ring fitted from the diffraction data.

6.4.4 Intersection Between Diffraction Cones

A series of diffraction cones can be produced from a polycrystalline (powder) sample. All diffraction cones share the same rotation axis, which is also the trajectory of the incident X-ray beam. The 2θ values of all diffraction rings can be evaluated from d-spacing values of the crystalline planes, but a diffraction ring does not reveal the γ value of a particular scattering direction. In order to calibrate a 2D detector position, some reference points corresponding to known scattering directions must be given by both 2θ and γ values. The reference points can be generated from the intersection between diffraction cones collected at different swing angles. On the left of Figure 6.10, a single diffraction cone is illustrated. The sample is located at the position O, and the straight line O-C is the rotation axis of the diffraction cone, which is also the direction of the incident X-ray. The apex angle of the cone is determined by 2θ. On the right of Figure 6.10, three diffraction cones with different swing angles are overlapping. Assuming the cone in the center has zero swing angle, and the other two have a swing angle of $\Delta\alpha$ in both positive and negative direction respectively, the lines O-C, O-C′, and O-C″ represent the rotation axes of the three diffraction cones respectively. Depending on the swing angles between diffraction cones, the intersection line

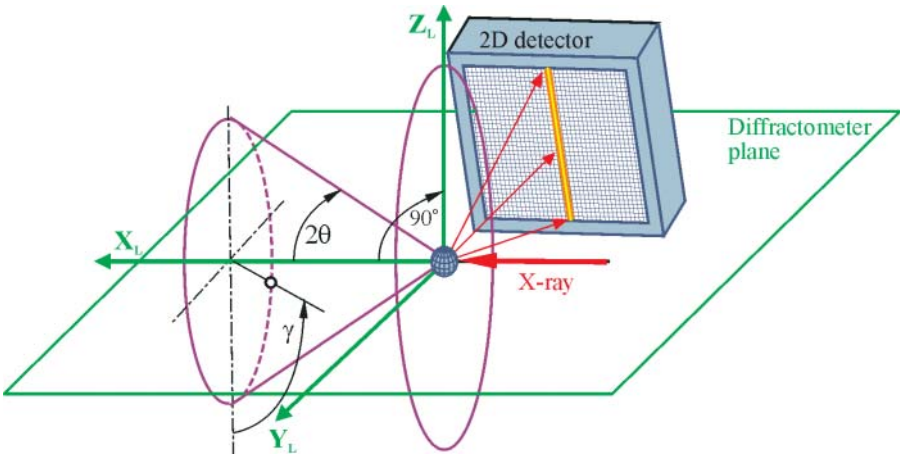


FIGURE 6.8 At $2\theta = 90°$, the diffraction cone becomes a plane perpendicular to the incident X-ray beams.

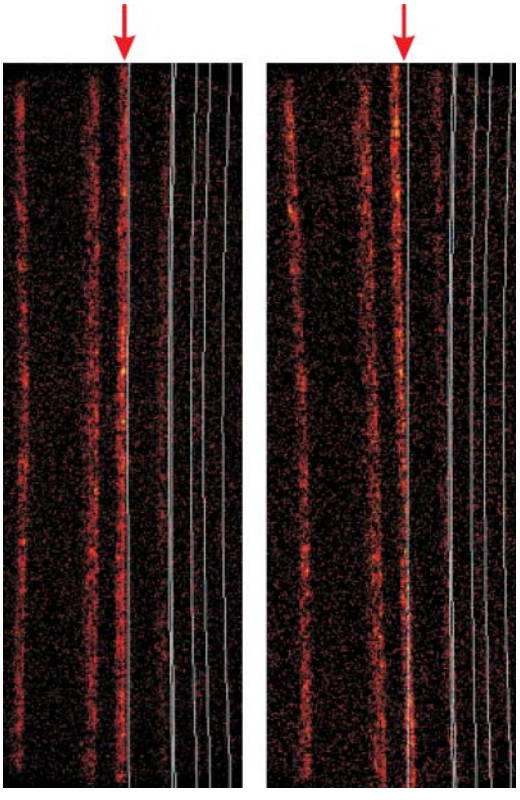


FIGURE 6.9 The 2D frames collected from corundum at 2θ near 90°: (left) minor or no roll error, (right) visible roll error.

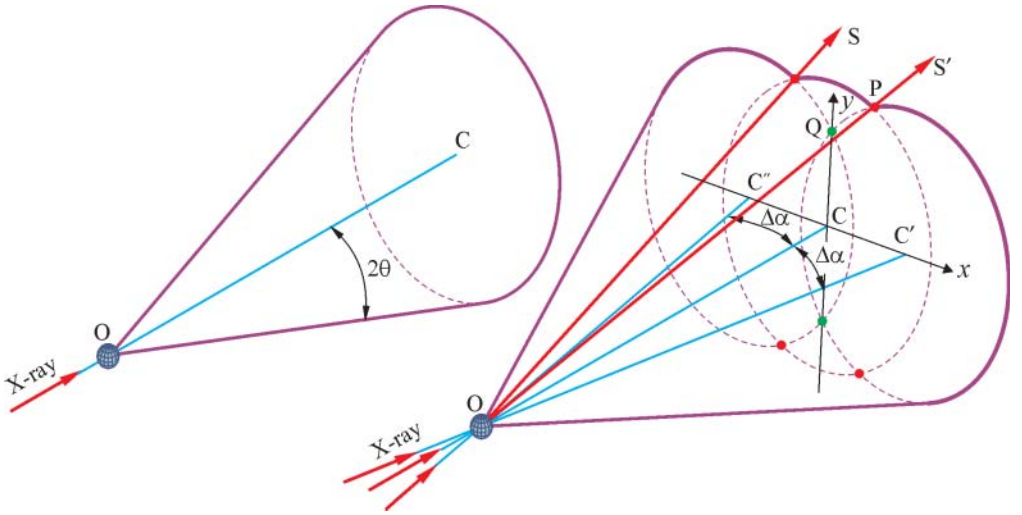


FIGURE 6.10 A single diffraction cone from one detector position (left), intersections between three diffraction cones with different swing angles (right).

between two diffraction cones defines a particular scattering direction. For instance, O-S and O-S′ represents two scattering directions from the intersection of the three cones. There are total of six scattering directions, which can be determined from the intersection of the three diffraction cones as marked by the red and green dots. Since all the scattering directions can be accurately defined regardless of the 2D detector position, the intersections can be used as references for calibration. For instance, the coordinate of the spot P on the detector can be given by

$$x_P = D \tan \frac{\Delta\alpha}{2} \tag{6.9}$$

$$y_P = D\sqrt{\tan^2 2\theta - \tan^2 \frac{\Delta\alpha}{2}} \tag{6.10}$$

The coordinates of all four red spots are given by (x_P,y_P), $(-x_P,y_P)$, $(-x_P,-y_P)$, and $(x_P,-y_P)$ respectively.

The coordinate of the spot Q is from the intersection of the two cones with positive and negative swing angles. The coordinate of the spot Q on the detector can be given by

$$y_Q = D \cos\Delta\alpha \sqrt{\tan^2 2\theta - \tan^2 \frac{\Delta\alpha}{2}} \tag{6.11}$$

The coordinates of the two green spots are given by $(0,y_Q)$ and $(0,-y_Q)$ respectively. The above equations can be used to calculate the cross point coordinates for the specific cases. The γ value for spot P can be calculated by

$$\gamma_P = \arccos \frac{\tan \frac{\Delta\alpha}{2}}{\tan 2\theta} + 90^\circ \tag{6.12}$$

The γ_P is determined only by the 2θ and swing angle difference $\Delta\alpha$, regardless the actual swing angle. So the above equation can be expressed for a general case:

$$\gamma_P = \arccos \frac{\tan \frac{\alpha_2 - \alpha_1}{2}}{\tan 2\theta} + 90^\circ \tag{6.13}$$

where α_1 and α_2 are the two swing angles at which the diffraction image was collected and assuming $\alpha_2 > \alpha_1$. The γ angle for the four intersection spots should be γ_P, $-\gamma_P$, $180^\circ - \gamma_P$, and $-180^\circ + \gamma_P$ respectively. Then, the (x,y) coordinates of the intersection spots on the detector can be calculated from $(2\theta,\gamma)$ by the following equations:

$$x = \frac{\cos\alpha \sin 2\theta \sin\gamma + \sin\alpha \cos 2\theta}{\cos\alpha \cos 2\theta - \sin\alpha \sin 2\theta \sin\gamma} D, \quad (-\pi \le \alpha \le \pi, \quad 0 \le 2\theta < \pi) \tag{6.14}$$

$$y = \frac{-\sin 2\theta \cos\gamma}{\cos\alpha \cos 2\theta - \sin\alpha \sin 2\theta \sin\gamma} D, \quad (-\pi \le \alpha \le \pi, \quad 0 \le 2\theta < \pi) \tag{6.15}$$

For any two rings of $(2\theta_1,\alpha_1)$ and $(2\theta_2,\alpha_2)$ with the condition that $2\theta_1 + 2\theta_2 > \alpha_2 - \alpha_1$, assuming $\alpha_2 > \alpha_1$, a set of the cross point coordinates can be determined by solving the above two equations with their respective parameters or computer iteration.

With various strategies based on the above principle, many reference patterns can be generated. For instance with powder samples containing large d-spacing lattice plane, such as silver behenate, plenty of intersection points can be collected at several swing angles. Figure 6.11(a) is a diffraction pattern collected from silver behenate powder at a nominal detector distance of 30 cm. Due to the large d-spacing lattice plane ($d_{001} = 58.38$Å), a set of concentric and evenly spaced diffraction rings from (00l) planes are observed. Figure 6.11(b) illustrates the intersections with the overlapping of three such diffraction patterns collected at three swing angles. Figure 6.11(c) is a single diffraction ring collected from a corundum sample in transmission mode and (d) illustrates the intersections with the overlapping of such diffraction patterns collected at many swing angles.

Figure 6.12 shows an experimental example of the intersection grid generated with a Pilatus3 R 100K-A 2D detector on a corundum sample. The left of the figure (a) shows a 2D frame with the (012) diffraction ring at $2\theta = 25.60$, collected at sample-to-detector distance $D = 14$ cm, Cu-K_α radiation, and swing angle $\alpha = 20^\circ$. The middle of the figure (b) shows both of the (012) and (104) rings at swing angle $\alpha = 26^\circ$. The right of the figure shows the intersection grid generated by overlapping frames collected at 10 swing angles of $\pm 18^\circ$, $\pm 20^\circ$, $\pm 22^\circ$, $\pm 24^\circ$, and $\pm 26^\circ$. For a detector without position error, the intersection points coordinates (x,y) can be calculated based on the equations (6.9–15). The intersection points on the measured frame can be estimated from the diffraction image. The errors between the measured intersection points and the calculated intersection points can then be used to calculate the detector position error. In order to improve the accuracy of the calibration, many intersection grid images can be measured with various diffractions rings at various detector swing angles. For calibration purposes, a set of intersection points for a given calibration procedure and standard sample can be stored as a reference. Only the measured intersection points need to be evaluated during the calibration.

The scattering angles calculated from the intersections between diffraction rings collected at various swing angles can be used as reference to calibrate the detector position. In addition to the detector distance, detector center as described in the previous section, the detector orientation (rotation) errors (roll, pitch, and yaw) can be determined from the intersections. The detector orientation (rotation) errors (roll, pitch, and yaw) can be determined from the intersections. Figure 6.13 illustrates the basic concept of the calibration. The upper-left (a) of the figure

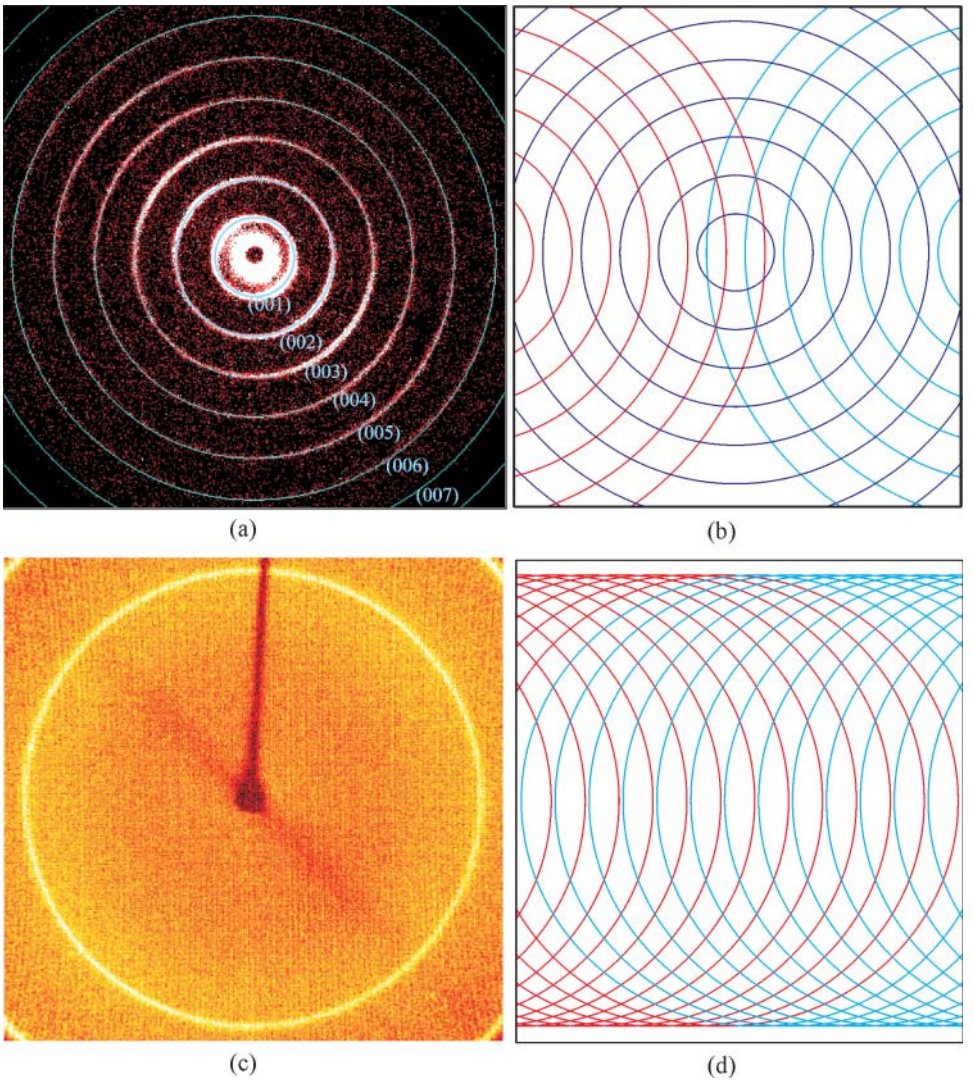


FIGURE 6.11 (a) Diffraction pattern collected from silver behenate, (b) intersections from silver behenate rings at three swing angles, (c) single diffraction ring collected from a corundum in transmission mode, (d) intersections with the overlapping of patterns collected at many swing angles.

shows four intersections produced by overlapping three diffraction rings collected at equal swing angle steps. If the detector has no orientation error, the green box connecting all four intersections is rectangular. The rectangular box will distort in shape or orientation if there is any detector orientation error. The upper-right (b) of the figure illustrates the rotation of the box distortion (red spots) caused by "roll". The bottom-left (c) shows the distortion of the box due to "pitch" where the left and right sides of the box are not equal length because the actual pixel-to-sample distances are not symmetric to the detector center. For the same reason, the top and bottom sides of the box are not equal length due to "yaw" as shown in the bottom-right (d) of the figure.

Figure 6.13 illustrates a simplified mode for the concept. The actual detector orientation error can be a combination of any or all of the three (roll, pitch, and yaw). The intersection points used for the calibration can also be much more than four, so the detector orientation error can be

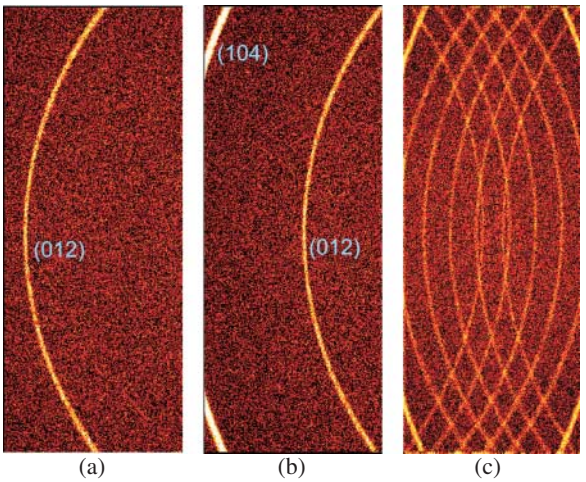


FIGURE 6.12 Measured diffraction rings from corundum at two swing angles (a) and (b) (middle) and the intersection grid by overlapping multiple frames at various swing angles (right).

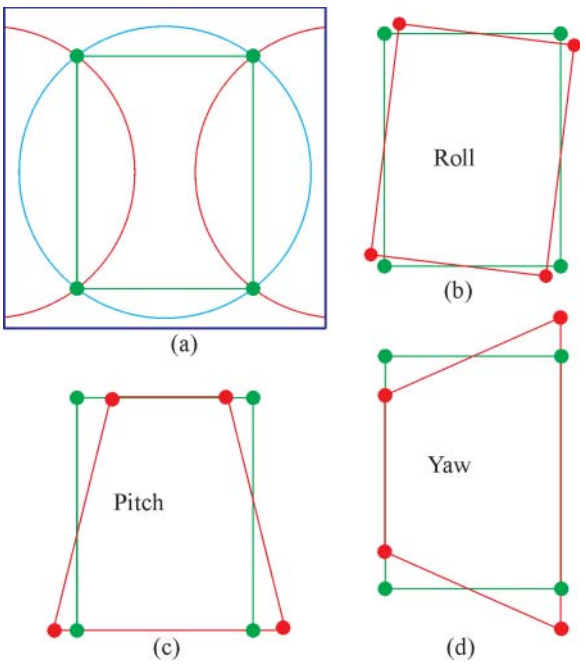


FIGURE 6.13 Relationship between intersection points and detector orientation errors (roll, pitch, yaw).

calculated more accurately with proper fitting and regression to all the available reference points. With small swing angle steps or a powder sample containing large d-spacing lattice plane, such as silver behenate, plenty of intersection points can also be used for a comprehensive correction covering detector distance, location, orientation, and spatial distortion. The correct x and y coordinates of the spots based on the diffraction cone intersection are first computed. Then the x and y coordinates of the measured intersection points are determined from the collected image by fitting all the diffraction rings. Then, similar to the spatial correction in the previous section,

the accurate diffraction patterns can be produced by 2D spline algorithms without any physical adjustment to the detector.

6.5 FRAME INTEGRATION

The 2D frame integration is a data reduction process that converts a two-dimensional frame into a one-dimensional intensity profile. Three forms of integration are generally of interest in analysis of a 2D diffraction frame from polycrystalline materials: γ-integration, 2θ-integration, and area integration. The γ-integration sums the counts within each 2θ steps ($\Delta 2\theta$) for the selected integration region. It produces a data set with intensity counts as a function of 2θ. The γ-integration region can be a "wedge" bounded by the 2θ range and two constant γ values, or a "slice" bounded by the 2θ range and a constant number of pixels in the vertical direction. The integration region can also be full frame or other selected region. The 2θ-integration sums the counts with given γ steps ($\Delta\gamma$) along the constant γ line and between two constant 2θ conic lines. The 2θ-integration produces a data set with intensity counts as a function of γ. The γ-integration is typically used for phase identification. The 2θ-integration is used to generate γ-profile which may be of interest for texture analysis and will be discussed more in Chapter 8 on texture analysis. The area integration sums all the counts within a selected region, which is typically used to generate a map of the interested diffraction features over an area of the sample.

6.5.1 Definition of Frame Integration

The γ-integration with wedge region can be expressed as

$$I(2\theta) = \int_{\gamma_1}^{\gamma_2} J(2\theta, \gamma) d\gamma \qquad 2\theta_1 \le 2\theta \le 2\theta_2 \tag{6.16}$$

or

$$I(2\theta) = \sum_{\gamma_1}^{\gamma_2} J(2\theta, \gamma) \qquad 2\theta_1 \le 2\theta \le 2\theta_2 \tag{6.17}$$

where J(2θ, γ) represents the two-dimensional intensity distribution in the 2D frame and I(2θ) is the integration result as a function of intensity versus 2θ. The γ_1 and γ_2 are the lower and upper limits of the integration. Due to the discrete nature of the diffraction frame, equation (6.17) is used to sum the counts within each $\Delta 2\theta$ step. If γ_1 and γ_2 are constants for γ-integration, the integration region in the most of the 2θ range looks like a wedge. If the γ range covers the complete 360° for an on-axis frame or frame collected with low swing angle, the integration region looks like a ring. If the lower and upper limits of integration are given by a constant vertical pixel range, the integration region looks like a slice. The γ-integration with a slice region can be expressed as

$$I(2\theta) = \int_{\gamma_1(2\theta, y_1)}^{\gamma_2(2\theta, y_2)} J(2\theta, \gamma) d\gamma \qquad 2\theta_1 \le 2\theta \le 2\theta_2 \tag{6.18}$$

or

$$I(2\theta) = \sum_{\gamma_1(2\theta, y_1)}^{\gamma_2(2\theta, y_2)} J(2\theta, \gamma) \qquad 2\theta_1 \le 2\theta \le 2\theta_2 \tag{6.19}$$

where the lower limit γ_1 is a function of 2θ and constant y_1, and the upper limit γ_2 is a function of 2θ and constant y_2. Alternatively, the γ-integration region can also be defined by a rectangular

region defined by a pixel range in both horizontal and vertical directions. For detectors without inferior quality near the edge, the full frame may be used as the γ-integration region.

A 2D diffraction frame collected with a 2D detector consists of a series of diffraction rings, as shown in Figure 6.14. The 2D detector is the Hi-Star detector positioned at a sample-to-detector distance $D = 7.5$ cm and swing angle $\alpha = -60°$. The frame format is 512×512 pixels. The sample is corundum (α-Al_2O_3) powder with a diffraction pattern that matches the PDF card 46-1212. The 2θ range is from 20° to 60° and the 2θ integration step size is 0.05°. Figure 6.14(a) shows γ-integration from 60° to 120° with a wedge region, and (b) shows γ-integration with a slice region and the same 2θ range, from 20° to 60° and with a 2θ integration step size of 0.05°. The lower limit y_1 is the lowest pixel position in the integration range, which is 100 pixels below the center of the detector and the upper limit y_2 is the highest pixel position in the integration range, which is 100 pixels above the detector center. A diffraction profile similar to the conventional diffraction result can be obtained by γ-integration with either wedge, slice region, or other regions over a selected 2θ range. Phase ID can then be done with conventional search/match methods. However, discrepancies in the relative intensities between the profiles from different integration region selection may occur due to the preferred orientation.

It can be observed from Figure 6.14(a) and (b) that the overall intensities of the two diffraction patterns are about the same, although the γ-integration ranges are significantly different. This is because the diffraction profiles are normalized by the solid angle. In order to reduce or eliminate the dependence of the integrated intensity on the integration interval, the integrated value at each 2θ step can be normalized by the number of pixels, the arc length, or the solid angle. The γ-integration with normalization by the solid angle can be expressed as

$$I(2\theta) = \frac{\int_{\gamma_1}^{\gamma_2} J(2\theta, \gamma)(\Delta 2\theta) d\gamma}{\int_{\gamma_1}^{\gamma_2} (\Delta 2\theta) d\gamma} \qquad 2\theta_1 \le 2\theta \le 2\theta_2 \tag{6.20}$$

Since $\Delta 2\theta$ step is a constant, this equation becomes

$$I(2\theta) = \frac{\int_{\gamma_1}^{\gamma_2} J(2\theta, \gamma) d\gamma}{\gamma_2 - \gamma_1} \qquad 2\theta_1 \le 2\theta \le 2\theta_2 \tag{6.21}$$

or

$$I(2\theta) = \frac{\sum_{\gamma_1}^{\gamma_2} J(2\theta, \gamma) \Delta\gamma}{\gamma_2 - \gamma_1} \qquad 2\theta_1 \le 2\theta \le 2\theta_2 \tag{6.22}$$

Following the same principle of the γ-integration, the 2θ integration can be expressed as

$$I(\gamma) = \int_{2\theta_1}^{2\theta_2} J(2\theta, \gamma) d(2\theta) \qquad \gamma_1 \le \gamma \le \gamma_2 \tag{6.23}$$

or

$$I(\gamma) = \sum_{2\theta_1}^{2\theta_2} J(2\theta, \gamma) \qquad \gamma_1 \le \gamma \le \gamma_2 \tag{6.24}$$

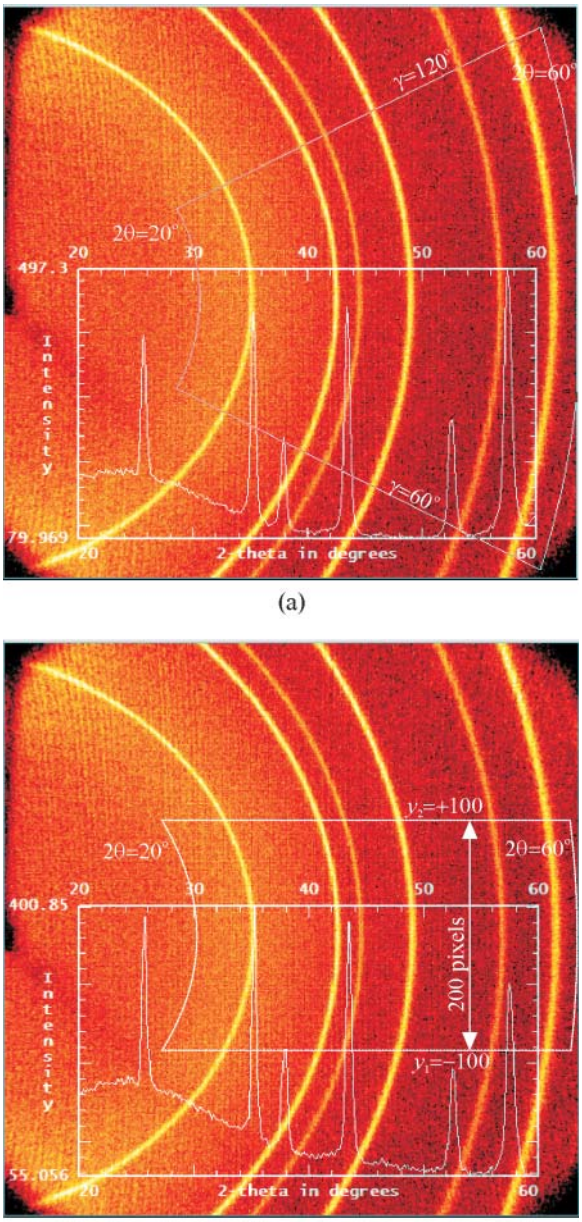


FIGURE 6.14 A 2D frame from corundum powder: (a) the γ-integration within a "wedge" region from 60° to 120°, (b) the γ-integration with a slice region of 200 pixels.

where $I(\gamma)$ is the integration result as a function of intensity versus γ within the range of γ_1 and γ_2. The area integration can be expressed as

$$I = \int_{\gamma_1}^{\gamma_2} d\gamma \int_{2\theta_1}^{2\theta_2} J(2\theta, \gamma) d(2\theta) \tag{6.25}$$

or

$$I = \sum_{\gamma_1}^{\gamma_2} \sum_{2\theta_1}^{2\theta_2} J(2\theta, \gamma) \tag{6.26}$$

In the following sections, various algorithms for γ-integration will be discussed. The same principle applies to the 2θ-integration and area integration.

6.5.2 Algorithm of Frame Integration – Flat Image

The γ-integration region is defined by two conic lines at $2\theta_1$ and $2\theta_2$ and two γ lines at γ_1 and γ_2. For each integration step, conic lines need to be calculated for 2θ and $\Delta 2\theta$ steps. In Chapter 2, equations were given for calculating 2θ and γ values for any point on a flat detector from its coordinates (x,y):

$$2\theta = \arccos \frac{x \sin\alpha + D\cos\alpha}{\sqrt{D^2 + x^2 + y^2}}, \quad (0 < 2\theta < \pi) \tag{6.27}$$

$$\gamma = \frac{x\cos\alpha - D\sin\alpha}{|x\cos\alpha - D\sin\alpha|} \arccos \frac{-y}{\sqrt{y^2 + (x\cos\alpha - D\sin\alpha)^2}}, \quad (-\pi < \gamma \le \pi) \tag{6.28}$$

The (x,y) coordinates of any point on the detector can be calculated from (2θ,γ) by the inverse functions of the above equations:

$$x = \frac{\cos\alpha \sin 2\theta \sin\gamma + \sin\alpha \cos 2\theta}{\cos\alpha \cos 2\theta - \sin\alpha \sin 2\theta \sin\gamma} D, \quad (-\pi \le \alpha \le \pi, \quad 0 \le 2\theta < \pi) \tag{6.29}$$

$$y = \frac{-\sin 2\theta \cos\gamma}{\cos\alpha \cos 2\theta - \sin\alpha \sin 2\theta \sin\gamma} D, \quad (-\pi \le \alpha \le \pi, \quad 0 \le 2\theta < \pi) \tag{6.30}$$

By setting either 2θ or γ to the given constant values of the integration region, conic lines or γ lines can be calculated. For slice integration, the lower limit γ_1 is a function of 2θ and constant y_1, and the upper limit γ_2 is a function of 2θ and constant y_2. Both functions $\gamma_1(2\theta,y_1)$ and $\gamma_2(2\theta,y_2)$ can be calculated from equation (6.28).

There is a range of integration software and algorithms available for reducing 2D frames into 1D diffraction patterns for polycrystalline materials [4, 17, 18]. An efficient algorithm to produce a line with pixels on a computer was first initiated by Bresenham [19]. The Bresenham line algorithm determines which pixels in an image should be connected to form a close approximation to a straight line between two given points. The original algorithm was modified later so that the algorithm can also be used to draw curves. Following a similar approach, the Bresenham algorithm can be used to integrate the 2D frame. Figure 6.15(a) shows γ-integration with the Bresenham algorithm. The pixels are represented by circles on the nodes of the grid. The conic line at a 2θ value is approximated by a series of pixels labeled with a dark dot inside the circle. The integration is a simple sum of all pixels approximating the conic line within the γ-interval.

$$I(2\theta) = \sum_{i=1}^{n} p_i \qquad 2\theta_1 \le 2\theta \le 2\theta_2 \tag{6.31}$$

where p_i is the counts of the ith pixel, and n is the total number of pixels integrated at the 2θ position. The intensity can be normalized by the number of pixels to average pixel count:

$$I(2\theta) = \sum_{i=1}^{n} p_i/n \qquad 2\theta_1 \le 2\theta \le 2\theta_2 \tag{6.32}$$

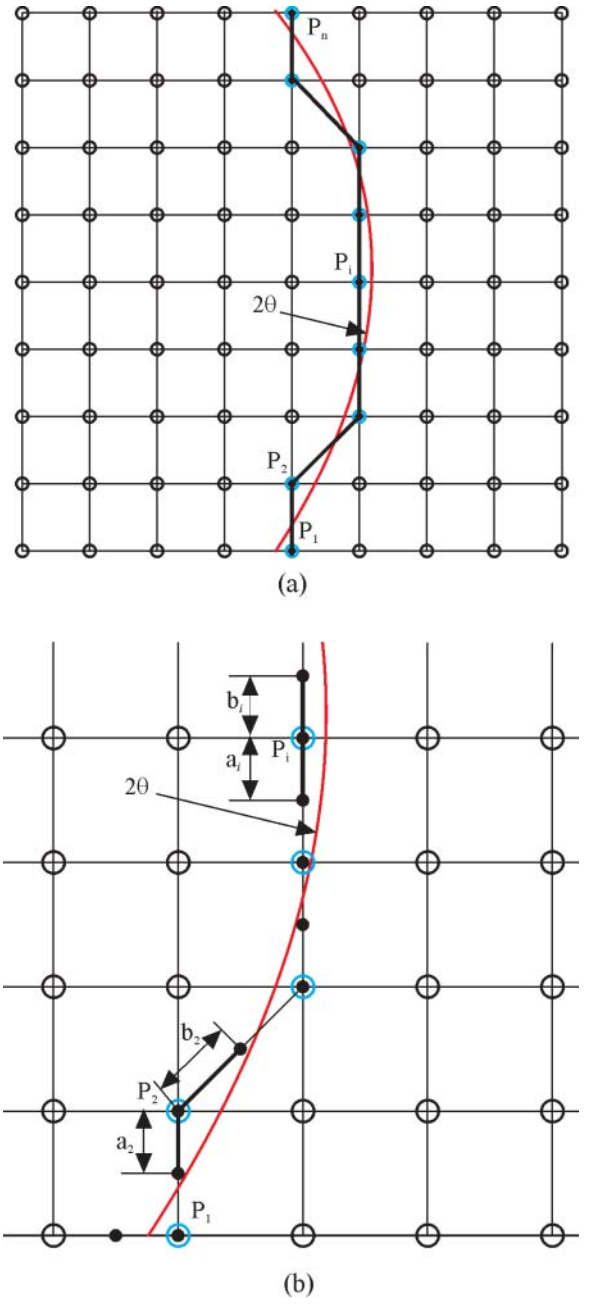


FIGURE 6.15 Illustration of integration by Bresenham algorithm: (a) conic line approximated by a series of pixels labeled with a dark dot inside the circle, (b) modified algorithm calculated the arc length for each pixel.

The integrated intensity can be normalized by the arc length by a Siemens modified algorithm [17]. Figure 6.15(b) gives a schematic of this modified algorithm. This modified algorithm must consider both the previously chosen pixel and the following chosen pixel by the Bresenham algorithm. The arc length is approximated by the two half distances to both the previous and the next pixel. For pixel P_2, the arc length is $a_2 + b_2$ and $a_i + b_i$ for pixel P_i. The arc normalized integration is then given by

$$I(2\theta) = \frac{\sum_{i=1}^{n} p_i(a_i + b_i)}{\sum_{i=1}^{n}(a_i + b_i)} \qquad 2\theta_1 \le 2\theta \le 2\theta_2 \tag{6.33}$$

The integrated intensity can also be normalized by the solid angle of each pixel:

$$I(2\theta) = \frac{\sum_{i=1}^{n} p_i \Delta\Omega_i}{\sum_{i=1}^{n} \Delta\Omega_i} \qquad 2\theta_1 \le 2\theta \le 2\theta_2 \tag{6.34}$$

where $\Delta\Omega_i$ is the corresponding solid angle of the pixel P_i given by equation (6.2). The Bresenham algorithm uses only simple addition, which can be done very fast. This was critical when computer power was very limited. However, satisfactory results can be achieved only if the pixel size is smaller than the $\Delta 2\theta$ step. When the $\Delta 2\theta$ step is only a fraction of the pixel size, it may generate a stair-like profile due the same group of pixels being used to approximate adjacent conic lines.

With the availability of much higher computer power today, the Bresenham algorithm and its modified versions have lost their advantages. Due to the way the Bresenham algorithm treats pixels as discrete points in the grid and the approximation of conic lines, it is hard to generate a smooth and accurate diffraction profile, especially when the integration step is smaller than the pixel size or the counts are low. A relatively new method is the bin method, which treats pixels as having a continuous distribution in the detector. It demands more computer power, but delivers much more accurate and smooth results, even with integration $\Delta 2\theta$ steps significantly smaller than the pixel size. Figure 6.16 illustrates the bin method. Figure 6.16(a) shows that the conic line and $\Delta 2\theta$ define the region to be integrated into a data point in the output diffraction profile. The pixels with gray areas are the contributing pixels. Depending on the relative size of $\Delta 2\theta$ and the pixel size, each contributing pixel is divided into one to three bins. A pixel may be contained in only one bin if the pixel size is smaller than $\Delta 2\theta$ and the entire pixel is enclosed in the integration step. Figure 6.16(b) shows magnified images of the pixels P_1, P_3, and P_i in which A_1, A_3, and A_i are the areas of respective pixels inside the integration step. The conic lines inside each pixel can be approximated by straight lines so that the values of A_i can be calculated for each pixel by simple formulas. The integration is then given as

$$I(2\theta) = \sum_{i=1}^{n} p_i \frac{A_i}{(\Delta x)^2} = \frac{1}{(\Delta x)^2} \sum_{i=1}^{n} p_i A_i \qquad 2\theta_1 \le 2\theta \le 2\theta_2 \tag{6.35}$$

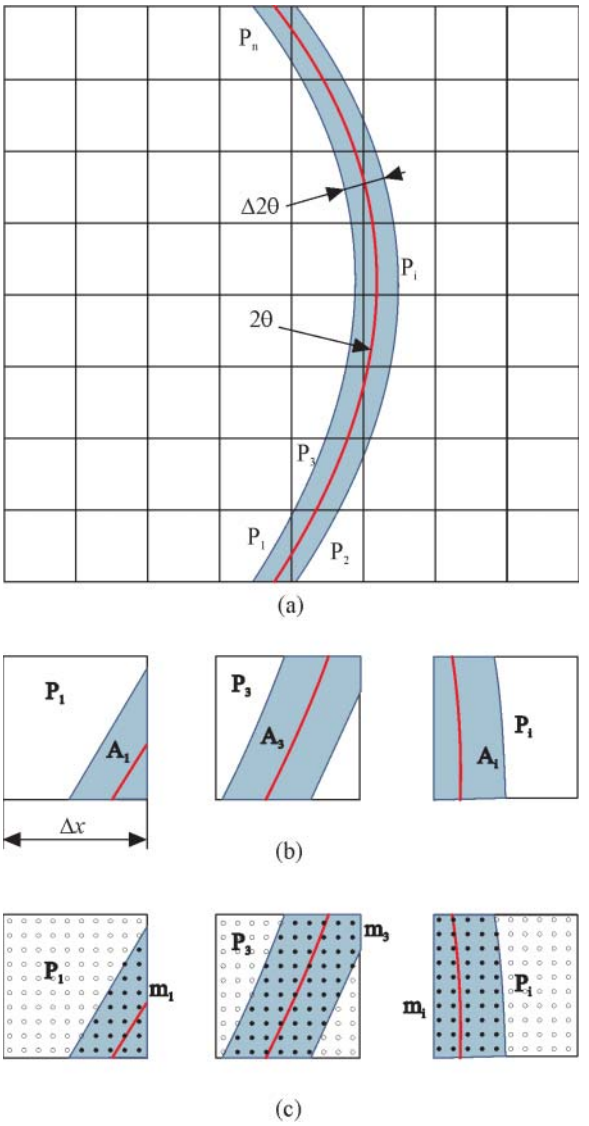


FIGURE 6.16 Illustration of integration by bin method: (a) conic line and $\Delta 2\theta$ define the region to be integrated, (b) each contribution pixel is divided into two or three bins, (c) each pixel is divided into subpixels.

where p_i is the count of the i-th pixel, Δx is the pixel size and n is the total number of contributing pixels integrated at the 2θ position. The intensity can be normalized by the solid angle:

$$I(2\theta) = \frac{\sum_{i=1}^{n} p_i \frac{A_i}{(\Delta x)^2} \Delta\Omega_i \frac{A_i}{(\Delta x)^2}}{\sum_{i=1}^{n} \Delta\Omega_i \frac{A_i}{(\Delta x)^2}} = \frac{1}{(\Delta x)^2} \frac{\sum_{i=1}^{n} p_i A_i^2 \Delta\Omega_i}{\sum_{i=1}^{n} \Delta\Omega_i A_i} \qquad 2\theta_1 \le 2\theta \le 2\theta_2 \tag{6.36}$$

where the solid angle $\Delta\Omega_i$ of each pixel is given by equation (6.2) and solid angle for the contributing (gray) area is calculated by multiplying the ratio of the gray area with the constant pixel area. Consider the $\cos^3\varphi$ falloff for the i-th pixel:

$$\Delta\Omega_i = \frac{(\Delta x)^2 D}{(D^2 + x_i{}^2 + y_i{}^2)^{3/2}} = \frac{(\Delta x)^2}{D^2}\cos^3\varphi_i \tag{6.37}$$

in which $\cos\varphi_i = \frac{D}{\sqrt{D^2+x_i{}^2+y_i{}^2}}$

The integration equation can also be rewritten as

$$I(2\theta) == \frac{1}{(\Delta x)^2}\frac{\sum_{i=1}^{n} p_i A_i^2 \cos^3\varphi_i}{\sum_{i=1}^{n} A_i \cos^3\varphi_i} \qquad 2\theta_1 \le 2\theta \le 2\theta_2 \tag{6.38}$$

In the above equations, square pixels are assumed. For a flat detector with rectangular pixel size of $\Delta x \times \Delta y$, replacing $(\Delta x)^2$ by $\Delta x \cdot \Delta y$. The above approach involves complicated algorithms to divide a pixel area into different $\Delta 2\theta$ regions. There are alternative computational approaches for achieving the same goal. One approach is to redistribute the counts of each pixel into a set of identical subpixels as shown in Figure 6.16(c). The subpixels are discrete points evenly distributed inside the pixel area marked by the blank circles or dark spots. The total number of subpixels within each pixel is M. The contributing subpixels are those that fall into the gray area (within the $\Delta 2\theta$ range) and labeled by the dark spots. The number of contributing subpixels in P_1, P_3, and P_i are m_1, m_3, and m_i respectively. The integration is then given by

$$I(2\theta) = \sum_{i=1}^{n} p_i \frac{m_i}{M} = \frac{1}{M}\sum_{i=1}^{n} p_i m_i \qquad 2\theta_1 \le 2\theta \le 2\theta_2 \tag{6.39}$$

Assuming the solid angles of subpixels within a pixel are identical, we can have the integration normalized by solid angle

$$I(2\theta) = \frac{\sum_{i=1}^{n} p_i \frac{m_i}{M}\Delta\Omega_i \frac{m_i}{M}}{\sum_{i=1}^{n} \Delta\Omega_i \frac{m_i}{M}} = \frac{1}{M}\frac{\sum_{i=1}^{n} p_i m_i^2 \Delta\Omega_i}{\sum_{i=1}^{n} m_i \Delta\Omega_i} \qquad 2\theta_1 \le 2\theta \le 2\theta_2 \tag{6.40}$$

or

$$I(2\theta) = \frac{1}{M}\frac{\sum_{i=1}^{n} p_i m_i^2 \cos^3\varphi_i}{\sum_{i=1}^{n} m_i \cos^3\varphi_i} \qquad 2\theta_1 \le 2\theta \le 2\theta_2 \tag{6.41}$$

The subpixel size should be at least smaller than the integration step $\Delta 2\theta$. The integration accuracy improves as the size of the subpixel decreases, while the computing time increases accordingly. The subpixel method is a better approach for computer programming since it counts a subpixel only based on its 2θ location.

All the normalization methods in the above integration, either by pixel, arc, or solid angle, result in an intensity level of one pixel. Since a pixel is much smaller than the active area of a typical point detector, the normalized integration leads to a diffraction pattern with fictitious low intensity counts, even though the true counts in the corresponding $\Delta 2\theta$ range are significantly higher. In order to avoid this misleading outcome, it is reasonable to introduce a scaling factor. For example, in GADDS™ (Bruker AXS) software, a factor of 10 is applied to all normalized integration results, but it is far from enough to reflect the true effect of the speed gain and statistic gain. A reasonable scaling factor can be chosen based on two considerations. One consideration is to find the number of pixels that have a total active area equivalent to the area of the receiving slit in a point detector system. For example, if the slit opening is 0.1×10 mm^2, and the pixel size of the 2D detector is 0.1×0.1 mm^2, then a reasonable scaling factor is 100.

Another consideration is to maintain total counting statistics. In this case the scaling factor should be the ratio of the average solid angle of the integration step to the solid angle of a pixel. Although this method can more closely reflect the true counts level at each $\Delta 2\theta$ range, the intensity level of the diffraction profile is dependent on the γ-integration range. That means the relative intensity will be higher at the low 2θ and high 2θ angles away from $2\theta = 90°$ as the $\Delta\gamma$-2θ relations described in the Chapter 4 of this book. Overall, there is no reasonable formula to make the integrated profile from a 2D frame to be comparable to a conventional point detector scan. The best practice is to be aware of the differences and to try not to make direct comparisons purely based on misleading intensity levels.

6.5.3 Algorithm of Frame Integration – Cylindrical Image

A cylindrical 2D diffraction image can be obtained by direct data collection with cylindrical detector, merged multiple frame and scanning of 1D or 2D detectors. The integration of a cylindrical 2D image follows the same principle as the integration of flat 2D images except a different conversion equations between pixels and 2θ and γ, and pixel solid angle coverage. The 2θ and γ values can be calculated by the following equations:

$$2\theta = \arccos \frac{D\cos\left(\frac{u}{D}\right)}{\sqrt{D^2 + v^2}} \quad (0 < 2\theta < \pi) \tag{6.42}$$

$$\gamma = \frac{u}{|u|} \arccos \frac{-\mathrm{v}}{\sqrt{\mathrm{v}^2 + D^2 \sin^2\left(\frac{u}{\mathrm{D}}\right)}} \quad (-\pi < \gamma \leq \pi) \tag{6.43}$$

where D is the radius of cylindrical images. The coordinates on the cylindrical 2D image (u,v) can be calculated from the 2θ and γ value:

$$\mathrm{v} = \frac{-\mathrm{D}\sin 2\theta \cdot cos\gamma}{\sqrt{1 - \sin^2 2\theta \cdot \cos^2\gamma}} \tag{6.44}$$

$$\mathrm{u} = \frac{\sin\gamma}{|\sin\gamma|}\mathrm{D} \cdot \arccos\left(\frac{\sqrt{\mathrm{D}^2 + v^2}}{D}\cos 2\theta\right) \tag{6.45}$$

The above two equation can used to generate the integration box over the cylindrical image or simulate a diffraction ring. The line curve representing a diffraction ring can be drawn on the cylindrical 2D image with variable γ at a given 2θ.

For the equations with normalization by the solid angle, $\Delta\Omega_i$ of the i-th pixel is given by

$$\Delta\Omega_i = \frac{\Delta u \cdot \Delta v \cdot D}{(D^2 + {v_i}^2)^{3/2}} = \frac{\Delta u \cdot \Delta v}{D^2}\cos^3\varphi_i \tag{6.46}$$

in which $\cos\varphi_i = \frac{D}{\sqrt{D^2+{v_i}^2}}$.

6.6 MULTIPLE FRAME MERGE

At a given sample-to-detector distance and swing angle, a diffraction frame collected by a flat 2D detector covers a limited 2θ and γ range, depending on the active area of the detector. In order to extend the 2θ coverage, multiple frames at various swing angles can be collected. The steps between each swing angle should be equal to or smaller than the 2θ range covered by a single 2D frame. Each of the 2D frames can be reduced to a one-dimensional diffraction profile by the γ-integration described in the previous section, and then all the profiles are merged into a single diffraction profile with the desired 2θ range. The preferable approach is to create a single 2D image by merging the multiple frames. The merged image can be displayed and evaluated more conveniently and accurately.

6.6.1 Merging Multiple Frames

The frames collected at various swing angles can be merged and displayed in one image. Figure 6.17(a) illustrates a 2D detector at three sequential swing angles. In order to get a continued coverage of the merged image, the swing angle step ($\Delta\alpha$) between two adjacent detector positions should be equal to or smaller than the angular coverage ($\Delta 2\theta$) of a single detector. When $\Delta\alpha = \Delta 2\theta$, the two adjacent detection planes meet at the edge of the detection region. In practice, to avoid the low image quality near the edge of some detectors and to get enough integration region for each frame, some overlapping between adjacent detector positions is used ($\Delta\alpha < \Delta 2\theta$). In this case, the adjacent detection planes intersect with an angle equal to the swing angle step ($\Delta\alpha$). The data collected in the region outside the intersection line is redundant. The swing angle step ($\Delta\alpha$) does not have to be equal at all adjacent detector positions, but is normally set as equal unless forbidden by the instrument or experimental condition. Figure 6.17(b) shows the merged image from the three frames collected at the above detector swing angles. The diffraction frames are collected with a Bruker Photon II™ detector from 1 μm Al_2O_3 powder in 1 mm glass capillary at a nominal sample-to-detector distance of 9 cm. The actual sample-to-detector distance should be approximately 100.6 mm based on the active area of the detector 103.9 mm × 138.5 mm. The measured angular coverage of a single frame is about 54.6°, and the three frames are collected at swing angle $\alpha = 0$, 40°, and 80° ($\Delta\alpha = 40°$) respectively. In the merged image, only the region within the two intersection lines is displayed; the redundant regions outside the intersection lines are not used. As discussed in the Section 2.3.2, the conic section takes a different shape for a different swing angle. The diffraction rings collected with the first frame at $\alpha = 0$ are circles, and the diffraction rings collected by the frames 2 and 3 may be ellipse, parabola or hyperbola depending on the value of 2θ and α angles. A discontinuity (kink) can be observed for the diffraction rings across two diffraction frames, especially between the frames 1 and 2 when the diffraction rings have strong curvature. The merged image by the above method is mainly for display purpose. Further data integration can be done on each individual frame and then merged to produce a continuous diffraction profile. The swing angles corresponding to each of the original frames should be used for generating an integration region and 2θ and γ conversion from the pixels or subpixels.

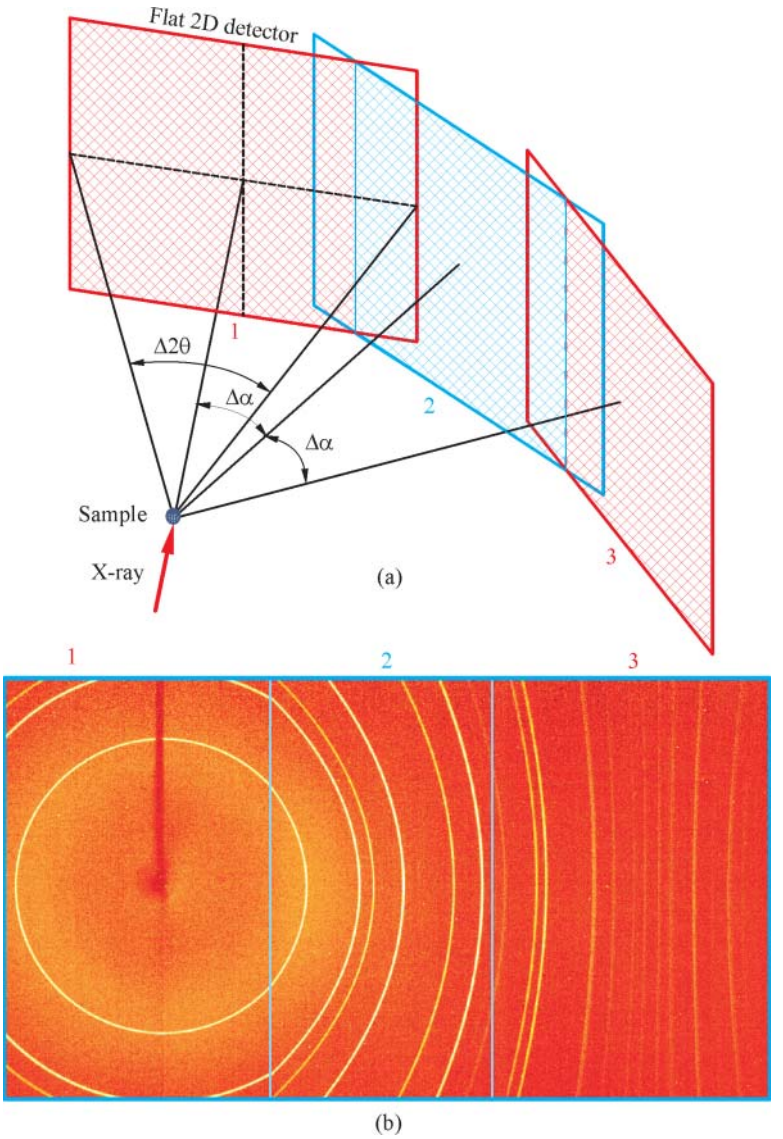


FIGURE 6.17 Merging of multiple frames collected with a flat 2D detector: (a) illustration of three detector swing angles, (b) merged 2D pattern from three flat frames.

6.6.2 Cylinder Projection of Flat 2D Frames

In order to accurately merge all frames collected at each detector position into a single 2D image, it is best to project all the frames to a cylindrical surface based on the scattering angle from the incident beam. As shown in Figure 6.18, the position of a flat 2D detector is determined by the detector distance D and the detector swing angle α. The cross point o is the detector center or origin of the pixel position (x,y). In the figure, three detector positions are displayed as detector, 1, 2, and 3 respectively. The detector at position 1 is set at swing angle $\alpha_1 = 0$, so the detector center is on the laboratory coordinate axis $\mathbf{X_L}$. The detector at positions 2 and 3 are set with a swing angle step $\Delta\alpha$, so the swing angles are $\alpha_2 = \Delta\alpha$ and $\alpha_3 = 2\Delta\alpha$ respectively. The y axis

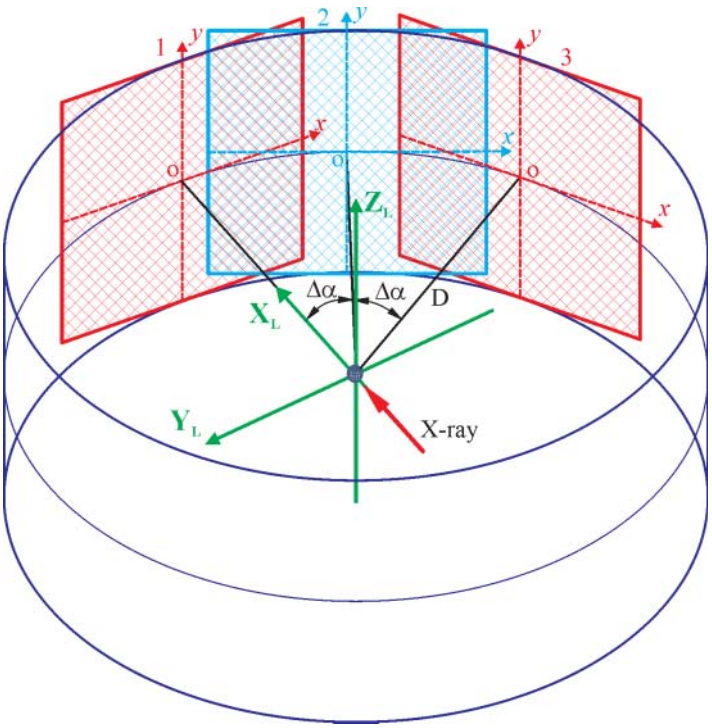


FIGURE 6.18 Projection of multiple frames collected with a flat 2D detector onto a cylindrical surface.

of the detector is always on the cylindrical surface at different swing angles. The radius of the cylinder is the same as the detector distance D. To merge the frames collected at all swing angles, the pixels in the flat detector are projected to the cylindrical surface through a straight line from the instrument center (sample) to the corresponding pixels. The direction of the straight line can be determined from the scattering angle given by the 2θ and γ or a different set of angles.

The projected image gives the correct scattering angles for all projected pixels and all the projected images collected at sequential detector positions fall to the same cylindrical surface. Therefore, the merged 2D image by the cylindrical projection can accurately show the diffraction rings without any distortion or discontinuity, as if the diffraction pattern had been collected by a cylinder-shaped detector. Once the multiple frames are merged into a cylindrical surface, the diffraction pattern can be displayed in a flattened 2D image and evaluated without discontinuity in conversion of the pixel position to the scattering angles 2θ and γ.

The projection of the flat 2D detector onto the cylindrical surface introduces distortion of the detection area and pixel. Figure 6.19(a) illustrates the geometry of projection of a single frame onto a cylindrical surface. If the image collected by the flat 2D detector is rectangular (or square) in shape, the cylindrical surface has the same height as the flat detector and the projected image onto the cylindrical surface will have the same height as the flat image in the center line (y axis), but it will gradually shrink in height away from the center line. The horizontal dimension of the flat detector is L and the arc length of the cylindrical surface covering the same 2θ range is C. The relation between the two lengths is given by

$$C = D \cdot \Delta 2\theta = 2D \arctan \frac{L}{2D} \tag{6.47}$$

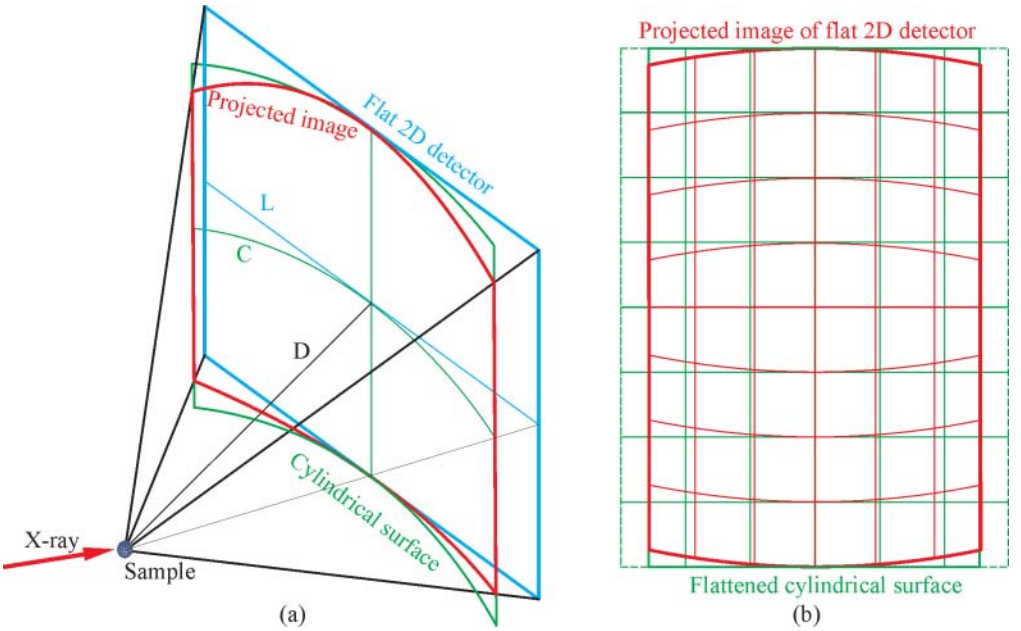


FIGURE 6.19 Projection of single frame collected with a flat 2D detector onto a cylindrical surface: (a) projection geometry, (b) flattened image of the projection.

Since C is always smaller than L, the projected image is also shrunk in the horizontal direction. Figure 6.19(b) illustrates the flattened surface and the projected image. Assuming that the pixel shape and size in the flattened cylindrical image are the same as in the flat 2D detector, the projected pixel shape and size are also changed correspondingly as illustrated by the grid box. If the pixels in the flat 2D detector are square (or rectangular) in shape, the projected pixels are no long square (or rectangular), and the shape and size vary depending on the position of the original pixel in the flat detector. The projected image gives the correct scattering angles for all projected pixels if treated as a cylindrical image.

Figure 6.20 illustrates the geometry and algorithms to project a flat 2D image into the cylindrical surface in the laboratory coordinates. The cross point between the $\mathbf{X_L}$ axis and the cylindrical surface is the origin of the cylindrical surface. The image on the cylindrical surface can be displayed as a flattened image with axes u and v in rectangular coordinates. The direction of an arbitrary scattered beam **S** can be defined by the angles β and ρ. β is the angle between **S** and $\mathbf{X_L}$ projected on the diffractometer plane $\mathbf{X_L}$-$\mathbf{Y_L}$, and ρ is the angle between **S** and diffractometer plane. For the flat 2D detector, the scattering angle of a point P(x,y) can be given as

$$\rho = \arctan \frac{y}{\sqrt{x^2 + D^2}} \tag{6.48}$$

and

$$\beta = \alpha - arctan\frac{x}{D} \tag{6.49}$$

For the cylindrical image, the scattering angle of a point P′(u,v) is given as

$$\rho' = arctan\frac{v}{D} \tag{6.50}$$

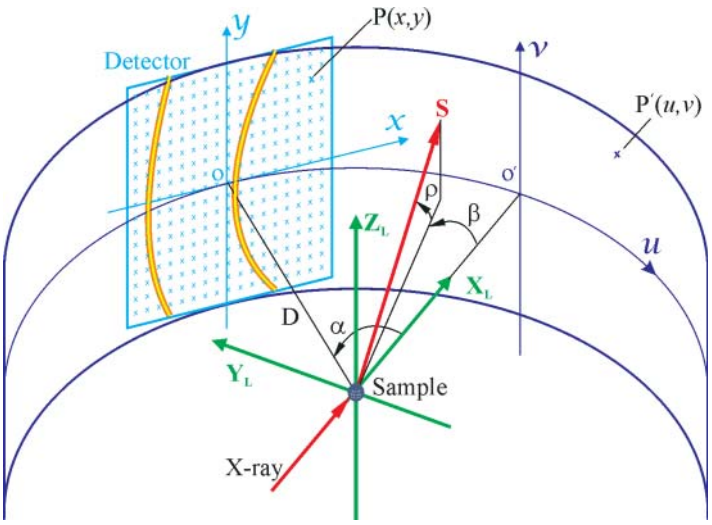


FIGURE 6.20 Geometry and algorithms to project flat 2D image onto the cylindrical surface.

and

$$\beta' = -\frac{u}{D} \tag{6.51}$$

Any point on the flat 2D detector should be projected to the point on the cylindrical surface with the same scattering angle, i.e. $\rho = \rho'$ and $\beta = \beta'$. Therefore, we can derive from the above four equations the following projection equation:

$$\boxed{u = D(arctan\frac{x}{D} - \alpha)} \tag{6.52}$$

$$\boxed{v = \frac{Dy}{\sqrt{x^2 + D^2}}} \tag{6.53}$$

When $x = 0$, $u = -D\alpha$ and $v = y$, equation (6.52) gives the center position of the flat image relative to the cylindrical image, and equation (6.53) indicates that the pixels on the y axis projected to the cylindrical image with the same vertical position above the diffractometer plane.

The above equations can be used for the pixel-to-pixel projection from the flat 2D detector into the image flattened from the cylindrical surface (cylindrical image). As shown in Figure 6.21, the pixels in the flat 2D detector projected onto the cylindrical image are defined by the box of red lines. The pixels in the flattened cylindrical image are defined by the box of green lines with the pixel size of $\Delta \boldsymbol{u} \times \Delta \boldsymbol{v}$. Due to the projection geometry as described previously, each pixel from the flat 2D detector may contribute to several pixels in the cylindrical image. For example, the pixel P(x,y) in the flat 2D detector contributes to four pixels in the cylindrical image.

The direct one pixel to one pixel projection will be too coarse to get an accurate projection. There are many methods to accurately project the pixels. For instance, the overlapping areas of the pixel $\mathbf{P}_{(x,y)}$ with pixel 1, 2, 3, and 4 are calculated based on equations (6.52) and (6.53). The intensity counts collected by the pixel P(x,y) can then be assigned to the pixels 1, 2, 3, and 4 proportional to the area respectively.

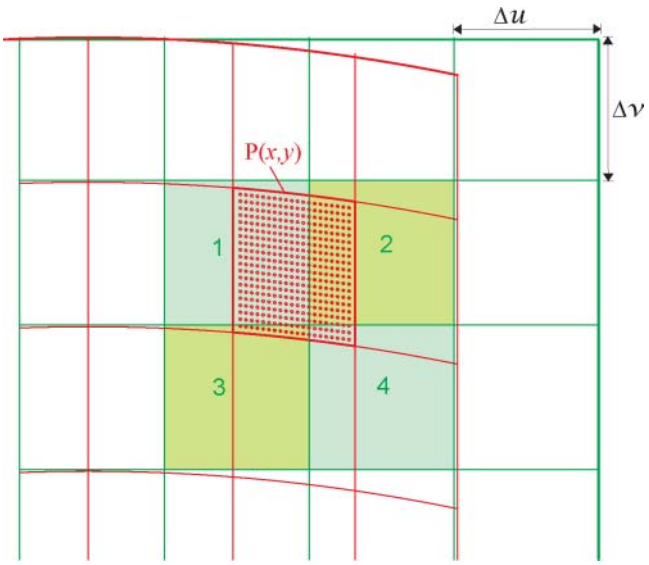


FIGURE 6.21 Pixel-to-pixel projection from the flat 2D image onto the flattened cylindrical image.

Calculating the contributing area for each pixel is not a programmer-friendly approach. The area of the curved pixel boundary is difficult to calculate. An alternative approach is to redistribute the counts of each pixel in the flat 2D image into a set of identical subpixels as shown in Figure 6.21. The subpixels are discrete points evenly distributed inside the pixel area marked by circular dots. If the total number of subpixels within each pixel is M, the scattering intensity counts of each subpixel is the pixel counts divided by M. The subpixels that fall into pixel 1 (dots in the upper-left region) are assigned to the pixel 1. The subpixels that fall into pixel 2 (dots in the upper-right region) are assigned to pixel 2. The same is for the pixels 3 and 4. Each subpixel in the flat 2D image can be assigned to the cylindrical image pixels by equations (6.52) and (6.53). The desired projection accuracy can be achieved by selecting a sufficient number of subpixels.

6.6.3 Merging of the Overlapping Region

The overlapping region of the frames collected by two adjacent detector swing angles can be simply ignored in the merged 2D image. However, a sharp seam line may be observed along the intersection of the two detection planes due to the inhomogeneity of scattering background or the sensitivity of a particular detector. The data within the overlapping region can be treated to produce a smooth transition between adjacent frames. Figure 6.22(a) illustrates the flattened cylindrical image merged from two frames collected by a round detector. Figure 6.22(b) is the top view of the merge geometry. The projected images from the round frames are no longer circular in shape. The radius of the active area is R. The vertical line passing the center of frame is the y axis of the flat detector. Since the y axis is also on the cylindrical surface, the vertical dimension of the projected image along y axis is the same (R). The horizontal line crossing both frames are the projection of the x axis in the original flat image, and also indicates the intersection of the detection plane with diffractometer plane. The horizontal dimension of the overlapping region varies with the pixel coordinates v:

$$l(v) = D\left(2\arctan\frac{\sqrt{R^2 - v^2}}{\sqrt{D^2 + v^2}} - \Delta\alpha\right) \tag{6.54}$$

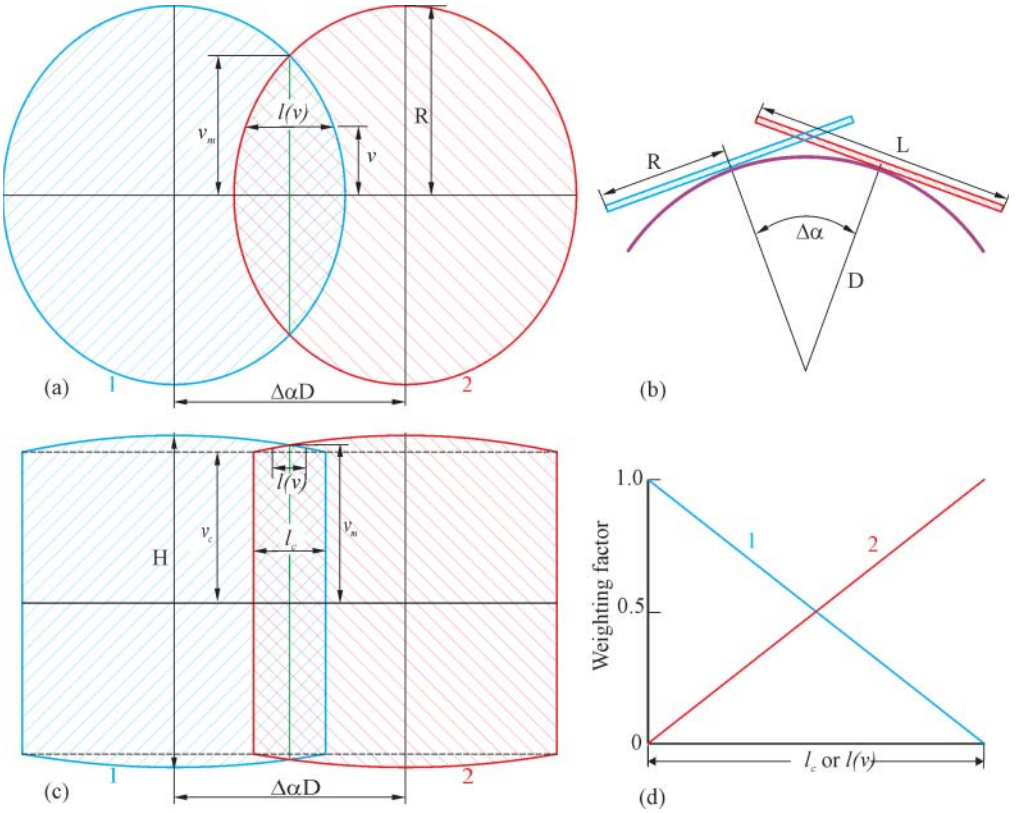


FIGURE 6.22 Merging of overlapping region: (a) detector with round active area, (b) detector with rectangular active area, (c) top view of two detection planes, (d) weighting factor to combine overlapping pixels.

The maximum overlapping at $v = 0$ is

$$l(v) = D\left(2\arctan\frac{R}{D} - \Delta\alpha\right) \tag{6.55}$$

The maximum v value in the overlapping region of two round frames is

$$v_m = \sqrt{R^2\cos^2\frac{\Delta\alpha}{2} - D^2\sin^2\frac{\Delta\alpha}{2}} \tag{6.56}$$

Figure 6.22(c) illustrates the flattened cylindrical image merged from two frames collected by a 2D detector with rectangular active area. The top view of the merge geometry can also be illustrated by Figure 6.22(b). The projected images from the rectangular frames are no longer rectangular in shape. The active area of the detector is H in height and L in width. Since the y axis is on the cylindrical surface, the vertical dimension of the projected image along y axis is the same as the original frame (=0.5H). The broken lines mark the height of the image projected from the edge of the detector:

$$v_c = \frac{DH}{\sqrt{L^2 + 4D^2}} \tag{6.57}$$

The horizontal dimension of the overlapping region is constant from $v = 0$ to v_c:

$$l = D\left(2\arctan\frac{L}{2D} - \Delta\alpha\right) \quad (0 \le v < v_c) \tag{6.58}$$

The maximum v value in the overlapping region of two rectangular frames is

$$v_m = H\cos\frac{\Delta\alpha}{2} \tag{6.59}$$

The overlapping region between v_c and v_m is a small arch shaped region. In most cases, the data evaluation can be done only within the rectangular region defined by v_c so that the overlapping region for $v > v_c$ can be ignored. If the data in this region is also merged, the horizontal dimension of the overlapping region is a function of v:

$$l(v) = D\left(2\arccos\frac{2v}{H} - \Delta\alpha\right) \quad (v_c < v \le v_m) \tag{6.60}$$

In order to produce a smoothly merged frame, the pixel counts of both frames are combined with a weighting factor, as described in Figure 6.22(d). Taking the case illustrated in the figure, both the flat frames are first projected onto the cylindrical surface to produce the frames at left (frame 1) and right (frame 2). At any v value, the pixel of the merged image at the left end takes 100% of the pixel counts from frame 1 and 0% from frame 2. At the center of the overlapping region, the merged pixel takes 50% of the pixel counts from both frames. At the right end, the merged pixel takes 100% of the counts from frame 2 and 0% from frame 1. By the gradual transition from frame to frame, a smoothly merged final 2D image can be created. Figure 6.23 shows a flattened image of the merged cylindrical frame from the same set of frames used in Figure 6.17(b). Based on the measured angular coverage of 54.6° for the single frame, the overlapping range covers about 14.6°. Due to the smooth transition from one frame to the next, no discontinuity within the overlapping regions is observed. The final merged diffraction pattern can be used for further data evaluation as if the data had been collected by a cylindrical detector.

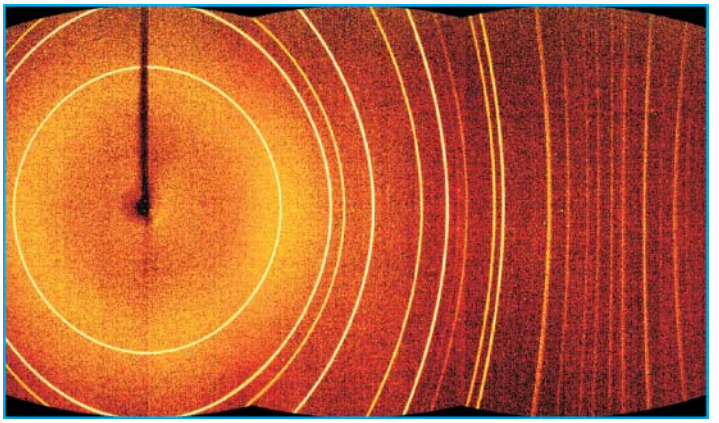


FIGURE 6.23 Merged cylindrical image from three frames collected with a Bruker Photon II™ detector from 1 μm Al_2O_3 powder.

6.7 SCANNING 2D PATTERN

Multiple frame merge is one way to extend the angular range of a 2D detector. Another method is to scan the 2D detector over a large 2θ range. As shown in Figure 6.24, a rectangular 2D detector scans over the swing angle continuously or in small steps during the data collection. The y axis of the detector forms a cylindrical surface during the data collection scan. The radius of the cylinder is the sample-to-detector distance (D). The edge of the detector forms another cylindrical surface with a radius of E. The trace of all the pixels of the scanning 2D detector falls into the space between two cylindrical surfaces. Due to the variable pixel-to-sample distance and the variable solid angle covered by a different pixel at a different detector position, if the frames collected at sequential detector positions are simply superposed from the original rectangular frames, the smearing effect will be produced on the diffraction ring as illustrated in Figure 6.25.

In order to accurately add all frames collected at each detector position to a single 2D image, it is best to project all the frames onto the cylindrical surface based on the scattering angle from the incident beam [20]. The same algorithms for the multiple frame merge onto a cylindrical image in the previous section can be used to produce the scanned 2D image. The projected image gives the correct scattering angles for all projected pixels, and all the projected images collected at sequential detector positions fall onto the same cylindrical surface. Therefore, the scanned image by superposition of the cylindrical projections can accurately show the diffraction rings without smearing effect, as illustrated in Figure 6.26. On the top and bottom of the final scanned image, there are regions with reduced total exposure time due to the arch shape of the projected image. The pixel counts in this region can be either normalized or ignored. The final scanned diffraction

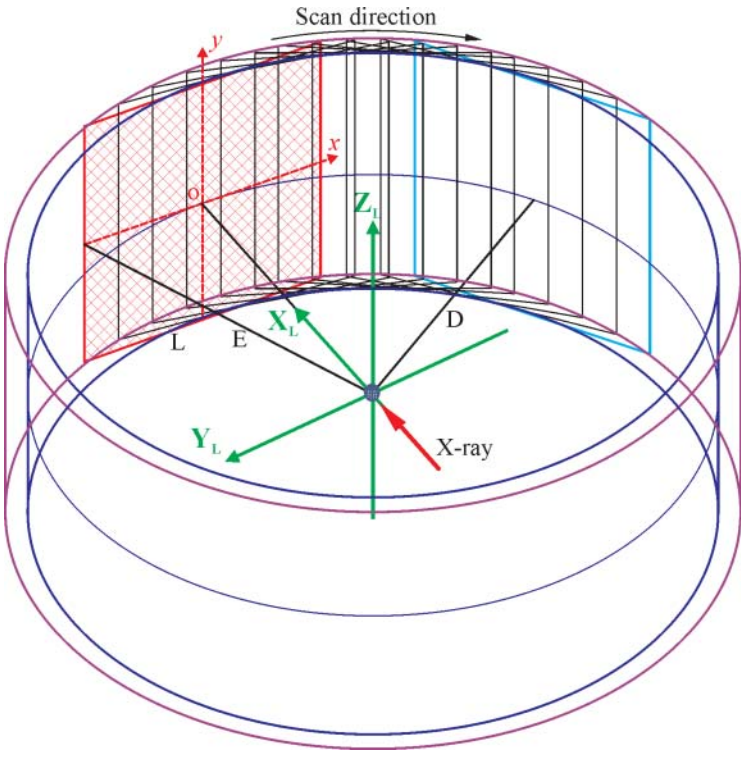


FIGURE 6.24 The 2D detector scans along the detection circle while collecting diffraction signals.

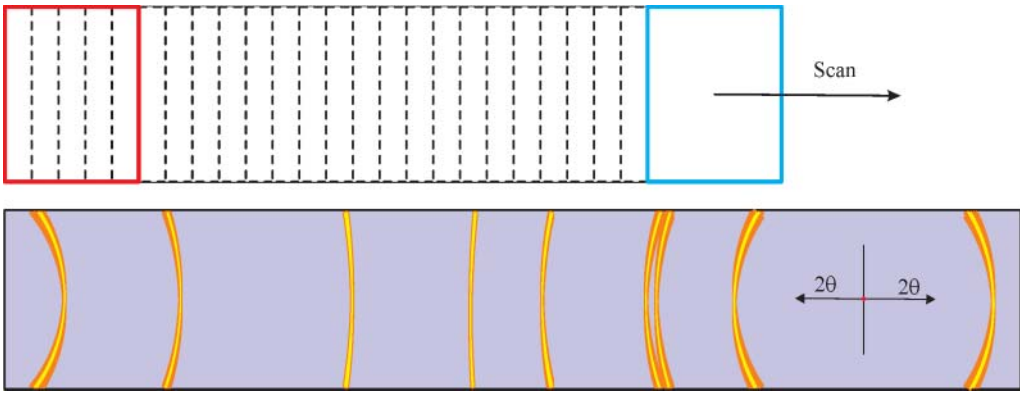


FIGURE 6.25 Smearing effect when the sequential 2D frames are simply superposed from the original rectangular frames.

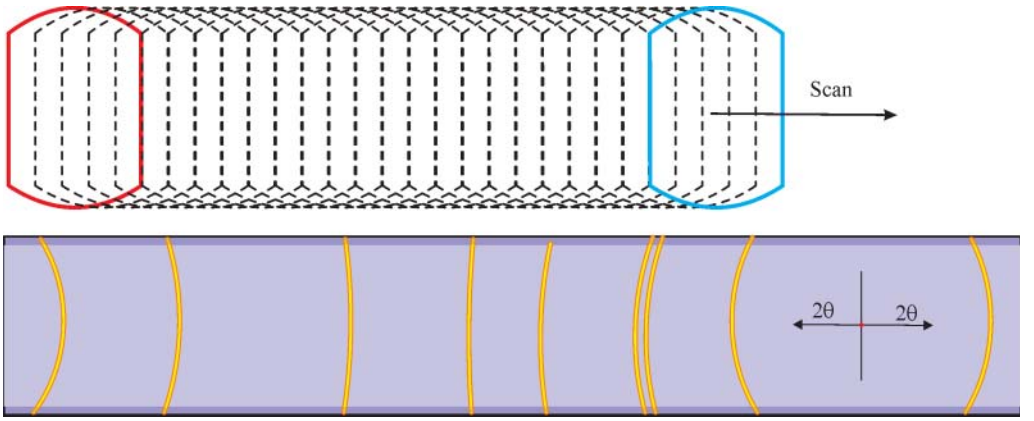


FIGURE 6.26 Accurate diffraction rings without smearing effect when the cylindrical projections from sequential 2D frames are combined.

pattern can be used for further data evaluation as if the data had been collected by a cylindrical detector.

Figure 6.27 illustrates the total exposure time of the scanned image and each of the sequential positions including the start and end position. As seen from the figure, there is a ramping up region at the left side and a ramping down region at the right side, in terms of the exposure time. In order to collect a 2D diffraction pattern with consistent counting statistics, it is necessary to collect the diffraction pattern with homogenous exposure time over the desired 2θ range. The common practice is to start the scanning with an under travel equivalent to the angular coverage of the 2D detector ($\Delta 2\theta$), and finish the scanning with an over travel of the same range. Because the swing angle (α) of the 2D detector is based on the center of the detector, the actual start swing angle (α_1) should have an offset of $\Delta 2\theta/2$ below the starting 2θ position and the final swing angle (α_2) with the same offset above the final 2θ position. If the instrument condition or experiment do not allow the under and/or over travel of the detector, the final image should be normalized against the exposure time or some other strategy to produce a 2D pattern with homogeneous exposure time [21].

Figure 6.28 shows a 2D image collected by scanning an Eiger2 detector in γ-optimized mode covering all diffraction rings within the 2θ range of 20° to 80° at a detector distance of 150 mm.

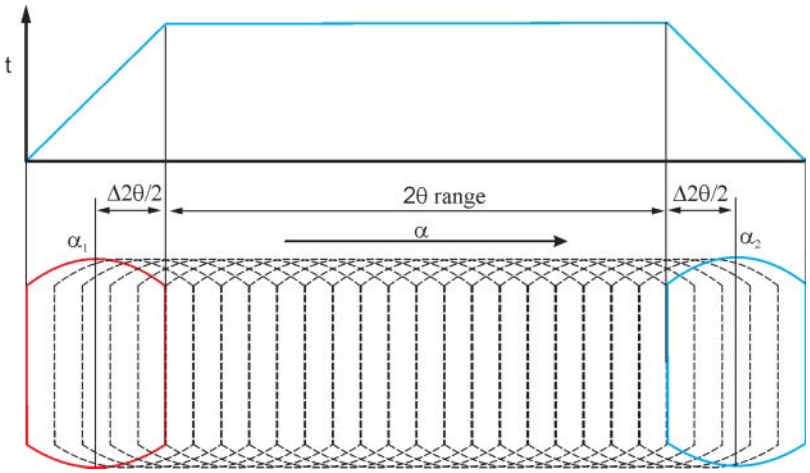


FIGURE 6.27 Exposure time of scanned 2D image and ramping up and ramping down regions.

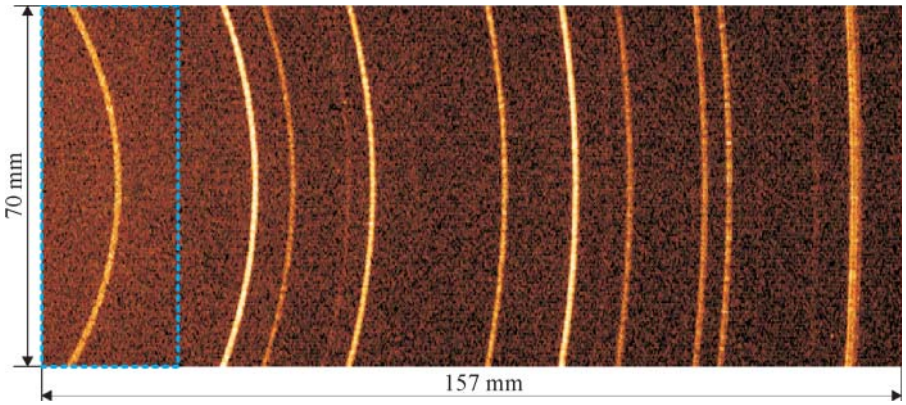


FIGURE 6.28 The 2D diffraction pattern collected from corundum by scanning an Eiger2 detector in γ-optimized mode within 2θ range of 20° to 80°.

The region to the left within a box of blue dotted lines corresponds to the coverage of a single frame. The 2D diffraction pattern is obtained by integration from consecutive flat 2D frames with scanning step of 0.02°. Due to the accurate projection in subpixel level, there is no smearing effect. The vertical dimension of the active area is 77.25 mm. The area with reduced exposure time near the top and bottom region is removed from the final 2D image. The regions covered by the under and over travel are also removed. The final 2D image is as accurate as if it had been collected with a cylindrical detector of 70 mm × 157 mm (arc length) with a radius of 150 mm.

The purpose of scanning the 2D detector is to extend 2θ range. The data collection scan can be achieved by either coupled scan (θ_1-θ_2 simultaneously) or detector scan (keep incident fixed while scanning detector swing angle α). The coupled scan changes the sample orientation with respect to the incident beam. As a consequence, the sample orientation information related diffraction pattern is lost or smeared out. The coupled scan can improve sampling statistics, equivalent to the sample rotation oscillation of $\Delta\omega = 2\arctan(L/2D)$. For stress or texture measurement, it is normally not necessary to extend the 2θ range by 2D scanning. But if 2D scanning is necessary, it should be a detector scan with fixed incident angle so as to maintain the sample orientation information.

6.8 LORENTZ, POLARIZATION, AND ABSORPTION CORRECTIONS

Lorentz, polarization, air scatter, Be-window, and sample absorption corrections may be applied to the diffraction frame to remove their effect on the relative intensities of Bragg peaks and background. The 2θ angular dependence of the relative intensity is commonly given as a Lorentz-polarization factor, which is a combination of Lorentz and polarization factors. In two-dimensional diffraction, the polarization factor is a function of both 2θ and γ, therefore it should be treated in the 2D frames, while the Lorentz factor is a function of 2θ only. The Lorentz correction can be done either on the 2D frames or on the integrated profile. In order to obtain relative intensities equivalent to a conventional diffractometer with a point detector, reverse Lorentz and polarization corrections may be applied to the frame or integrated profile.

6.8.1 Lorentz

The Lorentz factor is the same as with a conventional diffractometer. For a completely random sample, the Lorentz factor is given as [22]

$$L = \frac{\cos\theta}{\sin^2 2\theta} = \frac{1}{4\sin^2\theta\cos\theta} \tag{6.61}$$

The Lorentz factor may be given by a different equation for a different diffraction geometry [23–25]. The correction to the intensity of a pixel with a Lorentz factor is given as

$$p_c(x,y) = \frac{p_o(x,y)}{L} = 4\sin^2\theta\cos\theta \cdot p_o(x,y) \tag{6.62}$$

where $p_o(x,y)$ is the original pixel intensity of the pixel P(x,y) and $p_c(x,y)$ is the corrected intensity. The θ angle for each pixel is given by equation (6.27). The forward and reverse Lorentz corrections are exactly reciprocal and effectively cancel each other. Therefore, it is not necessary to perform the Lorentz correction to the frame before integration if relative intensities equivalent to a conventional Bragg–Brentano diffractometer is expected. The Lorentz correction can be done on the integrated diffraction profiles in the same way as on the diffraction profiles collected with conventional diffractometers.

6.8.2 Polarization

When a non-polarized X-ray beam is scattered by matter, the scattered X-rays are polarized. The intensity of the diffracted beam is affected by the polarization, called the polarization factor. The polarization factor for a single bounce scattering of a non-polarized X-ray beam is given as

$$P = \frac{1+\cos^2 2\theta}{2} \tag{6.63}$$

where 2θ is the scattering angle. For the polarization factor of a diffraction peak from a crystal, 2θ is the Bragg angle. If a diffracted beam crystal monochromator is used, the overall polarization factor for the measured intensity is a superposition of the monochromator scattering and the sample scattering. The overall polarization factor is dependent on the orientation relationship between the monochromator reflection and the sample reflection. The primary beam to the monochromator, the diffracted beam from the monochromator, and the normal of the monochromator crystal plane (the diffraction vector of the monochromator) form a plane, referred to as the

incident plane. The incident beam to the sample, the diffracted beam from the sample, and the normal of the diffraction crystal plane in the sample (the diffraction vector of the sample) form a plane, referred to as the diffraction plane. If the incident plane and the diffraction plane are the same plane, the overall polarization factor is given as

$$P = \frac{1 + \cos^2 2\theta_M \cos^2 2\theta}{2} \tag{6.64}$$

where $2\theta_M$ is the Bragg angle of the monochromator crystal and 2θ is the Bragg angle of the peak. With an incident beam monochromator, the incident beam to the sample is the diffracted beam from the monochromator. The polarization factor is conveniently expressed in terms of the intensity that is incident to the sample. Therefore, the polarization factor for the conventional diffractometer with an incident beam monochromator and the incident plane coincident to the diffractometer plane, P_I, is given as

$$P_I = \frac{1 + \cos^2 2\theta_M \cos^2 2\theta}{1 + \cos^2 2\theta_M} \tag{6.65}$$

Correspondingly, the polarization factor for the conventional diffractometer with an incident beam monochromator and the incident plane perpendicular to the diffractometer plane, P_{II}, is given as

$$P_{II} = \frac{\cos^2 2\theta_M + \cos^2 2\theta}{1 + \cos^2 2\theta_M} \tag{6.66}$$

In two-dimensional X-ray diffraction the diffraction vectors of the monochromator diffraction and sample crystal diffraction are not necessarily in the same plane or perpendicular planes. Therefore, the overall polarization factor is a function of both 2θ and γ. Figure 6.29 illustrates the geometric relationship between the monochromator and the detector in the laboratory coordinates, $\mathbf{X_L Y_L Z_L}$. The monochromator is located at the coordinates $\mathbf{X_L Y'_L Z'_L}$, which is a translation of the laboratory coordinates along the $\mathbf{X_L}$ axis in the negative direction. The monochromator crystal is rotated about the $\mathbf{Z'_L}$ axis for an angle of θ_M. The X-rays from the source reach the monochromator with an angle of $2\theta_M$ from the negative $\mathbf{X_L}$ direction. The diffracted beam from the monochromator propagates along the $\mathbf{X_L}$ direction. This is the incident beam to the sample located at the instrument center O. The incident plane, containing the monochromator diffraction vector $\mathbf{H_M}$, is coincident with the diffractometer plane $\mathbf{X_L - Y_L}$. The area detector location is given by the sample-to-detector distance D and swing angle α. The pixel P(x,y) represents an arbitrary pixel on the detector. The 2θ and γ are the corresponding diffraction space parameters for the pixel. The diffraction vector $\mathbf{H_P}$ represents the scattered X-rays collected by the pixel P(x,y). The angle ρ is the angle between the diffraction plane containing the diffraction vector $\mathbf{H_P}$ and the incident plane containing the monochromator diffraction vector. In this particular case, the angle ρ is also the angle between the diffraction plane and the diffractometer plane $\mathbf{X_L}$-$\mathbf{Y_L}$. Since a monochromator or other beam conditioning optics can only be used on the incident beam for two-dimensional diffraction system, the general polarization factor is given as [26, 27]

$$P_G = \frac{(\cos^2 2\theta \cos^2 \rho + \sin^2 \rho)\cos^2 2\theta_M + \cos^2 2\theta \sin^2 \rho + \cos^2 \rho}{1 + \cos^2 2\theta_M} \tag{6.67}$$

where 2θ angle for each pixel is given by equation (6.27), and $\cos^2\rho$ and $\sin^2\rho$ can be calculated from 2θ and γ. The γ angle for each pixel is given by equation (6.28).

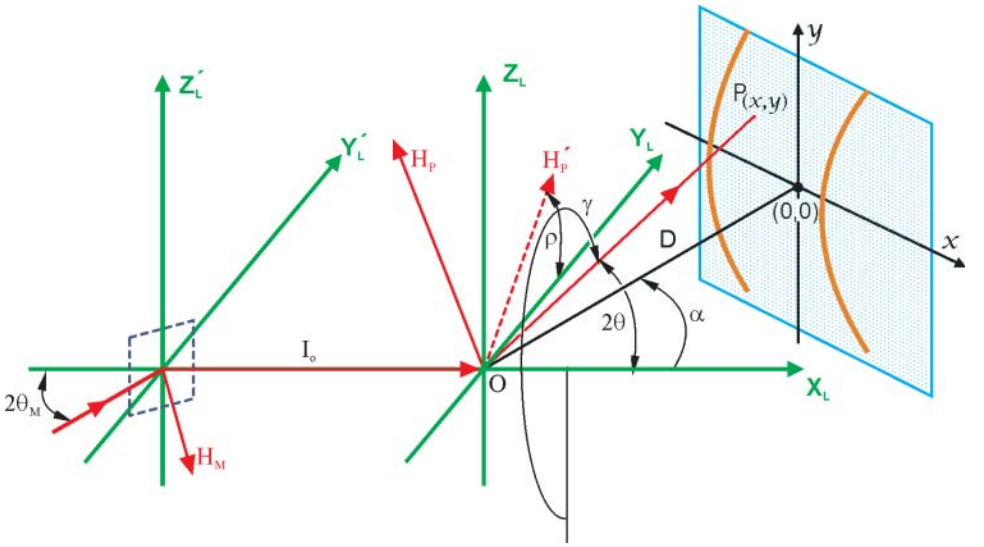


FIGURE 6.29 Illustration of geometric relationship between the monochromator and the detector in the laboratory coordinates, $\mathbf{X_L Y_L Z_L}$.

The unit vector of the diffraction vector $\mathbf{H_P}$ in the laboratory system is given in Chapter 2 as

$$\mathbf{h}_{\mathrm{L}} = \begin{bmatrix} h_x \\ h_y \\ h_z \end{bmatrix} = \begin{bmatrix} -\sin\theta \\ -\cos\theta\sin\gamma \\ -\cos\theta\cos\gamma \end{bmatrix} \tag{6.68}$$

The projection of the diffraction vector $\mathbf{H_P}$ onto the $\mathbf{Y_L}$–$\mathbf{Z_L}$ plane is the vector $\mathbf{H'_P}$. The unit vector of the vector $\mathbf{H'_P}$ is given as

$$\mathbf{h}'_{\mathrm{L}} = \begin{bmatrix} 0 \\ h'_y \\ h'_z \end{bmatrix} = \begin{bmatrix} 0 \\ -\sin\gamma \\ -\cos\gamma \end{bmatrix} \tag{6.69}$$

The unit vector of $\mathbf{Y_L}$ is given as $\mathbf{y_L} = [0,1,0,]$. Then we have

$$\cos\rho = \cos(\mathbf{h}'_L, y_{\mathrm{L}}) = \mathbf{h}_L \bullet y_{\mathrm{L}} = -\sin\gamma \tag{6.70}$$

Therefore

$$\cos^2\rho = \sin^2\gamma \tag{6.71}$$

and

$$\sin^2\rho = \cos^2\gamma \tag{6.72}$$

Introducing equations (6.71) and (6.72) into equation (6.67), the polarization factor for two-dimensional X-ray diffraction can then be given as a function of both θ and γ

$$P(\theta,\gamma) = \frac{(1+\cos^2 2\theta_M \cos^2 2\theta)\sin^2\gamma + (\cos^2 2\theta_M + \cos^2 2\theta)\cos^2\gamma}{1+\cos^2 2\theta_M} \tag{6.73}$$

Comparing with equations (6.65) and (6.66), we have

$$P(\theta,\gamma) = P_I \sin^2\gamma + P_{II}\cos^2\gamma \tag{6.74}$$

For the pixels that fall on the diffractometer plane, γ takes values of 90° or 270°, i.e. $\cos\gamma = 0$, and equation (6.73) reduces to equation (6.65). Therefore, we can conclude that the polarization equation for conventional diffraction is a special case of the more general polarization equation for two-dimensional X-ray diffraction. The correction to the intensity of a pixel with the polarization factor is calculated as

$$p_c(x,y) = \frac{p_o(x,y)}{P(\theta,\gamma)} = \frac{(1+\cos^2 2\theta_M)p_o(x,y)}{(1+\cos^2 2\theta_M\cos^2 2\theta)\sin^2\gamma + (\cos^2 2\theta_M + \cos^2 2\theta)\cos^2\gamma} \tag{6.75}$$

where $p_o(x,y)$ is the original pixel intensity of the pixel P(x,y) and $p_c(x,y)$ is the corrected intensity, and $2\theta_M$ is a constant for a specific monochromator crystal and radiation wavelength – for instance, $2\theta_M = 26.53°$ for Cu-K_α radiation with a graphite monochromator. The θ and γ angles for each pixel can be calculated from equations (6.27) and (6.28) respectively. The reverse polarization correction may be applied to the frame so that the relative intensities in the integrated profile are equivalent to the profile collected with a conventional diffractometer. Equation (6.65) can be used to perform the reverse polarization correction:

$$p_{rc}(x,y) = P_I \cdot p_c(x,y) = \frac{1+\cos^2 2\theta\cos^2 2\theta_M}{1+\cos^2 2\theta_M} p_c(x,y) \tag{6.76}$$

where $p_{rc}(x,y)$ is the pixel intensity after reverse correction and $p_c(x,y)$ is the pixel intensity after forward correction. The forward and reverse corrections can be combined into the following equation:

$$p_{rc}(x,y) = \frac{P_I \cdot p_o(x,y)}{P(\theta,\gamma)} = \frac{(1+\cos^2 2\theta\cos^2 2\theta_M)p_o(x,y)}{(1+\cos^2 2\theta_M\cos^2 2\theta)\sin^2\gamma + (\cos^2 2\theta_M + \cos^2 2\theta)\cos^2\gamma} \tag{6.77}$$

Since the forward and reverse Lorentz corrections cancel each other, this equation can be considered to be a combined equation for forward and reverse corrections for the Lorentz-polarization factor. All the above equations are based on the geometry that the monochromator diffraction vector falls in the diffractometer plane. If the crystal monochromator rotates about the $\mathbf{Y'_L}$ axis, i.e. the incident plane is perpendicular to the diffractometer plane, the polarization factor for two-dimensional X-ray diffraction can then be given as

$$P(\theta,\gamma) = \frac{(1+\cos^2 2\theta_M\cos^2 2\theta)\cos^2\gamma + (\cos^2 2\theta_M + \cos^2 2\theta)\sin^2\gamma}{1+\cos^2 2\theta_M} \tag{6.78}$$

In the above equations, the term $\cos^2 2\theta_M$ can be replaced by $|\cos^n 2\theta_M|$ for different monochromator crystals. The more general expression of the polarization factor for two-dimensional X-ray diffraction is then given as

$$\boxed{P(\theta,\gamma) = \frac{(1+|\cos^n 2\theta_M|\cos^2 2\theta)\sin^2\gamma + (|\cos^n 2\theta_M| + \cos^2 2\theta)\cos^2\gamma}{1+|\cos^n 2\theta_M|}} \tag{6.79}$$

For a mosaic crystal, such as a graphite crystal, $n = 2$. For most real monochromator crystals, the exponent n takes a value between 1 and 2. For near perfect monochromator crystals, n approaches 1 [28]. All the above equations for polarization factors may apply to multilayer optics. However, since multilayer optics have very low Bragg angles, $|\cos^n 2\theta_M|$ approximates to unity. The γ dependence of the polarization factor diminishes in this case. The polarization factor approaches

$$P(\theta, \gamma) \approx \frac{1 + \cos^2 2\theta}{2} \tag{6.80}$$

In this case, the polarization correction can be performed either to the 2D frame or to the integrated profile. The combined forward and reverse Lorentz-polarization correction becomes unnecessary for low polarization multilayer optics and non-polarization capillary optics.

6.8.3 Air Scatter and Be-Window Absorption

Air scatter results from X-rays being scattered by air molecules between the X-ray source and the sample, and between the sample and the detector. Air scatter results in two effects: the attenuation of the X-ray intensity and added background in the diffraction pattern. Air scatter within the enclosed primary beam path – for instance, in the mirror, monochromator housing, labyrinth, or collimator – results in attenuation of only the incident beam. The enclosed beam path can be purged by helium gas [29] or kept in vacuum to reduce the attenuation so that no correction is necessary for this part of air scatter. The open beam between the tip of the collimator and the sample generates an air scatter background pattern, which is the major part of the air scatter. The space between the sample and the detector is referred to as the secondary beam path. In the secondary beam path, the air scatter from the diffracted beam may generate background too, but the main effect of the air scatter is inhomogeneous attenuation to the diffraction pattern due to the different beam path lengths between the center and the edge of the detector.

The background generated by air scattering from the open incident beam path has a strong 2θ dependence. The air molecules are distributed randomly in space, but molecules have a preferred distance between atoms within each molecule. The scattering curve shows no peak at all, although the scattered intensity drops continuously with the increase in 2θ angle [30–32]. The specific scattering curve depends on the length of the open primary beam path, beam size, and the wavelength of the incident beam. There are two approaches to correct air scatter background noise. One is to collect an air scatter background frame in the same condition as the diffraction frame except without a sample. The background frame is then subtracted from the diffraction frame. Another approach is to remove the background from the integrated profile, since the background is 2θ dependent.

The attenuation of the diffracted beam by air absorption depends on the distance between the sample and the pixel. For a flat detector, air absorption can be corrected by

$$p_c(x, y) = p_o(x, y) \cdot \exp(\mu_{air} \sqrt{D^2 + x^2 + y^2}) \tag{6.81}$$

where $p_o(x,y)$ is the original pixel intensity of the pixel P(x,y) and $p_c(x,y)$ is the corrected intensity. The detector center is given by (0,0). μ_{air} is the linear absorption coefficient of air. The value of μ_{air} is determined by the radiation wavelength. As an approximation, for air with 80% N_2 and 20% O_2 at sea level and at 20°C, $\mu_{air} = 0.01\,\text{cm}^{-1}$ for Cu-K_α. Air scatter and absorption increases with increasing wavelength. For example, $\mu_{air} = 0.015\,\text{cm}^{-1}$ for Co-K_α and $\mu_{air} = 0.032\,\text{cm}^{-1}$ for Cr-K_α. The absorption coefficient for Mo-K_α is only one tenth of that for

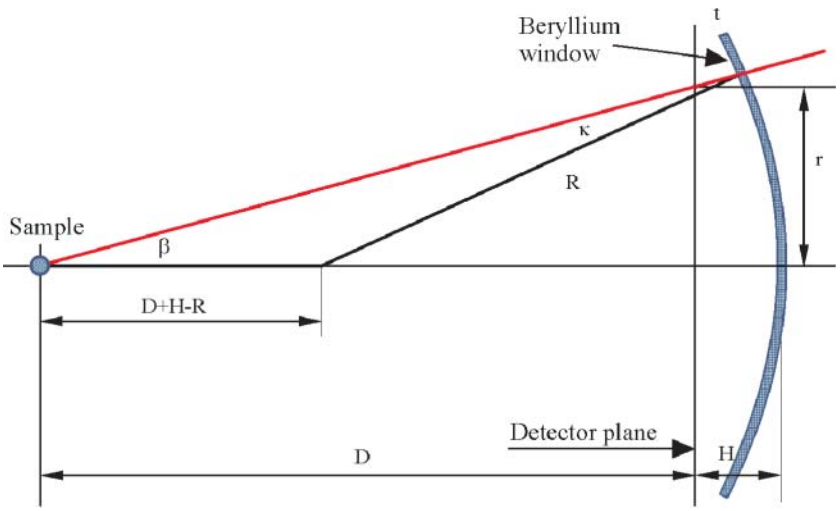


FIGURE 6.30 Geometry of the window absorption correction.

Cu-K$_\alpha$, $\mu_{air} = 0.001\,\text{cm}^{-1}$. Therefore air absorption correction is not necessary. Alternatively, absorption correction may be normalized to the absorption level in the beam center as

$$p_c(x, y) = p_o(x, y) \cdot \exp[\mu_{air}(\sqrt{D^2 + x^2 + y^2} - D)] \tag{6.82}$$

In this normalized correction the attenuation of air scatter is not fully corrected for each pixel, but rather corrected to the same attenuation level as the pixel in the detector center. This means that the effect of path length differences between the detector center pixel and other pixels is ignored.

Be-window absorption can create uneven attenuation in the diffraction pattern. Figure 6.30 shows the geometry of window correction, in which R is the radius of curvature of the Be window, D is the sample-to-detector distance measured from the sample to the detector plane, which is the contact plane between the front face of the detector and the fiducial plate during spatial correction. H is the gap between the detector plane and the center of the Be-window. The thickness of the window is t. When $D + H$ is equal to R, and all diffracted X-rays reach the window in the radial direction, the penetration thickness is t for all pixels. In this case, the Be-window absorption correction factor is a constant for all pixels. Therefore, window absorption correction is not necessary. In Figure 6.30, $D + H$ is greater than R. For an arbitrary pixel with a distance r from the center of the detector, the diffracted X-rays pass the Be-window with a tilt angle κ from the radial direction. The penetration thickness is

$$\tau = \frac{t}{\cos\kappa} \tag{6.83}$$

From the geometry, we have

$$\frac{D + H - R}{\sin\kappa} = \frac{R}{\sin\beta} \tag{6.84}$$

and

$$\sin\beta = \frac{r}{\sqrt{D^2 + r^2}} \tag{6.85}$$

where $r = \sqrt{x^2 + y^2}$. Then we have the penetration thickness for an arbitrary pixel as

$$\tau = \frac{t}{\sqrt{1 - \frac{r^2}{D^2+r^2}\left(\frac{D+H}{R} - 1\right)^2}} \tag{6.86}$$

The same equation can be derived for $D + H$ less than R. When the detector is used at a sample-to-detector distance such that $D + H = R$, then $\tau = t$. For a flat Be-window, as R approaches infinity ($R \to \infty$), the above equation becomes

$$\tau = \frac{t\sqrt{D^2 + r^2}}{D} = \frac{t}{\cos\beta} \tag{6.87}$$

The correction is then given as

$$p_c(x, y) = p_o(x, y) \cdot \exp(\mu_{Be}\tau) \tag{6.88}$$

where $p_o(x,y)$ is the original intensity of the pixel P(x,y) and $p_c(x,y)$ is the corrected intensity. μ_{Be} is the linear absorption coefficient of Be. The value of μ_{Be} is 1.86 cm^{-1} for Cu-K_α, and 2.82 cm^{-1}, 5.89 cm^{-1}, and 0.453 cm^{-1} for Co-K_α, Cr-K_α, and Mo-K_α respectively. Alternatively, the Be-window absorption correction may be normalized to the absorption level in the beam center as

$$p_c(x, y) = p_o(x, y) \cdot \exp[\mu_{Be}(\tau - t)] \tag{6.89}$$

In this normalized correction the attenuation of the Be-window is not fully corrected for each pixel, rather it is corrected to the same attenuation level as the pixel in the detector center. That means the effects of the penetration thickness differences between the detector center pixel and other pixels are removed.

6.8.4 Sample Absorption

The absorption of X-rays by the sample reduces the diffracted intensity. Many approaches are used to calculate and correct the absorption effect for various sample shapes and geometries [27, 33–41]. The absorption can be measured by the transmission coefficient (also referred to as the absorption factor):

$$A = \frac{1}{V}\int_V e^{-\mu\tau} dV \tag{6.90}$$

where A is the transmission coefficient, μ is the linear absorption coefficient, and τ is the total beam path in the sample, which includes the incident beam path and the diffracted beam path.

6.8.4.1 Reflection Mode Figure 6.31(a) shows reflection mode diffraction with flat plate sample. The thickness of the plate is t. The normal of the reflection surface is represented by the unit vector $\boldsymbol{n}$ which is in the direction S_3 as defined in Chapter 2. The incident beam is represented by the unit vector $\boldsymbol{s_o}$ and the diffracted beam by the unit vector $\boldsymbol{s}$. The beam path length in the sample, τ, for the element dV located at a distance z from the sample surface is given as.

$$\tau = \left(\frac{1}{\cos\eta} + \frac{1}{\cos\zeta}\right) z \tag{6.91}$$

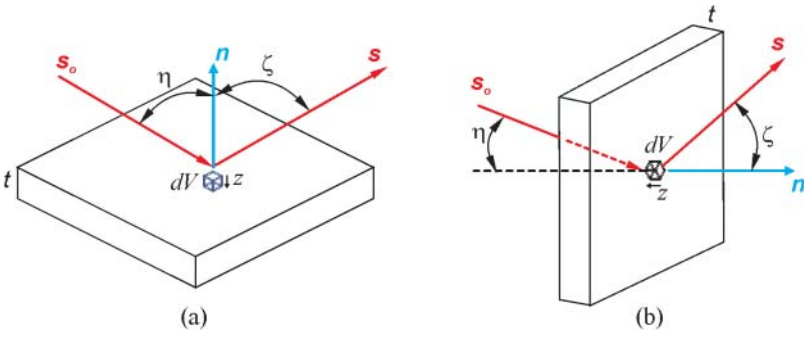


FIGURE 6.31 Absorption correction of flat slab: (a) reflection, (b) transmission.

The transmission coefficient is given as [17, 34]

$$A = \frac{1 - \exp\left[-\mu t\left(\frac{1}{\cos\eta} + \frac{1}{\cos\zeta}\right)\right]}{\mu\left(\frac{\cos\zeta}{\cos\eta} + 1\right)} \tag{6.92}$$

where η is the angle between the incident beam and the normal of the sample surface and ζ is the angle between the diffracted beam and the sample normal. In absorption correction for conventional diffractometers, the incident beam, sample normal, and diffracted beam are typically within the same plane. It is common in the absorption equation to use $\sin(\theta - \varphi)$ in place of $\cos\eta$ and $\sin(\theta + \varphi)$ in place of $\cos\zeta$, where φ is the tilt angle which reduces the incident angle to a value below the Bragg angle θ. For two-dimensional X-ray diffraction, the incident beam, sample normal, and diffracted beam are not necessarily in the same plane, so it is more convenient to use $\cos\eta$ and $\cos\zeta$ in the equation. For a thick plate with negligible transmission, the above equation becomes

$$A = \frac{\cos\eta}{\mu(\cos\eta + \cos\zeta)} \tag{6.93}$$

For two-dimensional X-ray diffraction, there is a single incident beam direction at a time, but various diffracted beam directions simultaneously. The unit vectors of the incident beam, diffracted incident beam, and the sample normal are given respectively in Chapter 2 as

$$\boldsymbol{s_o} = \begin{bmatrix} 1 \\ 0 \\ 0 \end{bmatrix}, \quad \boldsymbol{s} = \begin{bmatrix} \cos 2\theta \\ -\sin 2\theta \sin\gamma \\ -\sin 2\theta \cos\gamma \end{bmatrix} \quad \text{and} \quad \boldsymbol{n} = \begin{bmatrix} -\sin\omega\cos\psi \\ \cos\omega\cos\psi \\ \sin\psi \end{bmatrix} \tag{6.94}$$

Then we have

$$\cos\eta = -\boldsymbol{s_o} \cdot \boldsymbol{n} = \sin\omega\cos\psi \tag{6.95}$$

and

$$\cos\zeta = \boldsymbol{s} \cdot \boldsymbol{n} = -\cos 2\theta \sin\omega\cos\psi - \sin 2\theta \sin\gamma\cos\omega\cos\psi - \sin 2\theta\cos\gamma\sin\psi \tag{6.96}$$

It can be proven that $\cos\zeta$ is always positive for the reflection mode even though all the terms in the equation bear a negative sign. For a geometry equivalent to the Bragg–Brentano geometry, $\omega = \theta$, $\psi = 0$, and $\gamma = -90°$, $\cos\eta = \cos\zeta = \sin\theta$, and the transmission coefficient $A_{BB} = 1/(2\mu)$.

In the Bragg–Brentano geometry, the transmission coefficient is independent of the θ angle. Since it is a constant, it is usually neglected in the relative intensity calculation [42]. The transmission coefficients from the equation (6.92) and (6.93) also contain a length unit, which creates ambiguity if they are used to correct the intensity pixel by pixel. In order to make the relative intensity comparable to the results from the Bragg–Brentano geometry, we introduce a new transmission coefficient which is normalized by the transmission coefficient of the Bragg–Brentano geometry, $A_{BB} = 1/(2\mu)$. The normalized transmission coefficient is also a numerical factor without units. The transmission coefficient with normalization will be denoted by T hereafter in this chapter. The transmission coefficient for reflection mode diffraction with a flat sample of thickness t is then given as

$$T = A/A_{BB} = \frac{2\cos\eta\left\{1 - \exp\left[-\mu t\left(\frac{1}{\cos\eta} + \frac{1}{\cos\zeta}\right)\right]\right\}}{\cos\eta + \cos\zeta} \tag{6.97}$$

For a thick plate, or material with a very high linear absorption coefficient, the transmission through the sample thickness is negligible, and the above equation becomes

$$T = \frac{2\cos\eta}{(\cos\eta + \cos\zeta)} \tag{6.98}$$

Equations (6.97) and (6.98) are derived for a flat sample. When concave or convex sample geometries are used, the absorption correction involves more complicated formulae [43]. When the irradiated area on the curved surface is kept smaller than half the radius of curvature, the effects of the curved surface on absorption are negligible. Therefore, the transmission coefficients for flat samples can apply to samples with concave or convex samples in this case. Since the beam size for two-dimensional X-ray diffraction is typically smaller than 1 mm, the above equations for transmission coefficients can be used most of the time.

Taking the ratio of equations (6.97) and (6.98), we can obtain the fraction of the diffracted intensity G_t contributed by a surface layer of depth t.

$$G_t = 1 - \exp\left[-\mu t\left(\frac{1}{\cos\eta} + \frac{1}{\cos\zeta}\right)\right] \tag{6.99}$$

Therefore, the depth of penetration t corresponding to a given G_t can be calculated from

$$t = \frac{-\ln(1 - G_t)\cos\eta\cos\zeta}{\mu(\cos\eta + \cos\zeta)} \tag{6.100}$$

As an approximation, we only consider diffraction within the diffractometer plane ($\gamma = -90°$) and ignore the penetration dependence on γ. We obtain

$$t = \frac{-\ln(1 - G_t)\sin\omega\sin(2\theta - \omega)\cos\psi}{\mu[\sin\omega + \sin(2\theta - \omega)]} \tag{6.101}$$

For penetration corresponding to 95% and 50% diffracted intensity, we have

$$t_{95\%} = \frac{2.996\sin\omega\sin(2\theta - \omega)\cos\psi}{\mu[\sin\omega + \sin(2\theta - \omega)]} \tag{6.102}$$

and

$$t_{50\%} = \frac{0.693\sin\omega\sin(2\theta - \omega)\cos\psi}{\mu[\sin\omega + \sin(2\theta - \omega)]} \tag{6.103}$$

6.8.4.2 Transmission Mode Figure 6.31(b) shows the transmission mode diffraction with a flat plate sample. The thickness of the plate is t. The normal of the reflection surface is represented by the unit vector $\boldsymbol{n}$. The incident beam is represented by the unit vector $\boldsymbol{s}_0$ and the diffracted beam by the unit vector $\boldsymbol{s}$. Also, η is the angle between the incident beam and the normal of the sample surface and ζ is the angle between the diffracted beam and the sample normal. The beam path length in the sample, τ, for the element dV located at a distance z from the sample surface is given by

$$\tau = \left(\frac{z}{\cos\eta} + \frac{t-z}{\cos\zeta}\right) = z\sec\eta + (t-z)\sec\zeta \tag{6.104}$$

The transmission coefficient normalized by $A_{BB} = 1/(2\mu)$ is given by [34, 38]

$$T = \frac{2\sec\eta[\exp(-\mu t\sec\eta) - \exp(-\mu t\sec\zeta)]}{\sec\zeta - \sec\eta} \quad \text{for} \quad \sec\zeta \neq \sec\eta \tag{6.105}$$

It is a very common practice to set the incident angle perpendicular to the sample surface, i.e. $\eta = 0$. For most translation mode data collection, the above equation becomes

$$T = \frac{2[\exp(-\mu t) - \exp(-\mu t\sec\zeta)]}{\sec\zeta - 1} \tag{6.106}$$

When $\eta = \zeta$, both the numerator and denominator approach zero, and the transmission coefficient should be given by

$$T = 2\mu t\sec\zeta\exp(-\mu t\sec\zeta) \tag{6.107}$$

For two-dimensional X-ray diffraction, there is a single incident beam direction at a time, but various diffracted beam directions simultaneously. The unit vectors of the incident beam and diffracted incident beam are given respectively in Chapter 2 as

$$\boldsymbol{s}_0 = \begin{bmatrix} 1 \\ 0 \\ 0 \end{bmatrix} \quad \text{and} \quad \boldsymbol{s} = \begin{bmatrix} \cos 2\theta \\ -\sin 2\theta\sin\gamma \\ -\sin 2\theta\cos\gamma \end{bmatrix} \tag{6.108}$$

The unit vector of the normal to the sample depends on the sample loading orientations relative to the goniometer angles. If the sample is loaded such that $\omega = \psi = \phi = 0$, the sample surface is perpendicular to the X-ray beam and the sample normal is in the X-ray beam direction. Since $\boldsymbol{n}$ is in the opposite direction as S_1 as defined in Chapter 2, the unit vector of the sample normal for arbitrary goniometer angles is then given by

$$\boldsymbol{n} = \begin{bmatrix} \sin\omega\sin\psi\sin\phi + \cos\omega\cos\phi \\ -\cos\omega\sin\psi\sin\phi + \sin\omega\cos\phi \\ \cos\psi\sin\phi \end{bmatrix} \tag{6.109}$$

Then we have

$$\cos\eta = \boldsymbol{s}_0 \cdot \boldsymbol{n} = \sin\omega\sin\psi\sin\phi + \cos\omega\cos\phi \tag{6.110}$$

and

$$\begin{aligned} \cos\zeta = \boldsymbol{s}\cdot\boldsymbol{n} = {} & (\sin\omega\sin\psi\sin\phi + \cos\omega\cos\phi)\cos 2\theta \\ & + (\cos\omega\sin\psi\sin\phi - \sin\omega\cos\phi)\ \sin 2\theta\sin\gamma \\ & - \cos\psi\sin\phi\ \sin 2\theta\cos\gamma \end{aligned} \tag{6.111}$$

It is common practice for the sample to be loaded perpendicular to the incident X-ray beam at the goniometer angles $\omega = \psi = \phi = 0$. Therefore, $\cos\eta = 1$ and $\cos\zeta = \cos 2\theta$, and the transmission coefficient becomes

$$T = \frac{2\cos 2\theta \left[\exp(-\mu t) - \exp\left(-\frac{\mu t}{\cos 2\theta}\right)\right]}{1 - \cos 2\theta} \tag{6.112}$$

The transmission coefficient is a function of 2θ for a given sample thickness and absorption coefficient. To find the sample thickness that gives the maximum transmission coefficient, we let the first derivative of the above equation equal 0:

$$\frac{dT}{dt} = \frac{2\cos 2\theta}{1 - \cos 2\theta}\left[-\mu\exp(-\mu t) + \frac{\mu}{\cos 2\theta}\exp\left(-\frac{\mu t}{\cos 2\theta}\right)\right] = 0 \tag{6.113}$$

Then the maximum scattered intensity occurs when

$$t = \frac{\cos 2\theta \ln(\cos 2\theta)}{\mu(\cos 2\theta - 1)} \tag{6.114}$$

This equation can be used to select the optimum sample thickness for transmission mode diffraction. For example, if the measurement 2θ range is between 3° and 50°, the preferred sample thickness should be given by $\mu t = 0.8 \sim 1.0$. When $2\theta \to 0, t = 1/\mu$, and the maximum scattering intensity is achieved at small 2θ angles.

In order to do a pixel to pixel correction from equations (6.97) or (6.98) for reflection mode or equations (6.105) or (6.112) for transmission mode, we can obtain the transmission coefficient as a function of angles θ, γ, ω, ψ, plate thickness t, and linear absorption coefficient μ:

$$T = T(\theta, \gamma, \omega, \psi, t, \mu) = T(x, y, D, \alpha, \omega, \psi, t, \mu) \tag{6.115}$$

where θ, γ are given by the equations (6.27) and (6.28) for any pixel on the detector. The sample absorption correction can then be done pixel by pixel with the following equation

$$p_c(x, y) = p_o(x, y)/T(x, y, D, \alpha, \omega, \psi, t, \mu) \tag{6.116}$$

where $p_o(x,y)$ is the pixel intensity of the pixel P(x,y) before the absorption correction and $p_c(x,y)$ is the sample absorption corrected intensity.

6.8.5 Combined Intensity Correction

Lorentz, polarization, air scatter, Be-window, and sample absorption corrections as well as other pixel by pixel intensity corrections can all be combined into one correction with a combined correction factor C:

$$C = C_L \cdot C_P \cdot C_{Air} \cdot C_{Be} \cdot C_S \cdot C_i \cdot C_j \cdot C_k \cdot \cdots \tag{6.117}$$

where C_L, C_P, C_{Air}, C_{Be}, and C_S are correction factors for the Lorentz, polarization, air scatter, Be-window, and sample absorption effects, respectively. C_i, C_j, and C_k are correction factors of any other unspecified intensity effects. The correction for any effect can be disabled by setting

the corresponding correction factor to unity. The correction is then given as

$$p_c(x, y) = Cp_o(x, y) \tag{6.118}$$

where $p_o(x,y)$ is the intensity of the pixel P(x,y) before any intensity correction and $p_c(x,y)$ is the pixel intensity corrected by the combined intensity correction factor. The correction factors for Lorentz, polarization, air scatter, Be-window, and sample absorption effects are summarized in Table 6.3. When all the appropriate corrections are applied to the 2D diffraction data, the relative intensities from a random powder sample should match the profile collected with a diffractometer in Bragg–Brentano geometry.

Table 6.3 Correction Factors for Pixel to Pixel Intensity Correction

Effects	Correction Factors and Comments
Lorentz	$C_L = 4\sin^2\theta\cos\theta$
	Set $C_L = 1$ to get Bragg–Brentano equivalent pixel intensity
Polarization	$C_P = \dfrac{(1+\cos^2 2\theta_M\cos^2 2\theta)\sin^2\gamma + (\cos^2 2\theta_M + \cos^2 2\theta)\cos^2\gamma}{(1+\cos^2 2\theta_M)}$
	Incident monochromator reflection is within the diffractometer plane.
	$C'_P = \dfrac{1+\cos^2 2\theta\cos^2 2\theta_M}{1+\cos^2 2\theta_M}$
	Reverse correction to get Bragg–Brentano equivalent pixel intensity.
	Set $C_p = C'_P = 1$ for multilayer optics or capillary optics.
Air scatter	$C_{Air} = \exp[\mu_{air}(\sqrt{D^2 + x^2 + y^2} - D)]$
	Normalized to the pixel intensity at the detector center.
Be-window correction	$C_{Be} = \exp\left\{\mu_{Be}t\left(\sqrt{\dfrac{(D^2+x^2+y^2)R^2}{(D^2+x^2+y^2)R^2 - (x^2+y^2)(D+H-R)^2}} - 1\right)\right\}$
	Normalized to the pixel intensity at the detector center.
Sample absorption (reflection on flat sample)	$C_S = \dfrac{\cos\eta + \cos\zeta}{2\cos\eta\cdot\{1-\exp[-\mu t(\sec\eta + \sec\zeta)]\}}$
	$\cos\eta = \sin\omega\cos\psi$
	$\cos\zeta = -\cos 2\theta\sin\omega\cos\psi - \sin 2\theta\sin\gamma\cos\omega\cos\psi - \sin 2\theta\cos\gamma\sin\psi$
	Normalized by the absorption factor of the Bragg–Brentano geometry.
Sample absorption (transmission through flat sample)	$C_S = \dfrac{\sec\zeta - \sec\eta}{2\sec\eta[\exp(-\mu t\sec\eta) - \exp(-\mu t\sec\zeta)]}$ for $\sec\zeta \neq \sec\eta$
	$C_S = \dfrac{\exp(\mu t\sec\zeta)}{2\mu t\sec\zeta}$ for $\sec\zeta = \sec\eta$
	$\cos\eta = \sin\omega\sin\psi\sin\phi + \cos\omega\cos\phi$
	$\cos\zeta = (\sin\omega\sin\psi\sin\phi + \cos\omega\cos\phi)\cos 2\theta$ $+(\cos\omega\sin\psi\sin\phi - \sin\omega\cos\phi)\sin 2\theta\sin\gamma - \cos\psi\sin\phi\sin 2\theta\cos\gamma$
	Normalized by the absorption factor of the Bragg–Brentano geometry.

REFERENCES

1. S. N. Sulyanov, A. N. Popov, and D. M. Kheiker, Using a two-dimensional detector for X-ray powder diffractometry, *J. Appl. Cryst.* (1994) **27**, 934–942.
2. S. Scheidegger, A. Estermann, and W. Steurer, Correction of specimen absorption in X-ray diffuse scattering experiments with area-detector systems, *J. Appl. Cryst.* (1999) **33**, 35–48.
3. A. Cervellino, et al., Folding a two-dimensional powder diffraction image into a one-dimensional scan: a new procedure, *J. Appl. Cryst.* (2006) **39**, 745–748.
4. P. Boesecke, Reduction of two-dimensional small- and wide-angle X-ray scattering data, *J. Appl. Cryst.* (2007) **40**, 423–427.
5. R. Jenkins and R. L. Snyder, *Introduction to X-ray Powder Diffractometry*, 319–320, John Wiley, New York, 1996
6. ICDD, Release 2007 of the Powder Diffraction File, http://www.icdd.com, 2008.
7. P. R. Rudolf and B. G. Landes, Two-dimensional X-ray diffraction and scattering of microcrystalline and polymeric materials, *Spectroscopy*, **9**(6), pp. 22–33, 1994.
8. A. Fujiwara, et al., Synchrotron radiation X-ray powder diffractometer with a cylindrical imaging plate, *J. Appl. Cryst.* (2000) **33**, 1241–1245.
9. B. B. He, Introduction to two-dimensional X-ray diffraction, *Powder Diffraction*, *Vol.* **18***, No* 2, 71–90, June 2003.
10. G. Ning and R. L. Flemming, Rietveld refinement of LaB_6: data from μXRD, *J. Appl. Cryst.* (2005) **38**, 757–759.
11. M. W. Tate, et al., A large-format high resolution area X-ray detector based on a fiber-optically bonded charge-coupled device (CCD), *J. Appl. Cryst.* (1995) **28**, 196–205.
12. M. Stanton, et al., Correcting spatial distortions and non-uniform response in area detectors, *J. Appl. Cryst.* (1992) **25**, 549–558.
13. J. P. Moy, A novel technique for accurate intensity calibration of area X-ray detectors at almost arbitrary energy, *J. Synchrotron Rad.* (1996) **3**, 1–5.
14. B. B. He, Test report on Hi-Star calibration with glassy Fe foil, *Bruker AXS, April* **23**, 1997.
15. J. W. Campbell, Spatial-distortion corrections, for Laue diffraction patterns recorded on image plates, modeled using polynomial functions, *J. Appl. Cryst.* (1995). **28**, 43–48.
16. Z. Derewenda and J. R. Helliwell, Calibration tests and use of a Nicolet/Xentronics imaging proportional chamber mounted on a conventional source for protein crystallography, *J. Appl. Cryst.* (1989). **22**, 123–137.
17. Bruker AXS, General area detector diffraction software (GADDS) reference manual, doc# 269–017203, May, 1996.
18. A. B. Rodriguez-Navarro, XRD2DScan: new software for polycrystalline materials characterization using two-dimensional X-ray diffraction, *J. Appl. Cryst.* (2006) **39**, 905–909.
19. J. E. Bresenham, Algorithm for computer control of a digital plotter, *IBM Systems Journal*, Vol. **4**, No.1, January 1965, pp. 25–30.
20. B. B. He, et al., Method for collecting accurate X-ray diffraction data with a scanning two-dimensional detector, US Patent application, Dec 22, 2015, Publication number: US20170176355 A1.
21. B. B. He, Patent application: “Method to extend angular coverage for scanning 2D detector”, filed to USPTO on April 5, 2017, Application number: US 15/479,335.
22. B. D. Cullity, *Elements of X-ray Diffraction*, 2nd ed., Addison-Wesley, Reading, MA, 1978.
23. H. P. Klug and L. E. Alexander, *X-ray Diffraction Procedures for Polycrystalline and Amorphous Materials*, 2nd ed., John Wiley and Sons, New York, 1974.
24. O. Robach et al., Corrections for surface X-ray diffraction measurements using the Z axis geometry: finite size effects in direct and reciprocal space *J. Appl. Cryst.* (2000). **33**, 1006–1018.

25. D. J. Thomas, Modern equations of diffractometry: diffraction geometry, *Acta Cryst.* (1992). **A48**, 134–158.
26. L. V. Azaroff, Polarization correction for crystal-monochromatized x-radiation, *Acta Cryst.* (1955). **8**, 701.
27. C. Giacovazzo, et al., *Fundamentals of Crystallography*, Oxford Science, New York, 1992.
28. K. A. Kerr and J. P. Ashmore, Systematic errors in polarization corrections for crystal-monochromatized radiation, *Acta Cryst.* (1974). **A30**, 176.
29. M. Polentarutti, R. Glazerb, and K. D. Carugo, A helium-purged beam path to improve soft and softer X-ray data quality, *J. Appl. Cryst.* (2004). **37**, 319–324.
30. M. Krieger, et al., Data collection in protein crystallography: capillary effects and background corrections, *Acta Cryst.* (1974). **A30**, 740.
31. M. Krieger and R. M. Stroud, Data collection in protein crystallography: experimental methods for reducing background radiation, *Acta Cryst.* (1976). **A32**, 653.
32. R. W. Alkire, et al., Re-thinking the role of the beamstop at a synchrotron-based protein crystallography beamline, *J. Appl. Cryst.* (2004). **37**, 836–840.
33. W. R. Busing and H. A. Levy, High-speed computation of the absorption correction for single crystal diffraction measurements, *Acta Cryst.* (1957). **10**, 180.
34. E. N. Maslen, X-ray absorption, *International Tables for Crystallography*, Vol. C, edited by A. J. C. Wilson, IUCR by Kluwer Academic Publisher (1992), 520–529.
35. S. Scheidegger, et al., Correction of specimen absorption in X-ray diffuse scattering experiments with area-detector systems, *J. Appl. Cryst.* (2000). **33**, 35–48.
36. W. Pitschke, Absorption corrections of powder diffraction intensities recorded in transmission geometry, *J. Appl. Cryst.* (1996). **29**, 561–567.
37. A. D. Zuev, Calculation of the instrumental function in X-ray powder diffraction, *J. Appl. Cryst.* (2006). **39**, 304–314.
38. C. R. Ross II, Measurement of powder diffraction sample absorption coefficients using monochromated radiation and transmission geometry, *J. Appl. Cryst.* (1992). **25**, 628–631.
39. R. M. F. Leal, et al., Absorption correction based on a three-dimensional model reconstruction from visual images, *J. Appl. Cryst.* (2008). **41**, online 6 June.
40. J. Collazo, et al., Microabsorption of X-rays in planar powder samples in the non-symmetric reflection case, *J. Appl. Cryst.* (1997). **30**, 312–319.
41. S. Sulyanov, A. Gogina, and H. Boysen, Spatial distribution of the absorption factor for an infinite cylindrical sample used with a two-dimensional area detector, *J. Appl. Cryst.* (2012). **45**, 93–97.
42. V. K. Pecharsky and P. Y. Zavalij, *Fundamentals of Powder Diffraction and Structural Characterization of Materials*, Kluwer Academic Publisher (2003), 193–196.
43. M. E. Hilley, Ed., *Residual Stress Measurement by X-ray Diffraction*, SAE J784a, Society of Automotive Engineers, Warrendale, PA, 1971, p. 38–45.

7

PHASE IDENTIFICATION

7.1 INTRODUCTION

The majority of solid materials have crystalline atomic structure. The diffraction pattern from crystalline materials contains many peaks corresponding to various crystal planes in the material. Based on Bragg's law, the peaks at low 2θ angles are from crystal planes of large d-spacing and vice versa at the high 2θ angles. A set of data or plots showing the diffraction peak intensities at various 2θ positions or d-spacing values is called an X-ray diffraction pattern. In order to satisfy the Bragg condition at all crystal planes, the crystal diffraction pattern is actually generated from polycrystalline or powder materials. Therefore, the diffraction pattern is also called a powder diffraction pattern. In materials science, a phase is defined as a region that has relatively uniform chemical composition and physical properties, including crystal structure. Therefore, every phase should give a unique diffraction pattern. An X-ray diffraction sample may contain a single phase or multiple phases. Analysis of the diffraction pattern can precisely determine the contents of the sample. This process is called phase identification (phase ID) or qualitative analysis. One of the most efficient methods of diffraction data analysis is to compare the diffraction pattern from an unknown material to a list of standard diffraction patterns. A list containing standard diffraction patterns has been available since the 1930s and has gradually grown into an extensive database containing thousands of standard diffraction patterns [1]. The most comprehensive database is the Powder Diffraction File (PDF) updated annually by the International Center for Diffraction Data (ICDD). The 2007 release of the PDF contains over 550,000 unique material data sets. Each data set contains diffraction, crystallographic, and bibliographic data, as well as experimental, instrument, and sampling conditions, and select physical properties in a common standardized format [2].

The X-ray diffractometer in the Bragg–Brentano geometry has been the preferred configuration for collecting phase identification data from bulk powder or polycrystalline samples. However, the reality is that more and more users are using linear or area detectors to collect

Two-Dimensional X-Ray Diffraction, Second Edition. Bob Baoping He.
© 2018 John Wiley & Sons, Inc. Published 2018 by John Wiley & Sons, Inc.

phase ID data for many reasons, such as high speed, small sample size, or for samples with a large grain size and/or a preferred orientation. With the increased usage of linear and area detectors, many users have also noticed some discrepancies between the diffraction patterns collected with a Bragg–Brentano system and a system with linear or area detector. In the Bragg–Brentano geometry, the 2θ resolution is controlled by the selection of the divergence slit and receiving slit in the diffractometer plane, and the axial divergence is controlled by soller slits, while in a diffractometer with a linear or area detector, the 2θ resolution is mainly determined by the spatial resolution of the detector and the sample-to-detector distance. The complete diffraction pattern can be collected by a single scan in Bragg–Brentano geometry, but several 2θ ranges may have to be collected and merged with a linear or area detector. The 2θ resolution may vary with the 2θ measurement range and sample geometry. The relative peak intensity in a diffraction pattern from a sample with texture measured with linear or area detector can be significantly different from the results measured with the Bragg–Brentano geometry.

It is imperative to study the nature of these discrepancies so that the diffraction patterns collected with linear and area detectors can be used for phase ID with proper understanding and correction if necessary. In this chapter we compare the conventional Bragg–Brentano diffractometer with diffractometers using linear or area detectors in terms of geometry conventions, X-ray optics, data collection and processing strategies. Two-dimensional X-ray diffraction has enhanced phase identification in many respects [3–6]. Because of its ability to collect diffracted X-rays over a large angular range in both 2θ and γ directions, it can collect diffraction data with high speed and better sampling statistics. Due to point beam illumination on the sample, a relatively small sample size is required for phase identification. The large area detector allows for a large 2θ range to be analyzed without any movement of the sample and detector. This makes it possible to perform in-situ phase investigation on samples measured during phase transformation. The diffraction information in the γ direction allows accurate phase identification of samples with large gains and a preferred orientation.

When two-dimensional diffraction is used for phase identification, the first step is to integrate the 2D diffraction frame into a diffraction profile resembling the diffraction pattern collected with a conventional diffractometer. This diffraction pattern can then be interpreted by all existing concepts for conventional X-ray diffraction, and phase ID can be done by many available software programs [7–12]. The integrated diffraction profiles can be analyzed with all existing algorithms and methods, including profile fitting with conventional peak shapes and fundamental parameters, quantification of phases, and lattice parameter indexing and refinement [13]. The results can be used to search and match with the ICDD PDF database. Since there are many books and literature covering the topics [1, 8, 9], this chapter will focus on the special characteristics of two-dimensional X-ray diffraction as well as system geometry, data collection strategies, and data analysis in dealing with relative peak intensities, peak width (2θ resolution), grain size and distribution, and preferred orientations. Many factors and correction algorithms described in the chapter can aid understanding of the characteristics of two-dimensional diffraction compared to conventional Bragg–Brentano geometry. In most applications, the γ-integrated profile can be used for phase identification without these corrections.

7.2 RELATIVE INTENSITY

The integrated intensity diffracted from random polycrystalline materials is given by

$$\mathbf{I}_{hkl} = k_I \frac{p_{hkl}}{v^2}(LPA)\lambda^3 F_{hkl}^2 \exp(-2M_t - 2M_s) \tag{7.1}$$

where k_I is an instrument constant that is a scaling factor between experimental observed intensities and calculated intensity, p_{hkl} is the multiplicity factor of the crystal plane (hkl), v is the volume of the unit cell, (LPA) is the Lorentz-polarization and absorption factors, λ is the X-ray wavelength, F_{hkl} is the structure factor of the crystal plane (hkl) and $\exp(-2M_t - 2M_s)$ is the attenuation factor due to lattice thermal vibrations and weak static displacements [14, 15].

The instrument constant is the scaling factor converting the theoretically calculated intensities to the experimentally observed integrated intensities. The instrument constant is determined by the specific instrument configuration, geometry, and operational settings of many instrument parameters. Many physical parameters not explicitly expressed in the above relation are also covered in the instrument constant. The Lorentz-polarization and absorption factors need special treatment with two-dimensional diffraction data and have been covered in the Chapter 6. The rest of the factors in the above equation do not need special treatment for two-dimensional data and are briefly introduced in the following subsections.

7.2.1 Multiplicity Factor

In a single crystal lattice, a crystal plane (hkl) has several equivalent crystal planes with the exact same atomic arrangement and d-spacing but different orientations. This group of equivalent planes are referred to as planes of a form and expressed by the symbol {hkl}. For example, in the cubic system all the planes (100), (010), (001), $(\bar{1}00)$, $(0\bar{1}0)$, and $(00\bar{1})$ belong to the form {100}. The X-ray diffraction from each of the equivalent planes produces the same intensity at the same Bragg angle. Therefore, the total diffracted intensity from the planes of a form is the diffraction intensity from one of the equivalent crystal plane times the number of equivalent planes. The number of equivalent crystal planes for a form is referred to as the multiplicity factor. The multiplicity factor is a function of both the Miller indices and the lattice symmetry. A crystal plane of the same Miller index has a higher multiplicity factor for a crystal lattice of high symmetry. For example, a crystal plane with index (hkl) with $h \neq k \neq l$ has a multiplicity factor of 48 for cubic crystals, but only 24 for hexagonal crystals and 2 for triclinic crystals. Pairs of reflections from equivalent planes within the same form, but having opposite signs of indices, (hkl) and $(\bar{h}\bar{k}\bar{l})$ for instance, are referred to as Friedel pairs. The multiplicity factors of various crystalline planes are listed in Table 7.1.

Table 7.1 Multiplicity Factor p_{hkl} for Various Systems and Miller Indices

System	*hkl*	*hhl*	*hh0*	*0kk*	*hhh*	*hk0*	*h0l*	*0kl*	*h00*	*0k0*	*00l*
Cubic	48[a]	24	12[b]	12[b]	8	24[a]	24[a]	24[a]	6	6	6
Hexagonal	24[a]	12[a]	6	—[c]	—	12[a]	12[a]	12[a]	6	6	2
Trigonal	24[a]	12	6	—	—	12[a]	12	12	6	6	2
Tetragonal	16[a]	8	4	—	—	8[a]	8	8	4	4	2
Orthorhombic	8	—	—	—	—	4	4	4	2	2	2
Monoclinic	4	—	—	—	—	2	2	2	2	2	2
Triclinic	2	—	—	—	—	2	2	2	2	2	2

[a]The multiplicity factor may split to two or four parts for each set of the reflections having the same Bragg angle but different structure factors.

[b]Merged cells in the table represent equivalent crystal planes. For example, (110) and (011) planes are equivalent in cubic lattices.

[c]The cell filled with "—" means the Miller index is not counted as a form of plane. For example, {111} in a tetragonal lattices does not belong to {*hhh*}, but {*hhl*} since the lattice parameters $a = b \neq c$ in tetragonal lattice.

7.2.2 Electron and Atomic Scattering

X-ray scattering by matter is the collective effect of scattering by electrons. The intensity of a beam scattered by a free electron is given by the Thomson equation as

$$I = \left(\frac{e^4}{m^2c^4}\right)\left(\frac{I_o}{R^2}\right)\left(\frac{1+\cos^2 2\theta}{2}\right) \tag{7.2}$$

where e is the charge on an electron (1.60×10^{-19} coulomb), m is the mass of the electron (9.11×10^{-31} kg), c is the speed of light (3.00×10^8 m/sec), I_o is the intensity of the incident beam, I is the intensity of the scattered beam, R is the distance from the scattering electron (m), and 2θ is the scattering angle between the incident beam and the scattered beam. The combined term $e^4/(m^2c^4) = {r_e}^2$ is a constant (7.94×10^{-26} cm^2) and $r_e = e^2/(mc^2)$ is referred to as the classical electron radius. Both I and I_o are an average value over space and time. The term $(1 + \cos^2 2\theta)/2$ is the polarization factor for a non-polarized incident beam.

X-ray scattering by an atom is the net effect of all electrons in the atom based on the Thomson equation. The scattering power of an atom is given by the atomic scattering factor as

$$f = \frac{A_a}{A_e} \tag{7.3}$$

where f is the atomic scattering factor, A_a is the amplitude of the wave scattered by the atom and A_e is the amplitude of waves scattered by one electron. The differences in the locations of the electrons within an atom introduce phase differences between the waves scattered by different electrons. Therefore, the atomic scattering factor approaches the total number of electrons ($f = Z$) only for forward scattering with low scattering angle. The atomic scattering factor decreases with increasing scattering angle. The atomic scattering factor is also a function of the wavelength of the incident beam. The shorter the wavelength is, the faster the atomic scattering factor drops with the scattering angle. The atomic scattering factor is typically expressed as a function of $\sin\theta/\lambda$, which combines both the effects of scattering angle and wavelength in the atomic scattering factor. The atomic scattering factor with n electrons is determined by the electron distribution in the atom as

$$f_n = \int_0^\infty 4\pi r^2 \rho_n(r) \frac{\sin kr}{kr} dr \tag{7.4}$$

where $\rho_n(r)$ is the electron charge density distribution as a function of distance from the center of the atom and

$$\rho_n(r) = |\Psi_n^2| \tag{7.5}$$

Ψ_n is the Schrodinger's wave function. For the simplest case, the hydrogen atom in ground state, Ψ can be calculated exactly such that

$$\rho(r) = |\Psi^2| = (\pi a_o^3)^{-1} \exp\left(-2\frac{r}{a_o}\right) \tag{7.6}$$

where a_o is the Bohr radius of hydrogen (=0.529 Å). Then the atomic scattering factor for hydrogen atom can be given as

$$f_H = \left[1 + \left(\frac{2\pi a_o \sin\theta}{\lambda}\right)^2\right]^{-2} \tag{7.7}$$

The calculated atomic scattering factor f is valid if the wavelength of the incident beam is significantly less than the absorption edge. When the wavelength is close to the absorption edge, resonance effects are observed and f must be corrected by

$$f = f_o + \Delta f' + i\Delta f'' \tag{7.8}$$

where f_o is the atomic scattering factor without anomalous scattering, and $\Delta f'$ and $\Delta f''$ are the real and imaginary parts of the dispersion correction. Anomalous scattering is very important in single crystal diffraction (SCD), but trivial in most X-ray diffraction applications of polycrystalline materials. The atomic scattering factors f_o and the dispersion correction terms $\Delta f'$ and $\Delta f''$ for various atoms and ions can be found in the International Tables for Crystallography [16].

7.2.3 Structure Factor

X-ray scattering by a unit cell is the net effect of all atoms or ions in the unit cell or all the electrons in the unit cell. The net effect can be expressed as a summation of scattering from all atoms or ions in the unit cell

$$F_{hkl} = \sum_{1}^{N} f_n \exp[2\pi i(hu_n + kv_n + lw_n)] \tag{7.9}$$

where F_{hkl} is the structure factor for the hkl reflection, N is the total number of atoms or ions belonging to the unit cell, f_n is the atomic scattering factor of the n-th atom or ion in the unit cell, and the coordinates (u_n,v_n,w_n) give the location of the n-th atom or ion in the unit cell. The values of (u_n,v_n,w_n) are between 0 and less than unity with units of the lattice parameters (a,b,c) respectively. The other three lattice parameters (α,β,γ) are not included in the equation for the structure factor. Therefore, the structure factor is independent of the shape and size of the unit cell. F_{hkl} is a complex function containing both real and imaginary parts. F_{hkl} defines both the amplitude and phase of the resultant wave from all scattering atoms in the unit cell. The integrated intensity of the (hkl) peak in the diffraction pattern is proportional to $|F_{hkl}|^2$ and given by

$$\begin{aligned} |F_{hkl}|^2 = F_{hkl} \cdot F_{hkl}^* = &\left\{ \sum_{1}^{N} f_n \exp[2\pi i(hu_n + kv_n + lw_n)] \right\} \\ &\times \left\{ \sum_{1}^{N} f_n \exp[-2\pi i(hu_n + kv_n + lw_n)] \right\} \end{aligned} \tag{7.10}$$

where F_{hkl}^* is the complex conjugate of F_{hkl}. The value of $|F_{hkl}|$ is defined as

$$|F_{hkl}| = \frac{A_{hkl}}{A_e} \tag{7.11}$$

where A_{hkl} is the amplitude of the wave scattered by all the atoms in the unit cell in the (hkl) reflection and A_e is the amplitude of waves scattered by one electron. The structure factor calculation can yield many interesting results. For example, the body-centered cell contains two atoms located at 0 0 0 and ½ ½ ½, and the structure factor is given by

$$F = f\{1 + \exp[\pi i(h + k + l)]\} \tag{7.12}$$

Therefore, $F = 2f$ when $(h + k + l)$ is even, and $F = 0$ when $(h + k + l)$ is odd. This means that any crystal plane with $(h + k + l = 0)$ will miss reflection for crystals with body-centered unit cells. More examples can be found in the literature [8, 9]

7.2.4 Attenuation Factors

The relative intensity is also affected by two attenuation factors: $\exp(-2M_t)$ due to lattice thermal vibrations and $\exp(-2M_s)$ due to weak static displacements. The factor $\exp(-2M_t)$ is also called the Debye temperature factor and is given as

$$M_t = B_t\left(\frac{\sin\theta}{\lambda}\right)^2 \tag{7.13}$$

with $B_t = 8\pi^2\langle\mu_t^2\rangle$, where $\langle\mu_t^2\rangle$ is the mean square projected displacement of the thermal vibration normal to the diffracting planes, and θ is the Bragg angle. The attenuation to the sharp Bragg peak increases with high temperatures and high values of $\sin\theta/\lambda$. The attenuation factor due to a weak static displacement field has the same form

$$M_s = B_s\left(\frac{\sin\theta}{\lambda}\right)^2 \tag{7.14}$$

with $B_s = 8\pi^2\langle\mu_s^2\rangle$, and $\langle\mu_s^2\rangle$ is the mean square projected displacement of the static distortion normal to the diffracting planes, and θ is the Bragg angle. For example, for substitutional solid solutions without severe static distortions introduced by an aging treatment, B_s is given by [17]

$$B_s = 2a^2D_1c(1-c)\left(\frac{1+\nu}{1-\nu}\right)^2\left(\frac{1}{V}\frac{\partial V}{\partial c}\right)^2 \tag{7.15}$$

where a is the lattice parameter, D_1 is a constant related to the crystal type and defect type – for example, $D_1 = 0.0587$ for a FCC structure and $D_1 = 0.0932$ for a BCC structure – c is the atomic fraction of the solute, ν is Poisson ratio, and $\frac{1}{V}\frac{\partial V}{\partial c}$ is the volume size factor. The attenuation of the integrated intensity of the Bragg peak by weak static displacement is always associated with diffuse scattering background [14]. Weak displacement is typically caused by defects in the crystal, such as point defects from interstitial or substitutional atoms, dislocation, stacking fault, short range order clusters, or interphase mismatches. Due to the anisotropic nature of the defects, the diffuse scattering pattern can be better observed by a two-dimensional detector [18, 19]. The macroscopic scale displacement due to residual stresses mainly introduces peak shift instead of diffuse scattering. The intensity attenuation due to weak displacement can be ignored for most powder diffraction applications.

7.3 GEOMETRY AND RESOLUTION

Most conventional X-ray diffractometers have the Bragg–Brentano (BB) parafocusing geometry, in which, the sample surface normal is always a bisector between the incident beam and the diffracted beam. A divergent beam from the X-ray tube passes through soller slits and the divergent slit, then strikes the sample surface with an incident angle θ. The incident X-rays spread over the sample surface with various incident angles in the vicinity of θ. The diffracted rays from the irradiated area leave the sample at an angle 2θ from the corresponding incident rays, pass through the antiscatter slit and soller slits and focus at the receiving slit. A point X-ray

detector can be mounted at the position right after the receiving slit or after a crystal monochromator. The 2θ resolution with the BB geometry is controlled by the size of the slits. Smaller apertures of the divergence slit are used for higher 2θ resolution and larger apertures for fast data collection.

7.3.1 Detector Distance and Resolution

With a two-dimensional X-ray diffraction system, 2θ resolution is achieved by different approaches. A flat 2D detector has the flexibility to be used at different sample-to-detector distances. The detector resolution is determined by the pixel size and point spread function, which were discussed in Chapter 4. For the same detector resolution and detector active area, a higher resolution can be achieved at larger distances, and higher angular coverage at shorter distances. The sample-to-detector distance should be optimized depending on the 2θ range and resolution. When the 2θ range is not enough at the desired detector distance, several frames at sequential 2θ ranges can be collected. The integrated profiles can then be merged to achieve a large 2θ range. Figure 7.1 shows four 2D frames collected from NIST SRM 1976a Alumina Plate with a Bruker D8-Discover™ diffractometer with Våntec-500™ detector at detector distance of 20 cm and displayed with Bruker DIFFRAC.EVA™ software as a merged frame. The slice integration region is defined by two conic lines and two horizontal lines. The diffraction profile integrated from the merged frames is displayed in the bottom.

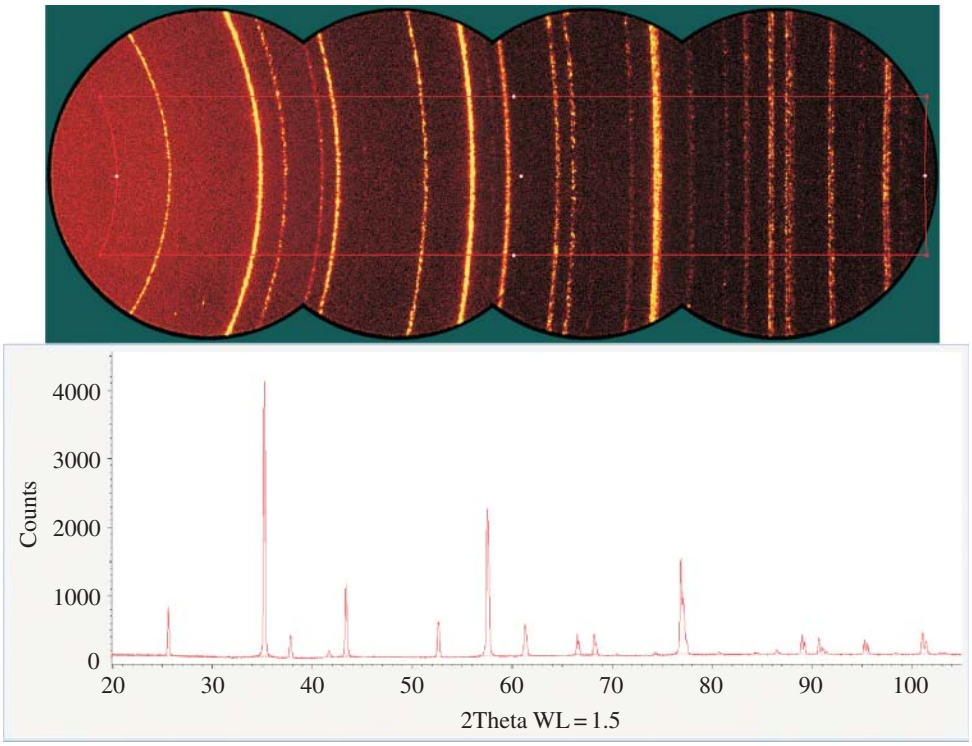


FIGURE 7.1 Diffraction pattern merged from three 2D frames collected from corundum and integrated diffraction profile.

7.3.2 Defocusing Effect

For a two-dimensional X-ray diffraction system with a single incident angle the diffracted X-rays are measured simultaneously in a two-dimensional range, so it is necessary to use an incident angle lower than the minimum 2θ angle. Since the reflected angle cannot always be the same as the incident angle, geometric aberrations are observed. The same is true for a line detector. The defocusing effect occurs when the incident angle is lower than the reflection angle. Figure 7.2 shows the geometry of two-dimensional diffraction in reflection mode with a flat sample. A parallel beam incident to the sample is reflected and measured by a 2D detector. At low incident angles, the incident beam spreads over the sample surface into an area much larger than the size of the original X-ray beam. The observed diffracted beam size is magnified by the defocusing effect if the diffracted beam makes an angle larger than the incident angle. If one looks at the cross-section on the diffractometer plane, the defocusing effect with reflection mode diffraction can be expressed as

$$\frac{B}{b} = \frac{\sin\theta_2}{\sin\theta_1} = \frac{\sin(2\theta - \omega)}{\sin\omega} \tag{7.16}$$

where θ_1 is the incident angle, b is the incident beam size, and B is diffracted beam size. The ratio of B to b is a measurement of the geometric aberration and will be referred to as the defocusing factor. In principle, defocusing occurs only when (B/b) is larger than 1. The reflected beam is actually focused to the detector when $\theta_2 < \theta_1$. The defocusing effect occurs when $\theta_2 > \theta_1$ and the defocusing factor increases with increasing θ_2 or decreasing θ_1. The maximum defocusing appears at $\theta_2 = 90°$. For the θ-2θ configuration, the incident angle $\omega\,(=\theta_1)$ is used in the equation.

For the Bragg–Brentano parafocusing geometry with the divergent slit and receiving slit of the same size, the defocusing factor is always 1. With an area detector (or linear) detector, the incident beam is fixed for a range of 2θ angles, and the defocusing factor varies with the 2θ angle. A cylindrical detector, like the Debye-Scherrer camera, can collect a diffraction pattern in a large 2θ range. However, the defocusing effect prevents it from being used for a large 2θ range for a flat sample. Figure 7.3 gives a comparison between the flat detector and the cylindrical detector. Figure 7.3(a) shows a cylindrical detector being used to collect a diffraction pattern from a flat sample for a 2θ range of 5° to 80°. The incident angle must be kept at 5° or lower. Figure 7.3(b) shows a flat detector being used to collect the diffraction pattern in the same 2θ range. In order to minimize the defocusing effect, the data collection is done at four different incident angles (5°, 15°, 25°, 35°) with four corresponding detector

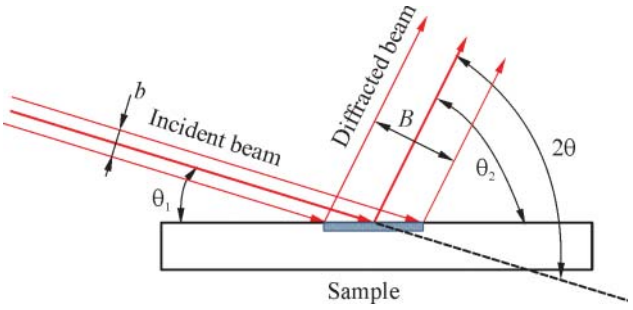


FIGURE 7.2 Geometry aberration of XRD[2] in reflection mode.

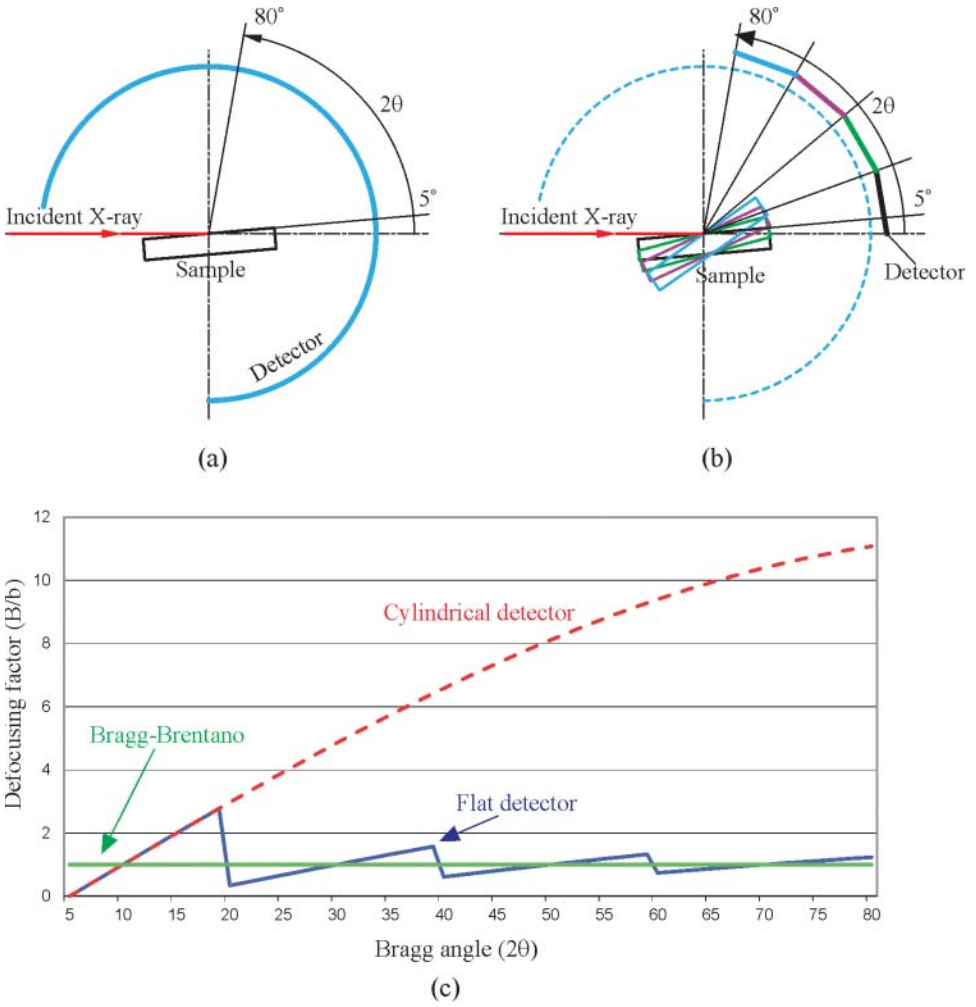


FIGURE 7.3 Defocusing effects: (a) 5° incident angle with cylindrical detector, (b) various incident angles (5°, 15°, 25°, 35°) and detector swing angles (10°, 30°, 50°, 70°), (c) comparison of defocusing factors.

swing angles (10°, 30°, 50°, 70°). Figure 7.3(c) is a comparison of the defocusing factors of both configurations. The horizontal blue line with defocusing factor $(B/b) = 1$ represents the situation with the Bragg–Brentano geometry. The defocusing factor for cylindrical detector (red broken line) continues to increase with 2θ angle up to (B/b) = 11. That means that the 2θ resolution would be 10 times worse than the BB geometry. For the diffraction pattern collected with a flat detector in four steps as in Figure 7.3(b), the defocusing factor fluctuated around 1, with the worst value being less than 3. By properly selecting the data collection strategy, the defocusing effect, like the 2θ resolution, can be controlled within a reasonable range. A large 2θ range cylindrical detector is not recommended unless dealing with a very small sample, similar to samples used for Debye–Scherrer cameras, such as thin wire or powder in a capillary. If a large 2θ range is required for a flat sample in reflection mode, it is always desirable to collect several frames at different incident (θ_1 or ω) angles for different 2θ ranges so as to improve the 2θ resolution.

7.3.3 Transmission Mode Diffraction

Geometric aberrations in the transmission mode have a very different effect. Figure 7.4 shows the geometric aberration of two-dimensional diffraction in transmission mode with a thin flat sample. A parallel incident beam enters the sample perpendicular to the sample surface and the diffracted beams exit the sample from the opposite surface of the sample. The beam size aberration can be expressed as

$$\frac{B}{b} = \cos 2\theta + \frac{t}{b}\sin 2\theta \tag{7.17}$$

where t is the sample thickness. It can be proved that when the sample thickness is less than 10% of the beam size, the defocusing factor (B/b) is equal to or less than 1 for all 2θ angles. The thickness of the transmission sample is typically negligible compared to the incident beam size ($t << b$), therefore $(B/b) = \cos 2\theta \leq 1$. There should be no defocusing effect at all when the incident beam is perpendicular to the sample surface.

Figure 7.5 is a comparison between reflection mode and transmission mode diffraction with data frames collected from corundum powder. Figure 7.5(a) is the data frame collected with a 0.5 mm collimator and a 5° incident angle. The diffraction rings and the integrated profile show severe peak broadening, especially at large 2θ angles. Figure 7.5(b) is the data frame collected with the same beam size in transmission mode. The diffraction rings and the integrated profile do not show the defocusing effect. Therefore, the transmission pattern has significantly better 2θ resolution. Transmission mode diffraction also has other advantages. For instance, the air scattering from the primary beam is blocked by the sample from reaching the detector, therefore the background at low angles is also lower for transmission diffraction. However, the transmission mode diffraction data can only be collected from samples with limited thickness. As given in Chapter 6, the maximum scattering intensity is achieved at low 2θ angles with the sample thickness of $t = 1/\mu$, where μ is the linear absorption coefficient. The scattering intensity drops dramatically when the thickness increases. Transmission mode diffraction becomes impractical for cases where the samples cannot be fabricated with the required thickness. For loose powder samples, the holder may attenuate the incident beam and introduce an amorphous background as is shown in Figure 7.5(b).

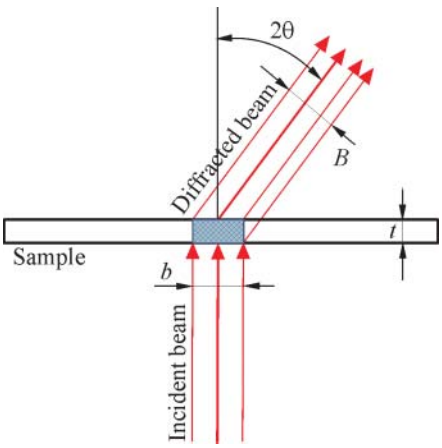


FIGURE 7.4 Geometry aberration of XRD[2] in transmission mode.

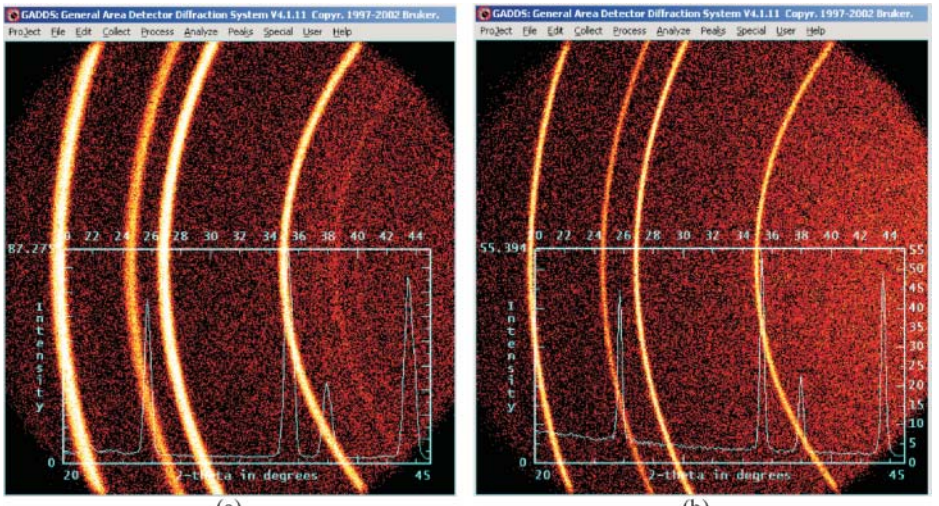


FIGURE 7.5 Diffraction pattern from corundum: (a) reflection mode diffraction with 5° incident angle, (b) transmission mode diffraction with perpendicular incident beam.

7.4 SAMPLING STATISTICS

In powder X-ray diffraction, the number of crystallites contributing to each reflection must be sufficiently large to generate reproducible integrated peak intensities. The standard deviation of the integrated peak intensity due to the number of contributing crystallites (N_s) is given by $\sqrt{N_s}$, assuming a Poisson distribution and equal intensity contribution from all participant crystals. A more revealing expression of the measurement precision can be given as the percent standard deviation

$$\sigma\% = \frac{100}{\sqrt{N_s}}\% \tag{7.18}$$

A larger number of contributing crystallites gives better precision or sampling statistics (also referred to as particle statistics). Sampling statistics are determined by both the sample structure and instrumentation. For a perfect random powder sample, the number of contributing crystallites for a measured line can be given as

$$N_s = p_{hkl} \cdot \frac{Vf_i}{v_i} \cdot \frac{\Omega}{4\pi} \tag{7.19}$$

where p_{hkl} is the multiplicity of the diffracting planes, V is the effective sampling volume, f_i is the volume fraction of the measuring crystallites ($f_i = 1$ for single phase materials), v_i is the volume of individual crystallites, and Ω is the angular window of the instrument in solid angle. The multiplicity term, p_{hkl}, effectively increases the number of crystallites contributing to the integrated intensity from a particular set of (hkl) planes. The volume of individual crystallites, v_i, is an average of various crystallite sizes or assumes that all crystallites have the same volume. Assuming sphere-shaped particles, the term v_i can be replaced by the particle size, $v_i = \pi d_i^3/6$, and d_i is

the diameter of the crystallite particles. The combination of the effective sampling volume and the angular window makes up the instrumental window, which determines the total volume of polycrystalline material making a contribution to a Bragg reflection. In two-dimensional X-ray diffraction, the instrumental window is not only determined by the incident beam size and divergence, but also by the detective area and distance of the area detector (γ angular coverage).

Sampling statistics should not be confused with the counting statistics covered in Chapter 4. Both are related and important for diffraction data quality, but can be influenced by different factors. For instance, increasing the brilliance of the X-ray source will improve counting statistics, but not necessarily sampling statistics, assuming the incident beam profile and size are the same. This is especially true in transmission mode when the effective diffraction volume is not affected by the penetration depth. Some of the following factors, such as effective sampling volume, angular window, and virtual oscillation, may improve both sampling statistics and counting statistics. Sample oscillation may improve the sampling statistics, but not necessarily the counting statistics. For the same diffraction condition with the same sample, the peak from the crystalline planes with high multiplicity will have better counting statistics and sampling statistics. Increasing the data collecting time and detector sensitivity will improve the counting statistics, but not necessarily the sampling statistics.

7.4.1 Effective Sampling Volume

The effective sampling volume is also referred as the effective irradiated volume in some literature. However, effective sampling volume seems to be a more appropriate term for two-dimensional diffraction. In conventional diffraction the effective irradiated volume can be uniquely calculated from the given incident angle and 2θ angle. In Bragg–Brentano geometry, the effective irradiated volume is a constant, but in two-dimensional diffraction, several 2θ angles at various γ angles are measured simultaneously, and the effective sampling volume is a function of both 2θ and γ. It can be hard to comprehend that the same instrument setup can result in variable irradiated volumes. The effective sampling volume can be obtained by multiplying the beam cross-section area with the transmission coefficients given in the Chapter 6 for absorption corrections. For the Bragg–Brentano geometry, it is given as

$$V = A_o A_{BB} = \frac{A_o}{2\mu} \tag{7.20}$$

where A_o is the cross-sectional area of the incident beam, $A_{BB} = 1/(2\mu)$ is the transmission coefficient for BB geometry, and μ is the linear absorption coefficient. The cross-sectional area A_o is a constant only if there is no divergence in the incident and diffracted beams. That means that the divergence slit and receiving slit have the same or smaller aperture size as the focal spot. For divergent beams commonly used with Bragg–Brentano geometry, the cross-section area A_o should be measured near the sample surface or given by the irradiated area, A_i, at a particular 2θ angle as $A_0 = A_i/\sin\theta$. For two-dimensional X-ray diffraction, the incident beam cross-section area can be considered a constant most of the time because of low divergence. For XRD^2 in reflection mode, the effective sampling volume is given by

$$V = \frac{A_o \cos\eta \left\{1 - \exp\left[-\mu t\left(\frac{1}{\cos\eta} + \frac{1}{\cos\zeta}\right)\right]\right\}}{\mu(\cos\eta + \cos\zeta)} \tag{7.21}$$

with $\cos\eta = \sin\omega\cos\psi$ and $\cos\zeta = -\cos 2\theta \sin\omega\cos\psi - \sin 2\theta \sin\gamma\cos\omega\cos\psi - \sin 2\theta \cos\gamma\sin\psi$ from equations (6.95) and (6.96), and t is the thickness of the sample. In XRD^2,

a round point beam is typically used, so the beam cross-section $A_o = \frac{1}{4}\pi b^2$ where b is the size of the incident beam in diameter. For a thick plate or material with a very high linear absorption coefficient, the transmission through the sample thickness is negligible, so the above equation becomes

$$V = \frac{\pi b^2 \cos\eta}{4\mu(\cos\eta + \cos\zeta)} \tag{7.22}$$

For XRD[2] in transmission mode and with the incident beam perpendicular to the sample surface, we have

$$V = \frac{\pi b^2 \cos 2\theta \left[\exp(-\mu t) - \exp\left(-\frac{\mu t}{\cos 2\theta}\right)\right]}{4\mu(1 - \cos 2\theta)} \tag{7.23}$$

For very small 2θ angles, the effective sampling volume is given by

$$V = \frac{1}{4}\pi b^2 t \exp(-\mu t) \tag{7.24}$$

The effective sampling volume reaches a maximum for transmission mode diffraction when $t = 1/\mu$. It can be observed from the above five equations that the effective sampling volume is proportional to the beam cross-sectional area and is lower for materials with higher linear absorption coefficients. In the above equations, a parallel incident beam was assumed. When a divergent (or convergent) incident beam is used, the incident beam size should be measured at the sample location (instrument center).

7.4.2 Angular Window

The angular window of the instrument is another factor that determines the number of crystallites contributing to a Bragg reflection. The angular window is given in solid angle. For a random polycrystalline material, the fraction contributing to a Bragg reflection is given by the ratio of the angular window of the instrument, Ω, divided by the full solid angle, 4π. Figure 7.6 illustrates the angular window of the instrument. The incident beam ($\mathbf{s_0}/\lambda$) has a divergence angle of β_1 within the diffraction plane and β_2 in the perpendicular direction. Since only the crystallites having a set of (hkl) planes perpendicular to the diffraction vector ($\mathbf{H}$) satisfy the Bragg condition, the angular

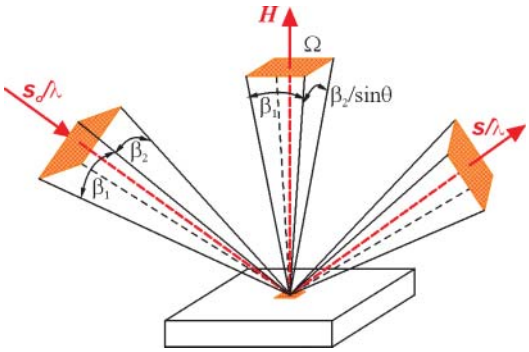


FIGURE 7.6 Angular window of instrument from the incident beam convergence.

window is measured as the solid angle containing all the diffraction vectors corresponding to the incident beam divergence, which is given by

$$\Omega = \beta_1\beta_2/\sin\theta = \beta^2/\sin\theta \tag{7.25}$$

where $\beta = \beta_1 = \beta_2$ is for the case that incident beam divergences in both direction are the same.

In the above equation, the angular window is calculated only with the contribution of the incident beam divergence. The sampling statistics increases with increasing incident beam divergence. However, there is a limit on the beam divergence. The angular window introduces an instrumental broadening effect on the Bragg peak, which convolutes with the other part of broadening effect. The divergence angle of the incident beam should be smaller than the required 2θ resolution. We have so far ignored the mosaicity of the crystallites. The angular window with contributions from both the instrumental broadening and the particle broadening should be given as

$$\Omega = (\beta_1 + \varepsilon)(\beta_2/\sin\theta + \varepsilon) \tag{7.26}$$

where ε is the FWHM of the rocking angle of the crystallites.

7.4.3 Virtual Oscillation

For XRD^2, the angular window is not only determined by the incident beam divergence, but also significantly increased by γ-integration. When γ-integration is used to generate the diffraction profile, it actually integrates the data collected in a range of various diffraction vectors. Figure 7.7 shows the relation between the γ-integration range, $\Delta\gamma$, and the angle between two extreme diffraction vectors within the γ-integration range. The incident beam vector is $\mathbf{s_0}/\lambda$. The diffracted beam vectors at the two extremes of the γ-integration range are $\mathbf{s_1}/\lambda$ and $\mathbf{s_2}/\lambda$ respectively, and the two diffraction planes (P_1 and P_2) are defined by the incident beam and the two diffracted beams respectively. The angle between the two diffraction planes is $\Delta\gamma$. The unit diffraction vectors for the two extreme diffraction vectors ($\mathbf{H_1}$ and $\mathbf{H_2}$) are respectively:

$$\mathbf{h}_{L1} = \begin{bmatrix} -\sin\theta \\ -\cos\theta\sin\gamma_1 \\ -\cos\theta\cos\gamma_1 \end{bmatrix} \quad \text{and} \quad \mathbf{h}_{L_2} = \begin{bmatrix} -\sin\theta \\ -\cos\theta\sin\gamma_2 \\ -\cos\theta\cos\gamma_2 \end{bmatrix}$$

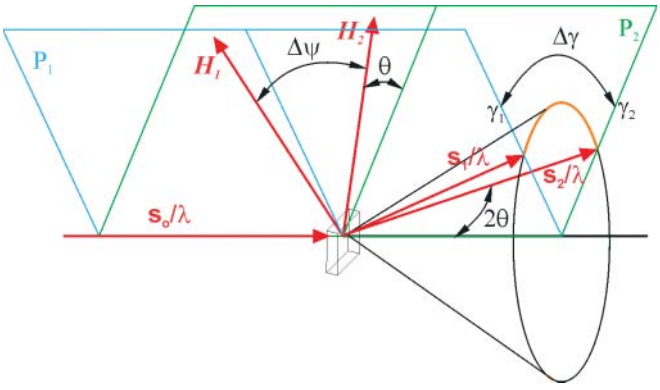


FIGURE 7.7 Relation between the γ-range, $\Delta\gamma$, and the virtual oscillation angle, $\Delta\psi$.

Then we have

$$\cos\Delta\psi = \mathbf{h}_{L1}\cdot\mathbf{h}_{L2} = \sin^2\theta + \cos^2\theta\sin\gamma_1\sin\gamma_2 + \cos^2\theta\cos\gamma_1\cos\gamma_2$$

Solving the above equation and introducing $\Delta\gamma = |\gamma_2 - \gamma_1|$, we obtain the angle between the two extreme diffraction vectors as

$$\boxed{\Delta\psi = 2\arcsin[\cos\theta\sin(\Delta\gamma/2)]} \tag{7.27}$$

Apparently, the above equation can also be used to calculate the angle between two diffracting crystalline planes if the corresponding two diffraction spots are observed in the same diffraction ring. Since the effect of γ-integration on sampling statistics is equivalent to the angular oscillation on the ψ axis in a conventional diffractometer, the effect is referred to as virtual oscillation and $\Delta\psi$ is the virtual oscillation angle. In conventional oscillation, mechanical movement may result in some sample position error. Since there is no actual physical movement of the sample stage during data collection, virtual oscillation can avoid this error.

The angular window with the contribution of both the incident beam divergence and the virtual oscillation is given by

$$\Omega = \beta\Delta\psi = 2\beta\arcsin[\cos\theta\sin(\Delta\gamma/2)] \tag{7.28}$$

where β is the divergence of the incident beam. Increasing the divergence angle β may introduce instrumental broadening which deteriorates the 2θ resolution, but virtual oscillation improves sampling statistics without introducing instrumental broadening. Considering the contribution of the crystallite mosaicity, the angular window can be given by

$$\Omega = (\beta + \varepsilon)\{\arcsin[\cos\theta\sin(\Delta\gamma/2)] + \varepsilon\} \tag{7.29}$$

Since the rocking angle of the crystallites is typically much less than the instrumental angular window, its effect on the angular window is negligible.

7.4.4 Sample Oscillation

In the case of materials with a large grain size or preferred orientation, or of microdiffraction with a small X-ray beam size, it is difficult to determine the 2θ position due to poor counting statistics. Increasing the beam size or divergence may become impractical for a limited sample size and required 2θ resolution. In these cases, some kind of sample oscillation, either by translation or rotation, can bring more crystallites into the diffraction condition. Translational oscillation is typically done by moving the sample in directions parallel to the sample surface. For reflection mode diffraction, it is the XY plane in the sample space coordinates. The oscillation can be linear in one direction, scanning in a region, or follow the trace of the powder sample on a filtration plate. Translational oscillation increases the effective sampling volume by summing the effective sampling volume at each sample location. For linear oscillation with reflection mode diffraction, due to beam spread on the sample surface along the projected line of the incident beam (X direction), oscillation in the perpendicular direction (Y direction) can achieve a better gain on sampling statistics. Translational oscillation is very effective in improving the sampling statistics of the sample with a large grain size or small beam size, but has very limited or no effect for samples with a preferred orientation. Therefore, translational oscillation may be used for texture data collection without smearing the pole-density distribution.

Angular oscillation is an enhancement to the angular window of the instrument. The effect is that the angular window scans over the oscillation angle. Any of the three rotation angles (ω,ψ,ϕ) or their combinations can be used as oscillation angles. Angular oscillation can effectively improve the sampling statistics for both large grain size and preferred orientation. As an extreme example, a powder diffraction pattern can be generated from a single crystal sample if a sufficient angular window can be achieved by sample rotation as a way to simulate the Gandolfi camera [20].

Figure 7.8 shows three diffraction frames from Si powder (NIST SRM 640c) [21] collected on a Bruker GADDS diffractometer in transmission mode with a Cu sealed tube, graphite monochromator, 0.2 mm collimator, and Hi-Star™ MWPC detector. The Si (100) ring is observed on the selected frame region. Figure 7.8(a) is for the sample in a still position with the X-ray beam perpendicular to the sample surface. The multiplicity of the Si (100) planes is only six for the cubic crystal structure. A beam diameter of 0.2 mm results in a small sampling volume. A spotty diffraction ring from Si (100) planes is observed due to poor sampling. Figure 7.8(b) is the frame collected with an oscillation within an area of $\Delta X \cdot \Delta Y = 1\ mm^2$, which increases the total sampling volume by at least a factor of 25. A smooth diffraction ring is observed due to this improved sampling. Figure 7.8(c) is the frame collected with an angular oscillation of $\Delta\omega = \pm 10°$. The divergence angle $\beta = 0.16°$, given in Chapter 3. The ω oscillation of 20° increases the total instrumental angular window by a factor of 125, hence a smooth diffraction ring is observed.

Figure 7.8 also shows the integrated (100) peak profile on each frame. The γ-integration range is 40° (from $\gamma = -70°$ to $\gamma = -110°$). Although Figure 7.8(a) has a very spotty ring, the integrated peak profile is as smooth and as accurate as the other two profiles integrated from 2D frames because of the virtual oscillation effect. The peak $2\theta = 28.5°$, the virtual oscillation angle $\Delta\psi$ is then given by equation (7.27) as 38.7°. Considering that the incident beam divergence is $\beta = 0.16°$, the virtual oscillation has improved the instrumental angular window by a factor of 240. Therefore, very good sampling statistics can be achieved without an actual oscillation. Comparing the three γ-integrated profiles from the three frames, it can be concluded that sample oscillations in

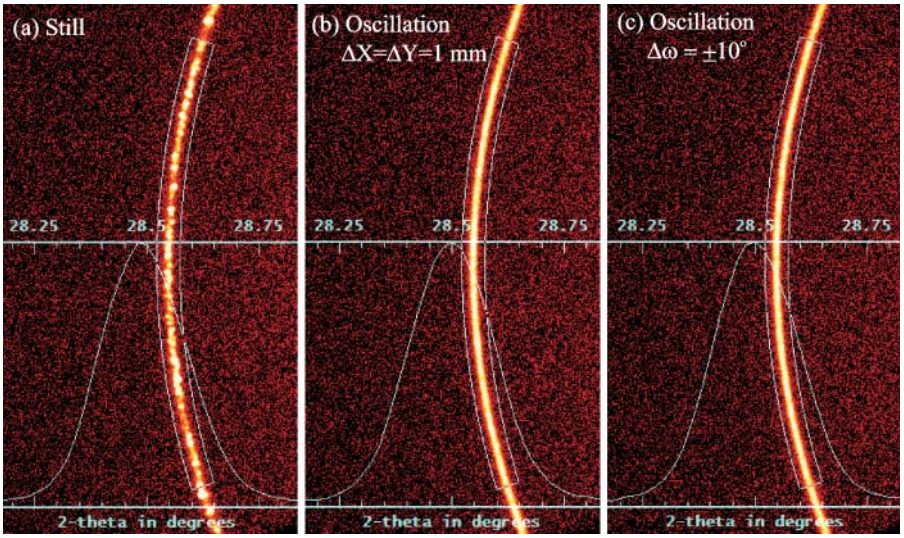


FIGURE 7.8 Diffraction frames from Si powder (NIST SRM 640c) collected on Bruker GADDS in transmission mode: (a) sample in still position, (b) sample oscillation in an area of $\Delta X = \Delta Y = 1 mm^2$, (c) sample angular oscillation with $\Delta\omega = \pm 10°$.

this case are not completely necessary since the virtual oscillation has already improved sampling statistics sufficiently. The effect of either translation oscillation or angular oscillation for this sample is mainly cosmetic. Virtual oscillation is one of the most important advantages of using XRD^2 for phase identifications.

7.5 PREFERRED ORIENTATION EFFECT

Phase identification studies by XRD are typically carried out on either ideal powders or single crystals. Textured materials are often avoided because relative intensities deviate from theoretical calculations or standard diffraction databases such as the PDF files. In this chapter so far, we have assumed that the orientation distribution of crystallites in the sample is perfectly random. In practice, a perfectly random sample is very hard to fabricate and most powder samples have a preferred orientation (texture) to a certain extent. The effect of the texture on the relative integrated intensities of the diffraction pattern is dependent on the geometry of the diffractometer. Discrepancies in the relative peak intensities between conventional diffraction and XRD^2 are largely due to the texture effect. The nature of the discrepancies will be analyzed and the correction algorithms are given in this section.

7.5.1 Relative Intensity with Texture

The integrated intensity diffracted from polycrystalline materials with texture is given by

$$\mathbf{I}_{hkl} = k_I \frac{p_{hkl}}{v^2}(LPA)\lambda^3 F_{hkl}^2 g_{hkl}(\alpha,\beta)\exp(-2M_t - 2M_s) \tag{7.30}$$

where $g_{hkl}(\alpha,\beta)$ is the normalized pole density distribution function. Each pole direction (equivalent to the diffraction vector direction) is defined by the radial angle α and azimuthal angle β. For a random powder sample, $g_{hkl}(\alpha,\beta) \equiv 1$. The normalized pole density distribution function is given by

$$g_{hkl}(\alpha,\beta) = \frac{2\pi P_{hkl}(\alpha,\beta)}{\int_0^{2\pi}\int_0^{\frac{\pi}{2}} P_{hkl}(\alpha,\beta)\cos\alpha d\alpha d\beta} \tag{7.31}$$

where $P_{hkl}(\alpha,\beta)$ is the pole density distribution function (or pole figure intensity) of the Bragg reflection (hkl) as will be defined in Chapter 8. The mapping of this function on the equatorial plane by stereographic projection is called a pole figure. The integration in the above equation is over the hemisphere above the equatorial plane, assuming the pole figure is at least symmetrical about the plane. The average of $g_{hkl}(\alpha,\beta)$ over the full sphere must be the same as the value for random powder, i.e. equal to unity,

$$\langle g_{hkl}(\alpha,\beta)\rangle = \frac{\int_0^{2\pi}\int_0^{\frac{\pi}{2}} g_{hkl}(\alpha,\beta)\cos\alpha d\alpha d\beta}{\int_0^{2\pi}\int_0^{\frac{\pi}{2}} \cos\alpha d\alpha d\beta} = 1 \tag{7.32}$$

or

$$\int_0^{2\pi}\int_0^{\frac{\pi}{2}} g_{hkl}(\alpha,\beta)\cos\alpha d\alpha d\beta = 2\pi \tag{7.33}$$

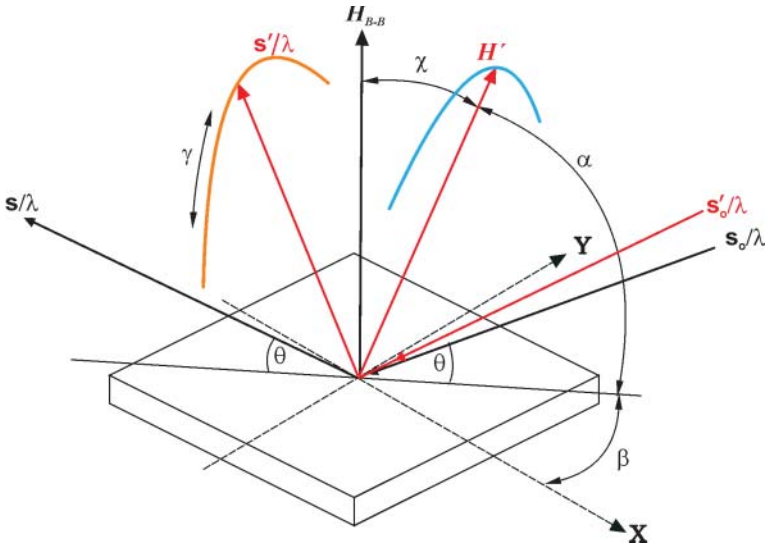


FIGURE 7.9 Relationship between the diffraction vector and pole density function for Bragg–Brentano geometry and XRD^2 geometry.

Figure 7.9 illustrates the relationship between the diffraction vector and the pole density function for the Bragg–Brentano geometry and the XRD^2 geometry. For the BB geometry, the vector of the incident beam is $\mathbf{s_0}/\lambda$ and the diffracted beam is $\mathbf{s}/\lambda$, and the diffraction vector, $\mathbf{H_{B\text{-}B}}$, is always perpendicular to the sample surface. The pole density in the sample normal direction, $g_{hkl}\left(\frac{\pi}{2},0\right)$, should always be used in the integrated intensity equation for the BB geometry. When $\alpha = \pi/2$, $g_{hkl}\left(\frac{\pi}{2},\beta\right)$ is independent of β, hence, we use $g_{hkl}\left(\frac{\pi}{2},0\right)$. With a strong texture, it is possible that the pole density of certain (hkl) reflections in the sample normal direction is very low or even approaches zero ($g_{hkl}\left(\frac{\pi}{2},0\right) \to 0$). In this case the peak disappears from the diffraction pattern collected in BB geometry.

In XRD^2, a single incident beam vector $\mathbf{s_0'}/\lambda$ may produce several diffraction rings. Each diffraction ring consists of continuously distributed diffracted beams, where $\mathbf{s}'/\lambda$ marks one diffracted beam. The corresponding diffraction vectors also form a ring with $\mathbf{H}'$ representing one of the diffraction vectors. The relationship between the pole figure angles (α,β), the sample orientation (ω,ψ,ϕ), and diffraction cone $(2\theta,\gamma)$ is given by

$$\begin{aligned} \alpha &= \sin^{-1}|h_3| = \cos^{-1}\sqrt{h_1^2+h_2^2}, \\ \beta &= \pm\cos^{-1}\frac{h_1}{\sqrt{h_1^2+h_2^2}} \quad \begin{cases} \beta \geq 0^\circ & if \quad h_2 \geq 0 \\ \beta < 0^\circ & if \quad h_2 < 0 \end{cases} \end{aligned} \tag{7.34}$$

where $\{h_1, h_2, h_3\}$ are components of the unit vector of the diffraction vector $\mathbf{H}$, which can be found in Chapter 2. At a particular sample orientation, the normalized pole density distribution function $g_{hkl}(\alpha,\beta)$ can be expressed as $g_{hkl}(\theta,\gamma)$ when (α,β) and $(2\theta,\gamma)$ maintain the relation given by equation (7.34). The diffraction profiles from 2D frames are produced by γ-integration, therefore the integrated intensity of a peak should be given as

$$\mathbf{I}_{hkl} = k_I \frac{p_{hkl}}{v^2}(LPA)\lambda^3 F_{hkl}^2 \langle g_{hkl}(\Delta\gamma)\rangle \exp(-2M_t - 2M_s) \tag{7.35}$$

where $\langle g_{hkl}(\Delta\gamma)\rangle$ is the average normalized pole density function within the γ-integration range and

$$\langle g_{hkl}(\Delta\gamma)\rangle = \frac{\int_{\gamma_1}^{\gamma_2} g_{hkl}(\theta,\gamma)\gamma d\gamma}{\gamma_2 - \gamma_1} \tag{7.36}$$

where θ is a constant in the integration, γ_1 and γ_2 are lower and upper limits of the γ-integration. Since the texture effect is an average over a select γ range, the possibility of missing a peak due to strong texture is much smaller with an XRD^2 instrument than with the conventional BB diffractometer. The texture effect on the integrated peak intensity from XRD^2 can be corrected by

$$\mathbf{I}^c_{hkl} = \frac{\mathbf{I}^m_{hkl}}{\langle g_{hkl}(\Delta\gamma)\rangle} \tag{7.37}$$

where $\mathbf{I}^c_{hkl}$ is the corrected intensity, which is equivalent to the intensity from a random sample. $\mathbf{I}^m_{hkl}$ is the measured intensity from XRD^2 including the effect of texture. Assuming the pixel corrections to the Bragg–Brentano equivalent pixel intensities have been done according to the algorithms given in Table 6.3, the integrated peak intensities can be corrected to the Bragg–Brentano equivalent with a texture effect by

$$\mathbf{I}^{BB}_{hkl} = \frac{g_{hkl}\left(\frac{\pi}{2},0\right)\mathbf{I}^m_{hkl}}{\langle g_{hkl}(\Delta\gamma)\rangle} \tag{7.38}$$

7.5.2 Intensity Correction on Fiber Texture

The correction of relative intensities by the normalized pole density distribution function $g_{hkl}(\alpha,\beta)$ requires the orientation distribution function (ODF) to be determined so that $g_{hkl}(\alpha,\beta)$ for all (*hkl*) peaks can be calculated. The determination of the ODF can be very time-consuming for a general texture. The ODF based on the three Eulerian angles can be significantly simplified, since the dependence on ϕ angle vanishes for fiber texture. The generally three-dimensional ODF then becomes two-dimensional, and usually a two-dimensional pole-figure becomes one-dimensional, as a so-called fiber texture plot (FTP) or simply fiber plot [22]. The pole density functions for each (*hkl*) peak can be determined by a series of harmonic functions. Compared to the general pole-figure with three-dimensional ODF, the pole density distribution functions for a fiber texture can be determined with much less experimental data and calculation effort. The effect of the texture can be corrected by the pole density distribution function of a fiber texture as long as either the sample has a fiber texture or by spinning the sample on the ϕ axis during the data collection. A pseudo-fiber texture is formed by spinning the sample during the data collection.

The fiber texture is mostly observed in two types of materials. One type of material is metal wires or rods formed by drawing, swaging, or extrusion. The other type is thin films formed by physical or chemical vapor deposition (PVD or CVD) or other deposition methods. The crystallites in materials with fiber texture have orientation distributions with a rotational symmetry about an axis, called the fiber axis. The fiber axis is the wire axis for a wire and normal to the sample surface for thin films. Due to the symmetry above the fiber axis, the effects of fiber texture on the integrated peak intensity can be treated with a simpler algorithm [15, 23]. For samples with fiber texture or artificially formed by spinning, the pole density function is conveniently expressed as

a function of a single variable, $g_{hkl}(\chi)$. Here, χ is the angle between the sample normal and pole direction as shown in Figure 7.9.

$$\chi = 90^\circ - \alpha \tag{7.39}$$

and

$$\chi = \cos^{-1} |h_3| \tag{7.40}$$

The pole density function for fiber texture can be expressed as a fiber plot. The fiber plot is the radial section of the pole figure, since the pole figure for fiber texture is symmetric above the fiber axis. When a fiber plot or pole figure is not available, the pole density function for a fiber texture can be calculated from discrete intensity measurements by fitting to a series of normalized Legendre polynomials,

$$g_{hkl}(\chi) = \sum_{n=0}^{\infty} G_n^{hkl} \bar{P}_n(\cos\chi) \tag{7.41}$$

where $\bar{P}_n(\cos\chi)$ are normalized Legendre polynomials and G_n^{hkl} are factors given by the coefficients of the orientation function. The series in the above equation can be truncated at a certain order of n since it is uniformly convergent. Due to symmetry, many terms in the above series vanish. The 0-th order term, $G_0^{hkl}\bar{P}_0(\cos\chi) = 1$. For a limited order N, we can write the series as

$$g_{hkl}(\chi) = 1 + \sum_{n=1}^{N} \sum_{m=0}^{n} C_{hkl}^{nm}(\chi) A_{nm} \tag{7.42}$$

where A_{nm} are the coefficients of the orientation function and $C_{hkl}^{nm}(\chi)$ are the coefficients determined by the crystal lattice symmetry and the order of the term in the series. There is limited number of coefficients for each order ($m \leq n$). For cubic crystallites, all odd order A_{nm} vanish and $A_{nm} \neq 0$ only if m is an integral multiple of four. Also, not all non-vanishing coefficients A_{nm} are independent. By combining the interdependent coefficients, we can obtain

$$g_i(\chi) = 1 + \sum_{j=1}^{q} C_{ij}(\chi) A_j \tag{7.43}$$

where i designates different (hkl) planes, j designates different nm combinations for non-vanishing independent coefficients, q is the total number of independent coefficients, and $C_{ij}(\chi)$ are the coefficients independent of the orientation function coefficients A_j. The measured integrated intensity for a peak at a particular χ angle can be expressed as

$$I_{hkl}^m(\chi) = kI_{hkl}^c g_{hkl}(\chi) = kI_{hkl}^c g_i(\chi) \tag{7.44}$$

where k is the scaling factor, $I_{hkl}^m(\chi)$ is the measured integrated intensity, and I_{hkl}^c is the calculated intensity for a random powder. Combining equations (7.43) and (7.44), we have

$$\sum_{j=1}^{q} C_{ij}(\chi) A_j - \frac{1}{k} \frac{\boldsymbol{I}_{hkl}^m(\chi)}{\boldsymbol{I}_{hkl}^c} = -1 \tag{7.45}$$

Table 7.2 Coefficients C_{hkl}^{nm} and $C_{ij}(\chi)$ to the Order of n = 16 for Cubic Structure

$C_{hkl}^{nm} = C_{ij}$	Expression as a function of (hkl) and χ
$C_{hkl}^{4,0} = C_{i1}$	$= \frac{4\pi\bar{P}_4(\cos\chi)}{(h^2+k^2+l^2)^2}\{0.375(h^2+k^2+l^2)^2 + 0.625(h^4+k^4+l^4) - 3.75(h^2k^2+l^2h^2+k^2l^2)\}$
$C_{hkl}^{6,0} = C_{i2}$	$= \frac{4\pi\bar{P}_6(\cos\chi)}{(h^2+k^2+l^2)^3}\{-0.3123(h^2+k^2+l^2)^3 + 1.3125(h^6+k^6+l^6)$ $- 6.5625(h^4k^2+h^4l^2+k^4l^2+k^4h^2+l^4h^2+l^4k^2) + 91.875h^2k^2l^2\}$
$C_{hkl}^{8,0} = C_{i3}$	$= \frac{4\pi\bar{P}_8(\cos\chi)}{(h^2+k^2+l^2)^4}\{0.2734375(h^2+k^2+l^2)^4 + 0.7265625(h^8+k^8+l^8)$ $- 15.09375(h^6k^2+h^6l^2+k^6l^2+k^6h^2+l^6h^2+l^6k^2)$ $- 3.28125(h^4k^2l^2+k^4l^2h^2+l^4h^2k^2) + 33.359375(h^4k^4+l^4h^4+k^4l^4)\}$
$C_{hkl}^{10,0} = C_{i4}$	$= \frac{4\pi\bar{P}_{10}(\cos\chi)}{(h^2+k^2+l^2)^5}\{-0{,}2461(h^2+k^2+l^2)^5 + 1.2461(h^{10}+k^{10}+l^{10})$ $- 21.2695(h^8k^2+h^8l^2+k^8l^2+k^8h^2+l^8h^2+l^8k^2)$ $+ 23.4609(h^6k^4+h^6l^4+k^6l^4+k^6h^4+l^6h^4+l^6k^4)$ $+ 508.9219(h^6k^2l^2+k^6l^2h^2+l^6h^2k^2) - 622.6172(h^4k^4l^2+k^4l^4h^2+l^4h^4k^2)\}$
$C_{hkl}^{12,0} = C_{i5}$	$= \frac{4\pi\bar{P}_{12}(\cos\chi)}{(h^2+k^2+l^2)^6}\{0.2256(h^2+k^2+l^2)^6 + 0.7744(h^{12}+k^{12}+l^{12})$ $- 34.3537(h^{10}k^2+h^{10}l^2+k^{10}l^2+k^{10}h^2+l^{10}h^2+l^{10}k^2)$ $+ 182.241(h^8k^4+h^8l^4+k^8l^4+k^8h^4+l^8h^4+l^8k^4)$ $+ 364.482(h^8k^2l^2+k^8l^2h^2+l^8h^2k^2) - 293.2617(h^6k^6+l^6h^6+k^6l^6)\}$ $- 879.7851(h^6k^4l^2+h^6l^4k^2+k^6l^4h^2+k^6h^4l^2+l^6h^4k^2+l^6k^4h^2) + 4310.9162h^4k^4l^4\}$
$C_{hkl}^{12,4} = C_{i6}$	$= \frac{4\pi\bar{P}_{12}(\cos\chi)}{(h^2+k^2+l^2)^6}\{118.6522(h^8k^4+h^8l^4+k^8l^4+k^8h^4+l^8h^4+l^8k^4)$ $+ 711.8822(h^8k^2l^2+k^8l^2h^2+l^8h^2k^2) - 332.20512(h^6k^6+l^6h^6+k^6l^6)$ $+ 1661.0289(h^6k^4l^2+h^6l^4k^2+k^6l^4h^2+k^6h^4l^2+l^6h^4k^2+l^6k^4h^2)$ $- 8305.0741h^4k^4l^4\}$
$C_{hkl}^{14,0} = C_{i7}$	$= \frac{4\pi\bar{P}_{14}(\cos\chi)}{(h^2+k^2+l^2)^7}\{-0.2095(h^2+k^2+l^2)^7 + 1.2095(h^{14}+k^{14}+l^{14})$ $- 44.0332(h^{12}k^2+h^{12}l^2+k^{12}l^2+k^{12}h^2+l^{12}h^2+l^{12}k^2)$ $+ 218.9013(h^{10}k^4+h^{10}l^4+k^{10}l^4+k^{10}h^4+l^{10}h^4+l^{10}k^4)$ $+ 1724.7982(h^{10}k^2l^2+k^{10}l^2h^2+l^{10}h^2k^2)$ $- 207.1684(h^8k^6+h^8l^6+k^8l^6+k^8h^6+l^8h^6+l^8k^6)$ $- 6413.0289(h^8k^4l^2+h^8l^4k^2+k^8l^4h^2+k^8h^4l^2+l^8h^4k^2+l^8k^4h^2)$ $- 12041.3267(h^6k^6l^2+k^6l^6h^2+l^6h^6k^2) + 44.10912(h^6k^4l^4+k^6l^4h^4+l^6h^4k^4)\}$
$C_{hkl}^{16,0} = C_{i8}$	$= \frac{4\pi\bar{P}_{16}(\cos\chi)}{(h^2+k^2+l^2)^8}\{0.1964(h^2+k^2+l^2)^8 + 0.8033(h^{16}+k^{16}+l^{16})$ $- 61.5720(h^{14}k^2+h^{14}l^2+k^{14}l^2+k^{14}h^2+l^{14}h^2+l^{14}k^2)$ $+ 677.0004(h^{12}k^4+h^{12}l^4+k^{12}l^4+k^{12}h^4+l^{12}h^4+l^{12}k^4)$ $+ 1354.0008(h^{12}k^2l^2+k^{12}l^2h^2+l^{12}h^2k^2) - 42151.974(h^6k^6l^4+k^6l^6h^4+l^6h^6k^4)$ $- 2513.4977(h^{10}k^6+h^{10}l^6+k^{10}l^6+k^{10}h^6+l^{10}h^6+l^{10}k^6)$ $- 7540.4936(h^{10}k^4l^2+h^{10}l^4k^2+k^{10}l^4h^2+k^{10}h^4l^2+l^{10}h^4k^2+l^{10}k^4h^2)$ $- 3847.2529(h^8k^8+l^8h^8+k^8l^8) + 44962.52(h^8k^4l^4+k^8l^4h^4+l^8h^4k^4)$ $+ 4449.5126(h^8k^6l^2+h^8l^6k^2+k^8l^6h^2+k^8h^6l^2+l^8h^6k^2+l^8k^6h^2)\}$

(continued)

Table 7.2 (***Continued***)

$$C_{hkl}^{16,4} = C_{i9} = \frac{4\pi \bar{P}_{16}(\cos\chi)}{(h^2+k^2+l^2)^8}\{371.1865(h^{12}k^4 + h^{12}l^4 + k^{12}l^4 + k^{12}h^4 + l^{12}h^4 + l^{12}k^4)$$
$$- 2227.1198(h^{12}k^2l^2 + k^{12}l^2h^2 + l^{12}h^2k^2) + 4199.7141(h^8k^8 + l^8h^8 + k^8l^8)$$
$$- 2449.8334(h^{10}k^6 + h^{10}l^6 + k^{10}l^6 + k^{10}h^6 + l^{10}h^6 + l^{10}k^6)$$
$$+ 12249.167(h^{10}k^4l^2 + h^{10}l^4k^2 + k^{10}l^4h^2 + k^{10}h^4l^2 + l^{10}h^4k^2 + l^{10}k^4h^2)$$
$$- 7349.4995(h^8k^6l^2 + h^8l^6k^2 + k^8l^6h^2 + k^8h^6l^2 + l^8h^6k^2 + l^8k^6h^2)$$
$$- 73494.998(h^8k^4l^4 + k^8l^4h^4 + l^8h^4k^4) + 68595.330(h^6k^6l^4 + k^6l^6h^4 + l^6h^6k^4)\}$$

Equations for the normalized Legendre polynomials $\bar{P}_n(\cos\chi)$

$$\bar{P}_n(\cos\chi) = \sqrt{\frac{2n+1}{2}} \text{ at } \chi = 0$$

In the range $0 < \chi \leq \frac{\pi}{2}$, $\bar{P}_n(\cos\chi)$ can be calculated from the Legendre polynomials

$$\bar{P}_n(\cos\chi) = \sqrt{\frac{2n+1}{2}} P_n(\cos\chi)$$

The Legendre polynomials $P_n(\cos\chi)$ can be calculated from the recurrence formula

$$P_{n+1}(\cos\chi) = \frac{2n+1}{n+1}\cos\chi P_n(\cos\chi) - \frac{n}{n+1}P_{n-1}(\cos\chi)$$

where $P_0(\cos\chi) = 1$ and $P_1(\cos\chi) = \cos\chi$

The orientation function coefficients A_j and the scaling factor k can be solved from the linear equations by least square regression as long as more than $q+1$ independent $I_{hkl}^m(\chi)$ values are available. The coefficients, $C_{hkl}^{nm}(\chi)$ and $C_{ij}(\chi)$ for a cubic structure, expressed as a function of (hkl) and χ up to the 16th order are listed in Table 7.2. A satisfactory fit to experimental data can be found with as low as 8th order polynomial textures in a metal sample formed by hot extrusion [14, 15]. The higher order terms are necessary only for very sharp textures and can be found in literature up to n = 22 [24] and up to n = 46 [25].

Figure 7.10 shows the pole density distributions, also called the fiber texture plot (FTP), of the peak (111), (200), and (220) from a Cu-Be alloy sample. The sample was a 0.24 cm disk cut perpendicular to the axis of a hot extruded rod 2.22 cm in diameter. This aligned the fiber axis to the surface normal. The relative peak intensities from 17 peaks were collected at $\chi = 0$ and averaged from three samples. The orientation function coefficients up to the 16th order were calculated from the relative peak intensities. The pole density functions of any (hkl) peak can be generated from the coefficients. The solid lines and dashed lines are the calculated pole density functions with and without the instrumental window correction, respectively. The experimental data points of pole densities for (111), (200), and (220) measured at various χ angles are also plotted over the calculated pole density function lines. The horizontal line at $g_{hkl} = 1$ is for random powder samples. The effect of the texture on peak intensities depends strongly on the χ angle. In this particular example, the maximum effect is observed at $\chi = 0$, with $g_{111}(0)/g_{220}(0) \approx 10$. While in the vicinity of $\chi = 20°$ and 50°, $g_{hkl}(\chi)$ for all three peaks approaches 1. The pole densities at $\chi = 0$ represent the texture effect with the Bragg–Brentano diffractometer, while the texture effect with XRD^2 can be the $g_{hkl}(\chi)$ values at any χ angle depending on the geometry of the data collecting settings. The average normalized pole density function $\langle g_{hkl}(\Delta\gamma)\rangle$ for the

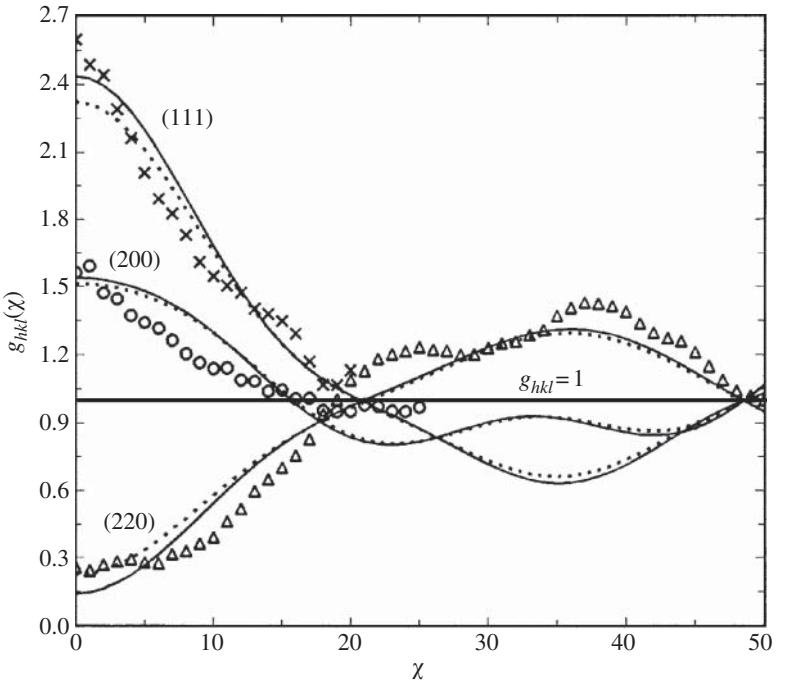


FIGURE 7.10 Fiber texture plot of the peak (111), (200), and (220) calculated and measured from a hot extruded rod of Cu-Be alloy.

intensity correction of the γ-integration peak with fiber texture is then given by

$$\langle g_{hkl}(\Delta\gamma)\rangle = \frac{\int_{\gamma_1}^{\gamma_2} g_{hkl}[\chi(\gamma)]\gamma d\gamma}{\gamma_2 - \gamma_1} \tag{7.46}$$

where $\chi = \cos^{-1}|\sin\theta\cos\psi\sin\omega - \cos\theta\sin\gamma\cos\psi\cos\omega - \cos\theta\cos\gamma\sin\psi|$, in which θ, ψ, ω are constants for a given 2D frame.

REFERENCES

1. R. Jenkins and R. L. Snyder, *Introduction to X-ray Powder Diffractometry*, 319–320, John Wiley, New York, 1996
2. ICDD, Release 2007 of the Powder Diffraction File, http://www.icdd.com, 2008.
3. P. R. Rudolf and B. G. Landes, Two-dimensional X-ray diffraction and scattering of microcrystalline and polymeric materials, *Spectroscopy*, **9**(6), pp. 22–33, 1994.
4. S. N. Sulyanov, A. N. Popov, and D. M. Kheiker, Using a two-dimensional detector for X-ray powder diffractometry, *J. Appl. Cryst.* (1994) **27**, 934–942.
5. A. Fujiwara, et al., Synchrotron radiation X-ray powder diffractometer with a cylindrical imaging plate, *J. Appl. Cryst.* (2000) **33**, 1241–1245.

6. Bob B. He, Introduction to two-dimensional X-ray diffraction, *Powder Diffraction*, 2003, **18** (2) 71–85.
7. G. W. Brindley, *The X-ray Identification and Crystal Structures of Clay Minerals*, 2nd ed., edited by G. Brown, Mineralogical Society, 1961.
8. B. D. Cullity, *Elements of X-ray Diffraction*, 2nd ed., Addison-Wesley, Reading, MA, 1978.
9. V. K. Pecharsky and P. Y. Zavalij, *Fundamental of Powder Diffraction and Structure Characterization of Materials*, Kluwer Academic Publishers, Boston, MA, 2003.
10. Bruker AXS, DIFFRACplus SEARC software, http://www.bruker-axs.com.
11. MDI, JADE, http://www.materialsdata.com/products.htm.
12. The Collaborative Computational Projects (CCP14), http://www.ccp14.ac.uk
13. G. Ning and R. L. Flemming, Rietveld refinement of LaB_6: data from μXRD, *J. Appl. Cryst.* (2005) **38**, 757–759.
14. B. He, X-ray Diffraction from Point-Like Imperfection, Ph.D dissertation, Virginia Tech, 1992, 93–125.
15. B. He, S. Rao, and C. R. Houska, A simplified procedures for obtaining relative X-ray intensities when a texture and atomic displacements are present, *J. Appl. Phys.* **75**, (9), May 1994.
16. A. J. C. Wilson, edited, *International Tables for Crystallography, Vol. C: Mathematical, Physical and Chemical Tables*, Kluwer Academic, Dordrecht, Netherlands, 1992.
17. M. A. Krivoglaz, *Theory of X-ray and Thermal-Neutron Scattering by Real Crystals*, Plenum Press, New York, 1969, p234.
18. S. Scheidegger, et al., Correction of specimen absorption in X-ray diffuse scattering experiments with area-detector systems, *J. Appl. Cryst.* (2000). **33**, 35–48
19. B. J. Campbell, Elucidation of zeolite microstructure by synchrotron X-ray diffuse scattering, *J. Appl. Cryst.* (2004). **37**, 187–192.
20. S. Guggenheim, Simulations of Debye–Scherrer and Gandolfi patterns using a Bruker Smart Apex diffractometer system, Bruker AXS Application Note 373 (2005).
21. J. P. Cline, NIST standard reference materials for characterization of instrument performance, *Industrial Applications of X-ray Diffraction*, edited by F. H. Chung and D. K. Smith, Marcel Dekker, New York, (2000) 903–917.
22. H. J. Bunge, *Texture Analysis in Materials Science, Butterworth*, London (1983)
23. R. D. Angelis, et al., Quantitative description of fiber textures in cubic metals, *Advances in X-ray Analysis*, **42**, 510–520 (2000).
24. R. J. Roe, Inversion of pole-figures for materials having cubic-crystal symmetry, *J. Appl. Phys.* **37**, 2069 (1966).
25. S. Rao and C. R. Houska, Quantitative analysis of fiber texture in cubic films, *J. Apply. Phys.* **54**, 1872 (1983).

8

TEXTURE ANALYSIS

8.1 INTRODUCTION

Most natural or artificial solid materials are polycrystalline, which means that they consist of many crystallites, also called grains, of various sizes, shapes and orientations. Each crystallite is a single crystal with anisotropic properties due to its periodic atomic arrangement in three-dimensional space. The properties of polycrystalline materials are determined by the combination of the single crystal's properties, the boundary between crystallites, and the orientation distribution of the crystallites within the material. In rare cases, the orientation of the crystallites in a material has a random distribution, which produces isotropic properties. In most cases, crystallites have an anisotropic orientation distribution and properties. This anisotropic orientation distribution is referred to as a preferred orientation or a texture. A sample having all crystallites fully randomly orientated is said to have no texture. Depending on the degree of the preferred orientation, a sample is referred to as having a weak, moderate, or strong texture. The extreme of having a preferred orientation is a single crystal. Many electrical, optical, or mechanical properties of materials are affected or determined by their texture. Numerous fabrication processes are developed to control the texture. The determination and interpretation of textures are therefore of fundamental importance in materials science and technology.

When a conventional X-ray diffractometer with a point detector is used for texture measurement, the crystallite orientation distribution is measured in one direction at a time, and full texture information is measured by rotating the sample to all the desired orientations. When used for texture measurement, two-dimensional X-ray diffraction systems have many advantages over conventional one-dimensional diffraction systems [1–7]. The orientation distribution of several crystallographic planes over a range of angles can be measured simultaneously so as to get better measurement results with less data collection time. The orientation relationship between different phases or between different layers of thin films and substrate can also be easily revealed by simultaneous measurement with the same sample rotation scan. The texture can also be observed and compared directly from the 2D diffraction frames without data processing.

Two-Dimensional X-Ray Diffraction, Second Edition. Bob Baoping He.
© 2018 John Wiley & Sons, Inc. Published 2018 by John Wiley & Sons, Inc.

8.2 POLE DENSITY AND POLE-FIGURE

XRD results from ideal randomly oriented powder normally serve as the basis for determining the relative intensity of each diffraction peak. Realistically, polycrystalline materials usually do not have randomly oriented grains (or crystallites). The deviation of the statistical grain orientation distribution of a polycrystalline material from the ideal powder is measured as a texture or preferred orientation. The pole-figure for a particular crystallographic plane is normally used to represent the texture of a sample. Assuming that all grains have the same volume, each "pole" represents a grain that satisfies the Bragg condition as shown in Figure 8.1(a). The pole is conveniently represented by the unit vector of the diffraction vector ($\boldsymbol{H_{hkl}}$). If we take the diffraction peak from a random powder sample as a reference in Figure 8.1(b), the diffraction peak intensity difference is due to the texture while the peak shift is due to stress. The number of grains satisfying the Bragg condition at a particular sample orientation can be larger or smaller than the number of grains for an ideal sample, and likewise for the integrated intensity of that peak. The stresses in a sample can be compressive or tensile so that the d-spacing in the corresponding direction will be smaller or larger than the stress-free sample, and the peak position changes correspondingly based on the Bragg law.

The measured 2D diffraction pattern contains two very important parameters at each γ angle: the partially integrated intensity $\mathbf{I}$ and the Bragg angle 2θ. Figure 8.2 illustrates two diffraction cones, with one for forward diffraction and one for backward diffraction. The regular diffraction cones are from the ideal powder sample with no stress, so that the 2θ angles and diffraction intensities are constant at all γ angles. The red rings are distorted diffraction cones due to stresses. For a stressed sample, 2θ becomes a function of γ and the sample orientation (ω,ψ,ϕ), i.e. $2\theta = 2\theta(\gamma,\omega,\psi,\phi)$. This function is uniquely determined by the stress tensor. The relationship between diffraction cone distortion and the stress tensor will be discussed in Chapter 9 on stress analysis. For a textured sample, the diffraction intensity varies along γ due to an anisotropic pole density distribution. The intensity is a function of γ and the sample orientation (ω,ψ,ϕ), i.e. $\mathbf{I} = \mathbf{I}(\gamma,\omega,\psi,\phi)$, which is uniquely determined by the orientation distribution function (ODF).

Texture is a measure of the orientation distribution of all grains in a sample with respect to the sample direction (e.g. the rolling direction in a sheet metal, or the substrate normal in a thin film). Texture characterization by X-ray diffraction involves the measurement of the peak intensity of a particular crystallographic plane at all tilt angles with respect to a sample direction. Typically, one to four independent crystallographic planes (different *hkl*-values) are measured to quantify the major orientation distribution of a material.

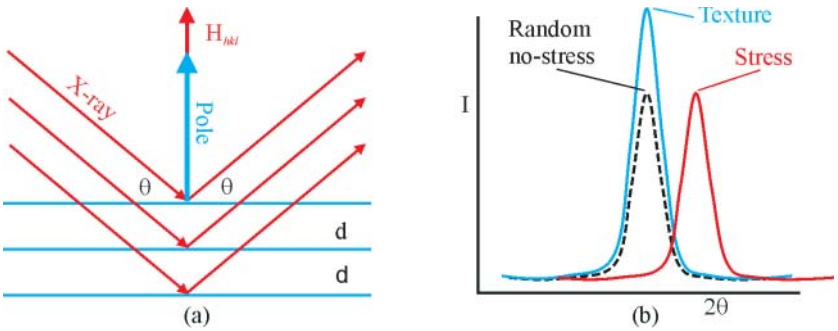


FIGURE 8.1 The definition of (a) pole and (b) diffraction peak intensity change due to texture and peak shift due to stress.

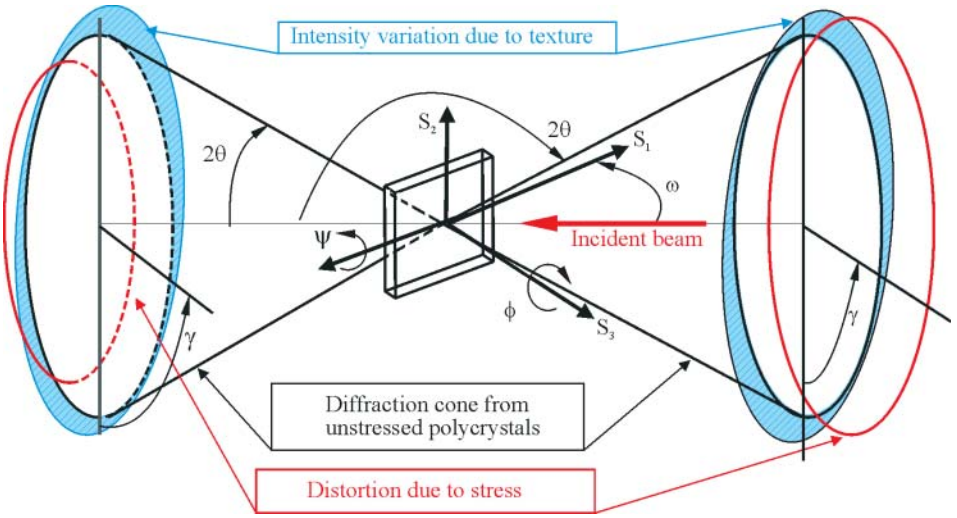


FIGURE 8.2 Diffraction cone distortion due to stress and intensity variation along γ due to texture.

Plotting the intensity of each (*hkl*) line with respect to the sample coordinates in a stereographic projection gives a qualitative view of the orientation of the crystallites with respect to a sample direction. These stereographic projection plots are called pole-figures. As shown in Figure 8.3(a), the rolling direction (RD) is aligned to the sample coordinate S_2, the transverse direction (TD) to S_1, and the plate normal direction (ND) to S_3. Let's consider a sphere with unit radius and the origin at O. A unit vector representing an arbitrary pole direction (also the unit vector of the diffraction) starts from the origin O and ends at the point P on the sphere. The pole direction is defined by a set of the radial angle α and azimuthal angle β. In some literature, the angle between the sample normal and the pole direction (χ) is used in the radial direction. The pole density at the point P projects to the point P′ on the equatorial plane through a straight line from P to the point S. The pole densities at all directions are mapped onto the equatorial plane by stereographic projection. As shown in Figure 8.3(b), this two-dimensional pole density mapping on the equatorial plane is called a pole-figure. The azimuthal angle β projects to the pole-figure as a rotation angle about the center of the pole-figure from the sample direction S_1. The radial angle α is projected to the pole-figure with a non-linear scale. If the distance from O to P′ is r, then r is given by

$$r = \tan\left(\frac{\pi}{4} - \frac{\alpha}{2}\right) \tag{8.1}$$

where a unit radius is assumed. When plotting the pole-density into a pole-figure of radius R, the location of the point P′ in the pole-figure should be given by β and

$$r = R\tan\left(\frac{\pi}{4} - \frac{\alpha}{2}\right) = R\tan\frac{\chi}{2} \tag{8.2}$$

For easy computer plotting and easy angular readout from the pole-figure, the radial angle α may be plotted on an equally spaced angular scale, similar to a two-dimensional polar coordinate system, except that the distance from the origin is expressed as the radial angle on a linear scale ($r = 2\chi R/\pi$). Other pole-figure mapping styles include perpendicular projection, in which the pole is projected to the pole-figure in a direction parallel to the sample normal ($r = R\sin\chi$), and equal area projection ($r = \sqrt{2}R\sin(\chi/2)$). The projection of the pole-figure must be properly noted to avoid confusion [8].

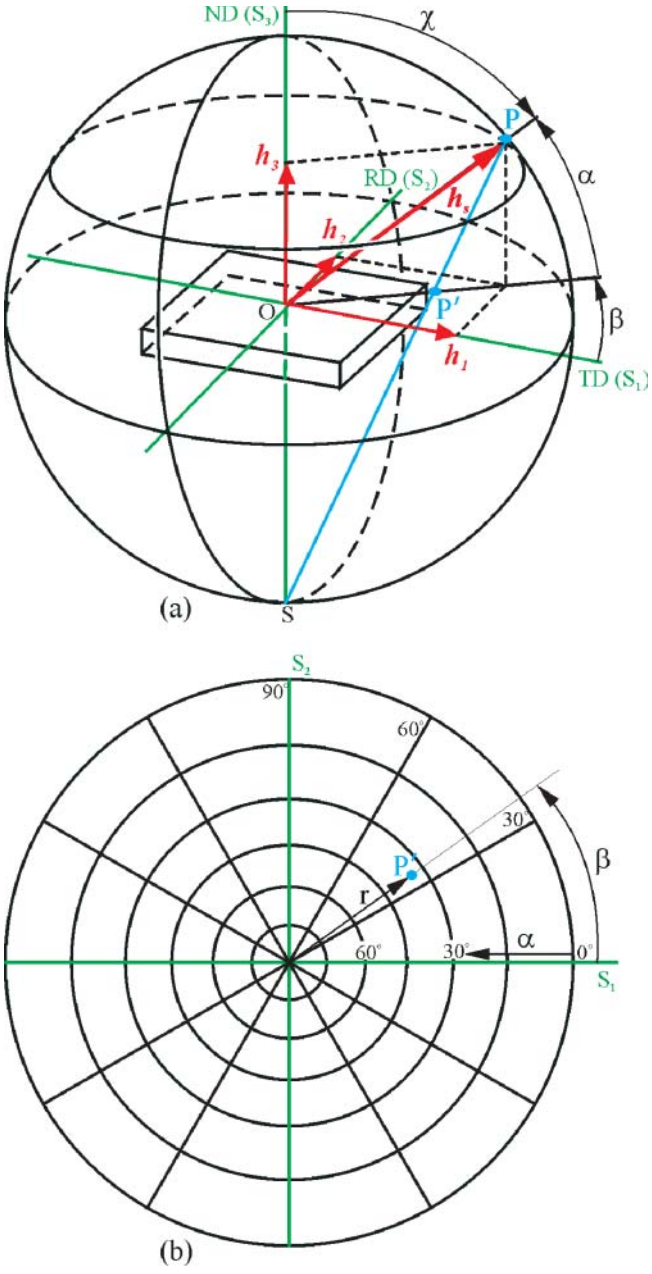


FIGURE 8.3 (a) Definition of pole direction angles α and β, (b) stereographic projection in pole-figure.

8.3 FUNDAMENTAL EQUATIONS

8.3.1 Pole-figure Angles

Each pole direction is defined by the radial angle α and azimuthal angle β. The α and β angles are functions of γ, ω, ψ, ϕ and 2θ. As shown in Figure 8.3(a), the pole, defined as a unit vector,

has three components h_1, h_2, and h_3 parallel to the three sample orientations TD (S_1), RD (S_2), and ND (S_3) respectively. The pole-figure angles (α,β) can be calculated from the unit vector components by the following pole mapping equations:

$$\boxed{\begin{aligned} &\alpha = \arcsin|h_3| = \arccos\sqrt{h_1^2 + h_2^2} \\ &\beta = \pm\arccos\frac{h_1}{\sqrt{h_1^2 + h_2^2}} \qquad \begin{cases} \beta \geq 0^\circ & \text{if} \quad h_2 \geq 0 \\ \beta < 0^\circ & \text{if} \quad h_2 < 0 \end{cases} \end{aligned}} \tag{8.3}$$

where α takes a value between 0° to 90° ($0^\circ \leq \alpha \leq 90^\circ$) and β takes values in two ranges ($0^\circ \leq \beta \leq 180^\circ$ when $h_2 \geq 0$ and $-180^\circ \leq \beta < 0^\circ$ when $h_2 < 0$). The condition for reflection mode diffraction with the sample plane on the S_1-S_2 plane is $h_3 > 0$. For transmission diffraction it is possible that $h_3 < 0$. In this case the pole with a mirror symmetry about the S_1-S_2 plane to the diffraction vector is used for the pole-figure mapping. The absolute value of h_3 is then used in the equation for the α angle. When $h_2 = 0$ in the above equation, β takes two values depending on the value of h_1 ($\beta = 0^\circ$ when $h_1 \geq 0$ and $\beta = 180^\circ$ when $h_1 < 0$). In many publications, the angle between the sample normal and the pole direction, χ, is used instead of α, as shown in Figure 8.3(a).

$$\chi = 90^\circ - \alpha \tag{8.4}$$

and

$$\chi = \arccos|h_3| \tag{8.5}$$

For Eulerian geometry, the unit vector components $\{h_1, h_2, h_3\}$ can be calculated from the sample orientation (ω,ψ,ϕ) and diffraction angles (2θ,γ) by

$$\begin{aligned} h_1 &= \sin\theta(\sin\phi\sin\psi\sin\omega + \cos\phi\cos\omega) + \cos\theta\cos\gamma\sin\phi\cos\psi \\ &\quad - \cos\theta\sin\gamma(\sin\phi\sin\psi\cos\omega - \cos\phi\sin\omega) \\ h_2 &= -\sin\theta(\cos\phi\sin\psi\sin\omega - \sin\phi\cos\omega) - \cos\theta\cos\gamma\cos\phi\cos\psi \\ &\quad + \cos\theta\sin\gamma(\cos\phi\sin\psi\cos\omega + \sin\phi\sin\omega) \\ h_3 &= \sin\theta\cos\psi\sin\omega - \cos\theta\sin\gamma\cos\psi\cos\omega - \cos\theta\cos\gamma\sin\psi \end{aligned} \tag{8.6}$$

The 2θ integrated intensity along the diffraction ring is then converted to the pole density distribution along a curve on the pole-figure. The α and β angles at each point of this curve are calculated from ω, ψ, ϕ, γ, and 2θ. The sample orientation (ω, ψ, ϕ) and 2θ for the diffraction ring are constants; only γ takes a range of values depending on the detector size and distance. Figure 8.4 is a comparison between the pole-figure measurement with conventional X-ray diffraction (XRD) and two-dimensional X-ray diffraction (XRD^2). With conventional X-ray diffraction, the diffraction vector $\mathbf{H}_{hkl}$ is measured at each sample angle, therefore a function of the sample orientation. For the ω scan as illustrated in the figure, the diffraction vector is denoted as $\mathbf{H}_{hkl}(\omega)$. As an example, with seven different ω positions, only seven poles are measured (red spots). Therefore, a conventional diffractometer needs to scan over a large number of sample orientations for data collection. There are many data collection scan strategies to fill the pole-figure with measured intensity spots. For instance, the hexagonal grid and spiral trace schemes have been suggested to fill a pole-figure with pole density data points collected at each sample orientation [9]. With

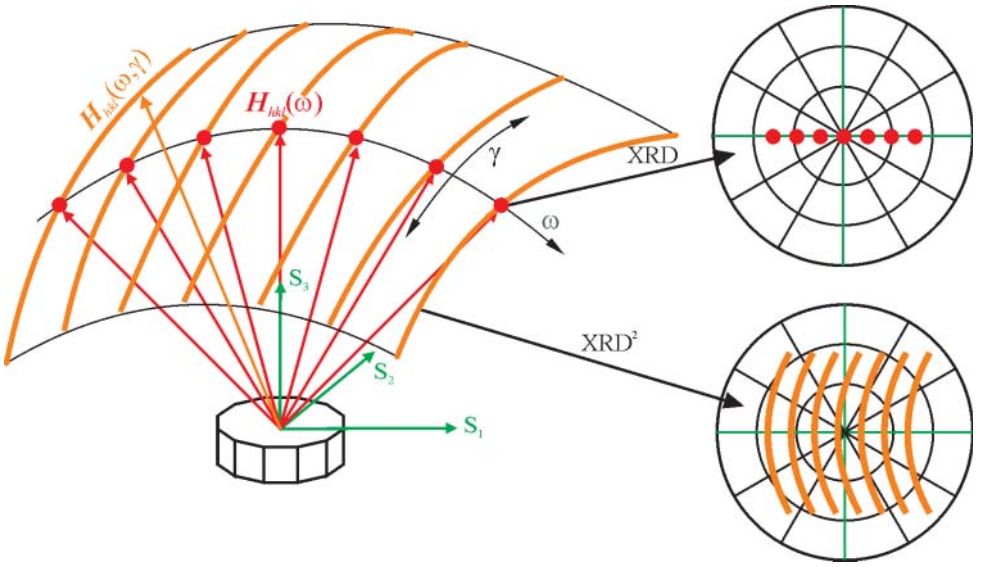


FIGURE 8.4 Comparison between the pole-figure measurement with the conventional X-ray diffraction and two-dimensional X-ray diffraction.

two-dimensional X-ray diffraction, numerous poles are measured at each sample angle (orange lines). The trace of the diffraction vector $\mathbf{H}_{hkl}$ measured at each sample orientation is not a single spot, but a distribution corresponding to the γ range. In this case, the diffraction vector becomes a function of both sample orientation and γ value, for instance, $\mathbf{H}_{hkl}(\omega, \gamma)$ for the ω scan. A one-dimensional pole mapping is created with each exposure. For the same seven ω positions, the poles measured can map a large area in the pole-figure. Therefore, when a two-dimensional diffraction system is used for texture measurement, much smaller scan steps can be used to achieve a high resolution pole-figure and the data collection time can also be dramatically reduced.

8.3.2 Pole Density

For a textured sample, the 2θ-integrated intensity of a diffraction ring from a family of (hkl) planes is a function of γ and the sample orientation (ω,ψ,ϕ), i.e. $I_{hkl} = I_{hkl}(\omega, \psi, \phi, \gamma, \theta)$, which is uniquely determined by the orientation distribution function (ODF). From the pole-figure angle mapping equations, we can obtain the integrated intensity in terms of pole-figure angles as

$$I_{hkl}(\alpha, \beta) = I_{hkl}(\omega, \psi, \phi, \gamma, \theta) \tag{8.7}$$

The pole density at the pole-figure angles (α,β) is proportional to the integrated intensity at the same angles:

$$P_{hkl}(\alpha, \beta) = K_{hkl}(\alpha, \beta) \cdot I_{hkl}(\alpha, \beta) \tag{8.8}$$

where $I_{hkl}(\alpha, \beta)$ is the 2θ-integrated intensity of the (hkl) peak corresponding to the pole direction (α, β), $K_{hkl}(\alpha, \beta)$ is the scaling factor covering the absorption, polarization, background corrections, and various instrument factors, if these factors are included in the integrated intensities, and $P_{hkl}(\alpha, \beta)$ is the pole density distribution function. The absorption correction, polarization correction, and detector related corrections have been discussed in previous chapters. Background

correction can be done during the 2θ-integration and will be discussed later in this chapter. The pole-figure is obtained by plotting the pole density function based on the stereographic projection.

The pole density function can be normalized such that it represents a fraction of the total diffracted intensity integrated over the pole sphere. The normalized pole density distribution function is given by

$$g_{hkl}(\alpha,\beta) = \frac{2\pi P_{hkl}(\alpha,\beta)}{\int_0^{2\pi}\int_0^{\frac{\pi}{2}} P_{hkl}(\alpha,\beta)\cos\alpha d\alpha d\beta} \tag{8.9}$$

The integration in the above equation is over the hemisphere above the equatorial plane, assuming the pole-figure is at least symmetric about the plane. The average of $g_{hkl}(\alpha,\beta)$ over the full sphere must be the same as the value for an ideal powder, i.e. equal to unity,

$$\langle g_{hkl}(\alpha,\beta)\rangle = \frac{\int_0^{2\pi}\int_0^{\frac{\pi}{2}} g_{hkl}(\alpha,\beta)\cos\alpha d\alpha d\beta}{\int_0^{2\pi}\int_0^{\frac{\pi}{2}} \cos\alpha d\alpha d\beta} = 1 \tag{8.10}$$

or

$$\int_0^{2\pi}\int_0^{\frac{\pi}{2}} g_{hkl}(\alpha,\beta)\cos\alpha d\alpha d\beta = 2\pi \tag{8.11}$$

The pole density distribution function is a constant for a sample with a random orientation distribution. Assuming the sample and instrument conditions are the same except for the pole density distribution, the scaling factor can then be determined experimentally from the integrated intensity collected with an ideal sample:

$$K_{hkl}(\alpha,\beta) = \frac{P}{I_{hkl}^{Random}(\alpha,\beta)} \tag{8.12}$$

where P is the constant pole density for the ideal sample. In practice, it can be given as an arbitrary scaling factor. The pole density function is then given by

$$P_{hkl}(\alpha,\beta) = \frac{PI_{hkl}(\alpha,\beta)}{I_{hkl}^{Random}(\alpha,\beta)} \tag{8.13}$$

Assuming the experimental conditions for the textured sample and the ideal sample are exactly the same, taking $P = 1$, we can obtain the normalized pole density function by

$$g_{hkl}(\alpha,\beta) = \frac{I_{hkl}(\alpha,\beta)}{I_{hkl}^{Random}(\alpha,\beta)} \tag{8.14}$$

The integrated intensity from the textured sample without any correction can be plotted according to the stereographic projection as an "uncorrected" pole-figure. The same can be done for the sample with a random orientation distribution to form a "correction" pole-figure that contains only the factors to be corrected. The normalized pole-figure is then obtained by dividing the "uncorrected" pole-figure by the "correction" pole-figure. This experimental approach is feasible only if a similar sample with random orientation is available.

8.4 DATA COLLECTION STRATEGY

8.4.1 Single φ Scan

Since a one-dimensional pole density mapping is created from each exposure with XRD^2, it is important to lay out a data collection strategy so as to have the optimum pole-figure coverage and less redundancy in the data collection. The pole-figure coverage can be simulated from the diffraction 2θ angle, detector swing angle, detector size and distance, goniometer angles, and scanning steps. Figure 8.5 shows examples of the scheme generated by GADDS™ (Bruker AXS) software for Hi-Star detector. Figure 8.5(a) shows an example of a scheme generated at $2\theta = 40°$,

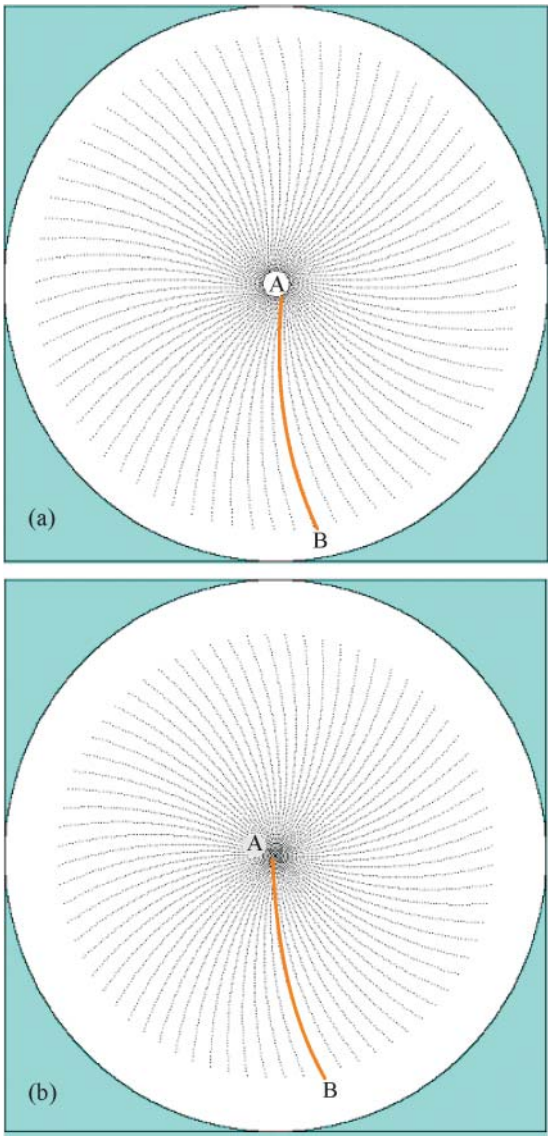


FIGURE 8.5 Data collection strategy: (a) a scheme generated at $2\theta = 40°$, $\omega = 20°$, $\psi = 35.26°$ has a hole in the center, (b) a modified scheme with $\omega = 23°$, $\psi = 30°$ covers the center of pole-figure.

$\omega = 20°$, $\psi = 35.26°$ ($\chi_g = 54.74°$ for a fixed-chi stage), and $D = 7$ cm with a ϕ scan of 5° steps. Real data collection can use smaller scanning steps, such as 1° to 2°. The data collected with a single exposure at $\phi = 0°$ would generate a one-dimensional pole-figure as shown in the curve marked by A and B. The pole-figure can be generated by a full circle rotation of 360°, but as shown by the scheme simulation, the pole-figure measured with this data collection strategy in the above example has a blank hole in the center. The pole density at the center represents the diffraction vector perpendicular to the sample surface. It is important to have the pole density information in the center region of the pole-figure, especially for fiber texture. The pole-figure angle at the center is $\alpha = 90°$, so the condition to achieve a filled center in a pole-figure is that one pole density within A-B curve is collected at

$$\alpha = \sin^{-1} h_3 = 90°$$

$$\text{or} \quad h_3 = \sin\theta\cos\psi\sin\omega - \cos\theta\sin\gamma\cos\psi\cos\omega - \cos\theta\cos\gamma\sin\psi = 1 \tag{8.15}$$

In order to avoid redundancy in the data collection, the best strategy is to put point A at the center of pole-figure. That is

$$h_3^A = \sin\theta\cos\psi\sin\omega - \cos\theta\sin\gamma_A\cos\psi\cos\omega - \cos\theta\cos\gamma_A\sin\psi = 1 \tag{8.16}$$

If we modify the parameters in the example of Figure 8.5(a) to $\omega = 23°$, $\psi = 30°$ (assuming the goniometer allows ψ rotation, such as an Eulerian cradle or a Kappa stage) for the same $2\theta = 40°$ and $D = 7$cm with a ϕ scan of 5° steps, and the γ angle measured on the same detector at point A is $\gamma_A = -122°$, then we have $h_3^A \cong 1$. The scheme generated with the new strategy is shown in Figure 8.5(b). The center of the pole-figure is filled with pole density data. The data collection parameters may be optimized by trial and error or calculation with the above equations.

8.4.2 Multiple ϕ Scans

The above data collection strategy uses a single ϕ scan to collect data for a single pole-figure. In some cases, a single ϕ scan is not enough to cover sufficient pole-figure angles due to a large detector distance or limited detector area. The data collection strategy should also be optimized for several crystallographic planes. It is necessary to collect a set of data with ϕ scans at several different sample tilt angles. Figure 8.6 shows an example of texture measurement on the magnetron sputter-deposited Cu film onto a Si (100) wafer [5]. Figure 8.6(a) shows the instrument (Bruker AXS GADDS™) with an area detector (Hi-Star™), quarter-circle Eulerian cradle, and a laser/video alignment system. The Cu thin film sample is mounted on the system, and the film thickness is 3 μm, as measured by a TEM. Figure 8.6(b) shows one of the diffraction frames for texture analysis collected from the Cu film. At a detector distance of 10 cm with Cu radiation, a total of three diffraction rings from the crystallographic planes of (111), (200), and (220) can be measured simultaneously. Therefore, three pole-figures can be measured simultaneously. The diffraction spot from the single crystal Si substrate may also be picked up by the detector at certain angles. The frame in the figure has a Si (311) spot. Since the detector distance has to be set at 10 cm for the rotation space of the Eulerian cradle, a single ϕ rotation is not sufficient to get a reasonable pole-figure angular coverage. In this case, each pole-figure requires two ϕ scans at different sample orientations.

Figure 8.7 illustrates the data collection scheme for the Cu thin film. The 2θ angles for the three crystallographic planes (111), (200), and (220) are 43.3°, 50.4°, and 74.1° respectively. There are three scans, A, B, and C, listed in the table, D is the detector distance, α is the detector swing

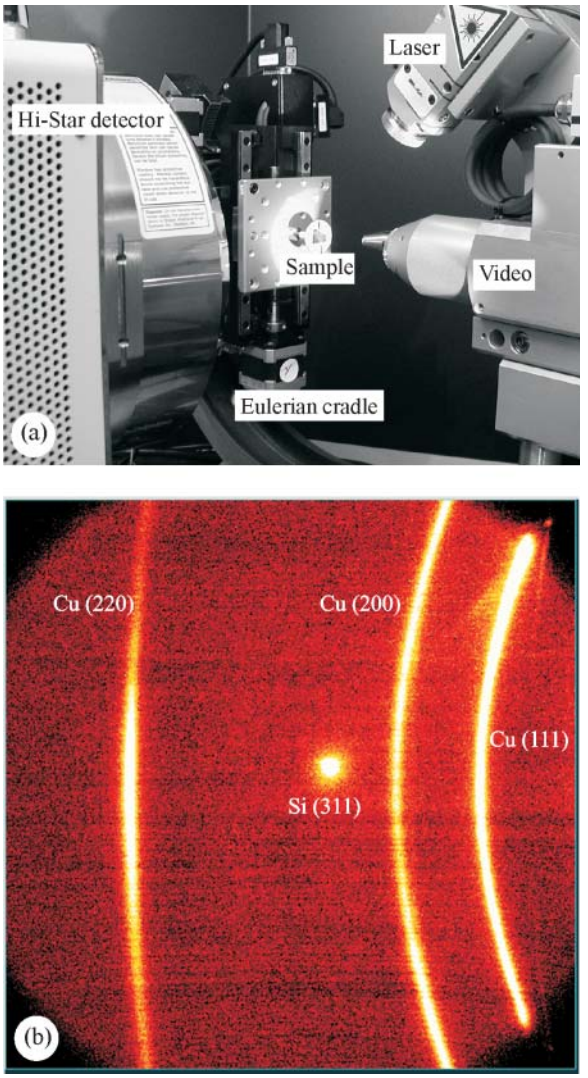
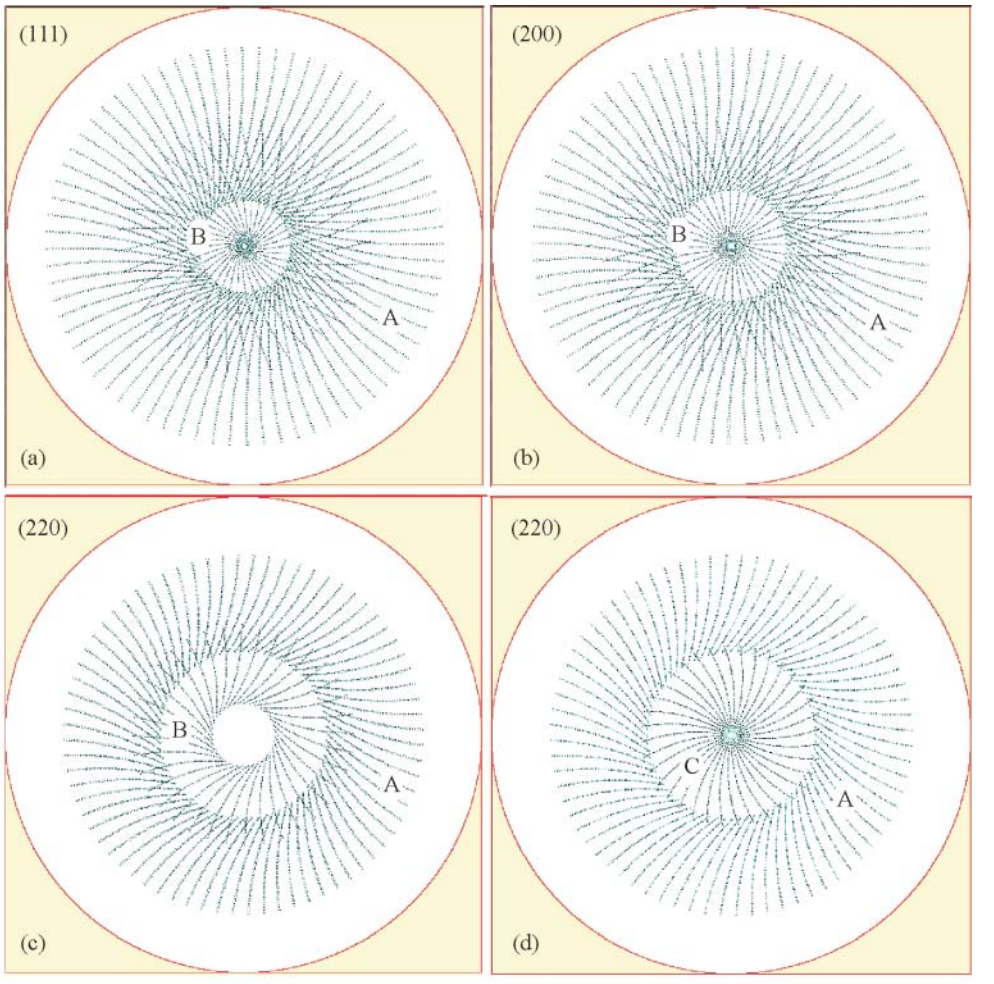


FIGURE 8.6 Texture analysis system and 2D frame: (a) Cu thin film sample mounted on a GADDS™ system (Bruker AXS), (b) each frame contains three Cu lines and a Si spot.

angle (should not be confused with the pole-figure angle α), and ω and ψ determine the normal orientation of the sample. Two ϕ scan steps are given for each scan, $\Delta\phi$ (s) is the scan step used to generate the schemes as shown in Figure 8.7, and $\Delta\phi$ (c) is the actual scan steps used for the data collection. The scan step for A is 1°, while the scan steps for B and C are 2°. This is because scan A covers the outer donut, which requires smaller scan steps to get a data point density on the pole-figure comparable to the 2° scan steps for the inner donut. We can get reasonable data point coverage on the pole-figures of (111) and (200) with the two ϕ scans, A and B, as shown in Figure 8.7(a) and (b). The pole density in the gaps between the data points will be generated by interpolation. We can see a small hole in the schemes of both (111) and (200), but the holes are small enough that interpolation will cover these holes in the center. When we use the same two scans (A+B) for the pole-figure of (220), we can find that there is a big hole in the center as



(*hkl*)	2θ
(111)	43.3°
(200)	50.4°
(220)	74.1°

Scan	D(cm)	α	ω	ψ	Δϕ (s)	Δϕ (c)
A	10	60°	10°	50°	5°	1°
B	10	60°	27°	29°	10°	2°
C	10	75°	40°	21.5°	10°	2°

FIGURE 8.7 Data collection strategy for Cu thin films with two ϕ scans: (a) (111) pole-figure with strategy A+B, (b) (200) with A+B, (c) (220) with A+B, (d) (220) with A+C.

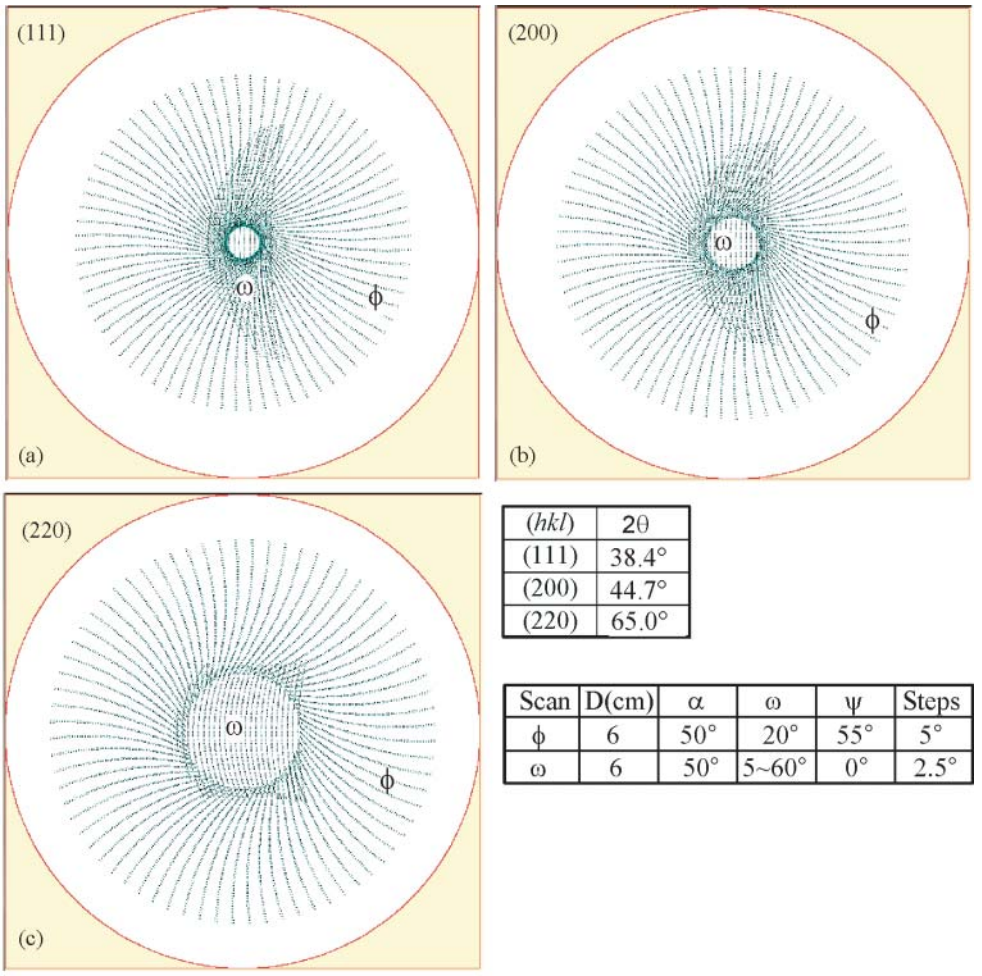
shown in Figure 8.7(c). Therefore, we need the third ϕ scan (C) at a different detector angle and sample normal orientation. In this case, the frames from the two ϕ scans A and C will cover the pole-figure region. Overall, we need three ϕ scans to get the three pole-figures for (111), (200), and (220).

The data collection strategy can be generated by trial and error or calculation. A good data collection strategy can save data collection time and improve data point coverage on the pole-figures. So far we have used ω and ψ to set the sample normal orientation and a ϕ scan to complete the pole-figure data point coverage. It is possible to measure textures with a ω scan or a ψ scan, but the

scheme will not cover a round region. This is acceptable if only a local region of the pole-figure is of interest – in industrial quality control, for instance. A motorized ϕ axis is highly recommended if an instrument is used for texture measurement. The step size of the data collection scan depends highly on the strength of the texture and the purpose of the texture measurements. For a weak texture, or for quality control for metal parts, ϕ (or ω, or ψ) scan steps of 5° may be sufficient. For strong textures, such as thin films with epitaxial structure, scan steps of 1° or smaller may be necessary.

8.4.3 Combination of φ and ω Scans

A data collection strategy may contain a combination of ϕ scans and ω scans. Figure 8.8 shows the data collection schemes generated by the GADDS™ (Bruker AXS) software for Al in reflection mode with a combination of a ϕ scan and ω scan. The ϕ scan is set as $\alpha = 50°$, $\omega = 20°$, $\psi = 55°$ for the Hi-Star detector at $D = 6$ cm with a ϕ scan of 5° steps. The data set with the ϕ scan contains pole density mapping for figures of (111), (200), and (220), but all with a "hole" in the center.



(*hkl*)	2θ
(111)	38.4°
(200)	44.7°
(220)	65.0°

Scan	D(cm)	α	ω	ψ	Steps
ϕ	6	50°	20°	55°	5°
ω	6	50°	5~60°	0°	2.5°

FIGURE 8.8 Data collection strategy for Al with a combination of a φ scan and an ω scan.

The missing pole density in the hole can be filled by an ω scan at $\alpha = 50°$, $\omega = 5{\sim}65°$, $\psi = 0°$ with ω steps of 2.5°. The combined ϕ and ω may reduce the total data collection time compared with multiple ϕ scans. But due to the more dramatic change in the incident angle with ω scan, the pole-figure may contain some artifact in the overlapping region or boundary between the ϕ and ω scans if the absorption is not properly corrected.

8.4.4 Goniometer ϕ Rotation Direction

The ϕ rotation in the XRD^2 diffractometer is defined as a left-handed rotation so that the diffraction vectors will make a right-hand rotation observed in the sample coordinates $\mathbf{S_1S_2S_3}$. All the algorithms for XRD^2 data interpretation and evaluation are based on the geometry convention that was defined in the Chapter 2. For some applications, such as phase identification, the direction of ϕ rotation may not cause a problem, but for applications depending on the sample orientation, the correct goniometer convention, especially the ϕ rotation direction, must be maintained to produce the correct results. Texture is one of the applications strongly associated with the sample orientation. Figure 8.9 shows the effect of a wrong ϕ rotation on the pole-figure mapping simulated with the Bruker GADDS™ software for Cu (111) with $2\theta = 43.3°$, $D = 10$ cm and $\alpha = 60°$. The region in the red box is the pole-figure mapping for positive ϕ scan from 10° to 57° with $\Delta\phi = 3°$ steps at $\omega = 10°$ and $\psi = 50°$. The region in the blue box is the pole-figure mapping for negative ϕ scan from $-10°$ to $-57°$ with $\Delta\phi = -3°$ steps at $\omega = 10°$ and $\psi = 50°$. Apparently, both regions are not symmetric to the $\mathbf{S_2}$ axis. If the ϕ scan is over the complete 360°, both the positive and negative

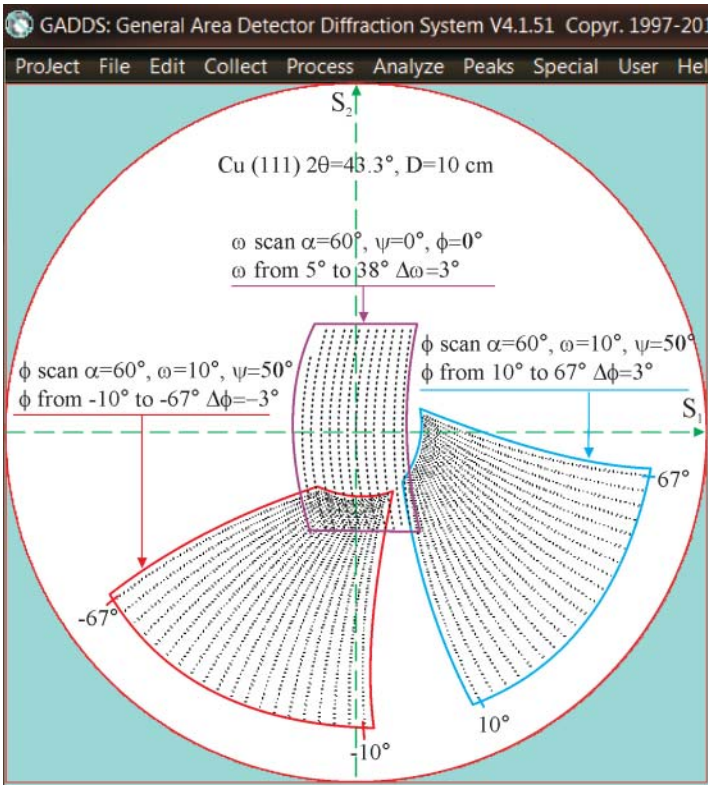


FIGURE 8.9 Effect of wrong φ rotation direction on pole-figure mapping.

ϕ scan will cover the same "donut" region. The hole in the center can be filled by an ω scan at $\alpha = 60°$, $\psi = 0°$, and $\phi = 0°$ from 5° to 38° with $\Delta\omega = 3°$ steps, as shown in the purple box. The region covered by the purple box will not be affected by the ϕ rotation direction at $\phi = 0°$, but the ω scanned region will merge with the ϕ scanned region in a different way if the ϕ rotation direction is mistakenly reversed.

The data frames collected by either a positive ϕ scan or a negative ϕ scan will produce a correct pole-figure as long as the ϕ angle definition is correct. But if the ϕ rotation direction is reversed in the system into a right-handed rotation, the pole-figure data points will be mapped into the wrong region, so that the pole-figure is distorted and misoriented relative to the sample orientation. The degree and form of the pole-figure distortion by the wrong ϕ rotation is also dependent on the data collection strategy. A pole-figure generated purely by wrong ϕ scans may be corrected by the combination of symmetry and rotation operation if the pole-figure has a clear and typical pattern, for instance, from a rolled metal sheet. For most unknown texture or weak texture, the pole-figure measured with wrong ϕ direction is incorrect and misleading, especially its orientation relationship to the sample. A pole-figure collected by a combination of ϕ scans in the wrong direction and ω scans will be so scrambled that it cannot be corrected by either rotation or symmetry operation.

8.4.5 Transmission Mode

The data collection strategies described in the previous section on multiple scan are based on reflection mode diffraction. The texture of a sample may be measured by transmission mode diffraction if the shape and dimension of the sample allows. Figure 8.10 illustrates texture

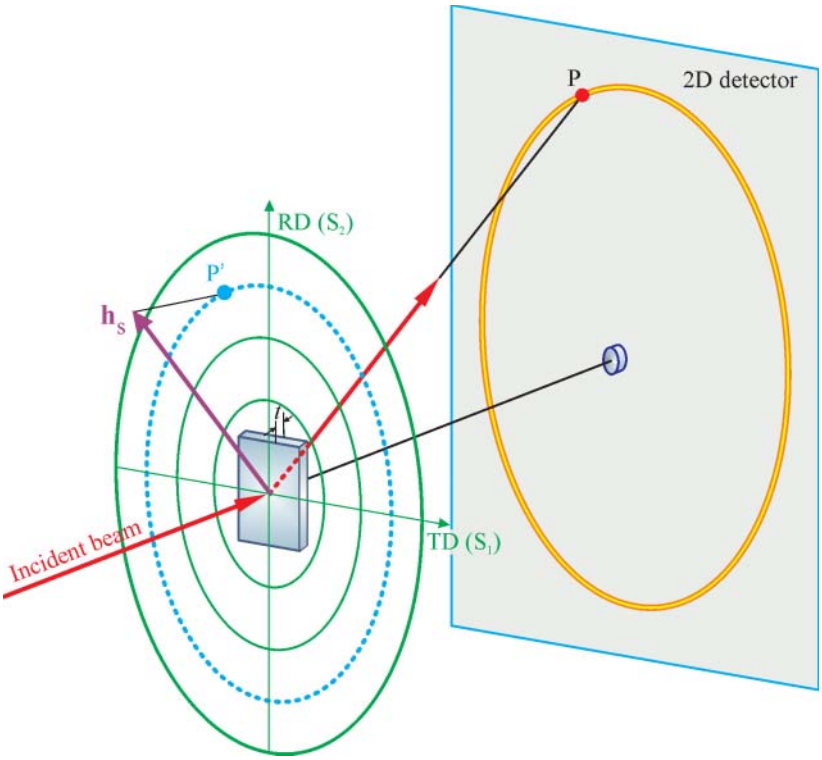


FIGURE 8.10 Texture measurement with transmission mode diffraction.

measurement with transmission mode diffraction. The sample thickness t should be thin enough to obtain sufficient diffraction intensity. The proper sample thickness depends on the linear absorption coefficient. The optimal sample thickness is $1/\mu$, but a sample with a few times greater than this value is acceptable with longer data collection time. The intensity on the point P of the diffraction ring is projected to the pole-figure as pole density P′. The location of point P′ in the pole-figure is determined by the unit diffraction vector $\mathbf{h_s}$. The intensity distribution of the complete diffraction ring is mapped to the pole-figure as pole density distribution indicated by the dotted blue circle. In the figure, the incident X-ray beam is normal to the sample surface, so the projected pole density is mapped to a circle concentric to the pole-figure boundary. With proper sample rotation, the measured pole intensity covers more area in the pole-figure. A typical sample rotation is about an axis on the sample, such as $\mathbf{S_1}$ and $\mathbf{S_2}$. In order to collect the complete diffraction ring in transmission, the rotation angle should be less than $90° - 2\theta$, plus or minus away from the sample normal direction.

Figure 8.11 shows the texture measurement on an aluminum plate 3 mm thick in transmission mode with a proprietary diffractometer [10]. The system uses an Mo-K_α incident X-ray beam from sealed tube and graphite monochromator, sample stage with single rotation axis, and Bruker Smart 1000 CCD detector at 2.7 cm distance. Figure 8.11(a) shows one of the diffraction frames. Because of the short detector distance, more than four complete diffraction rings are

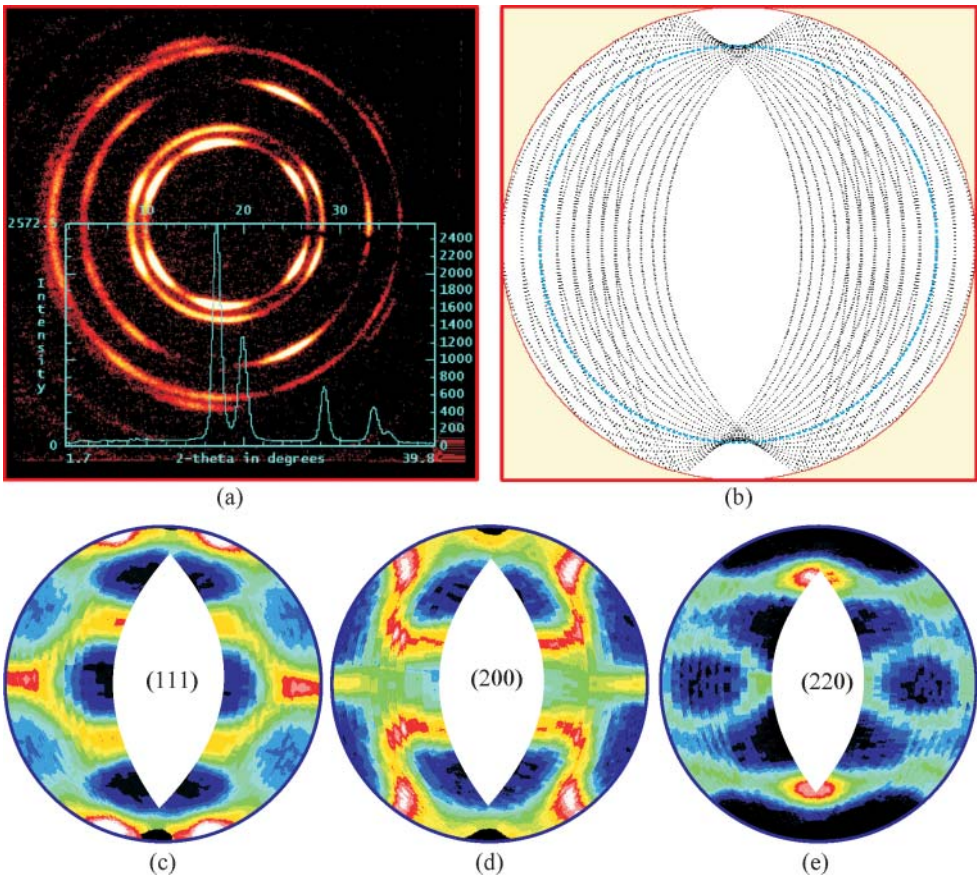


FIGURE 8.11 Texture measurement in transmission mode on an aluminum plate: (a) 2D diffraction frame, (b) data collection scheme for (200) pole-figure, (c) (111) pole-figure, (d) (200) pole-figure, (e) (220) pole-figure.

collected, including (111), (200), (220), and (311). The single rotation axis can be defined as the ω axis. For transmission mode diffraction, without change the sample coordinates, $\omega = 90°$ will put the sample surface normal to the incident beam direction. Figure 8.11(b) shows the scheme generated for (200) pole-figure from 20 frames with continuous ω scan from 42.5° to 142.5° with $\Delta\omega = 5°$ steps. With continuous scan, the central value of each scan step is used to calculate the pole-figure mapping projection. The blue circle in the scheme represents the projection from a frame at $\omega = 90°$ (actually collected within the ω range from 87.5° to 92.5°). The schemes for (111) and (220) would be similar because all three rings are complete. The single rotation may be defined as ϕ angle, but the sample coordinates and pole-figure projection would have to be redefined because ϕ axis is defined as a rotation above the sample normal ($\mathbf{S_3}$) in the standard XRD[2] geometry. Figure 8.11(c), (d), and (e) are the measured pole-figures for (111), (200), and (220) crystallographic planes respectively.

The scheme and measured pole-figures show that pole-figures collected by the transmission mode can reach the regions up to 90° from the sample normal (pole-figure center), but leave a blank region in the center. This is opposite to the reflection mode which tends to leave the region near the outer boundary circle blank. In either case, the missing region of the pole-figure can be constructed through the orientation distribution function (ODF) if multiple incomplete pole-figures are collected. The complete pole-figure may be measured by combining the data collected in both reflection mode and transmission mode, but discontinuity and other artifacts may be observed because of the absorption and geometry of the sample.

8.4.6 Comparison with Point Detector

The effectiveness of two-dimensional data collection for a texture can be compared to the point detector with the data collection strategy of the Cu thin film as an example. Figure 8.12(a) shows the data collection strategy for the (111) pole-figure from Figure 8.7(a) with the data scan steps shown as $\Delta\phi(s)$. The number of data frames, or exposures, for the displayed pole-figure coverage is 108. Figure 8.12(b) shows the pole-figure data collection strategy with a point detector. For the same resolution in the azimuthal angles and 5° steps in radial angles, a total of 973 measurements

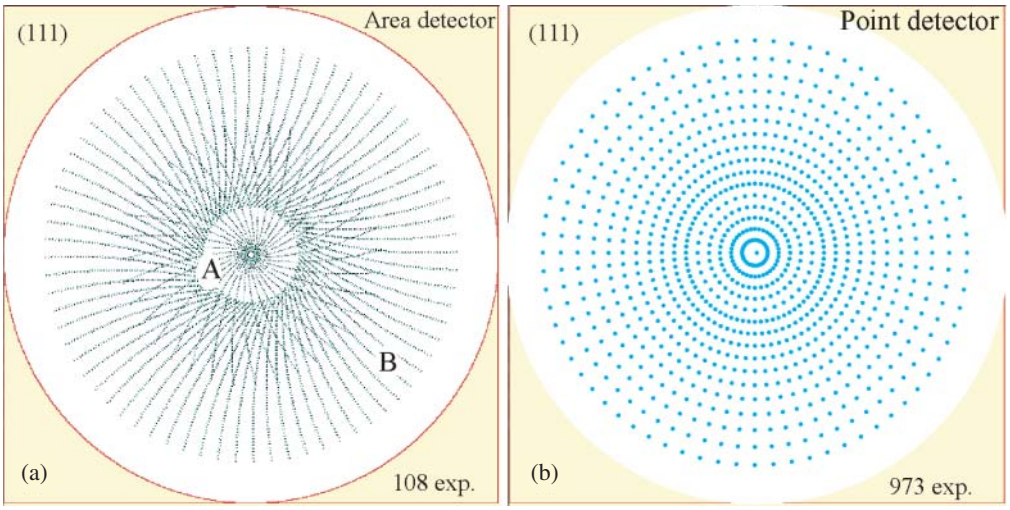


FIGURE 8.12 Comparison of data collection scheme: (a) strategy with area detector, (b) strategy with point detector.

are required to cover the same pole-figure area. It would require significantly more data points if the same resolution in the radial direction is expected. To collect all three pole-figures for (111), (200), and (220) with the area detector, a total of 144 exposures is required, as shown in Figure 8.7, while a total of 2919 measurements are required with a point detector. In this particular case, the pole-figure measurement with an area detector is more than 20 times faster than with a point detector. If pole-figures of higher resolution are expected, an area detector needs to reduce the data scan steps only at azimuthal angles, while the measurement with a point detector needs to reduce data scan steps for both azimuthal angles and radial angles. Taking the data collection scan steps shown as $\Delta\phi(c)$ in Figure 8.7 as an example, the resolution is increased by a factor of 5. The measurement of all three pole-figures with the area detector now requires 720 data frames. With a 5 second exposure per frame, the data collection time is about one hour, while with a point detector, the five-fold improvement in the pole-figure resolution would require a total of 72,975 data points. With a 5 second exposure per data point, the total data collection time would be more than 100 hours, which becomes impractical for most pole-figure studies. Therefore, for quantitative high resolution pole-figure measurement, a two-dimensional diffraction system is preferred over a conventional diffractometer with point detector [1].

8.5 TEXTURE DATA PROCESS

8.5.1 2θ Integration

A diffraction frame contains pixel intensities, and each pixel corresponds to a set of 2θ and γ values. In order to map the diffraction intensity distribution onto a pole-figure, it is necessary to calculate the diffraction intensity as a function 2θ, γ, and the sample orientation (ω,ψ,ϕ), i.e. $\mathbf{I} = \mathbf{I}(2\theta,\gamma,\omega,\psi,\phi)$. For a specific diffraction ring, 2θ is a constant or at least assumed to be constant for texture analysis, and the sample orientation angles (ω,ψ,ϕ) for a frame are also constants. Therefore, the pole-density information for a crystallographic plane in a frame is given by the diffraction intensity distribution as a function of γ only, or $\mathbf{I} = \mathbf{I}(\gamma)$. The diffraction intensities along a diffraction ring have a two-dimensional distribution, therefore, it is necessary to integrate the diffraction intensities in the vicinity of the diffraction ring in the 2θ direction so as to convert two-dimensional information into an one-dimensional function, $\mathbf{I}(\gamma)$.

Figure 8.13(a) shows one of the diffraction frames collected on an aluminum wire for texture analysis. At a detector distance of 6 cm with Cu radiation, a total of five diffraction rings from the crystallographic planes of (111), (200), (220), (311), and (222) can be measured simultaneously. Therefore, five pole-figures can be measured simultaneously. The low and high background and diffraction ring 2θ-γ range are defined by three boxes. All three boxes have the same γ range; in this example, $\gamma_1 = 55°$ and $\gamma_2 = 125°$. The 2θ ranges for the diffraction ring, low background, and high background should be determined based on the width of the 2θ peak and available background between adjacent peaks. It is assumed that the 2θ profile is a normal distribution, with FWHM $= 2.35\sigma$, and standard deviation σ. The 2θ range of two times the FWHM covers 98% of the intensity peak, and three times the FWHM covers more than 99.9%. In a set of data frames collected for texture measurement, the FWHM of the 2θ profile varies with the incident angle. The 2θ range should be sufficient to cover at least two times the FWHM of the broadest 2θ peak. The 2θ range should also be broad enough to cover the possible 2θ shifts caused by residual stresses in the sample. Figure 8.13(b) is the 2θ profile of the (220) plane integrated over the section $\Delta\gamma$ in Figure 8.13(a). The FWHM of the (220) peak is approximately 0.5°. The 2θ peak position is approximately 65.4° and a 2θ range of 3° is selected ($2\theta_1 = 64°$ and $2\theta_2 = 67°$), which is about six times the FWHM. Since there are large background ranges on both the low and

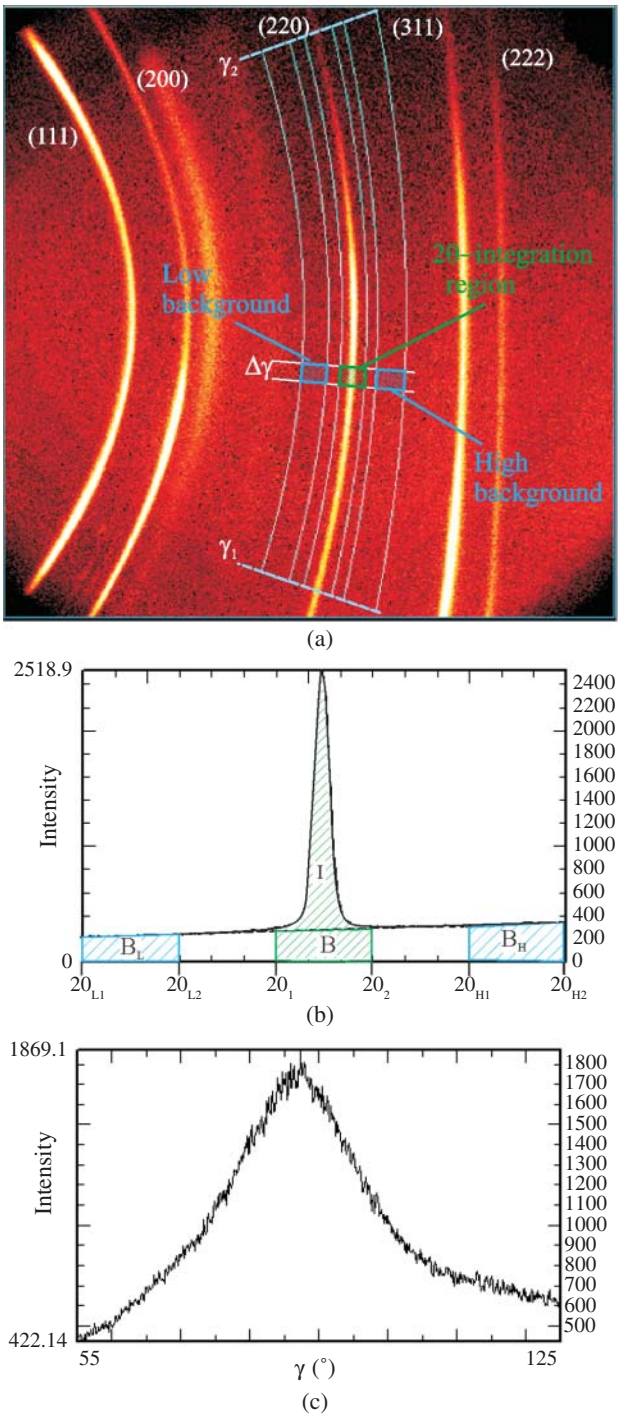


FIGURE 8.13 Pole-figure data process: (a) a frame from Al sample with the 2θ-integration ranges for (220) ring, (b) 2θ profile showing the background and peak, (c) integrated intensity distribution as a function of γ.

high 2θ sides, low background and high background 2θ ranges of 3° are selected. ($2\theta_{L1} = 58°$, $2\theta_{L2} = 61°$, $2\theta_{H1} = 70°$, $2\theta_{H2} = 73°$). The 2θ-integrated diffraction intensities as a function of γ is plotted in Figure 8.13(c). The background can be calculated and removed from the intensity values of the low and high backgrounds or ignored if the contribution of the background is trivial.

The 2θ-integration without background correction can be expressed as

$$I(\gamma) = \int_{2\theta_1}^{2\theta_2} J(2\theta, \gamma) d(2\theta) \quad \gamma_1 \le \gamma \le \gamma_2 \tag{8.17}$$

or

$$I(\gamma) = \sum_{2\theta_1}^{2\theta_2} J(2\theta, \gamma) \quad \gamma_1 \le \gamma \le \gamma_2 \tag{8.18}$$

where $J(2\theta, \gamma)$ represents the two-dimensional intensity distribution in the 2D frame and $I(\gamma)$ is the integration result as a function of intensity versus γ. $2\theta_1$ and $2\theta_2$ are the lower limit and upper limits of integration, which are constants for 2θ-integration. Due to the discrete nature of the diffraction frame, equation (8.18) is used to sum the counts within each $\Delta\gamma$ step. A similar equation can be used for 2θ-integration of the backgrounds:

$$B_L(\gamma) = \sum_{2\theta_{L1}}^{2\theta_{L2}} J(2\theta, \gamma) \text{ and } B_H(\gamma) = \sum_{2\theta_{H1}}^{2\theta_{H2}} J(2\theta, \gamma) \quad \gamma_1 \le \gamma \le \gamma_2 \tag{8.19}$$

where $B_L(\gamma)$ and $B_H(\gamma)$ are the integrated intensity of the low and high backgrounds within the $\Delta\gamma$ step, as are shown in Figure 8.13(b). Assuming a linear background change in the vicinity of the 2θ peak, the background under the peak, $B(\gamma)$, is then given by

$$\begin{aligned} B(\gamma) = {} & B_L(\gamma) \frac{(2\theta_2 - 2\theta_1)(2\theta_{H2} + 2\theta_{H1} - 2\theta_2 - 2\theta_1)}{(2\theta_{L2} - 2\theta_{L1})(2\theta_{H2} + 2\theta_{H1} - 2\theta_{L2} - 2\theta_{L1})} \\ & + B_H(\gamma) \frac{(2\theta_2 - 2\theta_1)(2\theta_2 + 2\theta_1 - 2\theta_{L2} - 2\theta_{L1})}{(2\theta_{H2} - 2\theta_{H1})(2\theta_{H2} + 2\theta_{H1} - 2\theta_{L2} - 2\theta_{L1})} \end{aligned} \tag{8.20}$$

Then the background stripped intensity distribution is given by

$$I(\gamma) = \sum_{2\theta_1}^{2\theta_2} J(2\theta, \gamma) - B(\gamma) \quad \gamma_1 \le \gamma \le \gamma_2 \tag{8.21}$$

The algorithms of γ-integration given in Chapter 4 can be easily modified for 2θ-integration by exchanging γ and 2θ in the equations. The algorithms with solid angle normalization should be used to get consistent integrated intensity over all areas of the detector. The 2θ-integrated intensity distribution can then be mapped onto a pole-figure based on the pole-figure angles given by equations (8.3). When a pole-figure pixel is overlapped by more than one data point from different scans, as shown in the region covered by two scans in Figure 8.7, the average value should be mapped to that pole-figure pixel. Figure 8.14 shows the processes of pole-density mapping and the pole-figure processes of the pole-figure data collected from an aluminum plate. The two-dimensional diffraction data frames were collected with GADDS™ with a Hi-Star™ area detector and quarter-circle Eulerian cradle (Bruker AXS). The aluminum plate was loaded in an orientation such that the sample surface is on the S_1-S_2 plane of the sample coordinates and the rolling direction (RD) is parallel to the S_2 direction. Row (a) shows pole density mappings of

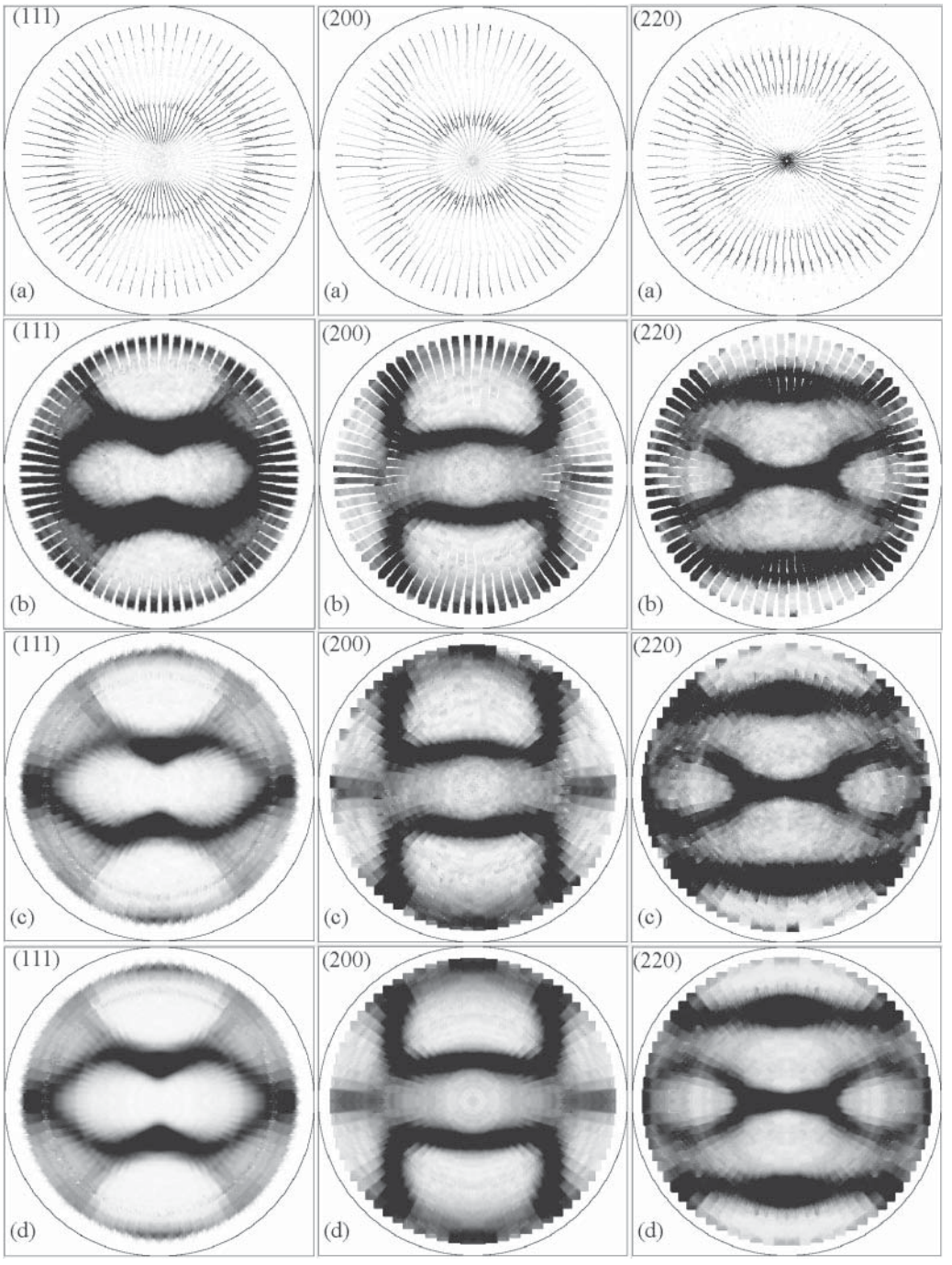


FIGURE 8.14 Pole-figure processes: (a) the 2θ-integrated pole density mapped to the pole-figure, (b) interpolation within five pixel half-width box, (c) second interpolation with the same box size, (d) symmetry process with Laue symmetry *mmm*.

three crystallographic planes: (111), (200), and (220). There are big gaps between the measured pole density data points due to the large ϕ scan of 5° steps. The gaps in the outer edge of the pole-figure are as large as 18 pixels.

8.5.2 Absorption Correction

All factors affecting relative intensities – such as Lorentz, polarization, air scattering, Be-window, and sample absorption – will have effects on the measured pole densities for the pole-figures. The corrections to these factors were given in Chapter 6. Some or all these corrections may be applied to the diffraction frames before 2θ-integration if the texture study demands high accuracy in the relative pole densities. The most important of these factors is sample absorption, since the data set for pole-figures is typically collected at several different incident angles, as shown in Figure 8.7. A ridge between the pole density regions covered by two different incident angles may be observed if sample absorption is not properly corrected. Sample absorption can either be applied to the data frames before the 2θ-integration or to the integrated results. The correction is

$$I_S(\gamma) = C_S(\gamma) \cdot I(\gamma) \tag{8.22}$$

where $I_S(\gamma)$ is the intensity distribution corrected by the sample absorption and $C_S(\gamma)$ is the absorption correction factor. For example, the absorption correction factor for a plate sample in reflection mode is given by

$$C_S(\gamma) = \frac{\cos\eta + \cos\zeta}{2\cos\eta \cdot \{1 - \exp[-\mu t(\sec\eta + \sec\zeta)]\}} \tag{8.23}$$

with $\cos\eta = \sin\omega\cos\psi$ and $\cos\zeta = -\cos 2\theta \sin\omega\cos\psi - \sin 2\theta \sin\gamma \cos\omega\cos\psi - \sin 2\theta\cos\gamma \sin\psi$.

Since all other angles are constants for a particular 2θ-integrated intensity distribution, $C_S(\gamma)$ is a function of γ only for each 2θ-integrated profile.

Sample absorption and all other instrumental factors affecting the relative intensity distribution can be corrected experimentally if a sample having the same content and crystal structure, but a random orientation distribution, is available. The "pole-figures" of the random sample are collected with the same strategy and experimental conditions. The corrected pole-figures can be obtained by normalizing the pole-figures of the textured sample by the "pole-figures" of the sample with random orientation, as given by equations 8.13 and 8.14.

8.5.3 Pole-Figure Interpolation

The pole-figure is stored and displayed as a bitmap image. Each pixel location represents a pole-figure orientation given by (α,β). The pole-density data points from all the collected frames may not fill up all the pixels of the pole-figure image due to the gap between data scan steps, as shown in Figure 8.14 row (a). The pixels without available data values should not be confused with the pixels that simply have zero pole-density. One method to make this distinction is to store all the filled pixels with the pole-density value plus one, while the unmapped pixels are given a value of 0. In order to generate a smooth pole-figure, the unmapped pixels are filled by the values generated from the interpolation of the surrounding pixels. A linear interpolation within a defined box is sufficient to fill the unmapped pixels. The size of the box should be properly chosen. A box too small may not be able to fill all unmapped pixels and a box too big may generate a smearing effect to the pole-figure, especially if a sharp pole-figure is processed. The box size can be determined by trial and error and should be at least as large as the largest pixel gap between

adjacent mapped pixel lines. Figure 8.14 row (b) shows the results from the interpolation of the three pole-figures in row (a) by GADDS™ software version 4.1. The interpolation box has a half width of five pixels, the maximum allowed by the software. Apparently, the box is not big enough to cover the largest gap, so there are still some gaps left in the rim of the pole-figure. Figure 8.14 row (c) shows the results after another interpolation with same box size. All the gaps between the measured pole density points are filled after this interpolation. For a sample with texture sharper than this example, smaller ϕ scan steps should be used. Single interpolation would be able to fill the gaps if the ϕ scan steps were smaller than 2.5° in this case.

8.5.4 Pole-Figure Symmetry

All pole-figure possess symmetry due to crystal Laue symmetry. Symmetry features can be used to fill the unmeasured pole-figure pixels or to smooth the pole-figure. For example, orthorhombic materials exhibit *mmm* symmetry, thus so we need to collect only an octant or quadrant of the pole sphere to generate the entire pole-figure. Laue symmetries that can be used for pole-figure data processes are triclinic (i), monoclinic ($2/m$), orthorhombic (mmm), tetragonal ($4/m$, $4/mmm$), trigonal ($\bar{3}$, $\bar{3}m$), hexagonal ($6/m$, $6/mmm$), and cubic ($m\bar{3}$, $m\bar{3}m$). The pole-figures of materials with higher symmetry may be treated by lower symmetry processes. For instance, we can use $2/m$ or mmm for hexagonal and mmm for cubic. In symmetry processes, all the symmetrical equivalent pole-figure pixels are filled by the average value of the measured pixels. For the unmeasured pole-figure pixels, the symmetry process fills in a value from the average of the all equivalent pixels. For the measured pixels, this average process serves as a smoothing function. Figure 8.14 row (d) shows the results from the symmetry processes of the pole-figures in row (c). Since the pole-figures in row (c) are complete in azimuthal angle β, the symmetry process made the pole-figure symmetric and smoothed the pole-figure.

8.5.5 Pole-Figure Normalization

The pole densities calculated from 2θ integration contain a factor proportional to the relative intensities of the different (hkl) peaks. For example, the crystallographic planes (111) and (222) should have identical orientation distributions, but the 2θ-integrated intensity can be significantly different due to different relative intensities. As given by equation (8.9), the pole-figure should be normalized such that it represents the ratio of the pole-densities relative to an ideal powder. The pole density of an ideal powder is defined as unity at any orientation. In practice, the pole density of an ideal powder may be defined as a different value, 100, for instance. The pole-figure may be pseudo-normalized to any scale for display.

8.6 ORIENTATION DISTRIBUTION FUNCTION

Each pole-figure can only define the orientation distribution of a particular crystal direction normal to the crystallographic plane, but the orientation distribution function (ODF) defines the full representation of the crystallographic orientation distribution. The ODF can be obtained by evaluations of several independent pole-figures. Accordingly, pole-figures of all orientations can be calculated from the ODF.

8.6.1 Eulerian Angles and Space

Three Eulerian angles are required to specify the orientation of a rigid body with respect to reference axes. As shown in Figure 8.15(a), the orientation of crystal coordinates can be expressed by the three Eulerian angles $\{\varphi_1, \Phi, \varphi_2\}$ [10]. The sample coordinates are denoted by the Cartesian

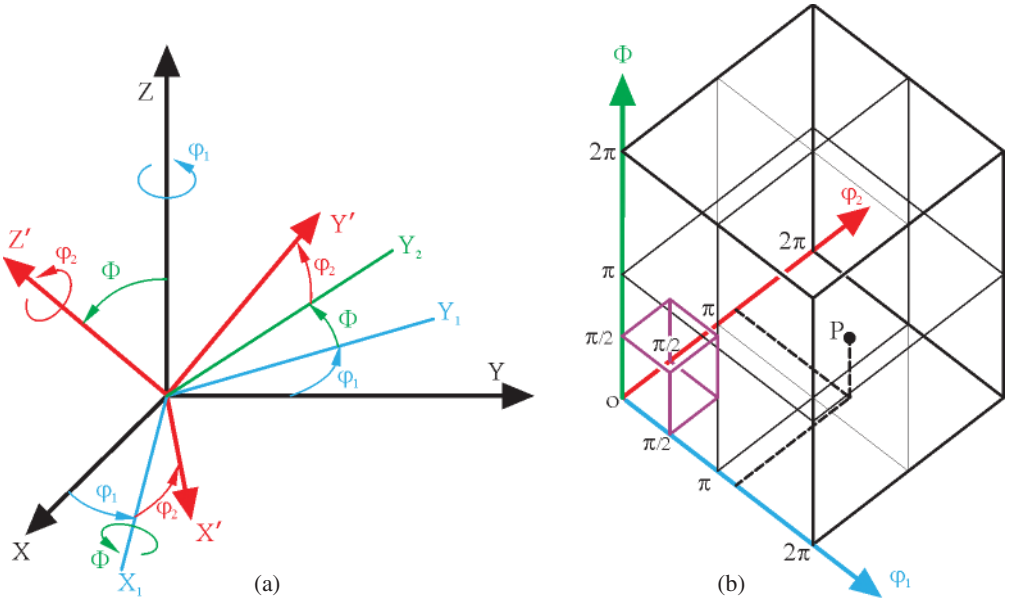


FIGURE 8.15 Eulerian angles and space: (a) Eulerian angles defining the orientation of the crystal coordinates in the sample coordinates, (b) Eulerian space given by the three Eulerian angles in Cartesian coordinates.

coordinates **XYZ** (equivalent to the previously defined $\mathbf{S_1S_2S_3}$ coordinates) with the **XY** plane parallel to the sample surface. When all three Eulerian angles equal 0, the crystal coordinates $\mathbf{X'Y'Z'}$ overlap to the corresponding sample coordinates **XYZ**. To reach a given orientation of the crystal coordinates with respect to the sample coordinates, the crystal coordinate system is first rotated about the **Z** axis by the angle ϕ_1. After this rotation, the crystal coordinates overlap to $\mathbf{X_1Y_1Z}$. Then the crystal coordinate system rotates (from its new orientation after the ϕ_1 rotation) about the $\mathbf{X_1}$ axis by the angle Φ. After this second rotation, the crystal coordinates overlap to $\mathbf{X_1Y_2Z'}$**.** Then the crystal coordinate system after the first two rotations is further rotated about the $\mathbf{Z'}$ axis by the angle ϕ_2. The final orientation of a crystal coordinates $\mathbf{X'Y'Z'}$ can be expressed by the three Eulerian angles as

$$g = \{\varphi_1, \Phi, \varphi_2\} \tag{8.24}$$

where g represents a combination of all three Eulerian angles, and should not be confused with the normalized pole density function $g_{hkl}(\alpha, \beta)$. Although the Eulerian angles $\{\varphi_1, \Phi, \varphi_2\}$ have the same rotation sequence as the Eulerian angles $\{\omega, \psi, \phi\}$ used for the sample orientation, they must not be confused. The Eulerian angles $\{\varphi_1, \Phi, \varphi_2\}$ define the crystallite orientation with respect to the sample coordinates, while the Eulerian angles $\{\phi, \psi, \omega\}$ define the sample orientation with respect to the laboratory coordinates. With a point detector, pole density data corresponding to a single pole or diffraction vector is measured at each sample orientation, so a direct relationship can be found between the orientation of the measured crystallites and the sample orientation. With an area detector, a series of g values can be achieved at each sample orientation. The Eulerian angles $\{\varphi_1, \Phi, \varphi_2\}$ can be expressed in three-dimensional Cartesian coordinates, referred to as the orientation space or Eulerian space, as shown in Figure 8.15(b). Any point, P, in Eulerian space represents a crystal orientation g. The number of crystallites having the orientation g can be considered the density at the point P. The full 3D representation of a crystallographic

texture is given by the orientation distribution function (ODF), which is a density function of the orientation g.

$$f(g) = f(\varphi_1, \Phi, \varphi_2) \tag{8.25}$$

Since all three coordinates are actually angular values, the Eulerian space has a periodicity of 2π in all three axes. Due to crystal symmetry, the Eulerian space can be divided in several subregions, for instance, the region within a $\pi/2$ range in all three axes, each containing complete information about the ODF.

By definition, the ODF is the volume fraction of crystallites oriented along a certain direction g.

$$f(g) = \frac{1}{V}\frac{dV(g)}{dg} \tag{8.26}$$

where V is the total sample volume, dV is the total volume of elements in the sample that possess the orientation g within an element of orientation dg (the orientation window between g and $g + dg$). Assuming all crystallites have the same shape and size, the orientation distribution function can be expressed as

$$n(g) = \frac{1}{N}\frac{dN(g)}{dg} \tag{8.27}$$

where N is the total number of crystallites in the sample, dN is the total number of crystallites that possess the orientation g within an element of orientation dg.

8.6.2 ODF Calculation

The ODF cannot be measured directly, but can be obtained through evaluation of a set of pole-figures. Different methodologies exist for obtaining the ODF from the pole-figures or measured pole density data [11–13]. One is the harmonic method, which expresses the ODF as a series of generalized spherical harmonic functions:

$$f(g) = \sum_{l=0}^{\infty} \sum_{m=-l}^{+l} \sum_{n=-1}^{+l} C_l^{mn} T_l^{mn}(g) \tag{8.28}$$

where C_l^{mn} represents the ODF coefficients, also referred as C-coefficients, $T_l^{mn}(g)$ are the generalized spherical harmonic functions, l is the order of the series, and m and n denote finite numbers of independent C-coefficient at each order. The three indices l, m, n, correspond to the dependence of the ODF on the three Eulerian angles with n related to ϕ_1 and m related to ϕ_2. The index l has to be a finite number to fit the experimentally determined pole density data with a finite number of independent C-coefficients. The series has to be truncated to fit the finite number of measured data points.

$$f(g) = \sum_{l=0}^{L} \sum_{m=-l}^{+l} \sum_{n=-1}^{+l} C_l^{mn} T_l^{mn}(g) \tag{8.29}$$

where L is the maximum order (also referred as degree or rank in various literature) of the series. L should be determined by the number of available pole-figures and the resolution of the ODF. Some of the $T_l^{mn}(g)$ terms vanish due to crystal symmetry, therefore fewer numbers of pole-figures are required for a crystal of high symmetry of the same order. Table 8.1 lists the order of series that can be solved from the number of pole-figures for each symmetry type [14].

Table 8.1 Order of the Series of Harmonics for the Number of Pole-Figures

Number of pole-figures (n)	Cubic	Hexagonal	Tetragonal	Trigonal	Orthorhombic
2	22	10	6	4	2
3	34	16	10	8	4
4	34	22	14	10	6
5	34	22	18	14	8
6	34	22	22	16	10
7	34	22	22	20	12
8	34	22	22	22	14
>8	46	22	22	22	2(n − 1) if n < 13 22 if n ≥ 13

In order to have an overview of the ODF values, it is typically visualized as contour plots in a series of cross-sections perpendicular to one of the three axes through the Eulerian space. The display is sometimes referred to as a Eulerian plot. Figure 8.16 shows the ODF calculated from the three pole-figures shown in row (c) of Figure 8.14. The pole-figures in row (d) were not used to generate the ODF because the symmetry process on the input pole-figures is not necessary. Symmetry features have been included in the ODF calculation with a spherical harmonic series. The ODF is displayed as 19 cross-sections at constant φ_1 angles of 0° to 90° with 5° steps. The ODF may also be displayed as contour plots with cross-sections at constant φ_2 or Φ angles.

8.6.3 Calculated Pole-Figures from ODF

Pole-figures can be recalculated from the ODF, which was generated from the measured pole-figures. Figure 8.17 shows the pole-figures used to generate the ODF and the pole-figures calculated from the ODF. Figure 8.17 row (a) shows the three measured pole-figures in contour plots for the (111), (200), and (220) planes of the aluminum plate as shown in Figure 8.14 row (c). The measured pole-figures were obtained by mapping the 2θ-integrated density distribution into the pole-figure and interpolated to fill the gap. The pole-figures have been measured up to a χ angle of approximately 85° ($\alpha = 5°$), so the pole-figures are not complete, as is shown by the broken line circles. The pole densities in the regions of $\chi > 85°$ are very difficult to measure due to the low incident and reflection angles. Due to crystal symmetry, the three incomplete pole-figures are sufficient to calculate the ODF. The ODF calculation takes advantage of the redundancy in pole-density information and crystal symmetry from all the measured pole-figures, so the ODF contains improved statistics and integrity of texture information. Therefore, the three recalculated pole-figures for (111), (200), and (220), as shown in row (b), are complete, symmetric, and smooth. This process has frequently been used to generate complete pole-figures from incompletely measured pole-figures or pole-density data. Once the ODF is obtained, pole-figures of any other orientation can be calculated. Row (c) of Figure 8.17 shows the calculated pole-figures for crystallographic planes of (311), (331), and (420). The pole-figures of the crystallographic planes with zero structure factors may never be measured by X-ray diffraction, but can be calculated from the ODF based on available measured pole-figures of other planes.

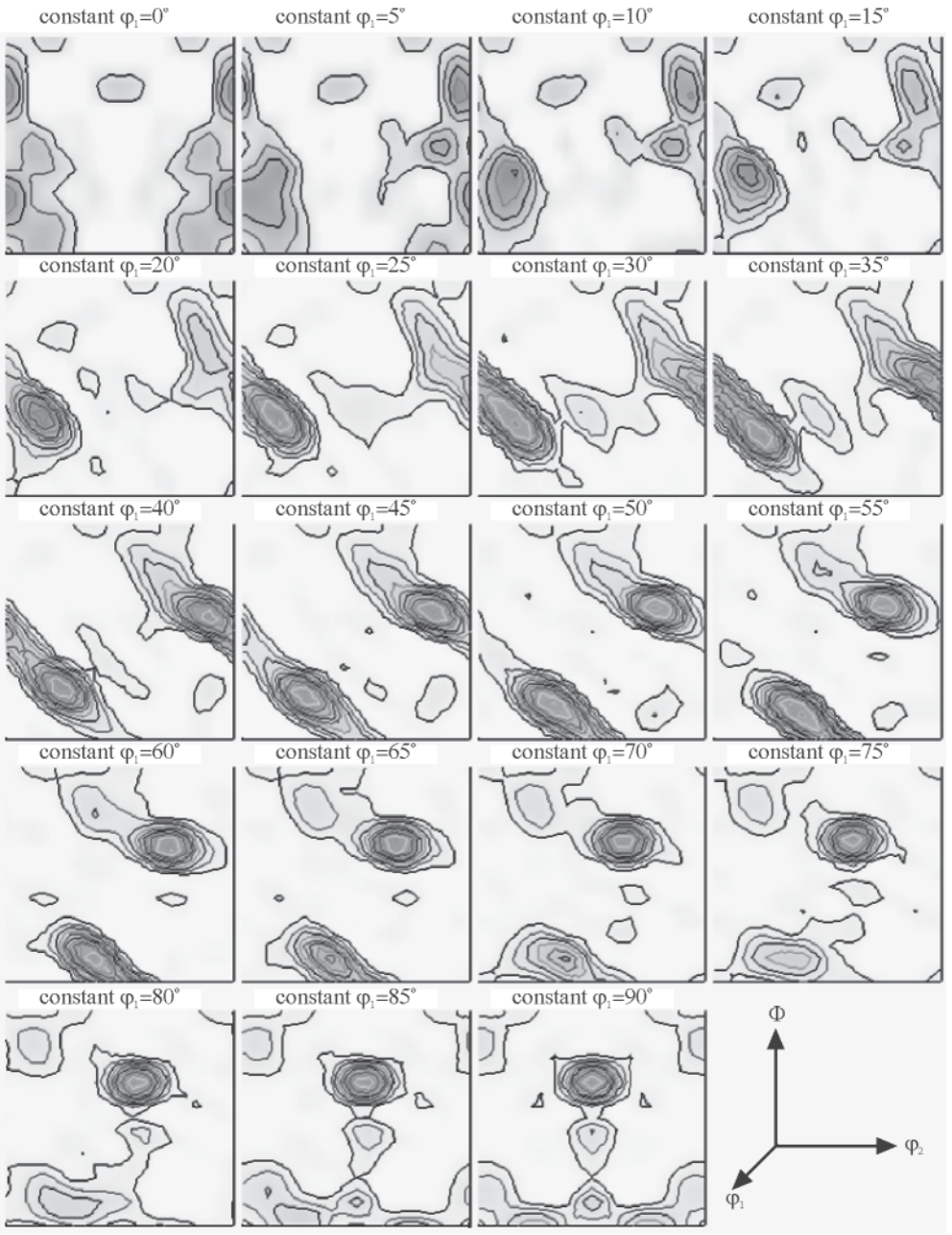


FIGURE 8.16 ODF of the aluminum plate calculated from the pole-figures (111), (200), and (222).

8.7 FIBER TEXTURE

If the texture has a rotational symmetry with respect to a sample orientation, the texture is referred to as a fiber texture. The sample orientation containing the symmetry axis is referred to as the fiber axis. If the fiber axis is aligned to the ND (S_3) direction as shown in Figure 8.3(a), the pole-density

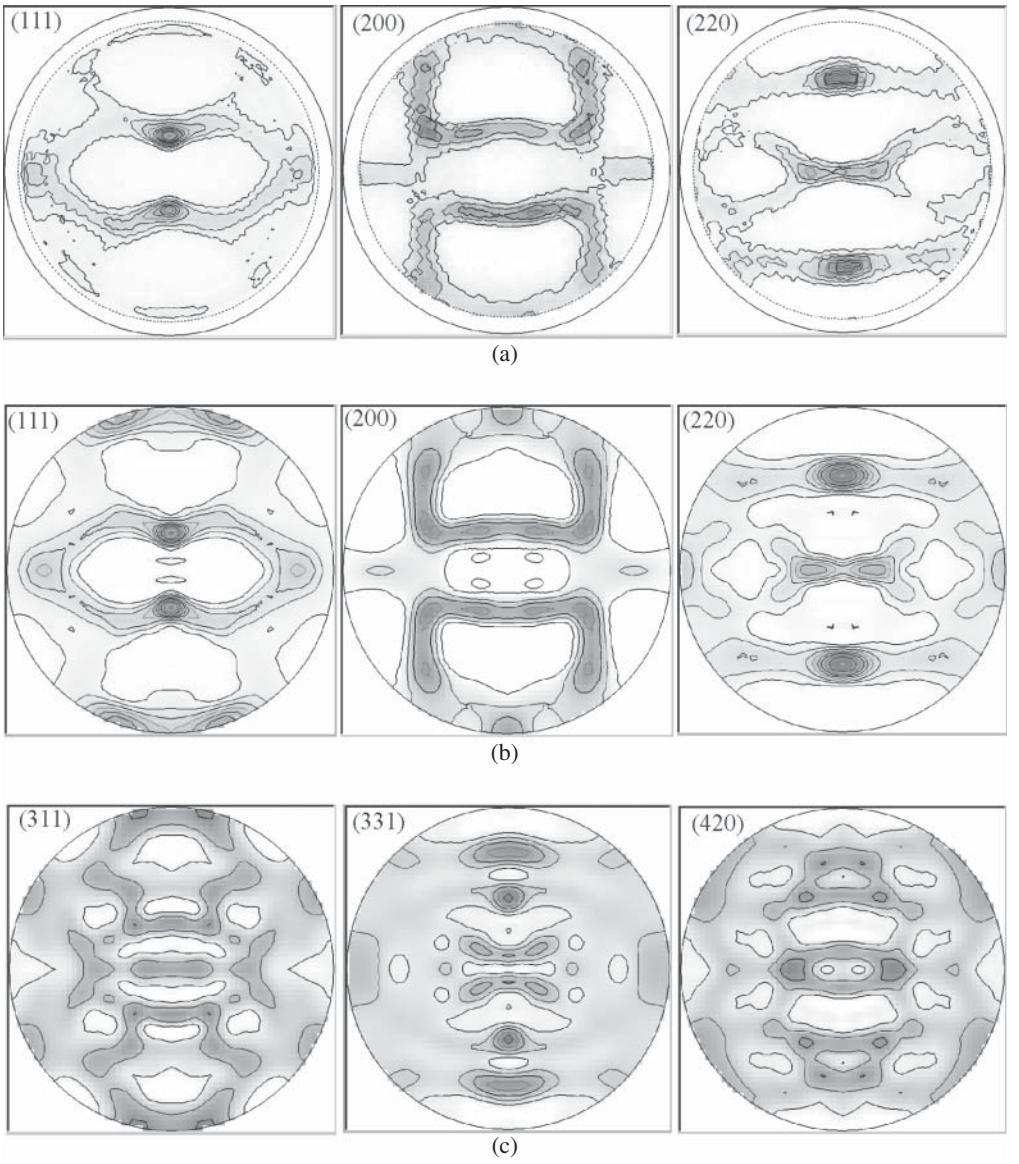


FIGURE 8.17 Pole-figure calculation from ODF: (a) Contour plots of three measured pole-figures, (b) recalculated pole-figures of the same planes from ODF, (c) calculated pole-figures of unmeasured crystallographic planes.

distribution function becomes independent of the azimuthal angle β. The fiber texture is mostly observed in two types of materials, metal wires or rods formed by drawing or extrusion, and thin films formed by physical or chemical deposition. The fiber axis is the wire axis of a wire and normal to the sample surface for thin films. Fiber texture can also be artificially formed by spinning a sample about its normal. This is a very useful feature since the relative intensity correction for a texture can be significantly simplified with sample spinning. The details were covered in Chapter 7 on phase identification.

8.7.1 Pole-Figures of Fiber Texture

Figure 8.18 show the pole-figures and ODF of fiber texture measured on a magnetron sputter-deposited Cu film onto a Si (111) wafer with the experimental conditions and data collection strategy illustrated in Figures 8.6 and 8.7. Figure 8.18(a) shows the 3D surface plots of the three measured pole-figures for the (111), (200), and (220) planes. The pole density distribution for (111) is concentrated in the center of the pole-figure. The pole density distributions of (200) and (220) are concentrated in the regions that match the corresponding angles of the (200) plane and the (220) plane with respect to the (111) plane. That means the (111) planes are mostly aligned approximately parallel to the film, or the [111] directions are aligned to the fiber axis or the sample normal direction. This fiber texture is called a (111) fiber texture. Figure 8.18(b) shows the contour plots of the three measured pole-figures. Figure 8.18(c) shows four cross-sections of the ODF at $\varphi_1 = 0°$, 30°, 60°, and 90° (19 cross-sections from 0° to 90° with 5° intervals were actually examined). Since the fiber axis is on the Z axis of the sample system, or the sample normal is the φ_1 axis of the Eulerian space, the ODF is independent of the φ_1 axis. All 18 (only four are shown) cross-sections of the ODF show almost identical pattern. Figure 8.18(d) shows three calculated pole-figures from the ODF for the same planes of the measured pole-figures. The measured pole-figures cover the angular region up to only $\chi = 80°$ approximately, but the calculated pole-figure covers all the angles up to $\chi = 90°$. The calculated complete pole-figures reveal the pole density distributions following the angles between planar normals in the cubic system [15]. The (111) pole-figure shows the concentrated intensity distribution in the center and in a ring making a 70.5° angle from the center, since the angle between (111) planes are either 0° or 70°32′. The (200) pole-figure shows the concentrated intensity distribution in a ring making a 54.7° angle from the center, since the angle between (111) plane and (200) plane is 54.74°. The (220) pole-figure shows the concentrated intensity distribution in two rings making 35.3° and 90° angles respectively from the center, since the angle between (220) and (111) planes are either 35.26° or 90°.

Since fiber texture has a pole density distribution symmetrical about the fiber axis or the sample normal, the fiber texture can be expressed by a fiber texture plot (FTP). Description and examples of a FTP were given in Chapter 6 on texture correction for phase identification.

8.7.2 ODF of Fiber Texture

The ODF based on the three Eulerian angles can be significantly simplified for fiber textures. The generally three-dimensional ODF can be expressed by its two-dimensional cross-section, since the dependence on the Eulerian angle ϕ_1 vanishes if the fiber axis is aligned with the Z axis in the Eulerian space. Consequently, general two-dimensional pole-figures can be expressed by one-dimensional fiber plots. The ODF for fiber texture can be determined with much less experimental data and calculation effort. The ODF calculation for fiber texture of cubic materials has been briefly discussed in Chapter 7, and more details can be found in the references [15–17].

Figure 8.19 shows the normalized ODF, $\bar{w}(\Omega, \psi)$, of a hot extruded rod of a Cu-Be alloy [16, 17]. Since the ODF for fiber texture is reduced to a two-dimensional distribution, the ODF can be expressed in a contour plot as in Figure 8.19(a) or a surface plot as in Figure 8.19(b). The Eulerian angles in this example are expressed as $\{\phi, \Omega, \psi\}$, which have the same definition as $\{\varphi_1, \Phi, \varphi_2\}$ respectively. The normalized ODF is calculated from the measured relative intensities of 17 peaks by a spherical harmonic series up to the 16th order. The fiber plots of various peaks can be calculated from the ODF and three calculated fiber plots were shown in Chapter 7 with comparison to measured data.

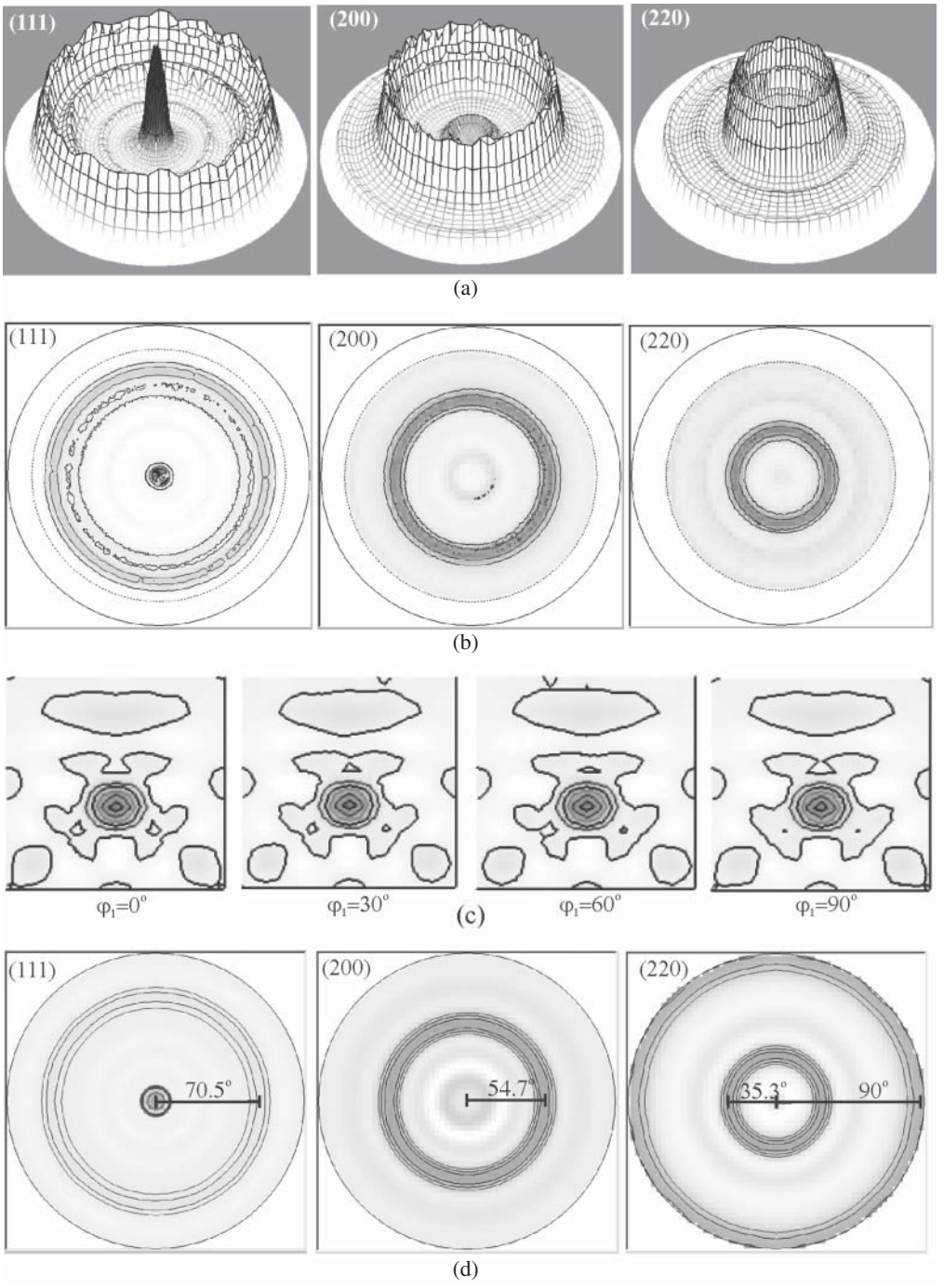
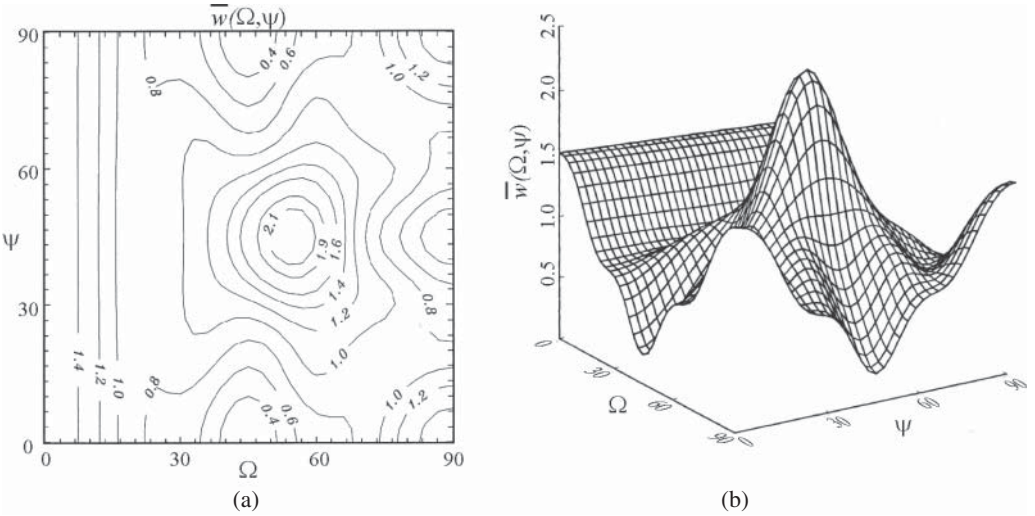


FIGURE 8.18 Pole-figures and ODF of fiber texture: (a) 3D surface plots of the three measured pole-figures, (b) contour plots of the three measured pole-figures, (c) ODF at four cross-sections, (d) calculated pole-figures from the ODF.



(a) (b)

FIGURE 8.19 Normalized ODF of fiber texture of a Cu-Be alloy sample: (a) in contour plot, (b) in 3D surface plot.

8.8 POLYMER TEXTURE

In general, X-ray diffraction can provide information on the atomic arrangement in materials with long range order, short range order, or no order at all. The atomic arrangement in polymer samples can be as random as amorphous, crystalline with long range order, or a structure between the two extremes. A polymer sample can contain a mix of domains in amorphous, crystalline, and intermediate phase. These domains, especially crystalline phase, may have a particular orientation distribution affecting the properties and performance of the polymers. The polymer sample evaluated by XRD can be in the form of powders, fibers, films, plate, and bulk solid. As such, the intensities and spatial distributions of the scattered X-rays from a polymer sample can be quite complex. An XRD^2 system is much preferred for polymer analysis since a 2D detector can easily capture a comprehensive diffraction pattern [18–22]. This is especially important when dealing with oriented polymers.

8.8.1 Data Collection Strategy for Polymers

Data collection for texture measurement of polymers can be in either transmission or reflection geometry. Due to the low density of polymers, the sample thickness for transmission can be as thick as several millimeters, depending on the linear absorption coefficient μ. The optimum thickness is approximately given as $1/\mu$, but a transmission diffraction pattern can be observed for a sample of a few times thicker. With a large 2D detector at on-axis position, several complete diffraction rings can be observed. For instance, with active area of 140 mm in diameter and detector distance 150 mm, complete diffraction rings up to 43° 2θ can be observed. This is sufficient to cover the crystalline peaks of most polymers. When the incident X-ray beam is normal to the sample surface, the projected pole density is mapped to a circle concentric to the pole-figure boundary. With sample rotation about an axis on the sample surface, the measured pole intensity covers more area in the pole-figure. The maximum rotation angle is less than $90 - 2\theta$. A relatively small 2θ angle of typical polymer peaks allows a large rotation angle away

from normal direction so as to have a large pole-figure coverage. A pole-figure by transmission can easily cover the region near the outer circle ($\chi = 90°$ or $\alpha = 0$), but cannot cover the region in the center of pole-figure.

The reflection mode data collection is preferred or necessary when the sample is too thick for transmission or when covering the center region of the pole-figure is desired. With the proper data collection strategy in reflection, a pole-figure can cover a circular region from the center up to certain χ angle ($\chi < 90°$). Due to large increase in absorption with low incident angle and exit angle from the sample surface, or sample surface roughness, it is difficult to collect the pole density near the boundary circle. Therefore, the pole-figure collected in reflection mode typically leaves uncovered region near the outer circle. For instance, most measured pole-figures cover a region up to $\chi = 70°{\sim}85°$. This is opposite to transmission mode which leaves a blank region in the center. A complete pole-figure may be measured by combining the data collected in both reflection and transmission modes, but discontinuity and other artifacts may be observed in the regions where reflection and transmission data meets. Most of the time, it is not necessary to collect complete pole-figures. Complete pole-figures can be generated from orientation distribution function (ODF). The ODF can be calculated from number of incomplete pole-figures of different crystalline planes.

8.8.2 Pole-Figure from Polymer Film

X-ray diffraction, especially XRD^2, has been largely used for texture analysis of polymer thin film [20, 23]. As an experimental example of texture analysis on polymer materials, Figure 8.20 shows pole-figures collected on biaxially oriented polyethylene (BOPE) films after various biaxial drawings [24]. Polyethylene (PE) sheets of 0.75 mm were stretched with a biaxial stretcher at 116°C. The samples were first uniaxially stretched in the MD direction with constrained deformation (0 strain) in the TD direction. The samples labeled as 1×0 and 3×0 were deformed with strain in MD direction of 1 and 3 respectively. The engineering strain is used here which is given by $\varepsilon = (l - l_0)/l$, where l_0 is the initial length in the drawing direction and l is the length after drawing. A set of samples uniaxially stretched to strain of 3 are further stretched in TD direction with constrained deformation (0 strain) in the MD direction. The biaxially stretched samples are labeled as 3×1, 3×2, 3×3, and 3×4 for strain of 1, 2, 3, and 4 in the TD direction respectively. Overall, the samples are labeled by its biaxial strain amount and sequence as $\varepsilon_{MD} \times \varepsilon_{TD}$.

An XRD^2 system in vertical θ-θ configuration (Bruker D8-Discover™) with IμS™ Cu microsource and Våntec-500™ 2D detector is used for texture measurement. The data collection was done in reflection mode at 19.8 cm detector distance and complete 360° continuous ϕ scan. Due to the large detector distance, two ϕ scans at different tilt angles ψ are performed to fill the pole-figure to a satisfactory χ angle. Different ϕ scan steps ($\Delta\phi$) are used at different ψ angle to have an relatively even distribution of the data points in the pole-figure. For instance, (110) pole-figure was collected at tilt angles of $\psi = 20°$ and $\psi = 65°$ with $\Delta\phi = 5°$ and $\Delta\phi = 3°$ respectively, and the pole-figure coverage reached $\chi = 70°$. Three diffraction rings corresponding to crystalline planes of (110), (200), and (020) are observed at 2θ about 21.4°, 23.6°, and 36.0° with Cu-K$_\alpha$ radiation. The Bruker MulTex™ software based on component method was used for processing pole-figure data [4]. Three pole-figures for (110), (200), and (020) are measured for each sample. In the pole-figures, red color indicates the highest pole density and green color indicates the lowest pole density. Artifacts are observed in some pole-figures at the boundary between the data points from low ψ tilt and higher ψ tilt. This can be avoided if the complete data is collected with a single ϕ scan at a shorter detector distance.

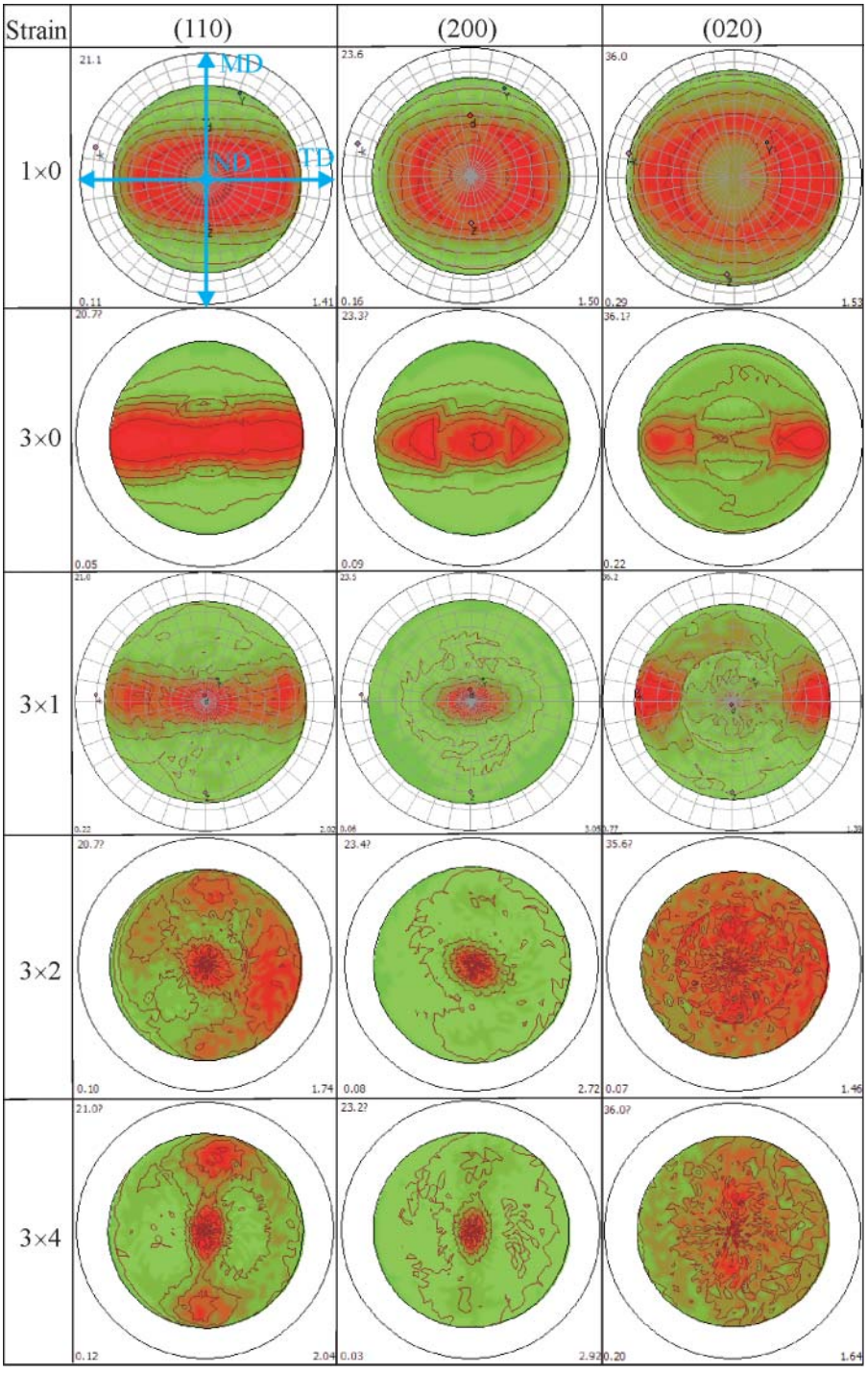


FIGURE 8.20 Pole-figures of biaxially oriented BOPE films after various biaxial drawings.

The crystalline phase in polyethylene is orthorhombic with lattice parameters $a = 0.741$ nm, $b = 0.495$ nm, and $c = 0.255$ nm. The (200) crystalline plane is normal to the crystal axis $\boldsymbol{a}$, so that the pole-figure represents the orientation distribution of the $\boldsymbol{a}$-axis. Similarly, the (020) pole-figure represents the orientation distribution of the $\boldsymbol{b}$-axis. For the samples 1×0 and 3×0, all three pole-figures show a stronger texture with increasing strain, with (110) pole density concentrated more along the TD-ND plane, (200) concentrated to ND and a direction between ND and TD, and (200) concentrated to a direction between ND and TD. For the samples 3×1, 3×2, 3×3, and 3×4, all three pole-figures show orientation rearrangement after the sample 3×0 were stretched in the second direction (TD). For instance, (110) pole density are refocused to the ND direction and a direction between ND and MD, and (200) pole density is concentrated to the ND direction. It should be noted that the above analysis is based on incomplete pole-figures, where the pole density distribution above $\chi = 70°$ cannot be revealed explicitly from the measured pole-figures.

The orientation distribution of the crystalline chain axis ($\boldsymbol{c}$-axis) has the strongest correlation to the mechanical and barrier properties of polymer films. Therefore, it is important to obtain the (002) pole-figure which represents the $\boldsymbol{c}$-axis. However, the (002) pole-figure cannot be measured directly by X-ray diffraction. Based on the three measured (110), (200), and (020) pole-figures, the (002) pole-figure can be calculated from the ODF with MulTex™ software. Figure 8.21 shows calculated (002) pole-figures for all five samples. The (002) pole-figure for sample 1×0 shows the crystalline chain axis ($\boldsymbol{c}$-axis) moved toward the drawing (MD) direction and heavily concentrated on the drawing direction after a large amount of drawing for sample 3×0. The sequential drawing in the TD direction (sample 3×1) defocused the crystal chain orientation, while further drawing in the TD direction (sample 3×2) rearranged most chains to the TD direction. After a large amount of drawings (sample 3×4), all the crystal chains are aligned to the TD direction. Overall, the crystal chain ($\boldsymbol{c}$-axis) tends to align to the drawing direction and the stretch in the second direction dominates the effect.

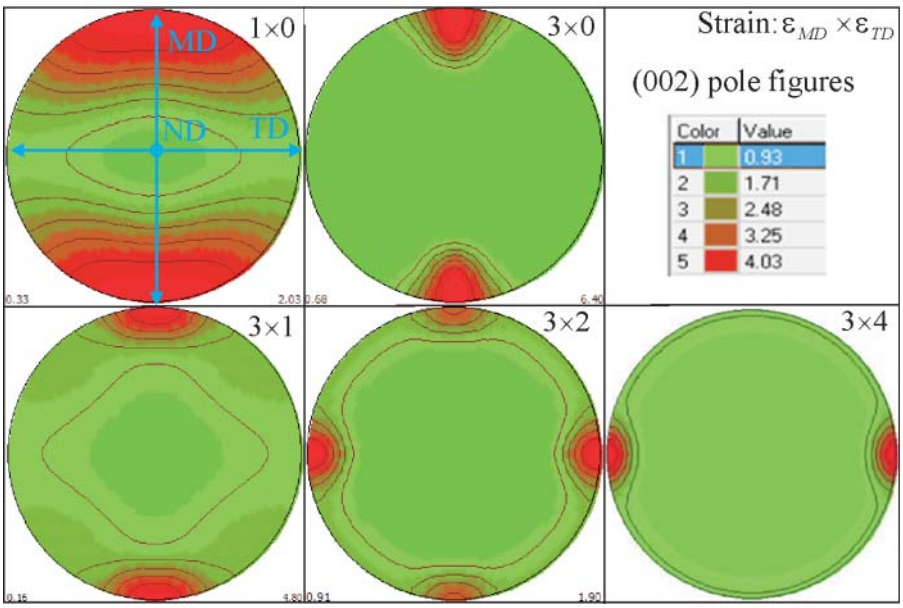


FIGURE 8.21 Calculated (002) pole-figures from ODF for various biaxial strains.

8.9 OTHER ADVANTAGES OF XRD^2 FOR TEXTURE

Two-dimensional X-ray diffraction (XRD^2) systems have many advantages over conventional one-dimensional diffraction systems when used for texture measurements. The capability of fast and simultaneous measurements of several pole-figures has been discussed previously in this chapter. Other advantages are given in the following examples.

8.9.1 Orientation Relationship

An XRD^2 system can measure texture from a sample containing a single phase, multiple phases, single crystals, or a mixture of these. The orientation relationship between different phases, or thin films and substrates, can be revealed because the measurements from all phases of the sample are done simultaneously. One example is the pole-figures measured on the magnetron sputter-deposited Cu film onto a Si (111) wafer with the experimental condition and data collection strategy illustrated in Figures 8.6 and 8.7. At certain angles, diffraction spots of the Si wafer may also appear on the frame. A pole-figure analysis at the 2θ angle of an Si plane can reveal the orientation of the substrate materials. Figure 8.22 shows the overlapped pole-figures of the film Cu (111) and substrate Si (400) in a 2D pole-figure (a) and 3D surface plot (b). The three sharp spots from the (400) spots of the Si wafer show the wafer cut orientation of (111). The Cu (111) pole density maximized in the center of the pole-figure shows a strong (111) fiber texture. The orientation relationship between the film fiber axis and the substrate is clearly described by the combined pole-figures. For samples with multiple thin film layers, the orientation relationships between the different layers of the films and the substrate can be revealed by superimposing their pole-figures.

8.9.2 Direct Observation of Texture

Two-dimensional diffraction frames can also directly reveal texture and grain size information qualitatively even before data processing. For example, Figure 8.23(a) and (b) show two frames collected from two γ-TiAl alloy samples with different microstructures, one with a large grain and weak texture, the other with a small grain and strong texture [6, 25]. We can immediately tell that (a) is from the sample with a larger grain and weak texture due to the spotty diffractions rings and relatively smaller intensity dependence on γ, while (b) is from the sample with a fine

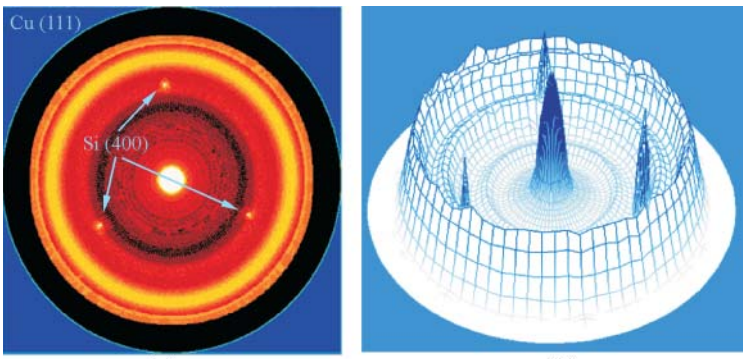


FIGURE 8.22 Combined pole-figure of Cu film (111) and substrate Si (400): (a) pole-figure in 2D projection, (b) pole-figure as a 3D surface plot.

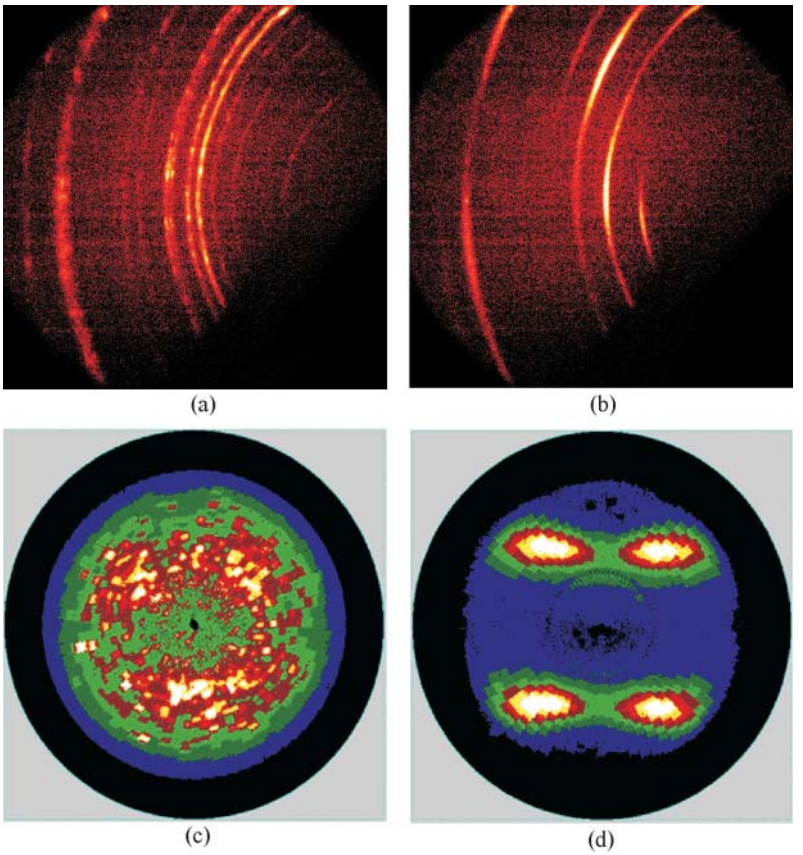


FIGURE 8.23 2D frames and (111) pole-figures collected from two γ-TiAl alloy samples with different microstructures: (a) and (c) larger grain and weak texture, (b) and (d) fine grain and strong texture.

grain and strong texture due to its smooth diffraction rings and large intensity variation with γ. Figure 8.23(c) and (d) show the corresponding pole-figures from the (111) planes of the same samples. The pole-figure in (c) has a scattered intensity distribution with high pole density spots corresponding to the large grains, while the pole-figure in (d) has a concentrated pole density distribution due to the strong texture.

REFERENCES

1. H. J. Bunge and H. Klein, Determination of quantitative, high resolution pole-figures with the area detector, *Z. Metallkd.* (1996) **87** (6), 465–475.
2. K. L. Smith and R. B. Ortega, Use of a two-dimensional, position sensitive detector for collecting pole-figures, *Adv. X-ray Anal.* (1993) **36,** 641–647.
3. T. N. Blanton, X-ray diffraction orientation studies using two-dimensional detectors, *Adv. X-ray Anal.* (1994) **37**, 367–373.
4. K. Helmings, M. Lyubchenko, B. He, and U. Preckwinfel, A new method for texture measurements using a general area detector diffraction system, *Powder Diffraction*, **18** (2), June 2003, 99–105.

5. B. B. He, K. Xu, F. Wang, and P. Huang, Two-dimensional X-ray diffraction for structure and stress analysis, *Residual Stresses VII*, (Proc. of the 7th Int. Conf. on Residual Stresses, Xian, China, 14–17 June 2004), *Mat. Sci. Forum*, **490–491** (July 2005), 1–6.
6. Bob B. He, Introduction to two-dimensional X-ray diffraction, *Powder Diffraction*, **18** (2), June 2003.
7. H. R. Wenk and S. Grigull, Synchrotron texture analysis with area detectors, *J. Appl. Cryst.* (2003). **36**, 1040–1049.
8. M. Birkholz, *Thin Film Analysis by X-ray Scattering*, Wiley-VCH, Weinheim (2006), 191–195.
9. A. C. Rizzie, T. R. Watkins, and E. A. Payzant, Elaboration on the hexagonal grid and spiral trace schemes for pole-figure data collection, *Powder Diffraction*, **23** (2), June 2008.
10. H. Weiland, A. Pitas, U. Preckwinkel, K. Smith, and B. He, A texture measurement instrument for industrial process control, presentation at the 12th International Conference on Textures of Materials, August 9–13, 1999, Montreal, Canada.
11. H. J. Bunge, *Texture Analysis in Materials Science,* Butterworth, London (1983).
12. Ed. by H. J. Bunge and C. Esling, *Advances and Applications of Quantitative Texture Analysis*, DGM Oberursel (1991).
13. S. Matthies, H. R. Wenk, and G. W. Vinel, Some basic concepts of texture analysis and comparison of three methods to calculate orientation distributions from pole-figures, *J. Appl. Cryst.* (1988), **21**, 285–304.
14. Bruker AXS, Texture evaluation program user's manual, TEXEVAL 2.0, doc# M85-E03010, Nov, 2000.
15. R. M. Bozorth, Orientations of crystals in electrodeposited metals, *Phys. Rev.* **26**, 390 (1925).
16. B. He, *X-ray Diffraction from Point-Like Imperfection*, Ph.D dissertation, Virginia Tech, 1992, 93–125.
17. B. He, S. Rao, and C. R. Houska, A simplified procedures for obtaining relative X-ray intensities when a texture and atomic displacements are present, *J. Appl. Phys.* **75**, (9), May 1994.
18. P. R. Rudolf and B. G. Landes, Two-dimensional X-ray diffraction and scattering of microcrystalline and polymeric materials, *Spectroscopy*, **9**(6), pp. 22–33, July/August 1994.
19. W. H. De Jeu, *Basic X-ray Scattering For Soft Matter*, Oxford Univ. Press, 2016.
20. N. E. Widjonarko, Introduction to advanced X-ray diffraction techniques for polymeric thin films, *Coatings*, (2016), **6**, 54, doi:10.3390/coatings6040054.
21. S. Ran, X. Zong, D. Fang, B. S. Hsiao, B. Chua, and R. Ross, Novel image analysis of two-dimensional X-ray fiber diffraction patterns: example of a polypropylene fiber drawing study, *J. Appl. Cryst.* (2000). **33**, 1031–1036.
22. D. Raabe, N. Chen, and L. Chen, Crystallographic texture, amorphization, and recrystallization in rolled and heat treated polyethylene terephthalate (PET), *Polymer* (2004) **45**, 8265–8277.
23. J. H. Butler, S. M. Wapp, and F. H. Chambon, Quantitative pole-figure analysis of oriented polyethylene films, *Adv. X-ray Anal.* (2000) **43.–141-150**.
24. Y. Tang, M. Ren, H. Shi, D. Gao, and B. He, X-ray pole-figure analysis on biaxially oriented polyethylene films with sequential biaxial drawing, presented at the 66th annual Denver X-ray Conference, August 2017 and submitted to *Adv. X-ray Anal.* (2018) **61.**
25. B. He, Application of two-dimensional X-ray diffraction, *Handout distributed in Denver X-ray Conference Workshop on Two-dimensional XRD*, 2001, 2003, 2005, 2007.

9

STRESS MEASUREMENT

9.1 INTRODUCTION

Polycrystalline materials consist of large amount of crystallites of various sizes, shapes and orientation. When a solid material is elastically deformed by a force, each crystallite in it changes shape or size. Assuming that the stresses in each crystallite represent the stresses in the solid, the stresses can be measured by measuring the lattice d-spacing change in the crystallites. The stress in a sample can be compressive or tensile, so that the d-spacing in the corresponding direction will be smaller or larger than the stress-free sample. This d-spacing change can be measured by the diffraction peak position change based on Bragg's law. In this case, the d-spacing in the crystallites serves as a gauge of the deformation. Strictly speaking, stresses are not directly measured by X-ray diffraction, but calculated from the measured strains based on the elasticity of the materials. In many cases, stress measurement by X-ray diffraction is for residual stress. However, there is no distinction between residual stress and applied stress in terms of the measurement principle and method.

The methods of stress measurement by X-ray diffraction can be classified as the conventional method and the 2D method (XRD^2). A point detector or line detector is typically used in the conventional method. The stress or stress tensor is calculated from many strain measurements from diffraction peak 2θ shifts of a specific lattice plane family. Each diffraction peak is measured at a sample orientation (ψ,φ). Stress measurement with two-dimensional X-ray diffraction (XRD^2) is based on the fundamental relationship between the stress tensor and the diffraction cone distortion. The diffraction peak 2θ shifts are measured along the diffraction rings. Since a diffraction ring in a 2D pattern contains far more data points than a conventional diffraction peak, an XRD^2 system can measure stress with higher accuracy and requires less data collection time, especially in dealing with highly textured materials, large grain size, small sample areas, weak diffraction, stress mapping, and stress tensor measurement. In this chapter we will first introduce the fundamentals of the conventional method, followed by the 2D method.

Two-Dimensional X-Ray Diffraction, Second Edition. Bob Baoping He.
© 2018 John Wiley & Sons, Inc. Published 2018 by John Wiley & Sons, Inc.

9.1.1 Stress

Stress is a measure of the deforming force applied to a solid per unit area. Figure 9.1 illustrates the basic definitions of stress and strain. Figure 9.1(a) shows a force F applied to a flat area A_o of a solid body. The force can be resolved into two components: F_n, normal to the flat area, and F_t, tangential to the flat area. In reaction to this external force, there exists an internal force to balance the external force to maintain equilibrium. The intensity of this internal force is referred to as stress. Assuming that the force is uniformly distributed over the flat area A_o corresponding to the normal force F_n, we have a normal stress given by

$$\sigma = \frac{F_n}{A_o} \tag{9.1}$$

The normal force takes a positive sign if the force points away from the area A_o or negative if the force points into the surface A_o. There are two kinds of normal stresses, tensile stress, with a positive value, which produces an elongation of the solid in the stress direction, and compressive

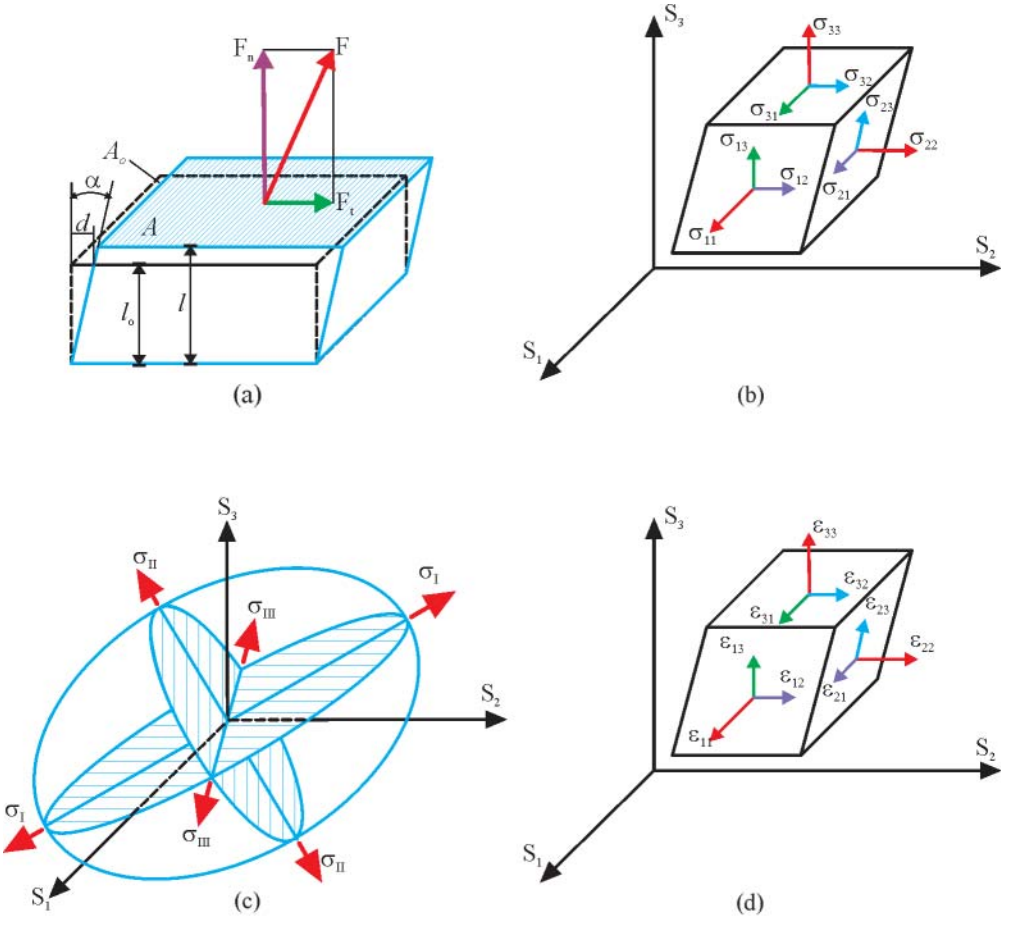


FIGURE 9.1 Stress and strain: (a) a force applied to an area A, (b) stress components on a volume element, (c) stress ellipsoid and principal stresses, (d) strain components on a volume element.

stress, with a negative value, which produces contraction in the stress direction. A shear stress is given by

$$\tau = \frac{F_t}{A_o} \tag{9.2}$$

In the above stress calculation, the original surface area A_o is used. The stress calculated from the original area is called the engineering stress. In reality, this area changes to A due to deformation as shown in Figure 9.1(a). Replacing the area A_o by A in equation (9.1) and (9.2), we obtain the so-called true stress. Since the difference between A_o and A is negligible in most cases within the stress range measured by X-ray diffraction, in practice it is not necessary to make a distinction. Thereafter in this chapter, we assume true stresses unless otherwise stated.

The SI (International System of Units) unit for stress is the Pa (shorthand for pascal), which is defined as a N/m^2 (one newton per square meter). The unit for stress is the same as that of pressure, which is also a measure of force per unit area. For most metals, stress is normally given in MPa (megapascal), which is defined as MN/m^2 (million newtons per square meter) or equivalently N/mm^2 (newtons per square millimeter). For polymers or other soft materials, kPa (kilopascal) may be a more appropriate unit. Other units can be converted to MPa by the following equations:

1 GPa = 1000 MPa = 1,000,000 kPa
1 ksi (1000 lb/in^2) = 6.895 MPa
1 kg/mm^2 = 9.807 MPa

The above is a simple model of stress. The stresses on an elemental volume in the sample coordinates $S_1S_2S_3$ contains nine components, given by [1, 2]

$$\sigma_{ij} = \begin{bmatrix} \sigma_{11} & \sigma_{12} & \sigma_{13} \\ \sigma_{21} & \sigma_{22} & \sigma_{23} \\ \sigma_{31} & \sigma_{32} & \sigma_{33} \end{bmatrix} \tag{9.3}$$

where the indices 1 and 2 may be expressed as x and y in some literature when the sample coordinates are expressed as XYZ. A component is normal stress when the two indices are identical, or shear stress when the two indices are mixed. Shear stress may be expressed in some literature as τ instead of σ. This grouping of the nine stress components is called the stress tensor. The stress tensor is a tensor of the second order. Figure 9.1(b) shows all nine components on an elemental volume, which was originally a unit cube, but distorted by the stresses. The three normal stress components are aligned with the three axes of the sample coordinates and each is normal to a face of the unit cube. The six shear components are within the three faces of cube perpendicular to the three axes of the sample coordinates. The first index denotes the cubic face that the shear component acted on and the second index denotes the direction of the shear stress component. Shear stress takes a positive value if the shear direction points to the sample coordinate direction corresponding to the second index, otherwise it is negative. Under equilibrium, the shear components must maintain the following relation:

$$\sigma_{12} = \sigma_{21},\ \sigma_{23} = \sigma_{32} \text{ and } \sigma_{31} = \sigma_{13} \tag{9.4}$$

Therefore, there are no more than six independent components to define the stress state in a solid. The following stress states are typically dealt with in stress measurement with X-ray

diffraction:

1. Uniaxial: All stress components are zero except one normal stress components:

$$\sigma_{ij} = \begin{bmatrix} \sigma_{11} & 0 & 0 \\ 0 & 0 & 0 \\ 0 & 0 & 0 \end{bmatrix} \text{ or } \sigma_{ij} = \begin{bmatrix} 0 & 0 & 0 \\ 0 & \sigma_{22} & 0 \\ 0 & 0 & 0 \end{bmatrix} \text{ or } \sigma_{ij} = \begin{bmatrix} 0 & 0 & 0 \\ 0 & 0 & 0 \\ 0 & 0 & \sigma_{33} \end{bmatrix}$$

   In this case, the indices can be omitted for the specified direction and the stress is denoted by σ. In X-ray stress analysis, the third case ($\sigma_{33} \neq 0$) is typically not considered because σ_{33} is in the sample surface normal direction.
2. Biaxial: All non-zero components are within a plane, for example, in the $\mathbf{S_1}$-$\mathbf{S_2}$ plane

$$\sigma_{ij} = \begin{bmatrix} \sigma_{11} & \sigma_{12} & 0 \\ \sigma_{21} & \sigma_{22} & 0 \\ 0 & 0 & 0 \end{bmatrix}$$

   This is the typical case on a sample surface where no balancing force is exerted in the normal direction of the sample surface. Due to the limited penetration of X-rays, most measured stresses by X-ray diffraction belong to this stress state.
3. Biaxial with shear: Except for $\sigma_{33} = 0$, all other components are not necessarily zero:

$$\sigma_{ij} = \begin{bmatrix} \sigma_{11} & \sigma_{12} & \sigma_{13} \\ \sigma_{21} & \sigma_{22} & \sigma_{23} \\ \sigma_{31} & \sigma_{32} & 0 \end{bmatrix}$$

   This is a general and typical case for X-ray stress analysis since the stress in the surface normal direction is considered zero due to the low penetration of the X-ray. In this case the stresses can be measured without accurate stress-free d-spacing. In some literature, this stress state is referred to as a triaxial stress state. However, it is helpful to make a distinction between this stress state and the general triaxial stress state, which requires accurate stress-free d-spacing for stress measurement.
4. Equibiaxial: This is a special case of the biaxial stress state where $\sigma_{11} = \sigma_{22} = \sigma$, so the stress tensor can be expressed as

$$\sigma_{ij} = \begin{bmatrix} \sigma & 0 & 0 \\ 0 & \sigma & 0 \\ 0 & 0 & 0 \end{bmatrix}$$

   There are no in-plane ($\mathbf{S_1}$-$\mathbf{S_2}$) shear components in the equibiaxial stress state. This stress state exists typically in the surface of metal parts after surface treatment, such as shot peening, or in thin films with no texture or with a fiber texture. In this stress state, there are only normal stress components having the same value in any direction within the plane.
5. Triaxial: This is the general case expressed by equation (9.3). This stress state exists only inside the solid body or a subsurface of metal parts. Due to the limited penetration of X-rays, in most cases, triaxial stresses cannot be directly measured by X-ray diffraction. It can be calculated from the results of layer by layer measurements in the layer removal method. Triaxial stresses may be measured with synchrotron radiation, high energy X-rays, or neutron radiation. Since stress-free d-spacing cannot be determined by measurement in this

stress state, the accurate stress-free d-spacing must be available to measure the triaxial stresses.

6. Equitriaxial: This is a special case of the triaxial stress state when $\sigma_{11} = \sigma_{22} = \sigma_{33} = \sigma$, so the stress tensor can be expressed as

$$\sigma_{ij} = \begin{bmatrix} \sigma & 0 & 0 \\ 0 & \sigma & 0 \\ 0 & 0 & \sigma \end{bmatrix}$$

There are no shear components in the equitriaxial stress state. In this stress state, the stress component in any direction has the same value and there is no shear stress component in any direction. This stress state exists typically in a solid body with forces uniformly distributed over the surface of the body and normal to the surface everywhere, such as a solid body submerged in a fluid under pressure. Therefore, the equitriaxial stress state is also referred as the hydrostatic state. Under limited hydrostatic stresses, where no phase transformation happens due to pressure, the crystal lattice parameters change in all directions linearly and proportionally. Therefore, the diffraction pattern from the crystal under equitriaxial stresses appears like a diffraction pattern from a crystal of the same structure but different unit cell size.

A stress tensor can be expressed as the sum of two other stress tensors: a mean hydrostatic stress tensor (or volumetric stress tensor or mean normal stress tensor) and a stress deviator tensor,

$$\sigma_{ij} = \begin{bmatrix} \sigma_{11} & \sigma_{12} & \sigma_{13} \\ \sigma_{12} & \sigma_{22} & \sigma_{23} \\ \sigma_{13} & \sigma_{23} & \sigma_{33} \end{bmatrix} = \begin{bmatrix} \sigma_m & 0 & 0 \\ 0 & \sigma_m & 0 \\ 0 & 0 & \sigma_m \end{bmatrix} + \begin{bmatrix} \sigma^d_{11} & \sigma^d_{12} & \sigma^d_{13} \\ \sigma^d_{12} & \sigma^d_{22} & \sigma^d_{23} \\ \sigma^d_{13} & \sigma^d_{23} & \sigma^d_{33} \end{bmatrix} \tag{9.5}$$

where σ_m is the mean stress given by

$$\sigma_m = \frac{\sigma_{11} + \sigma_{22} + \sigma_{33}}{3} \tag{9.6}$$

and σ^d_{ij} is the stress deviation tensor. While the hydrostatic tensor tends to change the volume of the crystal body, the stress deviator tensor tends to change the shape of the crystal.

The above stress components are expressed in the sample coordinates $\mathbf{S_1S_2S_3}$. The same stress tensor can be expressed in any other arbitrary Cartesian coordinates tilted away from the sample coordinates with different stress components. There exists a Cartesian coordinate system such that the stress tensor can be expressed by three normal stress components

$$\begin{bmatrix} \sigma_I & 0 & 0 \\ 0 & \sigma_{II} & 0 \\ 0 & 0 & \sigma_{II} \end{bmatrix}$$

Figure 9.1(c) shows the stress tensor ellipsoid relative the sample coordinates $\mathbf{S_1S_2S_3}$. The three principal stresses, σ_{I}, σ_{II}, and σ_{III}, also called eigenvalues, are in the directions of the three principal axes (axes of the ellipsoid). There is no shear stress component when the stress tensor is expressed in the principal axes. The principal stresses are typically assigned their values in the following order:

$$\sigma_I > \sigma_{II} > \sigma_{III} \tag{9.7}$$

The stress components are dependent of the coordinates in which they are expressed. The principal stresses are unique for a stress tensor. It is convenient to evaluate and compare the state of the elastic medium at a particular point in terms of the principal stresses. The values of the principal stress components (eigenvalues) and the orientation to the sample coordinates (eigenvectors) can be calculated from the stress tensor components in the sample coordinates. Detailed algorithms are given in Appendix 9.1.

9.1.2 Strain

Strain is a measure of the resulting deformation of a solid body caused by stress. Strain is calculated from the change in the size and shape of the deformed solid due to stress. Analogous to normal stresses and shear stresses are normal strains and shear strains. The normal strain is calculated from the change in length of the solid body along the corresponding normal stress direction. Figure 9.1(a) shows the length of the solid body in the normal force (F_n) direction changed from the original length of l_o to the deformed length of $\boldsymbol{l}$. The normal strain is given as

$$e_n = \frac{l - l_o}{l_o} = \frac{\Delta l}{l_o} \tag{9.8}$$

where e_n is the normal strain in the measured direction, which takes a positive sign for extension and a negative sign for contraction. The above strain definition is the relative elongation from the initial length to the final length. The strain calculated by this definition is called engineering strain. If the load is applied in a series of increments, the sum of all strains from each increment does not equal the strain calculated from the initial and final length. The true strain, also called natural strain or logarithmic strain, provides the correct measure of the final strain regardless of the strain path. The true strain is defined as

$$\varepsilon_n = \ln \frac{l}{l_o} = \ln(1 + e_n) \tag{9.9}$$

Most solid materials have a very small elastic limit. For instance, the elastic limit of most steel is less than 0.002 (0.2%), so a strain measured by the X-ray diffraction is generally a very small number. In practice, there is no difference between the engineering normal strain and true normal strain for such a small strain value.

Shear strain is typically given by two definitions: one is the change in angle between two mutually perpendicular reference axes following simple shear, and the other is the relative displacement of parallel planes at a unit distance. Figure 9.1(a) shows the angle between the original line and the deformed line along an edge of the solid body due to the shear force (F_t), α, which is also the angular change between the horizontal edge and the vertical edge. The engineering shear strain γ is given as

$$\gamma = \alpha \tag{9.10}$$

or based on the parallel plane displacement at a unit distance

$$\gamma = \frac{d}{l_o} = \tan \alpha \tag{9.11}$$

The shear strain values from both definitions are practically the same if the angular definition is given in radians and the value of the shear is much smaller than unity. The true shear strain,

also referred as the average strain, is given as

$$\varepsilon_t = \frac{\gamma}{2} \tag{9.12}$$

Shear strain cannot be directly measured by X-ray diffraction, but can be calculated from normal strains in other directions based on elasticity theory. Both the normal and shear strains contain a ratio of two length units and both length units cancel out. Therefore, strain is a dimensionless quantity, which can be expressed as a decimal fraction or as a percentage.

Figure 9.1(d) shows all components of the strain tensor expressed on an elemental volume in the sample coordinates $\mathbf{S_1S_2S_3}$.

$$\varepsilon_{ij} = \begin{bmatrix} \varepsilon_{11} & \varepsilon_{12} & \varepsilon_{13} \\ \varepsilon_{21} & \varepsilon_{22} & \varepsilon_{23} \\ \varepsilon_{31} & \varepsilon_{32} & \varepsilon_{33} \end{bmatrix} \tag{9.13}$$

Similar to the stress tensor, a component is normal strain when the two indices are identical, or shear strain when the two indices are mixed. This grouping of the nine strain components is called the strain tensor. The strain tensor is a second order tensor. The directions of all strain components are defined in the same way as for the stress tensor. Under equilibrium, the shear components must maintain the following relation:

$$\varepsilon_{12} = \varepsilon_{21},\ \varepsilon_{23} = \varepsilon_{32} \text{ and } \varepsilon_{31} = \varepsilon_{13} \tag{9.14}$$

Therefore, there are six independent components in the strain tensor.

9.1.3 Elasticity and Hooke's Law

Stresses cannot be directly measured by X-ray diffraction. The stress is calculated from the strains measured by X-ray diffraction. Therefore, the stress–strain relationship is very important in stress measurement. The stress–strain relationships are given by elasticity theory. When the deformation of a solid is within the elastic limit, stress is proportional to strain (Hooke's law). In general cases, the materials are anisotropic; for example, most single crystals or strongly textured materials, and the stress–strain relationship depends on the directions of the stress components relative to the material atomic arrangements. The stress–strain relations are given by the generalized Hooke's law

$$\sigma_{ij} = C_{ijkl}\varepsilon_{kl} \tag{9.15}$$

where C_{ijkl} are elastic stiffness coefficients. The stress–strain relations can also be expressed as

$$\varepsilon_{ij} = S_{ijkl}\sigma_{kl} \tag{9.16}$$

where S_{ijkl} are the elastic compliances. For most polycrystalline materials without texture or with weak texture, it is practical and reasonable to consider the elastic behavior to be isotropic and the structure to be homogeneous on a macroscopic scale. In these cases, the stress–strain relationship takes much simpler form. In stress measurement by X-ray diffraction, as discussed in this chapter, isotropic elasticity on a macroscopic scale is assumed unless otherwise suggested.

In a uniaxial stress state where only $\sigma_{11} \neq 0$, Hooke's law gives that

$$\varepsilon_{11} = \frac{\sigma_{11}}{E} \tag{9.17}$$

where E is a constant called the Young's modulus. While the solid elongates in the direction of stress with the strain ε_{11}, the solid also contracts in the perpendicular direction with

$$\varepsilon_{22} = \varepsilon_{33} = -\frac{\nu}{E}\sigma_{11} = -\nu\varepsilon_{11} \tag{9.18}$$

where ν is Poisson's ratio. In the case of a body under shear stress, the shear strain and shear stress follow the following relation

$$2\varepsilon_t = \gamma = \frac{\tau}{G} \tag{9.19}$$

where G is a constant called the shear modulus or modulus of rigidity. The Young's modulus E, Poisson's ratio ν and shear modulus G maintain the following relationship for homogeneous isotropic materials:

$$G = \frac{E}{2(1+\nu)} \tag{9.20}$$

Therefore, the Young's modulus E and Poisson's ratio ν are sufficient to describe the stress and strain relations for homogeneous isotropic materials. For an isotropic material in the triaxial state, we have the following stress and strain relationships:

$$\begin{aligned}
\varepsilon_{11} &= \frac{1}{E}[\sigma_{11} - \nu(\sigma_{22} + \sigma_{33})] \\
\varepsilon_{22} &= \frac{1}{E}[\sigma_{22} - \nu(\sigma_{33} + \sigma_{11})] \\
\varepsilon_{33} &= \frac{1}{E}[\sigma_{33} - \nu(\sigma_{11} + \sigma_{22})] \\
\varepsilon_{12} &= \frac{1+\nu}{E}\sigma_{12}, \quad \varepsilon_{23} = \frac{1+\nu}{E}\sigma_{23}, \quad \varepsilon_{31} = \frac{1+\nu}{E}\sigma_{31}
\end{aligned} \tag{9.21}$$

9.1.4 X-Ray Elasticity Constants and Anisotropy Factor

It is customary in the field of stress measurement by X-ray diffraction to use another set of macroscopic elastic constants, S_1 and $\frac{1}{2}S_2$, which are given by

$$\tfrac{1}{2}S_2 = (1+\nu)/E \quad \text{and} \quad S_1 = -\nu/E \tag{9.22}$$

Although polycrystalline materials on a macroscopic level can be considered isotropic, residual stress measurement by X-ray diffraction is done by measuring the strain in a specific crystal orientation of the crystallites which satisfy the Bragg condition. The stress–strain relationship on the crystallite level is generally different from that on a macroscopic level. Therefore, the stresses measured from diffracting crystallographic planes may have different values due to their elastic anisotropy. This discrepancy can be ignored in many industrial applications if the same crystallographic planes are used and consistent elasticity constants are used. In cases where the elastic anisotropy effect needs to be considered, the macroscopic elasticity constants should be replaced by a set of crystallographic plane-specific elasticity constants, $S_1^{\{hkl\}}$ and $\frac{1}{2}S_2^{\{hkl\}}$, called X-ray elastic constants (XEC). XECs for many materials can be found in literature, measured, or calculated from microscopic elasticity constants [3]. In the case of materials with cubic crystal symmetry, the equations for calculating the XEC from the macroscopic elasticity constants

Table 9.1 Values of A_{RX} for the Some Common Cubic Materials

Materials	A_{RX}
Body-centered cubic (bcc) Fe-base materials	1.49
Face-centered cubic (fcc) Fe-base materials	1.72
Face-centered cubic (fcc) Cu-base materials	1.09
Ni-base materials (fcc)	1.52
Al-base materials (fcc)	1.65

$\frac{1}{2}S_2$ and S_1 are:

$$\begin{aligned} \tfrac{1}{2}S_2^{\{hkl\}} &= \tfrac{1}{2}S_2\,[1 + 3(0.2 - \Gamma(hkl))\Delta] \\ S_1^{\{hkl\}} &= S_1 - \tfrac{1}{2}S_2[0.2 - \Gamma(hkl)]\Delta \end{aligned} \tag{9.23}$$

where $\Gamma(hkl) = \dfrac{h^2k^2 + k^2l^2 + l^2h^2}{(h^2 + k^2 + l^2)^2}$ and $\Delta = \dfrac{5(A_{RX} - 1)}{3 + 2A_{RX}}$

In the equations for stress measurement hereafter, either the macroscopic elasticity constants $\frac{1}{2}S_2$ and S_1 or the XEC $S_1^{\{hkl\}}$ and $\frac{1}{2}S_2^{\{hkl\}}$ are used in the expression, but both sets of elastic constants can be used depending on the application requirements. The factor of anisotropy (A_{RX}) is a measure of the elastic anisotropy of a material. Values of A_{RX} for some common cubic materials are given in Table 9.1; additional values may be taken from the literature. The A_{RX} value can also be calculated from two sets of XEC values from two independent directions, especially in the following cases:

$$A_{RX} = \frac{\frac{1}{2}S_2^{\{h00\}}}{\frac{1}{2}S_2^{\{hhh\}}} \tag{9.24}$$

9.1.5 Residual Stresses

Depending on the source of loading forces that produce stresses, there are two kinds of stress [4]. One kind is applied stress caused by external forces acting on the solid object. Applied stress changes when the loading forces change and it disappears once the forces are removed. The stresses measured by X-ray diffraction method are mostly residual stresses. Residual stress is caused by internal forces between different parts of a solid body. Residual stress exists without the external forces or remains after the external forces have been removed. The net force and moment on a solid body in equilibrium must be zero, so the residual stresses in the body must be balanced within the body. That means a compressive stress in one part of the body must come with a tensile stress in another part of the body. For example, the residual stress in a thin film is balanced by the stresses in the substrate. When residual stress in a solid body is mentioned it typically refers to a specific location.

There are many causes of residual stresses, typically related to the manufacturing processes. Inhomogeneous plastic deformation during the mechanical forming processes, such as rolling, extrusion, drawing, grinding, and mechanical polishing, can produce residual stresses. The forces applied to the materials during the processes produce both elastic deformation and plastic deformation. The elastic deformation and the corresponding stresses cannot be fully released after the processing forces are removed due to the inhomogeneous plastic deformation in the

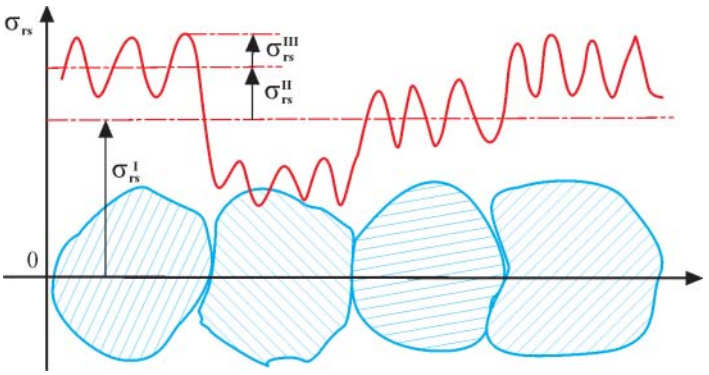


FIGURE 9.2 Illustration of the three kinds of residual stresses relative to the grain size.

material. Thermal incompatibilities between different parts of a component can also produce residual stresses. For instance, if the film and the substrate have different thermal expansion coefficients, residual stresses are produced if the component is placed at a temperature different from the stress-free temperature. Thermal processes, such as quenching, can also produce residual stresses due to an uneven cooling rate and phase transformation. For most mechanical parts, the compressive residual stresses in the surface can prevent or delay crack initiation and propagation processes, so residual stresses are also generated intentionally by some surface treatments, such as nitridation and carbonization of steel parts, ion implantation, and shot peening of metal surface [5–8].

Residual stresses are generally categorized as macroscopic or microscopic depending on the range in which the stresses are balanced. Some researchers prefer to categorize residual stresses into three kinds [9]. Figure 9.2 illustrates the three kinds of residual stresses relative to the scale of the grain size. The first kind, σ_{rs}^{I}, also called macroscopic residual stress, is stress measured over a large number of grains. It is the stress corresponding to the average of the strains in a range as large as 1 millimeter to several millimeters. The first kind of residual stress is balanced between different parts of the component. This kind of stress can be measured by X-ray diffraction through the shift of the Bragg peaks. The second kind, σ_{rs}^{II}, categorized as microscopic stress, is stress measured over one or a few grains. It is the stress corresponding to the average of the strains in a range of microns. This kind of stress may shift the diffraction peak if the X-ray beam is as small as several grains. The third kind, σ_{rs}^{III}, also categorized as microscopic stress, is stress corresponding to the strains in a range of 1–100 nm. This kind of stress is typically caused by crystal defects, such as dislocations, stacking faults and clusters of interstitials, and substitutional atoms. This kind of stress alone will not cause a detectable shift of diffraction peaks, but it can be measured by the peak broadening and peak profile modeling [10–16]. The γ-integrated diffraction profiles from 2D frames can be used in the peak broadening and peak profile analysis in the same way as diffraction profiles collected by a conventional diffractometer. In this chapter, we will focus on the X-ray diffraction method for stress measurement of the first kind.

9.2 PRINCIPLE OF X-RAY STRESS ANALYSIS

9.2.1 Strain and Bragg's Law

X-ray stress analysis is based on two fundamental theories: the theory of elasticity, which defines the relationship between stresses and strains, and X-ray diffraction theory, which gives the

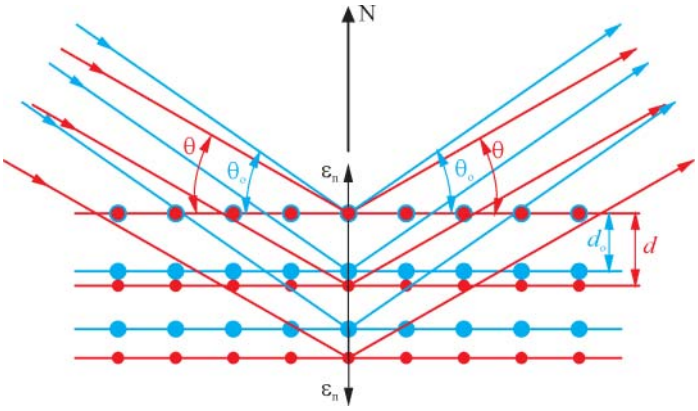


FIGURE 9.3 Illustration of the strain measurement based on Bragg's law.

relationship between the atomic arrangement in a solid and its diffraction pattern. Bragg's law is the basis of stress analysis by X-ray diffraction. Figure 9.3 illustrates the relationship between strain and diffraction angle. The blue spots represent the atomic positions in a strain-free crystal. The blue horizontal lines represent the crystal planes in the strain-free crystal. For the strain free crystal, Bragg's law is given by

$$2d_o \sin\theta_o = \lambda \tag{9.25}$$

where θ_o is the Bragg angle (the incident beam and the diffracted beam make the same angle to the crystal planes), d_o is the d-spacing between adjacent crystal planes, and λ is the wavelength of the X-ray beam. N denotes the plane normal direction. The red spots, lines, and symbols represent the Bragg condition for the crystal with strain. When a strain in the plane normal direction, ε_n is applied to the crystal, the d-spacing changes from d_o to d. For a crystal with strain, Bragg's law is given by

$$2d \sin\theta = \lambda \tag{9.26}$$

where θ is the diffraction angle measured from the crystal with strain. The strain in the plane normal direction, ε_n, can then be given by the following relations based on the engineering strain and true strain definitions:

$$\varepsilon_n = \frac{d}{d_o} - 1 = \frac{\sin\theta_o}{\sin\theta} - 1 = \frac{\lambda}{2d_o \sin\theta} - 1 \qquad \text{(engineering strain)}$$

or

$$\varepsilon_n = \ln\frac{d}{d_o} = \ln\frac{\sin\theta_o}{\sin\theta} = \ln\frac{\lambda}{2d_o \sin\theta} \qquad \text{(true strain)} \tag{9.27}$$

Since the difference between d_o and d is very small in the elastic range, the difference from the two definitions is negligible. For energy dispersive diffraction, the Bragg angle is a constant, and the strain is given by

$$\varepsilon_n = \ln\frac{\lambda}{\lambda_o} = \ln\frac{\lambda}{2d_o \sin\theta_o} \tag{9.28}$$

where λ is the wavelength at the peak for the strained crystal and λ_o is the wavelength at the peak for the strain-free crystal.

The strain calculation equation can also be obtained by taking a derivative of the Bragg equation. Starting from

$$2d \sin\theta = \lambda$$

both d and θ are variables, and by taking the first derivative, we have

$$2d \cos\theta \partial\theta + 2 \sin\theta \partial d = 0$$

The notation ∂ is used to denote the first derivative instead of d to avoid confusion with d-spacing. Replacing ∂d, $\partial\theta$, and θ by Δd, $\Delta\theta$, and θ_o respectively when both Δd and $\Delta\theta$ are very small, we have

$$\varepsilon_n = -\Delta\theta \cot\theta_o \tag{9.29}$$

Based on the above analysis, only the normal strain component perpendicular to the crystallographic planes may be measured directly by X-ray diffraction. The shear strains are calculated from the normal strains measured in various other directions. The stresses, either normal or shear, are calculated from the measured strains.

9.2.2 Strain Measurement

The normal strain along the crystallographic plane normal direction can be measured by the 2θ shift of the diffraction pattern. By measuring the normal strains in various directions in the sample coordinates, the strain in a desired direction can be calculated. The strain tensor in the measurement point can be determined if sufficient strains are measured. Figure 9.4 shows the relation between the direction of the measured normal strain and the sample coordinates. ϕ is the rotation angle around the sample normal (S_3), and ψ is the tilt angle from the sample normal within a plane defined by L and S_3. The fundamental equation governing the relationship between the measured normal strain and the strain tensor expressed in the sample coordinates is given by [2]

$$\begin{aligned}\varepsilon_{\phi\psi} = {} & \varepsilon_{11}\cos^2\phi\sin^2\psi + \varepsilon_{12}\sin 2\phi\sin^2\psi + \varepsilon_{22}\sin^2\phi\sin^2\psi \\ & + \varepsilon_{13}\cos\phi\sin 2\psi + \varepsilon_{23}\sin\phi\sin 2\psi + \varepsilon_{33}\cos^2\psi\end{aligned} \tag{9.30}$$

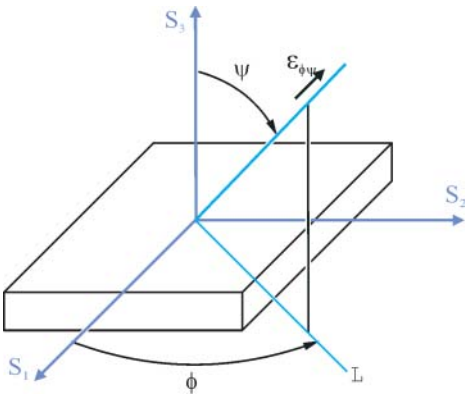


FIGURE 9.4 Schematic showing the strain measured by X-ray diffraction in the sample coordinates.

where $\varepsilon_{\phi\psi}$ is the measured strain in the orientation defined by ϕ and ψ and ε_{11}, ε_{12}, ε_{22}, ε_{13}, ε_{23} and ε_{33} are strain tensor components in the sample coordinates $S_1S_2S_3$. The above equation can be easily obtained from the unit vector in the $\varepsilon_{\phi\psi}$ direction expressed in the sample coordinates. The unit vector is given by

$$\mathbf{h}_{\phi\psi} = \begin{bmatrix} h_1^{\phi\psi} \\ h_2^{\phi\psi} \\ h_3^{\phi\psi} \end{bmatrix} = \begin{bmatrix} \cos\phi \sin\psi \\ \sin\phi \sin\psi \\ \cos\psi \end{bmatrix} \tag{9.31}$$

Then the relationship between the measured strain $\varepsilon_{\phi\psi}$ and the strain tensor can be given by

$$\varepsilon_{\phi\psi} = \varepsilon_{ij} \cdot h_i^{\varphi\psi} \cdot h_j^{\varphi\psi} \tag{9.32}$$

The scalar product of the strain tensor with the unit vector in the above equation is the sum of all components in the tensor multiplied by the components in the unit vector corresponding to the first and the second indices. Equation (9.30) can then be obtained by the expansion of this equation for i and j values of 1, 2, and 3. The measured strain can be given by any of the following equations with trivial discrepancy.

$$\varepsilon_{\phi\psi} = \frac{d_{\phi\psi} - d_o}{d_o} = \frac{\lambda}{2d_o \sin\theta} - 1 \approx -\Delta\theta \cot\theta_o$$

or

$$\varepsilon_{\phi\psi} = \ln\frac{d_{\phi\psi}}{d_o} = \ln\frac{\sin\theta_o}{\sin\theta} = \ln\frac{\lambda}{2d_o \sin\theta} \tag{9.33}$$

Equation (9.30) is a linear equation of the strain tensor components. The strain tensor can be obtained by solving the linear equations if six independent strains are measured or by linear least squares regression if more than six independent measured strains are available. In order to get a reliable solution from solving the linear equations or from least squares analysis, the independent strain should be measured at significantly different orientations.

9.2.3 Stress Measurement

In general, stresses can be determined from the measured strains by Hooke's law. For materials with homogenous and isotropic elasticity there are only two independent elasticity constants. So the stresses can be determined from the measured strains by the following equation [2, 3]:

$$\begin{aligned}\varepsilon_{\phi\psi} = &-\frac{\nu}{E}(\sigma_{11} + \sigma_{22} + \sigma_{33}) + \frac{1+\nu}{E}(\sigma_{11}\cos^2\phi + \sigma_{12}\sin 2\phi + \sigma_{22}\sin^2\phi)\sin^2\psi \\ &+ \frac{1+\nu}{E}(\sigma_{13}\cos\phi + \sigma_{23}\sin\phi)\sin 2\psi + \frac{1+\nu}{E}\sigma_{33}\cos^2\psi\end{aligned} \tag{9.34}$$

Considering the anisotropic nature of the crystallites, the equation can be given by [17]

$$\begin{aligned}\varepsilon_{\phi\psi}^{\{hkl\}} = &S_1^{\{hkl\}}(\sigma_{11} + \sigma_{22} + \sigma_{33}) + \tfrac{1}{2}S_2^{\{hkl\}}(\sigma_{11}\cos^2\phi + \sigma_{12}\sin 2\phi + \sigma_{22}\sin^2\phi)\sin^2\psi \\ &+ \tfrac{1}{2}S_2^{\{hkl\}}(\sigma_{13}\cos\phi + \sigma_{23}\sin\phi)\sin 2\psi + \tfrac{1}{2}S_2^{\{hkl\}}\sigma_{33}\cos^2\psi\end{aligned} \tag{9.35}$$

where $\varepsilon_{\phi\psi}^{\{hkl\}}$ is the strain measured from the specific lattice planes $\{hkl\}$ in the direction defined by ϕ and ψ, and $S_1^{\{hkl\}}$ and $\frac{1}{2}S_2^{\{hkl\}}$ are the XEC for the lattice planes. In the above equation, one

strain (2θ shift) value is considered at each sample orientation (ψ, ϕ). This is suitable for stress measurement with point detectors or one-dimensional position-sensitive detectors. The stress tensor can be obtained by solving the linear equations if six independent strains are measured or by linear least squares regression if more than six independent measured strains are available [3].

In most applications, the stresses in a very thin layer of material on the surface are measured by X-ray diffraction. The penetration depth varies with the incident angle. Maximum penetration occurs when both the incident angle and diffracted angle equal the Bragg angle θ ($\psi = 0$) with the penetration given by

$$t = -\frac{\sin\theta \ln(1 - G_t)}{2\mu} \tag{9.36}$$

where μ is the linear absorption coefficient, G_t is the fraction of the total diffracted intensity contributed by the surface layer of thickness t. A G_t of 0.95 is typically selected. For example, for iron (211) planes measured by Cr-K_α, the penetration depth $t \approx 16\,\mu m$. Due to the limited penetration of X-rays, normal stress at the sample surface diminishes to zero, $\sigma_{33} = 0$. The stress components along the L direction (Figure 9.4) are the normal stress σ_ϕ and shear stress τ_ϕ and are given by the stress tensor components in sample coordinates by

$$\begin{aligned} \sigma_\phi &= (\sigma_{11}\cos^2\phi + \sigma_{22}\sin^2\phi + \tau_{12}\sin 2\phi) \\ \tau_\phi &= (\sigma_{13}\cos\phi + \sigma_{23}\sin\phi) \end{aligned} \tag{9.37}$$

Then equation (9.33) simplifies to

$$\varepsilon_{\phi\psi}^{\{hkl\}} = S_1^{\{hkl\}}(\sigma_{11} + \sigma_{22}) + \tfrac{1}{2}S_2^{\{hkl\}}\sigma_\varphi \sin^2\psi + \tfrac{1}{2}S_2^{\{hkl\}}\tau_\phi \sin 2\psi \tag{9.38}$$

The stress state in this case is referred to as biaxial with shear. For a biaxial stress state, $\tau_\phi = 0$, so we have

$$\varepsilon_{\phi\psi}^{\{hkl\}} = S_1^{\{hkl\}}(\sigma_{11} + \sigma_{22}) + \tfrac{1}{2}S_2^{\{hkl\}}\sigma_\varphi \sin^2\psi \tag{9.39}$$

For a given sample, the measured strain is a linear function of $\sin^2\psi$. By taking the first derivative with respect to $\sin^2\psi$, we obtain

$$\frac{\partial \varepsilon_{\phi\psi}^{\{hkl\}}}{\partial(\sin^2\psi)} = \tfrac{1}{2}S_2^{\{hkl\}}\sigma_\varphi = m \tag{9.40}$$

where m is the slope of the measured strain in the $\varepsilon_{\phi\psi}^{\{hkl\}}$ - $\sin^2\psi$ plot as shown in Figure 9.5(a). Then we have

$$\sigma_\varphi = \frac{m}{\frac{1}{2}S_2^{\{hkl\}}} \tag{9.41}$$

With the macroscopic elasticity constants, it can also be expressed as

$$\sigma_\varphi = \frac{m}{\frac{1}{2}S_2} = \frac{mE}{1+\nu} \tag{9.42}$$

By collecting diffraction profiles of the $\{hkl\}$ peak at several ψ-tilt angles, the slope of the $\varepsilon_{\phi\psi}^{\{hkl\}}$ - $\sin^2\psi$ plot can be calculated by a linear least squares fitting and the stress is calculated from the slope and the elastic constant. The normal stress components σ_{11} and σ_{22} can be obtained by

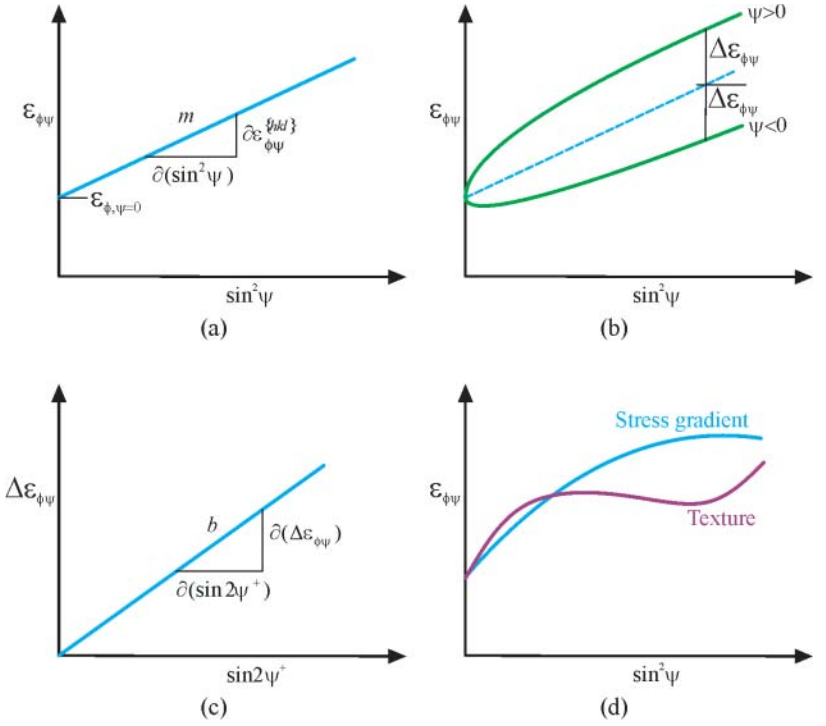


FIGURE 9.5 Stress measurement from the $\varepsilon_{\phi\psi}^{\{hkl\}}$ - $\sin^2\psi$ plot: (a) linear when $\tau_\phi = 0$, (b) ψ-split due to shear $\tau_\phi \neq 0$, (c) fluctuation due to texture, (d) curve due to stress or composition gradient.

measurements at $\phi = 0°$ and $\phi = 90°$ respectively. This method is often called the $\sin^2\psi$ method. The interception of the $\varepsilon_{\phi\psi}^{\{hkl\}}$ - $\sin^2\psi$ plot with the $\varepsilon_{\phi\psi}^{\{hkl\}}$ axis is the strain measured with the tilt angle $\psi = 0$,

$$\varepsilon_{\phi,\psi=0}^{\{hkl\}} = S_1^{\{hkl\}}(\sigma_{11} + \sigma_{22}) \tag{9.43}$$

In the case of biaxial stress with shear (only $\sigma_{33} = 0$), the shear strain results in a deviation from the linear relation of the $\varepsilon_{\phi\psi}^{\{hkl\}}$ - $\sin^2\psi$ plot, as shown in Figure 9.5(b). The deviations are both positive and negative from the linear relation, depending on the sign of the ψ tilt angle. Therefore, it is also referred to as ψ-split. The shear stress τ_ϕ can be measured from the amount of ψ-split. Assuming the strain $\varepsilon_{\phi\psi}^{\{hkl\}}$ has been measured at both positive and negative ψ tilt angles, by subtracting Equation (9.35) for ψ^+ and ψ^- and assuming $\sin 2\psi^- = -\sin 2\psi^+$ we obtain

$$\Delta\varepsilon_{\phi\psi} = \frac{\varepsilon_{\phi\psi+}^{\{hkl\}} - \varepsilon_{\phi\psi-}^{\{hkl\}}}{2} = \frac{\frac{1}{2}S_2^{\{hkl\}}\tau_\phi(\sin 2\psi^+ - \sin 2\psi^-)}{2} = \frac{1}{2}S_2^{\{hkl\}}\tau_\phi \sin 2\psi^+ \tag{9.44}$$

All other terms are cancelled out. Figure 9.5(c) is a plot of $\Delta\varepsilon_{\phi\psi}$ vs. $\sin 2\psi^+$. The slope of the plot can be calculated from a linear fitting of the data points. The shear stress is then given by

$$\tau_\phi = \frac{\partial(\Delta\varepsilon_{\phi\psi})}{\partial(\sin 2\psi^+)}\frac{1}{\frac{1}{2}S_2^{\{hkl\}}} = \frac{b}{\frac{1}{2}S_2^{\{hkl\}}} \tag{9.45}$$

where b is the slope of the $\Delta\varepsilon_{\phi\psi}$ - $\sin 2\psi^+$ plot. The value of $\sin 2\psi^+$ reaches a maximum at $\psi = 45°$, so a ψ-tilt of up to 45° is preferred to resolve shear stress. Further increase in the ψ-tilt beyond 45° is not necessary for resolving shear component. The shear stress components σ_{13} and σ_{23} can be obtained by measurements at $\phi = 0°$ and $\phi = 90°$ respectively.

The $\varepsilon_{\phi\psi}^{\{hkl\}}$ - $\sin^2\psi$ plot may deviate from a straight line for other reasons – for instance, texture, stress gradient, or composition gradient, as shown in Figure 9.5(d).

9.2.4 Stress Measurement Without d_o

In the above $\varepsilon_{\phi\psi}^{\{hkl\}}$ - $\sin^2\psi$ plots, the measured strain $\varepsilon_{\phi\psi}^{\{hkl\}}$ is given by equations (9.31), which requires both the measured d-spacing d (or 2θ) and the stress-free d-spacing d_o (or $2\theta_o$). d_o is not always available. For most metals or alloys, due to variations in composition, processing, and laboratory temperature, it is very hard to obtain an accurate d_o (or $2\theta_o$). Assuming an inaccurate stress-free d-spacing, d_o' is used in the calculation of $\varepsilon_{\phi\psi}^{\{hkl\}}$. With the true strain definition, we have

$$\varepsilon_{\phi\psi}^{\{hkl\}} = \ln\frac{d_{\phi\psi}^{\{hkl\}}}{d_o} = \ln\frac{d_{\phi\psi}^{\{hkl\}}}{d_o'}\frac{d_o'}{d_o} = \ln\frac{d_{\phi\psi}^{\{hkl\}}}{d_o'} + \ln\frac{d_o'}{d_o} = \varepsilon'^{\{hkl\}}_{\phi\psi} + \varepsilon_{ph} \tag{9.46}$$

where $\varepsilon_{ph} = \ln\frac{d_o'}{d_o}$ is the pseudo-hydrostatic strain caused by the error in d-spacing d_0'. The effect of pseudo-hydrostatic strain is as if the sample is first deformed by a hydrostatic strain ε_{ph} so the d-spacing of $\{hkl\}$ in all directions changes from d_o to d_o'. Introducing this effect into equation (9.36),

$$\varepsilon'^{\{hkl\}}_{\phi\psi} = S_1^{\{hkl\}}(\sigma_{11} + \sigma_{22}) + \tfrac{1}{2}S_2^{\{hkl\}}\sigma_\varphi\sin^2\psi - \varepsilon_{ph} \tag{9.47}$$

By taking the first derivative with respect to $\sin^2\psi$, we obtain:

$$\frac{\partial\varepsilon'^{\{hkl\}}_{\phi\psi}}{\partial(\sin^2\psi)} = \tfrac{1}{2}S_2^{\{hkl\}}\sigma_\phi = m' \tag{9.48}$$

One can easily conclude that the error in stress-free d-spacing only shifts the height of the $\varepsilon_{\phi\psi}^{\{hkl\}}$ - $\sin^2\psi$ plot, but does not change the slope ($m = m'$). Therefore, in a biaxial stress state or biaxial stress state with shear, it is not necessary to use an accurate stress-free d-spacing when the $\sin^2\psi$ method is used for stress measurement. Typically the d-spacing measured at $\psi = 0$, $d_{\phi,\psi=0}^{\{hkl\}}$, is used in place of d_o.

Following the same principle, the slope of the d vs. $\sin^2\psi$ plot has often been used for stress measurement. By the definition of engineering strain, in the biaxial stress state, we have

$$\frac{d_{\phi\psi}^{\{hkl\}} - d_o}{d_o} = S_1^{\{hkl\}}(\sigma_{11} + \sigma_{22}) + \tfrac{1}{2}S_2^{\{hkl\}}\sigma_\varphi\sin^2\psi \tag{9.49}$$

By taking the first derivative of $d_{\phi\psi}^{\{hkl\}}$ with respect to $\sin^2\psi$, we obtain

$$\frac{\partial d_{\varphi\psi}^{\{hkl\}}}{\partial(\sin^2\psi)} = \tfrac{1}{2}S_2^{\{hkl\}}d_o\sigma_\phi = m'' \tag{9.50}$$

where m'' is the slope of the d- $\sin^2\psi$ plot as shown in Figure 9.6(a). The error is negligible when d_o is replaced by $d^{\{hkl\}}_{\phi,\psi=0}$ in the denominator, therefore, we have

$$\sigma_\varphi = \frac{m''}{\frac{1}{2}S_2^{\{hkl\}} d^{\{hkl\}}_{\phi,\psi=0}} \tag{9.51}$$

As shown in Figure 9.6(b), the ψ-split in the d- $\sin^2\psi$ plot is given by

$$\Delta d_{\phi\psi} = \frac{d^{\{hkl\}}_{\phi\psi+} - d^{\{hkl\}}_{\phi\psi-}}{2} = \frac{\frac{1}{2}S_2^{\{hkl\}} d_o \tau_\phi (\sin 2\psi^+ - \sin 2\psi^-)}{2} = \frac{1}{2}S_2^{\{hkl\}} d_o \tau_\phi \sin 2\psi^+ \tag{9.52}$$

The shear stress can be calculated by

$$\tau_\phi = \frac{\partial(\Delta d_{\phi\psi})}{\partial(\sin 2\psi^+)} \frac{1}{\frac{1}{2}S_2^{\{hkl\}} d^{\{hkl\}}_{\phi,\psi=0}} = \frac{b'}{\frac{1}{2}S_2^{\{hkl\}} d^{\{hkl\}}_{\phi,\psi=0}} \tag{9.53}$$

where b' is the slope of the $\Delta d_{\phi\psi}$ - $\sin 2\psi^+$ plot and d_o is approximated by $d^{\{hkl\}}_{\phi,\psi=0}$. It is not necessary to take this approximation if the true (rational) strain definition has been used. From

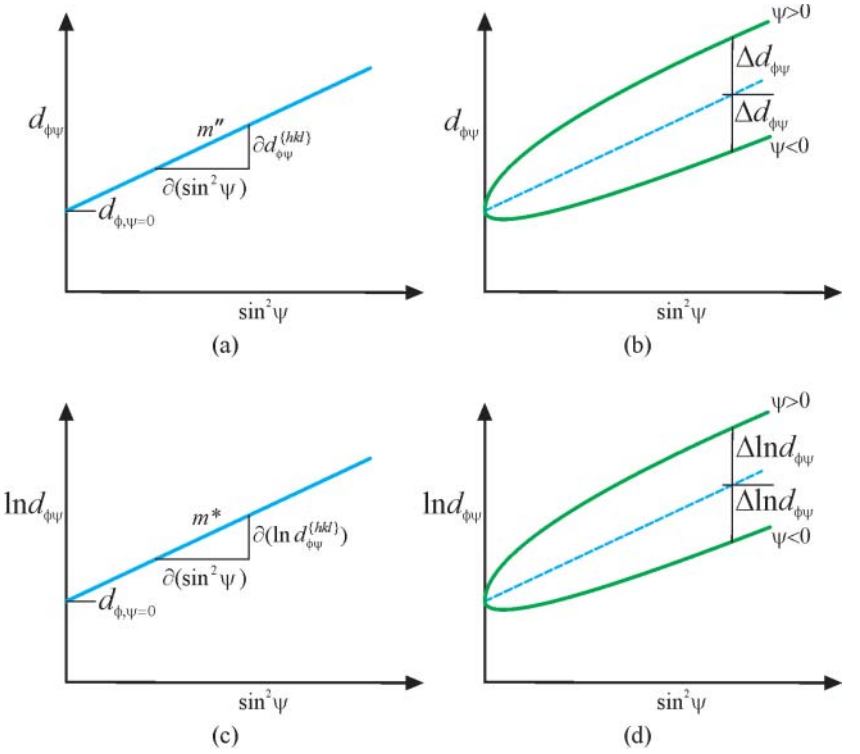


FIGURE 9.6 Stress measurement from the measured d vs $\sin^2\psi$ relations: (a) $d - \sin^2\psi$ plot for $\tau_\phi = 0$, (b) $d - \sin^2\psi$ plot for $\tau_\phi \neq 0$, (c) $\ln d - \sin^2\psi$ plot for $\tau_\phi = 0$, (d) $\ln d - \sin^2\psi$ plot for $\tau_\phi \neq 0$.

Equation (9.35), we obtain

$$\varepsilon_{\phi\psi}^{\{hkl\}} = \ln \frac{d_{\phi\psi}^{\{hkl\}}}{d_o} = S_1^{\{hkl\}}(\sigma_{11} + \sigma_{22}) + \tfrac{1}{2}S_2^{\{hkl\}}\sigma_\varphi \sin^2\psi + \tfrac{1}{2}S_2^{\{hkl\}}\tau_\phi \sin 2\psi \tag{9.54}$$

or

$$\ln d_{\phi\psi}^{\{hkl\}} = S_1^{\{hkl\}}(\sigma_{11} + \sigma_{22}) + \tfrac{1}{2}S_2^{\{hkl\}}\sigma_\varphi \sin^2\psi + \tfrac{1}{2}S_2^{\{hkl\}}\tau_\phi \sin 2\psi + \ln d_o \tag{9.55}$$

Then we have

$$\sigma_\varphi = \frac{\partial(\ln d_{\phi\psi}^{\{hkl\}})}{\partial(\sin^2\psi)} \frac{1}{\tfrac{1}{2}S_2^{\{hkl\}}} = \frac{m^*}{\tfrac{1}{2}S_2^{\{hkl\}}} \tag{9.56}$$

where m^* is the slope of the $\ln d$ - $\sin^2\psi$ plot, as shown in Figure 9.6(c). By using the true strain definition, the stress can be calculated without using the stress-free d_o and the approximation is therefore not necessary. The shear stress τ_ϕ can be measured from the amount of ψ-split in the $\ln d$ - $\sin^2\psi$ plot. Assuming the strain $d_{\phi\psi}^{\{hkl\}}$ has been measured at both positive and negative ψ tilt angles, by subtracting the expression of Equation (9.53) for ψ^+ and ψ^- and considering $\sin 2\psi^- = -\sin 2\psi^+$ we obtain

$$\Delta \ln d_{\phi\psi} = \frac{\ln d_{\phi\psi+}^{\{hkl\}} - \ln d_{\phi\psi-}^{\{hkl\}}}{2} = \frac{\tfrac{1}{2}S_2^{\{hkl\}}\tau_\phi(\sin 2\psi^+ - \sin 2\psi^-)}{2} = \tfrac{1}{2}S_2^{\{hkl\}}\tau_\phi \sin 2\psi^+ \tag{9.57}$$

The shear stress can be calculated by

$$\tau_\phi = \frac{\partial(\Delta \ln d_{\phi\psi})}{\partial(\sin 2\psi^+)} \frac{1}{\tfrac{1}{2}S_2^{\{hkl\}}} = \frac{s^*}{\tfrac{1}{2}S_2^{\{hkl\}}} \tag{9.58}$$

where s^* is the slope of the $\Delta \ln d_{\phi\psi}$ - $\sin 2\psi^+$ plot and the stress free d_o is not needed for the stress calculation.

9.2.5 ψ-Tilt and Goniometer

Measurement of a stress value with the $\sin^2\psi$ method requires at least the ψ-tilt, while measurement of a stress tensor requires at least two rotation axes to achieve the ψ-tilt and ϕ-rotation. The ψ-tilt is defined as the angle between the sample normal and the diffraction vector. Eulerian geometry has three sample rotation angles (ω,ψ,ϕ), hence, the ψ-tilt can be achieved by one of the two methods as shown in Figure 9.7(a). One is the iso-inclination mode (also called the ω-method or ω-diffractometer) in which both the sample normal ($\mathbf{S_3}$) and the diffraction vector are within the diffractometer plane. The ω rotation axis is perpendicular to the diffractometer plane containing the incident and diffracted beams. The other method is the side-inclination mode (also called the ψ-method or ψ-diffractometer) in which the sample normal ($\mathbf{S_3}$) is out of the diffractometer plane for all non-zero ψ-tilt angles. Both the sample normal ($\mathbf{S_3}$) and the diffraction vector are within a plane perpendicular to the diffractometer plane.

Since the ψ-tilt in the iso-inclination mode is achieved by a rotation axis parallel to the main axes of a goniometer, the iso-inclination mode can be achieved with most diffractometers. In a diffractometer with a θ-2θ configuration, the ψ-tilt is achieved by ω-rotation of the sample. The ψ-tilt is given by

$$\psi_{tilt} = \omega - \theta \tag{9.59}$$

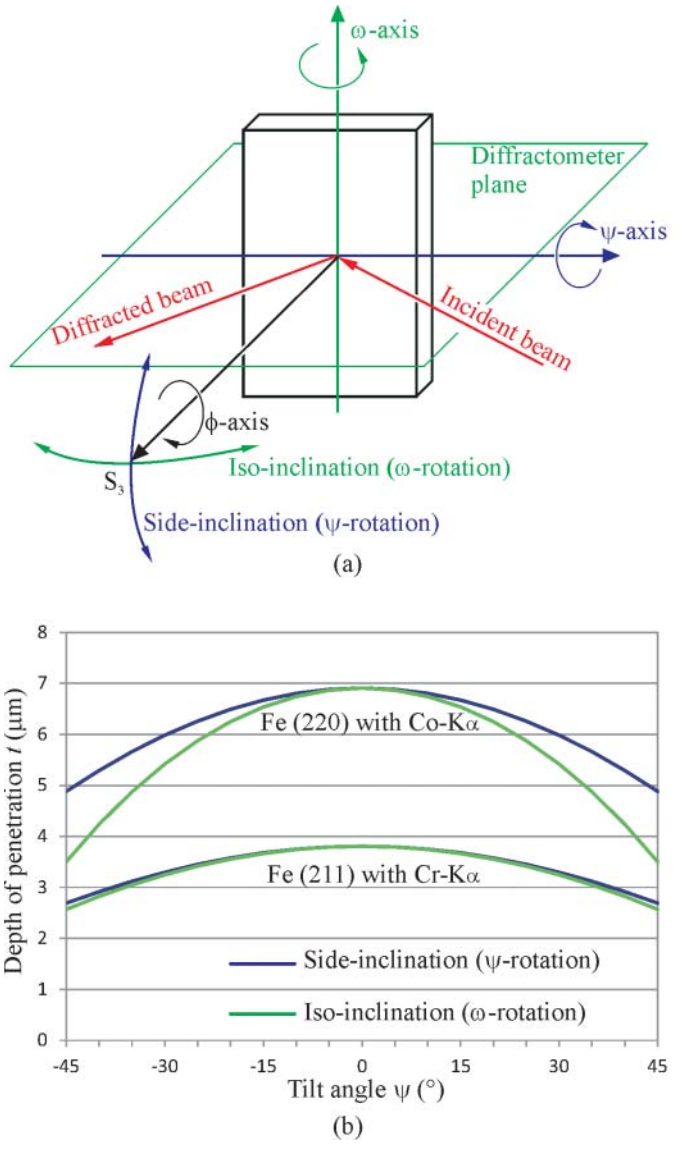


FIGURE 9.7 The ψ-tilt and depth of penetration: (a) ψ-tilt iso-inclination (ω-rotation) or side-inclination (ψ-rotation), (b) depth of penetration at different inclination modes.

where subscript "tilt" is used to distinguish the ψ-tilt from the goniometer angle ψ. When $\omega = \theta$, the diffraction vector and sample normal are in the same direction ($\psi_{tilt} = 0$). In a diffractometer with a θ-θ configuration, the ψ-tilt is achieved by the difference between the incident angle (θ_1) and the detector angle (θ_2). The ψ-tilt is given by

$$\psi_{tilt} = \frac{\theta_1 - \theta_2}{2} \tag{9.60}$$

The geometric relations between the incident beam, diffracted beam, and sample are equivalent in both the θ-2θ and θ-θ configurations. The incident angle to the sample varies with the

ψ-tilt angle, so X-ray penetration varies dramatically as well as the irradiated area on the sample surface due to the defocusing effect. These effects are more severe at the negative ψ-tilt angles where $\omega < \theta$. Measurement at low incident angle is also more sensitive to sample alignment error. Therefore, the iso-inclination mode should be used for samples with a mild stress gradient in depth and relatively homogeneous stress distribution on the surface. Measurement of the shear stress by ψ-split requires both positive and negative ψ-tilt angles. By rotating the sample by 180° in the ϕ axis, we have

$$\tau_{\phi+\pi} = [\sigma_{13}\cos(\phi+\pi) + \sigma_{23}\sin(\phi+\pi)] = (\sigma_{13}\cos\phi + \sigma_{23}\sin\phi) = -\tau_{\phi} \tag{9.61}$$

$$\tfrac{1}{2}S_2^{\{hkl\}}\tau_{\phi+\pi}\sin 2\psi^{+} = -\tfrac{1}{2}S_2^{\{hkl\}}\tau_{\phi}\sin 2\psi^{+} = \tfrac{1}{2}S_2^{\{hkl\}}\tau_{\phi}\sin 2\psi^{-} \tag{9.62}$$

This means that measurement at positive ψ-tilt angles with 180° sample rotation will create the same deviation from the straight line in the $\varepsilon_{\phi\psi}^{\{hkl\}}$ - $\sin^2\psi$ plot as at negative ψ-tilt angles. Therefore, measurement at negative ψ-tilts can be replaced by measurement at positive ψ-tilts with a 180° rotation of the sample in the φ axis.

The ψ-tilt in the side-inclination mode is achieved by a rotation axis within the diffractometer plane that is perpendicular to the main axes of a goniometer. Therefore, side-inclination mode requires an additional rotation axis beyond the main axes. This axis is also called the ψ-axis in Eulerian geometry. In some systems this axis is named the χ-axis. Hence, the side-inclination mode is also referred to as the χ-method in some literature. In a diffractometer with a θ-2θ configuration, the measurement is done at $\omega = \theta$, and at $\theta_1 = \theta_2 = \theta$ for the θ-θ configuration. The ψ-tilt is directly given by the goniometer ψ-angle or χ-angle.

The depth of penetration for diffraction with a point detector or diffraction within the diffractometer plane ($\gamma = -90°$ and ignore the penetration dependence on γ) for a 2D detector is given by

$$t = \frac{-\ln(1-G_t)\sin\omega\sin(2\theta-\omega)\cos\psi}{\mu[\sin\omega + \sin(2\theta-\omega)]} \tag{9.63}$$

where G_t is the fraction of the diffracted intensity contributed by a surface layer of depth t. It can be seen that the depth of penetration depends on the 2θ angle of the diffraction peak and also the mode of inclination, which determines the variation of ω and ψ angles. Figure 9.7(b) shows the depth of penetration at different inclination modes for steel (Fe) corresponding to 50% diffracted intensity. For {211} planes with Cr-K_α radiation, $2\theta_0 \approx 156°$, the difference between iso-inclination and side-inclination is small. But if the stress is measured with Co-K_α radiation for {220} planes, $2\theta_0 \approx 124°$, the difference between iso-inclination and side-inclination is significant. The depth of penetration with side-inclination has less variation at high tilt angle, while the depth of penetration with iso-inclination mode changes dramatically from 6.9 μm at zero tilt to 3.5 μm at $\psi = \pm 45°$. Overall, X-ray penetration is relatively more consistent with side-inclination and more variational with iso-inclination, especially for lower 2θ angle. Side-inclination is also less sensitive to the sample height error than the iso-inclination method due to lower variation of the incident angle. For instance, with $2\theta_0 \approx 156°$, at the typical maximum ψ-tilt angle of ±45°, the incident angle is 43.8° with side-inclination for both positive and negative ψ-tilt angles. But with iso-inclination mode, the incident angle varies from 33° to 123° from negative to positive ψ-tilt angles. Some diffractometer may not allow both the positive and negative ψ-tilt due to mechanical limitations. In this case, measurement at negative ψ tilts can be replaced by measurement at positive ψ tilts by rotating the sample by 180° around the ϕ axis, or vice versa.

9.2.6 $\sin^2\psi$ Method with Area Detector

Diffraction data from area detectors can be used for stress measurement with conventional methods, such as the $\sin^2\psi$ method or other algorithms developed for conventional diffractometers with a point or line detector. The diffraction profiles produced by γ-integration can be used in the same way as the diffraction profiles from a line detector or scanning point detector. Figure 9.8 shows an experimental example. The residual stress is measured with a GADDS™ (Bruker) microdiffraction system. The spring has a coil diameter of 10 mm, coil pitch of 4 mm and wire diameter of 0.7 mm. The spring was made of precipitation-hardened stainless steel 17–7PH. The residual stress on the inside surface of the spring was measured with a Cr tube and a 0.3 mm collimator. The (211) diffraction ring of the alpha phase was used for stress measurement. The laser-video sample alignment system was used to position the inside surface of the spring. Figure 9.8(a) shows that the laser beam passing through the spring pitch forms a bright spot on the inside surface of the spring wire. Figure 9.8(b) shows that the sample surface is aligned to the instrument center by overlapping the laser spot with the crosshair. A total of seven frames are collected with ω rotation corresponding to seven ψ-tilt angles between $\pm 45°$ with 15° steps. The total data collection time is 14 minutes with 2 minutes per frame. Figure 9.8(c) is the frame showing the γ-integration

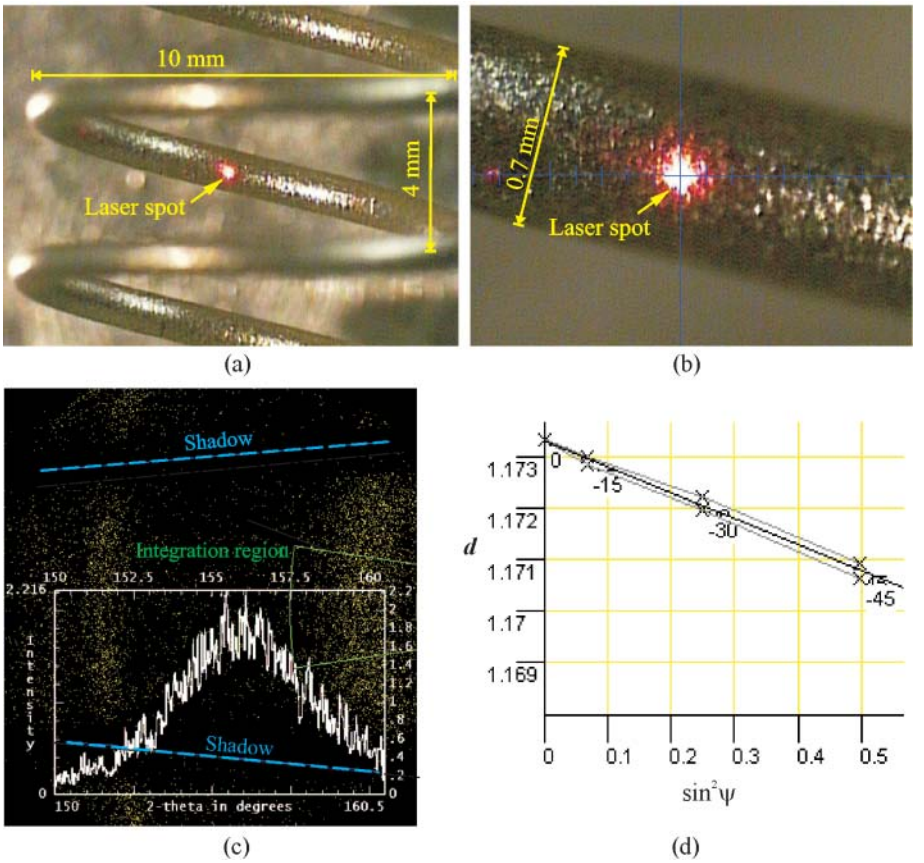


FIGURE 9.8 Experimental example of $\sin^2\psi$ method with area detector: (a) a spring with laser spot on inside surface, (b) alignment by laser-video system, (c) 2D diffraction frame with shadow of the spring wire. (d) The d- $\sin^2\psi$ curve.

region of 2θ from 150° to 160.5° and γ from 80° to 100°. The incident beam reaches the sample surface through the gap of spring wire and the diffracted X-rays reach the area detector through the gap. The low count regions, marked by the dashed lines, are the shadows of the spring wires. The diffraction signals from such a thin wire and small beam size are very weak, but γ-integration produced a profile with sufficient counts to determine the 2θ position. The seven integrated diffraction profiles are then used for stress analysis by the $\sin^2\psi$ method. The d- $\sin^2\psi$ curve is shown in Figure 9.8(d). The measured stress is −864 (±48) MPa. Another experiment with 19 frames (38 minutes) in the same setup but 5° steps measured the stress as −875 (±31) MPa.

The above example shows that an area detector can be used for residual stress measurement with a conventional method. Since γ-integration can produce a well-defined diffraction peak even from weak signals, an area detector can measure stress faster than the point detector and line detector, especially from a small sample area. However, the disadvantage with the conventional method is that only one strain value (2θ shift) is measured at one sample orientation. Although the profile is from γ-integration of the diffraction ring, the γ-range of the integration must be limited. In the above example, the measured 2θ value is actually an average over the γ-integration range of $\Delta\gamma = 20°$ (80–100°), but treated as if it was collected at the diffractometer plane ($\gamma = 90°$). This will cause a "smearing effect" to the sensitivity of the 2θ shift. Therefore, the complete diffraction ring cannot be used with the conventional method.

9.3 THEORY OF STRESS ANALYSIS WITH XRD^2

Two-dimensional X-ray diffraction (XRD^2) systems, when used for residual stress measurement, have many advantages over conventional one-dimensional diffraction systems [18–34]. First, the measurement time is significantly reduced due to the large portion of the diffraction ring being measured at each exposure. 2D data has a large angular coverage, which is beneficial to stress analysis of highly textured materials. γ-integration helps to smooth out rough diffraction profiles due to large grain size, small sample area or weak diffraction. The 2D fundamental equation, governing the relationship between the stress tensor and the diffraction cone distortion, is the basis of stress measurement in an XRD^2 system. The 2D fundamental equation can be used for both reflection mode and transmission mode diffraction. For biaxial stress measurement, the approximation of d-spacing or 2θ input for the stress-free condition does not cause error in the stress calculation. The true stress-free d-spacing can be calculated from the pseudo-hydrostatic term. The 2D method and the conventional method are consistent both in theory and applications.

9.3.1 2D Fundamental Equation for Stress Measurement

The diffraction cones from a stress-free polycrystalline sample are regular cones in which 2θ is a constant. The stress in the sample distorts the diffraction cone shape so that they are no longer regular cones. Figure 9.9 illustrates two diffraction cones with one for forward diffraction and one for backward diffraction. The regular diffraction cones (in black) are from the powder sample with no stress, so the 2θ angles are constant at all γ angles. The red rings are the cross-sections of the distorted diffraction cones due to stresses. For a stressed sample, 2θ becomes a function of γ and the sample orientation (ω,ψ,ϕ), i.e. $2\theta = 2\theta(\gamma, \omega, \psi, \phi)$. This function is uniquely determined by the stress tensor. For the diffraction cone from the lattice plane family $\{hkl\}$, there is a diffraction vector cone (in blue). For a point on the diffraction ring, P, the corresponding diffraction vector points to P′. The strain measured by the 2θ shift at point P is $\varepsilon^{\{hkl\}}_{(\gamma,\omega,\psi,\phi)}$, based on the true (rational) strain definition

$$\varepsilon^{\{hkl\}}_{(\gamma,\omega,\psi,\phi)} = \ln\frac{d}{d_o} = \ln\frac{\sin\theta_o}{\sin\theta} = \ln\frac{\lambda}{2d_o\sin\theta} \tag{9.64}$$

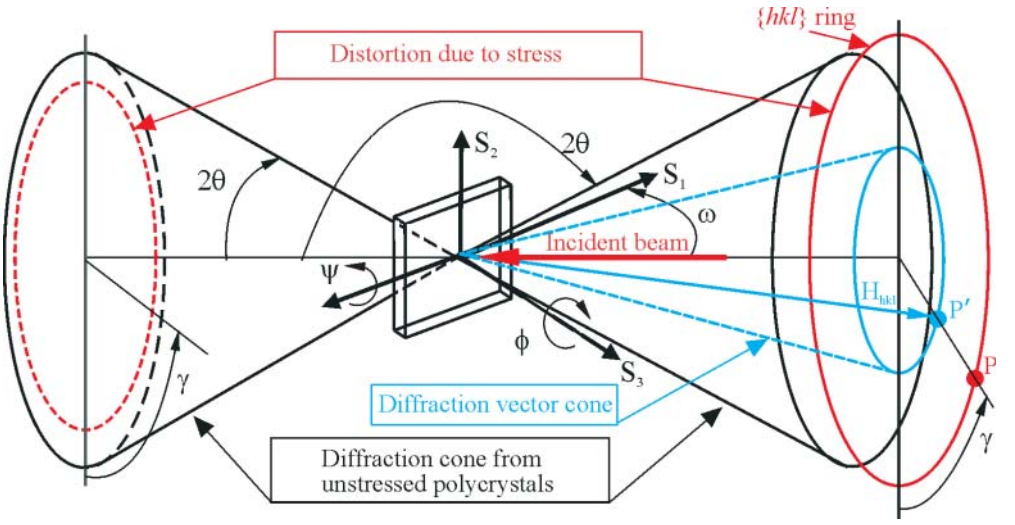


FIGURE 9.9 Diffraction cone distortion due to stresses.

where d_o and θ_o are the stress-free values and d and θ are measured values from a point on the diffraction ring corresponding to $(\gamma, \omega, \psi, \phi)$. The direction of $\varepsilon^{\{hkl\}}_{(\gamma,\omega,\psi,\phi)}$ in the sample coordinates $\mathbf{S_1S_2S_3}$ can be given by the unit vector of $\mathbf{H}_{hkl}$:

$$\mathbf{h}_S = \begin{bmatrix} h_1 \\ h_2 \\ h_3 \end{bmatrix} \tag{9.65}$$

which is given in Chapter 2 for Eulerian geometry by

$$\begin{aligned} h_1 &= \sin\theta(\sin\phi\sin\psi\sin\omega + \cos\phi\cos\omega) + \cos\theta\cos\gamma\sin\phi\cos\psi \\ &\quad - \cos\theta\sin\gamma(\sin\phi\sin\psi\cos\omega - \cos\phi\sin\omega) \\ h_2 &= -\sin\theta(\cos\phi\sin\psi\sin\omega - \sin\phi\cos\omega) - \cos\theta\cos\gamma\cos\phi\cos\psi \\ &\quad + \cos\theta\sin\gamma(\cos\phi\sin\psi\cos\omega + \sin\phi\sin\omega) \\ h_3 &= \sin\theta\cos\psi\sin\omega - \cos\theta\sin\gamma\cos\psi\cos\omega - \cos\theta\cos\gamma\sin\psi \end{aligned} \tag{9.66}$$

As a second order tensor, the relationship between the measured strain and the strain tensor components is then given by

$$\boxed{\varepsilon^{\{hkl\}}_{(\gamma,\omega,\psi,\phi)} = \varepsilon_{ij} \cdot h_i \cdot h_j} \tag{9.67}$$

The scalar product of the strain tensor with the unit vector in the above equation is the sum of all components in the tensor multiplied by the components in the unit vector corresponding to the first and the second indices. The expansion of this equation for i and j values of 1, 2, and 3 results in

$$\varepsilon^{\{hkl\}}_{(\gamma,\omega,\psi,\phi)} = h_1^2\varepsilon_{11} + 2h_1h_2\varepsilon_{12} + h_2^2\varepsilon_{22} + 2h_1h_3\varepsilon_{13} + 2h_2h_3\varepsilon_{23} + h_3^2\varepsilon_{33} \tag{9.68}$$

Or, taking the true strain definition

$$h_1^2\varepsilon_{11} + 2h_1h_2\varepsilon_{12} + h_2^2\varepsilon_{22} + 2h_1h_3\varepsilon_{13} + 2h_2h_3\varepsilon_{23} + h_3^2\varepsilon_{33} = \ln\left(\frac{\sin\theta_0}{\sin\theta}\right) \tag{9.69}$$

where θ_o is the stress-free d-spacing and θ are measured values from a point on the diffraction ring corresponding to $(\gamma, \omega, \psi, \phi)$, and $\{h_1, h_2, h_3\}$ are the components of the unit vector in the direction of the measured strain, $\varepsilon^{\{hkl\}}_{(\gamma,\omega,\psi,\phi)}$. As in the previous publications [24–27, 29, 30], the fundamental equation for strain measurement with XRD^2 can also be expressed as

$$f_{11}\varepsilon_{11} + f_{12}\varepsilon_{12} + f_{22}\varepsilon_{22} + f_{13}\varepsilon_{13} + f_{23}\varepsilon_{23} + f_{33}\varepsilon_{33} = \ln\left(\frac{\sin\theta_0}{\sin\theta}\right) \tag{9.70}$$

where f_{ij} are the strain coefficients given by

$$f_{ij} = \begin{cases} h_{ij}^2 & \text{if } i = j \\ 2h_ih_j & \text{if } i \neq j \end{cases}$$

Both θ and $\{h_1, h_2, h_3\}$ are functions of $(\gamma, \omega, \psi, \phi)$. By taking the γ value from 0° to 360°, the above equation establishes the relationship between the diffraction cone distortion and the strain tensor. Therefore, this equation is the fundamental equation for strain measurement with two-dimensional X-ray diffraction. The fundamental equation may be used to derive many other equations based on the stress–strain relationship, stress state, and special conditions. The fundamental equation and the derived equations may be referred to as 2D equations hereafter to distinguish them from the conventional equations. These equations can be used in two ways. One is to calculate the strain or strain tensor components (stress or stress tensor components) from the measured strain (2θ shift) values and corresponding directions. For this application, we need to measure the strain in different directions, at least as many as the independent unknown components, at independent directions. Another function of the fundamental equation is to calculate the diffraction ring distortion (normal strains at all directions corresponding to the full 360° range of γ angles) for a given stress (or strain) tensor at a particular sample orientation (ω, ψ, ϕ). Both functions will be further discussed later in the chapter.

Based on the above fundamental equation, the strain tensor can be measured by an XRD^2 system. In general, the stress tensor can be calculated from the measured strain tensor by Hooke's law. For materials with homogenous and isotropic elasticity, there are only two independent elasticity constants: Young's modulus E and Poisson's ratio ν or the macroscopic elastic constants $\frac{1}{2}S_2 = (1+\nu)/E$ and . $S_1 = -\nu/E$ We obtain

$$-\frac{\nu}{E}(\sigma_{11} + \sigma_{22} + \sigma_{33}) + \frac{1+\nu}{E}(\sigma_{11}h_1^2 + \sigma_{22}h_2^2 + \sigma_{33}h_3^2 + 2\sigma_{12}h_1h_2 + 2\sigma_{13}h_1h_3 + 2\sigma_{23}h_2h_3) = \ln\left(\frac{\sin\theta_0}{\sin\theta}\right) \tag{9.71}$$

or

$$S_1(\sigma_{11} + \sigma_{22} + \sigma_{33}) + \tfrac{1}{2}S_2(\sigma_{11}h_1^2 + \sigma_{22}h_2^2 + \sigma_{33}h_3^2 + 2\sigma_{12}h_1h_2 + 2\sigma_{13}h_1h_3 + 2\sigma_{23}h_2h_3) = \ln\left(\frac{\sin\theta_0}{\sin\theta}\right) \tag{9.72}$$

It is convenient to express the fundamental equation in a clear linear form

$$\boxed{p_{11}\sigma_{11} + p_{12}\sigma_{12} + p_{22}\sigma_{22} + p_{13}\sigma_{13} + p_{23}\sigma_{23} + p_{33}\sigma_{33} = \ln\left(\frac{\sin\theta_0}{\sin\theta}\right)} \tag{9.73}$$

where p_{ij} are stress coefficients and given by

$$p_{ij} = \begin{cases} (1/E)\,[(1+\nu)f_{ij} - \nu] = \frac{1}{2}S_2 f_{ij} + S_1 & \text{if } i = j \\ (1/E)\,(1+\nu)f_{ij} = \frac{1}{2}S_2 f_{ij} & \text{if } i \neq j \end{cases}$$

where

$$f_{ij} = \begin{cases} h_{ij}^2 & \text{if } i = j \\ 2h_i h_j & \text{if } i \neq j \end{cases}$$

So we have

$$p_{ij} = \begin{cases} (1/E)\,[(1+\nu)h_i^2 - \nu] = \frac{1}{2}S_2 h_i^2 + S_1 & \text{if } i = j \\ 2\,(1/E)\,(1+\nu)h_i h_j = 2\frac{1}{2}S_2 h_i h_j & \text{if } i \neq j \end{cases} \tag{9.74}$$

In the equations for the stress measurement above and hereafter, the macroscopic elastic constants $\frac{1}{2}s_2$ and S_1 are used for simplicity, but they can always be replaced by the XEC for the specific lattice plane $\{hkl\}$, $S_1^{\{hkl\}}$ and $\frac{1}{2}S_2^{\{hkl\}}$, if the anisotropic nature of the crystallites should be considered. For instance, Equation (9.72) can be expressed with the XEC as

$$S_1^{\{hkl\}}(\sigma_{11} + \sigma_{22} + \sigma_{33}) + \tfrac{1}{2}S_2^{\{hkl\}}(\sigma_{11}h_1^2 + \sigma_{22}h_2^2 + \sigma_{33}h_3^2 + 2\sigma_{12}h_1h_2 + 2\sigma_{13}h_1h_3 + 2\sigma_{23}h_2h_3) = \ln\left(\frac{\sin\theta_0}{\sin\theta}\right) \tag{9.75}$$

The fundamental equation for stress measurement with XRD^2 is a linear equation of the stress tensor components. The stress tensor can be obtained by solving the linear equations if six independent strains are measured or by linear least squares regression if more than six independent measured strains are available. In order to get a reliable solution from the linear equations or least squares analysis, the independent strain should be measured at significantly different orientations. The linear least squares regression calculation may not converge or may do so with large error if the diffraction vectors representing all measured strains are within a small solid angle range. In this case, a data set with various sample orientation is necessary to obtain accurate stress component or stress tensor. This data collection strategy will be further discussed later in the chapter.

The fundamental equation for stress measurement with XRD^2 in one of the above formats can be modified or simplified for various stress states or instrument configurations. For instance, the equations given in the cos α method has been proved to be a special case of the XRD^2 fundamental equation [34]. The next section will prove that the fundamental equation used for the conventional method can be considered as a special case of the XRD^2 fundamental equation.

9.3.2 Relationship Between Conventional Theory and 2D Theory

In order to find the relationship between conventional theory and the new 2D theory, we first compare the configurations used for data collection in the two cases. The conventional diffraction

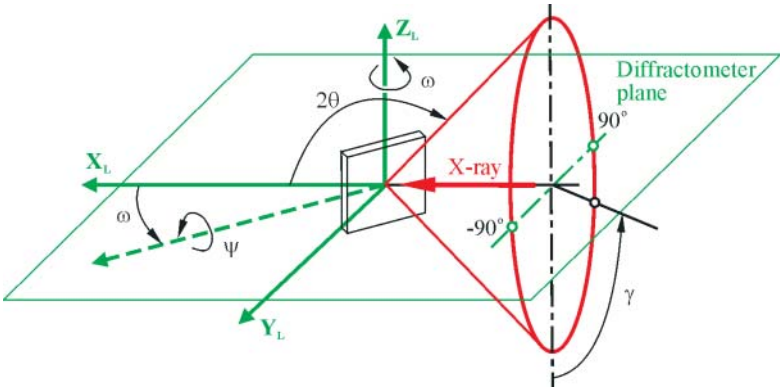


FIGURE 9.10 The diffraction cones and diffractometer plane.

profile is collected with a point detector scanning in the diffractometer plane or a position sensitive detector mounted in the diffractometer plane. 2D diffraction data consists of a diffracted X-ray intensity distribution on the detector plane. The intensity distribution along 2θ angles at any fixed γ is a diffraction profile analogous to the data collected with a conventional diffractometer. Figure 9.10 shows the relation between a 2D detector and a conventional detector. The diffraction profiles at $\gamma = 90°$ and $\gamma = -90$ (=270)° on the 2D detector are equivalent to the diffraction profiles collected in the conventional diffractometer plane. Therefore, we can use diffraction profiles at $\gamma = 90°$ and $\gamma = -90$ on a 2D frame to imitate a diffraction profile collected with a conventional diffractometer. It has been proven that the conventional fundamental equation is a special case of the 2D fundamental equation. In the same way, a conventional detector can be considered a limited part of a 2D detector. Depending on the specific conditions, we can choose either theory for stress measurement when a 2D detector is used. If conventional theory is used, we have to get a diffraction profile at $\gamma = 90°$ and $\gamma = -90$; this is normally done by integration of the data in a limited γ range. The disadvantage is that only part of the diffraction ring is used for stress calculation. When 2D theory is used, all of the diffraction ring can be used for stress calculation.

The 2D fundamental equations for stress and strain measurements define the relationship between diffraction cone distortion and the stress and strain tensors, so they should apply to both the conventional diffraction method and the two-dimensional diffraction method. The only difference is that the conventional method deals with the data points measured within a diffractometer plane while the two-dimensional diffraction method uses all the available data points. As shown in Figure 9.10, conventional diffraction is limited in the diffractometer plane. The diffraction data collected at $\gamma = 90°$ for negative detector swing and $\gamma = -90$ (=270)° for positive detector swing are within the diffractometer plane. Considering positive and negative detector swing angles and both the iso-inclination mode (ω-diffractometer) and side inclination mode (ψ-diffractometer), we have a total of four configurations to imitate the conventional system. For example, at a positive detector swing angle with a ψ-diffractometer condition, we have the following conditions:

$\gamma = -90°$,	using positive detector swing angle
$\omega = \theta$,	constant omega position with a ψ-diffractometer
$\psi' = \psi$	ψ-tilt angles achieved by ψ rotation
$\phi' = \phi + 90°$	tilt direction 90° away from the S_1 direction at $\phi = 0°$ when using a ψ-diffractometer

With above conditions, the unit vector components in the sample coordinates become

$$\begin{aligned}
h_1 &= \sin\theta(\sin\phi\sin\psi\sin\omega + \cos\phi\cos\omega) + \cos\theta\cos\gamma\sin\phi\cos\psi \\
&\quad - \cos\theta\sin\gamma(\sin\phi\sin\psi\cos\omega - \cos\phi\sin\omega) \\
&= \sin\psi'\cos\phi' \\
h_2 &= -\sin\theta(\cos\phi\sin\psi\sin\omega - \sin\phi\cos\omega) - \cos\theta\cos\gamma\cos\phi\cos\psi \\
&\quad + \cos\theta\sin\gamma(\cos\phi\sin\psi\cos\omega + \sin\phi\sin\omega) \\
&= \sin\psi'\sin\phi' \\
h_3 &= \sin\theta\cos\psi\sin\omega - \cos\theta\sin\gamma\cos\psi\cos\omega - \cos\theta\cos\gamma\sin\psi \\
&= \cos\psi'
\end{aligned}$$

Introducing these results into equations (9.69) and (9.72), and replacing $\ln\left(\frac{\sin\theta_0}{\sin\theta}\right)$ by $\varepsilon'_{\phi\psi}$, we then have exactly the same equations as the fundamental equations used for the conventional method of strain and stress measurement.

$$\begin{aligned}
\varepsilon'_{\phi,\psi} &= \varepsilon_{11}\cos^2\phi'\sin^2\psi' + \varepsilon_{12}\sin 2\phi'\sin^2\psi' + \varepsilon_{22}\sin^2\phi\sin^2\psi' \\
&\quad + \varepsilon_{13}\cos\phi'\sin 2\psi' + \varepsilon_{23}\sin\phi'\sin 2\psi' + \varepsilon_{33}\cos^2\psi' \qquad (9.76) \\
\varepsilon'_{\phi,\psi} &= S_1[\sigma_{11} + \sigma_{22} + \sigma_{33}] + \tfrac{1}{2}S_2[\sigma_{11}\cos^2\phi' + \sigma_{22}\sin^2\phi' + \sigma_{12y}\sin 2\phi']\sin^2\psi' \\
&\quad + \tfrac{1}{2}S_2[\sigma_{13}\cos\phi' + \sigma_{23}\sin\phi']\sin 2\psi' + \tfrac{1}{2}S_2\sigma_{33}\cos^2\psi' \qquad (9.77)
\end{aligned}$$

We can see that the fundamental equations for strain or stress measurement with two-dimensional diffraction are general equations that define the relationship between the strain (stress) tensor and diffraction cone distortion. When dealing with a single diffraction profile measured with a conventional diffractometer, the general equation reduces to the conventional equation. It can be proven that the same is true for all the other three configurations. All the above results show that the 2D fundamental equation covers the relations given by the conventional fundamental equation, or in other words, the conventional fundamental equation is a special case of the more general 2D fundamental equation. The four special conditions in an XRD^2 system imitating conventional diffractometers are summarized in Table 9.2.

Table 9.2 The Geometric Conditions Equivalent to the Conventional Diffractometer in an XRD^2 System

Detector swing angle	ω-diffractometer	ψ-diffractometer
Positive: $\alpha > 0$ $\gamma = -\frac{\pi}{2}$	$\psi = 0$ $\psi' = \theta - \omega$ $\phi' = \phi$	$\omega = \theta$ $\psi' = \psi$ $\phi' = \phi + \frac{\pi}{2}$
Negative: $\alpha < 0$ $\gamma = \frac{\pi}{2}$	$\psi = 0$ $\psi' = \pi - (\theta + \omega)$ $\phi' = \phi$	$\omega = \pi - \theta$ $\psi' = \psi$ $\phi' = \phi + \frac{\pi}{2}$

9.3.3 2D Equations for Various Stress States

The 2D fundamental equation can be used for stress measurement of the general triaxial stress state, in which all six stress tensor components have to be determined. The accurate stress-free d_o (or $2\theta_o$) must be available in this case. The general triaxial stress state is not typically measured by X-ray diffraction due to low penetration. For most applications, the stresses in a very thin layer of material on the surface are measured by X-ray diffraction. It is reasonable to assume that the average normal stress in the surface normal direction is zero within such a thin layer. Therefore, $\sigma_{33} = 0$, and the stress tensor has five non-zero components

$$\sigma_{ij} = \begin{bmatrix} \sigma_{11} & \sigma_{12} & \sigma_{13} \\ \sigma_{12} & \sigma_{22} & \sigma_{23} \\ \sigma_{13} & \sigma_{23} & 0 \end{bmatrix}$$

Some literature labels this stress state as triaxial. In order to distinguish this from the general triaxial stress state, we name this stress state as the biaxial stress state with shear. In this case, we have to be able to calculate the five stress tensor components with the following linear equation if more than five independent strains are measured and the accurate stress-free θ_o is known.

$$p_{11}\sigma_{11} + p_{12}\sigma_{12} + p_{13}\sigma_{13} + p_{22}\sigma_{22} + p_{23}\sigma_{23} = \ln\left(\frac{\sin\theta_0}{\sin\theta}\right) \tag{9.78}$$

However, for most metals or alloys, due to the variations in composition, processing conditions and laboratory temperature, it is very hard to obtain an accurate d_o (or $2\theta_o$). Assuming an inaccurate stress-free Bragg angle, θ_o' is used in the term $\ln\frac{\sin\theta_o}{\sin\theta}$, and faulty stress will be introduced into the calculation. The nature of this faulty stress is orientation independent, like a hydrostatic stress. In other words, the effect of the error in d_o (or $2\theta_o$) is as if the crystal lattice has been compressed or expanded uniformly in all directions. Therefore, this faulty stress is referred to as pseudo-hydrostatic stress, denoted by σ_{ph}. The stress tensor with $\sigma_{33} = 0$ now can be expressed as

$$\sigma'_{ij} = \begin{bmatrix} \sigma_{11} & \sigma_{12} & \sigma_{13} \\ \sigma_{12} & \sigma_{22} & \sigma_{23} \\ \sigma_{13} & \sigma_{23} & 0 \end{bmatrix} + \begin{bmatrix} \sigma_{ph} & 0 & 0 \\ 0 & \sigma_{ph} & 0 \\ 0 & 0 & \sigma_{ph} \end{bmatrix} = \begin{bmatrix} \sigma_{11}+\sigma_{ph} & \sigma_{12} & \sigma_{13} \\ \sigma_{12} & \sigma_{22}+\sigma_{ph} & \sigma_{23} \\ \sigma_{13} & \sigma_{23} & \sigma_{ph} \end{bmatrix} \tag{9.79}$$

Introducing this into the fundamental equation (9.73), we have

$$p_{11}(\sigma_{11}+\sigma_{ph}) + p_{12}\sigma_{12} + p_{22}(\sigma_{22}+\sigma_{ph}) + p_{13}\sigma_{13} + p_{23}\sigma_{23} + p_{33}\sigma_{ph} = \ln\left(\frac{\sin\theta_0}{\sin\theta}\right)$$

$$p_{11}\sigma_{11} + p_{12}\sigma_{12} + p_{22}\sigma_{22} + p_{13}\sigma_{13} + p_{23}\sigma_{23} + (p_{11}+p_{22}+p_{33})\sigma_{ph} = \ln\left(\frac{\sin\theta_0}{\sin\theta}\right)$$

$$p_{ij} = \begin{cases} (1/E)\,[(1+\nu)f_{ij} - \nu] = \frac{1}{2}S_2 f_{ij} + S_1 & \text{if } i = j \\ (1/E)\,(1+\nu)f_{ij} \quad\; = \frac{1}{2}S_2 f_{ij} & \text{if } i \neq j \end{cases}$$

$$\begin{aligned} p_{11}+p_{22}+p_{33} &= (1/E)\,[(1+\nu)(f_{11}+f_{22}+f_{33}) - 3\nu] \\ &= (1/E)\,[(1+\nu)(h_{11}^2+h_{22}^2+h_{33}^2) - 3\nu] \\ &= \frac{1-2\nu}{E} = \frac{1}{2}S_2 + 3S_1 = p_{ph} \end{aligned}$$

where $h_{11}^2 + h_{22}^2 + h_{33}^2 = 1$ since it is a scalar product of two identical unit vectors. Then, we obtain the linear equation for the biaxial stress state with shear:

$$\boxed{p_{11}\sigma_{11} + p_{12}\sigma_{12} + p_{22}\sigma_{22} + p_{13}\sigma_{13} + p_{23}\sigma_{23} + p_{ph}\sigma_{ph} = \ln\left(\frac{\sin\theta_0}{\sin\theta}\right)} \tag{9.80}$$

where the coefficient $p_{ph} = (1-2\nu)/E = \frac{1}{2}S_2 + 3S_1$, σ_{ph} is the pseudo-hydrostatic stress component caused by the approximate d-spacing d_0'. In this case the stresses can be measured without accurate stress-free d-spacing, since any error will be counted in the pseudo-hydrostatic stress term σ_{ph}. Six or more independent measured strains would be required since σ_{ph} is also one of the unknowns to be determined by the linear system. With the measured stress tensor components, the general normal stress (σ_ϕ) and shear stress (τ_ϕ) at any arbitrary angle ϕ can be given by

$$\sigma_\phi = \sigma_{11}\cos^2\phi + \sigma_{12}\sin 2\phi + \sigma_{22}\sin^2\phi \tag{9.81}$$

$$\tau_\phi = \sigma_{13}\cos\phi + \sigma_{23}\sin\phi \tag{9.82}$$

For the biaxial stress state, $\sigma_{33} = \sigma_{13} = \sigma_{23} = 0$, we have

$$p_{11}\sigma_{11} + p_{12}\sigma_{12} + p_{22}\sigma_{22} + p_{ph}\sigma_{ph} = \ln\left(\frac{\sin\theta_0}{\sin\theta}\right) \tag{9.83}$$

Here, four or more independent measured strains are required. The biaxial stress state corresponds to the straight line of the d-$\sin^2\psi$ plot. The biaxial stress with shear is the case when there is a split between the data points in $+\psi$ side and $-\psi$ side. For the equibiaxial stress state when $\sigma_{11} = \sigma_{22} = \sigma$, there are no in-plane ($\mathbf{S_1}$–$\mathbf{S_2}$) shear components, $\sigma_{12} = 0$. Therefore, we have

$$(p_{11} + p_{22})\sigma + p_{ph}\sigma_{ph} = \ln\left(\frac{\sin\theta_0}{\sin\theta}\right) \tag{9.84}$$

In this case two or more independent measured strains are required. This stress state exists typically in the surface of metal parts after surface treatment, such as shot peening, or thin films with no texture or with fiber texture. In this stress state, there are only normal stress components having the same value in any direction within the plane.

The above equations for the stress states of biaxial stress with shear, biaxial stress, and equibiaxial stress are based on $\sigma_{33} = 0$. For some measurement conditions with significant penetration or materials of multiphase or multilayers, $\sigma_{33} = 0$ may not be a valid assumption. The stress tensor with triaxial stress state ($\sigma_{33} \neq 0$) now can be expressed as

$$\sigma_{ij}' = \begin{bmatrix} \sigma_{11} & \sigma_{12} & \sigma_{13} \\ \sigma_{12} & \sigma_{22} & \sigma_{23} \\ \sigma_{13} & \sigma_{23} & \sigma_{33} \end{bmatrix} + \begin{bmatrix} \sigma_{ph} & 0 & 0 \\ 0 & \sigma_{ph} & 0 \\ 0 & 0 & \sigma_{ph} \end{bmatrix}$$

$$= \begin{bmatrix} \sigma_{11} - \sigma_{33} & \sigma_{12} & \sigma_{13} \\ \sigma_{12} & \sigma_{22} - \sigma_{33} & \sigma_{23} \\ \sigma_{13} & \sigma_{23} & 0 \end{bmatrix} + \begin{bmatrix} \sigma_{ph} + \sigma_{33} & 0 & 0 \\ 0 & \sigma_{ph} + \sigma_{33} & 0 \\ 0 & 0 & \sigma_{ph} + \sigma_{33} \end{bmatrix}$$

$$= \begin{bmatrix} (\sigma_{11} - \sigma_{33}) + (\sigma_{ph} + \sigma_{33}) & \sigma_{12} & \sigma_{13} \\ \sigma_{12} & (\sigma_{22} - \sigma_{33}) + (\sigma_{ph} + \sigma_{33}) & \sigma_{23} \\ \sigma_{13} & \sigma_{23} & \sigma_{ph} + \sigma_{33} \end{bmatrix}$$

$$= \begin{bmatrix} \sigma'_{11} + \sigma'_{ph} & \sigma_{12} & \sigma_{13} \\ \sigma_{12} & \sigma'_{22} + \sigma'_{ph} & \sigma_{23} \\ \sigma_{13} & \sigma_{23} & \sigma'_{ph} \end{bmatrix} \tag{9.85}$$

It can be seen that

$$\sigma'_{11} = \sigma_{11} - \sigma_{33},\ \sigma'_{22} = \sigma_{22} - \sigma_{33},\ \text{and}\ \sigma'_{ph} = \sigma_{ph} + \sigma_{33} \tag{9.86}$$

Introducing this into the fundamental equation (9.73), we have

$$p_{11}(\sigma'_{11} + \sigma'_{ph}) + p_{12}\sigma_{12} + p_{22}(\sigma'_{22} + \sigma'_{ph}) + p_{13}\sigma_{13} + p_{23}\sigma_{23} + p_{33}\sigma'_{ph} = \ln\left(\frac{\sin\theta_0}{\sin\theta}\right)$$

$$p_{11}\sigma'_{11} + p_{12}\sigma_{12} + p_{22}\sigma'_{22} + p_{13}\sigma_{13} + p_{23}\sigma_{23} + (p_{11} + p_{22} + p_{33})\sigma'_{ph} = \ln\left(\frac{\sin\theta_0}{\sin\theta}\right)$$

Since $p_{11} + p_{22} + p_{33} = p_{ph}$, we have

$$p_{11}\sigma'_{11} + p_{12}\sigma_{12} + p_{22}\sigma'_{22} + p_{13}\sigma_{13} + p_{23}\sigma_{23} + p_{ph}\sigma'_{ph} = \ln\left(\frac{\sin\theta_0}{\sin\theta}\right) \tag{9.87}$$

Introducing equation (9.86) back into (9.87), we have the linear equation for the triaxial stress state with pseudo-hydrostatic stress:

$$p_{11}(\sigma_{11} - \sigma_{33}) + p_{12}\sigma_{12} + p_{22}(\sigma_{22} - \sigma_{33}) + p_{13}\sigma_{13} + p_{23}\sigma_{23} + p_{ph}(\sigma_{ph} + \sigma_{33}) = \ln\left(\frac{\sin\theta_0}{\sin\theta}\right) \tag{9.88}$$

In this case the stresses can be measured without accurate stress-free d-spacing, since any error will be counted in the pseudo-hydrostatic stress term. The unknown stresses given by $\sigma_{11} - \sigma_{33}$, $\sigma_{22} - \sigma_{33}$, and $\sigma_{ph} + \sigma_{33}$ will all be treated as single terms to be evaluated by the least square regression. The exact value of σ_{11}, σ_{22}, σ_{33} cannot be given by the evaluation. Comparing equations (9.80) and (9.88), it can be seen that both equations have the same coefficients in the linear equation. Therefore, the same algorithms or software program can be used except the value of $\sigma_{11} - \sigma_{33}$, $\sigma_{22} - \sigma_{33}$, and $\sigma_{ph} + \sigma_{33}$ are reported instead of σ_{11}, σ_{22}, and σ_{ph} when $\sigma_{33} \neq 0$.

9.3.4 True Stress-Free Lattice d-Spacing

In the 2D stress equations for the biaxial and biaxial with shear states, we have assumed that σ_{33} is zero so that we can calculate stress with an approximation of d_{o} (or $2\theta_{\text{o}}$). Any error in d_{o} (or $2\theta_{\text{o}}$) will contribute only to a pseudo-hydrostatic term σ_{ph}. The measured stresses are independent of the input d_{o} (or $2\theta_{\text{o}}$) values. This can be proved by an experiment on an Almen strip. The Almen strip is a thin sample strip of metal used to quantify the intensity of a shot peening process. The Almen strip is named after John O. Almen for his invention of the method [35], which has been further modified by many [36]. The strip is placed in the shot peening chamber

where the machine parts are shot peened. The compressive stress introduced by the peening operation can then be measured by the strip deformation. In this experiment, the residual stress is measured by X-ray diffraction using a GADDS™ system with Cr-K_α radiation ($\lambda = 2.2897$ Å), generator power 35 kV/50 mA, and 0.5 mm collimator. The stress measurement parameters are: $E = 210$ GPa, $\nu = 0.28$, $A_{RX} = 1.49$. For each stress measurement, seven frames were taken at $\psi = -45°$, $-30°$, $-15°$, 0, 15°, 30° and 45° ($\omega = 57°$ to 147° with 15° steps). The (211) rings on the frame were used for stress calculation. Figure 9.11 shows the biaxial stress tensor measured with different input d'_o in the range of 1.165 Å to 1.175 Å. The measured stress tensor is independent of the input d'_o, ($\sigma_{11} = 623$MPa, $\sigma_{12} = 638$ MPa, $\sigma_{22} = 80$ MPa). All measured stress components are horizontal lines in the plot. The lines for σ_{11} and σ_{22} are almost overlapping due to their very close results, and the shear stress σ_{12} is very small. The stress state can be considered equibiaxial. The pseudo-hydrostatic term σ_{ph} changes with the input d'_o.

The true stress-free d-spacing d_o corresponds to the cross point of σ_{ph} line and zero stress. If we use d'_0 to represent the initial input, then the true d_o (or $2\theta_o$) can be calculated from σ_{ph} with the following equations:

$$d_o = d'_o \exp\left(\frac{1-2\nu}{E}\sigma_{ph}\right) \tag{9.89}$$

$$\theta_o = \arcsin\left[\sin\theta'_o \exp\left(\frac{2\nu-1}{E}\sigma_{ph}\right)\right] \tag{9.90}$$

Care must be taken that the σ_{ph} value contains the measurement error as does the true stress-free d-spacing d_o. If the purpose of the experiment is to determine the stress-free d-spacing d_o, the instrument should first be calibrated with a stress-free standard of a similar type of material.

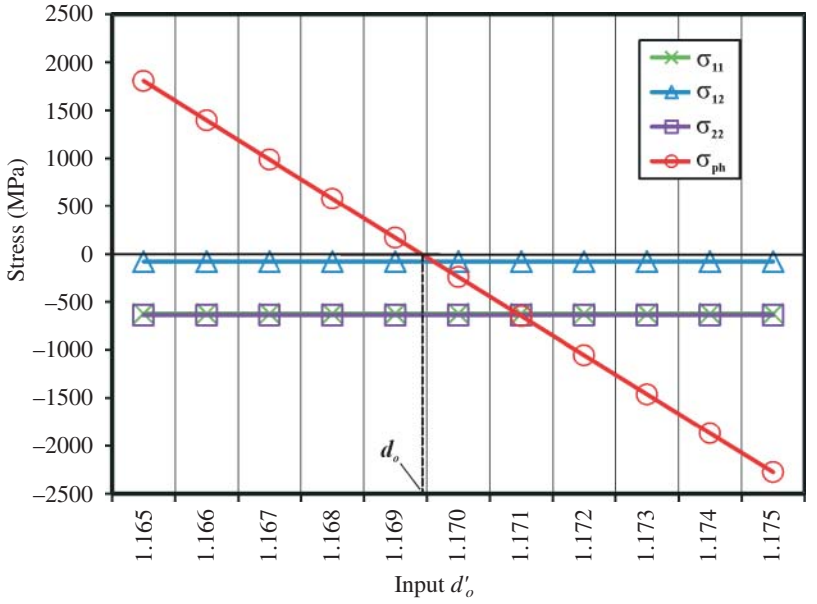


FIGURE 9.11 Measured biaxial stress tensor and pseudo-hydrostatic stress as a function of input d'_o.

9.3.5 Diffraction Cone Distortion Simulation

The 2D fundamental equation can also be used to simulate the diffraction cone distortion caused by a given stress tensor at a given sample orientation [37]. The simulated cone distortion can be displayed as a distorted ring in two dimensions. The visualization of the distorted ring can help us to understand the effects of the stress state, materials elasticity (anisotropy), and sample orientation. The visualization can also help in planning the stress measurement strategy by measuring the data at the most sensitive orientation range. Starting from the fundamental equation

$$p_{11}\sigma_{11} + p_{12}\sigma_{12} + p_{22}\sigma_{22} + p_{13}\sigma_{13} + p_{23}\sigma_{23} + p_{33}\sigma_{33} = \ln\left(\frac{\sin\theta_0}{\sin\theta}\right)$$

we obtain

$$\theta = \arcsin(e^{-D}\sin\theta_0) \tag{9.91}$$

where

$$D = p_{11}\sigma_{11} + p_{12}\sigma_{12} + p_{22}\sigma_{22} + p_{13}\sigma_{13} + p_{23}\sigma_{23} + p_{33}\sigma_{33}$$

The difficulty is that the 2θ angles on the diffraction ring are unknown values to be calculated, but 2θ values are also needed to determine the unit vector components $\{h_1, h_2, h_3\}$ so as to determine the stress coefficients (p_{ij}). The difference between θ and θ_o determines the measured strain, but it has negligible effect in determining the unit vector direction, so θ can be replaced by θ_o in the equation for D with negligible error for simulation purposes.

$$\theta = \arcsin(e^{-D_0}\sin\theta_0) \tag{9.92}$$

where

$$D_0 = p^0_{11}\sigma_{11} + p^0_{21}\sigma_{12} + p^0_{22}\sigma_{22} + p^0_{13}\sigma_{13} + p^0_{23}\sigma_{23} + p^0_{33}\sigma_{33}$$

and p^0_{ij} can be calculated from the equation given in Table 9.3 by taking $k = 0$. The equations are convenient for computer programming. The parameters (a, b, c) are calculated first, then the parameters (A, B, C), and then the stress coefficients p^k_{ij}. The unit vector components $\{h^k_1, h^k_2, h^k_3\}$ are replaced by (A, B, C) for convenience. The elasticity anisotropy can be introduced by replacing the macroscopic elasticity constants $\frac{1}{2}s_2$ and S_1 by the XEC $S_1^{\{hkl\}}$ and $\frac{1}{2}S_2^{\{hkl\}}$.

The above equations are generally sufficient for simulation purposes. In cases where accurate diffraction rings are required, the simulated diffraction ring can be generated through the

Table 9.3 The Equations of Stress Coefficients

$p^k_{11} = \frac{1}{2}S_2A^2 + S_1$	$p^k_{12} = \frac{1}{2}S_2 \cdot 2AB$
$p^k_{22} = \frac{1}{2}S_2B^2 + S_1$	$p^k_{13} = \frac{1}{2}S_2 \cdot 2AC$
$p^k_{33} = \frac{1}{2}S_2C^2 + S_1$	$p^k_{23} = \frac{1}{2}S_2 \cdot 2BC$
$a = \sin\theta_i\cos\omega + \sin\chi\cos\theta_i\sin\omega$	$A = a\cos\phi - b\cos\psi\sin\phi + c\sin\psi\sin\phi$
$b = -\cos\chi\cos\theta_i$	$B = a\sin\phi + b\cos\psi\cos\phi - c\sin\psi\cos\phi$
$c = \sin\theta_i\sin\omega - \sin\chi\cos\theta_i\cos\omega$	$C = b\sin\psi + c\cos\psi$
where $\frac{1}{2}S_2 = (1+\nu)/E$ and $S_1 = -\nu/E$	

following iterative equations:

$$\theta_{k+1} = \arcsin(e^{-D_k} \sin\theta_k) \qquad k = 0, 1, 2, \cdots\cdots \tag{9.93}$$

where

$$D_k = p_{11}^k \sigma_{11} + p_{21}^k \sigma_{12} + p_{22}^k \sigma_{22} + p_{13}^k \sigma_{13} + p_{23}^k \sigma_{23} + p_{33}^k \sigma_{33}$$

It must be noted that when calculating D_0, θ_0 is a constant for all of the diffraction ring, while $\theta_1, \theta_2, \theta_3, \cdots$ are functions of γ. The $\sin\theta_0$ term in the equation should always be the same. The iteration starts with $k = 0$ until a stop condition is satisfied:

$$\theta_{k+1} - \theta_k < \delta\theta \text{ at all } \gamma \text{ angles}$$

where $\delta\theta$ is the required accuracy. Typically, one or two iterations can achieve an accuracy better than 0.01°. The accurate simulation of the diffraction ring is typically used for displaying the measured data points against the simulated ring from the measured stress tensor. It is a useful way to observe the scatter of the measured data points to evaluate the quality of the measurement. If the approximate d-spacing d_0' has been used, the effect of the pseudo-hydrostatic term σ_{ph} should be included in the equation as

$$D_k = p_{11}^k \sigma_{11} + p_{21}^k \sigma_{12} + p_{22}^k \sigma_{22} + p_{13}^k \sigma_{13} + p_{23}^k \sigma_{23} + p_{ph} \sigma_{ph} \tag{9.94}$$

where the coefficient $p_{ph} = \frac{1-2\nu}{E} = \frac{1}{2}S_2 + 3S_1$, and the term $p_{ph}\sigma_{ph}$ is a constant. By definition, $\sigma_{33} = 0$, so the term $p_{33}^k \sigma_{33}$ is omitted.

The simulated diffraction ring can be displayed as a radar chart or a 2θ-γ plot. Figure 9.12 shows simulated diffraction rings for iron's (211) peak with Cr-K_α radiation and $E = 210$ GPa, $\nu = 0.28$, $d_0 = 1.1702$ Å, and $\lambda = 2.2897$ Å. The sample orientation is set at $\omega = 90°$ and $\psi = 0$ so that the incident beam is perpendicular to the sample surface. The stress tensor is $\sigma_{11} = -1000$ MPa and $\sigma_{22} = 1000$ MPa. The top of Figure 9.12 is a radar chart with a 2θ scale in the radial direction and γ in the azimuthal direction. The perfect circular ring corresponds to $2\theta_0 = 156°$, which can also be considered diffraction rings from a stress-free sample. There are two distorted rings. The one with the solid line is the diffraction ring, based on the isotropic assumption, that is calculated from the macroscopic elasticity constants. The one with the broken line stands for the diffraction ring, based on the anisotropic assumption, that is calculated with the XEC. In this model, the XEC are generated from the macroscopic elasticity constant, lattice plane index $\{hkl\}$ and the anisotropic factor $A_{RX} = 1.49$. The 2θ scale is enlarged to 155.80–156.25° from the center to the outer circle so that the 2θ shift from the stress-free ring can be easily observed.

At a sample rotation angle $\phi = 0°$, the 2θ values increase in the horizontal direction due to the compressive stress component $\sigma_{11} = -1000$ MPa and decreases in the vertical direction due to the tensile stress component $\sigma_{22} = 1000$ MPa. The ω and ψ rotation will change the shape of the distorted ring, and ϕ rotation will rotate the ring about its center but not change the shape, since the rotation axis is perpendicular to the plane of biaxial stress. The diffraction ring from the above stress condition at $\phi = 45°$ is identical to the diffraction ring from shear stress $\sigma_{12} = 1000$ MPa (other components are zero) at $\phi = 0°$. It is reasonable that, mechanically, the two stress conditions are equivalent with a $\phi = 45°$ offset. It should be noted that the actual diffraction ring shift is reversed on a 2D detector since the diffraction cone apex angles are twice the values of $180° - 2\theta$ for backward reflection ($2\theta > 90°$). In other words, if a flat detector is positioned at the backward diffraction position with a swing angle $\alpha = 180°$, the X-ray beam reaches the sample through

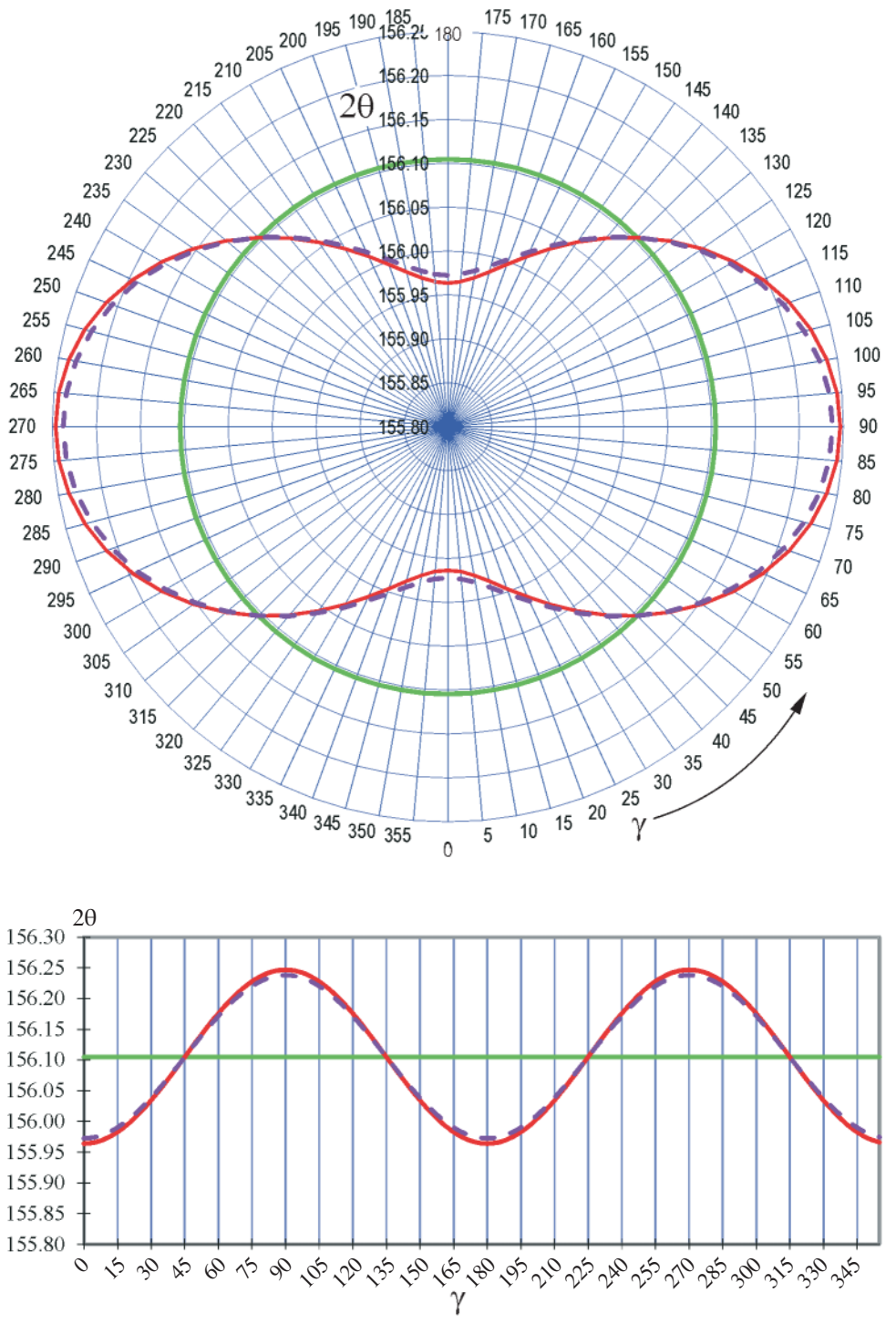


FIGURE 9.12 Simulated diffraction ring distortion due to stresses in radar chart (top) and 2θ vs. γ plot (bottom).

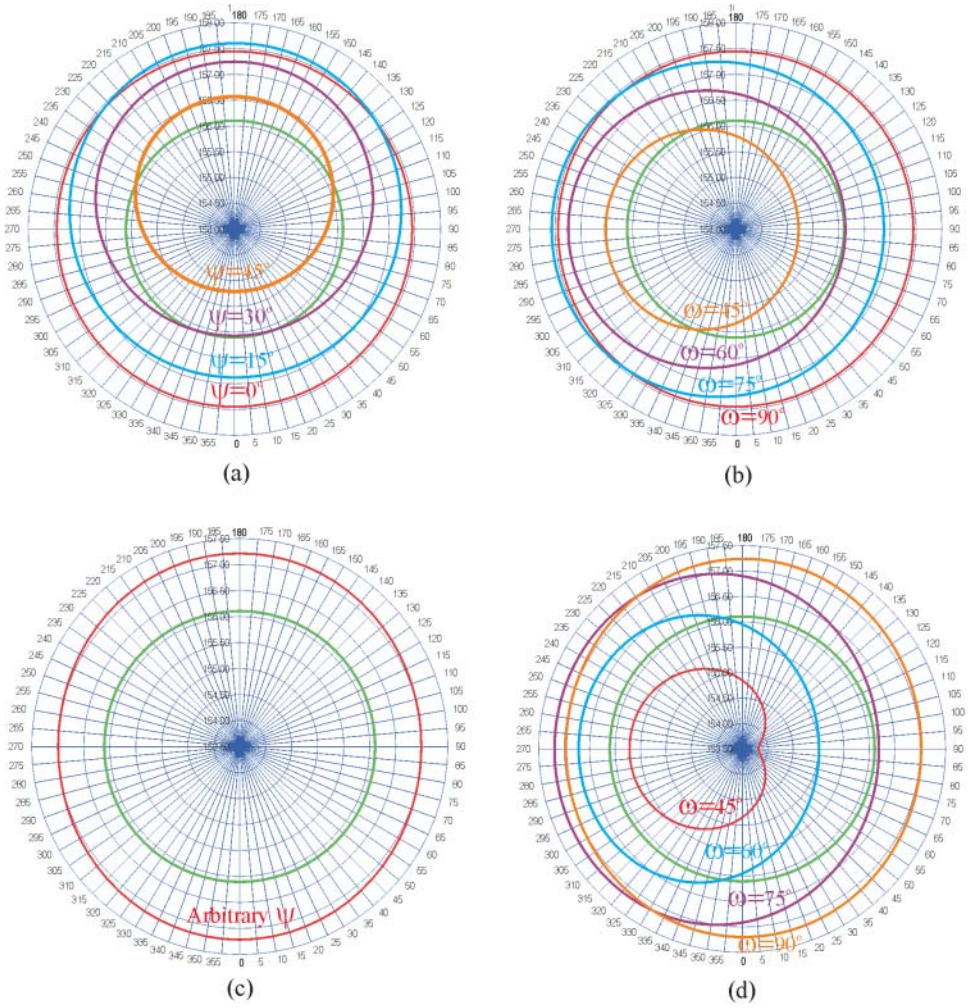


FIGURE 9.13 Simulated diffraction ring distortion in radar chart: (a) equibiaxial with ψ scans, (b) equibiaxial with ω scan, (c) uniaxial with ψ scans, (d) uniaxial with ω scan.

the detector. The center of the detector represents $2\theta = 180°$ and the pixel away from the center represents a 2θ angle smaller than 180°. The farther away the pixel is from the detector center, the smaller the 2θ angle. The bottom of Figure 9.12 is the 2θ shift vs. azimuthal angle γ. It shows that most 2θ shift values are observed in the vicinity of $\gamma = 0°$, 90, 180°, and 270°.

Figure 9.13 shows simulations of two stress conditions with ω and ψ scans for the iron (211) peak with E = 210 GPa, $\nu = 0.28$, $d_0 = 1.1702$ Å, and $\lambda = 2.2897$ Å. The anisotropic factor A_{RX} is set to 1 so the simulation shows only the isotropic model. As was shown in Figure 9.12, the difference between the isotropic model and the anisotropic model is small and can be ignored for this simulation. The green circle is the ring for the stress-free sample (θ_0). The other rings are the distorted diffraction rings labeled with the corresponding scanning angles. The four radar charts correspond to the simulation conditions listed in Table 9.4.

For equibiaxial stress condition $\sigma_{11} = \sigma_{22} = 1000$ MPa in the radar chart (a), the distorted diffraction rings for $\psi = 0°$, 15°, 30°, 45° are displayed. Due to the high 2θ angle ($\approx 156°$), the angle between the diffraction vector and the line of the incident X-ray beam is 12°. For $\psi = 0°$,

Table 9.4 The Simulation Conditions in Figure 9.13

Radar chart	Stress state	Goniometer angles	Scanning angles
(a)	$\sigma_{11} = \sigma_{22} = 1000$ MPa	$\omega = 90°, \phi = 0°$	$\psi = 0°, 15°, 30°, 45°$
(b)	$\sigma_{11} = \sigma_{22} = 1000$ MPa	$\psi = 0°, \phi = 0°$	$\omega = 90°, 75°, 60°, 45°$
(c)	$\sigma_{11} = 1500$ MPa	$\omega = 90°, \phi = 0°$	$\psi =$ arbitrary
(d)	$\sigma_{11} = 1500$ MPa	$\psi = 0°, \phi = 0°$	$\omega = 90°, 75°, 60°, 45°$

the sample is perpendicular to the X-ray beam and the measured strains along the diffraction rings are compressive strains with the same value due to Poisson contraction, so the distorted ring for $\psi = 0°$ is a circle with 2θ larger than $2\theta_0$. For $\psi = 15°$, the measured strains along the diffraction rings are still compressive, but not symmetric to the X-ray beam direction, and the top part of the diffraction ring has larger 2θ shift than the bottom part of the rings. For $\psi = 30°$, the measured strains along the diffraction rings are mostly compressive, but near zero at the bottom part of the ring where the distorted ring almost overlaps the stress-free ring. For $\psi = 45°$, the measured strains on the bottom part of the diffraction rings turned to tensile ($2\theta < 2\theta_0$) and the top part are still compressive($2\theta > 2\theta_0$), but with smaller 2θ shift. The radar chart (b) is for the same stress condition $\sigma_{11} = \sigma_{22} = 1000$ MPa, but with an ω scan. The chart shows almost identical diffraction ring distortions when the sample ω is rotated away from the initial orientation with X-ray beam perpendicular to the sample, except that the radar chart is rotated 90° from chart (a) for the ψ scan. For equibiaxial stress, the ψ scan and the ω scan have the same sensitivity to the diffraction cone distortion.

For the uniaxial stress condition, $\sigma_{11} = 1500$ MPa, in the radar chart (c), the distorted diffraction rings for all ψ angles are the same. With any arbitrary ψ angle, the uniaxial stress direction is perpendicular to the X-ray beam. The measured strains along the diffraction rings are all compressive, but more in the direction perpendicular to the uniaxial stress. The radar chart (d) is for the same uniaxial stress condition $\sigma_{11} = 1500$ MPa, but with ω scan. The diffraction ring distortions change dramatically with ω rotation. For $\omega = 90°$, the diffraction ring is the same as in the chart (c). For $\omega = 75°$, the measured strains along the diffraction rings are all compressive ($2\theta > 2\theta_0$), but near zero in the region around $\gamma = 90°$. For $\omega = 60°$, the measured strains on the left part of the diffraction rings turn to tensile ($2\theta < 2\theta_0$) and the right part is still compressive ($2\theta > 2\theta_0$). For $\omega = 45°$, all the measured strains along the diffraction rings become tensile ($2\theta < 2\theta_0$). We would expect the effects of ω scan and ψ scan on the diffraction ring distortion to exchange if the uniaxial stress were $\sigma_{22} = 1500$ MPa.

9.3.6 Goniometer ϕ Rotation Direction

The ϕ rotation in the XRD^2 diffractometer is defined as a left-handed rotation so that the diffraction vectors will make a right-hand rotation observed in the sample coordinates $\mathbf{S_1S_2S_3}$. All the algorithms for XRD^2 data interpretation and evaluation are based on the geometry convention defined in Chapter 2. For some applications, such as phase identification, the direction of ϕ rotation may not cause a problem, but for applications with dependence to the sample orientation, the correct goniometer convention, especially the ϕ rotation direction, must be maintained to produce the correct results. In addition to the explanation by the mix of even and odd functions in the unit diffraction vector equations, we can also prove it with the following experimental example. Figure 9.14 shows the residual stress measurement for an Al_2O_3 coating with correct ϕ rotation direction (a) and wrong ϕ rotation direction (b). The data set for the wrong ϕ rotation is created

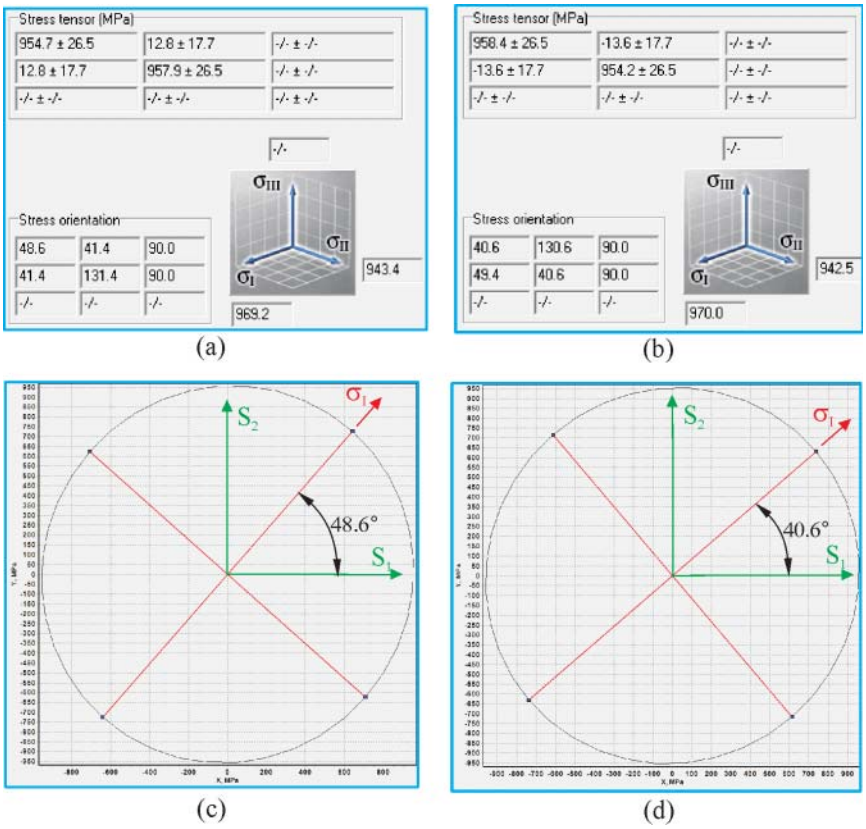


FIGURE 9.14 Effect of wrong ϕ rotation direction on stress results and principal tress orientation.

from the correct data set by reversing the ϕ values so that only the effects of ϕ rotation can be observed without introducing any instrument error or statistical error. The correct stress results are $\sigma_{11} = 954.7$ MPa, $\sigma_{22} = 957.9$ MPa and the results with wrong ϕ rotation are $\sigma_{11} = 958.4$ MPa, $\sigma_{22} = 954.2$ MPa. There are discrepancies, but not significant due to the stress state being almost equibiaxial. Much significant error can be observed for other stress states. By comparing the principal stress direction in Figure 9.14(c) and (d), we can see a discrepancy of 8° in the angle between σ_I and σ_{11} ($\mathbf{S_1}$). Both the measured stress value and the principal stress direction can be erroneous if the ϕ rotation is in the wrong direction, especially for the stress states with large difference between σ_{11} and σ_{22}.

9.4 PROCESS OF STRESS MEASUREMENT WITH XRD^2

The practice of stress analysis with two-dimensional X-ray diffraction (XRD^2) involves the selection of the diffraction system configuration, data collection strategy, data frame correction and integration, and stress calculation from the processed data points. Most concepts and strategies developed for stress analysis with the conventional diffractometer are still applicable for XRD^2, and will be briefly introduced with references. We will focus on the new concepts and practices due to the nature of the 2D detectors.

9.4.1 Instrument Requirements and Configurations

Most two-dimensional X-ray diffractometers can be used for stress measurement for certain samples. The overall functionality depends on the X-ray source, optics, goniometer, sample stage, and detectors.

X-ray sources are typically sealed tubes with spot focus, or point beams collimated with line focus. For stress analysis on thin films or a micro-area, rotating anode generators may be necessary to get enough diffraction intensity. Since most area detectors have limited energy resolution, the tube target must be properly chosen to avoid fluorescence from the sample. For example, Cu-K_α should not be used for samples containing a significant amount of iron or cobalt, Co-K_α should avoid Mn, Cr and V, and Cr-K_α should avoid Ti, Sc, and Ca. The size and divergence of the X-ray beam are another consideration. A large beam size or divergence may improve the sampling statistics, but a large beam size will reduce the spatial resolution on the sample, and a large divergence may reduce the angular resolution. The beam size and divergence should be chosen based on the sampling size and the grain size. One criterion is to get an accurate 2θ position from the diffraction profile. For samples with a large grain size, a large beam size and divergence can improve the sampling statistics. It will be discussed later that virtual oscillation by γ-integration can also help to improve the sampling statistics.

Any type of area detector as described in Chapter 4 can be used for stress measurement. At present, three kinds of 2D detector techniques are mostly used for stress measurements with XRD^2 systems: image plates (IP), multiwire proportional counters (MWPC), and charge coupled devices (CCD). Stress measurements using IPs have been reported in the literature [21, 23, 32]. The advantages of using multiwire area detector for stress measurements have also been discussed by the author [24–26, 28–30]. The most important characteristics of area detectors for stress measurement are sensitivity, linearity, count rate, and spatial resolution. Stress measurements are mostly performed on polycrystalline metal parts, and typically on high angle peaks, so diffraction intensities are not very high. Photon counting detectors, such as MWPC and microgap detectors, have high sensitivity with essentially no noise, which is very suitable for a stress measurement system using a laboratory source, such as sealed X-ray tubes or rotating anode generators. For stress measurements of ferrous metals, Cr or Co radiation is normally used to avoid fluorescence, and in this case, multiwire area detectors are, so far, the best choice. If an Mo X-ray source or synchrotron beam is used, a CCD detector is the better choice for its ability to handle high energy X-rays and high count rates. The spatial resolution requirement depends on the FWHM of the diffraction profile. In practice, a FWHM of 3–6 times the spatial resolution should be sufficient to precisely determine the peak position, provided that there are enough counts on the profile. Further reduction in the spatial resolution does not necessarily improve the peak position accuracy. The diffraction peak width for stress measurement is typically broad, so spatial resolution of most area detectors is sufficient for stress analysis.

The selection of the goniometer and sample stage is based on sample size, weight, and the stress or stress tensor components to be determined. For instance, one normal stress component on a large sample is better handled by a large XYZ stage on a goniometer with only two main axes. The ω scan can be achieved by the two main axes in either the θ-2θ or θ-θ configuration. In a vertical θ-θ configuration, the ω scan is achieved by moving the primary beam and detector, but keeping the sample still. This is especially beneficial for large samples. The vertical θ-θ configuration requires both the X-ray source and the detector to move for the ω scan. The horizontal θ-2θ configuration has the advantage of not having to move the X-ray source, which is convenient for a rotating anode generator. It is also easier to move a heavy 2D detector in the horizontal rotation. In 2D stress measurement, the data collection scan can imitate iso-inclination and side-inclination in the conventional method. The two main axes can only provide the iso-inclination scan (ω scan).

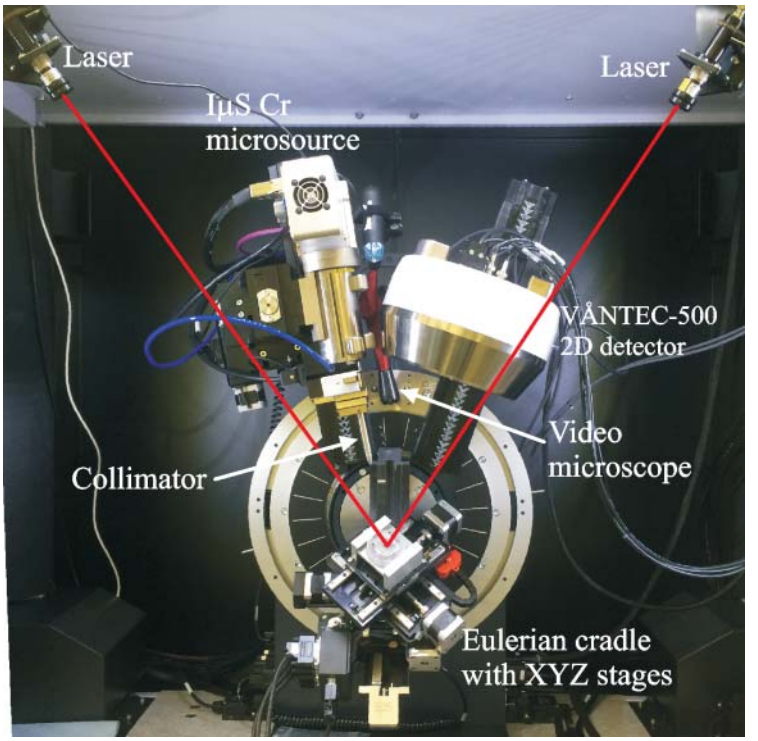


FIGURE 9.15 Two-dimensional XRD system for stress analysis in vertical θ-θ configuration (Bruker D8 Discover™).

The ψ axis is necessary to achieve the side-inclination scan (ψ scan). Just as in the conventional method, the ψ scan has less variation in the incident angle, so the depth of penetration is relatively consistent compared to the ω scan. For complete measurement of stress tensor components, the ϕ axis is necessary in addition to the ω and ψ axes. An XYZ stage is necessary to locate the measurement point on the sample and to collect data for stress mapping. The sample alignment device, such as a laser-video system, is desired for accurate alignment of the measurement spot to the instrument center.

Figure 9.15 shows a two-dimensional X-ray diffraction system in the vertical θ-θ configuration for stress measurement (Bruker D8-Discover™). The IμS™ Cr microsource and collimator are mounted on the primary track (θ_1). The Våntec-500™ 2D detector is mounted on the secondary track (θ_2). A Eulerian cradle with an XYZ stage is used to rotate the sample in ψ and ϕ, and to align and move the sample in the XYZ directions. A sample alignment system, including double lasers and a video microscope, is used to align the sample into the instrument center.

9.4.2 Data Collection Strategy

X-ray diffraction can measure stress by measuring the d-spacing change caused by the stress. The diffraction vector is in the normal direction of the measured crystalline planes. It is not always possible to have the diffraction vector in the desired measurement direction. In reflection mode X-ray diffraction, it is easy to have the diffraction vector normal to the sample surface, or tilted away from the normal, but impossible to have the vector on the surface plane. The stress on the surface plane, or biaxial stress, is calculated by elasticity theory from the measured strain in

other directions. The final stress measurement results can be considered an extrapolation from the measured values. In the conventional $\sin^2\psi$ method, several ψ-tilt angles are required, typically from −45° to +45°. The same is true with an XRD^2 system. The diffraction vectors corresponding to the data scan can be projected as a 2D plot in the same way as with the pole density distribution in a pole-figure. The 2D plot is called a data collection strategy scheme, or simply scheme.

Figure 9.16 shows a comparison between the conventional method and the 2D method in terms of the diffraction vector ($\mathbf{H}_{hkl}$) and sample coordinates $\mathbf{S_1S_2S_3}$ during the data collection scan. For conventional X-ray diffraction (XRD), seven normal strains are measured at the diffraction vector ($\mathbf{H}_{hkl}$) directions corresponding to seven tilt angles at −45°, −30°, −15°, 0°, 15°, 30°, 45°, achieved by ω rotation. The seven directions are mapped onto the scheme as seven solid dots. The direction of the measured stress components are plotted into the scheme as circles. Since the seven solid dots are aligned along the horizontal direction ($\mathbf{S}_1$), the stress component σ_{11} can be determined by the extrapolation of the seven measured data points ($\sin^2\psi$ method). The two filled circles represent the direction of σ_{11}. It would be impossible to calculate the stress component σ_{22} from the seven data points by extrapolation in the vertical direction ($\mathbf{S_2}$). The two empty circles represent the direction of σ_{22}. The $\sin^2\psi$ method also requires that the data points are distributed along the radial direction for each $\sin^2\psi$ plot. For XRD^2, it is assumed that the seven diffraction frames are taken at the same seven tilt angles. The measured strains along the diffraction ring at each tilt angle can be plotted into the scheme as a piece of curve corresponding to the γ range. Since the seven curves are distributed along the horizontal direction, the stress component σ_{11} can be determined by the extrapolation of the measured data points along the seven curves. In principle, it is also possible to calculate the stress component σ_{22}, since the measured strains also have some coverage in vertical direction ($\mathbf{S_2}$). But in practice, unless the γ range covers a large vertical range on the scheme, the data set is not suitable for a reliable σ_{22} result.

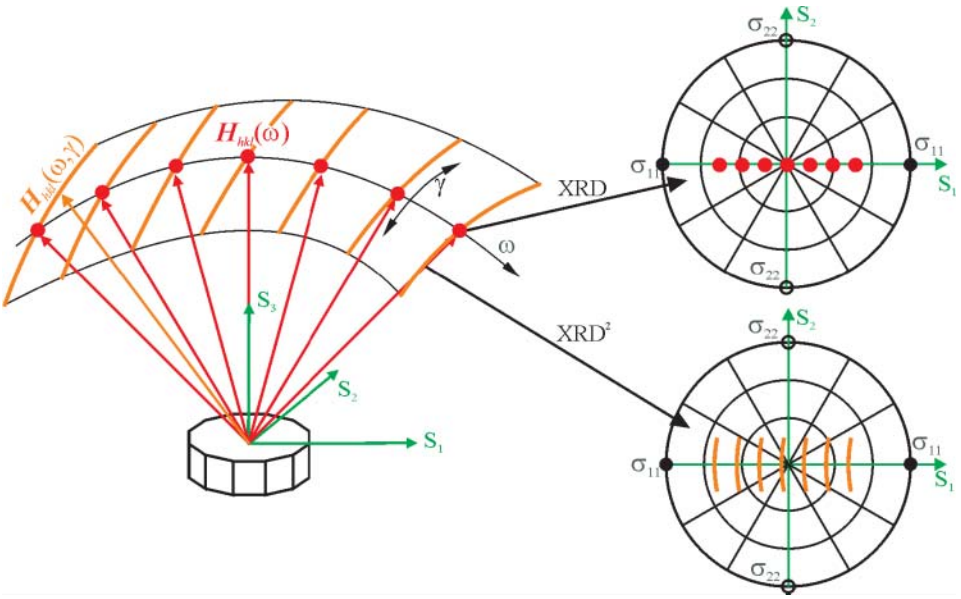


FIGURE 9.16 Diffraction vector distribution in stress measurement with conventional method and 2D method.

The scheme is generated by plotting the diffraction vector (pole) onto a 2D plot like a pole-figure. Each vector direction is defined by the radial angle α and azimuthal angle β. The α and β angles are functions of γ, ω, ψ, φ, and 2θ. The pole, defined as a unit vector, has three components, h_1, h_2, and h_3, parallel to the three sample orientations $\mathbf{S_1S_2S_3}$ respectively. The pole-figure angles (α,β) can be calculated from the unit vector components by the following pole mapping equations:

$$\alpha = \sin^{-1}|h_3| = \cos^{-1}\sqrt{h_1^2 + h_2^2},$$
$$\text{and } \beta = \pm\cos^{-1}\frac{h_1}{\sqrt{h_1^2 + h_2^2}} \qquad \begin{cases} \beta \geq 0^\circ & \text{if} \quad h_2 \geq 0 \\ \beta < 0^\circ & \text{if} \quad h_2 < 0 \end{cases} \tag{9.95}$$

where α takes a value between 0° to 90° ($0^\circ \leq \alpha \leq 90^\circ$) and β takes values in two ranges ($0^\circ \leq \beta \leq 180^\circ$ when $h_2 > 0$ and $-180^\circ \leq \beta < 0^\circ$ when $h_2 < 0$). By evaluating the measured strain distribution in the scheme, we can generate a data collection strategy suitable for the measurement of the intended stress components.

Figure 9.17 illustrates six schemes for data collection based on the iron (211) peak with Cr-K_α radiation and the stress-free $2\theta_0 = 156^\circ$. The two-dimensional X-ray diffraction system (Bruker D8-Discover™) for stress measurement is in the horizontal θ-2θ configuration with a Hi-Star™ MWPC detector. The schemes are generated by GADDS software. The detector position is set at a swing angle of $\alpha = -143^\circ$ and a sample-to-detector distance of $D = 15$cm. The diffraction vector corresponding to the center of the diffraction ring falls to the center of the scheme at $\omega = 102^\circ$ and $\psi = 0^\circ$. The goniometer angles and measurable stress components for the six schemes are listed in Table 9.5.

The scheme (a) is for an ω scan only from 57° to 147° with 15° steps. The rings corresponding to the measured strains are distributed along the horizontal direction. The rings cross the horizontal line at the points corresponding to −45° to +45° tilt angles from the sample normal (center of the scheme). It is obvious that this set of data would be suitable for calculating the stress components σ_{11} and σ_{13}. The ψ and ϕ axes are not required for this data collection strategy. This strategy is analogous to iso-inclination in the conventional method, which can be achieved by the two main axes of the goniometer.

In scheme (b), the Eulerian cradle is limited to a rotation range from −7° to 101° in ψ, so the ψ scan covers 0° to 45° with 15° steps. The ψ scan from 0° to 45° at $\phi = 180^\circ$ is equivalent to the ψ scan from 0° to −45°. The measured rings are distributed along the vertical direction with each ring tangential to the vertical line. This set of data is suitable for calculating the stress components σ_{22} and σ_{23}. This data collection strategy requires the ψ (or χ) axis in the goniometer, but not the ϕ axis. This strategy is analogous to side-inclination in the conventional method, which has a relatively consistent incident angle and X-ray penetration depth.

Scheme (c) is an enhancement to scheme (a). The same ω scan at $\phi = 90^\circ$ is good for σ_{22} and σ_{23}, so a data set with both $\phi = 0^\circ$ and $\phi = 90^\circ$ can be used to calculate the biaxial stress tensor. Since the diffraction ring distortion collected at $\phi = 0^\circ$ or $\phi = 90^\circ$ is not sensitive to the stress component σ_{12}, strategy (c) is suitable for the equibiaxial stress state. Scheme (d) is an enhancement to the scheme (b). The same ψ scan at eight ϕ angles with 45° intervals produces comprehensive coverage on the scheme chart in a symmetric distribution. The data set collected with this strategy can be used to calculate the complete biaxial stress tensor components and with shear stress (σ_{11}, σ_{12}, σ_{22}, σ_{13}, σ_{23}).

In scheme (e), an ω scan at $\phi = 45^\circ$ is added to scheme (c) so that the data set is suitable for calculating the complete biaxial stress tensor components with shear stress (σ_{11}, σ_{12}, σ_{22}, σ_{13}, σ_{23}).

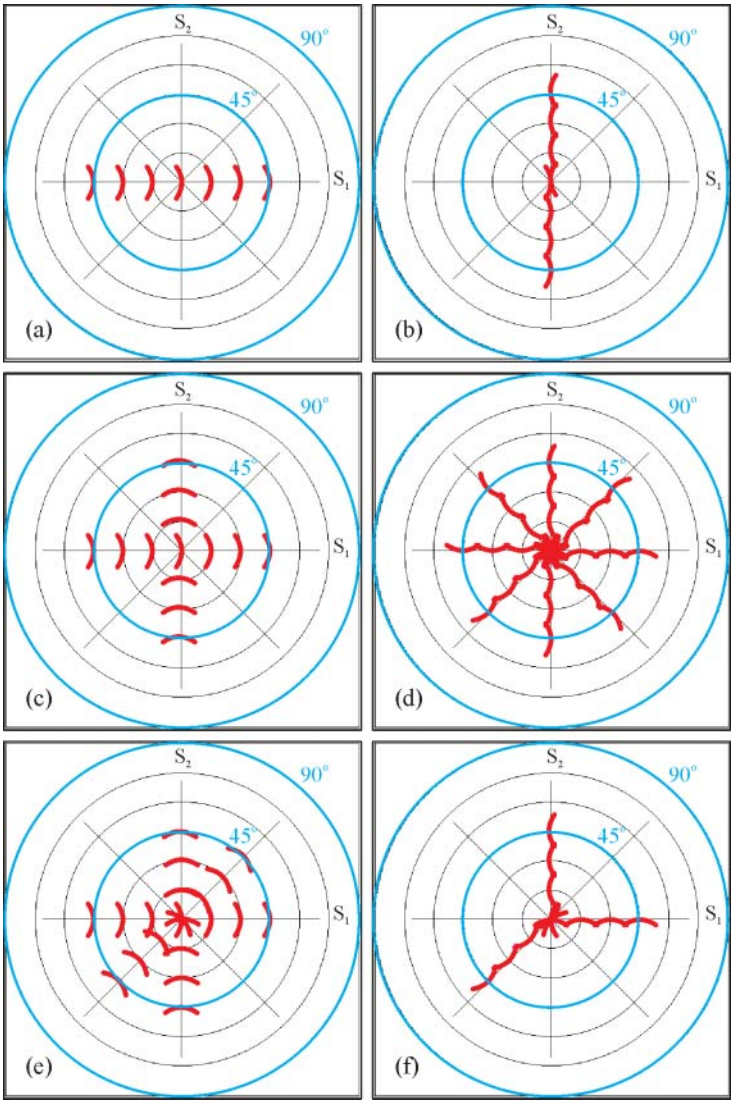


FIGURE 9.17 Data collection strategy schemes: (a) ω scan, (b) $\psi+\phi(180°)$ scan, (c) $\omega+\phi(90°)$ scan, (d) $\psi+\phi(45°)$scan, (e) $\omega+\phi(45°)$ scan, (d) $\psi+\phi(90°+135°)$ scan.

Table 9.5 Goniometer Angles and Measurable Stress Components for the Six Schemes. The Scanning Angles are Listed as Scan Range and Step in Parentheses

	Goniometer angles: scan range (step)			
Scheme	ω (°), $\alpha=-143$	ψ (°)	ϕ (°)	Measurable stress components
(a)	57–147 (15)	0	0	σ_{11}, σ_{13}
(b)	102	0–45 (15)	0–180 (180)	σ_{22}, σ_{23}
(c)	57–147 (15)	0	0–90 (90)	σ_{11}, σ_{22}, σ_{13}, σ_{23}
(d)	102	0–45 (15)	0–315 (45)	σ_{11}, σ_{12}, σ_{22}, σ_{13}, σ_{23}
(e)	57–147 (15)	0	0–90 (45)	σ_{11}, σ_{12}, σ_{22}, σ_{13}, σ_{23}
(f)	102	0–45 (15)	90, 180, 315	σ_{11}, σ_{12}, σ_{22}, σ_{13}, σ_{23}

Scheme (f) is a time-saving strategy with ψ scans at only three ϕ angles at $\phi = 90°$, 180°, and 315°. The rings on two ϕ angles are aligned to $\mathbf{S_1}$ and $\mathbf{S_2}$ and the rings on the third ϕ angle make 135° angles to the two arrays of rings. This is analogous to the configuration of a strain gage rosette. This data set is good for the complete biaxial stress tensor components with shear stress (σ_{11}, σ_{12}, σ_{22}, σ_{13}, σ_{23}). The three ϕ angles at $\phi = 90°$, 180°, and 315° are for easy visual description of the strategy, but the actual data collection can be done at $\phi = 0°$, 90°, and 225° with exactly the same effect. The three ϕ angles can also be separated equally by 120° steps. The six schemes discussed here are just some examples. An equivalent data collection strategy for vertical θ-θ system can be generated by using $\theta_1 = 78°$. Suitable schemes for a particular experiment should be determined by considering the stress components of interest, the diffractometer configuration, sample size, detector size and resolution, measurement accuracy, and data collection time.

9.4.3 Data Integration and Peak Evaluation

Stress measurement with two-dimensional X-ray diffraction is based on the fundamental equation between the stress tensor components and the diffraction cone distortion. For a stressed sample, 2θ becomes a function of γ and the sample orientation (ω,ψ,ϕ), i.e. $2\theta = 2\theta(\gamma, \omega, \psi, \phi)$, and this function is uniquely determined by the stress tensor. The purpose of data integration and peak evaluation is to generate a set of data points along distorted diffraction rings at various sample orientations so that stress components can be calculated by solving linear equations or by a least squares regression. Data integration for stress analysis is γ-integration over several defined subregions so as to generate diffraction profiles representing the corresponding subregions. The peak position can be determined by evaluating the data points by a procedure or by fitting the data points to a profile modeled by a given analytic function. Figure 9.18 illustrates data integration over a diffraction frame collected from a steel sample. The diffraction ring is from the lattice plane family {211}. With Co-K_α radiation, the stress-free $2\theta_0$ is in the vicinity of 99.8°. The total integration region is given by $2\theta_1 = 97°$, $2\theta_2 = 102.5°$, $\gamma_1 = -65°$, and $\gamma_2 = -115°$. The integration region is divided into ten subregions, with $\Delta\gamma = 5°$. One data point on the distorted diffraction ring is generated from each subregion. The γ value in the center (denoted by the dotted line) of each subregion is taken as the γ value of the data point. The γ-integration of the subregion produces a diffraction profile and the 2θ value is determined from the profile.

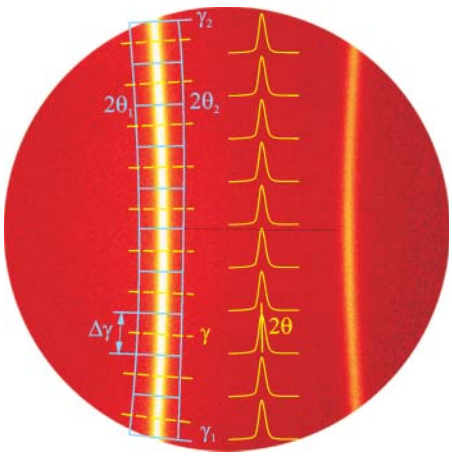


FIGURE 9.18 Data integration for stress measurement.

The number of subregions and the subregion size ($\Delta\gamma$) is selected based on the condition of the data frame. The larger the subregion size ($\Delta\gamma$), the better the integrated diffraction profile, due to more counts being integrated. The γ-integration also produces a smearing effect on the diffraction ring distortion because the counts collected within the subregion size ($\Delta\gamma$) are considered as a single γ value at the subregion center. The 2θ shift in the subregion is averaged. The subregion size ($\Delta\gamma$) should be sufficient to produce a smooth diffraction profile, but not so large as to introduce a significant smearing effect. For data frames containing high pixel counts, the integration subregion can be sufficiently small, $\Delta\gamma \leq 2^\circ$ for instance, and still have a smooth profile for each subregion. For data frames having low pixel counts, due to a micro-area, a small sample, or short data collection time, it is critical to choose an appropriate subregion size. The subregion size can be determined by observing the smoothness of the integrated profile or by comparing the stress results and standard error at various subregion sizes.

Peak evaluation on each subregion can be done by the same algorithm as used in the conventional method. The corrections on the integrated profiles are performed before or during the peak evaluation. Absorption correction eliminates the influence of the irradiated area and the diffraction geometry on the measured intensity distribution. The absorption for a given material and radiation level depends on the incident angle to the sample and the reflected angle from the sample. For XRD^2, the reflected angle is a function of γ on each frame. The polarization effect is also a function of γ. Therefore, the correction for polarization and absorption should be applied to the frame before integration. The details of these corrections were discussed in Chapter 6 on data reduction. The absorption correction is not always necessary if the error caused by absorption can be tolerated for the application, or if the data collection strategy involves only ψ and ϕ scans.

In most cases, the combined $K_{\alpha1}$ and $K_{\alpha2}$ radiation is used for stress measurement, in which case the weighted average wavelength is used in calculations. For samples with a broad peak width, the diffractions from the $K_{\alpha1}$ and the $K_{\alpha2}$ radiation are merged together as a single peak profile, and the profile can be evaluated as if there were a single K_α line without introducing much error to the measured d-spacing. For samples with a relatively narrow peak width, the diffraction profile shows strong asymmetry or may even reveal two peaks corresponding to the $K_{\alpha1}$ and $K_{\alpha2}$ lines, especially at high 2θ angles. This phenomenon has been referred to as a $K_{\alpha1}$-$K_{\alpha2}$ doublet or K_α doublet [38]. In this case the profile fitting should include contributions from both $K_{\alpha1}$ and $K_{\alpha2}$ lines. It is common practice to use the peak position from the $K_{\alpha1}$ line and the $K_{\alpha1}$ wavelength to calculate the d-spacing after the contribution of the $K_{\alpha2}$ line is eliminated. Therefore the correction is also referred to as $K_{\alpha2}$ correction or $K_{\alpha2}$ stripping. The line profiles of $K_{\alpha1}$ and $K_{\alpha2}$ are typically assumed to be identical, but with different intensities. The intensity ratio of the $K_{\alpha2}$ line to the $K_{\alpha1}$ line is approximately 0.5. The $K_{\alpha2}$ stripping can be done before the peak evaluation or during the profile fitting, depending on the algorithms used for peak evaluation [39, 40]. $K_{\alpha2}$ stripping is not necessary if the $K_{\alpha2}$ line has been removed from the incident X-ray beam – for instance, when a channel-cut monochromator is used.

Background correction is necessary if there is a strong background or the peak evaluation algorithms are sensitive to the background, such as in $K_{\alpha2}$ stripping, peak fitting, and peak intensity and integrated intensity evaluations. Background correction eliminates the scattered intensity not contributing to the diffraction profile. It is performed by subtracting a linear intensity distribution based on the background intensities at both the lower 2θ side and the higher 2θ side of the diffraction peak. The background region should be distanced sufficiently from the 2θ peak so that the correction will not truncate the diffraction profile. The 2θ ranges of the low background and high background should be determined based on the width of the 2θ peak and available background in the profile. Based on a normal distribution, a 2θ range of 2 times the FWHM covers of the 98% peak intensity, and 3 times the FWHM covers more than 99.9%, so the background intensity should be determined at more than 1 to 1.5 FWHM away from the peak position. In

cases where the diffraction profile contains background information only on one side of the peak, the background should be determined from either extrapolation of the available background or a flat background. The background correction can be neglected for a low background profile or if the error caused by the background is tolerable for the application.

Smoothing of the diffraction profile may be applied to reduce the effect of counting statistics on background determination, $K_{\alpha 2}$ corrections, and calculation of the peak position. Smoothing is not always necessary or beneficial because it may only provide a cosmetic effect to the diffraction profile, and may even smear or distort the diffraction profile.

The peak position can be evaluated by various methods, such as gravity, sliding gravity, and profile fitting by parabolic, Pseudo-Voigt, or Pearson VII functions [3, 17, 41]. In the gravity method (also called the centroid method), the center of gravity of the diffraction profile is calculated and used as the peak position. The intensities in the profiles are subtracted by a background value (threshold) for calculating the gravity center. The threshold value is a percentage of the net peak height, the recommended threshold being 20%. A lower threshold may introduce inconsistency in peak position determination. The sliding gravity method is a modified method which improves the final results by an iterative process. First, the center of gravity is calculated at several user-defined threshold values, typically 10% to 80%. A list of threshold dependent stress values and the corresponding standard deviations are then calculated. The final peak position is then generated from the weighted average of all gravity center values from the first step. The weight of each gravity center value is based on the standard deviation of the corresponding stress value. The stress value is then calculated from the final peak position.

When the peak position is evaluated by the profile fitting method, the measured data points on the diffraction profile are fitted to a given function with several unknown parameters by the least squares method. The peak position is then given by the resulting parameters. Many functions have been used, such as Gaussian, Cauchy (or Lorentz), Voigt, Pseudo-Voigt, or Pearson VII functions. [42]. All of these functions may be fitted to the complete diffraction profile with a large number of data points for good statistics. The quality of the fitting result depends on the consistency in shape between the measured profile and the fitting function. Among these functions, the Pearson VII function may be fitted to a broad range of profile shapes [43]. The Pearson VII function is given by

$$P(x) = H\left[1 + 4(2^{1/m} - 1)\left(\frac{x - x_0}{W}\right)^2\right]^{-m} \tag{9.96}$$

where H is a scaling factor that determines the height of the peak, W is the FWHM of the profile, and m is a shape parameter. When $m = 1$, 2, or ∞, the profile shape becomes a Cauchy, modified Lorentzian, or Gaussian shape as shown in Figure 9.19. The other m values represent a transition or combination of the above functions. In order to avoid confusion between the measured peak 2θ and stress-free $2\theta_0$, x represents the 2θ variables of the profile and x_0 represents the measured 2θ peak position. The parameters H, W, m, and peak position are evaluated by a non-linear least squares fitting of the diffraction profile to the above function. For a profile collected using $K_{\alpha 1}$ radiation, or a profile having been corrected by $K_{\alpha 2}$ stripping, the above equation is adequate to fit the diffraction profile. However, to account for the $K_{\alpha 1}K_{\alpha 2}$ doublet, the following pairs are summed to give

$$P(x) = H\left[1 + 4(2^{1/m} - 1)\left(\frac{x - x_{01}}{W}\right)^2\right]^{-m} + rH\left[1 + 4(2^{1/m} - 1)\left(\frac{x - x_{02}}{W}\right)^2\right]^{-m} \tag{9.97}$$

where r is the ratio of the $K_{\alpha 2}$ intensity to the $K_{\alpha 1}$ intensity, typically $r = 0.5$, and x_{01} and x_{02} are the peak positions corresponding to the $K_{\alpha 1}$ and $K_{\alpha 2}$ lines. It is assumed that the $K_{\alpha 1}$ line and

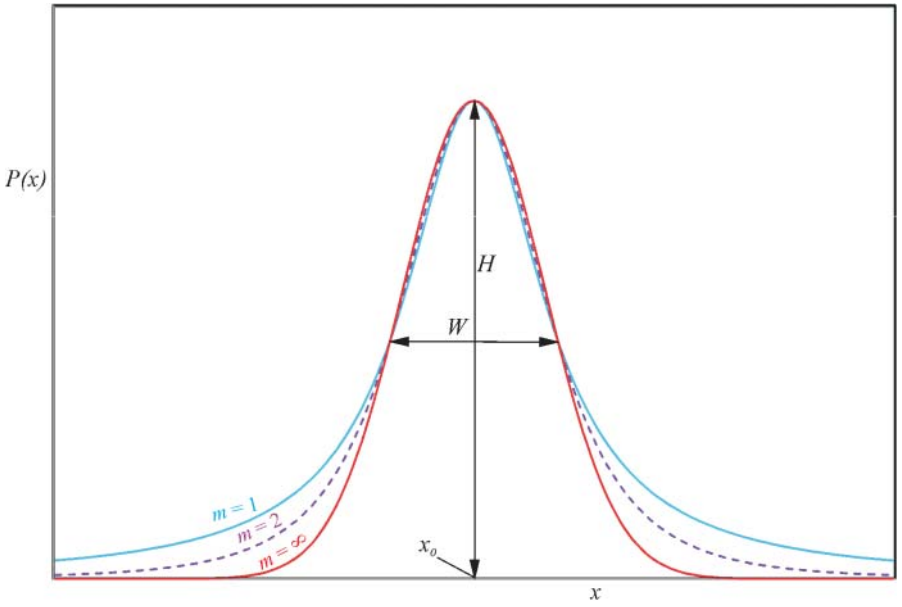


FIGURE 9.19 Pearson VII function with $m = 1$, 2, or ∞.

the $K_{\alpha 2}$ line have the exact same profile shape so that the same parameters H, m are used in both terms. Since x_{01} and x_{02} are not truly two independent parameters and only the peak position on the $K_{\alpha 1}$ line is needed for stress calculation, x_{02} in the above equation should be replaced by x_{01} by

$$x_{02} = 2\arcsin\left(\frac{\lambda_2}{\lambda_1}\sin\frac{x_{01}}{2}\right) \tag{9.98}$$

where λ_1 and λ_2 are the wavelengths of the $K_{\alpha 1}$ and $K_{\alpha 2}$ radiations respectively. This relation makes it possible to fit any peak with only four Pearson parameters: H, W, m, and peak position (x_{01}). In practice, the separation of two peaks is necessary only for profiles either showing two peaks or asymmetry due to the $K_{\alpha 1}K_{\alpha 2}$ doublet. For broad peaks, a single Pearson VII function and the weighted average wavelength can be used to evaluate the peak position and calculate stress without $K_{\alpha 2}$ stripping.

Non-linear least squares problems often have to be solved by an iterative procedure. The iteration starts with initial values for the parameters. Then, the parameters are refined iteratively until the convergence criterion is satisfied. The non-linear least squares regression may become unstable due to multiple minima or local minima in the sum of squares. Better convergence and stability can be achieved by using the shape parameter from the best fitting results from a similar sample. For example, the shape parameter of the Pearson VII function m can be set to a constant based on satisfactory fitting of a similar sample. The selection of the initial parameters based on raw data or other analysis can also make the fitting more stable and consistent – for example using the maximum count on the profile as an initial H factor and a centroid method to get the initial peak position x_0.

9.4.4 Stress Calculation

The final data set after integration and peak evaluation should contain many data points describing the diffraction ring shape for all collected frames. Each measured data point contains three

goniometer angles (ω,ψ,ϕ) and the diffraction ring position (γ,2θ). The peak intensity or integrated intensity of the diffraction profile is another value to be determined and may be used in stress calculation. In most cases the number of data points is more than the number of unknown stress components, so the linear least squares method can be used to calculate the stresses. In a general least squares regression, the residual for the i-th data point is defined as

$$r_i = y_i - \hat{y}_i \tag{9.99}$$

where y_i is the observed response value, $\hat{y}_i$ is the fitted response value, and r_i is the residual, which is defined as the difference between the observed value and the fitted value. The summed square of residuals is given by

$$S = \sum_{i=1}^{n} r_i^2 = \sum_{i=1}^{n} (y_i - \hat{y}_i)^2 \tag{9.100}$$

where n is the number of data points and S is the sum of squares error to be minimized in the least squares regression. For stress calculation, the observed response value is the measured strain at each data point

$$y_i = \ln\left(\frac{\sin\theta_0}{\sin\theta_i}\right) \tag{9.101}$$

and the fitted response value is given by the fundamental equation by

$$\hat{y}_i = p_{11}\sigma_{11} + p_{12}\sigma_{12} + p_{22}\sigma_{22} + p_{13}\sigma_{13} + p_{23}\sigma_{23} + p_{33}\sigma_{33} + p_{ph}\sigma_{ph} \tag{9.102}$$

where all possible stress components and stress coefficients are listed as a generalized linear equation. Since the response value function is a linear equation of unknown stress components, the least squares problem can be solved by a linear least squares regression. For programming convenience, all possible stress components are included in the linear expression, but they may not appear as non-zero values at the same time. For instance, the pseudo-hydrostatic stress term should be set to zero for the triaxial stress state. The stress components are either set as unknown (x) or set to zero for various stress states as listed in Table 9.6.

All stress components marked as unknown (x) will be calculated by the linear least squares regression, but the reliability and accuracy of each calculated stress component depends on the data collection strategy. The normal stress in a particular direction can be calculated with the setup of the biaxial stress state, but only the component corresponding to the preferred direction in the data collection strategy scheme should be used. For instance, σ_{11} should be measured with an ω scan at $\phi = 0°$, and σ_{22} with a ψ scan at $\phi = 0°$. The normal stress with shear in a particular direction can be calculated with the setup of the biaxial stress state with shear. For the same reason, σ_{11} and σ_{13} should be measured with an ω scan at $\phi = 0°$, and σ_{22} and σ_{23} are measured with a ψ scan at $\phi = 0°$.

Table 9.6 Unknown Stress Components to be Solved by Least Squares Regression

Stress states	σ_{11}	σ_{12}	σ_{22}	σ_{13}	σ_{23}	σ_{33}	σ_{ph}
Triaxial	x	x	x	x	x	x	0
Biaxial	x	x	x	0	0	0	x
Biaxial with shear	x	x	x	x	x	0	x

9.4.5 Effect of Texture and Large Grain

In the above stress calculation, all data points are assumed to have the same quality and are used equally in the least squares regression. This is acceptable when the diffraction ring is smooth and continuous along the γ angle. This requires that no strong textures are in the sample and that the grain sizes are relatively uniform and small. In this case, the diffraction profiles integrated from different γ ranges are smooth and with a consistent profile shape. In cases where the samples have strong texture and/or large grain sizes, the diffraction profiles at different data points may have a large variation in intensity, smoothness, and shape. The 2θ values evaluated from profiles of low quality carry large errors that can significantly affect the calculated stress. Figure 9.20(a) shows a diffraction frame from a textured Cu film sample. The total integration region for the Cu (222) ring is given by $2\theta_1 = 93°$, $2\theta_2 = 97.5°$, $\gamma_1 = -72.5$, and $\gamma_2 = -107.5°$. The integration region is divided into 14 subregions, with $\Delta\gamma = 2.5°$. The γ-integration from the subregion at $\gamma = -106.25°$ produces a smooth diffraction profile with relative peak intensity of 598. The 2θ value at this data point can be determined with good accuracy. Due to the strong texture in the Cu film, the intensity of the diffraction profile at $\gamma = -73.75°$ has a very low intensity of 87.5. The low diffraction intensity is typically associated with poor sampling statistics due to fewer grains contributing to the diffraction at this orientation. The 2θ value determined from this profile contains large error, and the error will pass on to the stress results if the data point is used without discrimination.

Figure 9.20(b) shows a diffraction frame collected from the transition area of a friction stir welded aluminum alloy plate with Cu-K_α radiation. The total integration region for the Al (311) ring is defined by $2\theta_1 = 137°$, $2\theta_2 = 142°$, $\gamma_1 = 65$, and $\gamma_2 = 115°$. The integration region is divided into 10 subregions, with $\Delta\gamma = 5°$. The γ-integration from the subregion at $\gamma = 67.5°$ produces a smooth diffraction profile with a relative peak intensity of 607.5. The 2θ value at this data point can be determined with good accuracy. Due to the large grain sizes, the diffraction ring is spotty. The intensity of the diffraction profile at $\gamma = 87.5°$ has a much lower intensity of 87.8. The diffraction profile is also rough, since fewer grains contribute to the diffraction at this orientation. The 2θ value determined from this profile will cause a large error in the stress results.

Large errors associated with texture and grain sizes can be avoided or reduced by several methods. One method is to inspect the diffraction profiles or the data points along the diffraction rings, and to remove the data points before the least squares regression. However, this method is tedious and subjective to human error or bias. Another method is to set an intensity threshold. The peak intensity or integrated intensity can be used as the threshold. The threshold can be set as an intensity level or as a given percentage of the profile with the highest intensity in the whole data set. Only the data points above the threshold are used for the least squares regression. The intensity weighted least squares regression is a more sophisticated approach and will be discussed in the next section. Figure 9.20(a) also shows a very strong Si (422) single crystal spot from the silicon substrate. This spot is so close to the Cu (311) ring that a big error will be produced if the Cu (311) ring is used for stress measurement. In this case, an intensity cap may be applied to eliminate the data points from the subregions containing strong diffraction from the single crystal substrate.

9.4.6 Intensity Weighted Least Squares Regression

The best approach is to calculate the stresses with the intensity weighted least squares regression. In the weighted linear least squares method, the weight of a data point on the diffraction ring is proportional to the diffraction intensity, which is directly related to the number of participating grains. Therefore, a high-quality data point influences the results more than a low-quality data point in stress determination. The weighted least square regression introduces a weighting factor

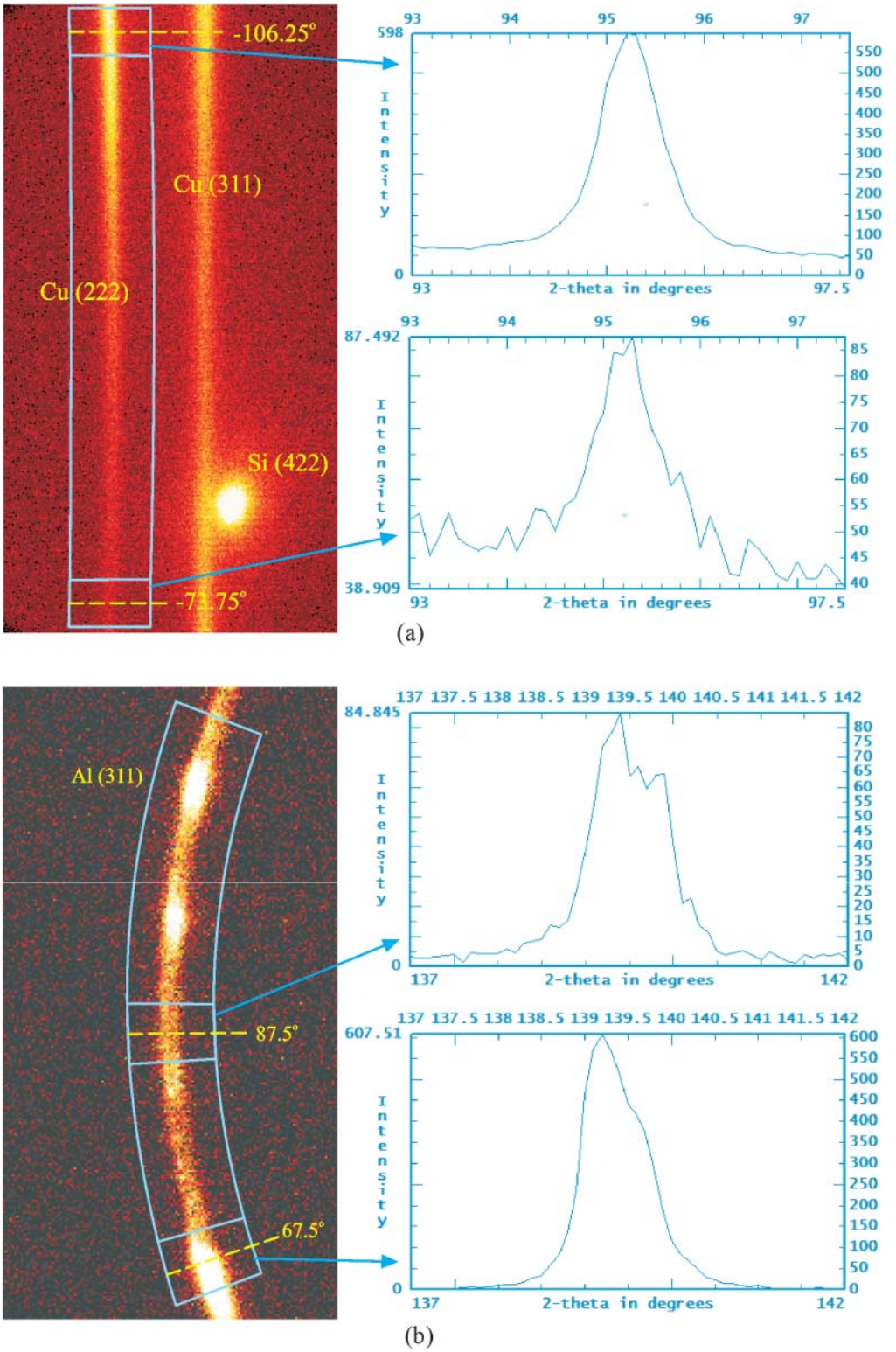


FIGURE 9.20 Quality of diffraction profiles: (a) strong texture, (b) large grain sizes.

in the summed square of residuals [44]:

$$S = \sum_{i=1}^{n} w_i r_i^2 = \sum_{i=1}^{n} w_i (y_i - \hat{y}_i)^2 \tag{9.103}$$

where w_i are the weighting factors. The peak intensity or the integrated intensity can be used as a weighting factor. The weighting factor can also be given by the standard error of profile fitting:

$$w_i = \frac{1}{\sigma_i^2} \tag{9.104}$$

where σ_i is the standard error of profile fitting on the i-th data point. In this case, a data point with a lower profile fitting error has more influence on the stress calculation than a data point with a larger profile fitting error. In order to consider the effects of both the profile intensity and the profile fitting error, the weighting factor can be given as

$$w_i = \frac{I_i}{\sigma_i^2} \tag{9.105}$$

where I_i can be either the peak height or the integrated intensity. In this case, data points with the combination of high intensity and good profile fitting will influence the stress calculation result more than data points of low intensity and/or poor profile fitting. The intensity threshold may be combined with the weighted least squares method, since the intensities of some data points may be so low that no reasonable results can be obtained from profile fitting. A high intensity threshold may be applied to eliminate the data points affected by the strong diffraction spots from large grains or single crystal substrate.

9.4.7 Stress-Free Sample and Standard Sample

There are many instrumentation factors affecting the accuracy of stress measurement, such as the sphere of confusion (SoC) of the goniometer, the sample surface height error, misalignment of the X-ray optics and detector position error (roll, pitch, and yaw). The measured stress is either false or beyond acceptable statistic error when any or a combination of the above factors are out of specification. Accuracy of an X-ray diffractometer for stress measurement can be verified by measuring the stress with a standard stress-free sample. With a well aligned and calibrated diffractometer, the measured stress value should be zero or within a specified deviation from zero.

As an example, the two-dimensional X-ray diffraction system shown in Figure 9.15 was tested with a stress-free Fe powder sample [45]. The Fe powder sample was measured immediately after the system was aligned and calibrated before all other stress measurement. The 32 frames from the combination of ψ (=0°, 15°, 30°, and 45°) and ϕ (0~360° with 45° steps) were collected with 60 second per frame. The measured stress values are: $\sigma_{11} = 12.9$ MPa, $\sigma_{22} = 9.3$ MPa with standard deviation 12.4 MPa. The stress-free Fe powder was measured again later, after 65 hours stress data collection runs with various Almen strip samples to check the system accuracy. With 180-second frames, the measured stress values are: $\sigma_{11} = 8.4$ MPa, $\sigma_{22} = 10.2$ MPa with standard deviation 8.6 MPa. The results satisfy the accuracy specs for the D8 Discover diffractometer.

The stress-free sample is typically made of fine powder of pure metal or alloy, having similar major elements or composition as the samples or parts to be measured. For example, Fe powder with particle size of a few microns is used to calibrate the system for stress measurement of ferrous metals. A fully annealed metal piece with fine grain and no strong texture can also be

used as a stress free sample. There are two major reasons to use the stress-free sample of the similar elements or composition. One reason is to have the same crystallographic plane, such as (211) for Fe, so that the instrument setup and data collection strategy are the same for both the stress-free sample and samples to be measured. Another reason is to have the same elastic constants so that the calibrated instrument error given in stress unit reflects the expected error for the following stress measurement due to the instrument. For example, if the maximum error of the above two-dimensional X-ray diffraction system (Bruker D8-Discover™) calibrated with stress-free Fe is 12.9 MPa, the stress error for following measurements on other ferrous metals should be in the same range.

Other powder samples, such as corundum, LaB6, silicon, and quartz, can also be used as a stress-free sample as long as the sample is prepared without residual stress and preferred orientation. This kind of stress-free sample standard is typically used to qualify the instrument with a given specification. When such a stress-free sample is used to evaluate the error in stress measurement for a particular type of material, three factors should be considered. First, the stress-free standard should have a peak with relatively strong diffraction intensity, well separated from adjacent peaks, and 2θ Bragg angle close to that of the samples to be measured, so that the instrument can be calibrated and used for further measurement with the same setup. Second, the stress-free standard is preferable to have an absorption coefficient not significantly different from the sample to be measured. Third, and most important, if the instrument is calibrated for stress measurement of a particular material, the elastic constants of that particular material should be used, instead of the stress-free sample. In this case, the stress-free standard provides a diffraction peak (d-spacing) as a strain gage, the actual impact of the instrument error on stress is evaluated based on the elasticity of the samples to be measured. Since the stress value is actually calculated from the measured strain, the measurement error evaluated from a stress-free sample does not represent the measurement error of the sample with different elastic constants. For instance, consider an instrument calibrated for stress measurement on polypropylene polymer (PP) samples with crystallinity around 50% [46]. The (060) diffraction peak of PP at 25.7° is used for stress evaluation. The diffraction peak at 25.6° for corundum (012) is used to calibrate the instrument. The Young's modulus given for a biaxially oriented PP film is 3880 MPa in TD direction and 2400 MPa in MD direction. While the Young's modulus of corundum (012) is 414,938 MPa, which is more than two orders of magnitude higher than the polymer. If the elastic constants of the corundum are used for the instrument calibration and the error is given in stress unit, the misleading stress may be much more than the stress to be measured on the polymer samples.

The accuracy of an X-ray diffractometer for stress measurement can also be verified by measuring a standard sample with known stress or stress tensor. The stress standard sample can be obtained from various sources, including well recognized laboratories or vendors, and samples measured in a well-calibrated instrument or alternative methods. The stability is a very important criterion for a stress standard. For instance, residual stresses in the Almen strips with residual stress produced by shot peening did not show a detectable change over 18 years [45].

9.4.8 Dynamic Sample Height Alignment

The SoC of goniometer and detector position error cannot be totally eliminated. It not only depends on the tolerance of all bearings for rotation axes and translation stages, but also the sample weight and instrument configuration. The weight of the sample produces extra displacements to all the mechanical parts on loading. The goniometer may be aligned to an acceptable SoC with the alignment fixture, but out of spec when a heavy sample is loaded. The detector position error also varies with different swing angles and detector distance, especially for the vertical system. Fortunately, most of the error is due to gravity and elastic deformation,

which is reproducible. Therefore, the SoC error can be compensated by a method called dynamic sample height alignment.

For a system with an automatic sample height alignment system, which typically includes laser video monitoring and motorized z translation stage, the sample height is adjusted automatically at each sample orientation. For a system with motorized z translation but without automatic alignment function, the dynamic alignment can be done by using calibrated z values at each sample orientation. The calibration can be done more precisely with a stress-free powder sample. Taking the 32 frames data collection strategy (combination of $\psi = 0°$, 15°, 30°, and 45° and $\phi = 0{\sim}360°$ with 45° steps) as an example, the calibrated z values at each of the 32 positions are obtained when a given 2θ value is measured by adjusting z. A list of 32 calibrated z values is saved for the instrument. The calibrated z values can then be used to position the sample for stress measurement. The stress evaluated with such a data set will have minimal error from the SoC of the goniometer.

9.4.9 Correction with Stress-Free Sample

As discussed above, the stress-free sample can be used to verify or calibrate an instrument on its accuracy for stress measurement. The dynamic sample height alignment can compensate the sample height error during the data collection at each sample orientation. For stress measurement with XRD^2 method, in order to follow the diffraction ring distortion, the 2θ values at various subregions along the diffraction ring are evaluated as a data point for stress calculation. The effect of instrument error on each data point (subregion) is not necessarily identical. Therefore, the correction with stress-free sample can be done more specifically on each data point. The approach is referred to as all data point correction (ADPC) or comprehensive instrument correction.

Figure 9.21 illustrates the concept of ADPC. The bottom is the 32 frames data collection scheme with combination of $\psi = 0°$, 15°, 30°, and 45° and $\phi = 0{\sim}360°$ with 45° steps. The 32 arcs are the orientation distribution of all unit diffraction vectors projected on the sample surface ($\mathbf{S_1}$-$\mathbf{S_2}$). The top-left shows three of the 32 diffraction frames collected from stress-free Fe powder. The three frames (A, B, and C) with the data points on the diffraction ring correspond to the three arcs (red) in the scheme. A total of 10 data points on each frame represents the integration and peak fitting results from 10 subregions. A total of 320 data points are produced from the complete data set of 32 frames. The top-right shows three 2θ-γ plots in rectangular coordinates corresponding to the three data frames on the top-left. The blue crosses mark the data points evaluated from each subregion. The horizontal black line and red lines represents the input $2\theta_0$ and calculated $2\theta_0$ respectively. Although the average measured 2θ is very close to input $2\theta_0$, the 2θ values measured at each data point have substantial deviation from the average value. A trend of higher to lower 2θ value from left to right along the γ angle can also be observed. The deviation is due to various instrument errors, such as misalignment of the optics, SoC, or roll of the detector.

With a perfect instrument, all the measured 2θ values from the stress-free Fe powder should be a constant ($2\theta_0$). Assuming the data collection time is sufficient and the statistical error is negligible, the deviation from $2\theta_0$ is caused by the instrument error. In the least squares regression for stress calculation, the observed response value is the measured true strain at each data point:

$$y_i = \ln\left(\frac{\sin\theta_0}{\sin\theta_i}\right) \tag{9.106}$$

in which the stress-free $2\theta_0$ is treated as a constant. θ_i is the measured value of the i-th data point. If a stress-free sample is measured with an imperfect instrument, the observed response value is

$$y_i^{SF} = \ln\left(\frac{\sin\theta_0}{\sin\theta_i^{SF}}\right) \tag{9.107}$$

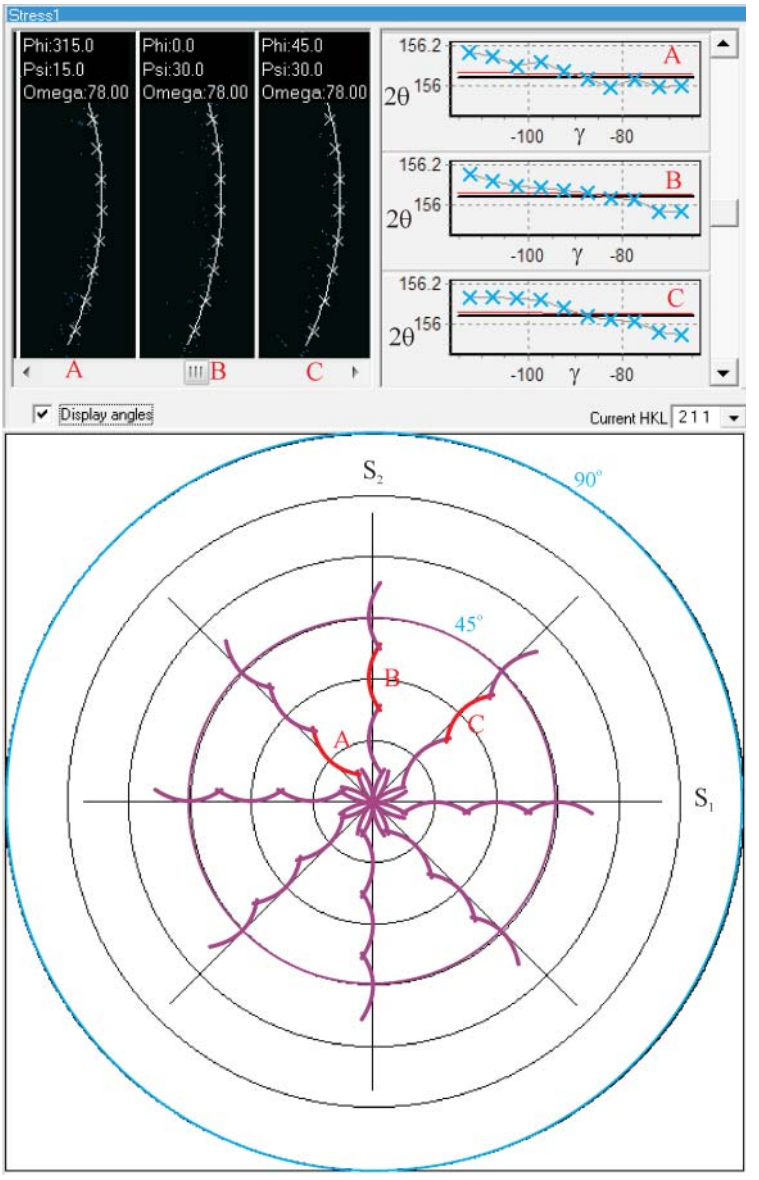


FIGURE 9.21 Stress-free 2θ values measured at various directions.

which can be considered as a pseudo-strain where θ_i^{SF} is the measured value of the i-th data point on the stress-free sample. When the same instrument is used for stress measurement on a sample with unknown stress, the observed response contains both the contribution from the measured true strain and the pseudo-strain. Assuming, the instrument error (pseudo-strain) is identical for both the measurement on the stress-free sample and stress sample, we can remove the pseudo-strain from the observed response:

$$y_i = \ln\left(\frac{\sin\theta_0}{\sin\theta_i}\right) - \ln\left(\frac{\sin\theta_0}{\sin\theta_i^{SF}}\right) = \ln\left(\frac{\sin\theta_i^{SF}}{\sin\theta_i}\right) \tag{9.108}$$

The instrument error is removed by replacing constant stress-free θ_0 with the measured θ_i^{SF} from the stress-free sample.

Stress measurement with all data point correction can be done with the following procedures. First, collect and process a complete data set to obtain $2\theta_i^{SF}$ for all data points (e.g. 320 data points for 32 frames with 10 subregions). Then collect a complete data set on the stress sample with the same instrument condition and data collection strategy and calculate stress from the data set using $2\theta_i^{SF}$ instead of $2\theta_0$ in the least square regression. The same set of $2\theta_i^{SF}$ values can be used for the subsequent stress measurement as long as the instrument condition remains the same. The composition and crystal structure of the stress-free sample should be consistent with the stress samples to be measured, for instance, stress-free Fe powder for ferrous metals with α phase. With the input of $2\theta_i^{SF}$ values in the stress evaluation, d_o (or $2\theta_o$) value input it is not needed. The actual d_o (or $2\theta_o$) is not necessarily the same for the stress-free sample and stress samples, but the discrepancy contributes only to the pseudo-hydrostatic term σ_{ph}. The measured stresses are not affected in the same principle as described earlier in this chapter.

9.4.10 Correction with Stress Standard

The accuracy of an instrument can be verified or compared with other instruments with a stress measurement on a stress standard. Following the same principle as in the previous section, all point data correction (APDC) can also be done with a stress standard sample. In the least squares regression for stress calculation, the observed response value is the measured strain at each data point:

$$y_i = \ln\left(\frac{\sin\theta_0}{\sin\theta_i}\right) \tag{9.109}$$

and the fitted response value is given by the fundamental equation by

$$\hat{y}_i = p_{11}\sigma_{11} + p_{12}\sigma_{12} + p_{22}\sigma_{22} + p_{13}\sigma_{13} + p_{23}\sigma_{23} + p_{33}\sigma_{33} + p_{ph}\sigma_{ph} \tag{9.110}$$

The stress components p_{ij} are either set as unknown (x) or set to zero for various stress states as listed in Table 9.6. If a stress standard sample is measured with an imperfect instrument, the observed response value is

$$y_i^{SS} = \ln\left(\frac{\sin\theta_0}{\sin\theta_i^{SS}}\right) \tag{9.111}$$

where θ_i^{SS} is the measured value of the i-th data point on the stress standard sample. The fitted response value for the stress standard is given by

$$\hat{y}_i^{SS} = p_{11}\sigma_{11}^{SS} + p_{12}\sigma_{12}^{SS} + p_{22}\sigma_{22}^{SS} + p_{13}\sigma_{13}^{SS} + p_{23}\sigma_{23}^{SS} + p_{33}\sigma_{11}^{SS} + p_{ph}\sigma_{ph}^{SS} \tag{9.112}$$

When the same instrument is used for stress measurement on a sample with unknown stress, the observed response contains both the contribution from the measured true strain and the pseudo-strain from the instrument error. Assuming, the instrument error (pseudo-strain) is identical for the measurements on both the stress standard and the stress samples, we can rewrite the summed square of residuals based on the difference between the stress standard and stress samples:

$$S = \sum_{i=1}^{n} R_i^2 = \sum_{i=1}^{n} (Y_i - \hat{Y}_i)^2 \tag{9.113}$$

where n is the number of data points and S is the sum of squares error to be minimized in the least squares regression. The observed response value is now the difference of the measured strain from the stress sample and the stress standard:

$$Y_i = y_i - y_i^{SS} = \ln\left(\frac{\sin\theta_0}{\sin\theta_i}\right) - \ln\left(\frac{\sin\theta_0}{\sin\theta_i^{SS}}\right) = \ln\left(\frac{\sin\theta_i^{SS}}{\sin\theta_i}\right) \tag{9.114}$$

Correspondingly, the difference between the fitted response values of the stress standard and stress samples is given as

$$\begin{aligned}\hat{Y}_i = \hat{y}_i - \hat{y}_i^{SS} &= p_{11}(\sigma_{11} - \sigma_{11}^{SS}) + p_{12}(\sigma_{12} - \sigma_{12}^{SS}) + p_{22}(\sigma_{22} - \sigma_{22}^{SS}) \\ &+ p_{13}(\sigma_{13} - \sigma_{13}^{SS}) + p_{23}(\sigma_{23} - \sigma_{23}^{SS}) + p_{33}(\sigma_{33} - \sigma_{33}^{SS}) + p_{ph}\sigma'_{ph}\end{aligned} \tag{9.115}$$

where $\sigma'_{ph} = \sigma_{ph} - \sigma_{ph}^{SS}$, with no need to be treated as two variables. In the above equations, the stress coefficient p_{ij} is assumed to be the same for either the stress standard and stress samples at each data point. The impact of the 2θ shift to the stress coefficient (or unit diffraction vector direction) is negligible. Since the stress components for the stress standard σ_{ij}^{SS} are already given, the stress values of the unknown stress sample can be calculated by the least square regression with the above equations. The instrument error is cancelled out by using the difference between the measured values from stress samples and the stress standard.

The same set of $2\theta_i^{SS}$ and σ_{ij}^{SS} values can be used for the subsequent stress measurement as long as instrument condition remains the same. The composition and crystal structure of the stress standard should be the same to the stress samples to be measured. Ideally, the stress standard is identical to the samples to be measured in terms of material, shape, size, and manufacturing process, but only the stress standard has been accurately measured by controlled condition, recognized laboratories, or other reliable alternative method.

It can be noted that the algorithms for the comprehensive instrument correction with stress standard are equivalent to the algorithms for stress-free sample if only we take σ_{ij}^{SS} as zero. Therefore, the same computer program can be used for the comprehensive instrument correction by either stress standard or stress-free sample, by using the proper σ_{ij}^{SS} values or setting it to zero. The weighted linear least squares method can also be combined with the comprehensive instrument correction. In addition to the correction for instrument error, the error due to the sample surface condition and shape can also be eliminated if the stress-free sample or stress standard has the same shape as the samples to be measured.

9.5 EXPERIMENTAL EXAMPLES

9.5.1 Comparison Between 2D Method and Conventional Method

Stress measurement on a polycrystalline material by X-ray diffraction is based on the strain measurements in single or several sample orientations. Each measured strain is calculated from the average d-spacing of specific lattice planes $\{hkl\}$ over many crystallites (grains). A larger number of contributing crystallites gives better accuracy and sampling statistics (also referred to as particle statistics). The sampling statistics are determined by both the crystal structure and the instrumentation. For a perfect randomly oriented powder sample, the number of contributing crystallites for a measured strain can be given as

$$N_s = \frac{p_{hkl}V\Omega}{4\pi v} = \frac{3p_{hkl}V\Omega}{2\pi^2 d^3} \tag{9.116}$$

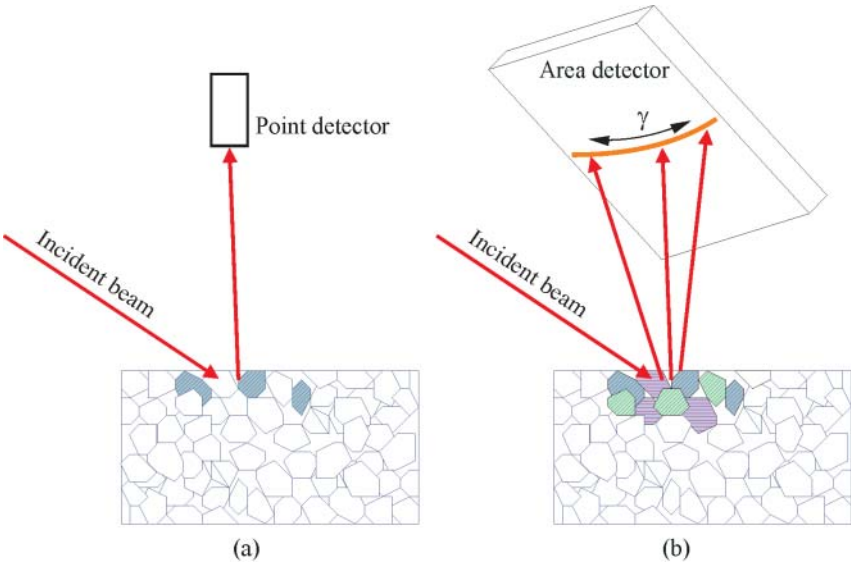


FIGURE 9.22 Number of diffraction contributing crystallites: (a) point detector, (b) area detector.

where p_{hkl} is the multiplicity of the diffracting planes, V is the effective sampling volume, v is the average volume of crystallites, d is the average diameter of crystallites, and Ω is the instrument window in solid angle. The instrument window is mainly determined by the divergence of the incident X-ray beam. The multiplicity term, p_{hkl}, effectively increases the number of contributing crystallites for a particular set of (hkl) planes. Therefore, the lattice plane families with large multiplicity are preferred for stress measurement. Figure 9.22 illustrates the diffraction contributing crystallites with (a) a point detector and (b) an area detector. The number of contributing crystallites measured by a conventional diffractometer with a point detector is limited to the crystallites with their orientation satisfying the Bragg condition given by the incident beam and diffracted beam to the point detector. In a two-dimensional diffraction system, the diffracted X-rays satisfying the Bragg condition are distributed over the diffraction ring at a range of γ angles. Therefore, many more crystallites can contribute to the diffraction. The larger γ is, the more crystallites contribute to the diffraction. Better precision or sampling statistics can be achieved with XRD[2].

One experimental example for stress calculation is residual stress measurement on the end surface of a carbon steel roller. The roller is a cylinder 1″ long and ¾″ in diameter. The stress data was taken from the center of the roller end. The sample was loaded on the XYZ stage of the GADDS™ microdiffraction system. A total of seven frames were taken with ω angles of 33, 48, 63, 78, 93, 108, and 123° (corresponding to ψ tilts of 69, 54, 39, 24, 9, 6, and −21° for a negative detector swing angle) with Cr-K_α radiation. The frame collected at $\omega = 123°$, as an example, is shown in Figure 9.23(a). The (211) ring covering the γ range of 67.5° to 112.5° was used for stress analysis. First, the frame data was integrated along γ with an interval of $\Delta\gamma = 5°$. A total of nine diffraction profiles were obtained from γ integration. The diffraction profile at each γ value is an integration in the range from $\gamma - \frac{1}{2}\Delta\gamma$ to $\gamma + \frac{1}{2}\Delta\gamma$. For example, the profile at $\gamma = 70°$ is from γ-integration from 67.5° to 72.5°. The peak position 2θ for each γ angle was then obtained by fitting the profile with a Pearson VII function. A total of 63 data points in the form of $2\theta(\gamma)$ can be obtained from the seven frames.

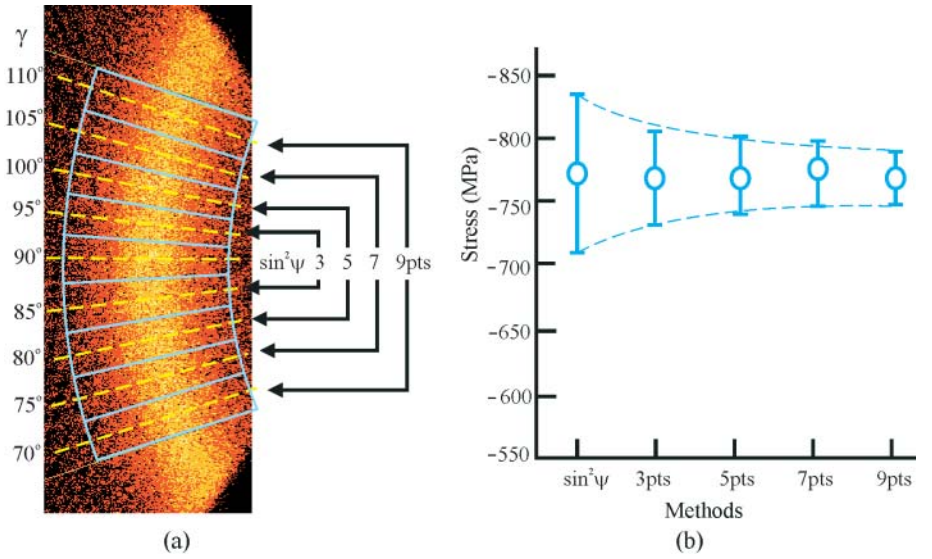


FIGURE 9.23 Stress calculation with 2D method and $\sin^2\psi$ method: (a) data points taken from the diffraction ring, (b) measured stress and standard deviation by different methods and from various numbers of data points.

Table 9.7 Measured Stress with the Conventional $\sin^2\psi$ Method and the 2D Method

Method	$\sin^2\psi$	2D method with various numbers of data points			
Data points per frame	1 points	3 points	5 points	7 points	9 points
Total data points	7 points	21 points	35 points	49 points	63 points
Stress (MPa)	−776 ±62	−769 ±38	−775 ±33	−777 ±26	−769 ±23

The data points at $\gamma = 90°$ from seven frames, a typical data set for an ω-diffractometer, were used to calculate stress with the conventional $\sin^2\psi$ method. In order to compare the gain from having increased data points with the 2D method, the stress was calculated from 3, 5, 7, and 9 data points on each frame. The results from the conventional $\sin^2\psi$ method and the 2D method are summarized in Table 9.7 and compared in Figure 9.23(b). The measured residual stress is compressive and the stress values from different methods agree very well. With the data taken from the same measurement (seven frames), the 2D method gives lower statistical error, and the error decreases with increasing number of data points from the diffraction ring.

9.5.2 Sample Oscillation and Virtual Oscillation

In the case of materials with large grain size or microdiffraction with a small X-ray beam size, the diffraction profiles are distorted due to poor counting statistics. To solve this problem with conventional detectors, some kind of sample oscillation, either translational oscillations or angular oscillations, are used to bring more crystallites into the diffraction condition. In other words, the purpose of oscillations is to bring more crystallites into the condition, in which the normal of the diffracting crystal plane coincides with the instrument diffraction vector. Sample oscillation by

rotation or translation can also be used to improve residual stress measurement with 2D detectors [47, 48]

For 2D detectors, when γ-integration is used to generate the diffraction profile, we actually integrate the data collected in a range of various diffraction vectors. Since the effect of γ-integration on sampling statistics is equivalent to angular oscillation on the ψ axis in a conventional diffractometer, the effect is referred to as virtual oscillation, and $\Delta\psi$ is the virtual oscillation angle. As given in Chapter 7, the virtual oscillation angle $\Delta\psi$ can be calculated from the integration range $\Delta\gamma$ by

$$\Delta\psi = 2\arcsin[\cos\theta \sin(\Delta\gamma/2)] \tag{9.117}$$

For large and flat sample surface with homogenous stress distribution parallel to the sample surface, mechanical oscillation can effectively improve the data quality. But with rough or curved sample surface, mechanical movement may result in some sample position error. Mechanical oscillation is not suitable for stress mapping when each stress measurement has to be limited within a small space step. Since there is no actual physical movement of the sample stage during data collection, virtual oscillation can avoid this error.

For example, Figure 9.24 is a frame taken from a SS304 stainless steel plate with Cr-K_α radiation. The large grain size results in a spotty (220) diffraction ring. A diffraction profile collected with a point detector may have a rough profile. The γ-integration from 80° to 100° results in a smooth diffraction profile so that the 2θ value can be accurately determined. In this case, $\Delta\gamma = 20°$

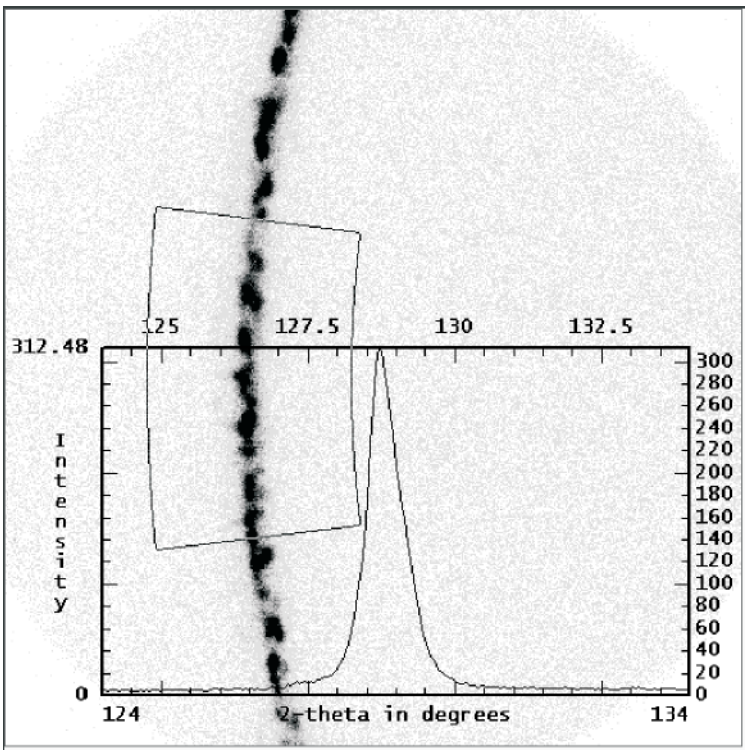


FIGURE 9.24 Virtual oscillation by γ-integration over $\Delta\gamma = 20°$ on a spotty diffraction ring taken from an SS304 stainless steel plate produces a smooth diffraction profile.

and $\theta \approx 64°$, so the virtual oscillation angle $\Delta\psi = 8.7°$. The γ-integrated profile is an average over the Debye ring defined by the γ-range. The averaging is over a region of orientation distribution, rather than a volume distribution. When 2D theory is used for stress measurement, the virtual oscillation effect is further enhanced due to the larger γ range. More importantly, the virtual oscillation effect for the 2D method is intrinsic; the data points along the diffraction ring are treated at almost their exact γ angle, while in the conventional method, the virtual oscillation is extrinsic. It doesn't matter if the profile is from γ-integration of a 2D frame or physical angular oscillation, the profile is still treated as if the data was collected at one orientation. Thus, the measured 2θ value is actually an average over the γ-integration range or angular oscillation range, the so-called smearing effect. For example, the 2θ value of the profile in Figure 9.24 is an average over $\Delta\gamma = 20°$ (80–100°), but treated as if it was collected at the diffractometer plane ($\gamma = 90°$). However, in the 2D method, the virtual oscillation range is the total range of the selected diffraction ring, and the smearing effect is only within the rather smaller $\Delta\gamma$ steps. For example, for the same frame in Figure 9.24, if the γ range of 70–110° and $\Delta\gamma = 4°$ are used for stress measurement with the 2D method, there will be 10 data points along the diffraction ring. The virtual oscillation range is 40°, but the smearing effect is only over $\Delta\gamma = 4°$ and can be even smaller with smaller $\Delta\gamma$ steps.

9.5.3 Stress Mapping on Weldment

Residual stress mappings on friction stir welded samples are measured using a two-dimensional X-ray diffraction (XRD^2) system [49]. The system with XYZ stage allows users to select the mapping area and steps. The stress results are processed and mapped to the grid based on the user-selected stress component. Friction stir welding is an innovative joining technique [50]. The weld is formed by mechanically tumbling a non-consumable tool between two pieces of material, as shown in Figure 9.25(a). During the welding process, the materials are kept in the solid phase. The welding tool generates enough frictional heat to soften the material in the contact area, and the two pieces of material are joined together by transferring the materials from the area in front of the tool to the area after the tool and mixing them together. Because the joint is formed in the solid state, friction stir welds are free of solidification defects. Residual stress distribution in Al-6061-T6 friction stir welds has been investigated with neutron diffraction [51]. The influence

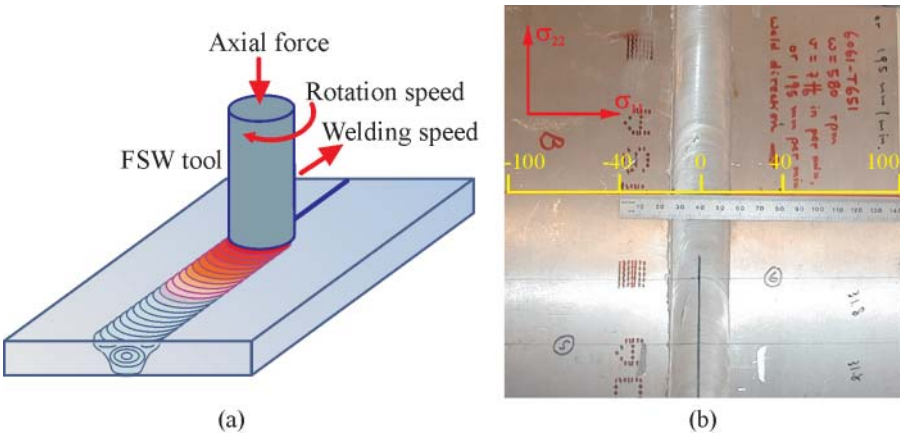


FIGURE 9.25 (a) Schematic illustration of the friction stir welding process, (b) specimen of friction stir welded aluminum alloy.

of welding speed was investigated. The residual stress distribution is a double-peak profile across the weld center line, with the peaks located in the middle of the heat-affected zone. In the experiment, the residual stress distribution on friction stir welded Al-6061-T651 samples was measured with a two-dimensional X-ray diffraction system.

Two specimens were made by friction stir welding with a rotation speed of 580 rpm and a welding speed of 113 mm/min and 195 mm/min respectively. The specimens will be denoted as 113 and 195 hereafter. The original specimen size is 200 mm (length) × 607 mm (width) × 9.5 mm (thickness). Each sample was cut to three 200 mm × 200 mm pieces and the center piece was used for residual stress measurement, as shown in Figure 9.25(b). The stress mapping takes a 1 mm stepwise scan for 0–40 mm from the center line and a 5 mm stepwise scan from 40 mm to the edges. The transverse direction across the welded zone is loaded in the sample direction $\mathbf{S_1}$ and the longitudinal direction is $\mathbf{S_2}$.

The instrument used for stress measurement is a Bruker D8-Discover GADDS™ with quarter-circle Eulerian cradle. The stress is measured on the aluminum (311) planes with Cr-K_α radiation. The X-ray beam size is 0.8 mm in diameter. Each diffraction frame is collected in 30 seconds with 5 frames per stress data point at various ψ and ϕ angles. The specimen is loaded on the XYZ stage of the Eulerian cradle as shown in Figure 9.26(a). Figure 9.26(b) is a magnified image of a mapping spot aligned to the instrument center with the laser-video alignment system.

In addition to the stress measurement, the diffraction frames collected with an area detector can reveal the microstructure [52]. Three typical diffraction frames collected on the original materials, stirred region, and the boundary between the two regions are shown in Figure 9.27. The original aluminum plate in the range of 18–100 mm from the center line has a large grain and strong texture, so the diffraction ring shows a large intensity variation along the ring and a spotty pattern. The friction stirred materials are within the area of 15 mm from the center line. The severe plastic deformation produced fine grains with almost no texture. As a result, the diffraction ring is very smooth with almost no intensity fluctuation. The diffraction ring from the materials in the range of 16–17 mm from the center line is a mixture of both the original and friction-stirred materials.

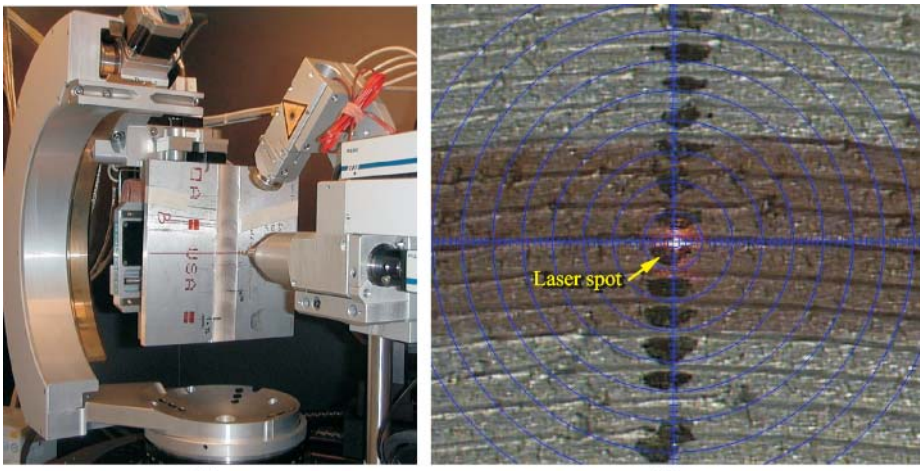


FIGURE 9.26 (a) Specimen loaded on the XYZ stage of Eulerian cradle and mapping spot is aligned with the laser-video system, (b) magnified image of the mapping area with the laser spot pointing to the instrument center.

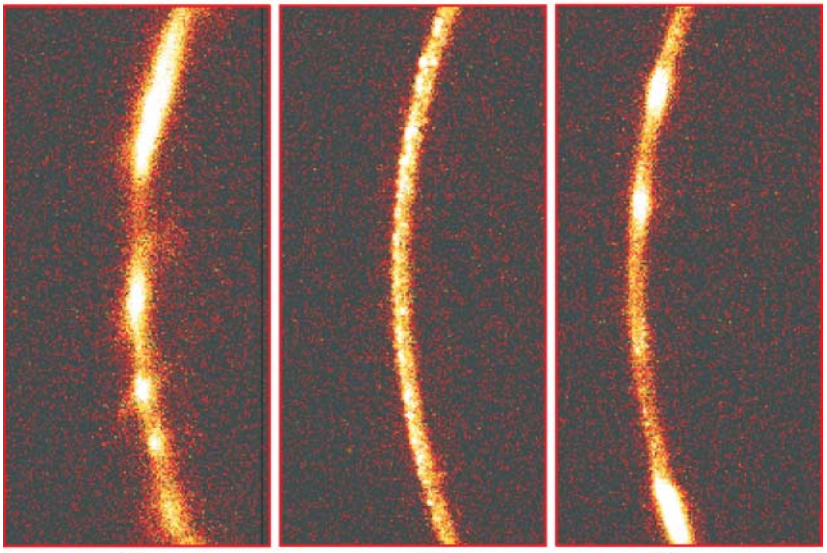


FIGURE 9.27 Diffraction frames collected at three typical regions: (a) original material, (b) friction-stirred region; and (c) mixture of both.

The residual stress mapping on both the top and bottom surfaces are measured. The stresses in the transverse direction (σ_{11}) are scattered around the zero stress line without a perceivable trend. The normal residual stress components in the longitudinal direction (σ_{22}) are shown in Figure 9.28. In mapping plot (a), the stresses in the longitudinal direction (σ_{22}) within 40 mm from the center line form a double-peak profile symmetric to the weld center line. The plots for specimens 113 and 195 are almost identical. A similar profile was observed with neutron diffraction [51]. The relatively small X-ray beam size compared to the large grain size is the

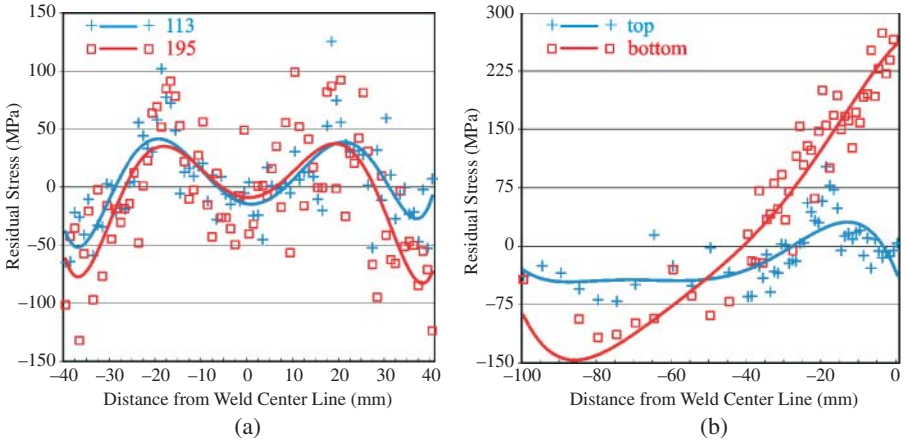


FIGURE 9.28 Residual stress mapping on friction stir welded Al alloy plate: (a) σ_{22} on the top surface within 40 mm from the weld center line of both specimens, (b) σ_{22} on both the top surface and the bottom surface from the specimen edge to the weld center line.

cause of the severe scattering data. The longitudinal stress mappings of both the top surface and the bottom surface from the specimen edge to the weld center line are shown in mapping plot (b). Small compressive residual stresses on the top surface are observed from the specimen edge to 40 mm from the center line. The bottom surface also has compressive stresses in the same range. However, strong tensile stresses are distributed from 40 mm to the center line with the maximum above 250 MPa at the center line.

9.5.4 Residual Stresses in Thin Films

Measurement of residual stresses in thin films by X-ray diffraction is always a challenging task due to the weak diffraction signals from the limited diffraction volume, sharp stress, or strain gradients, preferred orientations, anisotropic grain shape, and the inhomogeneous phase and microstructure distribution [53–55]. When residual stresses are measured by a conventional diffractometer, the $\sin^2\psi$ method is often used to calculate the residual stress on the sample surface in a particular ϕ direction, i.e. σ_ϕ. The non-linear d vs. $\sin^2\psi$ behavior commonly associated with thin films produces poor results. For a given material, the X-ray penetration depth is dependent on the incident angle. The lower the incident angle, the smaller the penetration depth. When residual stresses are measured on a thin film sample, it is preferable to keep a small incident angle to get the most X-ray scattering from the thin film layer. This is very difficult or impossible with the conventional $\sin^2\psi$ method. The ψ-tilt is achieved by two kinds of diffractometer configurations. One is iso-inclination (ω-diffractometer), in which the ψ-rotation axis is perpendicular to the diffractometer plane containing the incident and diffracted beams. The other is side-inclination (ψ-diffractometer), in which the ψ-rotation axis is in the diffractometer plane. With an ω-diffractometer, the incident angle varies during data collection, so the incident angle cannot be kept low during data collection, while with a ψ-diffractometer, the incident angle is determined by the Bragg angle θ, so the incident angle cannot be small unless the stress is measured using a peak with a very small 2θ angle. Figure 9.29 illustrates the diffraction vector distribution in the sample coordinates for stress measurement with the $\sin^2\psi$ method (in purple) and for the XRD^2

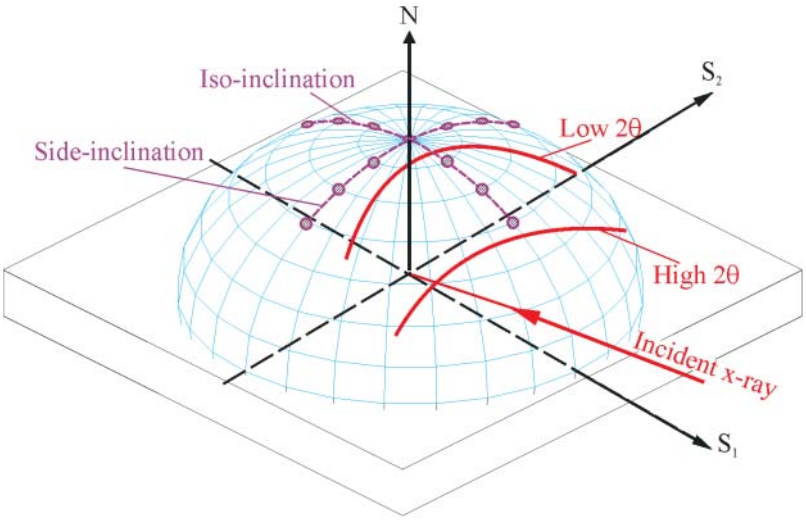


FIGURE 9.29 Diffraction vector distribution in the sample coordinates for the $\sin^2\psi$ method (in purple) and for the XRD^2 method with low incident angles for high and low 2θ angle peaks (in red).

method with low incident angles for high and low 2θ angle peaks (in red). The hemisphere covers all possible orientations of the diffraction vector. The $\sin^2\psi$ method can only be used when the diffraction data is measured with the diffraction vectors distributed along the longitudinal lines. **N** is the sample normal. At $\phi = 0$, the diffraction vector distribution along the longitudinal line passing the $\mathbf{S_1}$ coordinate and **N** represents a typical ω-goniometer, and that between $\mathbf{S_2}$ and **N** represents a typical ψ-goniometer. For any particular ϕ angle, the stress σ_ϕ is measured by a diffraction scan along the corresponding longitudinal line, that is, by rotating the sample about the ϕ axis so that the corresponding longitudinal line matches the type of goniometer.

The XRD^2 method has many advantages over the conventional method for stress measurement on thin film samples. With two-dimensional X-ray diffraction, stress measurement is based on a direct relationship between the stress tensor and diffraction cone distortion. The diffraction vectors cover more directions at each measurement and the diffraction vectors do not have to be distributed along a longitudinal direction, as is required for the conventional $\sin^2\psi$ method. In principle, data with diffraction vectors distributed in any direction can be used for stress calculation. This makes it possible to measure a set of diffraction data all at the same or within a small range of incident angles. Therefore, the depth of X-ray penetration can be controlled to reach a certain layer of the thin film or substrate. The stress gradient can be measured by measuring stresses at various incident angles. Figure 9.27 also illustrates the diffraction vector distribution with the XRD^2 method at low incident angles. The vector distribution depends on the incident angle and 2θ values. The figure shows one distribution for low 2θ angles and one for high 2θ angles. Either low or high 2θ angle peaks can be used for stress measurement with a low incident angle. With proper ϕ rotation, the diffraction vectors can have a good angular coverage for stress measurement.

Residual stress on TiO_2 films produced by microarc oxidation have been measured [31, 56, 57]. Samples numbered 1 to 4 are processed with pulsed DC power at a frequency of 100 Hz, duty ratio 20%, and a voltage of 240, 350, 400, and 450V respectively. The film thickness is about 5 μm. All four films contain anatase (TiO_2) and rutile (TiO_2), and the content of rutile (TiO_2) increases with increasing voltage. The residual stresses of the TiO_2 films are measured using the two-dimensional method with a fixed ω angle of 15°. This represents an incident angle of 15° at $\psi = 0$ and smaller than 15° at other ψ angles. Figure 9.30 shows one frame of the data as an example, in which the anatase (101) peak ($2\theta \approx 25.3°$) collected at an incident angle of 15° is used for stress calculation. The (101) peak ($2\theta \approx 40.2°$) of Ti from the same sets of data frames is used for stress measurement of the substrate at a lower depth of penetration. The (211) peak ($2\theta \approx 109.1°$) of Ti is used for stress measurement at a fixed ω angle of 54.5°. This represents an incident angle of 54.5° at $\psi = 0$ and is slightly smaller than 54.5° at other ψ angles. The measured results represent the residual stresses of the Ti substrate with larger depths of penetration. The results are summarized in Table 9.8.

The results show that all normal components of the residual stresses both from the substrates and the films are compressive. The in-plane shear stresses σ_{12} for all measurements are much less than the corresponding normal stress components σ_{11} and σ_{22}, and within the level of standard errors, so it can be concluded that all samples contain equibiaxial stresses. Residual stress values of the substrates measured with higher X-ray beam penetration are less than that with lower beam penetration. This is due to the stress gradient in the Ti substrates. The average standard error is 9% for Ti (211) and 12% for Ti (101). The residual stresses of TiO_2 film for sample #1 are about the same level of the standard error, and so can be considered trivial. The average standard error for TiO_2 films on sample #2 to #4 is 20%. The relatively weak diffraction intensity from the TiO_2 films is the major reason for the larger standard error.

The layer-removal technique is most commonly used to measure subsurface residual stress gradients [58–62]. Stress gradients within the maximum penetration depth can also be measured

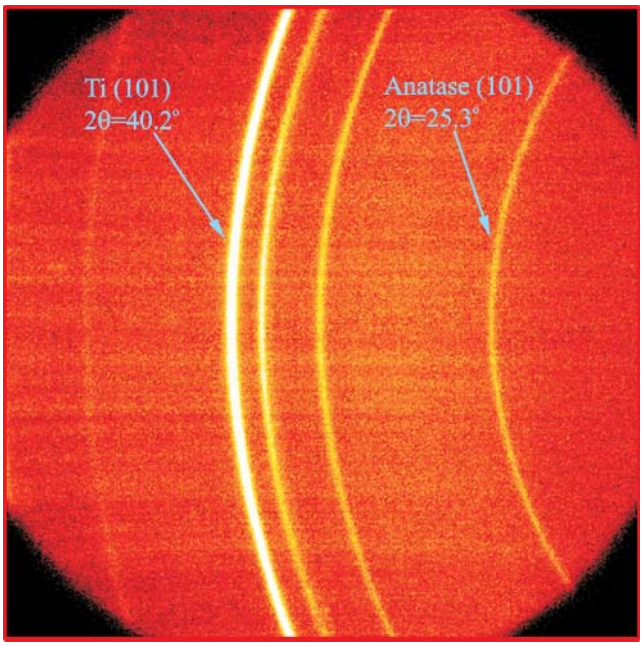


FIGURE 9.30 Anatase (101) and Ti (101) peaks collected at 15° incident angle used for stress measurement.

Table 9.8 Residual Stresses (MPa) of TiO_2 Films and Ti Substrates

Sample Stresses	#1: 240V			#2: 350V			#3: 400V			#4: 450V		
	σ_{11}	σ_{12}	σ_{22}	σ_{11}	σ_{12}	σ_{22}	σ_{11}	σ_{12}	σ_{22}	σ_{11}	σ_{12}	σ_{22}
TiO_2 film	−40	−20	−78	−341	−28	−237	−330	−51	−224	−640	131	−538
Ti (101)	−457	−1	−467	−331	−20	−331	−433	−30	−378	−646	253	−285
Ti (211)	−269	2	−315	−273	−26	−263	−332	−36	−285	−156	5	−90

non-destructively by using various incident angles. For two-dimensional diffraction with a given material, the X-ray penetration depth t depends on the linear absorption coefficient μ, the goniometer angles ω and ψ, Bragg angle 2θ, and the azimuthal angle γ. As an approximation, we only consider diffraction within the diffractometer plane and ignore the penetration dependence on γ. The fraction of the diffracted intensity G_t at the penetration depth t is given by [63]

$$G_t = 1 - \exp\left\{-\mu t\left[\frac{1}{\sin\omega\cos\psi} + \frac{1}{\sin(2\theta-\omega)\cos\psi}\right]\right\} \tag{9.118}$$

For a first order approximation, we can assume that the overall diffraction cone distortion contributed by each thickness element is proportional to the fraction of the diffracted intensity from that thickness element. Therefore the stress value at the penetration depth $\boldsymbol{t}$ corresponding to 50% of the total diffracted intensity is also the diffraction weighted average stress for the full penetration, assuming a linear stress depth gradient. In this case, $G_t = 0.5$ and

$$t = \frac{0.693\sin\omega\sin(2\theta-\omega)\cos\psi}{\mu[\sin\omega + \sin(2\theta-\omega)]} \tag{9.119}$$

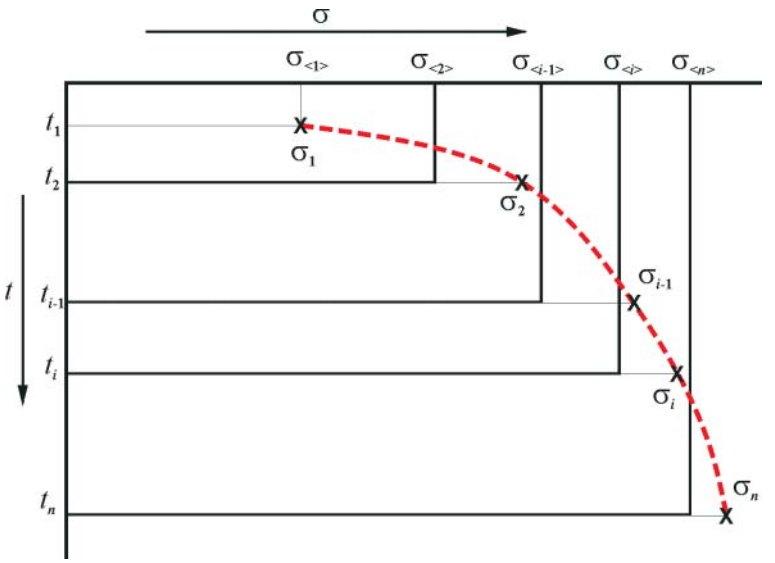


FIGURE 9.31 Measured average stress value $\sigma_{<i>}$ for each measurement depth t_i and the corresponding calculated stress value σ_i at the depth t_i.

As shown in Figure 9.31, with a series of incident angles we can have stress measured for $t_1, t_2, \cdots t_i \cdots t_n$ with t_1 corresponding to the lowest incident angle. The distribution above t extends to a much greater depth, so we only consider the stress distribution within each depth t_i. At t_1, we have

$$\sigma_1 = \sigma_{<1>} \tag{9.120}$$

We assume that the measured average stress in t_2 is a superposition of the contribution from the layers t_1 and $t_2 - t_1$, that is

$$\sigma_{<2>} = \sigma_{<1>}\left[1 - \exp\left(-\frac{t_1}{t_2}\right)\right] + \sigma_2 \exp\left(-\frac{t_1}{t_2}\right) \tag{9.121}$$

Then we have a general equation to calculate the stress value at depth t_i

$$\sigma_i = [\sigma_{<i>} - \sigma_{<i-1>}] \exp\left(\frac{t_{i-1}}{t_i}\right) + \sigma_{<i-1>} \tag{9.122}$$

The above equation is a rather simplified approximation. More sophisticated algorithms for stress depth profile analysis are available [58–62, 64, 65].

9.5.5 Residual Stress Measurement with Multiple {*hkl*} Rings

Since the diffraction frames collected with area detectors typically contains more than one diffraction ring, the stress can be calculated from diffraction rings from multiple {*hkl*} crystalline plane families. First, this will increase the number of available data points for stress calculation and so improve the sampling statistics. Second, due to the different orientation distributions from different {*hkl*} planes, the weak diffraction signal from one {*hkl*} plane is most likely compensated by a strong diffraction signal from another {*hkl*} plane. There are also many cases, such as thin films or

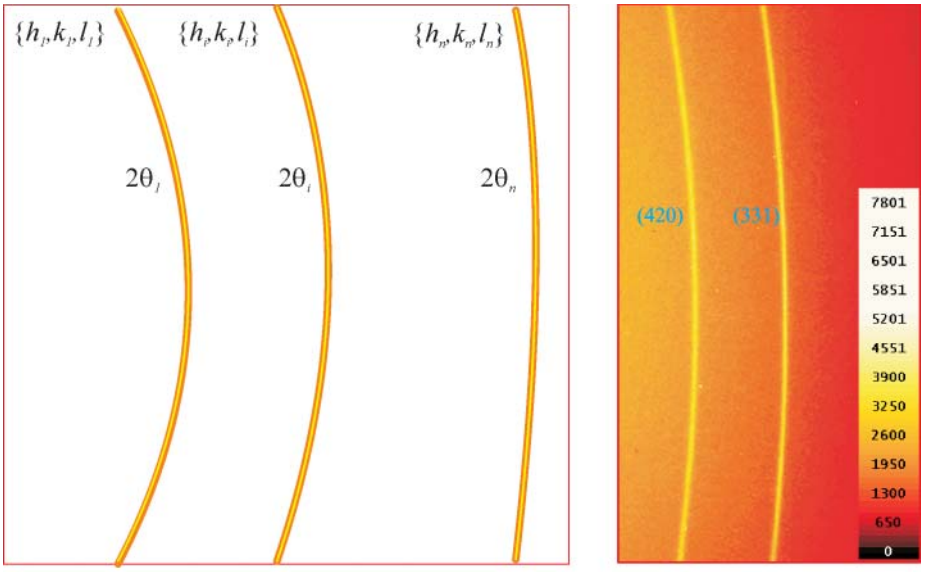


FIGURE 9.32 (a) Illustration of frame with multiple $\{hkl\}$ rings, (b) diffraction frame of Cu film containing (331) and (420) rings.

samples with strong texture, where multiple lines are necessary to get better stress measurement. The stress results are less impacted by preferred orientations and anisotropic elasticity. By using multiple diffraction rings, it is also possible to reduce the number of sample tilt angles without reducing the angular coverage. Figure 9.32(a) shows a sketch of a frame with multiple $\{hkl\}$ lines. The $2\theta_1$, $2\theta_i$, and $2\theta_n$ correspond to the diffraction rings from the crystalline planes $\{h_1, k_1, l_1\}$, $\{h_i, k_i, l_i\}$, and $\{h_n, k_n, l_n\}$, respectively. The approach to using multiple rings is to solve the stress components by putting the linear equations generated from multiple rings into one group and solving with a single least squares calculation. When multiple $\{hkl\}$ are used for the stress measurement, all the linear equations for all the stress state are the same as with a single $\{hkl\}$, except that there are different $2\theta_o$ values for each $\{hkl\}$ rings. The linear equation for biaxial stress with shear for the ith ring is given by

$$p_{11}\sigma_{11} + p_{12}\sigma_{12} + p_{22}\sigma_{22} + p_{13}\sigma_{13} + p_{23}\sigma_{23} + p_{ph}\sigma_{ph} = \ln\left(\frac{\sin\theta_{0i}}{\sin\theta_i}\right) \tag{9.123}$$

where θ_{0i} is the input stress free value for the $\{h_i, k_i, l_i\}$ ring. The linear equations are then generated for each $\{hkl\}$ ring at each data point and all linear equations are solved together by the least squares method. When multiple $\{hkl\}$ lines are used for stress calculation, it is most critical that the lattice symmetry and elastic anisotropy be consistent for all $\{hkl\}$ lines. For example, in a biaxial stress condition, the error of initial d_0 (or $2\theta_0$) values for each line should only create pseudo-hydrostatic (dilation or contraction) deformation, not a distortion. In order to maintain the same pseudo-hydrostatic stress component in the calculation, the initial stress free $2\theta_0$ values for all $\{hkl\}$s must be consistent with the crystal lattice structure. For instance, for a cubic crystal structure, the following relation should be maintained.

$$\frac{\sin\theta_{01}}{\sqrt{h_1^2 + k_1^2 + l_1^2}} = \cdots = \frac{\sin\theta_{0i}}{\sqrt{h_i^2 + k_i^2 + l_i^2}} = \cdots = \frac{\sin\theta_{0n}}{\sqrt{h_n^2 + k_n^2 + l_n^2}} \tag{9.124}$$

In order to make the initial d_0 (or $2\theta_0$) values consistent, only one $2\theta_0$ value for one $\{hkl\}$ ring should be used as initial stress free value, the stress free $2\theta_0$ values for other $\{hkl\}$ rings should be calculated based on the above relations. For cubic crystals, the $2\theta_0$ value for $\{h_1,k_1,l_1\}$ is used as initial input value, and the $2\theta_0$ values for other $\{hkl\}$ rings should be given as

$$\theta_{0i} = \arcsin\left\{\frac{\sqrt{h_i^2 + k_i^2 + l_i^2}}{\sqrt{h_1^2 + k_1^2 + l_1^2}} \sin\theta_{01}\right\} \quad i = 2,3, \ldots \quad n \tag{9.125}$$

For other non-cubic crystal lattices, the relation between θ_{0i} and θ_{01} are listed in Table 9.9. After all the data point for all the selected $\{hkl\}$ diffraction rings are processed, the stress can

Table 9.9 Equations of Dependent $2\theta_0$ for Stress Analysis with Multiple $\{hkl\}$ Rings

Crystal system	Equations
Cubic	$\theta_{0i} = \arcsin\left\{\frac{\sqrt{h_i^2 + k_i^2 + l_i^2}}{\sqrt{h_1^2 + k_1^2 + l_1^2}} \sin\theta_{01}\right\}$
Tetragonal	$\theta_{0i} = \arcsin\left\{\frac{\sqrt{h_i^2 + k_i^2 + (a/c)^2 l_i^2}}{\sqrt{h_1^2 + k_1^2 + (a/c)^2 l_1^2}} \sin\theta_{01}\right\}$
Hexagonal	$\theta_{0i} = \arcsin\left\{\frac{\sqrt{4h_i^2 + 4h_i k_i + 4k_i^2 + 3(a/c)^2 l_i^2}}{\sqrt{4h_1^2 + 4h_1 k_1 + 4k_1^2 + 3(a/c)^2 l_1^2}} \sin\theta_{01}\right\}$
Rhombohedral (trigonal)	$\theta_{0i} = \arcsin\left\{\frac{\sqrt{(h_i^2 + k_i^2 + l_i^2)\sin^2\alpha + 2(h_i k_i + k_i l_i + h_i l_i)(\cos^2\alpha - \cos\alpha)}}{\sqrt{(h_1^2 + k_1^2 + l_1^2)\sin^2\alpha + 2(h_1 k_1 + k_1 l_1 + h_1 l_1)(\cos^2\alpha - \cos\alpha)}} \sin\theta_{01}\right\}$
Orthorhombic	$\theta_{0i} = \arcsin\left\{\frac{\sqrt{h_i^2 + (a/b)^2 k_i^2 + (a/c)^2 l_i^2}}{\sqrt{h_1^2 + (a/b)^2 k_1^2 + (a/c)^2 l_1^2}} \sin\theta_{01}\right\}$
Monoclinic	$\theta_{0i} = \arcsin\left\{\frac{\sqrt{\frac{h_i^2}{a^2} + \frac{k_i^2 \sin^2\beta}{b^2} + \frac{l_i^2}{c^2} - \frac{2h_i l_i \cos\beta}{ac}}}{\sqrt{\frac{h_1^2}{a^2} + \frac{k_1^2 \sin^2\beta}{b^2} + \frac{l_1^2}{c^2} - \frac{2h_1 l_1 \cos\beta}{ac}}} \sin\theta_{01}\right\}$
Triclinic	$\theta_{0i} = \arcsin\left\{\frac{\sqrt{\frac{h_i^2}{a^2}\sin^2\alpha + \frac{k_i^2}{b^2}\sin^2\beta + \frac{l_i^2}{c^2}\sin^2\gamma + \frac{2k_i l_i}{bc}(\cos\beta\cos\gamma - \cos\alpha) + \frac{2l_i h_i}{ca}(\cos\gamma\cos\alpha - \cos\beta) + \frac{2h_i k_i}{ab}(\cos\alpha\cos\beta - \cos\gamma)}}{\sqrt{\frac{h_1^2}{a^2}\sin^2\alpha + \frac{k_1^2}{b^2}\sin^2\beta + \frac{l_1^2}{c^2}\sin^2\gamma + \frac{2k_1 l_1}{bc}(\cos\beta\cos\gamma - \cos\alpha) + \frac{2l_1 h_1}{ca}(\cos\gamma\cos\alpha - \cos\beta) + \frac{2h_1 k_1}{ab}(\cos\alpha\cos\beta - \cos\gamma)}} \sin\theta_{01}\right\}$

be calculated by least square regression of the linear equation (9.123) or equivalent for selected stress state with $\ln\left(\frac{\sin\theta_0}{\sin\theta}\right)$ replaced by $\ln\left(\frac{\sin\theta_{0i}}{\sin\theta_i}\right)$ $i = 1,2,\cdots n$ respectively.

If the anisotropic effect on the elastic constants is considered, the X-ray elastic constants (XEC), $\frac{1}{2}S_2\{hkl\}$ and $S_1\{hkl\}$ for each $\{hkl\}$ ring should be used in the stress coefficients, p_{ij} and p_{ph}.

An example is given of stress measurement on a Cu film using a 1.4Å synchrotron beam and a CCD detector. A highly textured Cu film with a thickness of 1 μm is deposited on a proprietary substrate. The stress calculations with a single (331) or (420) peak and combined analysis with both peaks are compared. Figure 9.32(b) is part of a diffraction frame collected in 30 seconds with the sample mounted on a loading stage. The data frames are collected at various levels of loading. At each loading level, two frames are collected for each stress measurement at $\omega = 106.1°$ and 79.5°. The frame contains two diffraction rings for the (331) and (420) planes. The macroscopic elastic constants for Cu are $E = 129{,}800$ MPa and $\nu = 0.343$. Based on the anisotropic factor $A_{RX} = 1.09$, the anisotropic elastic constants are $S_1\{331\} = -2.576 \times 10^{-6}$/MPa, $\frac{1}{2}S_2\{331\} = 1.015 \times 10^{-5}$/MPa, $S_1\{420\} = -2.678 \times 10^{-6}$/MPa and $\frac{1}{2}S_2\{420\} = 1.045 \times 10^{-5}$/MPa. Figure 9.33 shows the data analysis setting

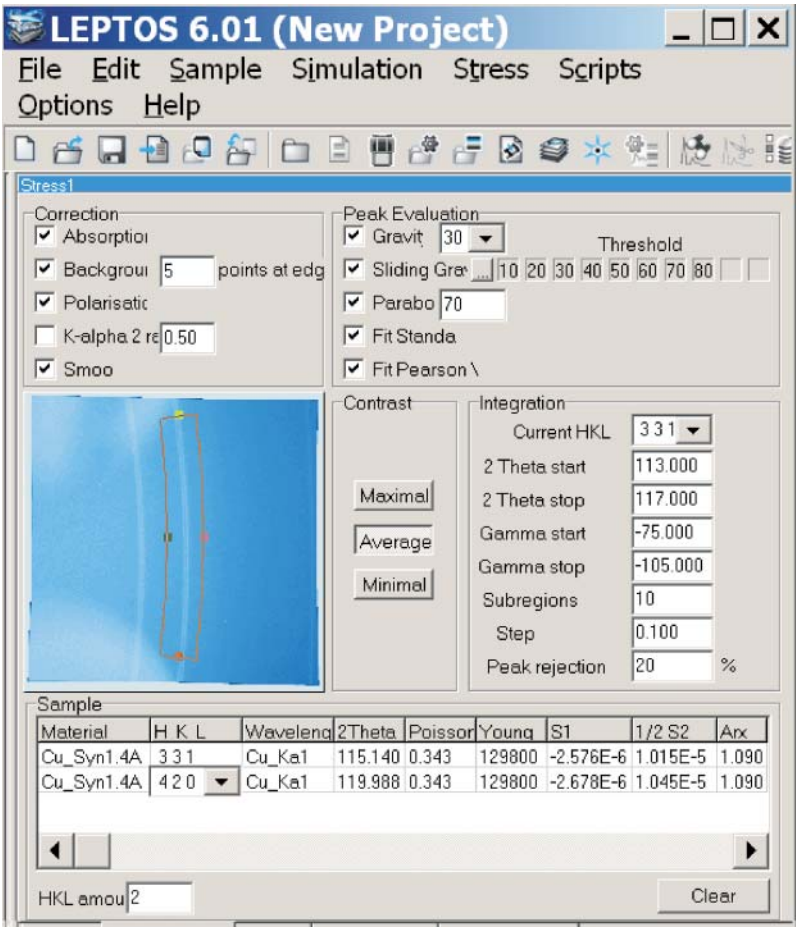


FIGURE 9.33 Data integration region and stress calculation settings with LEPTOS software (Bruker AXS).

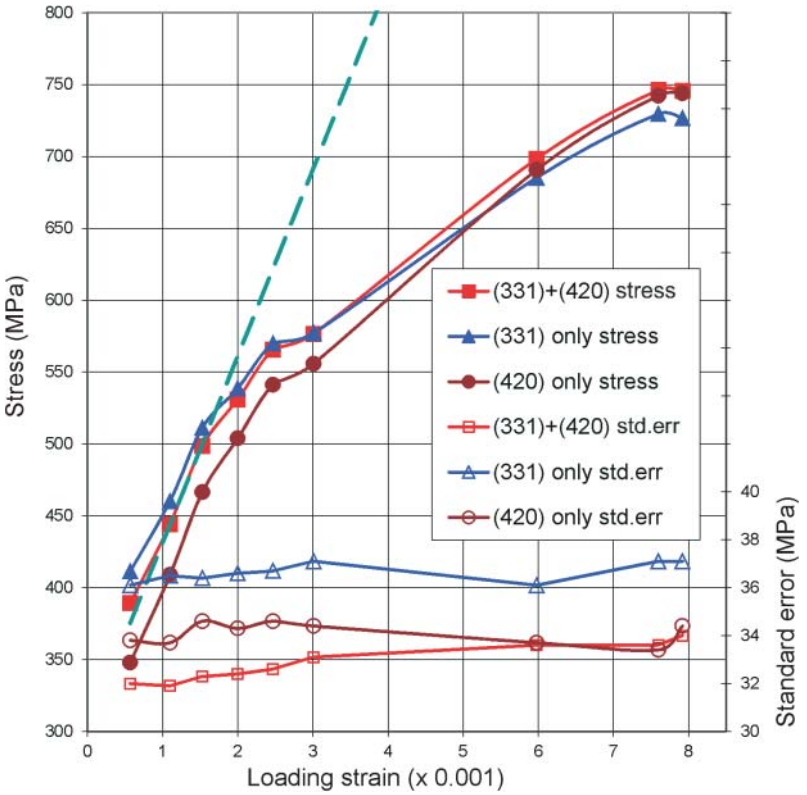


FIGURE 9.34 Stresses of Cu film measured at various loading strains.

for both (331) and (420) with the Bruker LEPTOS™ version 6.01 software. The integration range of (331) is displayed. The range for (420) is the same except at a different 2θ range of 118–122°.

Figure 9.34 shows the stress values measured at various loading strains. The three solid lines on top of the chart are stress values evaluated from three different settings, one from (331) ring only, one from (420) ring only, and one from both (331) and (420) rings. The three lines follow the same trend with increasing loading. The discrepancy between (331) and (420) are most likely from anisotropic elasticity, even though the anisotropic factor of 1.09 has been introduced. The standard deviations are displayed in the corresponding colors with the scale on the right. The standard error for the (331)+(420) case is relatively smaller than for (331) or (420) only. Considering the least squares regression for the combined (331)+(420) data points has to cover the systematic discrepancy between the two rings, the statistical error for (331)+(420) is actually much smaller than either (331) or (420).

The initial part of the stress vs. loading strain shows a linear trend. The dashed line follows the linear part of the relationship between the stress and loading strain from data points from combined (331)+(420) evaluation. The linear relation is maintained up to approximately 500 MPa which corresponds to the yielding point of the Cu film. This is slightly higher than the yield strength (471 MPa) given by the empirical equation obtained from a series of stress–strain curves of Cu thin films of various thickness on polyimide substrate measured by the microtensile tester [66]. The discrepancy is likely due to the Young's modulus of the thin film being typically about

20% lower than the value of single crystal Cu. The residual stress without loading was not measured, but can be estimated by the extrapolation as 320 MPa.

9.5.6 Single Tilt Method

Due to the large angular coverage with a 2D detector, residual stress may be measured with a single ψ tilt angle. The single tilt method can avoid the sample height error associated to ψ rotation, which is especially critical when measuring stress with a low 2θ peak. Another advantage is the consistent depth of penetration due to a constant incident angle, which is beneficial for stress measurement on thin films or samples with steep stress gradient. Generally, high 2θ peaks are preferred for stress measurement due to the more significant 2θ shift and being less sensitive to the sample height error. But for thin films, coatings, or polymer materials, high 2θ peaks may not be available or appropriate for stress measurement. With low 2θ peaks, it is difficult or even impossible to measure stress with the conventional $\sin^2\psi$ method. With the iso-inclination method, there is only limited angular range for the tilt. The tilt angle has to be smaller than θ to have the incident beam or diffracted beam above the sample surface. With the side-inclination method, the actual incident angle to the sample surface is further reduced, and the measurement results become extremely sensitive to the sample height error.

Figure 9.35 illustrates the diffraction vector distribution for the diffraction pattern collected with a point (0D) detector and a 2D detector. The hemisphere represents all the possible orientations from the origin O of the sample coordinate $S_1S_2S_3$. With a point detector, at $\psi = 0°$, the diffraction vector points to the sample normal direction N. In order to measure stress, the sample has to be tilted at several ψ angles, for instance 0°, 15°, 30°, and 45°, as indicated by the purple mark ⊗. With a 2D detector, the trace of the diffraction vector covers a range as shown by the red curve. The diffraction vectors $\mathbf{H_1}$ and $\mathbf{H_2}$ correspond to the two extreme values of γ_1 and γ_2 on the diffraction ring covered by the 2D detector, $\Delta\psi$ is the total angular range of the diffraction vector distribution, and $\Delta\gamma$ is the γ range. With a single tilt of ψ, for example 22.5°, the diffraction vector covers a range as shown by the green curve. For low 2θ diffraction rings at proper

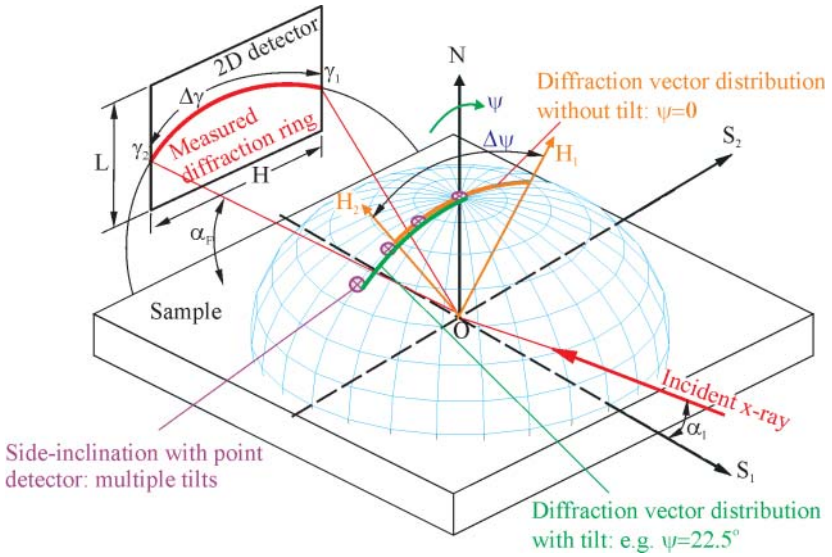


FIGURE 9.35 Diffraction vector distribution for 0D and 2D detectors.

detector distance, it is possible to cover sufficient angular range for stress evaluation with a single tilt. The complete data set for the stress tensor can be collected at several ϕ angles, for instance a 360° scan with 45° steps. Therefore the complete data set is collected with ϕ scan only at a fixed ψ angle. For most goniometers with Eulerian geometry, the ϕ axis is typically built on a precision bearing with very small spherical error, while ψ rotation is achieved by a circular track which tends to have much more significant spherical error. Avoiding ψ rotation can significantly reduce the sample height variation during data collection, therefore improving the measurement accuracy.

The diffraction vector distribution range ($\Delta\psi$) is determined by the detector distance D, detector height H, detector width L, Bragg angle 2θ, and swing angle α. In order to get $\Delta\psi$ coverage for a flat detector, the γ_1 and γ_2 are first calculated from the following two implicit equations:

$$H(\cos\alpha\cos 2\theta - \sin\alpha\sin 2\theta\sin\gamma_1) + 2D\sin 2\theta\cos\gamma_1 = 0 \tag{9.126}$$

$$H(\cos\alpha\cos 2\theta - \sin\alpha\sin 2\theta\sin\gamma_2) - 2D\sin 2\theta\cos\gamma_2 = 0 \tag{9.127}$$

Then, $\Delta\psi$ can be calculated from $\Delta\gamma = |\gamma_2 - \gamma_1|$ by

$$\Delta\psi = 2\arcsin[\cos\theta\sin(\Delta\gamma/2)] \tag{9.128}$$

It can be seen that this is the same equation as for the virtual oscillation. In a typical measurement configuration with a flat 2D detector, the swing angle, either positive or negative, is set in the vicinity of 2θ ($|\alpha| = 2\theta$), so that the aberration between the flat detector and cylindrical detector is small, especially when detector size H is smaller than D. In this case, $\Delta\gamma$ for the flat detector can be approximated from the equation for cylindrical detector with negligible error. For a cylindrical detector, $\Delta\gamma$ can be given by

$$\Delta\gamma = 2\arcsin\frac{H}{\sin 2\theta\sqrt{4D^2 + H^2}} \tag{9.129}$$

where D is used for the radius of the cylindrical detector because it is equivalent to the sample-to-detector distance for a flat detector.

Combining the above equation with equation (9.128), we have

$$\Delta\psi = 2\arcsin\left(\frac{H}{2\sin\theta\sqrt{4D^2 + H^2}}\right) \tag{9.130}$$

The measured γ range may be limited by the detector width L if the diffraction ring is cut off at the side edge of the detector, especially for low 2θ rings and the detector width significantly smaller than the detector height H ($L \ll H$). When the γ range is limited by the detector width, $\Delta\gamma$ is given by

$$\Delta\gamma = 2\arccos\frac{\cos 2\theta(2D\sin\alpha + L\cos\alpha)}{\sin 2\theta(L\sin\alpha - 2D\cos\alpha)} \tag{9.131}$$

Combining with equation (9.128), we have

$$\Delta\psi = 2\arcsin\left\{\cos\theta\sin\left[\arccos\frac{\cos 2\theta(2D\sin\alpha + L\cos\alpha)}{\sin 2\theta(L\sin\alpha - 2D\cos\alpha)}\right]\right\} \tag{9.132}$$

Figure 9.36(a) shows the diffraction vector distribution range $\Delta\psi$ as a function of 2θ calculated for flat 2D detector and cylindrical detector. Both the detector distance of the flat detector

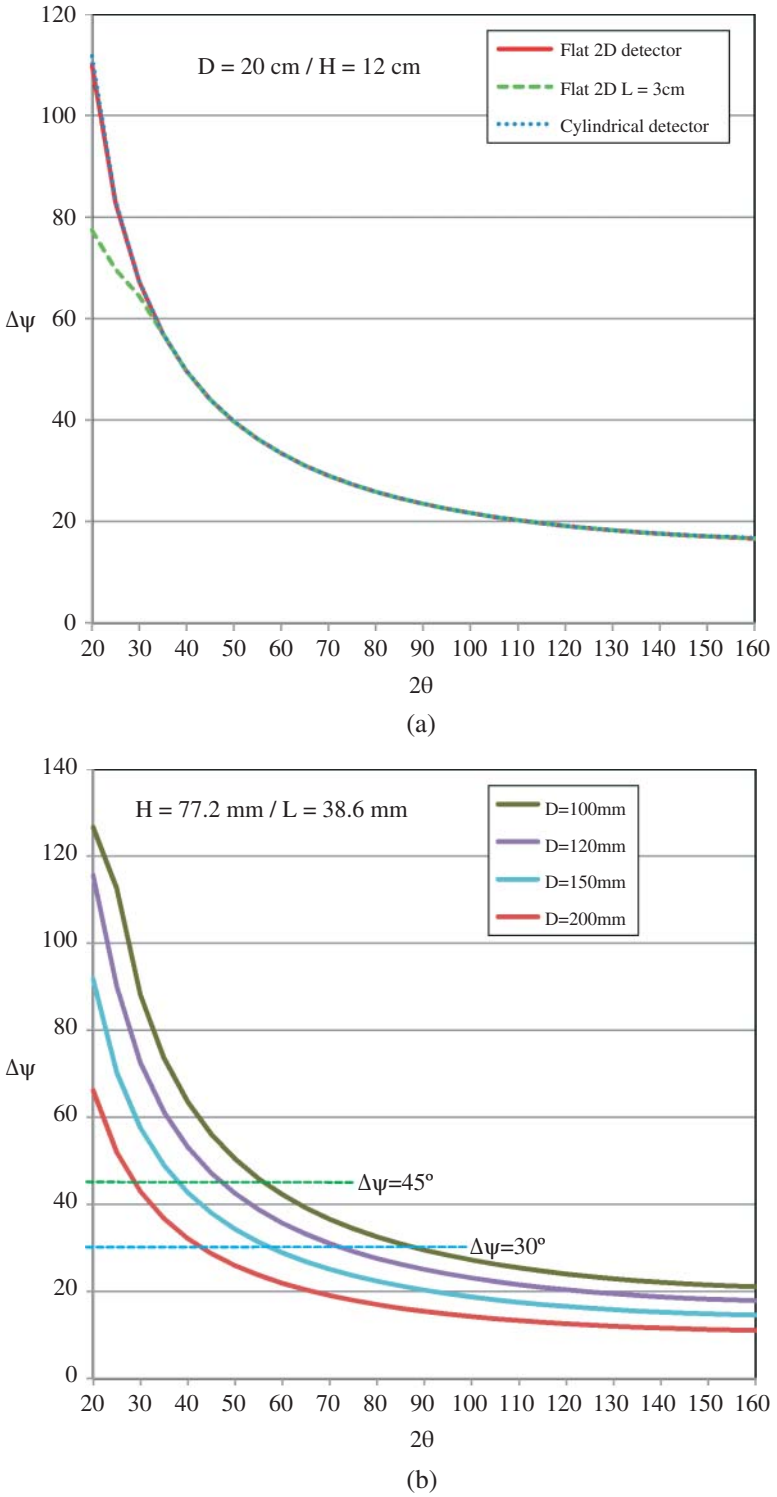


FIGURE 9.36 Diffraction vector distribution range $\Delta\psi$ as a function of 2θ: (a) for flat 2D detector and cylindrical detector, (b) for Eiger 2R 500k™ detector in γ-optimized orientation.

and the radius of the cylindrical detector are 20 cm and the detector height (perpendicular to the diffractometer plane) is 12 cm for both detectors. It can be seen that the two plots are almost identical. This is true as long as the detector width L for the flat detector is more than 6 cm. For a flat detector with $L = 3$cm and $|\alpha| = 2\theta$, the $\Delta\psi$ coverage is reduced in the low 2θ region as shown by the green curve. For a detector with small width L, the $\Delta\psi$ coverage can be increased by using a smaller swing angle α within the range of

$$2\theta - \arctan\frac{L}{2D} < |\alpha| < 2\theta \tag{9.133}$$

Figure 9.36(b) shows the diffraction vector distribution range $\Delta\psi$ as a function of 2θ calculated for the Eiger 2R 500k™ detector at various detector distances and in γ-optimized orientation ($H = 77.2$ mm and $L = 38.6$ mm). The $\Delta\psi$ vs. 2θ plot can be calculated from the equation for cylindrical detector with negligible error. For stress measurement with single tilt, $\Delta\psi$ of more than 30° is acceptable, but the most desirable $\Delta\psi$ coverage is 45° or above. A shorter detector distance can be used to increase $\Delta\psi$. In general, the angular coverage $\Delta\psi$ is significantly higher with low 2θ angles. Therefore, the single tilt method is more suitable for middle or low 2θ angles.

With a ψ tilt, the incident angle is given by

$$\alpha_I = \arcsin(\sin\omega\cos\psi) \tag{9.134}$$

The exit angle α_F varies with the γ value:

$$\alpha_F = \arcsin(-\cos 2\theta \sin\omega\cos\psi - \sin 2\theta \sin\gamma\cos\omega\cos\psi - \sin 2\theta\cos\gamma\sin\psi) \tag{9.135}$$

where α_F has a positive value for the reflection mode diffraction. Although the exit angle varies, it may affect the scattering intensity along γ, but not the stress evaluation since the shift of 2θ is evaluated at the same γ value for each data point. The ϕ rotation during the data collection does not change the incident angle and exit angles, so the depth of penetration is consistent.

Figure 9.37 illustrates the single tilt scheme generated with GADDS software. The left (a) is for PE polymer (020) with $2\theta = 36.3°$, $\psi = 22.5°$, and detector to sample distance $D = 20$ cm and the right (b) is for Al_2O_3(116) with $2\theta = 57.5°$, $\psi = 22.5°$, and $D = 15$ cm. The arcs represent the trace of the diffraction vector corresponding to the data set, and S_1 and S_2 are two sample orientations. The red broken curve marks the diffraction vector distribution covered by the frame collected at $\phi = 0$. With eight frames collected with complete ϕ rotations at 45° intervals, the scheme produces comprehensive coverage on the scheme chart in a symmetric distribution. The data set collected with this strategy can be used to calculate the complete biaxial stress tensor components. Since the diffraction ring collected by each frame covers the vector direction distribution from near the sample normal to the high tilt angle near 45°, the stress measurement with single tilt method is very sensitive to the detector roll error. The roll error of the detector should be measured and corrected before the data collection.

The residual stress in the Al_2O_3 coating of less than 1 μm thick on a proprietary cutting insert is measured with a Bruker D8-Discover system containing a centric Eulerian cradle and Våntec-500 2D detector. With Cu-K_α radiation, the diffraction ring from (116) planes at $2\theta = 57.5°$ is used for stress evaluation. The stress calculation is done with Bruker DIFFRAC.LEPTOS software version 7.9. Figure 9.38 shows the data evaluation setting. The data integration region is defined by 2θ range of 56° to 59° and γ range of −65° to −115°. The 50° γ range is divided into 10 subregions, 5° for each subregion. The counts within each subregion are integrated into a diffraction profile and the 2θ peak position is determined by one of the five peak evaluation algorithms. In this

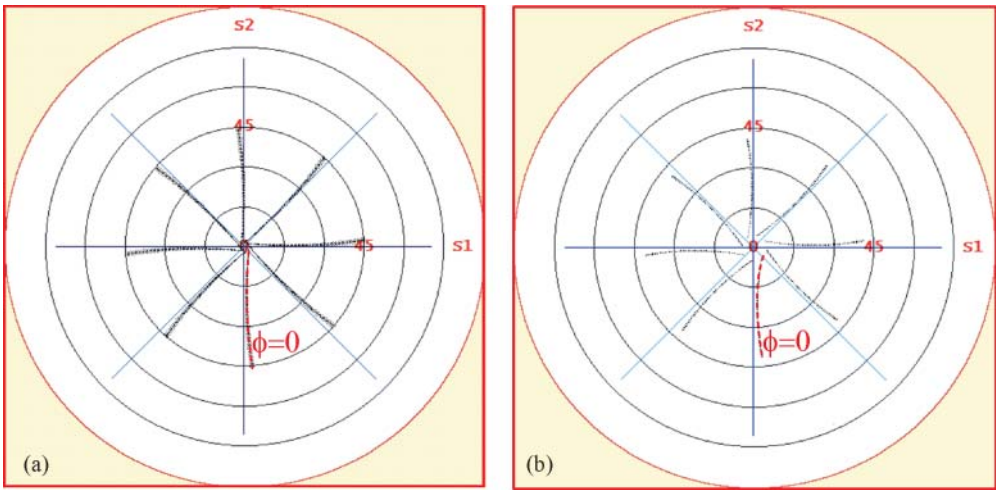


FIGURE 9.37 Data collection strategy schemes with single tilt at $\psi = 22.5°$ and complete ϕ rotation of 45° steps: (a) PE polymer (020), $2\theta = 36.3°$ and $D = 20$ cm, (b) Al_2O_3(116), $2\theta = 57.5°$ and $D = 15$ cm.

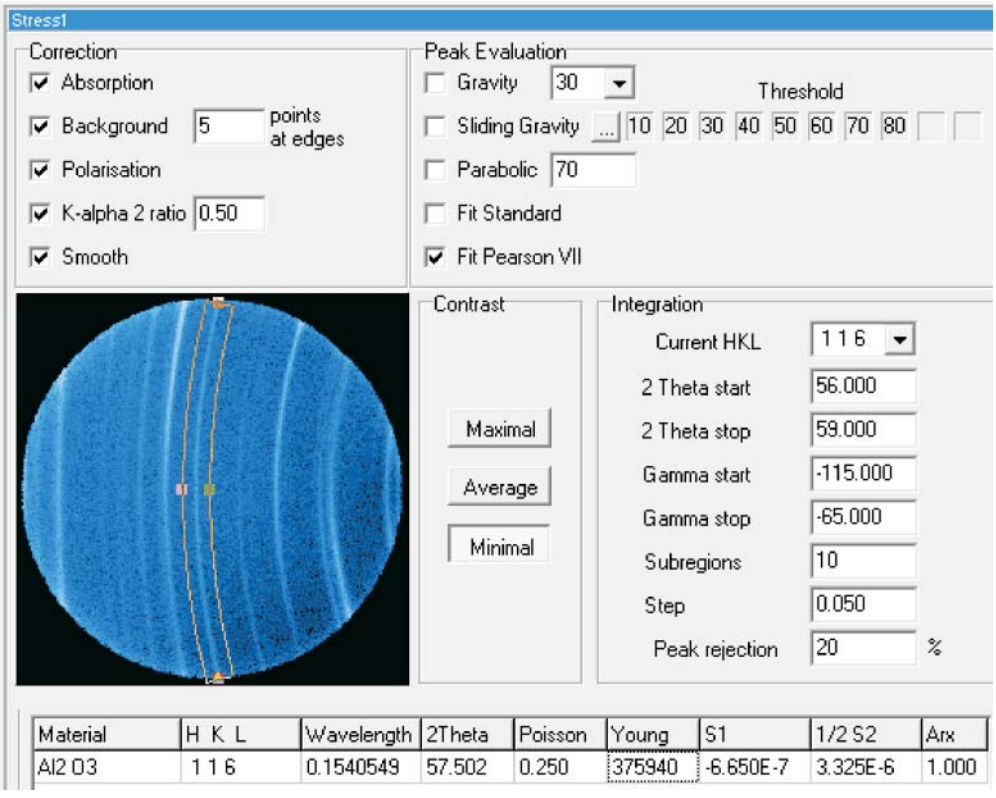


FIGURE 9.38 Data evaluation setting with LEPTOS software for 1 μm thick Al_2O_3 coating on cutting insert.

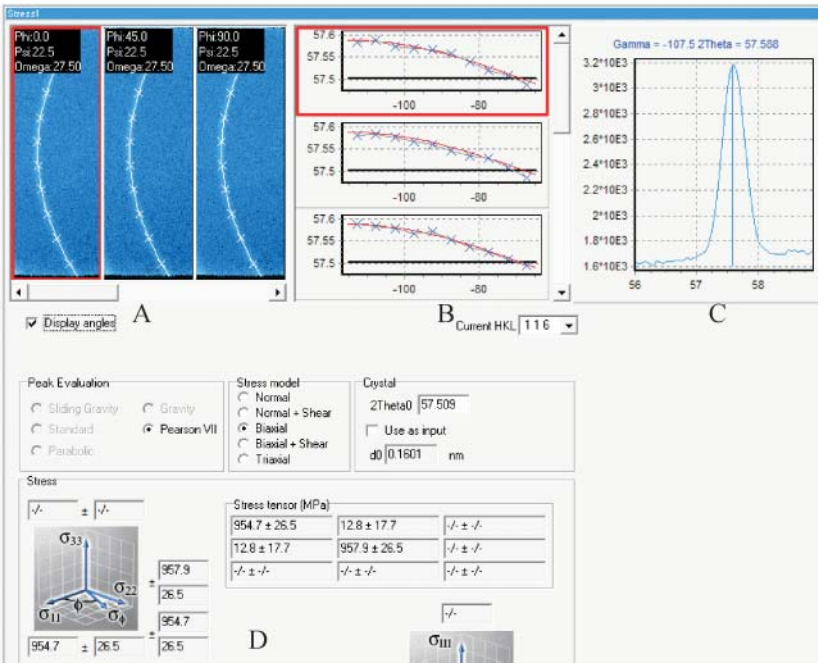


FIGURE 9.39 Data evaluation results with LEPTOS software for 1 μm thick Al_2O_3 coating on cutting insert.

experiment, the Pearson VII function is used to fit the profile and evaluate the 2θ peak position. Figure 9.39 shows the stress evaluation results from one of the data sets. The charts above "A" are the fitted data points on 2D frames. The charts above "B" are the fitted data points in γ-2θ rectangular coordinates with magnified 2θ scale, in which, the black line indicates $2\theta_0$, the blue cross and line indicate the data points from the profile fitting of each subregion, and the red line represents the calculated diffraction rings from the stress results. The scattering of the crosses about the red line represents the quality of the data, affecting the standard deviation of the stress results. Any roll error of the detector will change the trend of the fitted data points and the red line, thus the stress results. By clicking on any data point, the integrated profile displays above "C". With 60 seconds per frame, the total data collection time is 8 minutes. The measured stress values are given in the region "D" as $\sigma_{11} = 954.7$ MPa, $\sigma_{22} = 957.9$ MPa, and standard deviation 26.5 MPa (<3%).

The single tilt stress measurement method is especially suitable for measuring residual or loading stresses in polymers. For stress measurement by X-ray diffraction, the polymer sample must contain sufficient crystalline phase. The crystalline peaks from polymers are typically at low 2θ angles. For instance, polyethylene (PE) polymer contains mainly three diffraction rings at 2θ about 21.4°, 23.6°, and 36.3° with Cu-K_α radiation, corresponding to crystalline planes of (110), (200), and (020) respectively. Even with the 36.3° peak, a large error in the stress result can be introduced by the sphere of confusion with multiple sample tilt angles. The single tilt method can overcome this problem. One other challenge for stress measurement on polymers is the low stress value. However, due to the extremely low Young's modulus, such as 1070 MPa for high density polyethylene, the 2θ shift (strain) is also more significant for the same stress when compared to metals. Due to the large depth of penetration, the zero normal stress assumption ($\sigma_{33} = 0$ on sample surface) for polymers may not be as accurate as for metals.

Residual stresses on a high-density polyethylene (HDPE) pipe are measured with the single tilt method [67]. An XRD^2 system in vertical θ-θ configuration (Bruker D8-Discover™) with IμS™ Cu microsource and Våntec-500™ 2D detector is used for the measurement. The HDPE pipe has a diameter of 32 mm and wall thickness of 3 mm. The length of the sample is 50 mm, cut from a pipe. Residual stresses of a total seven points in the outer surface of the pipe and along the axial direction were measured. To avoid the relaxation effect near the cutting edges, the measurement starts at 10 mm from one end with 5 mm steps and completes at the last point 10 mm from the other end. A total of eight frames are collected for each measurement point with the data collection strategy given in Figure 9.37(a). Figure 9.40 shows the data evaluation setting and fitting results with LEPTOS software for one of the measurement point. The measured stresses are tensile in the pipe extrusion direction with variation of 1.3~2.2 MPa over the seven points, and compressive in the hoop direction with variation of 6.5~8.1 MPa.

In summary, for thin films, coatings, or polymers, when the diffraction peaks at high 2θ angles are not available or not appropriate, a low 2θ peak may be used for stress evaluation. With diffraction rings at low 2θ angle, the diffraction vector distribution can satisfy the angular coverage for stress or stress tensor measurement at a fixed tilt angle (ψ). Without ψ changing during data collection and with ϕ rotation only, the sample height is accurately maintained and data collection

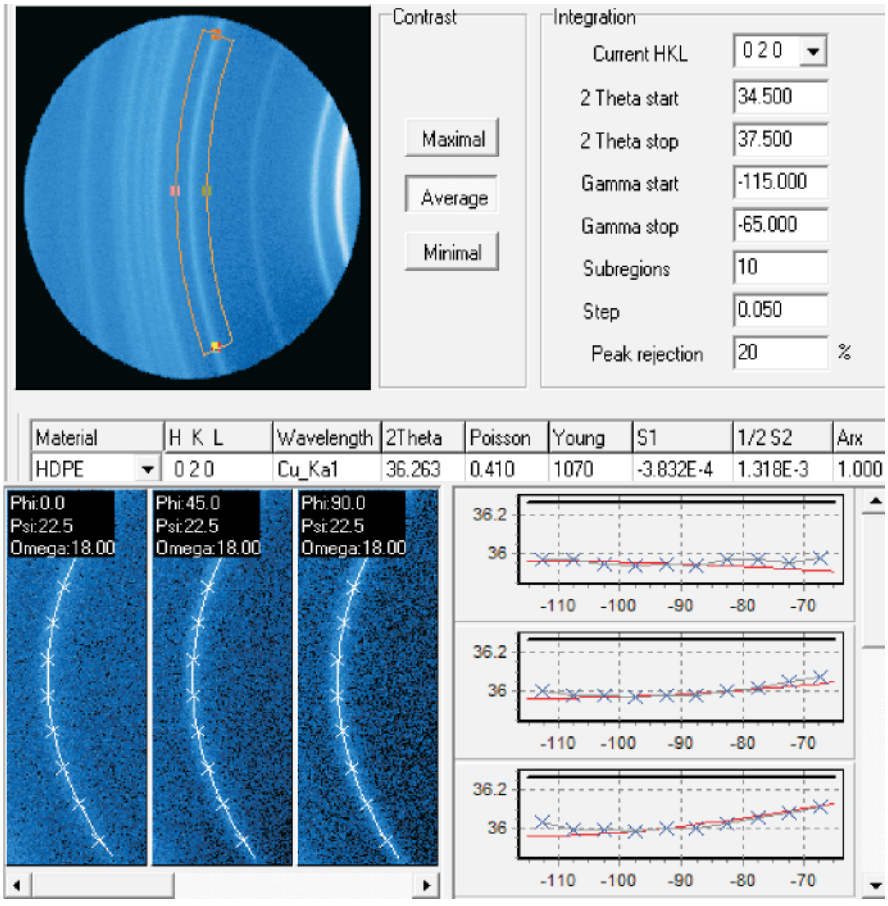


FIGURE 9.40 Data evaluation setting and fitting results with LEPTOS software for the HDPE pipe.

time is reduced. The single tilt method is a unique method only achievable with an XRD^2 system, which can measure residual stress with high accuracy and high speed for thin films, coatings, and polymers with low to medium 2θ peaks.

9.5.7 Gage Repeatability and Reproducibility Study

The gage repeatability and reproducibility (gage R&R or GRR) test has long been accepted as a standard by many industries, especially by the automotive industry [68–70]. Gage R&R is a statistical quality control method for evaluating the precision of a measurement system. By evaluating large amounts of measurements performed by several operators (appraisers) on a certain number of parts several times (trials), it produces a report that estimates the variation and percentage variation for a measurement system on its repeatability, reproducibility, part-to-part variation, and variation of the total system.

The residual stress measurement system evaluated in this study is the Bruker GADDS™, a two-dimensional X-ray diffraction (XRD^2) system [71, 72]. The system can measure residual stress with one of two approaches: the conventional approach and two-dimensional (2D) approach. The measurements were done with the following configuration: Cr-K_α radiation ($\lambda = 2.2897$ Å); generator power 35 kV/50 mA; 0.5 mm collimator with front pinhole only. The stress measurement parameters are: $2\theta_0 = 156°$ for (211) peak, $E = 210{,}000$ MPa, $\nu = 0.28$, $A_{RX} = 1.49$. For each stress measurement, seven frames were taken at $\psi = -45°$, $-30°$, $-15°$, 0, 15°, 30°, and 45° ($\omega = 57°$ to 147° with 15° steps). The data collection time is 1 minute per frame, 7 minutes for one stress measurement. The diffraction system was first calibrated with a stress-free sample. The measured stress with the stress-free sample was 0 ± 12 MPa. The calibration shows that the system was appropriately aligned.

Ten Almen strips were used for the residual stress measurement. The Almen strips have a hardness of 55 HRC and had been shot peened on both faces for 30 minutes with S170 cast steel shot. The samples were loaded by three operators, and each sample was measured three times by each operator. A total of 90 stress measurements were taken. There are four peak fitting methods available in the stress software program that use the conventional $\sin^2\psi$ method. The discrepancies between different fitting methods are observed. For example, the stress values for sample 1, trial 1 by operator A are -647, -649, and -643 MPa for gravity, sliding gravity, and curve-fitting methods, respectively. The discrepancy between the conventional method and the 2D method is also very small. The stress value calculated from the same data using the 2D method with a Gaussian fit is -644 MPa. The correlation between the conventional ($\sin^2\psi$) method and the 2D method for the 10 samples is shown in Figure 9.41. For consistency, the stress values from the curve-fitting method were used for the gage R&R test. The average for all 90 measurements is -627.8 ± 19.4 MPa. The average standard deviation is 3.1% of the average stress value.

The gage R&R test condition consists of three operators (appraisers), ten parts and three trials. The individual range value R_1 for each sample, under each operator, is calculated by the maximum of (trial 1, trial 2, trial 3) minus the minimum of (trial 1, trial 2, trial 3). The average range for each operator, R_{A1}, R_{B1} and R_{C1} is calculated by averaging all ten R_1 values for each operator. The equations for the gage R&R test are summarized below [70, 72, 73].

Repeatability – Equipment variation (*E.V.*) is the variation in measurements obtained by an instrument (gage) when it is used several times by one operator while measuring identical parameter on the same parts:

$$E.V. = \bar{R} \times K_1 \tag{9.136}$$

where $\bar{R}$ is the average of ranges for all operators, $K_1 = 3.05$ for three trials.

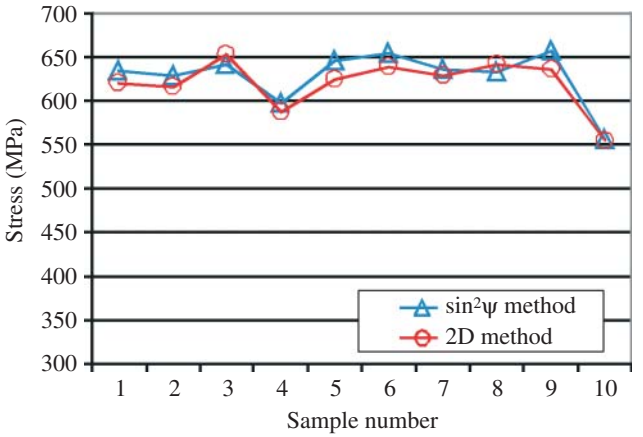


FIGURE 9.41 Stress values calculated by the conventional method and the 2D method from the ten samples, averaged over nine measurements for each sample.

Reproducibility – Appraiser Variation (*A.V.*) is the variation on the average of the measurements made by different operators using the same instrument while measuring identical characteristic on the same parts:

$$A.V. = \sqrt{(\bar{X}_{diff} \times K_2)^2 - (\text{E.V.})^2/nt} \tag{9.137}$$

where $\bar{X}_{diff}$ is the range of average values measured by each operator, $K_2 = 2.70$ for three operators, and $n = 10$ is the number of parts, $t = 3$ is the number of trials.

Gage accuracy (measurement error) – Repeatability and reproducibility (*R&R*) is the measurement system error, which determines the possible difference between the measured values and the "true values". *R&R* is a combination of repeatability (*E.V.*) and reproducibility (*A.V.*)

$$R\ \&\ R = \sqrt{(\text{E.V.})^2 + (\text{A.V.})^2} \tag{9.138}$$

Part variation (*P.V.*) is the variation of the average of the measurements made for different parts or samples. This variation is caused by the differences of the "true values" between different parts. *P.V.* does not represent the accuracy of the measurement system, but it does contribute to measurement variation:

$$P.V. = \sqrt{(\bar{R}_p \times K_p)^2 - (\text{E.V.})^2/t} \tag{9.139}$$

where $\bar{R}_p = (R_{A2} + R_{B2} + R_{C2})/3$, and R_{A2} , R_{B2} , and R_{C2} are ranges of part averages for each operator. $K_p = 1.66$ for ten parts with three trials.

Total variation (*T.V.*) is the total measurement variation due to the measurement system error and the part (sample) variation. *T.V.* is a combination of *R&R* and *P.V.:*

$$T.V. = \sqrt{(\text{E.V.})^2 + (\text{A.V.})^2 + (\text{P.V.})^2} \tag{9.140}$$

All the stress measurement results and gage R&R test results are listed in Table 9.10. Since the sign of the stress has no effect on the gage R&R test, all stress values referred to are in absolute values without negative signs. The results show that the measurement system error

Table 9.10 Gage R&R Test Results from Ten Sample by Three Operators for Three Measurements

	Operator A			Operator B			Operator C		
Part #	Trial 1	Trial 2	Trial 3	Trial 1	Trial 2	Trial 3	Trial 1	Trial 2	Trial 3
1	643	651	655	625	629	623	619	632	627
2	627	611	618	633	637	625	636	633	631
3	634	638	638	633	644	624	657	649	652
4	586	584	577	590	598	589	610	624	615
5	657	644	647	638	654	639	639	639	649
6	665	658	655	669	660	658	639	640	640
7	637	635	642	653	655	649	603	625	617
8	620	616	620	638	643	633	637	645	642
9	651	655	669	644	655	651	676	657	651
10	561	557	557	536	511	525	592	581	580
Repeatability		Reproducibility		Part variation		Total variation		R&R	
E.V. =	34.67	*A.V.* =	14.52	*P.V.* =	173.89	*T.V.* =	177.91	*R.R.* =	37.59
%T.V. =	19.49%	%T.V. =	8.16%	%T.V. =	97.74%	Avg. =	627.84	%T.V. =	21.13%
% Avg =	5.52%	% Avg =	2.31%	% Avg =	27.70%	% Avg =	28.34%	% Avg =	5.99%

(R&R) is 37.6 MPa, which is 6% of the average residual stress value (627.8 MPa) for all 90 measurements. The two components of the R&R value are: repeatability (*E.V.*) = 34.7 MPa and reproducibility (*A.V.*). = 14.5 MPa. The total variation (*T.V.*) is large (177.9 MPa); however, the majority of it comes from the part variation (*P.V.*). Taking the total measurement variation (*T.V.*) as 100%, the part variation (P.V.) is 97.7%, the measurement system error (*R&R*) is 21.1%. It must be noted that all component variations do not simply add up to 100% due to the square-root relation.

APPENDIX 9.1 CALCULATION OF PRINCIPAL STRESSES FROM THE GENERAL STRESS TENSOR

A9.1.1 Calculate Principal Stresses

The principal stress components, σ_{I}, σ_{II}, and σ_{III}, also called eigenvalues, can be calculated from the tensor:

$$\begin{bmatrix} \sigma_{11} & \sigma_{12} & \sigma_{13} \\ \sigma_{12} & \sigma_{22} & \sigma_{23} \\ \sigma_{13} & \sigma_{23} & \sigma_{33} \end{bmatrix}$$

The equations and procedures to calculate the principal stresses are:

1. Calculate the coefficients I_1, I_2, and I_3:

$$I_1 = \sigma_{11} + \sigma_{22} + \sigma_{33}$$

$$I_2 = \sigma_{11}\sigma_{22} + \sigma_{22}\sigma_{33} + \sigma_{33}\sigma_{11} - \sigma_{12}^2 - \sigma_{23}^2 - \sigma_{13}^2$$

$$I_3 = \sigma_{11}\sigma_{22}\sigma_{33} + 2\sigma_{12}\sigma_{23}\sigma_{13} - \sigma_{11}\sigma_{23}^2 - \sigma_{22}\sigma_{13}^2 - \sigma_{33}\sigma_{12}^2$$

2. Calculate the coefficients R, Q, and T:

$$R = \frac{1}{3}I_1^2 - I_2$$

$$Q = \frac{1}{3}I_1 I_2 - I_3 - \frac{2}{27}I_1^3$$

$$T = \left(\frac{1}{27}R^3\right)^{\frac{1}{2}}$$

3. Calculate the coefficients S and α:

$$S = (R/3)^{\frac{1}{2}}$$

$$\alpha = \arccos(-Q/2T)$$

4. Calculate the three principal stresses: σ_{p1}, σ_{p2} and σ_{p3}:

$$\sigma_{p1} = 2S\cos(\alpha/3) + I_1/3$$

$$\sigma_{p2} = 2S\cos[(\alpha/3) + 120^0] + I_1/3$$

$$\sigma_{p3} = 2S\cos[(\alpha/3) + 240^0] + I_1/3$$

5. Place the three principal stresses: σ_{p1}, σ_{p2}, and σ_{p3} in their normal conventional order, so that:

$$\sigma_I \geq \sigma_{II} \geq \sigma_{III}$$

A9.1.2 Calculate the direction cosines for principal stresses (Eigenvectors)

Having determined the three principal stresses for a given stress tensor, the directions of the principal stresses can be solved from the following equations:

$$\begin{bmatrix} (\sigma_{11} - \sigma_p) & \sigma_{12} & \sigma_{13} \\ \sigma_{12} & (\sigma_{22} - \sigma_p) & \sigma_{23} \\ \sigma_{13} & \sigma_{23} & (\sigma_{33} - \sigma_p) \end{bmatrix} \begin{bmatrix} l_p \\ m_p \\ n_p \end{bmatrix} = 0, \quad p = 1, 2, \text{ or } 3$$

l_p, m_p, and n_p are the direction cosines of the principal stress σ_p, and p takes values of 1, 2, or 3 respectively. The values of l_p, m_p, and n_p can be determined by solving the three linear equations generated from the above equation by taking $p = 1$, 2, and 3 respectively. An alternative procedure for determining the direction cosines is given by the following:

1. Calculate the cofactors of the determinant on the elements of the first row:

$$a = \begin{vmatrix} (\sigma_{22} - \sigma_p) & \sigma_{23} \\ \sigma_{23} & (\sigma_{33} - \sigma_p) \end{vmatrix} = (\sigma_{22} - \sigma_p)(\sigma_{33} - \sigma_p) - \sigma_{23}^2$$

$$b = -\begin{vmatrix} \sigma_{12} & \sigma_{23} \\ \sigma_{13} & (\sigma_{33} - \sigma_p) \end{vmatrix} = \sigma_{13}\sigma_{23} - \sigma_{12}(\sigma_{33} - \sigma_p)$$

$$c = \begin{vmatrix} \sigma_{12} & (\sigma_{22} - \sigma_p) \\ \sigma_{13} & \sigma_{23} \end{vmatrix} = \sigma_{12}\sigma_{23} - \sigma_{13}(\sigma_{22} - \sigma_p)$$

2. Calculate the factor k

$$k = \frac{1}{\sqrt{a^2 + b^2 + c^2}}$$

3. Calculate the direction cosines or eigenvectors:

$$l_p = ak \quad m_p = bk \quad n_p = ck$$

Repeat steps 1 to 3 for all three principal stresses, then obtain the eigenvector by

$$\begin{bmatrix} l_1 & m_1 & n_1 \\ l_2 & m_2 & n_2 \\ l_3 & m_3 & n_3 \end{bmatrix} \quad \text{or in angles} \quad \begin{bmatrix} \cos^{-1}l_1 & \cos^{-1}m_1 & \cos^{-1}n_1 \\ \cos^{-1}l_2 & \cos^{-1}m_2 & \cos^{-1}n_2 \\ \cos^{-1}l_3 & \cos^{-1}m_3 & \cos^{-1}n_3 \end{bmatrix}$$

APPENDIX 9.2 PARAMETERS FOR STRESS MEASUREMENT

The parameters required for X-ray stress determination are the crystal lattice parameter, d-spacing, Miller index, X-ray wavelength (target material), stress-free $2\theta_0$, Young's modulus E, Poisson's ratio ν, and the anisotropic factor A_{RX}. Another set of macroscopic elastic constants, S_1 and $\frac{1}{2}S_2$, can be calculated from E and ν. The crystallographic plane-specific elasticity constants (XEC), $S_1^{\{hkl\}}$ and $\frac{1}{2}S_2^{\{hkl\}}$, can be calculated from E, ν, and A_{RX}, or found in the literature. The following table lists the parameters for some commonly used materials. Stress evaluation software, such as Bruker LEPTOS™, also contains a database for most commonly used materials for the user's convenience. Since the parameters, especially E and ν, (or $S_1^{\{hkl\}}$ and $\frac{1}{2}S_2^{\{hkl\}}$) are very critical for the stress measurement, users are encouraged to use the parameters from more reliable sources if available for their specific materials and experiments.

Materials	***a* (*lc*)**	$\langle d_{hkl} \rangle$	**{*hkl*}**	***Target***	$2\theta_0$	***E***	ν	A_{RX}
Parameter Unit	Å	**Å**			degree	MPa		
Ferritic and martensitic steel (bcc)	2.866	1.170	211	Cr	156.0	210000	0.28	1.49
		1.013	220	Co	124.1			
Austenitic steel (fcc)	3.571	1.263	220	Cr	130.2	193000	0.3	1.72
		1.031	222	Co	120.5			
		0.798	420	Cu	149.8			
Aluminum (fcc)	4.049	1.221	311	Cr	139.5	70600	0.345	1.65
		0.929	331	Co	148.7			
		0.826	422	Cu	137.7			
Copper (fcc)	3.615	1.278	220	Cr	127.3	129800	0.343	1.09
		1.044	222	Co	118.1			
		0.829	331	Cu	136.7			

(continued)

Materials	a (/c)	$<d_{hkl}>$	{hkl}	*Target*	$2\theta_0$	E	ν	A_{RX}
Parameter Unit	Å	Å			degree	MPa		
Silicon (fcc-diamond)	5.431	1.246	331	Cr	133.6	167200	0.221	
		0.918	531	Co	154.0			
		0.828	533	Cu	136.9			
α-Brass (fcc)	3.680	1.301	220	Cr	123.4	100600	0.35	
		0.920	400	Co	153.2			
		0.823	420	Cu	139.1			
β-Brass (bcc)	2.945	1.202	211	Cr	144.6	74000	0.29	
		0.930	310	Co	146.4			
		0.850	222	Cu	130.1			
Chromium (bcc)	2.884	1.177	211	Cr	153.0	279000	0.21	
		1.020	220	Co	122.7			
		0.912	310	Cu	115.3			
Nickel (fcc)	3.529	1.248	220	Cr	133.7	199500	0.312	1.52
		1.019	222	Co	122.9			
		0.810	331	Cu	145.0			
Titanium (α-hcp)	2.951 /4.686	1.247	112	Cr	133.3	120200	0.361	
		0.918	114	Co	154.6			
		0.821	213	Cu	139.5			
Manganese (hcp)	3.210 /5.210	1.366	112	Cr	113.9	44700	0.291	
		0.976	105	Co	133.1			
		0.899	213	Cu	118.0			
Molybdenum (bcc)	3.147	1.285	211	Cr	126.0	324800	0.293	
		0.995	310	Co	128.0			
		0.841	321	Cu	132.6			
Niobium (bcc)	3.307	1.348	211	Cr	116.3	104900	0.397	
		1.045	310	Co	117.7			
		0.884	321	Cu	121.2			
Silver (fcc)	4.086	1.231	311	Cr	136.9	82700	0.367	
		0.938	331	Co	145.2			
		0.834	422	Cu	134.9			
Gold (fcc)	4.079	1.230	311	Cr	137.1	78000	0.44	
		0.936	331	Co	145.8			
		0.833	422	Cu	135.4			
Tungsten (bcc)	3.165	1.292	211	Cr	124.9	411000	0.28	1.00
		0.914	222	Co	156.8			
		0.791	400	Cu	155.0			

REFERENCES

1. S. P. Timoshenko and J. N. Goodier, *Theory of Elasticity*, McGraw-Hill, New York, 1970.
2. I. C. Noyan and J. B. Cohen, *Residual Stress*, Springer-Verlag, New York, 1987.
3. J. Lu, *Handbook of Measurement of Residual Stress*, The Fairmont Press, Lilburn, GA, 1996.
4. N. M. Walter et al., *Residual Stress Measurement by X-ray Diffraction* – SAE J784a, Society of Automotive Engineering, 1971
5. E. J. Mittemeijer, The relation between residual macro- en microstresses and mechanical properties of case-hardened steels, *Case-Hardened Steels: Microstructural and Residual Stress Effects*, edited by D. E. Diesburg, TMS-AIME, Warrendale, Pa., USA, 1984, 161–187.
6. C. K. Lowe-Ma and M. J. Vinarcik, Selected applications of X-ray diffraction in the automotive industry, *Industrial Applications of X-ray Diffraction*, edited by F. H. Chung and D. K. Smith, Marcel Dekker, New York, 2000, 179–192.
7. A. P. Voskamp and E. J. Mittemeijer, Residual stress development and texture formation during rolling contact loading, *Industrial Applications of X-ray Diffraction*, edited by F. H. Chung and D. K. Smith, Marcel Dekker, New York, 2000, 813–846.
8. S. I. Rao, B. He, and C. R. Houska, X-ray diffraction analysis of concentration and residual stress gradients in nitrogen-implanted niobium and molybdenum, *J. Appl. Phys.*, **69** (12) 15 June 1991.
9. M. R. James and J. B. Cohen, The measurement of residual stresses by X-ray diffraction techniques, *Treatise on Materials Science and Technology*, Vol. **19** Part A, edited by H. Herman, 1980.
10. T. Adler and C. R. Houska, Simplifications in X-ray line-shape analysis, *J. Appl. Phys*. (1979), **50** (5), 3282–3287.
11. C. R. Houska, Least-square analysis of X-ray diffraction line shapes with analytic functions, *J. Appl. Phys*. (1981), **52** (2), 748–754
12. R. Delhez et al., Determination of crystallite size and lattice distortions through X-ray diffraction line profile analysis: recipes, methods and comments, *Fresenius Z Anal Chem.* (1982) **312**, 1–16
13. S. Rao and C. R. Houska, X-ray diffraction profiles described by refined analytical functions, *Acta Cryst.* (1986). **A42**, 14–19
14. D. Balzar, Profile fitting of X-ray diffraction lines and Fourier analysis of broadening, *J. Appl. Cryst.* (1992). **25**, 559–570
15. R. W. Cheary and A. Coelho, A fundamental parameters approach to X-ray line-profile fitting, *J. Appl. Cryst.* (1992). **25**, 109–121
16. D. Balzar et al., Size-strain line-broadening analysis of the ceria round-robin sample, *J. Appl. Cryst.* (2004). **37**, 911–924
17. EN 15305:2008, *Non-destructive Testing – Test Method for Residual Stress analysis by X-ray Diffraction*, European Standard, July 2008.
18. G. M. Borgonovi, Determination of residual stress from two-dimensional diffraction pattern, *Non-destructive Methods for Material Property Determination*, edited by C. O. Ruud and R. E. Green, Jr., Plenum Publishing Corporation, 47–57, 1984.
19. G. M. Borgonovi and C. P. Gazzara, Stress measurement with two-dimensional real-time system, *Advances in X-ray Analysis*, **32**, 397–406, 1989.
20. M. A. Korhonen, V. K. Lindroos, and L. S. Suominen, Application of a new solid state X-ray camera to stress measurement, *Advances in X-ray Analysis*, **32**, 407–413, 1989.
21. Y. Yoshioka and S. Ohya, X-ray analysis of stress in a localized area by use of image plate, *Advances in X-ray Analysis*, **35**, 537–543, 1992.
22. N. Fujii and S. Kozaki, Highly sensitive X-ray stress measurement in small area, *Advances in X-ray Analysis*, **36**, 505–513, 1993.

23. Y. Yoshioka and S. Ohya, X-ray analysis of stress in a localized area by use of image plate, Proceedings of ICRS-4, Baltimore, USA, 1994
24. B. B. He and K. L. Smith, A new method for residual stress measurement using an area detector, *Proceedings of The Fifth International Conference on Residual Stresses (ICRS-5)*, Edited by T. Ericsson et al., pp. 634–639, Linkoping, Sweden, 1997.
25. B. B. He and K. L. Smith, Fundamental equation of strain and stress measurement using 2D detector, *Proceedings of 1998 SEM Spring Conference on Experimental and Applied Mechanics*, Houston, USA, 1998.
26. B. B. He, U. Preckwinkel, and K. L. Smith, Advantages of Using 2D Detectors for Residual Stress Measurement, *Advances in X-ray Analysis*, **42**, 429–438, 1998.
27. A. Kämpfe et al., X-ray stress analysis on polycrystalline materials using two-dimensional detectors, *Advances in X-ray Analysis*, **43**, 54–65, 1999.
28. B. B. HE, *The 20th ASM Heat Treating Society Conference Proceedings*, *Vol.* 1, pp. 408–417, St. Louis, Missouri, 2000.
29. Bob B. He, "Introduction to two-dimensional X-ray diffraction", *Powder Diffraction*, *Vol.* 18, *No.* 2, June 2003.
30. M. Francois, Unified description for the geometry of X-ray stress analysis: proposal for a consistent approach, *J. Appl. Cryst.* (2008). **41**, 44–55.
31. B. He, K. Xu, F. Wang, and P. Huang, Two-dimensional X-ray diffraction for structure and stress analysis, *ICRS-7 Proceeding, Mat. Sci. Forum*, **490–491**, 1–6, 2005.
32. T. Sasaki, Y. Kanematsu, and Y. Hirose, Determination of volume fraction of constituents in deformed stainless steel by means of image plate, ICRS-7 Proceeding, *Mat. Sci. Forum*, **490–491**, 190–193, 2005.
33. G. Geandier et al., Benefits of two-dimensional detectors for synchrotron X-ray diffraction studies of thin film mechanical behavior, *J. Appl. Cryst.* (2008). **41**, 1–13.
34. T. Miyazaki and T. Sasaki, A comparison of X-ray stress measurement methods based on the fundamental equation, *J. Appl. Cryst.* (2016). **49**, 426–432.
35. John O. Almen, Shot blasting test, US Patent number 2350440, (1944).
36. R. A. Thompson, Almen strip, US Patent number 5731509, (1998).
37. B. B. He and K. L. Smith, Computer simulation of diffraction stress measurement with 2D detectors, *Proceedings of 1998 SEM Spring Conference on Experimental and Applied Mechanics*, Houston, USA, 1998.
38. H. P. Klug and L. E. Alexander, *X-ray Diffraction Procedures*, John Wiley and Sons, New York, 1974.
39. R. Delhez, E. J. Mittemeijer, An improved $\alpha 2$ elimination, *J. Appl. Cryst.*, **8**–609-611, 1975.
40. W. Pfeiffer: The role of the peak location method in X-ray stress measurement, *Proc. of the 4th Int. Conf. on Residual Stresses.* SEM, Bethel, CT, USA, (1994)148-155.
41. J. M. Sprauel and H. Michaud, Global X-ray method for determination of stress profiles, *Materials Sciences forum*, **404–407**, 19–24, 2002.
42. W. Parrish, Powder and related techniques, *International Tables for Crystallography*, Vol. **C**, edited by A. J. C. Wilson, IUCR by Kluwer Academic Publisher (1992), 42–79.
43. V. N. Naidu and C. R. Houska, Profile separation in complex powder patterns, *J. Appl. Cryst.* (1982). **15**, 190–198.
44. E. Prince and P. T. Boggs, Least squares, *International Tables for Crystallography*, Vol. **C**, edited by A. J. C. Wilson, IUCR by Kluwer Academic Publisher (1992), 594–604.
45. B. B. He, Accuracy and stability of 2D-XRD for residual stress measurement, *Proceedings of the 10th International Conference on Residual Stresses*, Sydney, Australia, July **2–7**, 2016.
46. Y. Shi, C. Zheng, M. Ren, Y. Tang, L. Liu, and B. He, Evaluation of principal residual stress and its relationship with crystal orientation and mechanical properties of polypropylene films, *Polymer* **123**, 137–143, 2017.

47. O. Takakuwa, H. Soyama, Optimizing the conditions for residual stress measurement using a two-dimensional XRD method with specimen oscillation, *Advances in Materials Physics and Chemistry*, (2013), **3**, 8–18.
48. T. Miyazaki, Y. Fujimoto, and T. Sasaki, Improvement in X-ray stress measurement using Debye–Scherrer rings by in-plane averaging, *J. Appl. Cryst.* (2016). **49**, 241–249.
49. B. B. He, X. L. Wang, W. Tang, and Y. Chao, Stress mapping using a two-dimensional diffraction system, *Proc. of the SEM Annual Conference on Experimental and Applied Mechanics*, June 4–6, 2001, Portland, Oregon, 547–550.
50. W. M. Thomas, *International Patent Application*, No. PCT/GB92/02203, June 10, 1993.
51. X.-L. Wang et al., Neutron diffraction study of residual stresses in friction stir welds, *Proceedings of the 6th Intn'l Conference on Residual Stresses*, Oxford, UK, 2000.
52. I. J. Fiala and S. Nemecek, X-ray diffraction imaging as a tool of mesostructure analysis, *Advances in X-ray Analysis*, **44**, 24–31, 2001.
53. I. C. Noyan, Defining residual stresses in thin film structure, *Advances in X-ray Analysis*, **35**, 461–473, 1992.
54. L. Yu, B. Hendrix, K. Xu, J. He, and H. Gu, X-ray residual stress measurement in thin films with crystallographic texture and grain shape, *Mat. Res. Soc. Symp. Proc.* Vol. 403, 1996.
55. V. Hauk, Stress evaluation on materials having non-linear lattice strain distribution, *Advances in X-ray Analysis*, **27**, 101–120, 1984.
56. P. Huang, K. Xu, B. He, and Y. Han, An investigation of residual stress of porous titania layer by microarc oxidation under different voltages, *ICRS-7 Proceeding, Materials Science Forum*, **490–491**, 552–557, 2004.
57. B. B. He, Measurement of residual stresses in thin films by two-dimensional XRD, *Proceedings of the 7th European Conference on Residual Stresses*, September 13–15, 2006 Berlin, Germany.
58. I. Kraus and N. Ganev, Residual stress and stress gradients, *Industrial Applications of X-ray Diffraction*, edited by F. H. Chung and D. K. Smith, Marcel Dekker, New York, 2000, 793–811.
59. C. L. Azanza Ricardo, M. D'Incau, and P. Scardi, Revision and extension of the standard laboratory technique for X-ray diffraction measurement of residual stress gradients, *J. Appl. Cryst.* (2007). **40**, 675–683.
60. V. Hauk and B. Kruger, A new approach to evaluate steep stress gradients principally using layer remove, *Material Science Forum*, **347–349**, 80–82, 2000.
61. H. K. Tonshoff, J. Ploger, and H. Seegers, Determination of residual stress gradients in brittle materials using an improved spline algorithm, *Material Science Forum*, **347–349**, 83–88, 2000.
62. J. Koo and J. Valgur, Layer growing/removing method for the determination of residual stresses in thin inhomogeneous discs, *Material Science Forum*, **347–349**, 89–94, 2000.
63. B. D. Cullity, *Elements of X-ray Diffraction*, Addison Wesley, Reading, MA, 1978.
64. V. Hauk, *Structural and Residual Stress Analysis by Non-destructive Methods*, Elsevier, Amsterdam 1997.
65. M. Stefenelli et al., X-ray analysis of residual stress gradients in TiN coatings by a Laplace space approach and cross-sectional nanodiffraction: a critical comparison, *J. Appl. Cryst.* (2013). **46**, 1378–1385.
66. D. Y. W. Yu and F Spaepen, The yield strength of thin copper films on Kapton, *J. Appl. Phys.* (2004) **95** (6), 2991–2997.
67. M. Ren, C. Zheng, Y. Shi, Y. Tang, and B. He, Residual stress measurement of high-density polyethylene pipe with two-dimensional X-ray diffraction, presented at the 66th annual Denver X-ray Conference, August 2017 and submitted to Adv. X-ray Anal. (2018) **61.**
68. General Motors, *Statistical Process Control Manual*, Warren, MI, 1986, pp. 3-1–11.
69. J. W. Sinn, Introduction and overview of statistical process control, *Proceeding of Electrical/Electronics Insulation Conference*, Chicago, IL, Oct. 1993, pp. 729–36.

70. C. S. Ackermann, Evaluating destructive measurements using gage R & R, *Proceedings of 1993 IEEE/Semi-advanced Semiconductor Manufacturing Conference and Workshop*, Boston, Oct. 1993, pp. 101–5.

71. B. B. He, K. L. Smith, U. Preckwinkel, and W. Schultz, Micro-area residual stress measurement using a two-dimensional detector, *Materials Science Forum Vols. 347–349 (2000) pp. 166–171*, *Proceedings of the 5th European Conference on Residual Stresses*, The Netherlands, September 28–30, 1999.

72. B. B. He, K. L. Smith, U. Preckwinkel, and W. Schultz, Gage R&R study on residual stress measurement system with area detector, *Materials Science Forum Vols. 347–349 (2000) pp. 101–106*, *Proceedings of the 5th European Conference on Residual Stresses*, The Netherlands, September 28–30, 1999.

73. T. J. Kazmierski, *Statistical Problem Solving in Quality Engineering*, McGraw-Hill, New York, 1995.

10

SMALL ANGLE X-RAY SCATTERING

10.1 INTRODUCTION

Since the small angle X-ray scattering pattern was first observed in the late 1930s [1–3], the application of this technique has advanced significantly due to the demand for studies of the properties of materials on a nanoscale level. Small angle X-ray scattering (SAXS) is a reliable and economic method for analyzing nanostructured materials. SAXS yields information such as particle sizes and size distributions from 1 to 100 nm, shape and orientation distributions in liquid, and powders and bulk samples, and can help materials scientists and engineers to understand and improve the properties of these materials [2, 3]. Conventional SAXS data (1D), collected by a point detector, such as a Kratky camera, is a scattering curve of the scattered intensity verse the scattering angle [4]. This kind of SAXS data can be used for samples either with isotropic structure or with a particular orientation. SAXS data measured by two-dimensional detectors (2D) can reveal anisotropic features from specimens, such as from polymers, fibrous or layered materials, single crystals, and biomaterials. De-smearing correction is not necessary with the collimated point X-ray beam and an area detector [5–7]. Since one exposure provides all the required SAXS information, it is easy to scan over the sample to map the structure information from the small angle diffraction data. The instrumentation and data analysis of conventional 1D SAXS have been covered by many publications [8, 9]. This chapter gives an introduction to some basics of two-dimensional SAXS. There are many references available on the advantages, special characteristics, theoretical development, and application examples of area detectors for SAXS [10–41].

10.1.1 Principle of Small Angle Scattering

Small angle X-ray scattering (SAXS) and wide-angle X-ray scattering (WAXS) work on the same physical principles. Both techniques observe the coherent scattering from a sample as a

Two-Dimensional X-Ray Diffraction, Second Edition. Bob Baoping He.
© 2018 John Wiley & Sons, Inc. Published 2018 by John Wiley & Sons, Inc.

function of the electron distribution in the sample. A simple distinction between the two is that WAXS has a diffraction 2θ angle range of 0.5° to 180°, while SAXS is in the range from 0° up to roughly 2 or 3°. WAXS normally deals with long range periodicity in all three dimensions with a d-spacing range from a fraction of 1 Å to 10 Å (<1 nm). The crystal structures of most inorganic and organic materials fall into this category. Since the scale of structure and the scattering pattern are inversely proportional, SAXS patterns contain structure information on relatively large scales, typically in the size range between 10 Å to 1000 Å (1–100 nm). The scattering intensity distribution contains information about particle size, size distribution, particle shapes and orientation, and other structure information on this scale. Particles do not necessarily have long range order (crystal) within each particle. However, a SAXS pattern may contain features of a diffractive nature. Types of information obtainable from small-angle X-ray scattering include: lamellar repeat distance; radius of gyration (the first moment of the scattering center distribution function); large-scale structure and long-range order, the arrangement of a column structure, its diameter, and the distances between columns. Types of samples for small-angle X-ray scattering include: polymers, fibers, wood products, detergents, surfactants, lipids, membranes, biological tissues, liquid crystals, catalysts, ceramics, and glasses and also solutions containing various particles.

10.1.2 General Equation and Parameters in SAXS

SAXS patterns represents the scattering variation due to the point-to-point variations in electron density. The variation can be expressed by the scattering amplitude of the X-ray illuminated volume V by the following transformation:

$$A(\vec{q}) = A_e(\vec{q}) \int_v \rho(\vec{r}) \exp(-i\vec{q} \cdot \vec{r}) d^3\vec{r} \tag{10.1}$$

where $\vec{q}$ is the scattering vector with modulus $q = |\vec{q}| = \frac{4\pi}{\lambda} \sin\theta$, $A_e(\vec{q})$ is the scattering amplitude of a single electron, $\vec{r}$ is a vector that defines the position of a point relative to an arbitrary origin, and $\rho(\vec{r})$ is the spatial distribution of electron density. SAXS deals with a size range well above the interatomic distance, so $\rho(\vec{r})$ can be approximated as a continuous variable of the position $\vec{r}$ in the specimen. The actually measured intensity is given by the product amplitude $A(\vec{q})$ and its complex conjugate $A^*(\vec{q})$

$$I(\vec{q}) = A(\vec{q}) \cdot A^*(\vec{q}) = I_0 \left| \int_V \rho(\vec{r}) \exp(i\vec{q} \cdot \vec{r}) d^3\vec{r} \right|^2 \tag{10.2}$$

where I_0 is a constant defined by the conditions of the SAXS-instrument. The intensity distribution (SAXS pattern) as a function of $\vec{q}$ is uniquely determined by the structure in terms of its electron density distribution. Therefore, in principle, the structure associated with the electron density distribution can be uniquely determined from the SAXS pattern. For instance, if the scattering is spherically symmetric, i.e. $I(\vec{q})$ depends only on q, then we have

$$I(q) = 4\pi \int_0^\infty p(r) \frac{\sin qr}{qr} dr \tag{10.3}$$

where $p(r)$ is the so-called pair-distance distribution function (PDDF), which gives the number of different electron pairs with a mutual distance between r and $r+dr$ within the particle. We can see that, like the electron spatial distribution function $\rho(\vec{r})$, $p(r)$ is a function of the structure and

can be given by the inverse transformation from the scattering intensity

$$p(r) = \frac{1}{2\pi^2}\int_0^\infty I(q)qr\sin(qr)dq \tag{10.4}$$

The equation gives the direct relationship between the measured scattering intensity I(q) and the PDDF $p(r)$. More theories and equations for SAXS can be found in a number of textbooks and literature listed at the end of this chapter.

10.1.3 X-Ray Source and Optics for SAXS

In a two-dimensional SAXS system the scattered X-rays are measured in all 360° azimuthal angles simultaneously. Therefore, the X-ray source and optics have different requirements in terms of the spectrum purity, beam divergence, beam size, and beam cross-section profile. The X-ray source used for SAXS can be a sealed tube or rotating anode generator. Small focal spots with high specific power loading on the target is preferred since long beam path, low divergence, and small beam size are typically required for SAXS. Any of the commonly used target material, such as Cu, Co, Cr can be used for SAXS. The longer wavelength of Cr-K_α radiation may have a gain in scattering angle resolution compared to Cu-K_α, but suffer more from the absorption and scattering of the beam path. Therefore, Cu-K_α radiation is most commonly used for SAXS. Another consideration in the target selection is avoiding fluorescence. Due to the small scattering angles, the scattering pattern from the $K_{\alpha1}$ and $K_{\alpha2}$ lines are always merged together The monochromatization by graphite crystals or multilayer mirrors can provide sufficient spectrum purity. Collimation is the most critical part of a SAXS system. The collimation system defines the size, shape, and divergence of the X-ray beam. Collimation also determines the resolution of a SAXS system. Figure 10.1(a) shows the collimation of the SAXS system with a pinhole collimator, sample, beamstop, and detector. The primary beam, consisting of parallel and divergent components, is blocked by the beamstop. The maximum angular resolution α_{max} is given by

$$\alpha_{max} = \alpha_1 + \alpha_2 \tag{10.5}$$

where α_1 is the maximum angular divergence of the incident beam, which is given in Figure 3.14 of Chapter 3 and is denoted by β. The α_2 is the maximum angular deviation of the X-rays recorded in the detector, defined by the beam spot on the sample (S), the resolution element of the detector (r), and the sample-to-detector distance (D).

$$\alpha_2 = \frac{S + r}{D} \tag{10.6}$$

The resolution R, defined as the theoretically largest Bragg spacing, is given as

$$R = \lambda / \alpha_{max} \tag{10.7}$$

where λ is the wavelength of the X-ray radiation. R is chosen so that for a lattice spacing smaller than R, the angle between two consecutive orders of Bragg-reflections is larger than α_{max}. The actual achievable resolution is also limited by the low angle limit of the beamstop size (B_s), and the resolution limit of the beamstop (R_{BS}) is given by

$$R_{BS} = \lambda \cdot \frac{2L}{B_s} \tag{10.8}$$

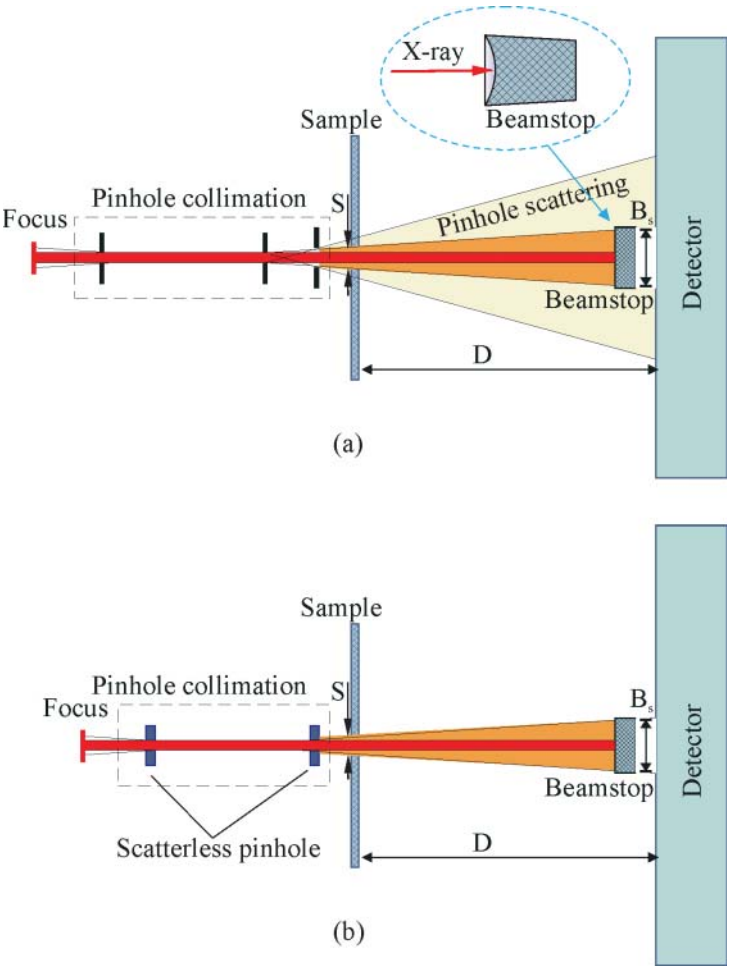


FIGURE 10.1 Pinhole collimation for SAXS: (a) conventional collimation with three pinholes, (b) collimation with two scatterless pinholes.

The pinhole scattering is due to the scattering from the material of the second pinhole. The region of pinhole scattering is partially blocked limited by the antiscattering pinhole (third pinhole). The size of the antiscattering pinhole should be small enough to block as much pinhole scattering as possible, but not so small as to 'touch' the primary beam. Pinhole scattering, observed as a halo around the shadow of the beamstop, is also called parasitic scattering. If the scattering signal from the sample is much stronger than the parasitic scattering, or if the halo is evenly distributed around the beamstop, the parasitic scattering will not limit the achievable resolution. Some effort is necessary to reduce the parasitic scattering, such as using a high parallel beam (Göbel mirrors), smaller pinhole size and appropriate pinhole combination.

The cross-section design of a beamstop is also shown in Figure 10.1(a). The function of the beamstop is to prevent the direct beam from hitting the detector. The diameter of the beamstop (B_s) should be sufficient to block the direct beam, including the parallel and divergent parts. In practice, it is a few times larger than the beam spot size on the detector plane to give enough tolerance to alignment error and to stop most of the tailing part of the beam profile. The side with

the larger diameter of the cone shaped beamstop should face the beam to avoid having the direct beam or scattered beams reflected from the side of the beamstop.

Parasitic scattering by pinholes or slits is a serious problem for SAXS, which results in high background and unwanted artifacts to the image as well as lower resolution limit (R_{BS}) due to the large beamstop. Using scatterless pinholes can significantly overcome the problem [42]. As can be seen in Figure 10.1(b), the collimation with two scatterless pinholes can reduce the system length, remove most of the parasitic scattering, and improve the resolution limit with smaller beamstop.

10.2 2D SAXS SYSTEMS

2D SAXS data can be collected on most two-dimensional X-ray diffraction systems used for WAXS with or without special attachments, depending on the required resolution and data quality. The angular resolution of a SAXS system depends mostly on the parallelism and size of the X-ray beam and resolution of the detector. A long distance between the 1st and 2nd pinholes in the collimator is preferred for the primary beam path to achieve high parallelism and to reduce the parasitic scattering from the collimator. Most area detectors, described in Chapter 4, can be used to collect 2D SAXS data. 2D SAXS has higher demands on some important characteristics of area detectors. Due to the high scattering intensity and the tailing part of the direct beam near the edge of the beamstop, and fast weakening of scattering intensity with the scattering angle, the area detector for 2D SAXS must have sufficient dynamic range to simultaneously record the high counts near the beamstop and low counts of high order features. For laboratory systems, photon counting detectors are preferred because of their high sensitivity and low noise. High spatial resolution is another requirement of detectors for 2D SAXS. SAXS patterns are compacted within a small angular range, but carry many details. The SAXS system must have a sufficient angular resolution to reveal the details of the scattering patterns. High angular resolution can be achieved by a high detector spatial resolution (r), long secondary beam path (D), and small beam size (S). The detector spatial resolution is determined by the point spread function of the selected detector and typically used in the mode with the highest possible pixel resolution. The limiting factor to using a smaller beam size is the sampling statistics. The sampling volume is approximately given by the product of the sample thickness and the beam spot size on the sample. The beam size should be sufficient to cover enough particles in the sample. The secondary beam path should be increased proportionately to maintain angular resolution if the beam size is increased to improve the sampling statistics. A long secondary beam path requires either a vacuum or a helium environment to reduce further scattering and attenuation of the scattered X-rays by the air molecules. This is typically available only for dedicated SAXS systems.

10.2.1 SAXS Attachments

The simplest 2D SAXS system is to add a beamstop to the center of the detector in an XRD^2 system designed for WAXS. Figure 10.2 shows the attachments used for SAXS. Figure 10.2(a) is a beamstop assembly attached to a Hi-Star™ MWPC detector. The beamstop is attached with nylon wires to two linear motion feedthroughs. The beamstop can be positioned accurately to the X-ray beam center by adjusting the micrometers on the feedthroughs. This attachment allows SAXS data to be collected with a relatively short sample-to-detector distance of 15–30 cm for Cu-K_α. The absorption and scattering of X-rays by air prevents the attachment from being used for longer distances. Air scattering increases rapidly with increasing wavelength. SAXS data collection in open air with Cr-K_α is not recommended. In order to reduce air scattering, a helium beam path may

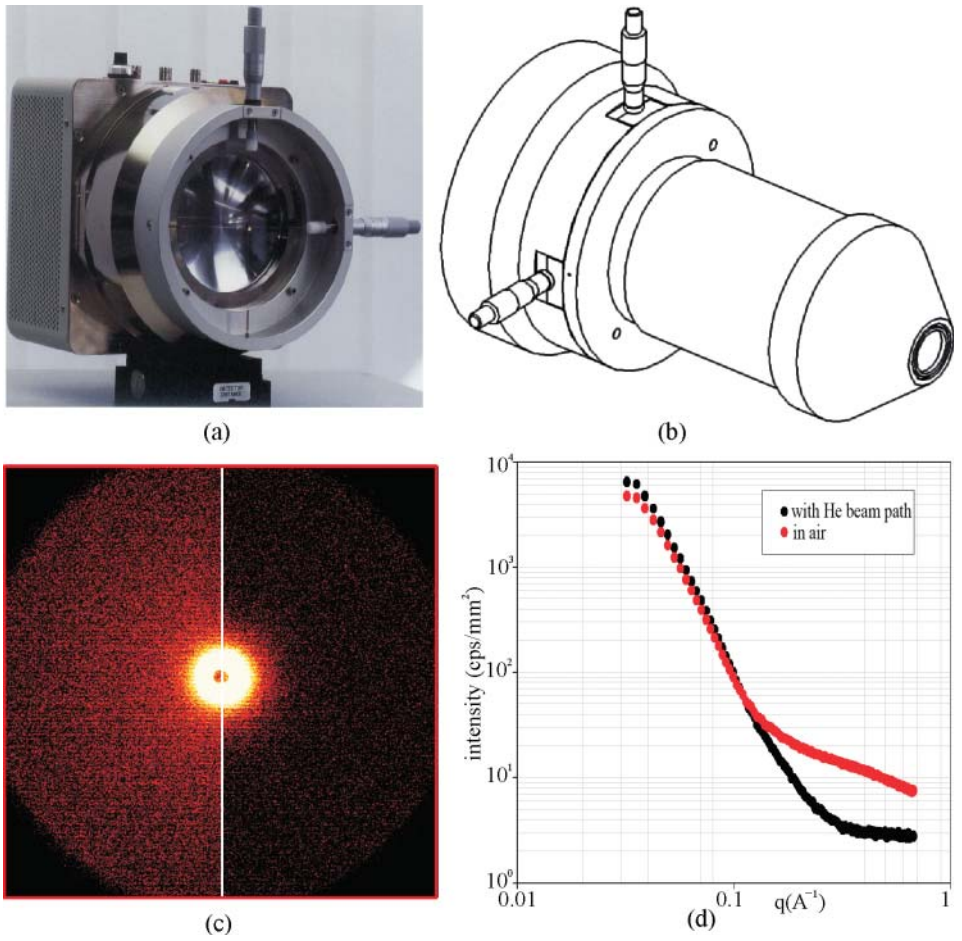


FIGURE 10.2 Attachments for SAXS: (a) beamstop attached to Hi-Star detector, (b) helium beam path, (c) 2D frame with air scatter background (left) and with helium beam path (right), (d) integrated scattering intensities showing the air scattering background.

be attached to the beamstop assembly as shown in Figure 10.2(b). The linear absorption coefficient for air μ_{air} is approximately 0.01 cm^{-1} at one atmosphere and 20°C with Cu-K_α radiation. The linear absorption coefficient for helium ($\mu_{He} \approx 4.7 \times 10^{-5}$ cm^{-1}) at one atmosphere is more than 200 times less. However, a window made of Mylar foil or Be is necessary to seal the helium gas, which can cause absorption and scattering too.

A comparison between an open air and helium beam path for SAXS data collection from a solid SiO_2 aerogel sample was investigated [43]. The data was collected at a 30 cm sample-to-detector distance with Cu-K_α radiation and a 100 seconds measurement time. One half of the 2D pattern was collected with the secondary beam path in open air (left) and one half of the 2D pattern was collected with a helium beam path (right), as shown in Figure 10.2(c). The increased background due to air scattering is obvious. Azimuthally (γ) integrated scattering intensities are displayed in a double logarithmic plot. The increased background due to air scattering dominates in the q-region higher than 0.12 $Å^{-1}$. An inflection point at around $q \sim 0.06$ $Å^{-1}$ is observed. This corresponds to a real space dimension of about $d \sim 10$ Å. The helium beam path attachment dramatically reduces

background scattering in the SAXS experiment. In this experiment, the background is reduced by about 75% at $q = 0.4$ Å^{-1}.

The helium beam path allows 2D SAXS data collection at sample-to-detector distances up to 30–40 cm. The vacuum beam path is required if the SAXS data is collected at larger sample-to-detector distances, 60 cm for instance. The vacuum level does not have to be very high. For example, vacuum level of 0.4 mbar reduces air density by more than 2500 times compared to atmospheric pressure.

Table 10.1 lists the resolution (R) and the resolution limit of beamstops (R_{bs}) for various collimator sizes (0.05–0.5 mm) calculated from the beam divergence (α_1), the primary beamstop on the sample (S), and the maximum angular resolution (α_{max}), as given in the Table 3.6 of Chapter 3. A detector spatial resolution of 0.2 mm and a beamstop diameter of 4 mm are assumed in the calculation. The sample-to-detector distance is 300 mm with an He beam path and 600 mm in vacuum. It can be seen that the beamstop determines the achievable resolution for most cases. The beamstop diameter (4 mm) and the available collimator sizes limit the achievable resolution to 200–250 Å (at the edge of the beamstop) for an He beam path with the detector positioned at 30 cm, and to 300–450 Å for a vacuum beam path with the detector positioned at 60 cm. Both the He beam path or vacuum beam path have to be sealed by a window. It is critical to select an appropriate window material with high transmission, mechanical strength, and low parasitic scattering [44, 45].

10.2.2 Dedicated SAXS System

A dedicated system is required for SAXS study requiring high resolution. Dedicated 2D SAXS systems typically have a long primary beam path for collimating the beam, a third pinhole precisely aligned to remove parasitic scatter, and a long sample-to-detector (secondary beam path) to enhance the angular resolution. The primary beam path, sample chamber, and the secondary beam path are all evacuated to eliminate air scattering. The 2D detector is the most essential component of a dedicated SAXS system. The detector should have a large active area, good spatial resolution, and a very low noise level. Figure 10.3 shows a two-dimensional SAXS system (Bruker Nanostar™) – (a) is the side view of the complete system and (b) is the top view with a complete description of components along the beam path [37]. The type of X-ray source is not shown in (a) and can either be a fine focus sealed tube or a rotating anode generator. The multilayer

Table 10.1 The Resolution of Various SAXS Configurations

Sample-detector distance:			$L = 300$ mm			$L = 600$ mm		
Collimator	α_1 (°)	D(mm)	α_{max}(°)	R (Å)	R_{bs}(Å)	α_{max}(°)	R (Å)	R_{bs}(Å)
Graphite Monochromator								
0.05	0.04	0.071	0.09	951	231	0.07	1320	462
0.10	0.08	0.143	0.15	599	231	0.11	770	462
0.20	0.16	0.286	0.26	344	231	0.21	420	462
0.30	0.23	0.418	0.34	257	231	0.28	311	462
0.50	0.27	0.639	0.43	207	231	0.35	255	462
Göbel Mirrors								
0.05	0.04	0.071	0.09	951	231	0.07	1320	462
0.10	0.06	0.131	0.12	716	231	0.09	963	462
0.20	0.06	0.231	0.14	620	231	0.10	872	462
0.30	0.06	0.331	0.16	546	231	0.11	797	462
0.50	0.06	0.531	0.20	442	231	0.13	680	462

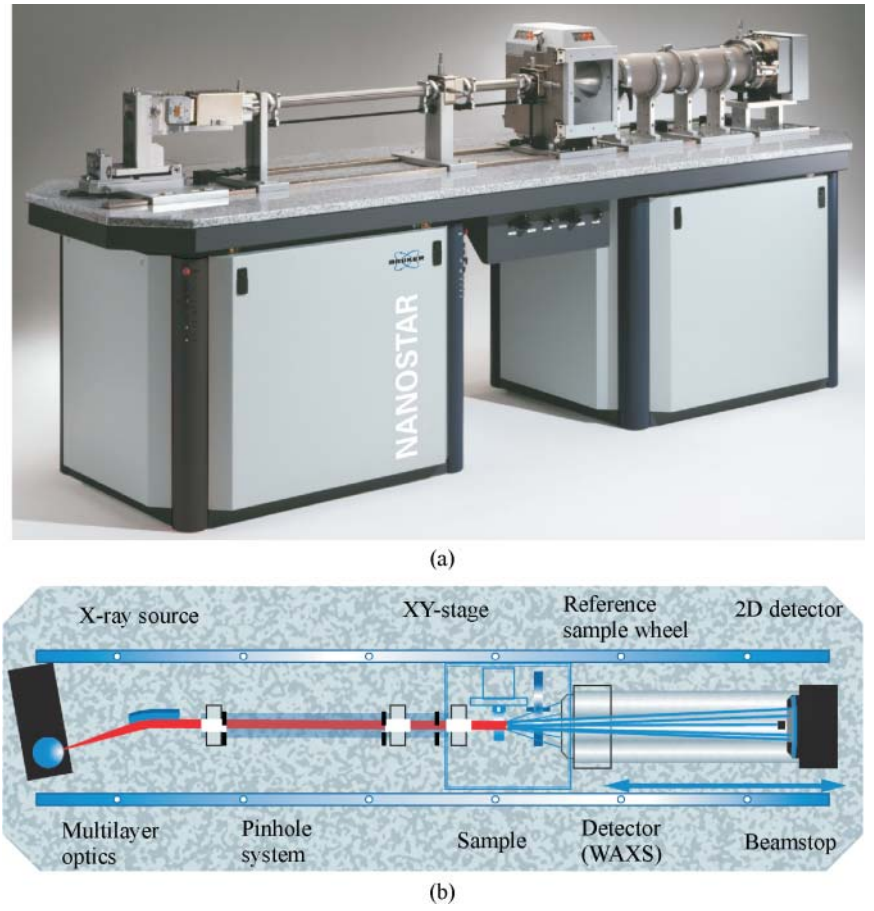


FIGURE 10.3 Two-dimensional SAXS system (Bruker AXS Nanostar™): (a) side view, (b) top view showing complete beam path.

optics monochromatize the X-rays to K_α-radiation and condition the divergent X-rays from the source into a two-dimensional parallel beam. Due to the low Bragg angles of the multilayer mirror and the cross-coupled configuration, the polarization of the primary beam is negligible. The three pinhole collimation system can control the beam divergence and deliver a clean beam with minimum parasitic scattering. The large space between the first and second pinholes results in a parallel beam with very low divergence. The third pinhole is also called the antiscatter pinhole. It has an aperture larger than the first and second pinholes. When properly aligned, no direct beam should reach the third pinhole, so no scatter is generated from the direct beam by the third pinhole. The function of the third pinhole is to block the scatter from the second pinhole.

The sample is mounted on an XY stage. The XY stage allows several samples to be loaded in the chamber at the same time. The XY stage can oscillate the sample while collecting data to improve the sampling statistics. The XY stage allows the sample to be scanned through the X-ray beam during SAXS data collection. Then a given SAXS feature can be mapped over the sample location to generate a radiograph. The reference sample wheel can hold glassy carbon samples and other reference samples. The sample chamber is typically evacuated together with the primary and secondary beam paths, but may also be separated from both beam paths by high transmission windows so that the sample chamber can be filled with other gas environments or pressurized.

The system has a module secondary beam path which allows different sample-to-detector distances, for instance 650–2000 mm for SAXS, or as close as the sample chamber for WAXS. A 2θ of 40° can be measured with either a MWPC Hi-Star™ or a Mikrogap Våntec-2000™ detector in a WAXS configuration. The primary beamstop is made of material with high absorption and low fluorescence, such as gold, tantalum, tungsten, or Pb-Sb alloy. The size of the beamstop is selected based on the beam size and divergence. It is held in place by two Kapton strings in a 90° cross and its position can be adjusted by micrometers through the vacuum feedthroughs.

10.2.3 Detector Correction and System Calibration

The 2D detector should be corrected for non-uniform efficiency (flood field) and geometric distortion (spatial). The detailed description on flood field and spatial correction is given in Chapter 6. For a SAXS system, since the detector cannot be driven away from the primary beam, amorphous fluorescence materials, such as glassy iron foil, cannot be used as a calibration source for the correction. Radioactive sources, such as ^{55}Fe, have to be used for collecting correction frames.

For accurate determination of the beam center and sample-to-detector distance, a diffraction pattern from a calibration standard should be measured. Silver behenate powder is a recommended standard for detector calibration at low angles [46]. Silver behenate [$CH_3(CH_2)_{20}COOAg$] has a large d-spacing lattice plane ($d_{001} = 58.38$ Å). A set of diffraction peaks from (00l) planes are evenly distributed in the low angle region, and can be used as reference peaks for 2θ angle calibration. With an area detector, a set of concentric and evenly spaced diffraction rings are observed and can be used to calibrate the detector distance and beam center. Figure 10.4 shows a diffraction frame collected from silver behenate powder at a nominal detector distance of 30 cm. Diffraction rings from seven orders of silver behenate (00l) reflections are observable. The calibration rings are generated from d-spacing values of (00l) planes based on beam center (x,y) and sample-to-detector distance (D). The size and the location of the rings can be changed by adjusting the beam center and distance. The calibration rings overlap with the measured diffraction rings when the calibrated beam center (x,y) and sample-to-detector distance (D) are reached. In the

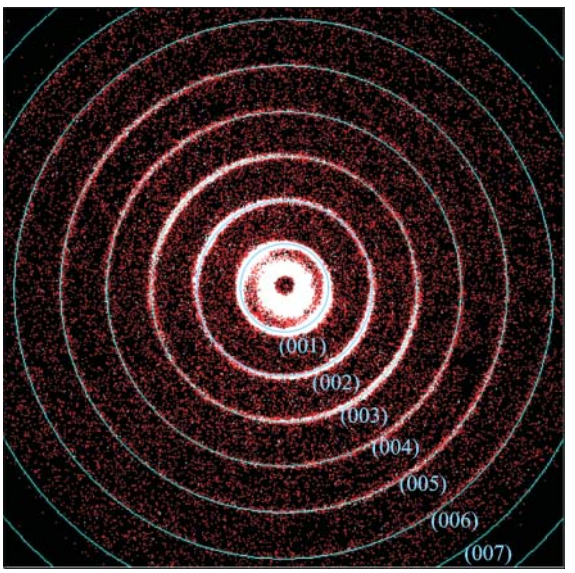
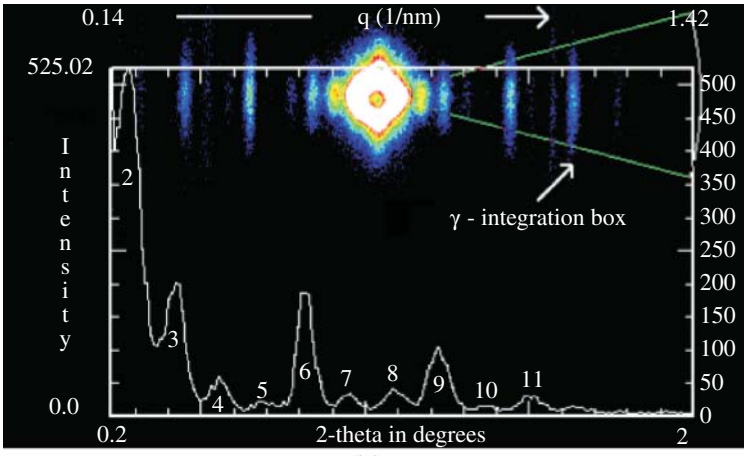
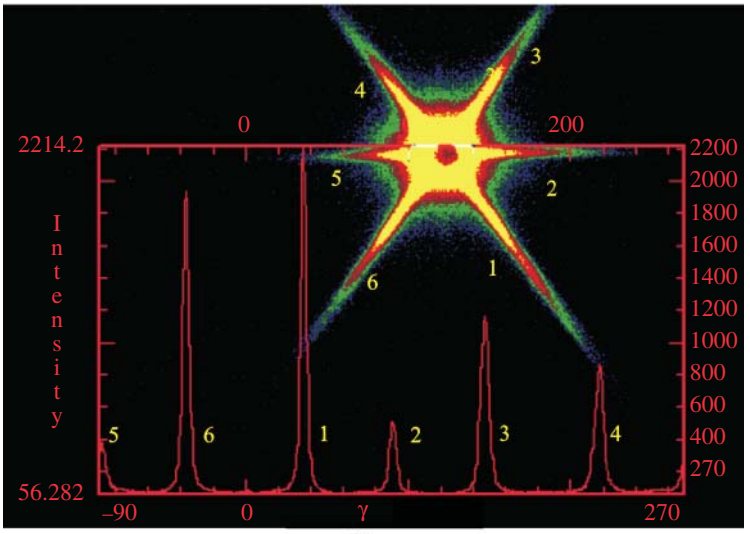


FIGURE 10.4 Diffraction pattern from silver behenate as a low-angle calibration material and calibration ring.



(a)



(b)

FIGURE 10.5 The 2D SAXS data frame integration (a) γ-integration of a frame from rat tail tendon, (b) 2θ-integration of a frame from plate-shaped iron-oxide precipitates inside single crystal Cu (reproduced from reference [49] with permission).

particular example, the calibrated beam center is $x = 517$, $y = 509$, and the sample-to-detector distance is $D = 30.20$ cm. The shadow of the beamstop should be concentric to the diffraction rings, or should be adjusted.

10.2.4 Data Collection and Integration

Using γ-integration converts the 2D SAXS frame into a plot of scattering intensity vs. scattering angle. The γ-integration range can be a full azimuthal angle for materials showing isotropic SAXS pattern. A limited γ-integration range is selected for anisotropic SAXS patterns to reveal the scattering in a specified direction. A 2θ-integration at a given 2θ range reveals the scattering at

the 2θ range as a function of azimuthal angle γ. The plot of scattering intensity vs. azimuthal angle reflects the shape and orientation information of the samples.

A rat tail tendon sample is used as an example of data collection and integration. Part of a frame collected with a dedicated SAXS system (Bruker Nanostar™) is shown in Figure 10.5(a). Since the SAXS pattern of the rat tail tendon shows strongly anisotropic features, γ-integration is done in the γ range of 75° to 105° and a 2θ range of 0.2° to 2° (corresponding to the q range of 0.14 to 1.42 nm^{-1}). The integrated profile shows second order to over 11th order peaks of the SAXS pattern from the rat-tail tendon sample.

Figure 10.5(b) shows a SAXS pattern from plate-shaped iron-oxide precipitates in a single crystal of copper [47–49]. Each streak corresponds to a particular orientation of such a plate with respect to the copper crystal lattice. A 2θ-integration is performed with an integration range of $2\theta = 0.6°$ to 2.4° and the full azimuthal angle range of $\gamma = 0°$ to 360°. The profile from the 2θ-integration results in an intensity distribution as a function of azimuthal angle. The profile can be used to accurately measure the angles between the six streaks. Such spectra can be measured in a number of different sample orientations. The reconstruction of three-dimensional SAXS patterns then gives the precise shape and orientation of the iron-oxide precipitates with respect to the orientation of the single crystal copper [49, 50].

10.3 APPLICATIONS EXAMPLES

10.3.1 Particles in Solutions

Particles kept in suspension in solutions typically have random orientation distributions, so the 2D SAXS pattern can be integrated over the full γ range or any selected γ-integration range. Scattering plots from different γ-integration ranges have the same profile, except that full azimuthal angle integration may give better sampling statistics. Figure 10.6 shows two examples of SAXS analysis with particles in solutions [51]. The solution samples are contained in a quartz capillary, and the sealed capillary is loaded in the vacuum sample chamber. The scattering intensities are normalized by the scattering from the pure solution sample. Figure 10.6(a) shows the plot of scattering intensity vs. scattering vector generated from the 2D SAXS frame collected with spherical gold colloidal particles in toluene. The gold particles are coated with thiols so that the particles can be suspended in the organic solvent toluene. The curve is a fit for a Gaussian size distribution of spherical particles. Figure 10.6(b) shows a Gaussian size distribution of spherical particles with an average radius of 25 Å.

SAXS can be used to study the structural and dynamic properties of concentrated protein solutions and mixtures as well as their dominant interaction forces, aggregation phenomena, liquid-liquid phase separation, crystal growth and glass formation [52, 53]. Figure 10.6(c) is the scattering plot from the protein β-lactoglobulin in water. The protein has a molecular weight of 18,300 Da. The protein is distributed between a monomeric and dimeric state. The scattering data is in agreement with this monomer-dimer equilibrium, and also with larger aggregates. The curve is a fit from an indirect Fourier transformation. Figure 10.6(d) is the pair-distance distribution function (PDDF), $p(r)$, produced from the fit. The $p(r)$ function has contributions from monomers, dimmers, as well as a small part from higher oligomers.

10.3.2 Scanning SAXS and Transmission Measurement

Structure information measured by SAXS over a selected area of the specimen can be mapped by scanning SAXS [54–60]. Figure 10.7(a) is a schematic view of the scanning SAXS system. The

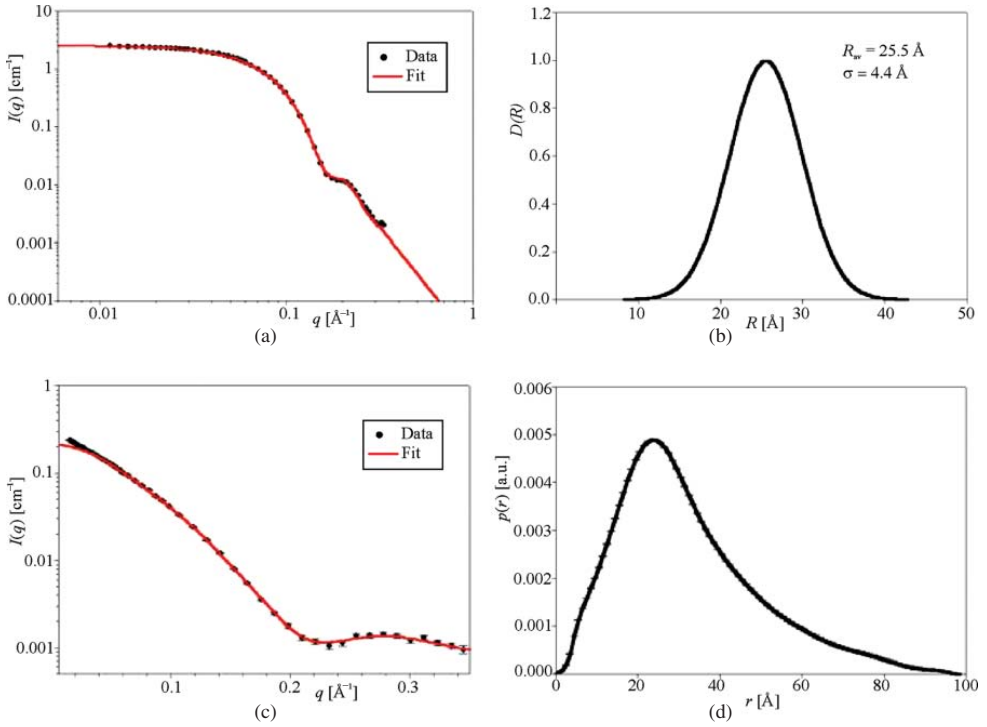


FIGURE 10.6 SAXS from solution samples: (a) scattering plot of spherical gold colloidal particles in toluene, (b) size distribution of gold particle, (c) scattering plot of protein in water, (d) distance distribution function of the protein in water. (Reproduced from Bruker AXS Application Notes [51] with permission.)

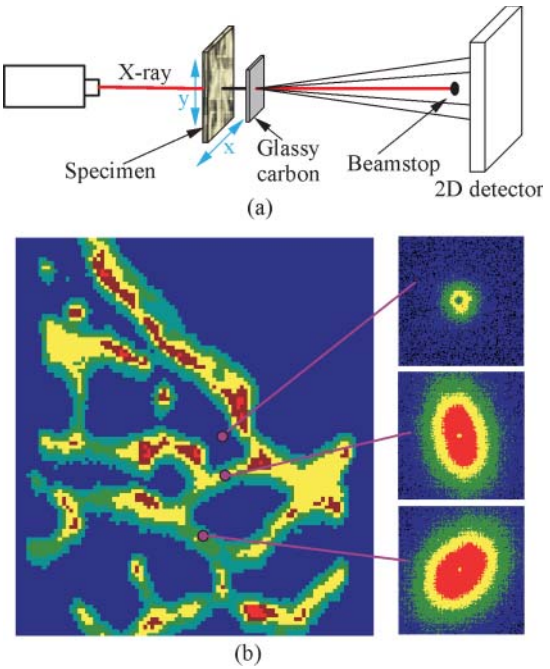


FIGURE 10.7 Scanning SAXS: (a) SAXS system with XY stage, (b) radiography and SAXS patterns from selected spots (reproduced from Bruker Application Notes with permission [50]).

2D SAXS frames are collected with the specimen moving across the X-ray beam with steps in the μm range over a selected area of the specimen. X-ray radiography can be generated from the transmission at each spot of the sample and the SAXS can then be collected at selected sample locations corresponding to the spots of interest on the radiograph. As an example, Figure 10.7(b) shows a radiograph collected from a section of a human vertebra and three SAXS patterns recollected on selected spots on the radiograph [54–56]. The specimen is kept on the motorized XY stage for the radiograph and SAXS data collection so that the measurement spots based on the radiograph can be accurately reproduced. A nanostructural image based on SAXS intensity or other features in a selected region of the 2D SAXS frames can also be generated from scanning SAXS. The specimen is loaded on a motorized XY stage so that the specimen is moved automatically along the x and y directions. The minimum scanning steps are selected based on the desired spatial resolution and the X-ray beam size. It is necessary to have the transmission coefficient measured when doing SAXS scanning over an inhomogeneous sample, so that SAXS data can be normalized against density variations. In typical operation, the radiograph is first taken by inserting a glassy carbon foil behind the specimen. The transmission of the specimen at each spot is proportional to the scattering intensity of the glassy carbon. The transmission factor of the glassy carbon, T_{GC}, is measured by collecting two frames, one with only an absorber in the beam path and one with both the absorber and glassy carbon. The value of T_{GC} is given by

$$T_{GC} = \frac{I_{Abs+GC}}{I_{Abs}} \tag{10.9}$$

where I_{Abs} is the integrated intensity over the complete detector area from the frame collected with the absorber and I_{Abs+GC} is the integrated intensity from the frame of both the absorber and

glassy carbon. The transmission of each spot on the specimen, $T_{x,y}$, is determined by

$$T_{x,y} = \frac{I_{x,y+GC} - T_{GC} I_{x,y}}{I_{GC} - T_{GC} I_0} \tag{10.10}$$

where $I_{x,y+GC}$ is the integrated intensity with both the specimen and glassy carbon in the beam path, $I_{x,y}$ is the integrated intensity with the specimen only, I_{GC} is for glassy carbon only, and I_0 is the background intensity without the specimen and glassy carbon in the beam path. The background is collected without the sample only for solid samples. For samples in a liquid, the background should be collected with the liquid and its container.

10.4 SOME INNOVATIONS IN 2D SAXS

10.4.1 Simultaneous Measurements of Transmission and SAXS

The scanning SAXS method in the previous section requires that the sample is first scanned with the GC to measure the transmission coefficients at each scanning position, and then the scanning SAXS data is collected after removing the glassy carbon. More techniques for measuring the transmission and SAXS simultaneously can be found in literature [29, 61]. An innovative method has been developed to measure the SAXS patterns and transmission coefficients simultaneously [62, 63]. The beamstop is normally used in the transmission mode to prevent the direct beam from striking the detector. In this new method, the beamstop is modified to allow the direct beam to pass through the center of the beamstop. Figure 10.8 is a drawing of the modified beamstop (Bruker SAXSEye™). The beamstop has a through-hole with a diameter of B_L to allow the direct beam to pass. The pinhole and the attenuator are used to control the size and intensity of the direct beam passing through the beamstop. The pinhole aperture diameter is d and the attenuator thickness is t_0.

The integrated intensity of the measured primary beam passing through the above beamstop is approximately given by

$$I_0 = kP_G \frac{d^2}{s^2} \exp(-t_0 \cdot \mu) \tag{10.11}$$

where k is a scaling factor determined by the SAXS system, P_G is the power of the X-ray generator, μ is the linear absorption coefficient of the attenuator, and s is the size of the primary beam spot on the detector if the beamstop is removed. Although both the pinhole size d and the attenuator thickness t_0 determine the integrated intensity I_0, the two parameters play different roles.

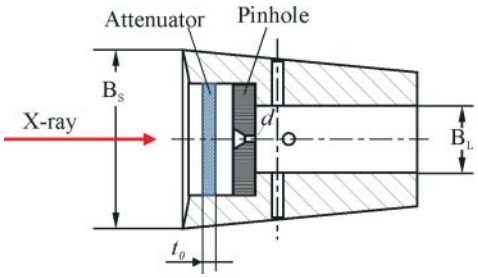


FIGURE 10.8 modified beamstop in which the transmitted direct beam from the sample passes the beamstop through an attenuator and the transmission size is limited by the pinhole.

The beam leak pinhole (d) allows a small portion of the direct beam to pass through the beamstop. The attenuator with an appropriate thickness (t_0) attenuates the transmitted beam below the detector saturation level. A good combination of d and t_0 should limit the intensity below the maximum count rate per pixel when I_0 is measured, but give enough counting statistics when a relatively thick sample is loaded. The ideal situation is that I_0 is measured near the maximum linear counting rate.

An experiment with the SAXSEye™ was done on the Bruker D8-Discover GADDS™ system with the following parameters: Cu-tube, 40 kV/40 mA power, 0.3 mm collimator, 150 mm detector distance, beamstop size $B_S = 4$ mm and $B_L = 2$ mm, pinhole diameter $d = 30$ μm, and an Al foil attenuator $t_0 = 60$ μm. The latter two parameters were determined by gradually increasing the power and reducing the absorber in front of the 2D detector. The SAXSEye makes beamstop positioning easier and more accurate, since we can adjust the beamstop to the beam center by maximizing the transmission intensity. With the above configuration, I_0 was measured at the maximum counting rate of 125 c/s/p, which is below the detector linear counting rate. The transmission coefficients of various layers of an oriented polyester film 0.2 mm thick are measured. The intensity (I_0) was taken as the average of the measurements before the sample was added and after completion of the test and with the sample removed. The result shows that the intensity fluctuation within 24 hours is less than 3%, so the one measurement made before the sample was added can also be used as I_0 without introducing much error. Figure 10.9 is a magnified frame collected with six layers of the oriented polyester films. The majority of the transmitted direct beam is blocked by the beamstop. The dark center spot (the darkness is proportional to the brightness) bounded by the white donut-shaped beamstop shadow represents transmission intensity. It is given by the integrated intensity from a circular region by its user-defined center pixel position and radius.

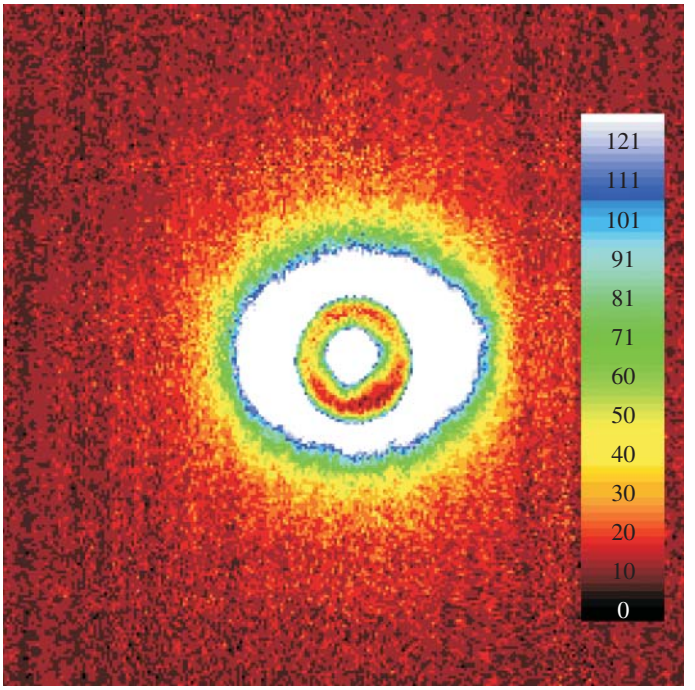


FIGURE 10.9 Center portion of the frame collected with six layers of the oriented polyester films with magnification of 8×. The bright spot inside the shadow of the beamstop represents the transmission.

The transmissions of various stacks of 1 to 14 layers of the oriented polyester films are measured. The transmission of the nth layer is given by

$$\Delta T_n = \frac{I_n}{I_{n-1}} \tag{10.12}$$

where I_n is the total counts of the transmitted beam through n layers of the film and the SAXSEye. ΔT_n is the transmission coefficient of the n-th layer, calculated from the intensity ratio with the consecutive measurement. The average transmission coefficient of each layer is 87.3% with a standard deviation of 1.3%. The transmission coefficient of a single layer T_1 is given by

$$T_1 = \exp(-\mu \cdot t) \tag{10.13}$$

where t is the thickness of one layer. From the measured average transmission, the linear absorption coefficient of the polyester film is 6.79 cm^{-1}. Then the transmission coefficient for a stack of n layers is given by

$$T_n = \exp(-\mu \cdot nt_1) = T_1^n \tag{10.14}$$

or

$$\ln T_n = n \ln T_1 \tag{10.15}$$

The equation shows that the logarithm of total transmission of n layers is proportional to the number of layers. Figure 10.10 is the measured transmission coefficient for various layers on a logarithmic scale plotted against the number of layers. A linear correlation is observed with an almost perfect correlation, with a coefficient of determination of 0.999.

10.4.2 Vertical SAXS System

Instead of the conventional horizontal beam direction in a SAXS system, there are some advantages to having a two-dimensional small angle X-ray scattering system with the X-ray

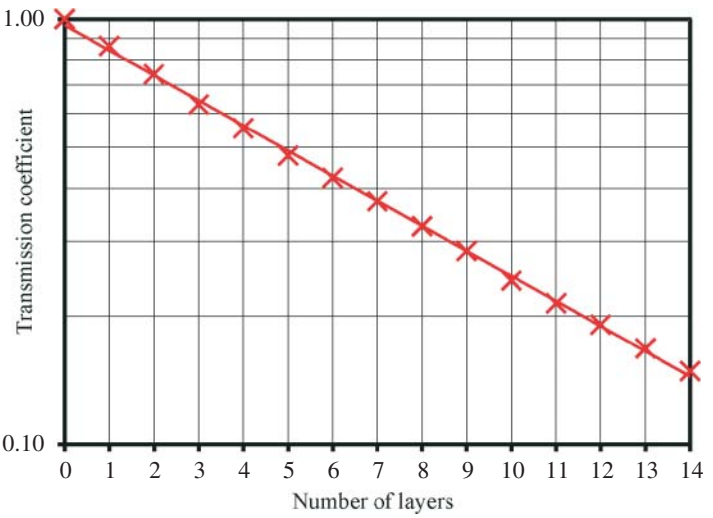


FIGURE 10.10 Transmission coefficient as a function of sample thickness (number of 0.2 mm polyester layers).

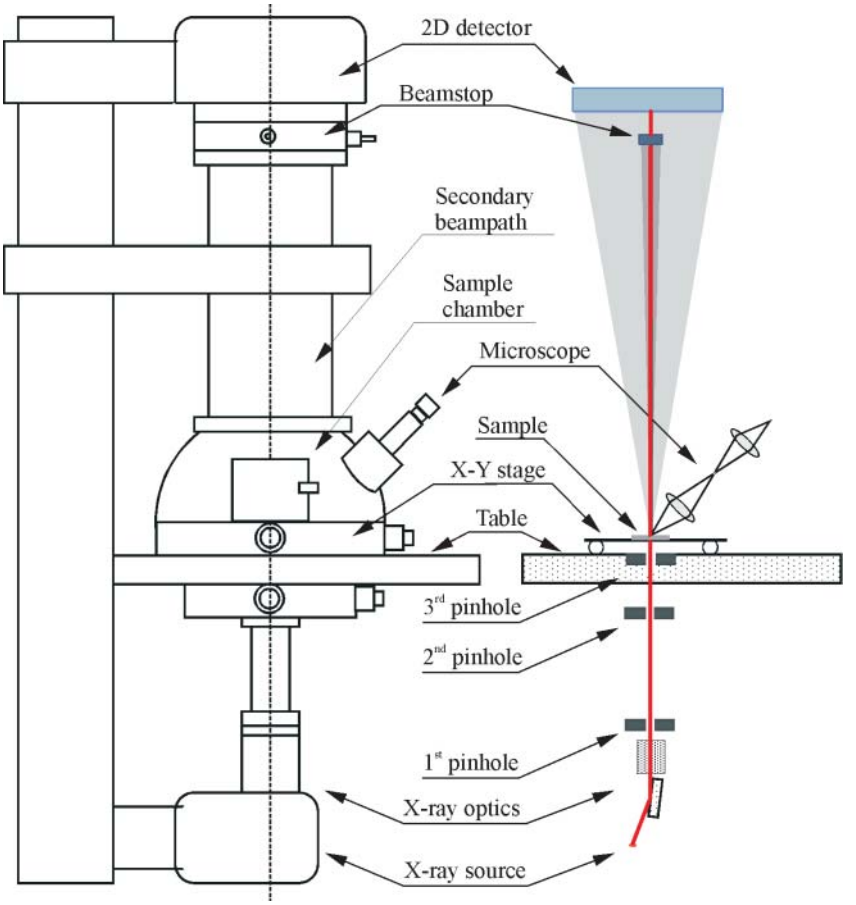


FIGURE 10.11 Schematics of the vertical small angle X-ray scattering system.

beam in the vertical direction [64]. The vertical SAXS configuration allows the samples to be placed on a horizontal XY stage relying on gravity. This is especially advantageous for loose powder or a sample in a liquid solution. Incorporated with a video microscope or optical microscope, it is possible to observe and position the sample precisely to the X-ray beam for SAXS data collection. The configuration and operation of the vertical SAXS system is analogous to the typical transmission electron microscope. Therefore, it is convenient to observe and manipulate the sample in the vertical SAXS system.

Figure 10.11 shows the concept of a vertical SAXS system. The system consists of an X-ray source, X-ray optics, primary beam path with pinhole collimation, sample XY stage, microscope, secondary beam path, beamstop, and a two-dimensional detector. The X-ray source is at the bottom of the system. It can be either a sealed X-ray tube or a rotating anode generator (RAG). Spot focus is preferred. The X-ray optics can be a crystal monochromator, capillaries, X-ray filters, X-ray mirror, or mirror group as well as any device capable of conditioning the X-rays into the desired spectrum and distribution profiles. The primary beam path contains three pinholes for collimation and suppression of parasitic scattering. Each pinhole position can be adjusted independently relative to the X-ray beam. In order to maximize the transmission efficiency of the X-ray beam, the primary beam path is either under a vacuum or filled with a low density gas,

such as helium. The sample chamber is a confined space with air, under a vacuum or with some other controlled environment. The chamber has a door for loading and unloading the sample. The sample chamber may be separated from the primary and the secondary beam path by diaphragms. The diaphragms are made of materials with low X-ray absorption, such as beryllium or kapton foils. Therefore, the sample chamber can be under an environment different from the primary or secondary beam path. The sample chamber may also have adapting ports for other sensors or accessories.

The sample stage is a precision XY (or XYZ) stage mounted inside the sample chamber. XY translation can be done manually and/or be motorized with remote operation. The sample can be supported on a frame, a foil or nylon net. The sample may also be fixed on the support mechanically or glued on a loading cartridge. It is ideal to maintain the sample position on the XY stage while minimizing the X-ray attenuation caused by the support materials. A sample observation microscope is mounted on the sample chamber. This microscope can be either optical and/or with a video camera. The secondary beam path for the scattered X-rays from the sample is in a vacuum to eliminate air scattering. A high sensitivity, low noise, and high resolution two-dimensional detector is located at the top of system. A beamstop is mounted right in front of the two-dimensional detector to protect the detector from being hit by the direct beam. The position of the beamstop can be adjusted precisely to the direct beam. The beamstop can be a conventional beamstop or an innovative beamstop for transmission measurement [62, 63]. One or more accessory ports in various sizes and forms can be built on the shell of the sample chamber. Those ports can be used to accommodate other measurement devices or sample environment stages. For instance, the accessory port may be used for a second 2D detector, so that the system can measure WAXS and SAXS simultaneously.

REFERENCES

1. A. Guinier and G. Fournet, *Small-Angle Scattering of X-rays*, John Wiley, New York, 1955.
2. L. E. Alexander, *X-ray Diffraction Methods in Polymer Science*, Krieger Publishing Company, Malabar, Florida, 1985.
3. F. J. Baltá-Calleja and C. G. Vonk, *X-ray Scattering of Synthetic Polymers*, Elsevier Science Publishing Company, New York, 1989.
4. G. Fritz and A. Bergmann, SAXS instruments with slit collimation: investigation of resolution and flux, *J. Appl. Cryst.* (2006). **39**, 64–71.
5. O. Glatter, A new method for the evaluation of small-angle scattering data, *J. Appl. Cryst.* (1977). **10**, 415–421.
6. O. Glatter, Small-angle techniques, *International Tables for Crystallography, Volume C*, edited by A. J. C. Wilson, pp. 89–112, Kluwer Academic Publishers, Dordrecht, The Netherlands, 1995.
7. R. A. Register and S. L. Cooper, Smearing effects in 'pinhole' collimation with one-dimensional detection, *J. Appl. Cryst.* (1988). **21**, 550–557.
8. O. Glatter and O. Kratky, eds. *Small Angle X-ray Scattering* (Academic Press, New York, 1982).
9. H. P. Klug and L. E. Alexander, *X-ray Diffraction Procedures for Polycrystalline and Amorphous Materials*, 1st ed., John Wiley, New York, 1954.
10. R. W. Hendricks, The ORNL 10-meter small-angle X-ray scattering camera. *J. Appl. Cryst.* (1978). **11**, 15–30.
11. J. Schelten and R. W. Hendricks, Recent developments in X-ray and neutron small-angle scattering instrumentation and data analysis, *J. Appl. Cryst.* (1978). **11**, 297–324.
12. J. S. Higgins and R. S. Stein, Recent developments in polymer applications of small-angle neutron, X-ray and light scattering, *J. Appl. Cryst.* (1978). **11**,346–375.

13. T. Furuno, H. Sasabe, and A. Ikegami, A small-angle X-ray camera using a two-dimensional multiwire proportional chamber, *J. Appl. Cryst.* (1987). **20**, 16–22.
14. G. D. Wignall, J. S. Lin, and S. Spooner, Reduction of parasitic scattering in small-angle X-ray scattering by a three-pinhole collimating system, *J. Appl. Cryst.* (1990). **23**, 241–245.
15. J. S. Pedersen, D. Posselt, and K. Mortensen, Analytical treatment of the resolution function for small-angle scattering, *J. Appl. Cryst.* (1990). **23**, 321–333.
16. A. R. Faruqi, R. A. Cross, and J. Kendrick-Jones, Solution small-angle X-ray scattering studies on myosin with a multiwire area detector, *J. Appl. Cryst.* (1991). **24**, 852–856.
17. F. Né et al., Characterization of an image-plate detector used for quantitative small-angle-scattering studies, *J. Appl. Cryst.* (1993). **26**, 763–773.
18. P. Fratzl and A. Daxer, Structural transformation of collagen fibrils in corneal stoma during drying: an X-ray scattering study, *Biophys. J.* (1993). **64**, 1210–1214.
19. A. Gupta, I. R. Harrison, and J. Lahijani, Small-angle X-ray scattering in carbon fibers, *J. Appl. Cryst.* (1994). **27**, 627–636.
20. M. W. Tate et al., A large-format high resolution area X-ray detector based on a fiber-optically bonded charge-coupled device (CCD), *J. Appl. Cryst.* (1995). **28**, 196–205.
21. D. J. Hughes et al., Time-resolved simultaneous SAXS/WAXS of the drawing of polyethylene at the Daresbury SRS, *J. Synchrotron Rad.* (1996). **3**, 84–90.
22. V. Le Flanchec et al., Two-dimensional de-smearing of centrosymmetric small-angle X-ray scattering diffraction patterns, *J. Appl. Cryst.* (1996). **29**, 110–117.
23. S. Pol1zzi et al., Two-dimensional small-angle X-ray scattering investigation of stretched borosilicate glasses, *J. Appl. Cryst.* (1997). **30**, 487–494.
24. J. A. Pople, P. A. Keates, and G. R. Mitchell, A two-dimensional X-ray scattering system for in-situ time-resolving studies of polymer structures subjected to controlled deformations, *J. Synchrotron Rad.* (1997). **4**, 267–278.
25. Z. Bu et al., A small-angle X-ray scattering apparatus for studying biological macromolecules in solution, *J. Appl. Cryst.* (1998). **31**. 533–543.
26. B. B. He, K. Smith, U. Preckwinkel, and H. F. Jakob, Small angle X-ray scattering systems with point focus and area detector, *American Crystallography Association Annual Meeting*, Washington, DC, 1998.
27. S. Ran et al., Novel image analysis of two-dimensional X-ray fiber diffraction patterns: example of a polypropylene fiber drawing study, *J. Appl. Cryst.* (2000). **33**, 1031–1036.
28. T. Fujisawa, Y. Inoko, and N. Yagi, The use of a Hamamatsu X-ray image intensifier with a cooled CCD as a solution X-ray scattering detector, *J. Synchrotron Rad.* (1999). **6**, 1106–1114.
29. S. Seifert et al., Design and performance of a ASAXS instrument at the Advanced Photon Source, *J. Appl. Cryst.* (2000). **33**, 782–784.
30. I. Zizak et al., Investigation of bone and cartilage by synchrotron scanning-SAXS and -WAXD with micrometer spatial resolution, *J. Appl. Cryst.* (2000). **33**, 820–823.
31. D. Pontoni, T. Narayanana, and A. R. Rennieb, High-dynamic range SAXS data acquisition with an X-ray image intensifier, *J. Appl. Cryst.* (2002). **35**, 207–211.
32. P. Fratzl, Small-angle scattering in materials science – a short review of applications in alloys, ceramics and composite materials, *J. Appl. Cryst.* (2003). **36**, 397–404.
33. T. Kamiyama et al., Change in the nanostructure of Al-base alloy ribbons in response to tensile stress – a small angle X-ray scattering study, *J. Appl. Cryst.* (2003). **36**, 464–468.
34. Volker Urban et al., Two-dimensional camera for millisecond range time-resolved small-and wide-angle X-ray scattering, *J. Appl. Cryst.* (2003). **36**, 809–811.
35. A. Orthen et al., Development of a two-dimensional virtual-pixel X-ray imaging detector for time-resolved structure research, *J. Synchrotron Rad.* (2004). **11**, 177–186.

36. E. Mathew, A. Mirza, and N. Menhart, Liquid-chromatography-coupled SAXS for accurate sizing of aggregating proteins, *J. Synchrotron Rad.* (2004). **11**, 314–318.
37. J. S. Pedersen, A flux- and background-optimized version of the Nanostar small-angle X-ray scattering camera for solution scattering, *J. Appl. Cryst.* (2004). **37**, 369–380.
38. C. A. Dreiss, K. S. Jack, and A. P. Parker, On the absolute calibration of bench-top small-angle X-ray scattering instruments: a comparison of different standard methods, *J. Appl. Cryst.* (2006). **39**, 32–38.
39. P. L. Guzzo et al., Two-dimensional small-angle X-ray scattering from as-grown and heat-treated synthetic quartz, *J. Appl. Cryst.* (2007). **40** (Supplement), s132–137.
40. P. Boesecke, Reduction of two-dimensional small- and wide-angle X-ray scattering data, *J. Appl. Cryst.* (2007). **40** (Supplement), s423–427.
41. W. Ruland and B. M. Smarsly, Two-dimensional small-angle X-ray scattering of self-assembled nanocomposite films with oriented arrays of spheres: determination of lattice type, preferred orientation, deformation and imperfection, *J. Appl. Cryst.* (2007). **40**, 409–417.
42. Incoatec Product Flyer, SCATEX – Scatterless pinholes for home-lab systems, IDO-F20-005A (2015), *Incoatec GmbH*, www.incoatec.de.
43. K. Erlacher, SAXS experiments using the D8 Discover with GADDS, Bruker Lab report, May 2005.
44. S. J. Henderson, Comparison of parasitic scattering from window materials used for small-angle X-ray scattering: a better beryllium window, *J Appl. Cryst.* (1995). **28**, 820–826.
45. L. Lurio et al., Windows for small-angle X-ray scattering cryostats, *J. Synchrotron Rad.* (2007). **14**, 527–531.
46. T. C. Huang, H. Toraya, T. N. Blanton, and Y. Wu, X-ray powder diffraction analysis of silver behenate, a possible low-angle diffraction standard, *J Appl. Cryst.* (1993). **26**, 180–184.
47. P. Fratzl, F. Langmayr, and O. Paris, Evaluation of 3D small-angle scattering from non-spherical particles in single crystals, *J. Appl. Cryst.* (1993). **26**, 820–826.
48. O. Paris, P. Fratzl, F. Langmayr, G. Vogl, and H. G. Haubold, Internal oxidation of Cu-Fe. I. small-angle X-ray scattering study of oxide precipitation, *Acta Metall. Mater*. (1994). **42**, 2019–2026.
49. P. Fratzl and H. F. Jakob, Nanostar: small-angle X-ray scattering on alloys, Bruker AXS Lab Report XRD **37**, L86-E00037, 2002.
50. P. Fratzl and H. F. Jakob, Nanostar: small-angle X-ray scattering with area detector, Bruker AXS Application Note #359, A89-E00001, 2000.
51. J. S. Pedersen and K. Erlacher, Nanostar: small-angle X-ray scattering from solutions, Bruker AXS Application Note #369, A88-E00009, 2004.
52. A. Stradner and P. Schurtenberger, Nanostar: small-angle X-ray scattering (SAXS) on proteins, Bruker AXS Application Note #367, A88-E00008, 2004.
53. K. Erlacher and P. Doppler, Nanostar: SAXS studies on drug components embedded in a polymer matrix, Bruker AXS Lab Report XRD **50**, L88-E00050, 2004.
54. P. Fratzl et al., Position-resolved small-angle X-ray scattering of complex biological materials, *J. Appl. Cryst.* (1997). **30**, 765–769.
55. H. F. Jakob, Nanostructure of Natural Cellulose and Cellulose Composites, Ph.D. dissertation, Universität Wien, Austria, April, 1996.
56. B. B. He, H. F. Jakob, K. Smith, and U. Preckwinkel, *SAXS with area detector and scanning – SAXS, Proceedings SAXS99*. Brookhaven, NY, USA, 1999.
57. A. Gourrier, Scanning X-ray imaging with small-angle scattering contrast, *J. Appl. Cryst.* (2007). **40** (Supplement), s78–82.
58. Y. Kajiura et al., Structural analysis of single wool fibre by scanning microbeam SAXS, *J. Appl. Cryst.* (2005). **38**, 420–425.
59. O. Paris et al., Scanning-SAXS: a tool for structural characterization of complex materials at the micrometer and the nanometer scale, *Acta Cryst.* (2002). **A58** (Supplement), c25.

60. G. A. Maier, G. Wallner, R. W. Lang, and P. Fratzl, Scanning X-ray scattering study on structural changes at crack tips in PVDF, *Acta Cryst.* (2005). **A61**, c391.
61. T. Morita et al., Apparatus for the simultaneous measurement of the X-ray absorption factor developed for a small-angle X-ray scattering beamline, *J. Appl. Cryst.* (2007). **40**, 791–795.
62. B. B. He and K. L. Smith, An innovation in transmission coefficient measurement, *Advances in X-ray Analysis*, (1999) **43**, 281–286.
63. B. B. He and K. L. Smith, Beam scattering measurement system with transmitted beam energy detection, US Patent No. 6,136,592, Dec. 19, 2000.
64. B. B. He and R. D. Schipper, Vertical small angle X-ray scattering system, US Patent No. 6,956,928, Oct. 18, 2005.

11

COMBINATORIAL SCREENING

11.1 INTRODUCTION

11.1.1 Combinatorial Chemistry

Combinatorial chemistry is an innovative method of synthesizing and analyzing a large number of many different substances quickly and simultaneously. The concept of combinatorial chemistry was introduced about 40 years ago [1–5]. Instead of the traditional way of making and testing one or a few new materials, one at a time, combinatorial technology allows scientists to fabricate, test, evaluate, and store the resulting data for a material library containing tens, hundreds, or even thousands of different materials or compounds. Combinatorial synthesis and rapid screening methods promise to make materials discovery more efficient and less wasteful [6]. Combinatorial chemistry is the art and science of synthesizing and testing compounds for bio-activity to discover drugs and materials more quickly and inexpensively. It has been one of the most popular approaches to drug discovery [7]. Many excellent results in the discovery and synthesis of new phosphors, catalysts, zeolites, and new drugs were reported ten years ago [3–9]. In the past ten years, combinatorial chemistry has been one of the most dynamic and rapidly evolving fields. The most significant progress has been achieved in the drug discovery process. These concepts and techniques have also had a big impact on other fields such as semiconductors, superconductors, catalysts, and polymers. Since reliable and consistent processes can be applied to a material library, the productivity and quality of materials research are significantly advanced by the combinatorial approach. Combinatorial processes can also be more effectively automated by computer controlled processes, since the operations are repeated on all cells of a material library.

11.1.2 High Throughput Screening

With the increased productivity in material synthesis and processing facilitated by combinatorial techniques, it becomes a challenge to efficiently screen all the samples produced in the material

Two-Dimensional X-Ray Diffraction, Second Edition. Bob Baoping He.
© 2018 John Wiley & Sons, Inc. Published 2018 by John Wiley & Sons, Inc.

library. The characterization of a large amount of samples requires high-throughput screening techniques to test and evaluate the variation of composition, structure, and properties of the entire material library. Many proprietary material libraries have been designed not only considering material processing, but also the requirements for fast and unambiguous characterizations. X-ray diffraction is one of the most suitable rapid screening techniques because of the penetrating power of the X-ray beam, non-destructive to samples, rapid data collection, and the abundant information contained in the diffraction pattern about the materials. In the pharmaceutical industry, powder X-ray diffraction (PXRD) is one of the primary techniques used in drug discovery and process analysis [10–18]. X-ray diffraction, especially two-dimensional X-ray diffraction, can be used to measure the structural information of a material library with high speed and high accuracy [19–21].

The method of XRD combinatorial screening and the corresponding systems and devices are introduced in this chapter. The method and system design are based on two-dimensional X-ray diffraction (XRD^2) theory. Various configurations and components designed to deal with special needs of the screening are introduced. The combined screening method with XRD and Raman is also introduced.

11.2 XRD^2 SYSTEMS FOR HIGH THROUGHPUT SCREENING

Two-dimensional X-ray diffraction is one of the preferred methods for high-throughput combinatorial screening. An XRD^2 system designed for combinatorial chemistry contains equipment with the latest technological advances needed to perform high throughput, easy-to-use screening on a wide variety of analytical parameters. When material libraries are analyzed by a conventional X-ray diffractometer, the material on each cell has to be measured individually. In most cases, the material libraries are not suitable for loading on a conventional diffractometer, so the materials may have to be removed from the libraries after the combinatorial reaction process. The quantity of the material in each cell is also typically much less than the amount required to fill a standard sample holder. A material library may have to be kept horizontal since the products of the reaction are loose powders or even in solution. An X-ray diffraction system dedicated to high-throughput screening of a combinatorial material library should be able to handle material library plates of various sizes and designs. Ideally, the materials are measured in the library without disturbance, and can be measured between the material processing steps or even during processing. The X-ray optics, detector, and system configuration should be able to measure materials in small quantity and confined in the library cell. The system should be able to move each sample on the library plate to the measurement location (instrument center) automatically and accurately. The software should be able to collect, store, retrieve, analyze, and present the data for combinatorial screening [20–22].

11.2.1 Screening in Reflection Geometry

Figure 11.1(a) shows the schematic of an XRD^2 system for high throughput combinatorial screening in reflection mode and, as an example, (b) is a picture of a Bruker D8 Discover GADDS™ CS (combinatorial screening). All components are mounted on a vertical θ-θ goniometer. The X-ray tube and optics are mounted on a dovetail track, referred to as the θ_1 track. The X-ray beam can be monochromatized with either a graphite monochromator or a multilayer mirror. The X-ray beam can be collimated to various sizes from 50 to 1000 μm, by using a pinhole collimator or a monocapillary. A two-dimensional detector is mounted on another dovetail track, referred to as the θ_2 track. The picture shows a Hi-Star™ multiwire detector. The detector has a pixel resolution

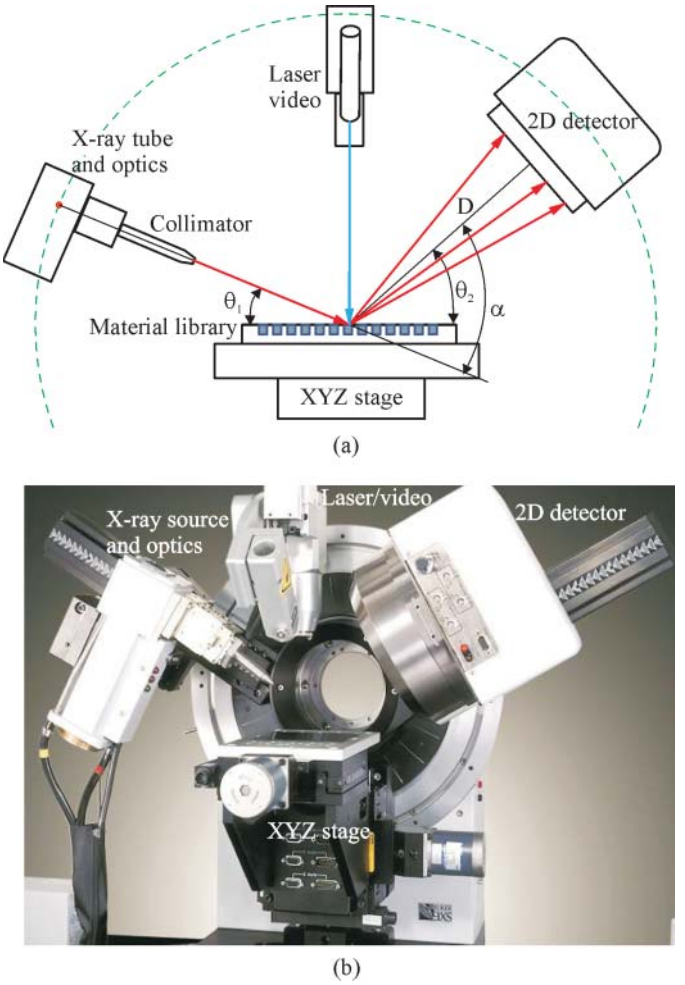


FIGURE 11.1 The XRD^2 system for combinatorial screening: (a) schematics, (b) Bruker D8 Discover GADDS™ CS.

of 100 μm or 200 μm with a frame size of 1024 × 1024 or 512 × 512. The detector can be set at a sample-to-detector distance between 6 cm and 30 cm depending on the application. Larger angular coverage is achievable at shorter distances (65° measuring range at 6 cm) and higher angular resolution is achievable at longer distances (0.02° resolution at 30 cm). A two-dimensional detector can collect a large area of a diffraction pattern with high speed, high sensitivity, low noise, and in real time. A 2D-diffraction pattern contains information about the structure, quantitative phase contents, crystal orientation, and deformation.

The vertical θ-θ geometry and horizontally mounted XYZ stage allow us to load the combinatorial library with ease, even for loose powders or liquids. The horizontal plate on the XYZ stage can hold material library plates of various sizes. The laser-video system together with the XYZ stage allows each cell on the plate to be moved to the instrument center accurately and automatically [23]. The diffraction results are processed and mapped to the screening grid based on user-selected parameters.

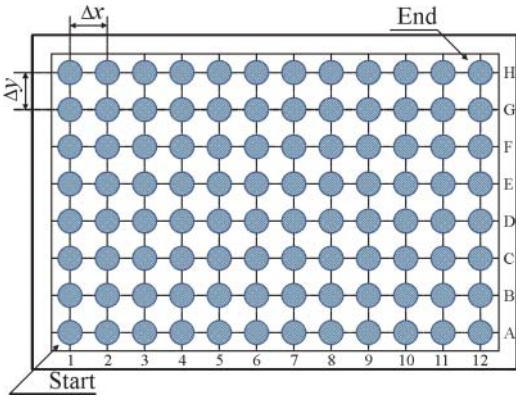


FIGURE 11.2 Grid points are determined by the starting and ending points and the steps.

The instrument center is defined by the intersection of the incident X-ray beam and the center line of the detector. The system automatically and sequentially puts each cell in the material library into the instrument center, based on the predetermined XYZ grid points. The system can also generate an XYZ grid file by inputting the XY coordinates of the starting point, the end point, and the well pitches (steps Δx and Δy) between each grid point, as is illustrated in Figure 11.2. The sample heights (Z coordinates) at each cell are determined by the laser-video system. The laser beam and optical axis of the microscope intercept the instrument center so that the sample position can be determined by the laser spot position on the sample image. The distance between the surface of each cell and the instrument center is calculated from the offset of the laser spot from the crosshair center. The sample height (Z) is automatically adjusted to move the sample surface into the instrument center. Since the video image can be captured with the safety enclosure closed, the video microscope can record the image and position of each cell of the material library during data collection.

A 2D detector can capture a large area of diffraction data containing information for various analyses, such as phase identification, crystal structure and polymorphous, percent crystallinity, particle size and shape, orientation and strain, etc. Almost all the parameters measured by X-ray diffraction can be used for the screening of material libraries. Figure 11.3 shows one form of the screening results display, in which an arbitrary screening parameter is plotted against the cells in a 96 well material library plate. In high-throughput XRD screening, hundreds or thousands of powder diffraction patterns on a series of chemically or structurally related compounds, such as polymorphs, are analyzed. It is necessary to process and analyze the diffraction data set in an integrated approach so that the relationships and effects of sophisticated differences in chemistry, process, and structure can be revealed. Comprehensive algorithms are suggested that can analyze such data, automatically sort the patterns into related clusters or classes, characterize each cluster, and identify any unusual samples containing, for example, unknown or unexpected polymorphs [24–27]. Mixtures may be analyzed quantitatively based on a database of pure phases [28]. The analysis and results can be visualized by dendrograms, cluster analysis, pie charts, principal-component-based score plots, and metric multidimensional scaling. Applications for pharmaceutical data and inorganic compounds are presented. The procedures have been incorporated into the computer program PolySNAP™, which is available commercially from Bruker AXS [29–33]. The software can run data sets from as many as 1500 samples on phase identification, pass/fail analysis, similarity analysis, automatic mixture detection, automatic amorphous phase detection, and quantitative analysis of mixtures.

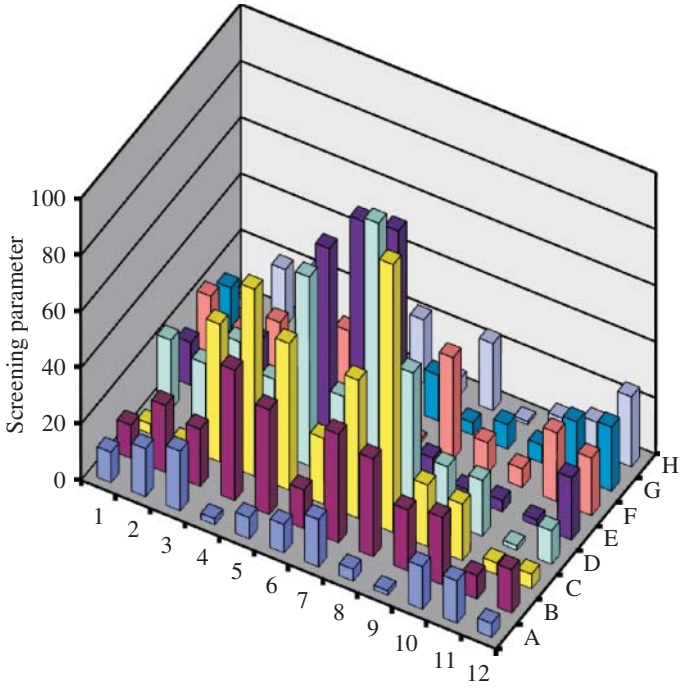


FIGURE 11.3 Screening parameters displayed against the cells in the material library plate.

11.2.2 Retractable Knife-Edge

In many combinatorial screening applications, such as polymorphism studies in pharmaceutical chemistry and catalyst development in the oil industry, a typical 2θ measurement range is from 2° to 60°. With an XRD^2 system in reflection mode, the diffracted X-rays are measured simultaneously in a two-dimensional range, so it is necessary to use an incident angle lower than the minimum 2θ. However, the defocusing effect associated with low incident angles reduces the 2θ resolution and has the possibility of producing cross-cell contamination. Figure 11.4 shows the geometry of two-dimensional diffraction screening in reflection mode. A defocusing effect is observed with low incident angle over a flat sample surface. If one looks at the cross-section on the diffractometer plane, the defocusing factor (B/b) is given by

$$\frac{B}{b} = \frac{\sin\theta_2}{\sin\theta_1} = \frac{\sin(2\theta - \omega)}{\sin\omega} \tag{11.1}$$

where θ_1 is the incident angle, b is the incident beam size, and B is the diffracted beam size. The ratio of B to b is the defocusing factor. The diffracted beam is focused to the detector when $\theta_2 < \theta_1$. The defocusing effect increases with increasing θ_2 or decreasing θ_1. The maximum defocusing appears at $\theta_2 = 90°$. For the θ-2θ configuration, the incident angle ω is used in the equation. Due to the defocusing effect, the incident X-ray beam is spread over the sample surface onto an area much larger than the size of the original X-ray beam. In combinatorial screening applications, sample cells are located close to each other. Therefore, the defocusing may produce cross contamination in the collected diffraction data. The measured diffraction pattern includes not only diffraction from the intended cell but also diffraction from adjacent cells. Cross contamination happens when

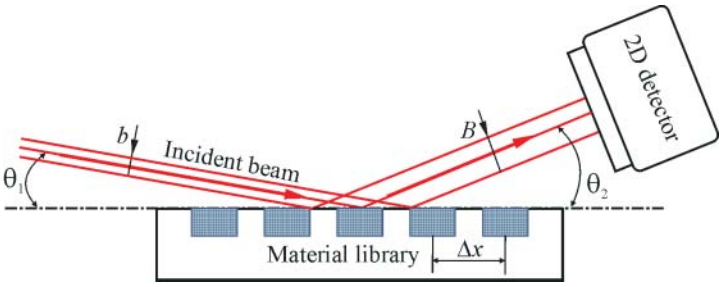


FIGURE 11.4 Defocusing and cross-cell contamination with XRD^2 screening in reflection mode.

the size of the irradiated area is greater than the sum of the well pitch and the gap between the neighboring cells. With half of the gap as a safety margin, the X-ray beam spread over the sample should be smaller than the pitch between adjacent cells to avoid cross contamination, i.e.

$$\frac{b}{\sin\theta_1} < \Delta x \tag{11.2}$$

One approach for avoiding cross contamination is to reduce the beam size, but this sacrifices diffraction intensity. Cross contamination happens only when the data is collected at low incident angles, so the beam size should be reduced only at these angles. One strategy is to insert a knife-edge collimator at low incident angle and remove it at higher incident angle. A motorized retractable knife-edge can be used for this strategy. It can improve resolution and eliminate cross contamination when it is driven into the beam path [34, 35].

Figure 11.5 shows a picture of the motorized retractable knife-edge designed for the Bruker D8 Discover with GADDS™ for combinatorial screening. In a conventional diffraction system, a knife-edge is typically mounted on the sample stage. Combinatorial screening requires that the knife-edge to be mounted on a separate stationary base so that the knife-edge does not move with

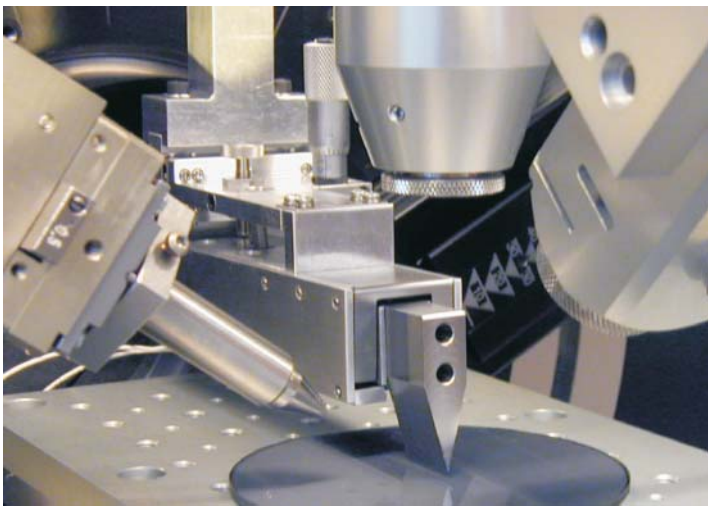


FIGURE 11.5 Motorized retractable knife-edge designed for the Bruker D8 Discover with GADDS for combinatorial screening.

the sample. Instead, each cell is moved to the set instrument center and measured with the same knife-edge setting. The knife-edge has two operational positions: the retracted position and the extended position, as shown in the picture. It is necessary to expose each cell to the laser and video camera during alignment. The motorized retractable knife-edge in the retracted position allows automated alignment. The diffraction patterns are measured at the extended knife-edge position. The knife-edge tilt angle is adjusted with an adjusting knob to form a parallel gap between the knife-edge and the sample surface. The size of the gap is adjusted with a micrometer. The knife-edge moves with a 3° takeoff angle relative to the sample surface so that the gap between the knife-edge and sample surface gradually increases during the retracting operation. This is to reduce the risk of the knife-edge striking adjacent sample cells.

Figure 11.6 illustrates the function of the knife-edge in the extended position. The θ_1 and θ_2 are the incident and diffracting angles respectively, and δ is the gap between the knife-edge and the sample surface. A part of the primary X-rays are blocked by the knife-edge, so they will not reach the adjacent cells on the right side of the knife-edge. The diffracted X-rays from the adjacent cells on the left side of the knife-edge are also blocked by the knife-edge. Therefore, only the diffraction from the defined area can reach the detector. The knife-edge can also prevent the direct beam from hitting the detector.

The triangle in Figure 11.6 shows the relationship between the size of the diffracted area S and the incident angle θ_1, diffracting angle θ_2, and the gap between the knife-edge and sample surface δ.

$$S = \delta(\cot\theta_1 + \cot\theta_2) \tag{11.3}$$

For a given cell pitch Δx, with half of the gap as a safety margin, the required knife-edge gap δ is given as

$$\delta \leq \frac{\Delta x}{\cot\theta_1 + \cot\theta_2} \tag{11.4}$$

If a range of θ_1 and θ_2 angles is used, the lowest possible angles should be used for this calculation. The performance of the retractable knife-edge was tested with a corundum powder sample. The sample-to-detector distance was 15 cm. The primary X-ray source and optics included a Cu tube, 40 kV/50 mA, a graphite monochromator and a 0.5 mm pinhole collimator. Both frames with or without knife-edge were collected at an incident angle of $\theta_1 = 1°$ and the detector at $\theta_2 = 29°$. The gap of the knife-edge was approximately 0.05 mm. Figure 11.7 shows the diffraction profiles

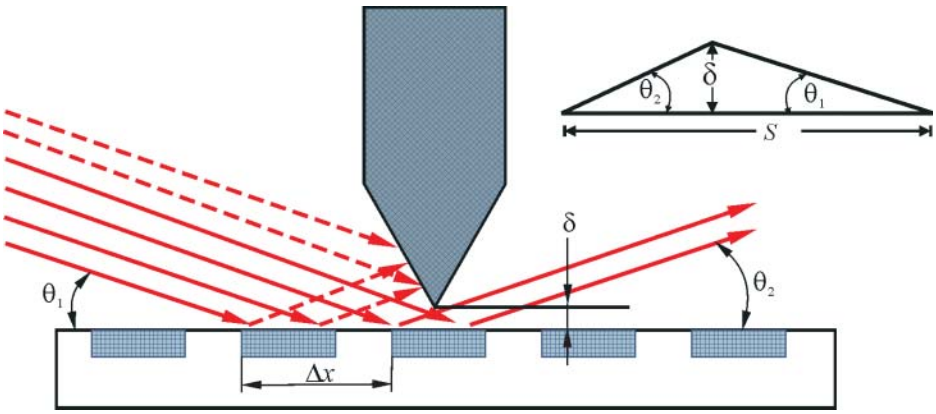


FIGURE 11.6 Knife-edge defining the irradiated area of diffraction.

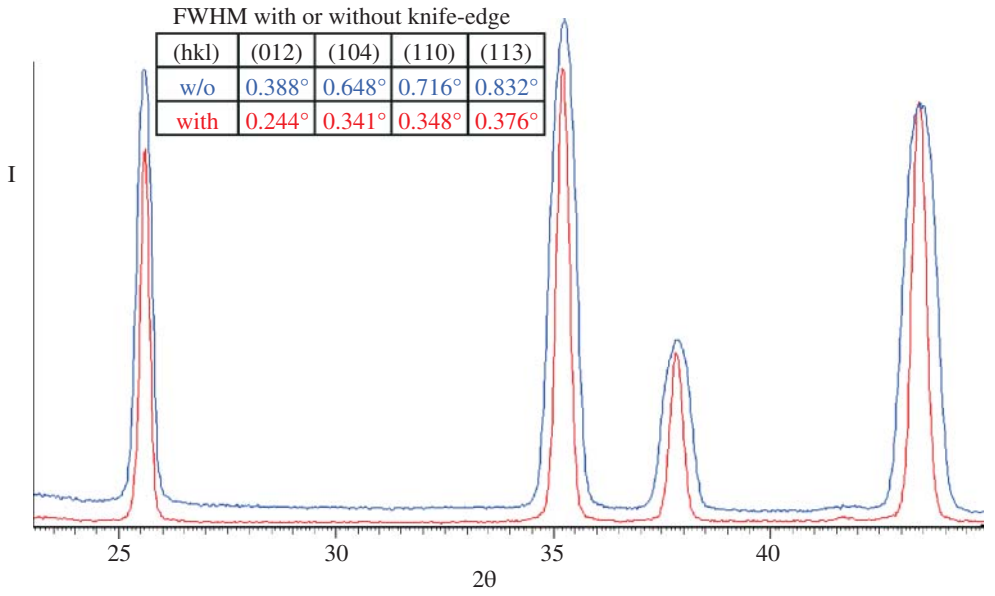


FIGURE 11.7 Diffraction profiles from corundum power without knife-edge (blue line) and with knife-edge (red line).

from γ-integration of both 2D frames. The profile with knife-edge (red line) is scaled up by a factor of 1.5 for easy comparison. The tabulated FWHM values show that diffraction peaks without the knife-edge (blue line) are much broader than those with the knife-edge. The knife-edge dramatically improves the 2θ resolution of the instrument for this experiment. The profile with knife-edge also has significantly lower background in this experiment.

Cross contamination was tested with a proprietary fixture designed for microdiffraction alignment and screening system verification. The fixture has an area with three Cu wires 1 mm in diameter and with a 5 mm separation. The minimum incident angle without cross contamination for a 0.5 mm beam and 5 mm separation is about $\theta_1 = 6°$. Figure 11.8 shows two frames collected at an incident angle of $\theta_1 = 4°$ and the detector at $\theta_2 = 41°$. The first frame in the figure is collected without the knife-edge, where both (111) and (200) peaks appear as three peaks. The center of the three peaks is from the Cu wire aligned to the instrument center and the two peaks on both sides are from the adjacent Cu wires. The second frame is collected with knife-edge in which no cross contamination is observed.

11.2.3 Screening in Transmission Geometry

The defocusing effect and cross-contamination can also be reduced or eliminated by using a XRD^2 system in transmission mode. The defocusing effect is observed with low incident angle over a flat sample surface in reflection mode diffraction. In reflection mode, for the same low incident angle, the diffracted beam at a low 2θ angle is sharper than the diffracted beam at a high 2θ angle. In transmission mode with the incident beam perpendicular to the sample surface, no such a defocusing effect is observed. A detailed description of transmission mode diffraction and a comparison between reflection mode and transmission mode diffraction with data frames collected from corundum powder are given in Chapter 7. In many combinatorial screening applications, such as polymorphism studies in pharmaceutical chemistry and catalyst development in the oil

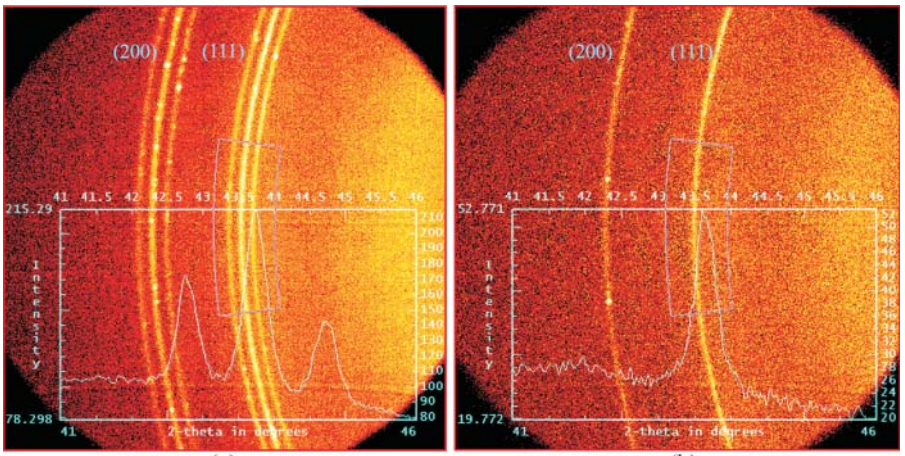


FIGURE 11.8 Diffraction profiles from the combinatorial screening verification fixture (1 mm Cu wire with 5 mm separation): (a) cross contamination without the knife-edge, (b) no cross contamination with knife-edge.

industry, a typical 2θ measurement range is 2–60°. It is preferable to run the combinatorial XRD screening in transmission mode in order to avoid the defocusing effect.

A two-dimensional diffraction system is designed for XRD screening in transmission mode for various applications, including screening of material libraries for combinatorial chemistry. Figure 11.9(a) shows a schematic of an XRD^2 system for combinatorial screening in transmission mode, and as an example, (b) is a picture of Bruker D8 Discover GADDS™ CST (combinatorial screening transmission) [36]. The system is built on a vertical two-circle goniometer. An offset mounted XYZ translation stage yields space for the X-ray source, optics, and area detector, while providing translations in the X, Y, and Z directions for material library scanning and sample alignment. The laser/video sample alignment system is mounted on one of the main axes of the goniometer so that it can be driven away after alignment. In the transmission mode X-ray diffraction measurement, the incident beam is typically perpendicular to the sample, so the irradiated area on the specimen is limited to a size comparable to the X-ray beam size, allowing the X-ray beam to be concentrated to the intended measuring area. In combinatorial screening applications, sample cells are located close to each other. Therefore, transmission mode diffraction can also avoid cross contamination between adjacent samples.

The transmission system can be built in two configurations: vertical θ-2θ geometry and vertical θ-θ geometry. With the θ-2θ configuration, the source and primary optics are mounted stationary and the 2D detector can be driven to a desired swing angle relative to the director beam. When low angle data is measured, a beamstop can be mounted on the stationary base of the goniometer to protect the detector from the direct beam. With the θ-θ geometry, both the primary beam (source and optics) and the detector can be driven independently to achieve various detector swing angles relative to the direct beam. For a given swing angle, both the primary beam and detector can move in a synchronized mode to achieve a sample oscillation effect equivalent to omega oscillation in the conventional X-ray diffractometer. In the system with the θ-θ configuration, the beamstop has to be mechanically connected to the primary beam so that the beamstop stays in the direct beam during θ_1 motion.

The choice between reflection and transmission modes is restricted mostly by the design of the sample plate and the way the sample was prepared. In reflection mode XRD screening, the

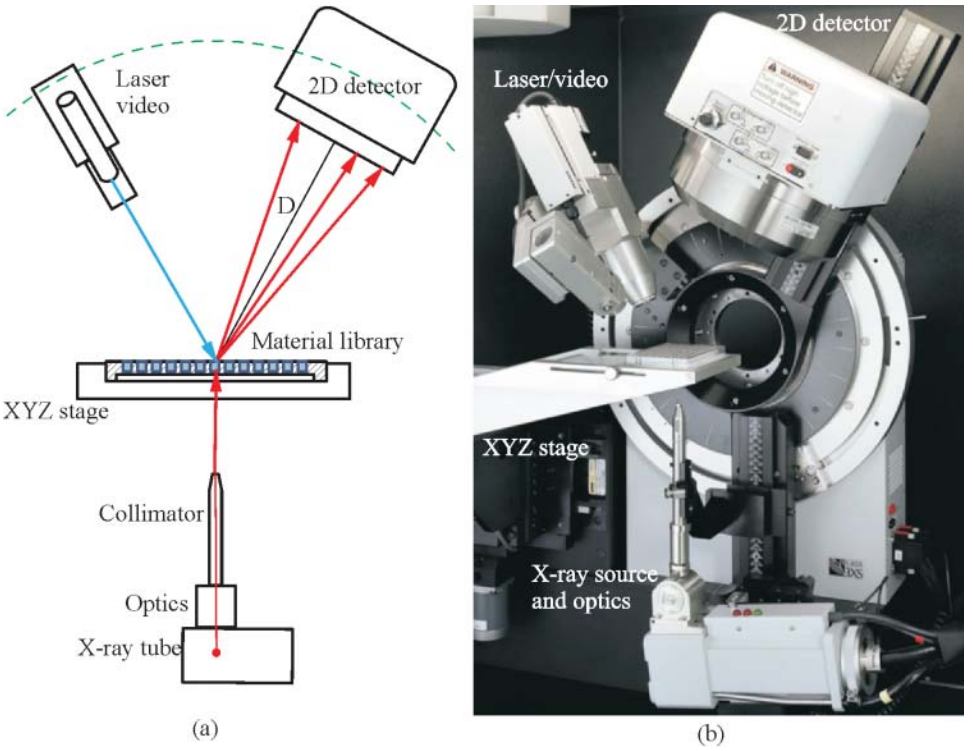


FIGURE 11.9 XRD^2 system for combinatorial screening in transmission mode: (a) schematic, (b) Bruker D8 Discover GADDS™ CST.

2D detector is on the same side of the sample plane as where the incident X-ray beam enters the sample. Reflection mode requires open space on at least one surface of the sample for both the incident X-ray beam and diffracted X-rays. This condition can be satisfied by most library plates. Figure 11.10 are some schemes of various material library plates and the corresponding XRD^2 system configurations for combinatorial screening. Scheme (a) represents plates without a beam path for transmission. The transmission beam path is either blocked by thick material on the plate or other components for material processing or conditioning in the library plate. Material library plates of this type can only be used in reflection mode XRD screening. In cases where the surface of the sample can only be exposed on the bottom of the plate, there is a special configuration with the incident beam reaching the sample from the bottom and detector positioned below the plate. The configuration can be illustrated by scheme (a) turned upside down.

The transmission mode requires that the incident X-ray beam enters the sample from one surface and that the 2D detector collects the diffracted X-rays at the other surface. Transmission mode requires open space on both sides of the sample plane to allow the primary optics and detector. In most cases the samples are kept in place by a layer of plate material or other materials. The incident X-ray and the diffracted X-rays are attenuated by the supporting material and the X-ray scattering from the supporting material also contributes a background to the collected data frames. The supporting material should be kept minimum in thickness and made of materials with light (low density) elements and that are amorphous in atomic structure, such as mylar or Kapton foils. Scheme (b) represents a type of material library plate in which a narrow beam path is below the sample, and open space is available above the sample. It is desirable to screen this material

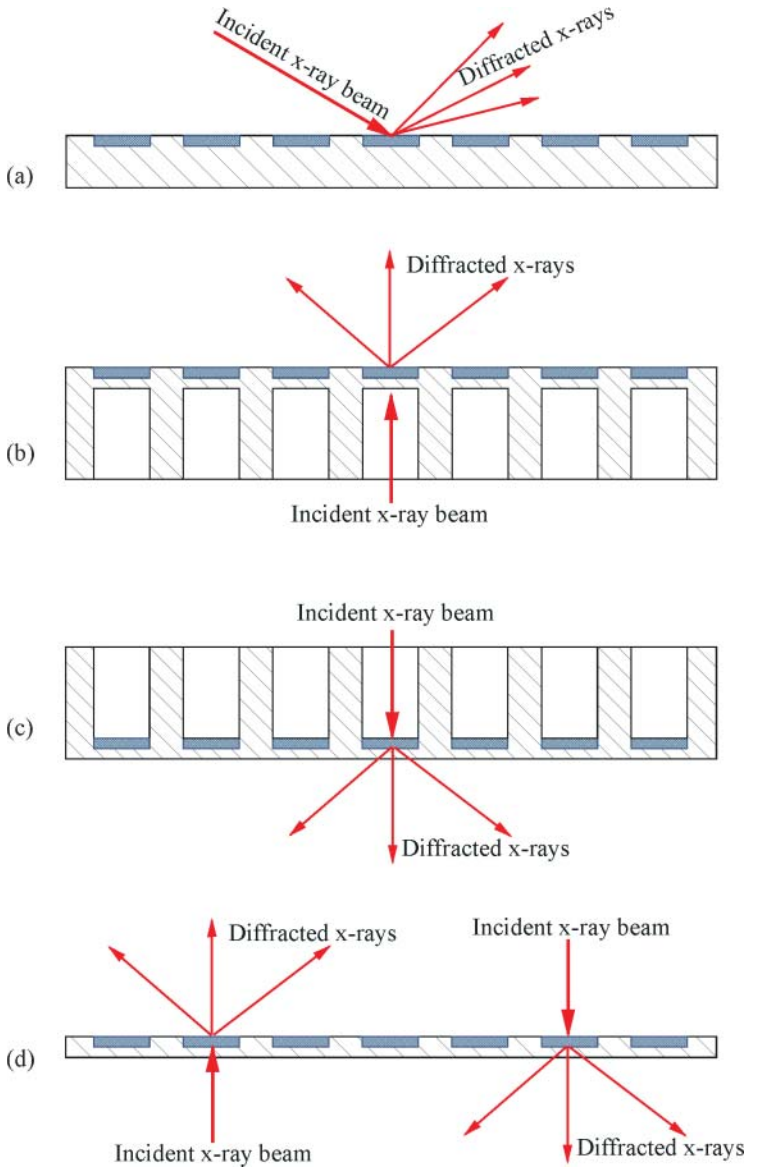


FIGURE 11.10 Schemes of various material library plates with: (a) no transmission beam path, (b) transmission path for beam-up configuration, (c) transmission path for beam-down configuration, (d) transmission path for both beam-up and beam-down configurations.

library with the beam-up configuration, in which the incident X-ray beam reaches the sample from below the library plate and the diffracted X-rays are measured above the plate. Scheme (c) shows a material library plate in which a narrow beam path is above the sample and open space is available beneath the sample. It is desirable to screen this material library with the beam-down configuration. Scheme (d) shows a material library plate in which open space is available both above and below the sample. Both beam-up and beam-down configurations can be used for this type of material library plate. The XRD combinatorial screening strategy should be considered

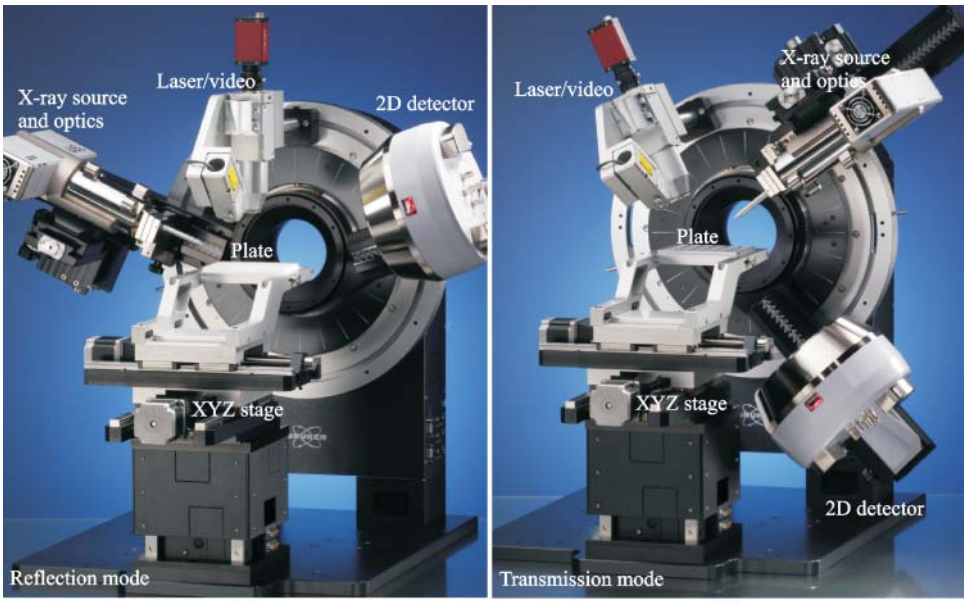


FIGURE 11.11 One system with automated reflection (a) and transmission (b) conversion (Bruker AXS D8 Discover™ HTS).

in the material library design. For instance, the material library may consist of several layers for various functions, with a layer designed for screening that can be removed from the assembly during XRD data collection.

A transmission mode X-ray diffraction screening system may be designed modularly to allow easy switching between the beam-up and beam-down configurations. Transmission mode diffraction data can be collected on a system dedicated to reflection mode screening, as shown in Figure 11.1, with the sample plate rotated 90°. The same is true when reflection mode diffraction data is collected on a system dedicated to transmission, as shown in Figure 11.9. In cases where both reflection and transmission modes are desired in one system, a system with automated reflection-transmission conversion while keeping the library plate in the horizontal position has been designed [37]. Figure 11.11 is a picture of a Bruker D8 Discover™ HTS (high-throughput screening). The system can run at an optimum configuration for both reflection (a) and transmission (b) modes while keeping the material library plate in the horizontal position. In reflection mode (a) both the X-ray source/optics assembly and 2D detector are on the same side (top) of the material library plate. The switch from reflection mode to transmission mode is simply done by driving the X-ray source and optics assembly from the same side (top) of the sample plate to the opposite side (bottom).

11.3 COMBINED SCREENING WITH XRD^2 AND RAMAN

Combinatorial screening with two-dimensional X-ray diffraction can be combined with other material characterization techniques. One example is to combine XRD^2 and Raman spectroscopy. Unlike most analytical techniques, both X-ray diffraction and Raman spectroscopy are non-destructive methods that require virtually no sample preparation, thus allowing samples to be

analyzed simply and quickly in their natural form. These two techniques are also complementary to one another in that X-ray diffraction provides abundant information on the atomic arrangement of the sample revealed through the diffraction pattern and Raman spectroscopy can measure the characteristic vibration frequencies determined by the chemical composition and chemical bonds [38, 39]. For crystal form analysis in pharmaceutical research, the primary technique is X-ray diffraction, since it is directly related to the crystal structure. Ideally, the effective diffraction volume should cover some 10^8–10^{10} crystallites with completely random orientation. However, in some cases it is very difficult to distinguish two crystal forms when they have very similar diffraction patterns due to preferred orientations and poor sampling statistics associated with a small amount of sample on the library plate. In these cases, cluster analysis based solely on XRD data may not be able to distinguish between relative intensity changes due to crystal structural changes and changes due to preferred orientation, crystal size, or even instrument alignment error, while Raman spectroscopy, or other vibration spectroscopy techniques (FTIR, NIR), may be able to distinguish the crystal forms without ambiguity [40].

As complex composite systems require sophisticated modeling to separate chemical and physical features, no single technique has proven to be universally applicable to suit all the analytical needs of pharmaceutical manufacturing and characterization [41]. Combinatorial screening based on spectroscopic and diffraction techniques is of high importance for drug substances and formulations since the polymorphism of active ingredients has to be controlled to achieve a reliable product quality that will satisfy regulatory authorities. In patent applications, two or more independent techniques are more likely to uniquely identify a particular solid form than one technique. For instance, the claims of a cocrystal describe it as having XRPD peaks at about 10.6 and 12.1 degrees 2θ and Raman peaks at about 735 cm^{-1} and about 809 cm^{-1} [42].

Figure 11.12 is a picture of a combinatorial screening system (Bruker AXS D8 ScreenLab™) consisting of a two-dimensional X-ray diffractometer, Raman spectrometer, and video microscope. The XRD pattern, Raman pattern, and optical image of a carbamazepine powder sample are shown below the picture of the instrument. X-ray detector, laser source, Raman probe, and an auto-zoomed video microscope are all integrated into a single platform so that the X-ray diffraction pattern, Raman spectrum, and optical image from the same sample or sample area can be measured simultaneously or sequentially. All three measurements (Raman spectrum, X-ray diffraction, and optical imaging) are non-destructive and need no special sample preparation. The information obtained from the three measurements are complementary. Therefore, a combination of the three functions into one instrument is beneficial to high-throughput combinatorial screening. The XYZ translation stage can bring each cell of the combinatorial library into both measurement positions. The laser and video microscope is mainly used to align the samples to the instrument center automatically. In addition, the optical video image can provide the surface condition, color, and shape of the sample. All three measurements can be done in a relative short time. Therefore, a combination of the three functions into one instrument is beneficial to high-throughput combinatorial screening analysis [43, 44].

Once the solid-state characterization data is collected and stored, samples can be generally classified into groups or quantified by novel, statistical, pattern-matching software. Besides fast evaluation of large databases, convenient access to each individual measurement result can yield a deeper insight on the molecular level. The software associated with the system can treat data from the various techniques and analyze the results in conjunction [45]. The results show that combined screening can distinguish forms better than either Raman or XRD individually, identification of pure phases or mixtures is improved, and the combined data can highlight any inconsistencies in separate analyses. The combined techniques are not limited to just Raman and XRD, and can be extended to Near IR; XRF, DSC, and so on.

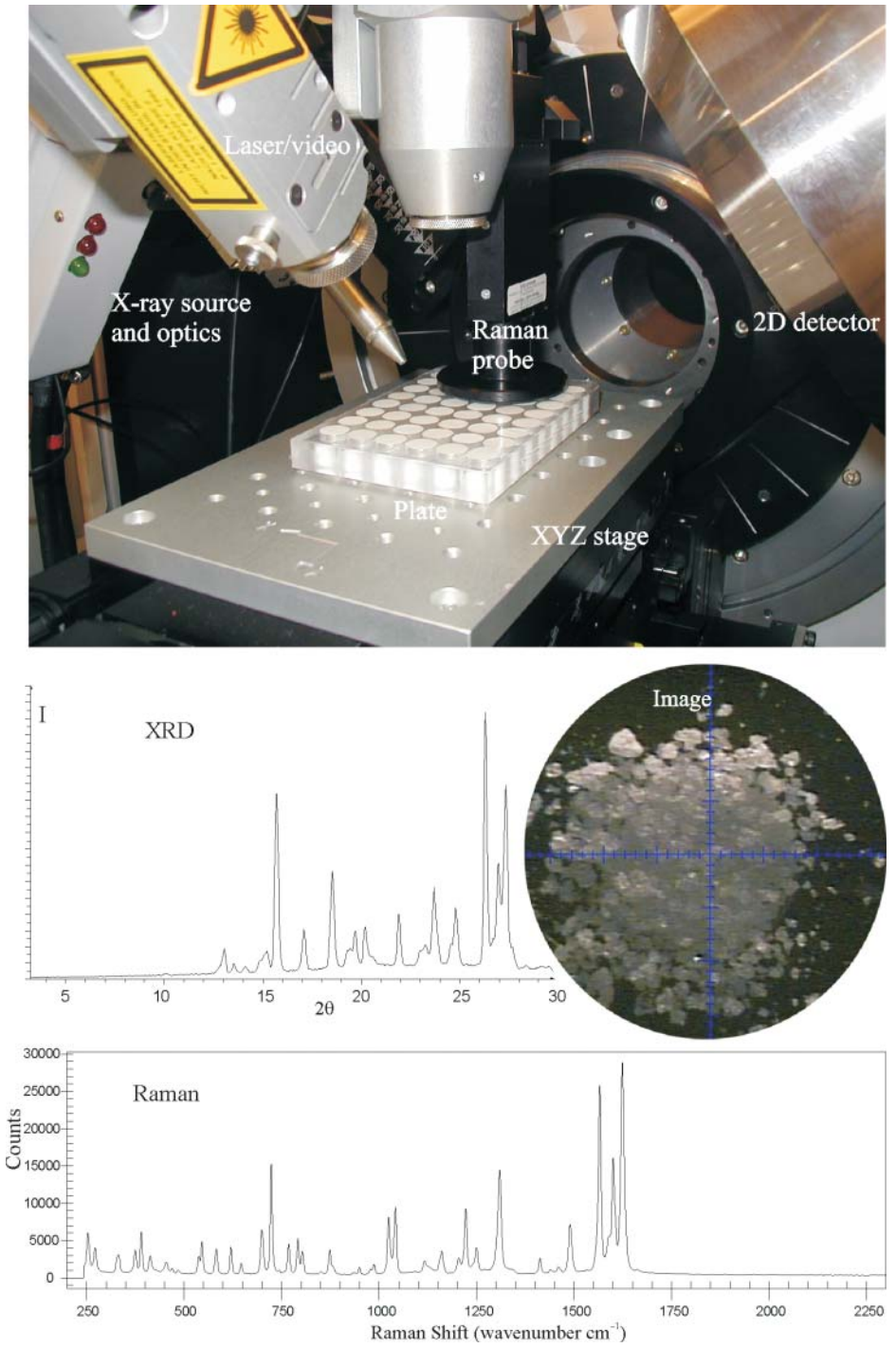


FIGURE 11.12 Combinatorial screening system (Bruker AXS D8 ScreenLab™) and XRD pattern, Raman pattern, and optical image of Carbamazepine powder.

REFERENCES

1. J. J. Hanak, The "multiple sample concept" in materials research: synthesis, compositional analysis and testing of entire multicomponent systems, *J. Mater. Sci.*, 1970, **5**, 964–971.
2. N. K. Terrett, *Combinatory Chemistry*, Oxford University Press, New York, 1998.
3. M. S. Lesney, The red queen's race: combinatorial chemistry feeds the need for speed, *Today's Chemist at Work*, January, 1999, **8** (1) 36–43.
4. R. Brown, Worldwide alliance pursues discovery tools, *Today's Chemist at Work*, January, 1999, **8** (1) 48–50.
5. J. S. MacNeil, Innovating in the material world, *Today's Chemist at Work*, December, 1999, **8** (12) 22–28.
6. R. Dagani, A faster route to new materials, *Chemical & Engineering News*, March **8**, 1999, 51–60.
7. S. Borman, Reducing time to drug discovery, *Chemical & Engineering News*, March **8**, 1999, 33–48.
8. X. D. Xiang et al., A combinatorial approach to materials discovery, *Science*, 1995, **268** (5218), 1738–1740.
9. B. Jandeleit, et al., Combinatorial materials science and catalysis, *Angew. Chem., Int. Ed. Engl.* 1999, **38**, 2494–2535.
10. J. Bernstein, Pharmaceuticals: development and formulation, *Industrial Applications of X-ray Diffraction*, edited by F. H. Chung and D. K. Smith, Marcel Dekker, New York, 2000, 527–538.
11. J. Anwar, Pharmaceuticals: design and development of drug delivery systems, *Industrial Applications of X-ray Diffraction*, edited by F. H. Chung and D. K. Smith, Marcel Dekker, New York, 2000, 539–553.
12. B. Litteer and D. Beckers, Increasing application of X-ray powder diffraction in the pharmaceutical industry, *American Laboratory*, June 2005, 22–24.
13. S. Yin et al., Simulated PXRD patterns in studies of the phase composition and thermal behavior of bulk crystalline solids, *American Pharmaceutical Review*, 2003, **6** (2), 80–85.
14. M. Davidovch et al., Detection of polymorphism by powder X-ray diffraction: interference by preferred orientation, *American Pharmaceutical Review*, 2004, **7** (1), 10–16.
15. P. J. Desrosiers, The potential of perform: an integrated approach to preformulation allows researchers to complete this crucial step earlier in the drug development process, *Modern Drug Discovery*, January, 2004.
16. S. Yin et al., Bioavailability enhancement of a COX-2 inhibitor, BMS-347070, from a nanocrystalline dispersion prepared by spray-drying, *J. Pharm. Sci.*, 2005, **94** (7), 1598–1607.
17. S. Yin et al., In-situ variable temperature powder X-ray diffraction and thermal analysis, *American Pharmaceutical Review*, 2005, **8** (2), 56–62.
18. S. Yin, C. J. Pommier, and R. P. Scaringe, The role of PXRD in QbD and PAT, PPXRD-6 organized by ICDD, Barcelona, Spain, February **19–22**, 2007.
19. J. Klein, C. W. Lehmann, H-W. Schmidt, and W. F. Maier, Combinatorial material libraries on the microgram scale with an example of hydrothermal synthesis, *Angew. Chem., Int. Ed. Engl.* 1998, **37** (24), 3369–3372.
20. B. B. He et al., XRD rapid screening system for combinatorial chemistry, *Advances in X-ray Analysis*, 2001, **44**, 1–5.
21. B. B. He, L. Brügemann, and U. Preckwinkel, Rapid combinatorial screening by means of X-ray diffraction, *Business Briefing: Pharmatech*, 2003.
22. R. D. Durst and B. B. He, Diffraction system for biological crystal screening, US Patent No. 6,836,532, Dec. 28, 2004.
23. J. Fink et al., X-ray micro diffractometer sample positioner, US Patent No. 5,359,640, Oct. 25, 1994.
24. C. J. Gilmore, G. Barr, and J. Paisley, High-throughput powder diffraction. I. A new approach to qualitative and quantitative powder diffraction pattern analysis using full pattern profiles, *J. Appl. Cryst.* (2004). **37**, 231–242.

25. G. Barr, W. Dong, and C. J. Gilmore, High-throughput powder diffraction. II. Applications of clustering methods and multivariate data analysis, *J. Appl. Cryst.* (2004). **37**, 243–252.
26. G. Barr, W. Dong, C. Gilmore, and J. Faber, High-throughput powder diffraction. III. The application of full-profile pattern matching and multivariate statistical analysis to round-robin-type data sets, *J. Appl. Cryst.* (2004). **37**, 635–642.
27. G. Barr, W. Dong, and C. J. Gilmore, High-throughput powder diffraction. IV. Cluster validation using silhouettes and fuzzy clustering, *J. Appl. Cryst.* (2004). **37**, 874–882.
28. T. G. Fawcett et al., Using PDF-4+/Organics to discover and analyze polymorphs, PPXRD-7 organized by ICDD, Orlando, FL, February **26**, 2008.
29. G. Barr, W. Dong, and C. J. Gilmore, PolySNAP: a computer program for analyzing high-throughput powder diffraction data, *J. Appl. Cryst.* (2004). **37**, 658–664.
30. G. Barr, C. J. Gilmore, and J. Paisley, SNAP-1D: a computer program for qualitative and quantitative powder diffraction pattern analysis using the full pattern profile, *J. Appl. Cryst.* (2004). **37**, 665–668.
31. G. Barr, W. Dong, C. J. Gilmore, A. Parkin, and C. C. Wilson, dSNAP: a computer program to cluster and classify Cambridge Structural Database searches, *J. Appl. Cryst.* (2005). **38**, 833–841.
32. PolySNAP: High-throughput XRD data analysis for research, development and production control, Bruker AXS Handout, Order No. DOC-H88-EXS010, 2007.
33. M. Norman et al., Characterization of insulin microcrystals using powder diffraction and multivariate data analysis, *J. Appl. Cryst.* (2006). **39**, 391–400.
34. B. B. He and F. F. Jin, X-ray diffraction screening system with retractable X-ray shield, US Patent No. 6,718,008, Apr. 6, 2004.
35. B. B. He et al., Retractable knife-edge for XRD combinatorial screening, *Advances in X-ray Analysis*, 2004, **47**, 194–199.
36. B. B. He, R. C. Bollig, and H. M. L. Brügemann, Transmission mode X-ray diffraction screening system, US Patent No. 6,859,520, Feb. 22, 2005.
37. B. B. He and R. C. Bollig, X-ray diffraction screening system convertible between reflection and transmission modes, US Patent No. 7,242,745, Jul. 10, 2007.
38. D. A. Long, *Raman Spectroscopy*, McGraw-Hill, 1977.
39. D. J. Gardiner and P. R. Graves, *Practical Raman Spectroscopy*, Springer-Verlag, 1989.
40. B. Sarsfield et al., When spectroscopy is better than powder X-ray diffraction for crystal form analysis of active pharmaceutical ingredients, *American Pharmaceutical Review*, 2007, **10** (1), 16–23.
41. L. D. Peter et al., Quantitative PXRD and complementary techniques: improving resolution for multicomponent compact systems using contemporary chemometric methods, PPXRD-7 organized by ICDD, Orlando, FL, February **25–28**, 2008.
42. E. H. Barash, Trends in solid form patents: cocrystal IP opportunities and challenges, PPXRD-6 organized by ICDD, Barcelona, Spain, February **19–22**, 2007.
43. B. B. He, C. S. Frampton, and F. W. Burgäzy, Combinatorial screening system with X-ray diffraction and Raman spectroscopy, US Patent No. 7,269,245, Sep. 11, 2007.
44. B. He, C. Frampton, J. Sawatzki, A. Kern, C. Gilmore, and G. Barr, Combined XRD and Raman combinatorial screening system, PPXRD-6 organized by ICDD, Barcelona, Spain, February **19–22**, 2007.
45. G. Barr and C. Gilmore, How to combine PXRD, Raman and other 1-D data in high throughput studies, PPXRD-6 organized by ICDD, Barcelona, Spain, February **19–22**, 2007.

12

MISCELLANEOUS APPLICATIONS

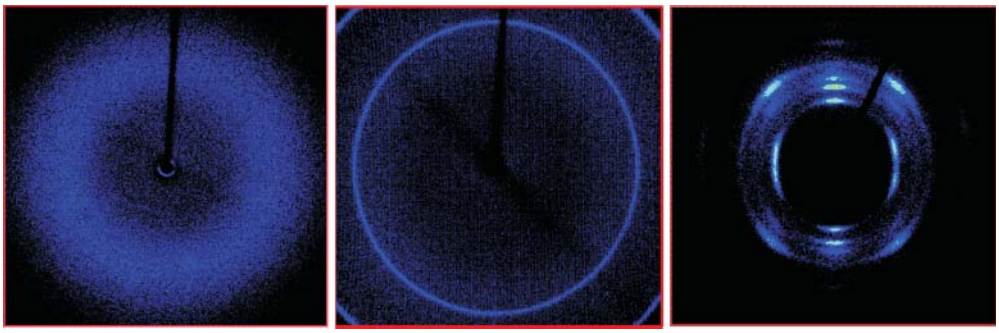
12.1 PERCENT CRYSTALLINITY

12.1.1 Introduction

The crystallinity of a polymer material influences many of its characteristics, including mechanical strength, opacity, and thermal properties. Crystallinity measurement provides valuable information for both materials research and quality control in material processing [1–6]. X-ray scattering occurs from both crystalline and non-crystalline materials, but the scattering intensity distribution in space is determined by the atomic arrangement in the materials. Crystalline materials have long range order and the diffraction pattern from a crystalline material has many sharp peaks corresponding to various crystal planes based on Bragg's law. Amorphous materials, either solid or liquid, do not have long range order as a crystal does, but the atomic distance has a narrow distribution due to the atoms being tightly packed. In this case, the intensity of the scattered X-rays forms one or two maxima with a very broad distribution in the 2θ range reflecting the distribution of the atomic distances. The diffraction pattern from a material containing both amorphous and crystalline solids has a broad background from the amorphous phase and sharp peaks from the crystalline phase.

The weight percentage of the crystalline phases in a material containing both crystalline and amorphous phases is referred to as percent crystallinity. Assuming that the X-ray scattering intensity from each phase in such a material is proportional to its weight percentage, and that the scattering intensities from all phases can be measured within a given 2θ range, the percent crystallinity can be determined by the ratio of the integrated intensity of the crystalline peaks to the total scattered intensity [7–10]. Therefore, deconvolution of the diffraction pattern from the contributions of the amorphous and the crystalline scatterings is the key to obtaining a reliable number that is consistent with other techniques such as NMR and calorimetry [2, 11]. Percent crystallinity as obtained by X-ray measurements is defined as the ratio of intensity from the crystalline peaks

Two-Dimensional X-Ray Diffraction, Second Edition. Bob Baoping He.
© 2018 John Wiley & Sons, Inc. Published 2018 by John Wiley & Sons, Inc.



(a) (b) (c)

FIGURE 12.1 (a) Amorphous scattering, (b) random polycrystalline scattering, (c) oriented polycrystalline and amorphous scattering.

to the sum of the crystalline and amorphous intensities:

$$x_{pc} = 100\% \frac{I_{crystal}}{I_{crystal} + I_{amorphous}}. \tag{12.1}$$

where x_{pc} is the percent crystallinity, $I_{crystall}$ is the integrated intensity of all crystalline peaks and $I_{amorphous}$ is the integrated intensity of the amorphous scattering. Figure 12.1 shows 2D frames from (a) amorphous materials, (b) crystalline materials, and (c) their mixtures. X-ray scattering from amorphous materials produces a diffuse halo of intensity, which when integrated over γ gives a very broad distribution in the 2θ range. X-ray scattering from polycrystalline materials produces well-defined rings which integrate to sharp, higher-intensity peaks. X-ray scattering from a material containing an amorphous matrix with an oriented crystalline phase produces a mixture of the broad background and sharp diffraction patterns with scattering intensity as a function of both 2θ and γ. Figure 12.2(a) shows an integrated diffraction profile from a polymer sample with crystallinity that consists of sharp crystalline peaks and a broad amorphous background. Figure 12.2(b) shows the separation of the sharp crystalline peaks and the amorphous background. The area under each profile represents the corresponding integrated intensity.

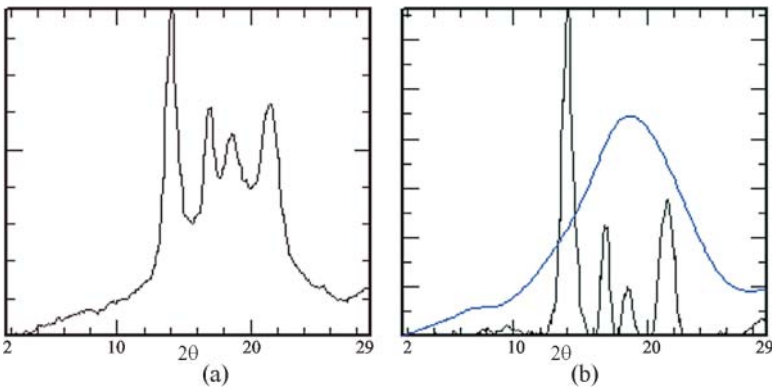


FIGURE 12.2 (a) Integrated diffraction profile showing the sharp crystalline peaks and broad amorphous background, (b) separation of the sharp crystalline peaks and amorphous background.

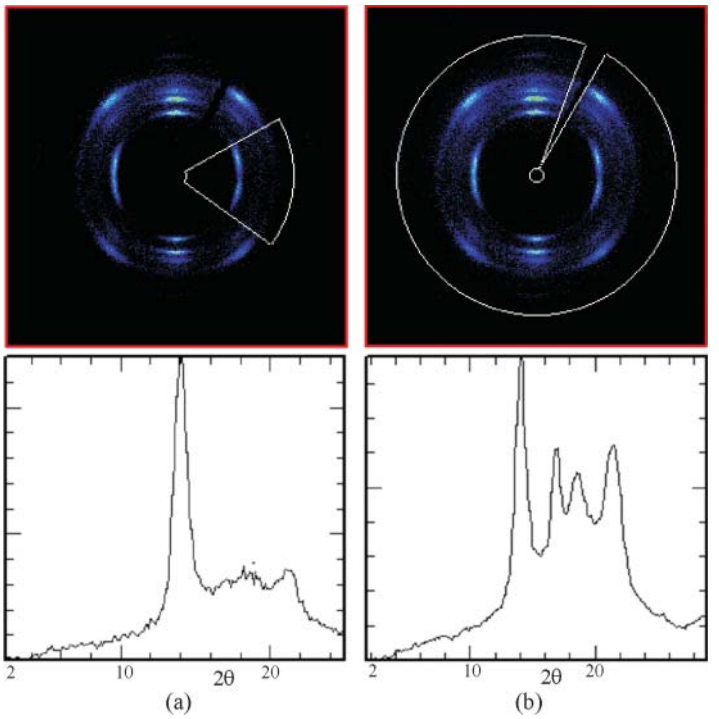


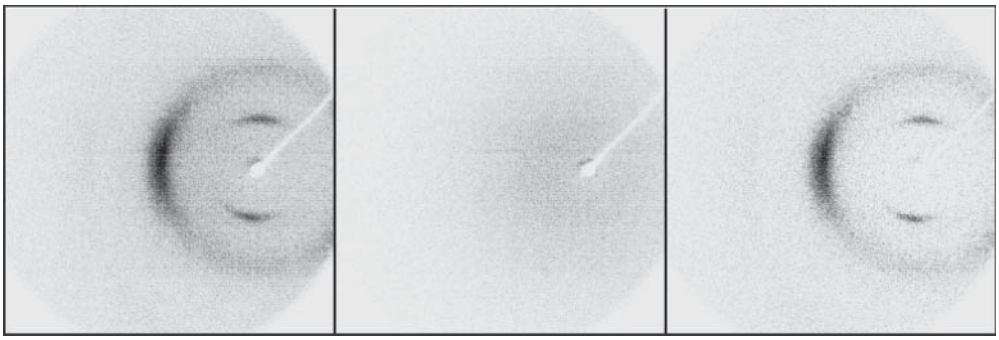
FIGURE 12.3 2D diffraction pattern from an oriented polycrystalline polymer sample, (a) diffraction profile integrated from a horizontal region analogous to a profile collected with point detector, (b) diffraction profile integrated from all part of the 2D frame.

12.1.2 Comparison of Conventional XRD and XRD^2

The accuracy of measured percent crystallinity is dependent on the integrated diffraction profile. Since most crystallinity samples have a preferred orientation, it is very difficult to have a consistent crystallinity measurement with a conventional diffractometer. Figure 12.3 shows a 2D diffraction frame collected from an oriented polycrystalline sample. The diffraction is in transmission mode with the X-ray beam perpendicular to the plate sample surface. Figure 12.3(a) shows a diffraction profile integrated from a horizontal region analogous to a profile collected with the conventional diffractometer. Only one crystalline peak can be observed from the profile. This means that the diffraction profile would look like the one in Figure 12.3(a) had a conventional diffractometer been used for data collection in the same sample orientation. It is also possible that a different peak or no peak would be measured if the sample is loaded in other orientations. Figure 12.3(b) is the diffraction profile integrated from the region covering all crystalline peaks over almost all azimuthal angles. A total of four crystalline peaks are observed. Apparently, the percent crystallinity measured with the conventional diffractometer is not consistent if the preferred orientation is not considered. The sample orientation has no effect on the full circle integrated diffraction profile from a 2D frame, therefore, an XRD^2 system can measure percent crystallinity more accurately with consistent results [12, 13].

12.1.3 Scatter Correction

The measured total intensity may have significant contributions other than from crystalline and amorphous scattering from the sample. Air scatter, specimen holder scatter (e.g. capillary glass



(a) (b) (c)

FIGURE 12.4 (a) Nylon frame with air scatter, (b) air scatter frame without sample, (c) nylon frame with air scatter subtracted.

scatter), and Compton (or incoherent) scatter must also be taken into account. Air scatter occurring after the specimen and specimen holder scatter can be corrected for by measuring "blank" frames under identical conditions as the sample (with the exception of the measurement time). Note that the beamstop must not be repositioned between the measurement of the blank and data frames for measurements in transmission mode. Figure 12.4 shows an example of this correction. Figure 12.4(a) is a transmission frame collected from a nylon sheet which includes air scatter, (b) is a frame with air scatter only collected without the sample, and (c) is a frame with air scatter subtracted.

The beamstop will also cause considerable scattering if it is not properly aligned (to block the primary beam). Another air scatter effect arises from incident-beam scattering, which is a function of the sample geometry. The best approach is to reduce this effect by putting the sample as close to the tip of the incident beam collimator as possible or use a sample plate significantly larger than the incident beam in transmission mode so that the air scatter from the primary beam is blocked by the sample. This eliminates the shadow on the detector that is absorption of air scatter before the sample.

Compton or incoherent scattering can make a substantial contribution to the background intensity. If it is not corrected, the percent crystallinity value can be artificially low, especially for polymeric materials. Compton scattering can be modeled and removed in both the internal and external methods. This correction is unnecessary if the same material is examined and its density varies no more than ~20%. More discussion on correction of Compton effects can be found in literature [1, 14–17].

12.1.4 Internal and External Methods

The internal method is used when there is overlap of the crystalline and amorphous regions, especially when the frames contain continuous Debye rings, for which the external method cannot be used. While this method can be used for oriented peaks, the external method is better suited for such materials. For unoriented materials as shown in Figure 12.5(a), separate integration regions are selected as amorphous regions and crystalline regions. The start and end γ values for all the regions must be the same, otherwise the region bounded by the difference in the γ values is also considered amorphous. To determine the boundaries of the crystalline and amorphous regions, the areas are integrated into a diffraction profile, and profile fitting is used to deconvolute the crystalline and amorphous peaks. In the crystalline region, a linear boundary is assumed to

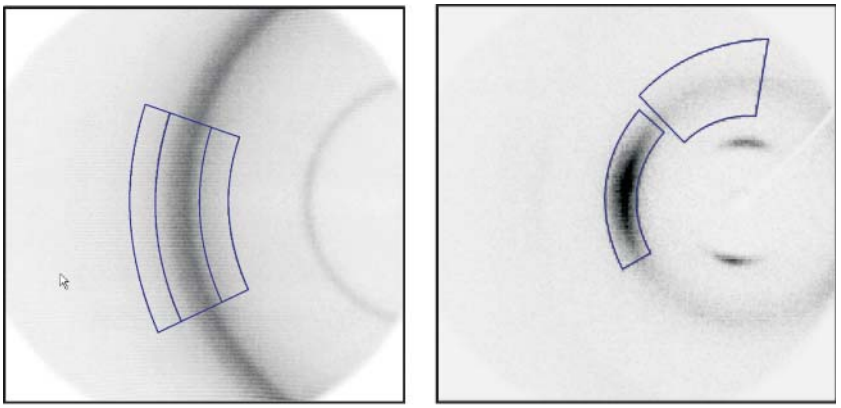


FIGURE 12.5 (a) Internal method for γ-nylon powder, (b) external method for γ-nylon fiber.

separate the crystalline intensity and the amorphous background. A non-linear background fit, such as a second order polynomial, may be used as a curved surface to separate the crystallinity intensity and the background intensity. Then the percent crystallinity with internal method is calculated from

$$x_{pc} = 100\% \cdot \frac{I_{crystalline\ region} - I_{background}}{I_{crystalline\ region} + I_{amorphous\ region}} \tag{12.2}$$

where $I_{crystalline\ region}$ is the integrated intensity of the crystalline region containing the crystalline peaks and background, $I_{background}$ is the background intensity of the crystalline region, and $I_{amorphous\ region}$ is the integrated intensity of the amorphous region.

The external method calculates percent crystallinity within a user-defined region. Both an amorphous-only region and a crystalline-plus-amorphous region must be specified. Figure 12.5(b) shows the external method. The external method is used for oriented polymers. The amorphous region, rather than the region containing both crystalline and amorphous scatter, will give the best information on the extent of amorphous scatter. These values are used for the lower and upper limits on the amorphous external function. The same 2θ limits can also be used for the crystalline region. Examine the crystalline region with a 2θ integration to determine the boundary in γ to set for the crystalline scattering. Note that the crystalline region contains amorphous scatter too. However, this region must not overlap with the previously selected amorphous region. The amorphous γ range does not have to match the crystalline γ range if the area of the amorphous region is scaled to the area of the crystalline region. There can be multiple oriented crystalline peaks in the crystalline region, unlike in the internal method. The amorphous region must have no crystalline scatter within its boundaries. If the sample has unoriented crystallites, then it is impossible to have a pure amorphous region, and the external method will include this scatter in the amorphous component. This will lead to a lower crystallinity. If the amount of material that is randomly oriented is constant, this method is still valid as a relative measure of crystallinity. Then the percent crystallinity with the external method is calculated from

$$x_{pc} = 100\% \cdot \frac{I_{crystalline\ region} - I_{amorphous\ region}}{I_{crystalline\ region}} \tag{12.3}$$

where $I_{crystalline\ region}$ is the integrated intensity of the crystalline region containing the crystalline peaks and amorphous background, and $I_{amorphous\ region}$ is the integrated intensity of the amorphous region.

12.1.5 Full Method

The external and internal methods employ user-specified areas of frame data for a relative measurement of percent crystallinity. The full method is the best to use when there is overlap of the crystalline and amorphous regions over the measured azimuthal angles. The full method calculates the percent crystallinity by directly extracting an amorphous background frame from the original frame and uses

$$x_{pc} = 100\% \cdot \frac{I_{original\ frame} - I_{background\ frame}}{I_{original\ frame}} \tag{12.4}$$

where $I_{original\ frame}$ is the integrated intensity of the frame containing the crystalline scattering and amorphous scattering and $I_{background\ frame}$ is the integrated intensity of the background. This method for background estimation is based on morphological processing. The amorphous background of a diffraction pattern can be estimated with a composite morphological operation, called a "rolling ball algorithm" [18, 19]. As shown in Figure 12.6, the operation can be interpreted physically as taking a "ball" and pressing it up against the underside of the intensity surface of the frame. The background is found by tracking the highest point reached by the "ball" at each pixel. As long as the ball is large enough, it cannot enter the positive excursions that correspond to the peaks. However, the ball can track the broad background very well. Since the ball may be forced down by sharp noise "spikes", noise reduction by smoothing the background is necessary. The radius of the ball is a user-defined parameter for optimum and consistent background estimation. In order to have flexibility to the various amorphous background levels and sharpnesses of the crystalline peaks, a "sliding ellipsoid" is actually used instead of a rolling ball. The radius and height parameters affect the shape of the sliding ellipsoid used to characterize the amorphous background. The smaller the radius parameter, the closer the background surface follows the frame image. The height parameter affects the shape of the "sliding" ellipsoid. The smaller the height parameter is relative to the radius, the flatter the ellipsoid. A height of zero represents a flat disk. A height equal to the radius parameter represents a sphere. For sharp crystalline peaks,

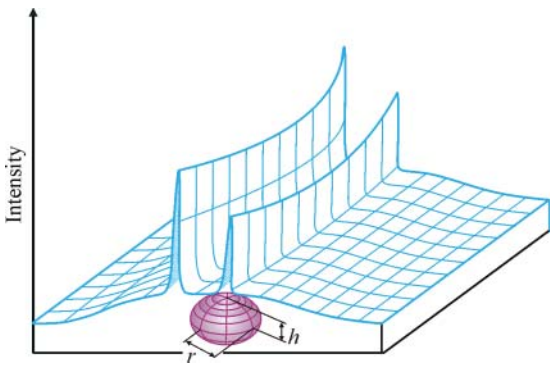


FIGURE 12.6 Schematic of rolling ball background subtraction.

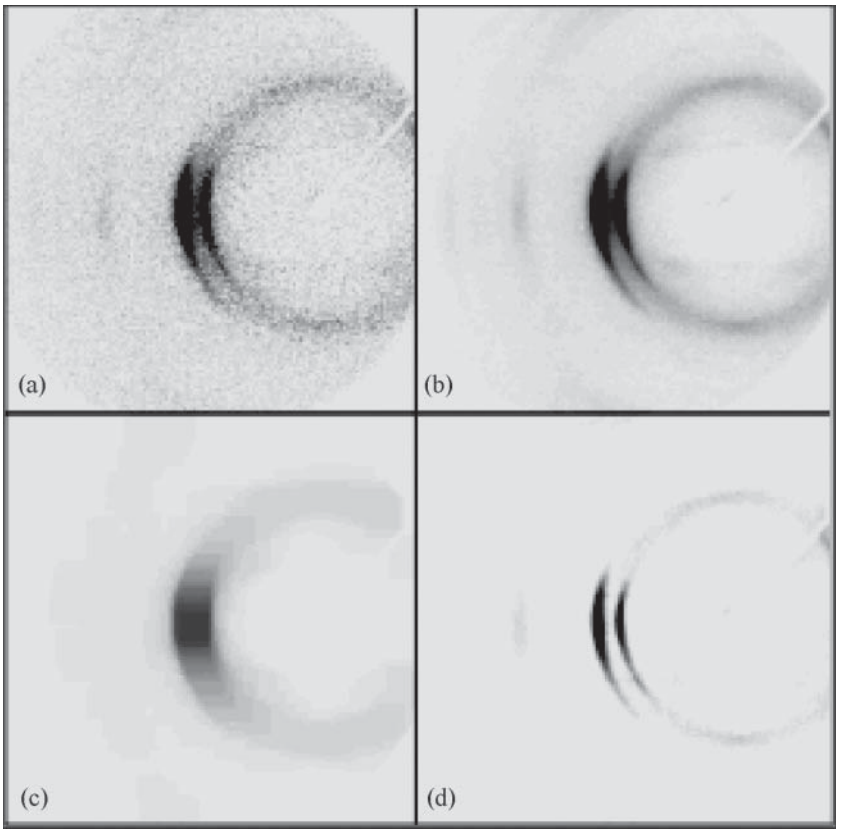


FIGURE 12.7 Percent crystallinity data process with a frame collected from a nylon fiber: (a) original frame with air scatter removed, (b) smoothed frame with air scatter removed, (c) amorphous background frame generated from frame (b), (d) crystalline scattering.

a larger height parameter can be used to make the ellipsoid fit better to the amorphous intensity surface. The radius should be the smallest possible value, but not so small that the crystalline features remain in the resultant background frame.

Figure 12.7 illustrates the data process of percent crystallinity measurement with the full method using a frame collected from a nylon fiber as an example. The frame (a) is the original frame with air scatter removed, (b) is the smoothed frame with air scatter removed, (c) is the amorphous background frame generated from frame (b) by the rolling ball algorithm, and (d) is a frame containing crystalline scattering only which is generated by subtracting frame (c) from frame (a). The percent crystallinity in this example is given by

$$x_{pc} = 100\% \cdot \frac{I_a - I_c}{I_a} = 100\% \cdot \frac{I_d}{I_a} \tag{12.5}$$

where I_a, I_c, and I_d are the integrated intensities (total frame counts) of the frames (a), (c), and (d) respectively.

12.2 CRYSTAL SIZE

12.2.1 Introduction

The properties of polycrystalline materials are determined by the properties of each crystallite and the boundaries between crystallites. The size of the crystallites in a polycrystalline material has significant effects on many of its properties, such as thermal, mechanical, electrical, magnetic, and chemical properties. For instance, the mechanical strength of polycrystalline metals and alloys are strongly dependent on the crystallite size. The deformation of metals is caused by the motion of dislocations and other defects under loading stress. Different crystallographic orientations and the boundaries between adjacent crystallites serve as barriers to the motion of dislocations and other crystal defects. A metal with finer crystallites therefore has more boundaries to impede dislocation motion. For most metal materials, the relation between yield strength σ_y and grain size d is described mathematically by the Hall–Petch equation [20]

$$\sigma_y = \sigma_o + k_y d^{-1/2} \tag{12.6}$$

where σ_0 and k_y are constants for a particular material. A crystallite is also referred to as a grain or particle, but may be used with preference for a particular microstructure. For instance, the metal phase or its solid solution phase are typically referred to as grains, but the fine and hard crystallites of metallic or non-metallic compounds, such as carbides in metallic matrix, are often referred to as particles. Crystallites size can be measured by many techniques, such as optical microscopy or electron microscopy on polished and etched surfaces. X-ray diffraction has been used for crystallites size measurement for over 100 years since Scherrer and subsequent contributions were made by Stokes & Wilson and Warren & Averbach. All these methods are based on diffraction line broadening and line profile analysis. Many publications are available with detailed discussion and modified algorithms of the line profile analysis for crystallite size and size distribution [21–24]. This section will give a brief introduction to crystallite size analysis by line profile analysis. Another approach in crystallite size measurement is based on the spotty diffraction rings collected with two-dimensional detectors when a small X-ray beam is used [25, 26]. Line profile analysis is based on the diffraction profile in the 2θ direction, while crystallite size analysis with the spotty 2D diffraction pattern is based on the diffraction profile in the γ direction. The latter may be referred to as γ-profile analysis. Line profile analysis is suitable for crystallite sizes below 100 nm (1000 Å), while γ-profile analysis is suitable for crystallite sizes from as large as tens of μm down to 100 nm with a small X-ray beam size. Therefore, the technique is categorized as microbeam X-ray diffraction (MXRD).

12.2.2 Line Broadening for Crystallite Size

The broadening of diffraction peaks can be observed when the crystallite size is smaller than approximately 100 nm. The term "particle size" is usually used in this size range. The crystallite size can be measured by measuring the broadening given by the Scherrer equation:

$$B = \frac{C\lambda}{t\cos\theta} \tag{12.7}$$

where λ is the X-ray wavelength (Å), B is the full width at half maximum (FWHM) of the peak (in radians) corrected for instrumental broadening and strain broadening, θ is the Bragg angle, C is a factor, typically from 0.9 to 1.0, depending on crystallite shape [24], and t is the crystallite size (Å). This equation shows an inverse relationship between crystallite size and peak profile width. The wider the peak, the smaller the crystallites. Although line broadening appears when the

particle size is smaller than 100 nm, in practice, the Scherrer equation can adequately determine the average size of crystallites smaller than 30 nm when the broadening is significant enough to be resolved from instrumental broadening.

The diffraction peak broadening or peak shape is normally due to crystallite size (particle broadening), microstrain (strain broadening), and diffractometer condition (instrumental broadening). Only peak broadening due to crystallite size should be considered in the crystallite size calculation. Instrumental broadening is determined by many instrumental parameters, such as X-ray source focal spot, optics, collimator size, beam divergence, and detector resolution. The NIST SRM (standard reference material) 660 LaB_6 (lanthanum hexaboride) is commonly used to measure instrumental broadening. The LaB_6 standard powder has no strain and the particle size is larger than 1 μm. The entire peak width measured with this standard is due to instrumental broadening. The NIST SRM 640 silicon powder may also be used as a standard for instrumental broadening. With a two-dimensional detector, data from a standard and an unknown must be collected at the same incident angle (ω angle) to avoid the defocusing effect. It is recommended that the incident angle is set as the θ value so that the defocusing factor is 1 (similar to Bragg–Brentano geometry). For reflections below ~25° 2θ, the ω value may be selected to be larger than the θ value to avoid unnecessarily large instrumental broadening caused by the large projected area of the X-ray beam at low incident angles.

Particle broadening can be calculated from the breadth of the measured profile with unknown crystallite size and instrumental broadening determined with the standard. The formula for subtraction of the standard peak from the unknown peak is dependent on the shape of diffraction profile. There are many sophisticated algorithms to deconvolute the particle broadening from the measured profile and instrumental broadening, some involving Fourier analysis of the full diffraction profile [21–41]. Simplified formulas are given for two special cases, depending on whether the peaks have been fit with Gaussian or Cauchy (Lorentzian) functions. These two functions have different mathematical properties concerning the addition properties of their FWHMs. For Gaussian profiles,

$$B^2 = U^2 - S^2 \tag{12.8}$$

while for Cauchy profiles,

$$B = U - S \tag{12.9}$$

where B is the corrected FWHM for crystallite size calculation by Scherrer equation, and U and S are the FWHMs of the unknown and standard peaks, respectively. Figure 12.8(a) is a 2D frame and γ-integrated profile from NIST SRM 660 (LaB_6). Profile fitting of the peak shown gives a FWHM of 0.162° with a Gaussian profile and 0.133° with a Cauchy. Figure 12.8(b) is a 2D frame and γ-integrated profile of Cu (111) peak from a semiconductor tab tape. Profile fitting with a Cauchy function gives a peak location of 43.455° 2θ and a FWHM of 0.300°. Using LaB6 as an instrumental broadening standard with a Cauchy FWHM of 0.133°, the corrected FWHM is 0.167°, and the Scherrer equation gives a crystallite size of 512 Å. Usually Cauchy profiles are used for two-dimensional detectors, although the incident beam profile is Gaussian. The differences between the two fitting functions become smaller with smaller crystallite size. For example, assume a sample has a diffraction line at 30° 2θ and a line width of 2.83° and that a standard LaB_6 pattern has been measured with a line width of 0.09°. This would yield crystallite sizes of 29 Å with a Gaussian fit and 30 Å with a Cauchy fit. Now, we assume that the unknown has a line width of 0.26°. This would produce crystallite sizes of 348 Å with a Gaussian fit and 545 Å with a Cauchy fit. Both equations assume no strain broadening.

If the material is suspected to possess microstrain, Warren–Averbach or single line methods should instead be used. This technique usually involves analysis of the peak profile shape, from which contributions due to crystallite size and microstrain are separated. Microstrain in materials

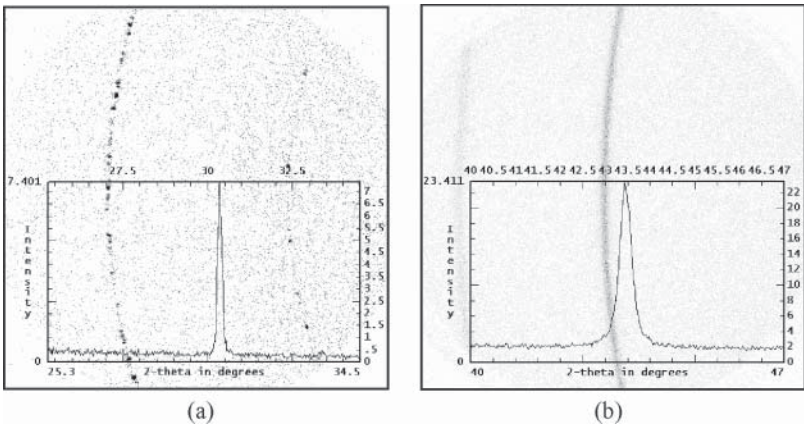


FIGURE 12.8 2D frames and γ-integrated profile for crystallite size analysis: (a) NIST SRM 660 (LaB_6), (b) Cu (111) peak from a semiconductor tab tape.

increases the line width as a function of 2θ. The deconvolution of the width from crystallite size and lattice distortion is based on the Warren–Averbach method. This method involves the measurement of the complete profile of multiple orders of the same reflection, such as (100), (200), (300) peaks. In summary, the peak profiles of the standard and unknown are deconvoluted into Fourier coefficients that are then corrected for instrumental broadening. Plotting the Fourier coefficients as a function of the (hkl) values of the measured reflections, a crystallite size distribution and a microstrain distribution are obtained, which yield an average crystallite size and a root mean squared microstrain. The single line method is based on the Warren–Averbach method with additional assumptions, i.e. that crystallite size broadening has a Cauchy profile, while microstrain broadening has a Gaussian profile. It can be used when only one diffraction peak is available for analysis, provided that both crystallite size and microstrain effects are present in the sample of interest. The single line method also provides a crystallite size distribution, but one of the assumptions is that the microstrain is constant. Since the derivations and assumptions behind the Scherrer method and the Warren–Averbach method are different, discrepancy exists in the average crystallite size values obtained from each method. For many applications, such as quality-control, reproducibility is more important than absolute accuracy.

When a 2D detector is used for data collection for crystallite size analysis, a long sample-to-detector distance should be used to maximize resolution. In this way, peak broadening due to crystallite size is not obscured by the point spread function of the detector. Small beam size and low convergence should be used to reduce instrument broadening. In crystallite size measurements on randomly oriented materials (e.g. fine powders), there is no reason to rotate or oscillate the sample. If sample characteristics warrant sample rotation or oscillation, for instance, with a highly textured sample, then the standard should be collected under identical measurement conditions. If crystallite size measurements are made in transmission, it is important to match the thickness of the sample and the standard.

12.2.3 Crystallite Size Using γ-Profile Analysis

Line profile analysis for crystallite size measurement is based on the diffraction intensity distribution as a function of 2θ. The diffraction profiles for line profile analysis can be obtained either by a conventional diffractometer with a point or line detector, or by γ-integration from

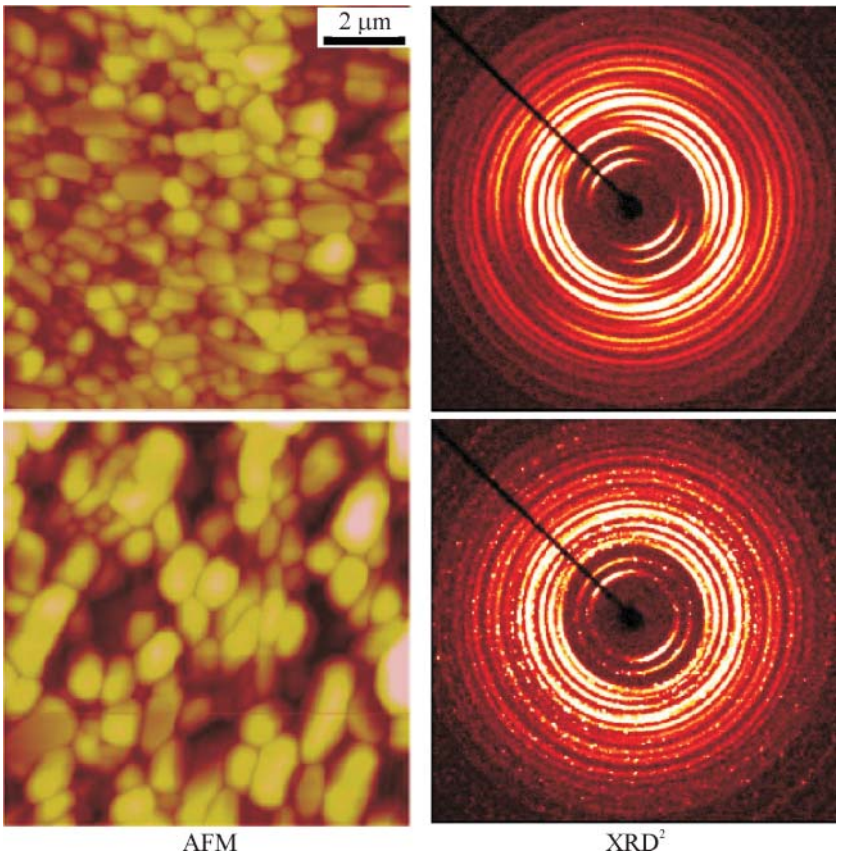


FIGURE 12.9 Atomic force microscope (AFM) images and XRD^2 patterns of samples crystallized from organic glass with large and small particle size. (Reproduced from [42] with permission.)

the diffraction pattern collected with area detector. The availability of an area detector makes it possible to analyze the crystallite size from spotty diffraction rings. Figure 12.9 shows the atomic force microscope (AFM) images and the XRD^2 pattern of a sample crystallized from an organic glass with large and small crystal size [42]. The XRD^2 pattern from the sample with fine crystal size shows a smooth diffraction ring, while the XRD^2 pattern from the sample with larger crystals shows spotty diffraction rings. The crystal size can be measured by the spottiness of the diffraction ring by γ-profile analysis [43].

Line profile analysis is suitable for measuring crystallite size smaller than 100 nm (1000 Å), while γ-profile analysis is more suitable for larger crystallites from 0.1 μm to 100 μm depending on the X-ray incident beam size, divergence, sample shape and size, instrument geometry, and detector resolution. The term "grain size" is usually used in this size range. The γ-profile analysis is based on the sampling statistics. Sampling statistics believed to be "poor" for other applications are actually preferred for crystallite size determination. The sampling statistics are determined by both the sample structure and instrumentation. For a perfect random powder sample, the number of contributing crystallites for a measured diffraction line can be given by

$$N_s = p_{hkl} \cdot \frac{Vf_i}{v_i} \cdot \frac{\Omega}{4\pi} \tag{12.10}$$

where p_{hkl} is the multiplicity of the diffracting planes, V is the effective sampling volume, f_i is the volume fraction of the crystallites being measured, and $f_i = 1$ for single phase materials, v_i is the volume of individual crystallites and Ω is the angular window of the instrument in solid angle. The factor Vf_i/v_i is the number of the crystallites being measured within the effective volume. The factor $\Omega/4\pi$ is the ratio of the effective volume satisfying the Bragg condition. The multiplicity factor, p_{hkl}, effectively increases the number of crystallites contributing to the integrated intensity from a particular set of (hkl) planes. The volume of individual crystallites, v_i is an average of various crystallite sizes or assumes all crystallites have the same volume. Assuming sphere-shaped particles, the term v_i can be replaced by the particle size, $v_i = \pi d_i^3/6$, where d_i is the diameter of the crystallite particles. The combination of the effective sampling volume and the angular window makes up the instrumental window, which determines the total volume of polycrystalline material making a contribution to the diffraction pattern. In two-dimensional X-ray diffraction, the instrumental window is not only determined by the incident beam size and divergence, but also by the γ angular range (the detective area and sample-to-detector distance). As shown in Figure 12.10, the instrumental window Ω is given by

$$\Omega = \beta_1\beta_2 = 2\beta \arcsin[\cos\theta \sin(\Delta\gamma/2)] \tag{12.11}$$

where β_1 is the instrument angular window in the 2θ direction and β_2 is the instrumental window in the γ direction, or the diffraction vector angular range corresponding to the azimuthal angular range $\Delta\gamma$. Neglecting the instrumental broadening effect of the detector, the instrument window in the 2θ direction can be given by the divergence of the incident angle ($\beta_1 = \beta$).Particle broadening may also affect the above relation, but since γ-profile analysis is mostly used for dealing with relative large crystallites, particle broadening is negligible.

For XRD^2 in reflection mode, the effective sampling volume is given by

$$V = \frac{A_0 \cos\eta}{\mu(\cos\eta + \cos\zeta)} = \frac{\pi b^2 \cos\eta}{4\mu(\cos\eta + \cos\zeta)} \tag{12.12}$$

with $\cos\eta = \sin\omega\cos\psi$

and $\cos\zeta = -\cos 2\theta \sin\omega\cos\psi - \sin 2\theta \sin\gamma \cos\omega\cos\psi - \sin 2\theta \cos\gamma \sin\psi$

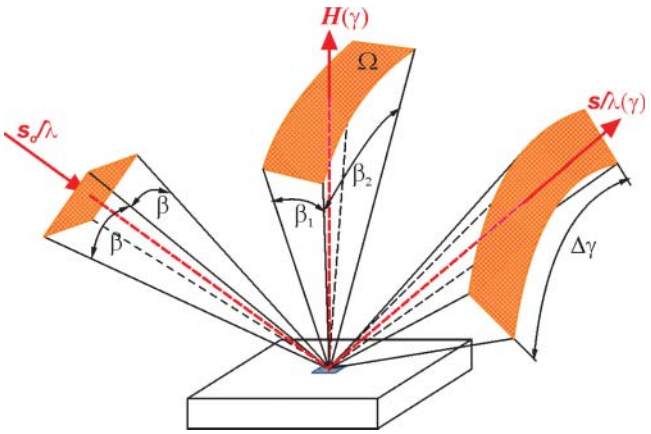


FIGURE 12.10 Instrumental window with two-dimensional diffraction.

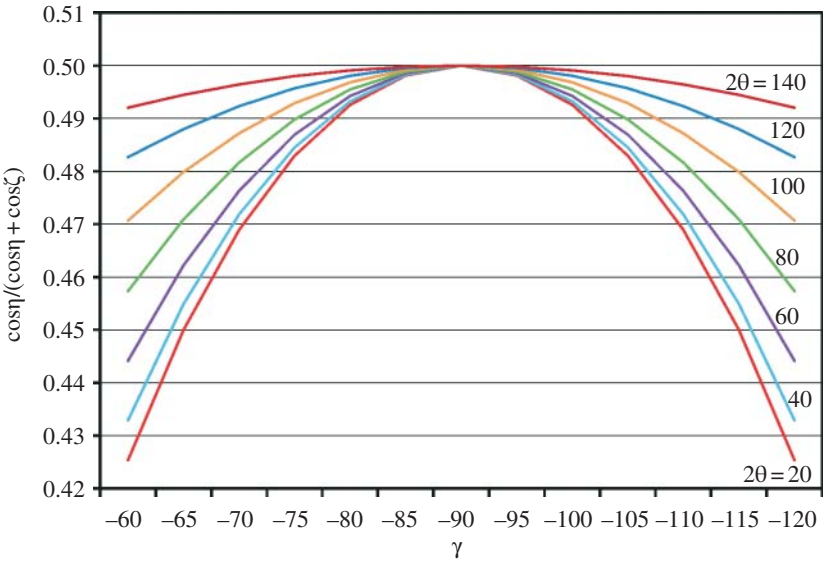


FIGURE 12.11 Relative variation of effective sampling volume as a function of 2θ and γ.

where A_o is the cross-section of the incident X-ray beam and μ is the linear absorption coefficient. In XRD[2], a round point beam is typically used, so the beam cross-section $A_o = \frac{1}{4}\pi b^2$ and b is the size of the incident beam in diameter. For crystallite size measurement, it is not necessary to tilt the sample normal away from the diffractometer plane, so we can set $\psi = 0$. The effective sampling volume is also a function of 2θ and γ. In reflection mode, the diffraction rings are typically in a γ range symmetric to $\gamma = -90°$. Figure 12.11 shows the relative variation of the effective volume $\cos\eta/(\cos\eta + \cos\zeta)$ as a function of 2θ and γ with $\omega = \theta$. Within the angular range of 2θ from 20° to 140° and γ from −60° to −120°, a very small variation from 0.425 to 0.5, and approaching 0.5 with increasing 2θ and γ near −90°. The variation of effective sampling volume can be ignored by using the value at $\gamma = -90°$. Considering $\psi = 0$, the effective volume is given by

$$V = \frac{A_0 \sin\omega}{\mu[\sin\omega + \sin(2\theta - \omega)]} = \frac{\pi b^2 \sin\omega}{4\mu[\sin\omega + \sin(2\theta - \omega)]} \tag{12.13}$$

This can be further simplified by collecting data at $\omega = \theta$,

$$V = \frac{A_0}{2\mu} = \frac{\pi b^2}{8\mu} \tag{12.14}$$

Introducing equations (12.14) and (12.11) into (12.10), we obtain the crystallite volume for the i-th phase as

$$v_i = \frac{p_{hkl} f_i A_0 \beta \arcsin[\cos\theta \sin(\Delta\gamma/2)]}{4\pi\mu N_s} \tag{12.15}$$

where N_s is the number of crystallites contributing to the diffraction pattern within the instrumental window and effective sampling volume. Given a material with single phase, $f_i = 1$, and replacing v_i by the diameter of the crystallite particles d (from $v = \pi d^3/6$), the crystallite size is

then given by

$$d = \left\{ \frac{3p_{hkl}A_0\beta \arcsin[\cos\theta \sin(\Delta\gamma/2)]}{2\pi^2\mu N_s} \right\}^{1/3} \tag{12.16}$$

Introducing a scaling factor covering all the numeric constants, incident beam divergence, and calibration factor for the instrument, we obtain an equation for the crystallite size measurement in reflection mode:

$$\boxed{d = k\left\{ \frac{p_{hkl}b^2 \arcsin[\cos\theta \sin(\Delta\gamma/2)]}{\mu N_s} \right\}^{1/3}} \tag{12.17}$$

where $k = \left(\frac{3\beta}{8\pi}\right)^{1/3}$ if the instrumental broadening in 2θ direction is given, but we may treat k as a calibration factor which can be determined from the 2D diffraction pattern of a known standard. Since only a limited number of spots along the diffraction ring can be resolved, it can be seen from the equation that a smaller X-ray beam size and low multiplicity peak should be used if a smaller crystallite size is to be determined.

For XRD^2 in transmission mode and with the incident beam perpendicular to the sample surface, we have the effective sampling volume:

$$V = \frac{\pi b^2 \cos 2\theta \left[\exp(-\mu t) - \exp\left(-\frac{\mu t}{\cos 2\theta}\right)\right]}{4\mu(1 - \cos 2\theta)} \tag{12.18}$$

where t is the thickness of the sample. For small 2θ angles, the effective sampling volume can be approximated by

$$V = A_0 t \exp(-\mu t) = \frac{1}{4}\pi b^2 t \exp(-\mu t) \tag{12.19}$$

The effective sampling volume reaches a maximum for transmission mode diffraction when $t = 1/\mu$. It can be observed from the above equations that the effective sampling volume is proportional to the beam cross-section area and is lower for materials with higher linear absorption coefficients. The effective sampling volume given by the above two equations (12.18), (12.19) takes into account the sampling statistics and their effect on the scattering intensities. For crystallite size analysis, sample absorption has a different effect on the sampling volume in reflection and transmission modes. In reflection mode, the linear absorption coefficient determines how fast the incident beam is attenuated within the sample, but there is no clear cutoff for the penetration depth. Therefore, the effective sampling volume has to be used. In transmission mode with the incident beam perpendicular to the sample surface, the linear absorption coefficient affects the relative scattering intensity (counting statistics), but not the actual sampling volume. In other words, all the sample volume within the beam path contributes to the diffraction. Therefore, it is reasonable to ignore the absorption effect, $\exp(\mu t)$, for crystallite size analysis as long as the sample is thin enough for transmission mode diffraction. The actual sampling volume can then be given simply by

$$A_0 t = \frac{1}{4}\pi b^2 t \tag{12.20}$$

In the above equations, a parallel incident beam was assumed. If a divergent (or convergent) incident beam is used, the incident beam size should be measured at the sample location

(instrument center). Introducing equations (12.20) and (12.11) into (12.10), we obtain the crystallite volume for the i-th phase as

$$v_i = \frac{p_{hkl} f_i A_0 t \beta \arcsin[\cos\theta \sin(\Delta\gamma/2)]}{2\pi N_s} \tag{12.21}$$

Considering a material with a single phase, $f_i = 1$, and replacing v_i by the diameter of the crystallite particles d (from $v = \pi d^3/6$), the crystallite size is then given by

$$d = \left\{ \frac{3 p_{hkl} b^2 t \beta \arcsin[\cos\theta \sin(\Delta\gamma/2)]}{4\pi N_s} \right\}^{1/3} \tag{12.22}$$

Introducing a scaling factor k to cover all the numeric constants, incident beam divergence, and the calibration factor for the instrument, we obtain an equation for crystallite size measurement in transmission mode:

$$\boxed{d = k \left\{ \frac{p_{hkl_i} b^2 t \arcsin[\cos\theta \sin(\Delta\gamma/2)]}{N_s} \right\}^{1/3}} \tag{12.23}$$

where $k = \left(\frac{3\beta}{4\pi}\right)^{1/3}$ if the instrumental broadening in the 2θ direction is given, but we may treat k as a calibration factor which can be determined from the 2D diffraction pattern of a known standard. By using the relationships given by either equation (12.17) or (12.23), crystallite size analysis becomes a task of resolving the number of crystallites measured in a section of diffraction ring.

Figure 12.12 shows a frame collected from a SRM660a (LaB_6) sample with an XRD^2 system (GADDS™ CST) for combinatorial screening in transmission mode and with Cu-K_α X-rays. The 2D detector (Hi-Star™) is set at 23.75 cm from the instrument center. The beam (collimator pinhole) size b is 200 μm. An accurate sample thickness value should be used in system calibration. One way is to calculate the sample thickness from the measured transmission coefficient. This is especially practical for packed loose powder samples. Based on the calculated linear absorption coefficient of 1138 cm^{-1} (0.1138 μm^{-1}) and the measured transmission of 0.45 for the LaB_6 sample, the sample thickness t is 7.0 μm. The SEM analysis on the SRM660a indicated that the particles of LaB_6 consist of aggregates of crystallites on the size range from 2 μm to 5 μm [44]. We take the average crystallite size d as 3.5 μm. Three rings from (100), (110), and (111) planes are observed. The 2θ-integrated plots (γ-profiles) are shown under the γ-profile. There may be many different algorithms developed in the future. The author suggests counting the number of crystallites by checking the number of intersections of the γ-profile with a threshold line. This line can be a horizontal straight line based on the average intensity or background. For example, we can use a straight horizontal line representing the average intensity of the γ-profile. Every two intersections of γ-profile with this horizontal line represent a crystallite. In order to cancel out the effects of preferred orientation and other material and instrumental factors on the overall intensity fluctuation along the γ-profile, we can use a trend line as a threshold line. In Figure 12.12, a second order polynomial trend line of the intensities is fitted to each γ-profile. The number of crystallites is counted as half of the number of intersections between the γ-profile and the trend line. Since the SRM660a (LaB_6) sample has a known average crystallite size, we use all three diffraction rings to calibrate the instrument for crystallite size determination. The calibration results with the

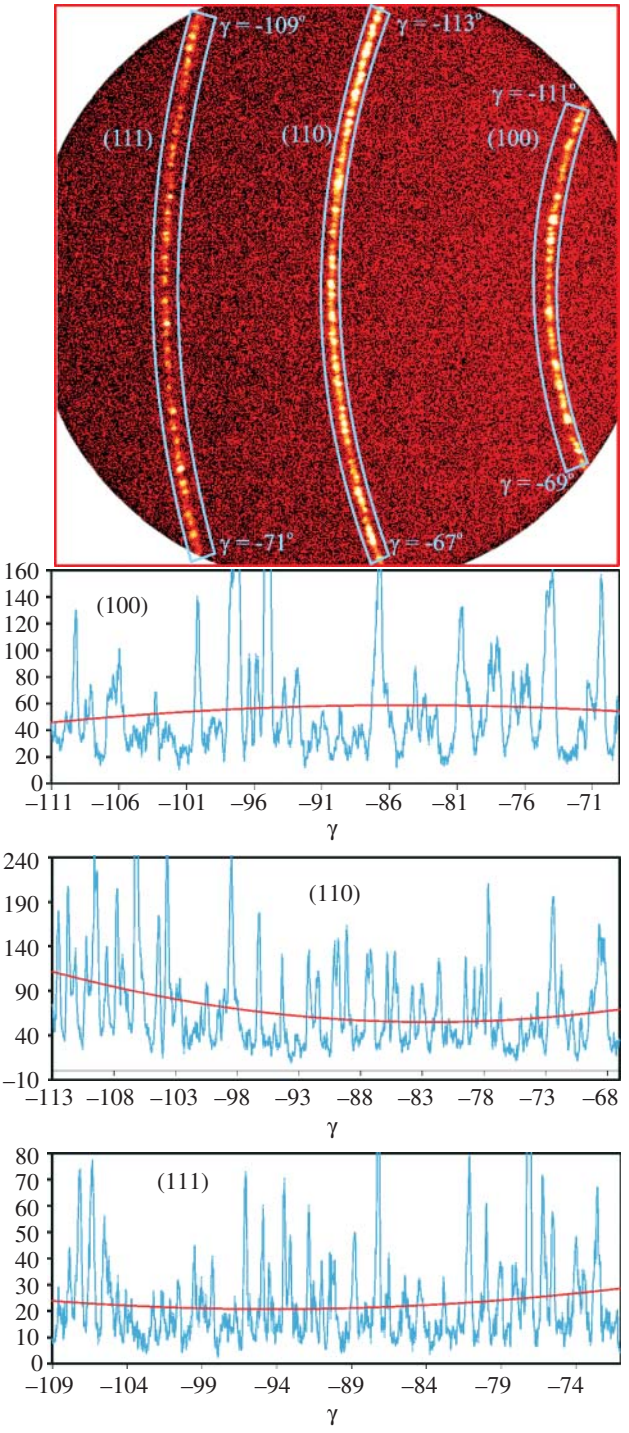


FIGURE 12.12 Three diffraction lines collected from SRM660a (LaB_6) illustrate the γ-profile analysis for crystallite size analysis.

Table 12.1 Instrumental Calibration for Crystallite Size with LaB_6

(*hkl*)	P_{hkl}	2θ	$\Delta\omega$	N_s	k
(100)	6	21.36	38	23	0.1217
(110)	12	30.38	46	41	0.1106
(111)	8	37.44	42	38	0.1281

LaB_6 standard are listed in Table 12.1. The average scaling factor k is 0.12 in this calibration. The system can then be used to measure the crystallite size of unknown materials if the data can be collected in approximately the same condition. The divergence of the 0.2 mm collimator was given in Chapter 3 as 0.164° (or 0.00286 in radians). The calculated k is then given by.

$$k = \left(\frac{3\beta}{4\pi}\right)^{1/3} = \left(\frac{3 \times 0.00286}{4\pi}\right)^{1/3} = 0.088$$

This is more than 2/3 of the calibrated value of 0.1201. In this case, primary beam divergence is the primary part of the instrumental window in the 2θ direction. The discrepancy is due to many factors, including errors in the spot count N_s, sample thickness t, detector resolution, and other instrumental errors. Therefore, it is always necessary to calibrate the system with a known standard, preferably with a comparable sample geometry and crystallite size. For reflection mode, it is critical to have a standard with a comparable linear absorption coefficient so as to have similar penetration.

The purpose of the above example is to explain the γ-profile analysis and calibration technique. The trend line from a certain percentage of the intensities may also be used to count the intersections. The lower the percentage is, the more sensitive the analysis is to weak spots, but the analysis will be more affected by background noise. The most important thing is to be consistent with the threshold line for the standard and unknown materials. The γ-resolution on crystal spots can be improved by using a long sample-to-detector distance. Reducing the X-ray beam size, beam divergence and sample thickness can reduce the number of spots along the γ-profile so as to reduce the demand for γ-resolution. Using a diffraction line with low multiplicity also reduces the demand for γ-resolution. In cases where too few diffraction spots can be observed in the diffraction ring, a large beam size or sample oscillation (by rotation or translation) may improve the sampling statistics. However, the system should be calibrated in the same condition with a known sample having comparable crystallite size. The linear absorption coefficient has been built into the equation for reflection mode and the sample thickness has been built into the equation for transmission mode. In principle, the linear absorption coefficient or the thickness of the calibration standard sample does not have to match the sample to be measured. The extent of the effect of discrepancies in the linear absorption coefficient or in the thickness on the γ-profile has not been rigorously studied. But in order to reduce the geometry error or any unknown factors caused by such a discrepancy, the standard material may be diluted by light and amorphous materials. For example, a diluted LaB6 sample with various linear absorption coefficients or matching thickness for profile analysis can be made by mixing with different amounts of starch [45].

The crystal size analysis from FWHM of 2θ peaks by Scherrer equation is limited to crystal size below 100 nm, while γ-profile analysis is a complementary method which can extend the crystal size measurement range up to a few millimeters by proper instrumentation and data collection strategy. The algorithms given in this section for evaluating crystal size from γ-profile is based on a rather simplified model. Many factors, such as the crystal size distribution, peak intensity variation in γ-profile, statistics of overlapping spots, and preferred orientation, are not considered.

Some recent progress in experiments and more sophisticated models have shed more light on this approach [46–49].

12.3 RETAINED AUSTENITE

Austenite is an interstitial solid solution of carbon in γ-iron at temperatures above 723°C. Austenite has face-centered cubic (FCC) crystal structure and therefore is more densely packed. The carbon content in austenite can be as high as 2%. Austenite may contain other elements either as interstitial or substitutional solid solutions. Below 723°C, austenite normally decomposes into ferrite, a solid solution of carbon in α-iron, and cement (Fe_3C). Ferrite has a body-centered cubic (BCC) crystal structure and is less densely packed. The carbon content in ferrite is much lower, with a 0.025% maximum at 723°C. During quenching at a cooling speed faster than a threshold, carbon and other alloy elements may delay or prevent the transformation process. Instead of decomposing into ferrite and carbide, the austenite transforms to an unstable body-centered tetragonal (BCT) phase, referred to as martensite. Some residual untransformed austenite remains in the steel parts at room temperature. The retained austenite has significant effects on the mechanical properties of steels, such as dimensional stability, wearing resistance, crack initiation and propagation, and fatigue life. The volume percentage of retained austenite within a sample also containing martensite, ferrite, and carbide is typically measured. Quantitative X-ray diffraction is one of the best methods for determining the volume percentage of retained austenite [50].

X-ray diffraction technique normally does not make a distinction between martensite and ferrite – both are referred to as the α phase for retained austenite measurement. It is assumed that no preferred orientation exists in either phase and that the diffraction intensity from carbides is negligible. The volume percentage of retained austenite (RA) is calculated from

$$\%RA = 100\left(\frac{I_\gamma/R_\gamma}{I_\gamma/R_\gamma + I_\alpha/R_\alpha}\right) \tag{12.24}$$

Where I_γ and I_α are the measured integrated intensities of the γ and α phases respectively. R_γ and R_α are the reflection factors of the γ and α phases respectively. The reflection factor for phase i is proportional to the theoretic relative intensity and is given by

$$R_i^{hkl} = \frac{p_{hkl}}{v^2}(LP)F_{hkl}^2 \exp(-2M) \tag{12.25}$$

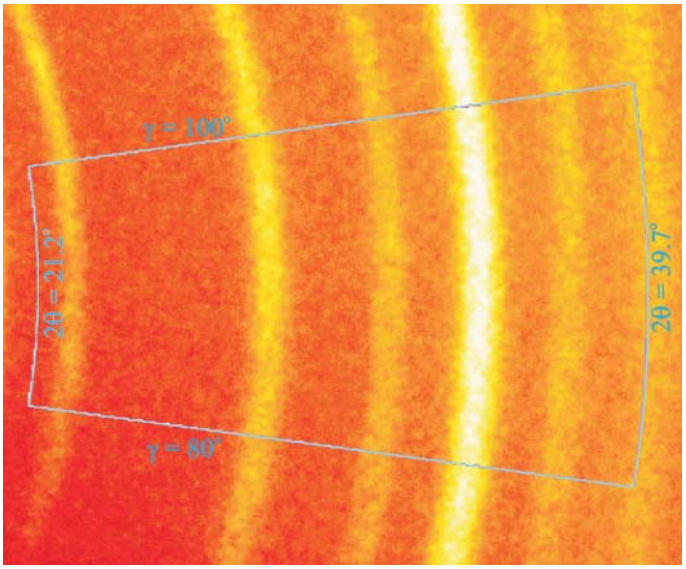
where p_{hkl} is the multiplicity factor of the crystal plane (hkl), v is the volume of the unit cell, (LP) are the Lorentz-polarization factors, F_{hkl}^2 is the structure factor of the crystal plane (hkl) and $\exp(-2M)$ is the Debye–Waller factor or temperature factor. The reflection factor R can be calculated from the above equation or found in literature [51].

If a carbide phase is present, the volume percentage of retained austenite is calculated from

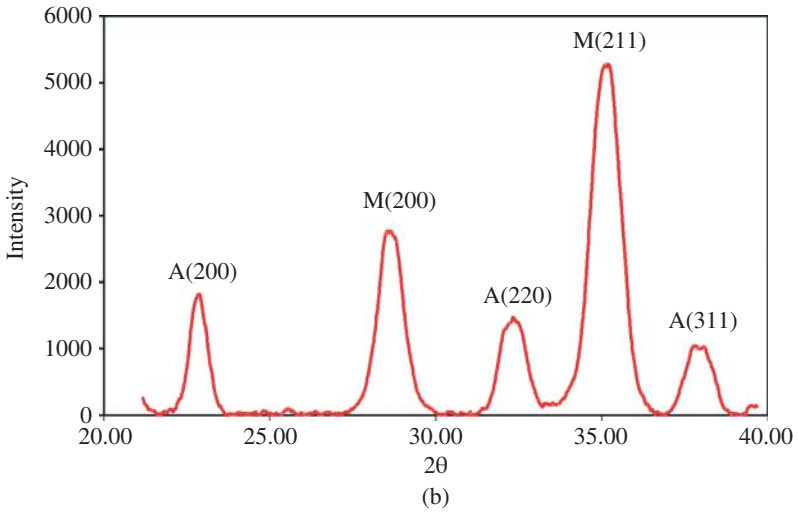
$$\%RA = 100\left(\frac{I_\gamma/R_\gamma}{I_\gamma/R_\gamma + I_\alpha/R_\alpha + I_c/R_c}\right) \tag{12.26}$$

where I_c is the measured integrated intensities of the carbide and R_c is the reflection factor (theoretic relative intensities) of the carbide. The equation may be modified for multiple γ and α peaks and multiple carbides by averaging the intensity ratio of the same phases:

$$\left\langle I_i/R_i \right\rangle = \frac{1}{n}\sum_{j=1}^{n}\left(I_i/R_i\right)_j \tag{12.27}$$



(a)



(b)

FIGURE 12.13 Retained austenite measurement from a steel roller: (a) 2D frame collected by CCD detector, (b) γ-integrated profile showing three peaks, (200), (220), and (311), from the retained austenite and two peaks, (200) and (211), from the martensite.

where n is the number of peaks measured for the phase i and $\left({}^{I_i}/_{R_i}\right)_j$ is the intensity ratio of the j-th peak of the phase i. A two-dimensional detector can measure retained austenite with fast data collection, good sampling statistics, and a lower measurement limit [52]. The preferred orientation effect can also be reduced by virtual oscillation. Figure 12.13(a) shows a 2D frame collected from a steel roller with an APEX II™ CCD detector and Mo-K_α radiation. Figure 12.13(b) is a profile integrated from the 2D frame in the range of 2θ from 21.1° to 39.7° and γ from 80° to 100°. The background has been subtracted from the integrated profile. The profile shows three peaks, (200), (220), and (311), from the retained austenite and two peaks, (200) and (211), from the martensite.

Table 12.2 Retained Austenite Measurement of a Steel Roller: %RA = 21.3

Phase	(*hkl*)	2θ	*R*[51]	*I*	*I*/*R*	<*I*/*R*>
Martensite	200	28.72	288.6	278618.3	965.4	1053.7
	211	35.36	530.0	605242.4	1142.0	
Austenite	200	22.78	644.3	124335.5	193.0	285.1
	220	32.42	376.7	148181.2	393.4	
	311	38.22	390.0	104891.8	269.0	

The above five peaks are chosen for the retained austenite measurement because of good separations between each adjacent peak [53]. The other peaks may be too close to be resolved. For instance, the 2θ values for martensite (110) and austenite (111) are 20.20° and 19.68° respectively, and for martensite (310) and austenite (400) are 46.16° and 46.52° respectively. These peaks should be avoided because of the difficulty of separating the peaks and determining the integrated intensities from scrambled peaks. The diffraction profile from γ-integration has been normalized by the γ-integration range, so the intensity is independent of the γ-range. In this case, the reflection factors used for conventional diffraction can be used to calculate the retained austenite. Table 12.2 lists peak position (2θ), reflection factors from reference [51], measured integrated intensities, and the ratio of the intensity to the reflection factor. The retained austenite in the steel roller is measured as 21.3%. This example shows the basic concept of the measurement. Since the published reflection factors are based on the Bragg–Brentano geometry, for improved accuracy, the corrections given in Chapter 7 should be applied to obtain integrated intensities equivalent to the value from the Bragg–Brentano geometry.

The integrated intensities of each phase can also be obtained by area integration over the defined regions for each peak. Then the reflection factors should be determined experimentally by measuring samples with a known percentage of retained austenite (and carbide). The number of samples with different percentages of retained austenite for calibration should be the same or more than the number of reflection factors to be determined. Calibration by experimental method is especially preferred for the integrated intensity determined by area integration. The "reflection factors" determined experimentally contain all the instrument factors or corrections. No further correction is necessary as long as the instrument condition and the integration regions are the same. The maximum integrated area for each phase can be used as long as it is consistent with the calibration. Background subtraction may be avoided if a low noise photon-counting detector is used.

12.4 CRYSTAL ORIENTATION

Investigation on the orientation distribution of crystallites in polycrystalline materials have been covered in Chapter 8. In some cases, the crystalline orientations associated with features in 2D diffraction pattern may need to be evaluated without a comprehensive texture analysis, for example the orientation of a crystal plane relative to the sample orientation, the angles between two crystal planes, and offcut of silicon wafers.

12.4.1 Orientation with Respect to Sample

For any diffraction feature, such as a diffraction spot, the orientation of the diffracting crystal plane with respect to the sample can be calculated from the spot location in the 2D frame (2θ,γ) and

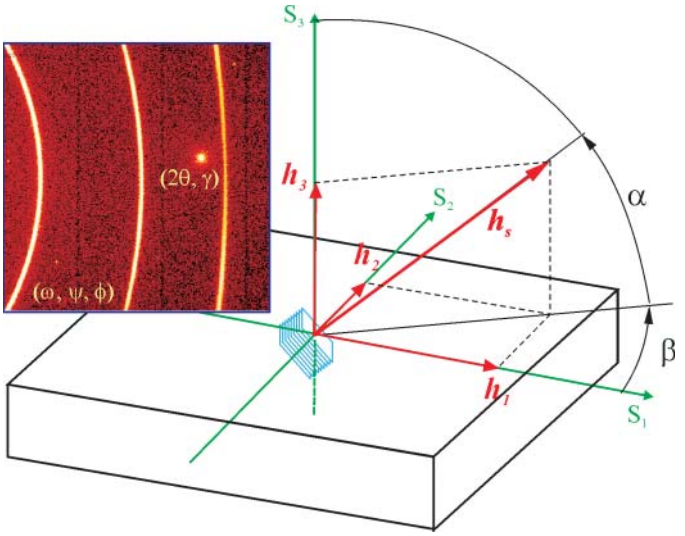


FIGURE 12.14 Orientation of the crystalline planes with respect to the sample orientation.

sample orientation (ω,ψ,ϕ). Figure 12.14 shows a diffraction frame with a spot and the orientation of crystal plane in the sample coordinate. The 2θ and γ values can be evaluated from the location (gravity center) of the diffraction spot. The normal direction of the crystal planes is given by the unit vector $\boldsymbol{h}_s$, which has three components h_1, h_2, and h_3 parallel to the three sample orientations S_1, S_2, and S_3 respectively. The normal direction of the crystal planes with respect to the sample coordinates is given by the radial angle α and azimuthal angle β:

$$\begin{aligned} \alpha &= \arcsin h_3, \\ \beta &= \pm \arccos \frac{h_1}{\sqrt{h_1^2 + h_2^2}} \begin{cases} \beta \geq 0^\circ & if \quad h_2 \geq 0 \\ \beta < 0^\circ & if \quad h_2 < 0 \end{cases} \end{aligned} \tag{12.28}$$

where α takes a value between -90° to 90° ($-90^\circ \leq \alpha \leq 90^\circ$) and β takes values in two ranges ($0^\circ \leq \beta \leq 180^\circ$ when $h_2 \geq 0$ and $-180^\circ \leq \beta < 0^\circ$ when $h_2 < 0$). When $h_2 = 0$ in the above equation, β takes two values depending on the value of h_1 ($\beta = 0^\circ$ when $h_1 \geq 0$ and $\beta = 180^\circ$ when $h_1 < 0$). Equations (12.28) are similar to the fundamental equations for pole-figure mapping, except α can be positive or negative. The condition for reflection mode diffraction with the sample plane on the S_1-S_2 plane is $h_3 > 0$. For transmission diffraction it is possible that $h_3 < 0$. In this case, α is negative. For Eulerian geometry, the unit vector components $\{h_1, h_2, h_3\}$ can be calculated from the sample orientation (ω,ψ,φ) and diffraction angles (2θ,γ) by

$$\begin{aligned} h_1 &= \sin\theta(\sin\phi \sin\psi \sin\omega + \cos\phi \cos\omega) + \cos\theta \cos\gamma \sin\phi \cos\psi \\ &\quad - \cos\theta \sin\gamma(\sin\phi \sin\psi \cos\omega - \cos\phi \sin\omega) \\ h_2 &= -\sin\theta(\cos\phi \sin\psi \sin\omega - \sin\phi \cos\omega) - \cos\theta \cos\gamma \cos\phi \cos\psi \\ &\quad + \cos\theta \sin\gamma(\cos\phi \sin\psi \cos\omega + \sin\phi \sin\omega) \\ h_3 &= \sin\theta \cos\psi \sin\omega - \cos\theta \sin\gamma \cos\psi \cos\omega - \cos\theta \cos\gamma \sin\psi \end{aligned} \tag{12.29}$$

The above method can only obtain the orientation of the normal to a crystal plane, but not the orientation of the crystal. The orientation of at least one more non-parallel crystal plane of the same crystal has to be obtained in order to uniquely define the crystal orientation with respect to the sample coordinates.

12.4.2 Angle Between Two Crystal Planes

For any spot (or feature) in a 2D diffraction frame, the normal direction of the corresponding diffracting crystal plane is given by the unit vector $\boldsymbol{h}_s$. For any two diffraction spots a and b, the unit vectors are given by

$$\mathbf{h}_S^b = \begin{bmatrix} h_1^b \\ h_2^b \\ h_3^b \end{bmatrix} \text{ and } \mathbf{h}_S^a = \begin{bmatrix} h_1^a \\ h_2^a \\ h_3^a \end{bmatrix} \tag{12.30}$$

The angle between the two unit vectors is then given by

$$\cos\alpha = \frac{\boldsymbol{h}_S^a \cdot \boldsymbol{h}_S^b}{|\boldsymbol{h}_S^a||\boldsymbol{h}_S^b|} = \boldsymbol{h}_S^a \cdot \boldsymbol{h}_S^b \tag{12.31}$$

For unit vector, $|\mathbf{h}_S^a| = |\mathbf{h}_S^b| = 1$, so we have

$$\alpha = \arccos(h_1^a h_1^b + h_2^a h_2^b + h_3^a h_3^b) \tag{12.32}$$

The spots a and b are not necessarily from the same frame so that all five parameters $(2\theta,\gamma,\omega,\psi,\phi)$ in the unit vectors can be different. The equation can be used to calculate the angle between any two diffraction features, for instance, the angle between two families of crystal planes from either the same or different crystals, angle between a crystal plane in a thin film and the substrate. If the two spots are from the same diffraction ring, all four parameters $(2\theta,\omega,\psi,\phi)$ are the same. The angle can then be calculated from the difference in γ between two spots $(\Delta\gamma)$:

$$\alpha = 2\arcsin[\cos\theta \sin(\Delta\gamma/2)] \tag{12.33}$$

12.4.3 Miscut Angle of Single Crystal Wafer

Miscut of a single crystal is defined as the angle between the crystal surface plane and a crystalline plane (hkl). For instance, the angle of between Si (111) plane and Si wafer surface is called Si wafer (111) miscut. The miscut angle can be measured by XRD^2 method as illustrated in Figure 12.15. In (a), the miscut angle between crystal plane ABCD and crystal surface is α. The incident X-ray $\mathbf{s_0}$ makes an incident angle ω from the crystal surface. The data frame is collected while the sample rotates ϕ continuously about its surface normal N. With the miscut, Bragg condition can be satisfied at two ϕ angles, for instance, with crystal plane at ABCD and A′B′C′D′ positions.

Two diffraction spots in Figure 12.15 (b) can be observed with each corresponding to the diffracted beams $\mathbf{s_1}$ and $\mathbf{s_2}$ respectively. The separation between two spots $\Delta\gamma$ can be evaluated from the 2D frame by 2θ-integration. Two diffraction vectors $\mathbf{H_1}$ and $\mathbf{H_2}$ are defined by the incident X-ray $\mathbf{s_0}$ and two diffracted beams $\mathbf{s_1}$ and $\mathbf{s_2}$ respectively. Two diffraction vectors $\mathbf{H_1}$ and $\mathbf{H_2}$ represent the normal directions of crystal plane at ABCD and A′B′C′D′ positions. The miscut

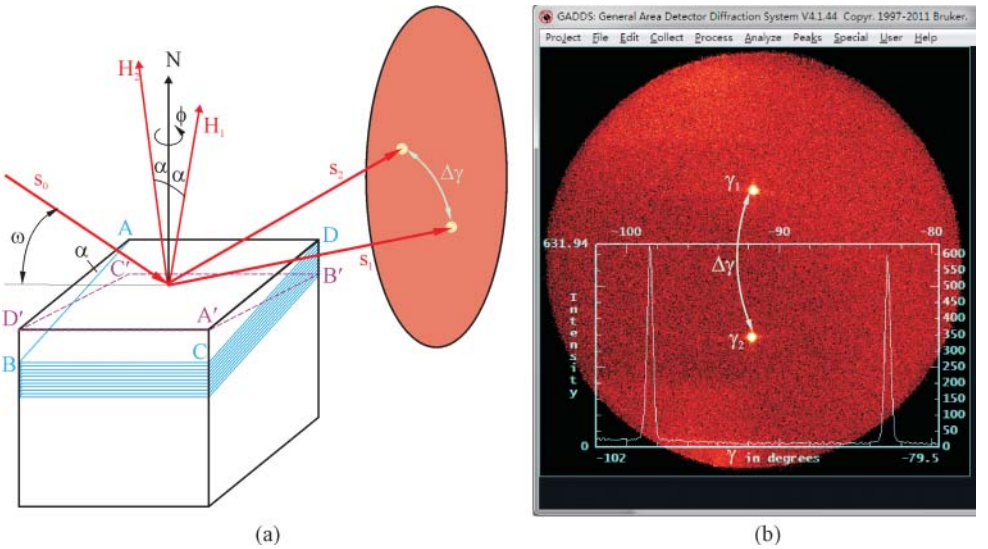


FIGURE 12.15 Measurement of miscut angle: (a) geometry, (b) 2D frame with two spots.

angle α is the angle between $\mathbf{H_1}$ and N, or equally between $\mathbf{H_2}$ and N. The unit vectors representing N, $\mathbf{H_1}$, and $\mathbf{H_2}$ are given as

$$\boldsymbol{n} = \begin{bmatrix} 0 \\ 0 \\ 1 \end{bmatrix}, \quad \boldsymbol{h}_s(\gamma_1) = \begin{bmatrix} h_1(\gamma_1) \\ h_2(\gamma_1) \\ h_3(\gamma_1) \end{bmatrix}, \quad \boldsymbol{h}_s(\gamma_2) = \begin{bmatrix} h_1(\gamma_2) \\ h_2(\gamma_2) \\ h_3(\gamma_2) \end{bmatrix} \tag{12.34}$$

Then we have

$$\cos\alpha = \boldsymbol{n} \cdot \boldsymbol{h}_s(\gamma_1) = h_3(\gamma_1) \quad \text{and} \quad \cos\alpha = \boldsymbol{n} \cdot \boldsymbol{h}_s(\gamma_2) = h_3(\gamma_2) \tag{12.35}$$

The ψ tilt is not necessary for measuring miscut, so $\psi = 0$. In the reflection mode with positive ω angle, the γ should be negative, $-\pi < \gamma < 0$. Considering that

$$\gamma_1 = -(90^\circ - \Delta\gamma/2) \quad \text{and} \quad \gamma_2 = -(90^\circ + \Delta\gamma/2)$$

we can obtain

$$\alpha = \arccos[\sin\theta \sin\omega + \cos\theta \cos\omega \cos(\Delta\gamma/2)] \tag{12.36}$$

If the incident angle is set at $\omega = \theta$, the equation can be further simplified to

$$\alpha = 2\arcsin[\cos\theta \sin(\Delta\gamma/4)] \tag{12.37}$$

For a single crystal wafer with zero miscut ($\alpha = 0$), there is only one diffraction spot on the diffractometer plane ($\gamma = -90^\circ$). The diffraction vector is in the sample normal direction, the Bragg condition is satisfied when $\omega = \theta$, and ϕ rotation will not change the Bragg condition. With miscut angle, $\omega = \theta$ does not necessarily satisfy the Bragg condition. The Bragg condition can be satisfied with a combination of ω and ϕ when the incident X-ray beam makes θ angle to

the crystal planes. The ω angle should be in the vicinity of θ, typically $\omega = \theta$, so that the ϕ rotation can bring the crystal planes into Bragg condition. Within full 360° ϕ rotation, the Bragg condition can be satisfied twice at two different ϕ angles, as illustrated by the crystal plane position ABCD and A′B′C′D′. The larger the miscut angle, the larger the separation ($\Delta\gamma$) between two diffraction spots.

12.5 THIN FILM ANALYSIS

Thin films, referring to materials with thickness of a few Å to several μm, can have significantly different properties compared to the similar bulk materials. X-ray diffraction has been largely used for characterization of all kind of thin films, including single layer films, coatings, and multilayer films. Most of the principles and methods covered in previous chapters apply to thin films. Some experimental examples are given for thin film samples. However, due to the relative high penetration of X-rays compared to the thickness of thin films, the instrumentation configuration, data collection, and evaluation methods may be different from that of the bulk materials. The instrumentation and applications with a 2D detector are also different from the diffractometer with a point detector.

12.5.1 Grazing Incidence X-Ray Diffraction

Grazing incidence X-ray diffraction (GIXRD) is a commonly used technique for thin films analysis by X-ray scattering [54, 55]. Figure 12.16(a) shows the configuration for GIXRD with a point detector. A single parabolic bent Göbel mirror transforms the divergent primary beam from the X-ray tube into a parallel beam. The parallel incident beam may be produced by other X-ray source and optics. The incident angle α_I is kept at a low angle (grazing incident) to control the penetration of the incident X-rays so that most scattering occurs within the thin film and there is less contribution from substrate scattering. The optimal grazing incident angle is determined by the thin film thickness (t) and the linear absorption coefficient of the thin film material (μ):

$$\alpha_I \approx \arcsin(\mu t) \tag{12.38}$$

The grazing incidence angle should also be higher than the critical angle of total reflection, which is typically between 1° and 3°, depending on the wavelength of the incident X-rays and the thin film material. A line focus incident beam is typically used with a point detector. At such a low incident angle, the incident X-rays spread over a large area of the sample surface with the same incident angle θ. A set of soller slits, with the plates perpendicular to the diffractometer plane and aligned in the direction between the instrument center and detector, is attached in front of the point detector. This soller slits may also be referred to as, soller plates collimator, soller collimator, and secondary collimator. The scattered X-rays from the irradiated region may point to various directions, but only the diffracted X-rays in the direction of 2θ defined by the soller slits can reach the point detector. The soller slits can maintain a good 2θ resolution while collecting diffraction signal from a large irradiated area on the sample. Depending on the length of the soller slits and the gap between the adjacent plates, a good 2θ resolution, for instance, 0.1°, 0.2°, 0.3°, or 0.4°, can be maintained. The Göbel mirror can only collimate the beam in planes parallel to the diffractometer plane. In order to remove the axial divergence, additional soller slits (not shown in the figure), in either or both the incident and secondary sides, may be used in the same way as in the Bragg–Brentano geometry. During the data collection, the incident beam is kept in a fixed direction, while the soller slit and detector scan over the desired 2θ range. Although the incident

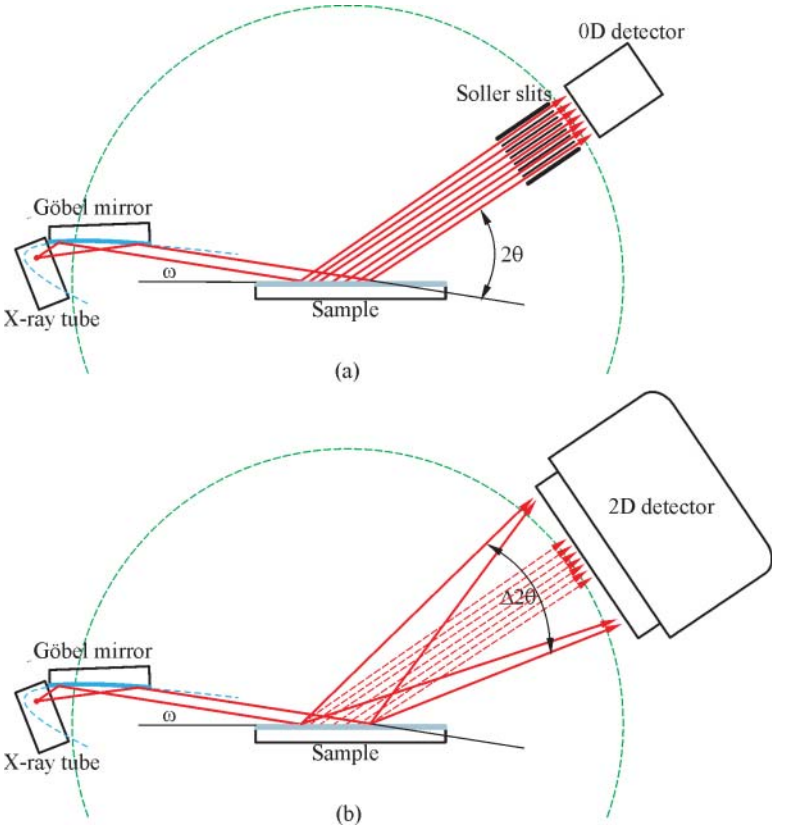


FIGURE 12.16 (a) GIXRD with a point detector, (b) GIXRD with a 2D detector.

beam spread over the sample, a diffraction pattern can be collected with a 2θ resolution as good as defined by the soller slits and scanning steps.

Figure 12.16(b) shows the configuration for GIXRD with a 2D detector. The primary beam is also a parallel beam. It may look identical as the primary beam in Figure 12.16(a), but spot focus X-ray source, or additional slit or pinhole collimator (not shown) are used to obtain a point beam. In an XRD^2 system, the diffracted X-rays are measured simultaneously in a two-dimensional range so that no soller slits can be attached to the 2D detector. The scattered X-rays over the large irradiated range cannot be selected by soller slits. Instead, all scattered X-rays within the coverage of the 2D detector ($\Delta 2\theta$) are collected simultaneously. Therefore, the data collection speed can be dramatically higher than the system with a point detector, but the 2θ resolution is significantly deteriorated.

In-plane grazing incidence X-ray diffraction (IP-GIXRD) is also referred to as grazing incidence in-plane diffraction (GIIXD) or non-coplanar GIXRD in some literature [52]. Correspondingly, the GIXRD with diffraction vector within diffractometer plane ($\psi = 0$) is called out-of-plane GIXRD (OP-GIXRD) or coplanar GIXRD. Both in-plane and out-of-plane GIXRD have been widely used to characterize sample surface, thin films, and coatings. With a 2D detector, it is possible to obtain diffraction information simultaneously from the OP direction to the IP direction [56].

Figure 12.17 shows the geometry of grazing incidence X-ray diffraction with a 2D detector (GIXRD^2). (a) is the standard geometry with the sample orientation set at $\psi = 0°$ and the sample

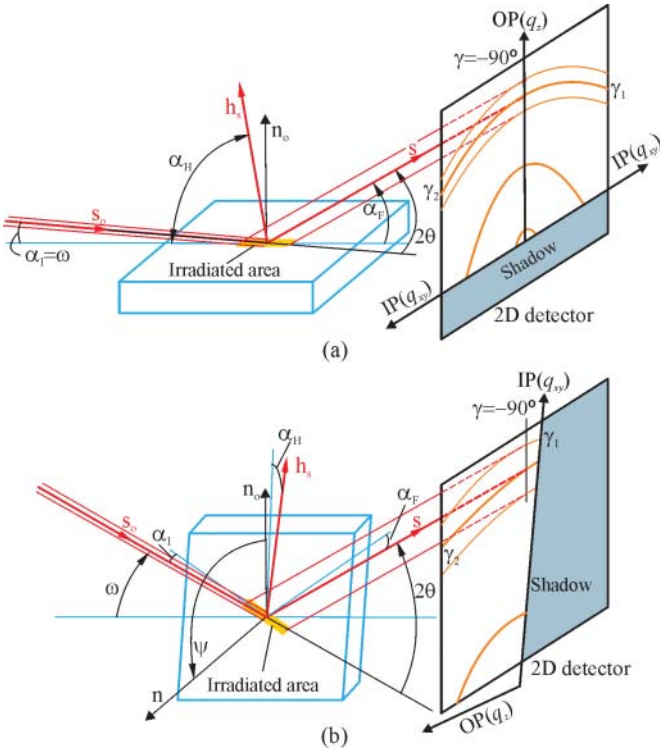


FIGURE 12.17 Grazing incidence X-ray diffraction with a 2D detector (GIXRD^2): (a) standard geometry, (b) in-plane geometry.

surface normal is within the diffractometer plane. The sample normal at $\psi = 0°$ is $\mathbf{n_0}$. The shadowed region on the 2D image (viewed from the back of detection plane in the figure as if the detection plane is transparent) represents the scattering direction blocked by the sample surface. For a system with a point detector or if only the diffracted X-rays within the diffractometer plane ($\gamma = -90°$) are considered for a 2D detector, the diffraction vector is normal to the sample surface when $\omega = \theta$. In this geometry, the incident angle is given by ω (θ-2θ configuration) or θ_1 (θ-θ configuration) and the exit angle α_F (defined as the angle between the diffracted beam and the sample surface) varies with the γ value:

$$\alpha_F = \arcsin(-\cos 2\theta \sin\omega - \sin 2\theta \sin\gamma \cos\omega) \tag{12.39}$$

For the diffracted beam within the goniometer plane ($\gamma = -90°$), $\alpha_D = 2\theta - \omega$. The angle between the diffraction vector and sample surface (α_H) is given by

$$\alpha_H = \arcsin(\sin\theta \sin\omega - \cos\theta \sin\gamma \cos\omega) \tag{12.40}$$

For diffraction pattern with a 2θ angle smaller than the coverage of the detector size, γ covers a large range over the 2D frame. Therefore, the diffraction pattern may cover a large range of diffraction vector directions from the in-plane (q_{xy}) direction to out-of-plane (q_z) direction. The same geometry is also used for grazing incidence small angle scattering (GISAXS) with long detector distance for better resolution and evacuated beam path to eliminate air scatters.

Figure 12.17(b) shows GIXRD^2 in in-plane geometry (IP-GIXRD^2). The grazing incidence angle is achieved by ψ rotation. When ψ approaches 90°, the diffraction vector makes a very small angle (=90° – ψ when $\omega = \theta$) with the sample surface plane. The unit vectors of the incident beam, diffracted beam and the sample normal are given respectively in Chapter 2 as

$$\boldsymbol{s_o} = \begin{bmatrix} 1 \\ 0 \\ 0 \end{bmatrix}, \quad \boldsymbol{s} = \begin{bmatrix} \cos 2\theta \\ -\sin 2\theta \sin\gamma \\ -\sin 2\theta \cos\gamma \end{bmatrix} \text{ and } \boldsymbol{n} = \begin{bmatrix} -\sin\omega\cos\psi \\ \cos\omega\cos\psi \\ \sin\psi \end{bmatrix} \tag{12.41}$$

We have

$$\sin\alpha_I = \cos(90^\circ - \alpha_I) = -\boldsymbol{s_o}\cdot\boldsymbol{n} = \sin\omega\cos\psi \tag{12.42}$$

Then the incident angle is given by

$$\alpha_I = \arcsin(\sin\omega\cos\psi) \tag{12.43}$$

The exit angle α_F varies with the γ value. Considering

$$\begin{aligned} \sin\alpha_F &= \cos(90^\circ - \alpha_F) = \boldsymbol{s}\cdot\boldsymbol{n} \\ &= -\cos 2\theta \sin\omega\cos\psi - \sin 2\theta \sin\gamma\cos\omega\cos\psi - \sin 2\theta\cos\gamma\sin\psi \end{aligned} \tag{12.44}$$

we have

$$\alpha_F = \arcsin(-\cos 2\theta \sin\omega\cos\psi - \sin 2\theta \sin\gamma\cos\omega\cos\psi - \sin 2\theta\cos\gamma\sin\psi) \tag{12.45}$$

Although all three terms in the arcsine function bear a negative sign, α_F has a positive value for the reflection mode diffraction. The region with negative α_F value represents the scattering direction blocked by the sample surface, which shows as a shadowed region on the 2D image. When ψ is near 90° (but not at 90°), the γ range of the diffraction ring starts at a value near $\gamma = -90^\circ$. For example, if $\omega = 30^\circ$, $2\theta = 60^\circ$, and $\psi = 89^\circ$, the grazing incidence angle α_I is 0.5°, and the exit angle α_F for the diffracted beam at $\gamma = -90^\circ$ is also 0.5°. But the γ value at the boundary between the "bright" region and shadowed region is $\gamma_1 \approx -89.43^\circ$ and γ_2 is determined by the detector size.

The angle between the diffraction vector and the sample surface is given by

$$\alpha_H = \arcsin h_3 = \arcsin(\sin\theta\cos\psi\sin\omega - \cos\theta\sin\gamma\cos\psi\cos\omega - \cos\theta\cos\gamma\sin\psi) \tag{12.46}$$

For the above example ($\omega = 30^\circ$, $2\theta = 60^\circ$, and $\psi = 89^\circ$) with $\gamma = -90^\circ$, the angle between the diffraction vector and sample surface $\alpha_H = 90^\circ - \psi = 1^\circ$. The minimum α_H angle corresponding to the edge of the shadow ($\gamma_1 \approx -89.43^\circ$) is then 0.5°. Since the grazing incidence angle cannot be 0, the diffraction vector can approach the sample plane, but never be within the plane.

With the in-plane condition achieved by setting ψ near 90°, a large 2θ range can be measured by multiple 2D frames or scanning 2D detector. The configuration can be used to collect 2D diffraction data for phase analysis, strains, stresses, and texture measurement. With either configuration (a) or (b) in Figure 12.17, the irradiated area on the sample spreads over an elongated area, resulting in a deteriorated 2θ resolution, especially when diffraction pattern at large 2θ angle is collected. A detailed analysis on the 2θ resolution for both in-plane and out-of-plane configurations can be found in reference [57].

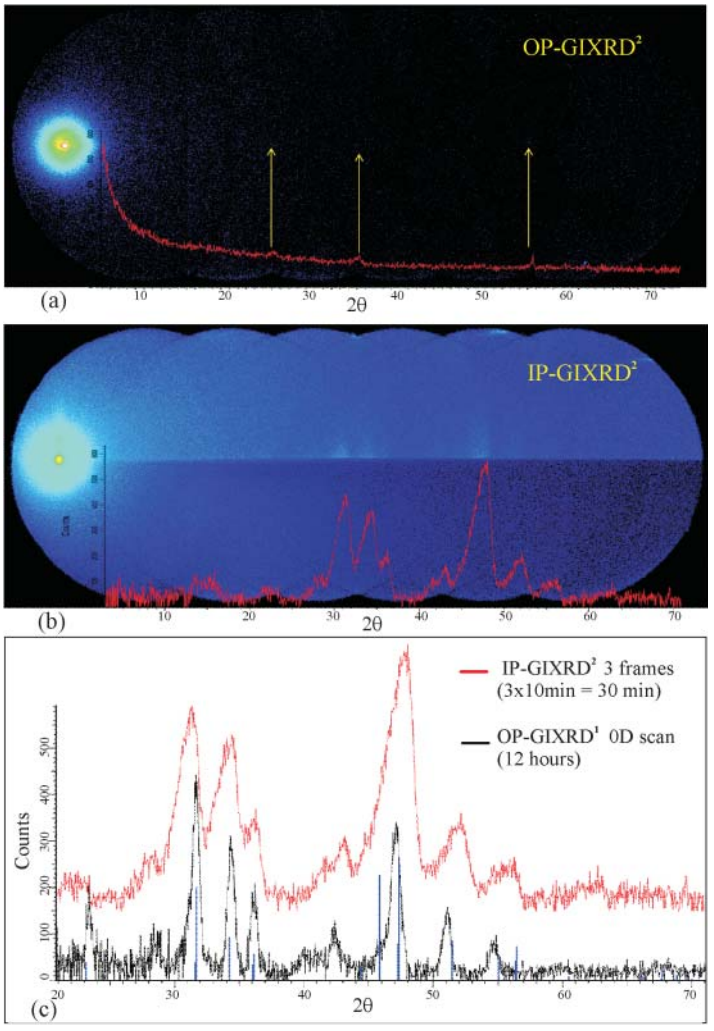


FIGURE 12.18 Diffraction data collected on 10 nm polycrystalline NiSi file on Si wafer with (a) OP-GIXRD^2, (b) IP-GIXRD^2, and (c) comparison of IP-GIXRD^2 and OP-GIXRD^1 (reproduced from [58] with permission).

Figure 12.18 shows a comparison of diffraction data collected on 10 nm polycrystalline NiSi file on Si wafer with different diffractometers and configurations [58]. The figure shows: (a) 2D pattern collected in out-of-plane GIXRD configuration (OP-GIXRD^2), (b) 2D pattern collected in IP-GIXRD configuration (IP-GIXRD^2, and (c) a comparison of 1D diffraction pattern from integration of IP-GIXRD^2 pattern and from conventional 0D detector scanning with grazing incidence (OP-GIXRD^1). It can be seen that the diffraction pattern with OP-GIXRD^2 is so weak that the three peaks marked by the yellow arrow are hardly visible. IP-GIXRD^2 can obtain a strong diffraction pattern over a large 2θ range with 30 minutes data collection time (three 10 minute frames), while the diffraction pattern collected with the conventional 0D detector (OP-GIXRD^1) takes 12 hours. Although with inferior 2θ resolution and high background, IP-GIXRD^2 is still a good choice for fast thin film characterization.

12.5.2 Reflectometry with 2D Detector

X-ray reflectometry, also known as X-ray reflectivity or XRR, is used to measure thickness, density, and roughness of single layer film or multilayer films on a substrate [59–61]. When X-rays are applied to a sample surface at an incident angle below or equal to the critical angle θ_c, total reflection will occur. The critical angle varies depending upon the electronic density of the material. Therefore, density of the material can be determined from the critical angle. When the incident angle is above the critical angle, the incident X-rays penetrate into the sample, the reflected intensity drops dramatically with increasing incident angle. The reflections from the sample surface and interfaces between different layers and substrate produce interference fringes. The period of the interference fringes and the fall in the intensity are related to the thickness and the roughness of the film or multilayers. Since the reflection of X-rays is due to the contrast in electron densities, XRR does not work effectively if there is no difference between the electron density of different layers or between layer and substrate. However, XRR analysis can be performed on both crystalline and amorphous materials.

The interference of X-ray reflected from the sample surface and the interface between the thin film and the substrate results in oscillations of the reflected intensity as a function of the incident angle. The reflected intensity may be plotted as a function of 2θ (or θ) for a specific wavelength λ, or as a function of q ($q = 4\pi \sin\theta/\lambda$ is the magnitude of the scattering vector $\mathbf{Q}$). The thickness of single film on a substrate can be given approximately by

$$t \approx \frac{\lambda}{2} \cdot \frac{1}{\Delta\theta} \approx \frac{\lambda}{\Delta(2\theta)} \approx \frac{2\pi}{\Delta q_Z} \tag{12.47}$$

Where $\Delta(2\theta)$ is the difference in 2θ angle between two adjacent maxima in the reflectivity plot, Δq_Z is the difference when the reflectivity is plotted against q, and the subscript z indicates that the scattering vector is perpendicular to the sample surface. The above equation is a simplified approximation to describe the relationship between the reflectivity plot and the single film thickness. More sophisticated mathematic models are typically used in the reflectivity evaluation software. The reflectivity from multiple layers is a combination of the interference of X-rays reflected from interfaces between the layers and the substrate, therefore more complicated models are necessary to fit the XRR pattern. The sample surface roughness and interface roughness results in diffuse scattering, so the reflected intensity drops more dramatically with a rough surface or interfaces. Therefore, the surface roughness and interface roughness can be evaluated from the fall of the reflectivity plot.

Total external reflection can be several orders of magnitude stronger than the interference fringes. The maximal observable thickness is limited by the 2θ resolution. For reflectometry with conventional a point (0D) detector, we can add an absorber in the beam path for data collection in the vicinity and below the critical angle. The 2θ resolution can be controlled by the soller slits attached in front of the 0D detector. The absorber may be added to the primary beam side for reflectometry with a 2D detector, but adding soller slits in front of the 2D detector would defeat the purpose of having a 2D detector. This is the main reason that 2D detectors have not been used for reflectometry as much as 0D detectors. With the availability of 2D detectors having high dynamic range and high resolution, XRR with a 2D detector becomes more practical and will be used more frequently in the near future. Figure 12.19 shows an example of thin film thickness measurement by XRR with a 2D detector. The left (a) shows four 2D pattern collected from thin films (not specified in the reference) with various thicknesses and the right (b) are fitted results from the integrated XRR profile.

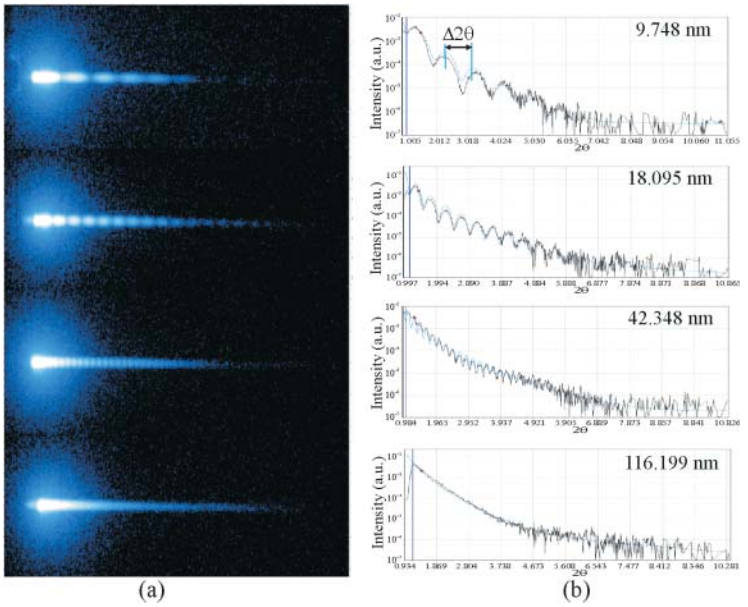


FIGURE 12.19 Thin film thickness measurement with 2D detector. (a) 2D XRR pattern and (b) thickness evaluation from the integrated profiles. (Reproduced from [58] with permission.)

12.5.3 Reciprocal Space Mapping

Reciprocal space mapping (RSM) is a powerful tool to visualize and analyze the diffraction patterns from highly oriented structures, diffuse scattering from crystal defects, and thin films [57, 62–65]. RSM by the conventional diffractometer with a 0D detector takes a long data collection time because each exposure measures a point in the reciprocal space. The RSM data points generated from a 2D diffraction pattern can cover a 2D area in the reciprocal space. The RSM in three-dimensional space can be collected by using a 2D detector with energy resolution and X-rays with a broad spectrum or tunable energy [66]. Since it requires a 2D detector with high pixel resolution and high energy coverage and resolution, this method is not practical with today's detector technology. Alternatively, scanning 2D coverage over the reciprocal space by sample rotation is still the best way to collect data for RSM.

Figure 12.20 illustrates the concept of RSM by a 2D detector. The coverage of a 2D detector in reciprocal space is the orange region on the surface of the Ewald sphere centered on C. The size of the region is determined by the angular coverage of the 2D detector $\Delta 2\theta$ and $\Delta\gamma$. The location of the region with respect of the Ewald sphere is determined by the detector swing angle α (not shown in the figure, but is equal to 2θ if measured from the detector center). The position of the Ewald sphere with respect to the sample direction may be changed in terms of the laboratory coordinates (determined by the incident X-ray beam and diffractometer plane) by ω, ψ, and ϕ rotations. At original sample orientation ($\omega = \psi = \phi = 0$), the rotation axes are in parallel to the three sample axes S_1, S_2, and S_3 (not marked in the figure, but in overlap with q_x, q_y, q_z axes respectively). But due to the stacking sequence of the rotation axes, the orientation of a rotation axis may be altered by the other rotations. The effects of all rotations are defined in Chapter 2.

In a classic illustration, the crystal is located in the center of the Ewald sphere. The diffracted beam vector $\mathbf{s}/\lambda$ ends at the point O. In order to clearly illustrate the orientation relationship between the incident beam and sample, we translate the sample rotation center to the point O.

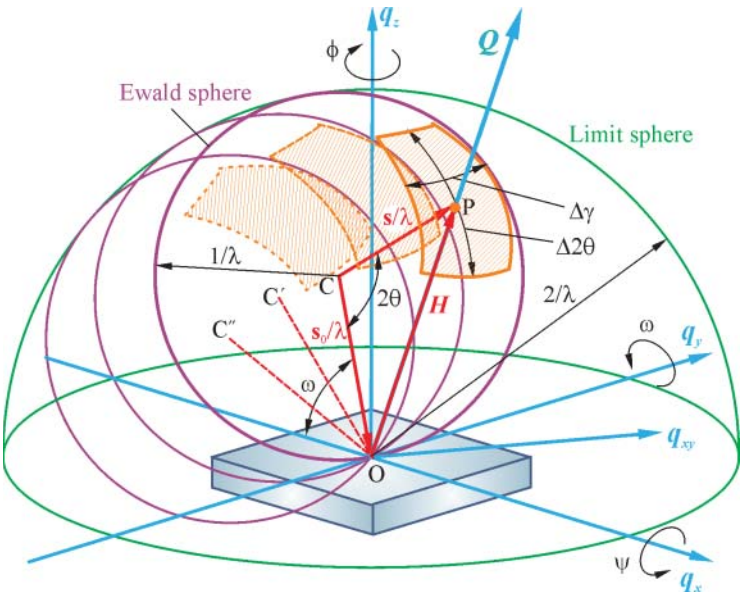


FIGURE 12.20 Reciprocal space mapping with a 2D detector.

The point O of the Ewald sphere remains in the instrument center with sample rotation as well as the rotation of Ewald sphere. With all possible sample orientations, the Ewald sphere covers a sphere of $2/\lambda$ in radius, referred to as limit sphere. For reflection mode diffraction, only half of the limit sphere above the sample surface is available. For an arbitrary spot P within the coverage, both incident beam vector $\mathbf{s_0}/\lambda$ and diffracted beam vector $\mathbf{s}/\lambda$ start at point C, but end at points O and P respectively. The angle between the incident beam and the diffracted beam is 2θ. The vector from O to P is the diffraction vector $\boldsymbol{H}$. The diffracted beam vector and the diffraction vector meet at the point P on surface of the Ewald sphere. Considering the diffraction vectors corresponding to all the pixels of the 2D detector, the coverage of the 2D diffraction can be mapped on the surface of the Ewald sphere. For simplicity, the area are marked within the angular ranges of $\Delta 2\theta$ and $\Delta\gamma$. The actual coverage depends on the size and shape of the detector, but it is not likely to have such a regular shape after being mapped into the reciprocal space. The Ewald spheres with the centers at point C, C′, and C″ represents the Ewald sphere at three different ω values. A three-dimensional mapping can be obtained by collecting many 2D frames with fine scanning steps. The RSM can be achieved by scanning any one or a combination of the Eulerian angles (ω,ψ,ϕ).

In RSM construction, we project data points corresponding to the scattering intensities (in X-ray counts) from a pixel or small region in 2D frame into diffraction space, then into reciprocal space: i.e.

$$I(x,y) \Rightarrow I(2\theta,\gamma) \Rightarrow I(\boldsymbol{H}) \tag{12.48}$$

The location of a data point is determined by the diffraction vector. Since RSM is typically displayed respect to the sample coordinates, we have

$$\boldsymbol{H} = \frac{2\sin\theta}{\lambda}\boldsymbol{h}_s = \frac{2\sin\theta}{\lambda}\begin{Bmatrix} h_1 \\ h_2 \\ h_3 \end{Bmatrix} \tag{12.49}$$

where $\boldsymbol{h_s}$ is the unit vector of the diffraction vector with three components $\{h_1, h_2, h_3\}$ expressed in the sample coordinates. Considering that RSM is typically displayed in Q space and $\boldsymbol{Q} = 2\pi\boldsymbol{H}$, an illustration scaling up by a factor of 2π from Figure 12.20 can be drawn with $\boldsymbol{k_0}$, $\boldsymbol{k}$, and $\boldsymbol{Q}$ instead of $\boldsymbol{s_0}$, $\boldsymbol{s}$, and $\boldsymbol{H}$ respectively. Then we have the RSM as

$$\boldsymbol{I}(\boldsymbol{Q}) = \boldsymbol{I}(q_x, q_y, q_z) \tag{12.50}$$

where q_x, q_y, and q_z are the three components of the $\boldsymbol{Q}$ vector expressed in sample orientation, which can be obtained from 2D diffraction pattern $(2\theta,\gamma)$ and sample orientation (ω,ψ,ϕ) by the following equations:

$$q_x = \frac{4\pi \sin\theta}{\lambda}[\sin\theta(\sin\phi \sin\psi \sin\omega + \cos\phi \cos\omega) + \cos\theta \cos\gamma \sin\phi \cos\psi - \cos\theta \sin\gamma(\sin\phi \sin\psi \cos\omega - \cos\phi \sin\omega)] \tag{12.51}$$

$$q_y = \frac{4\pi \sin\theta}{\lambda}[-\sin\theta(\cos\phi \sin\psi \sin\omega - \sin\phi \cos\omega) - \cos\theta \cos\gamma \cos\phi \cos\psi + \cos\theta \sin\gamma(\cos\phi \sin\psi \cos\omega + \sin\phi \sin\omega)] \tag{12.52}$$

$$q_z = \frac{4\pi \sin\theta}{\lambda}[\sin\theta \cos\psi \sin\omega - \cos\theta \sin\gamma \cos\psi \cos\omega - \cos\theta \cos\gamma \sin\psi] \tag{12.53}$$

The above equations are general RSM equations for XRD[2] with all possible rotations. Some special case can be considered with simplified equations. For example, if a 2D RSM contains the out-of-plane direction (q_z) and a particular in-plane direction (q_{xy}), we have the same equation for q_z, but

$$q_{xy} = \frac{4\pi \sin\theta}{\lambda}\sqrt{1 - (\sin\theta \cos\psi \sin\omega - \cos\theta \sin\gamma \cos\psi \cos\omega - \cos\theta \cos\gamma \sin\psi)^2} \tag{12.54}$$

Diffraction with a 0D detector can be considered as a special case with the above general equations. The diffraction intensity at a point with $\gamma = -90°$ in a 2D frame is equivalent to the diffraction intensity collected with a 0D detector. With $\psi = \phi = 0$, the above equations can be reduced to

$$q_x = \frac{2\pi}{\lambda}[\cos\omega - \cos(2\theta - \omega)] \tag{12.55}$$

$$q_z = \frac{2\pi}{\lambda}[\sin\omega + \sin(2\theta - \omega)] \tag{12.56}$$

The above two equations gives the $\boldsymbol{Q}$ vector for various scan types of the conventional diffractometer with a point detector and only two main axes in either θ-2θ or θ-θ configurations, for instance, a rocking curve by scanning ω with a fixed 2θ, detector scan by scanning 2θ with a fixed ω, or coupled scan by scanning 2θ and ω simultaneously (radial scan or $\omega/2\theta$ scan). The coupled scan with $\theta = \omega$ (symmetric $\theta/2\theta$ scan) sets $q_x = 0$ and scans only in q_z direction.

The resolution of RSM constructed from 2D frames depends on the scanning steps of any one or a combination of the Eulerian angles (ω,ψ,ϕ), the size and parallelism of the incident X-ray beam, as well as the detector pixel resolution. Fine scanning steps can be easily achieved with a modern goniometer, and the incident beam can be conditioned by various optics, such as

monochromator, pin holes, and slits. Thus, the pixel size and detector distance become the most critical factors for RSM resolution. The 2θ resolution associated to an arbitrary pixel in a 2D detector is given as

$$\Delta 2\theta = \frac{D}{D^2 + x^2 + y^2}\Delta x \tag{12.57}$$

where D is sample-to-detector distance, x and y are the location of the pixel in the detector, and Δx is the pixel size assuming a square pixel. The resolution within the Ewald sphere surface corresponding to a pixel can be given in Q space is

$$\Delta q = \frac{2\pi}{\lambda} \cdot \frac{D \cdot \Delta x}{D^2 + x^2 + y^2} \tag{12.58}$$

where Δq is the best resolution within the Ewald sphere surface covered by a 2D detector. The actual resolution is smeared by the other instrument broadening effects. Assuming the only instrument broadening contribution is from a parallel incident beam with beam size b, the resolution is then given as

$$\Delta q = \frac{2\pi}{\lambda} \cdot \frac{D\sqrt{\Delta x^2 + b^2}}{D^2 + x^2 + y^2} \tag{12.59}$$

For instance, with a detector pixel of 75 μm, $b = 50$ μm, $D = 200$ mm, and $\lambda = 0.154059$ nm, the best RSM resolution in the center of the covered Ewald sphere surface ($x = y = 0$) is 0.0184 nm^{-1}.

RSM by XRD^2 can be measured and displayed in many ways. The three-dimensional reciprocal space mapping can be obtained by applying the pixel intensities to the corresponding reciprocal points. With various sample orientations, the scattered intensities recorded by all pixels, or pixels within a selected region, can be mapped into three-dimensional reciprocal space within a sphere of maximum radius of $2/\lambda$ (limiting sphere). Actual radius of limit sphere is smaller than $2/\lambda$ because most diffractometers cannot reach 180° 2θ. For the study of epitaxial structure, heterostructure, superlattice, microstrain, and other crystal detects, high resolution RSM in the vicinity of Bragg reflections is necessary. For instance, diffuse scattering can be observed outside the Bragg peak associated with crystal defects. This requires a high resolution XRD^2 system with bright and parallel incident X-ray beam with small beam size, a precise goniometer, and a 2D detector with high resolution and high dynamic range.

The software to construct RSM from XRD^2 data set can be found from commercial vendors or academies. One example is MAX3D, which is a software package designed to read a series of 2D diffraction images and provide a visualization of a solid volume of reciprocal space (also referred to as XRD^3). Figure 12.21 shows six examples of projected views of RSM created by MAX3D, and 3D visualization can be realized by direct access to the software or website [67, 68].

The 2D frames collected at various sample orientations may be combined to form an integrated RSM. The integrated RSM can be collected either by rotating the sample while collecting data in a single exposure or by integrating 2D frames collected at various sample orientations. The $\boldsymbol{Q}$ vectors expressed in q_x, q_y, q_z vary with the 2D frames collected at different sample orientations, but the diffraction space (2θ, γ) values are kept the same with the sample orientation. Therefore, integrated RSM is better displayed in diffraction space, or in another words, on the original 2D frame format. The integrated RSM has no specific (or accurate) reference to the sample orientation, but a combined diffraction pattern covering a range of sample orientation. A 2D frame collected by the Gandolfi method or angular oscillation, in principle, is an integrated RSM displayed in diffraction space. Figure 12.22 shows an integrated RSM collected by a GADDS™ system with Hi-Star 2D detector from 200 nm $BiFeO_3$ thin film on (001) $SrTiO_3$ substrate by ω

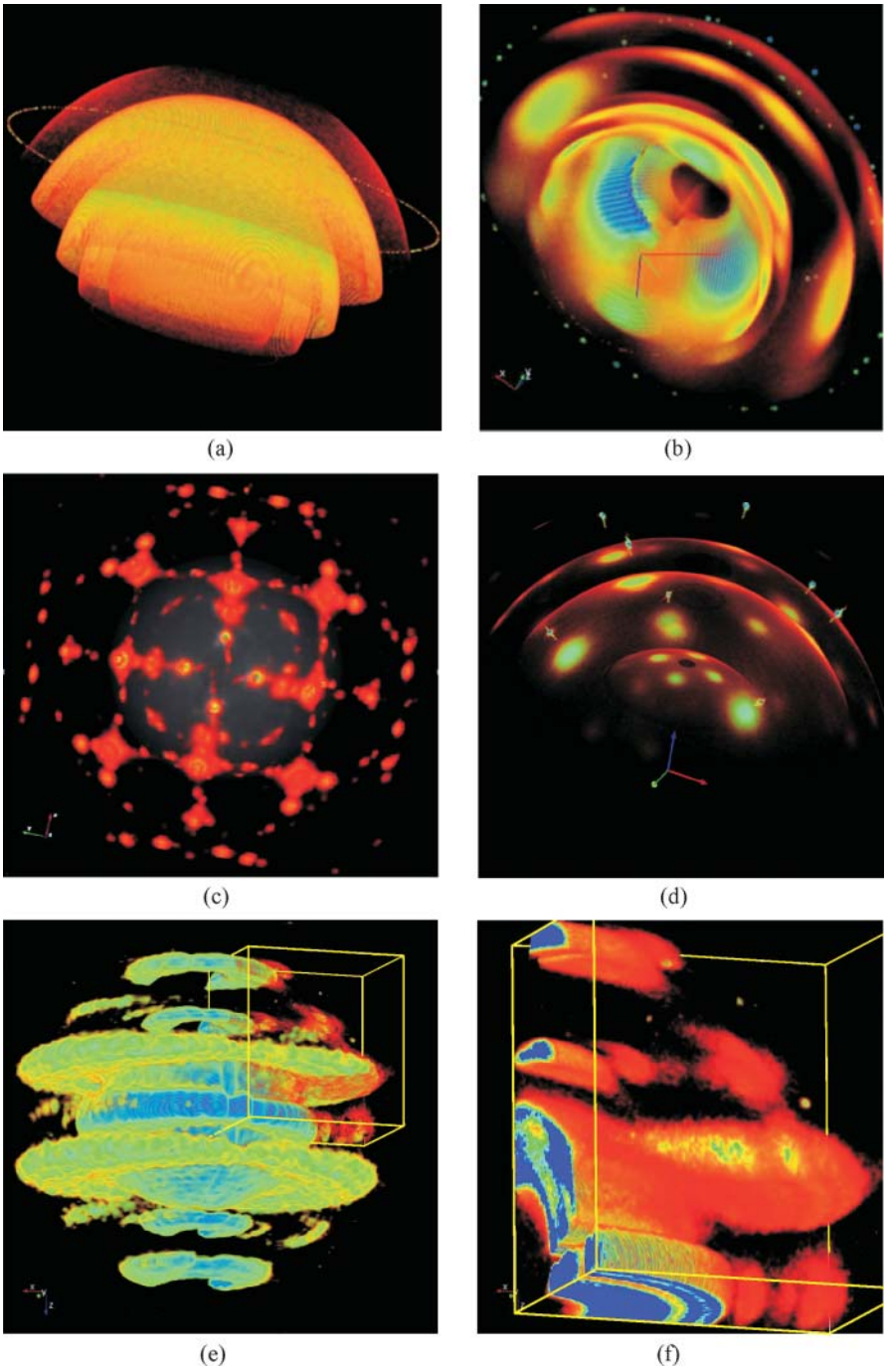


FIGURE 12.21 Three-dimensional RSM constructed by MAX3D with 2D frames collected at various sample rotation angles: (a) random corundum powder, (b) Au/Pt nanolayered sheet with rolled texture, (c) GaAs nanowires on Si substrate, (d) epitaxial thin film with texture on substrate, (e) extruded, distorted polypropylene, and (f) subsection of (e) with higher resolution. (Reproduced from [67, 68] with permission.)

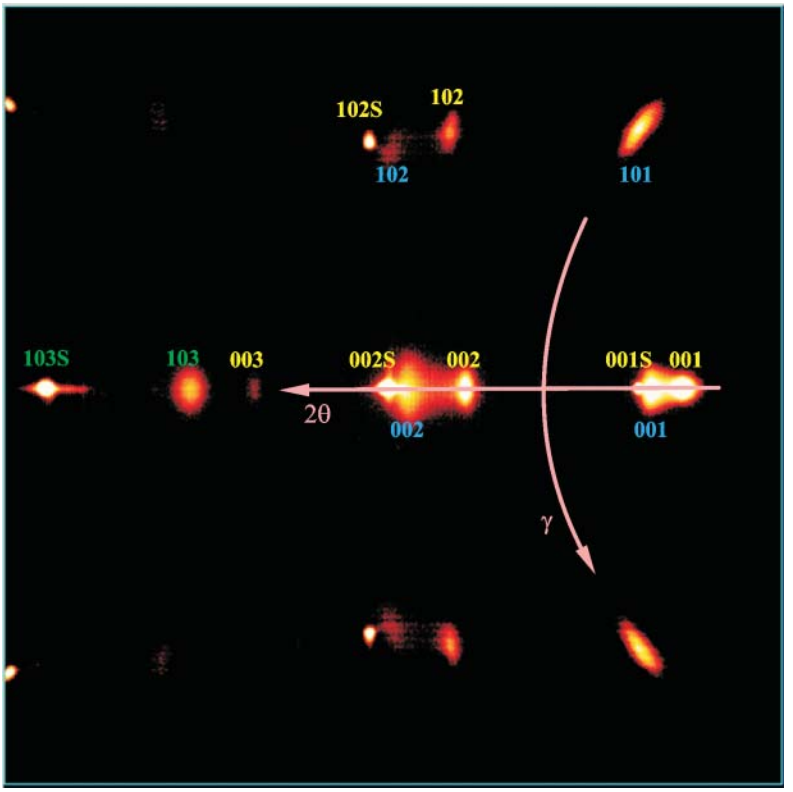


FIGURE 12.22 Integrated RSM from 200 nm $BiFeO_3$ thin film on (001) $SrTiO_3$ substrate. (Reproduced from [69] with permission.)

scan from 8° to 30° with detector distance $D = 6$ cm [69]. The integrated RSM shows all diffraction spots from the film, substrate, and in-plane epitaxial relation as well as impurity phase which can be collected at any angle of ω between 8° and 30°. Since the integrated RSM is actually a 2D frame, it can be γ-integrated into a 1D diffraction profile for further analysis, such as phase identification. The integrated RSM may also be displayed in a rectangular q-γ coordinates, here $q = 4\pi \sin\theta/\lambda$.

REFERENCES

1. L. E. Alexander, *X-ray Diffraction Methods in Polymer Science*, Krieger Publishing Company, Malabar, FL, 1985.
2. N. Kasai and M. Kakudo, *X-ray Diffraction by Macromolecules*, Kodansha and Springer, Tokyo, 2005, 393–417.
3. N. S. Murthy and H. Minor, General procedure for evaluating amorphous scattering and crystallinity from X-ray diffraction scans of semi-crystalline polymers, *Polymer* **31**, 996–1002 (1990).
4. N. S. Murthy, H. Minor, M. K. Akkapeddi, and B. V. Buskirk, Characterization of polymer blends and alloys by constrained profile-analysis of X-ray diffraction scans, *J. Appl. Polym. Sci.* **41**, 2265–2272 (1990).

5. K. B. Schwartz et al., Crystallinity and unit cell variations in linear high-density polyethylene, *Adv. in X-ray Anal*, 1995–**38**, 495–502.
6. N. S. Murthy and R. Barton Jr., Polymer Industry, *Industrial Applications of X-ray Diffraction*, edited by F. H. Chung and D. K. Smith, Marcel Dekker, New York, 2000, 495–509.
7. S. Krimm and A. V. Tobolsky, Quantitative X-ray studies of order in amorphous and crystalline polymers. Quantitative X-ray determination of crystallinity in polyethylene, *J. Polymer Sci.*, 1951, **7**, 57–76.
8. C. G. Vonk, Computerization of Ruland's X-ray method for determination of the crystallinity in polymers, *J. Appl. Cryst.* (1973). **6**, 148–152.
9. S. Polizzi et al., A fitting method for the determination of crystallinity by means of X-ray diffraction, *J. Appl. Cryst.* (1990). **23**, 359–365.
10. C. G. Vonk and G. Fagherazzi, The determination of the crystallinity in glass-ceramic materials by the method of Ruland, *J. Appl. Cryst.* (1983). **16**, 274–276.
11. F. H. Chung and R. W. Scott, A new approach to the determination of crystallinity of polymers by X-ray diffraction, *J. Appl Cryst.* (1973). **6**, 225–230.
12. J. A. Pople, P. A. Keates, and G. R. Mitchell, A two-dimensional X-ray scattering system for in-situ time-resolving studies of polymer structures subjected to controlled deformations, *J. Synchrotron Rad.* (1997). **4**, 267–278.
13. Percent crystallinity in polymer, Bruker AXS Lab Report No. L86-E00005, 2000.
14. S. Ran et al., Novel image analysis of two-dimensional X-ray fiber diffraction patterns: example of a polypropylene fiber drawing study, *J. Appl. Cryst.* (2000). **33**, 1031–1036.
15. M. Shimazu and A. Watanabe, Effective elimination of the Compton component in amorphous scattering by experimental means, *J. Appl. Cryst.* (1974). **7**, 531–535.
16. W. Ruland, X-ray determination of crystallinity and diffuse disorder scattering, *Acta Cryst.* (1961). **14**, 1180–1185.
17. P. Pattison, P. Suortti, and W. Weyrich, An X-ray spectrometer for inelastic scattering experiments. III. Design and performance, *J. Appl. Cryst.* (1986). **19**, 353–363.
18. S. R. Sternberg, Biomedical image processing computer. *IEEE Computer Society*, 1983, **6**, 22–34.
19. S. R. Sternberg, Greyscale morphology, *Computer Vision, Graphics, and Image Processing*, 1986, **35**, 333–355.
20. D. R. Askeland and P. P. Phule, *The Science and Engineering of Materials*, Thomson, 2003.
21. S. Rao and C. R. Houska, X-ray particle-size broadening, *Acta Cryst.* (1986). **A42**, 6–13.
22. A. J. C. Wilson, Some further considerations in particle-size broadening, *J. Appl. Cryst.* (1971). **4**, 440–443.
23. T. Ungár, Warren-Averbach applications, *Industrial Applications of X-ray Diffraction*, edited by F. H. Chung and D. K. Smith, Marcel Dekker, New York, 2000, 847–867.
24. H. P. Klug and L. E. Alexander, *X-ray Diffraction Procedures for Polycrystalline and Amorphous Materials*, John Wiley & Son, New York, 1974, 618–708.
25. B. D. Cullity, *Elements of X-ray Diffraction*, 2nd ed., Addison-Wesley, Reading, MA, 1978.
26. R. P. Goehner et al., Microbeam crystallographic and element analysis, *Industrial Applications of X-ray Diffraction*, edited by F. H. Chung and D. K. Smith, Marcel Dekker, New York, 2000, 869–890.
27. G. Allegra and S. Brückner, Crystallite-size distributions and diffraction line profiles near the peak maximum, *Powder Diffraction*. (1993), **8**(2), 102–106.
28. H. Ebel, Crystallite size distributions from intensities of diffraction spots, *Powder Diffraction*. (1988), **3**(3), 168–171.
29. J. I. Langford, The variance and other measures of line broadening in powder diffractometry. I. Practical considerations, *J. Appl. Cryst.* (1968). **1**, 48–59.
30. J. I. Langford, The variance and other measures of line broadening in powder diffractometry. II. Determination of particle size, *J. Appl. Cryst.* (1968). **1**, 131–138.

31. J. P. Urban, X-ray measurements of strain and mosaic particle size in annealed tungsten powder, *J. Appl. Cryst.* (1975). **8**, 459–464.
32. J. I. Langford and A. J. C. Wilson, Scherrer after sixty years: A survey and some new results in the determination of crystallite size, *J. Appl. Cryst.* (1978). **11**, 102–113.
33. T. Adler and C. R. Houska, Simplifications in X-ray line-shape analysis, *J. Appl. Phys*. (1979), **50** (5), 3282–3287.
34. C. R. Houska, Least-square analysis of X-ray diffraction line shapes with analytic functions, *J. Appl. Phys*. (1981), **52** (2), 748–754.
35. R. Delhez et al., Determination of crystallite size and lattice distortions through X-ray diffraction line profile analysis: recipes, methods and comments, *Fresenius Z Anal Chem.* (1982) **312**, 1–16.
36. S. Rao and C. R. Houska, X-ray diffraction profiles described by refined analytical functions, *Acta Cryst.* (1986). **A42**, 14–19.
37. D. Balzar, Profile fitting of X-ray diffraction lines and Fourier analysis of broadening, *J. Appl. Cryst.* (1992). **25**, 559–570.
38. R. W. Cheary and A. Coelho, A fundamental parameters approach to X-ray line-profile fitting, *J. Appl. Cryst.* (1992). **25**, 109–121.
39. T. Ungár, J. Gubicza, G. Ribárik, and A. Borbély, Crystallite size distribution and dislocation structure determined by diffraction profile analysis: principles and practical application to cubic and hexagonal crystals, *J. Appl. Cryst.* (2001). **34**, 298–310.
40. D. Balzar et al., Size-strain line-broadening analysis of the ceria round-robin sample, *J. Appl. Cryst.* (2004). **37**, 911–924.
41. Z. W. Wilchinsky, Effect of crystal, grain, and particle size on X-ray power diffracted from powders, *Acta Cryst.* (1951). **4**, 1–9.
42. L. Yu, Polymorphs and glasses of organic molecules, presentation provided by Professor Lian Yu, University of Wisconsin – Madison, School of Pharmacy & Dept. of Chemistry, (2011).
43. B. B. He, Materials characterization from diffraction intensity distribution in the γ-direction, *Powder Diffraction*, (2014), **29** (2), 113–117.
44. S. W. Freiman and N. M. Trahey, NIST Certificate of standard reference material 660a, lanthanum hexaboride powder for line position and line shape standard for powder diffraction, September **13**, 2000.
45. T. Ida and K. Kimura, Effect of sample transparency in powder diffractometry with Bragg–Brentano geometry as a convolution, *J. Appl. Cryst.* (1999). **32**, 982–991.
46. B. Ingham, Statistical measures of spottiness in diffraction rings, *J. Appl. Cryst.* (2014). **47**, 166–172.
47. K. G. Yager and P. W. Majewski, Metrics of graininess: robust quantification of grain count from the non-uniformity of scattering rings, *J. Appl. Cryst.* (2014). **47**, 1855–1865.
48. M. S. Bramble1, R. L. Flemming, and P. J. A. McCausland, Grain size, 'spotty' xrd rings, and chemin: two-dimensional x-ray diffraction as a proxy for grain size measurement in planetary materials, *45th Lunar and Planetary Science Conference* (2014) 1658.
49. S. Thakral, N. K. Thakral, and R. Suryanarayanan, Estimation of drug particle size in intact tablets by 2-dimensional X-ray diffractometry, *Journal of Pharmaceutical Sciences*, (2017) 1–8. DOI: https://doi.org/10.1016/j.xphs.2017.08.021.
50. C. F. Jatczak, Retained austenite and its measurement by X-ray diffraction – SAE 800426, *Society of Automotive Engineering*, 1980.
51. Standard practice for X-ray determination of retained austenite in steel with near random crystallographic orientation, designation: E 975–03, *ASTM International*, 2003.
52. D. Stephan, G. Grosse, and K. Wetzig, Simultaneous position-resolved determination of phase and stress distributions by means of an X-ray diffractometer with a two-dimensional position-sensitive detector, *J Appl. Cryst.* (1995). **28**, 561–567.

53. J. D. Makinson et al., Diffracting particle size analysis of martensite-retained austenite microstructure, *Adv. in X-ray Anal*, 2000.–**43**, 326–331.
54. M. Birkholz, *T*hin Film Analysis by X-ray Scattering, Wiley-VCH, Weinheim, 2006, 143–182.
55. B. K. Tanner, et al., Grazing incidence in-plane X-ray diffraction in the laboratory, *Adv. in X-ray Anal*, 2004.–**47**, 309–314.
56. H. Morioka, et al., In situ observation of the fatigue-free piezoelectric microcantilever by two-dimensional X-ray diffraction, *Jpn. J. Appl. Phys.* **48** (2009) 09KA03.
57. M. Schmidbauer et al., A novel multidetection technique for three-dimensional reciprocal-space mapping in grazing-incidence X-ray diffraction, *J. Synchrotron Rad.* (2008). **15**, 549–557.
58. J. Giencke, Innovative applications for XRD^2, McMaster University and Bruker XRD^2 Seminar, June **12**, 2013.
59. J. Daillant and A. Gibaud, *X-Ray and Neutron Reflectivity: Principles and Applications*. Springer, (2009).
60. J. Als-Nielsen, D. McMorrow, *Elements of Modern X-Ray Physics*, Wiley, New York, (2001).
61. M. Tolan, *X-Ray Scattering from Soft-Matter Thin Films*, Springer, (1999).
62. D.-M. Smilgies and D. R. Blasini, Indexation scheme for oriented molecular thin films studied with grazing-incidence reciprocal-space mapping, *J. Appl. Cryst.* (2007). **40**, 716–718.
63. S. T. Mudie, et al., Collection of reciprocal space maps using imaging plates at the Australian National Beamline Facility at the Photon Factory, *J. Synchrotron Rad.* (2004). **11**, 406–413.
64. N. Stribeck and U. Nöchel, Direct mapping of fiber diffraction patterns into reciprocal space, *J. Appl. Cryst.* (2009). **42**, 295–301.
65. S. Bauer, et al., Three-dimensional reciprocal space mapping with a two-dimensional detector as a low-latency tool for investigating the influence of growth parameters on defects in semi-polar GaN, *J. Appl. Cryst.* (2015). **48**, 1000–1010.
66. T. W. Cornelius, et al., Three-dimensional diffraction mapping by tuning the X-ray energy, *J. Synchrotron Rad.* (2011). **18**, 413–417.
67. J. Britten, W. Guan, MAX3D – a program for the visualization of reciprocal space, http://max3d.mcmaster.ca., *IUCr Commission on Crystallographic Computing Newsletter*, No. 8, November 2007, 96–108.
68. J. Britten, W. Guan, and V. Jarvis, Visualization of 3D reciprocal space with MAX3D, Invited presentation at NYU-Bruker XRD Workshop, June 15–16, 2011.
69. K. Saito, et al., Introduction to thin film analysis with XRD^2, Bruker marketing presentation, 2005.

13

INNOVATION AND FUTURE DEVELOPMENT

13.1 INTRODUCTION

Significant developments in two-dimensional X-ray diffraction have been demonstrated in the past 30 years. Two-dimensional detectors have been adapted for many X-ray diffraction techniques and applications. The previous chapters in this book have covered some of these accomplishments. Many advantages of two-dimensional X-ray diffraction have been recognized in these applications. However, two-dimensional X-ray diffraction is relatively new in the history of X-ray diffraction. More innovation and development are expected in two major categories. One is technology development in the detector, X-ray source and optics, computing power, and software, and the other is theoretical development in two-dimensional diffraction pattern interpretation and data analysis. Three examples of innovation and future development were given in the first edition of this book and the author would like to keep them in this chapter with a little update. The first example is an innovation in collecting two-dimensional diffraction data with a scanning line detector. The second example is the concept of a three-dimensional detector and its potential applications. The third example is an approach for data analysis of two-dimensional diffraction data. The scanning line detector for collecting XRD^2 data has been implemented; the other two examples are mostly at the conceptual stage. Further developments and experiments are necessary.

Many innovations since the publication of the first edition of this book have been included in the previous chapters. In this chapter, we give one more example: the high resolution two-dimensional X-ray diffractometer. Prediction of future development in two-dimensional X-ray diffraction is next to impossible, but it is certain that the potential of two-dimensional X-ray diffraction is boundless.

Two-Dimensional X-Ray Diffraction, Second Edition. Bob Baoping He.
© 2018 John Wiley & Sons, Inc. Published 2018 by John Wiley & Sons, Inc.

13.2 SCANNING LINE DETECTOR FOR XRD[2]

13.2.1 Working Principle

A two-dimensional detector has been perceived as a mandatory component of a two-dimensional diffraction system [1–3]. An innovative geometry and design of a two-dimensional X-ray diffraction system using a line detector is introduced [4]. The line detector is positioned perpendicular to the diffractometer plane. During data collection, the line detector scans along the detection circle while collecting diffraction signals. The line signals at sequential detector positions forms a two-dimensional diffraction image. The two-dimensional diffraction image can then be displayed and analyzed using two-dimensional diffraction theory.

As shown in Figure 13.1, a line detector is mounted perpendicular to the diffractometer plane. In still mode, the detector collects X-rays scattered from the sample along a vertical linear range. When the detector is scanned over an angular range while collecting data, the trace of the detection line forms a cylindrical surface that is a two-dimensional diffraction image. In order to analyze the two-dimensional diffraction data collected by a scanning line detector, 2θ and γ angles in the diffraction space should be calculated for each pixel in the diffraction frame. As shown in Figure 13.2, the position of the line detector is determined by the detector distance D and the detector swing angle α. The detector distance D is measured between the detection line and the instrument center within the diffractometer plane. The detector swing angle α is defined as

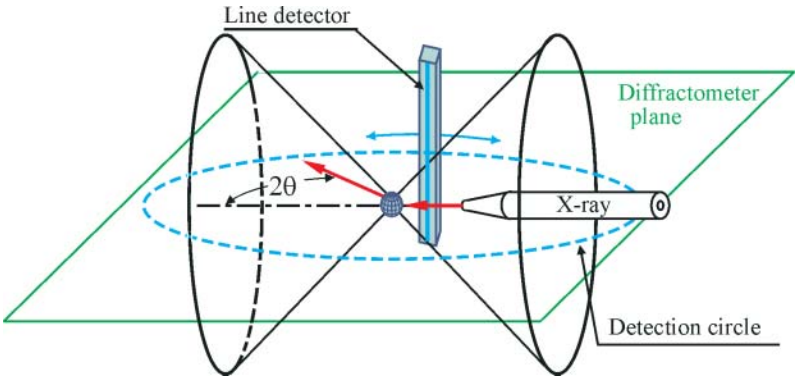


FIGURE 13.1 Geometrical features of two-dimensional diffraction by scanning line detector.

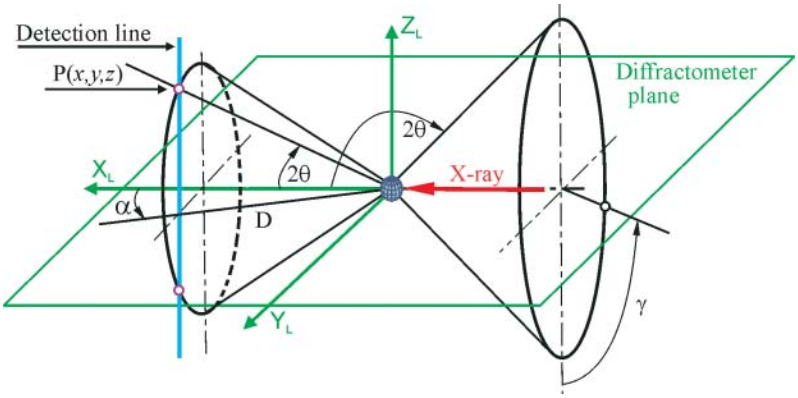


FIGURE 13.2 Line detector position and a point of line detector in the diffraction space.

the angle measured in the diffractometer plane between the $\mathbf{X_L}$ axis and the line extended from the origin to the detector. For a given point on the line detector, P(x,y,z), the position of the point in the diffraction space is determined by (x,y,z) in the laboratory coordinates, where z is given as the distance from the diffractometer plane to the point on the line detector and

$$x = D\cos\alpha$$
$$y = D\sin\alpha \tag{13.1}$$

The γ and 2θ angles of each pixel can be calculated from

$$\gamma = \begin{cases} \arccos\dfrac{-z}{\sqrt{z^2 + D^2\sin^2\alpha}} & -\pi \le \alpha < 0 \\ \pi + \arccos\dfrac{z}{\sqrt{z^2 + D^2\sin^2\alpha}} & 0 \le \alpha \le \pi \end{cases} \tag{13.2}$$

and

$$2\theta = \arccos\frac{D\cos\alpha}{\sqrt{D^2 + z^2}} \tag{13.3}$$

During data collection, the line detector scans along the detection circle while collecting diffraction signals. Figure 13.3 is an illustration of the data collected with a line detector. The line signals at sequential detector positions form a two-dimensional diffraction image. The horizontal axis corresponds to the detector swing angle α, and the vertical axis corresponds to the pixel height z. The equations (13.2) and (13.3) convert each pixel position (in α and z) into a point in diffraction space (γ and 2θ). The two-dimensional diffraction image can then be displayed and analyzed using two-dimensional diffraction theory. Other equations may be used to calculate the diffraction space parameters (γ and 2θ) for the same geometry or different geometry. All the previous algorithms for phase identification, stress analysis, texture analysis, and other diffraction applications are applicable to the diffraction frame collected by scanning line detector, except those equations specifically developed for the geometry of flat 2D detectors.

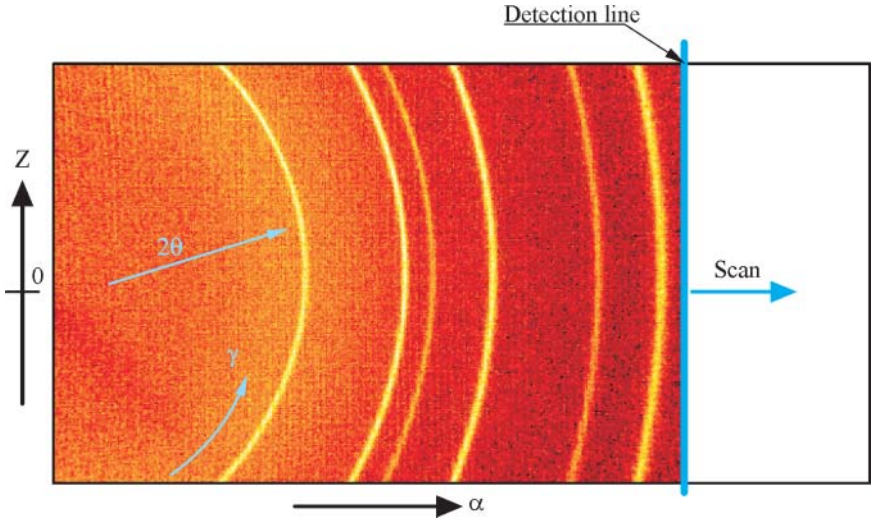


FIGURE 13.3 Illustration of a two-dimensional diffraction image.

13.2.2 Advantages of Scanning Line Detector

There are many advantages of two-dimensional diffraction with a line detector. In additional to most functions of a conventional two-dimensional diffraction with a 2D detector, there are other advantages which include, but are not limited to, the following:

- **Low cost** – With current technology, the cost of a line detector is typically much less than an area detector. The low cost makes two-dimensional diffraction more affordable to many users.
- **Higher resolution** – There are at least three factors resulting in higher resolution with line scan diffraction. First, a line detector can be built with smaller pixel size, which translates to higher resolution. Second, the line scan step with a typical goniometer can be much smaller than the pixel size in a typical 2D detector. Third, it is possible to add slits along the line direction to control the detection line width.
- **No defocusing effect** – The defocusing effect is observed with the data collected by a 2D detector when a diffraction peak is collected with the low incident angle ($< \theta$) over a flat sample surface. With line scan diffraction, the incident angle θ_1 can change simultaneously with detector scan scanning angle α so as to keep $\theta_1 = \theta_2$ in the diffractometer plane. In this case, the defocusing effect is eliminated with a constant defocusing factor of 1.
- **Reduces air scattering from the diffracted beam** – Air scatter with a 2D detector is a significant contribution to the intensity background due to the open space between the sample and 2D detector. The intensity of the air scatter from the incident beam is proportional to the length of the open incident beam path, which is the distance between the sample and the beam collimation exit. With a line detector, air scatter may be blocked by an air scatter shield as shown in Figure 13.4. The air scatter from the primary beam between the collimator exit and the sample is blocked by the scatter shield. The air scatter from the diffracted X-rays is also blocked by the scatter shield. Only the diffracted X-rays from the sample and in the correct direction can reach the line detector through the narrow channel of the scatter shield.
- **Secondary monochromator on the detector side** – The spectrum impurity of the incident beam and/or radiation fluorescence from the sample are sources of intensity background with a 2D detector, for example when Cu-K_α radiation is used for iron or ferrous alloys. Most two-dimensional detectors have a very limited energy resolution and it is impossible to add a diffracted beam monochromator in front of a 2D detector. However, it is possible to use a specially designed monochromator in front of a line detector. Figure 13.5 is an illustration of a multilayer used as such a monochromator. The lines OE and EG are a diffracted beam

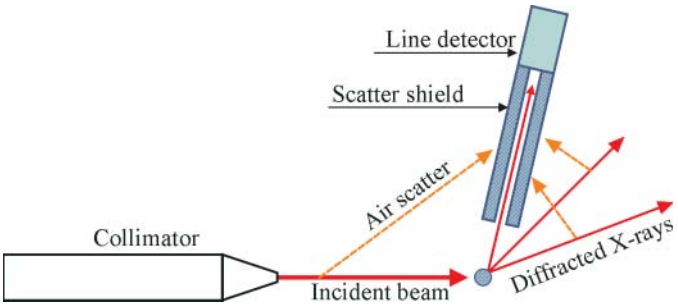


FIGURE 13.4 Air scatter from incident X-ray beam and diffracted X-rays is blocked by a scatter shield for the line detector.

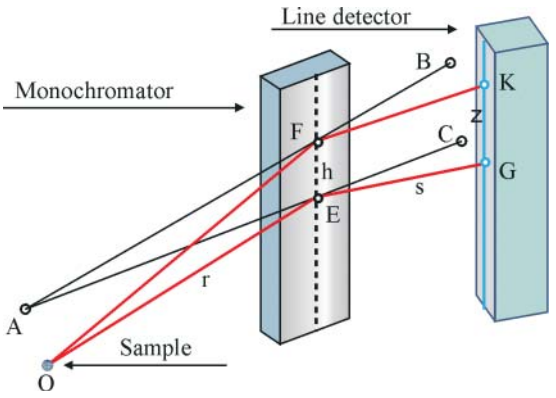


FIGURE 13.5 A multilayer mirror used as a monochromator in front of the scanning line detector.

from the sample to the mirror and from the mirror to the line detector in the diffractometer plane. The line AC is the projection of OE and EG on the mirror surface. The lines OF and FK are a diffracted beam from the sample to the mirror and from the mirror to the line detector above the diffractometer plane. The distance between the sample and the mirror (OE) is r and between the mirror and detector is s. Both r and s are measured within the diffractometer plane. The distance between F and E is h and the distance between K and G is z, corresponding to the touch point of a diffracted beam on the mirror and detector, respectively, and we have that

$$z = \frac{r+s}{r}h \tag{13.4}$$

The angles ∠OEA and ∠GEC are the Bragg angle of the mirror in the diffractometer plane, $\theta_0 = \angle\text{OEA} = \angle\text{GEC}$. The angles ∠OFA and ∠KFB are the Bragg angle of the mirror at the position h above the diffractometer plane, $\theta_h = \angle\text{OFA} = \angle\text{KFB}$. θ_h is given by

$$\sin\theta_h = \frac{r}{\sqrt{r^2+h^2}}\sin\theta_0 \tag{13.5}$$

The corresponding mirror d-spacing distribution is given by

$$d = \frac{\sqrt{r^2+h^2}}{r}d_0 \tag{13.6}$$

where d_0 is the d-spacing of the mirror at the diffractometer plane. A multilayer mirror designed with such a d-spacing distribution can be used as a monochromator in front of the line detector.

- **Imitation of a point detector** – The line detector can also be used alternatively as a conventional point detector. By using a limited detection region and corresponding divergent slits, an antiscatter slit and soller slits, the line detector can function as a point detector for Bragg–Brentano parafocusing geometry and parallel beam geometry.
- **Variable detector distance with a line detector** – Some two-dimensional diffraction systems use a cylinder shaped 2D detector, such as a cylindrical image plate. A cylindrical detector is designed for a fixed radius. Although the trace of a scanning line detector forms a cylinder, the radius of the cylinder can be selected by changing the detector distance D. A user can choose a short distance for large angular coverage or long distance for better angular resolution.

13.3 THREE-DIMENSIONAL DETECTOR

13.3.1 Third Dimension of a Detector

In Chapter 4, we discussed detectors with zero dimensions (point detector), one dimension (line detector), and two dimensions (area detector). This naturally extends to the concept of three-dimensional detectors. However, the three-dimensional detector is not a straightforward extension of the 0D, 1D, and 2D detectors. As described by the ideal (4π) detector, a two-dimensional detection surface provides the maximum number of dimensions needed in real space to capture all the X-rays. An extension into the third dimension in real space – for instance, by stacking a set of identical semi-transparent 2D detectors to improve performance – has been referred to as a three-dimensional detector [5]. Although this kind of detector extends the 2D sensitive area to a 3D sensitive volume, the purpose of detecting X-rays at different layers of a 2D detector is to improve the quality of X-ray detection in a two-dimensional space distribution, but not to add a third dimension. It is feasible and valuable to add the third dimension based on a parameter physically and mathematically orthogonal to the two-dimensional image – for instance, the energy of the incoming photons. Three-dimensional X-ray detectors with energy dispersive resolution have been introduced with encouraging results [6]. A spectral resolution of $\Delta E = 150\,\text{eV}$ has been achieved with a $75\,\mu\text{m} \times 75\,\mu\text{m}$ pixel size and 256×256 frame size. A 3D detector with the energy resolution is also referred to as a color camera for X-rays compared to 2D detectors for monochromatic X-rays. With today's technology, it is still a big technical challenge to build a 3D detector with detection area, spatial resolution, count rate, and readout speed comparable to a 2D detector, and still have an energy resolution comparable to a dedicated energy dispersive point detector. This section will not discuss technologies to produce 3D detectors, but focus on some geometry concepts and potential applications.

13.3.2 Geometry of Three-Dimensional Detector

Figure 13.6 illustrates the geometry and some definitions of three-dimensional detectors based on energy dispersive pixels. The sensor of the 3D detector is a two-dimensional array of pixels, with each pixel acting like an energy dispersive point detector. The values x and y are the coordinates in real space. A pixel is denoted by P(x,y). The third coordinate z represents an imaginary dimension and can be given as a function of wavelength λ (Å) or photon energy E (eV). X-ray photons measured by each energy dispersive pixel can be displayed as counts at each energy interval. The complete three-dimensional dataset can be considered a 3D image. The smallest distinguishable volume element in the 3D image is referred to as a voxel – short for volume pixel – representing a value on a regular grid in three-dimensional space. This is analogous to a pixel, which represents 2D image data. In Figure 13.6, the data measured by the pixel P(x,y) contains a series of voxels, such as V(x,y,z), V′(x,y,z'), and V″(x,y,z''), all having the coordinates (x,y). The series of voxels with the same (x,y) may be referred to as a voxel column. The term voxel has been frequently used in the visualization and analysis of three-dimensional scientific data. The size of voxels in a 3D image can be used to describe the resolution. For example, a 3D X-ray detector may be defined by $512 \times 512 \times 512$ voxels with the voxel size of $100\,\mu\text{m} \times 100\,\mu\text{m} \times 100\,\text{eV}$. In most cases, all voxels are assumed to have the same size and shape. The value of a voxel is the count measured within the pixel area and the energy (or wavelength) range. The position of a voxel is given by the position of its center. The boundaries of a voxel are exactly halfway between the centers of neighboring voxels along the three coordinate directions.

The slice in the 3D image containing voxels of the same z value forms a 2D image equivalent to a 2D frame collected by a 2D detector at that energy level. Therefore, each slice parallel to

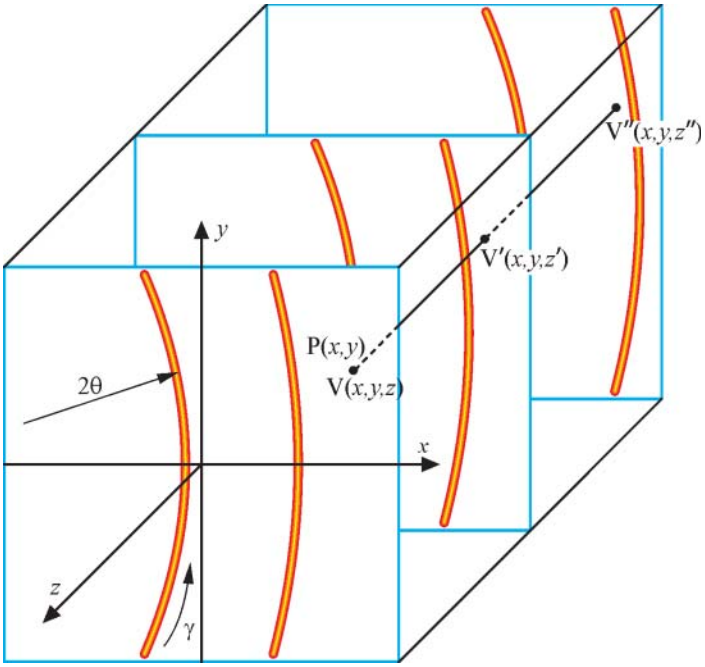


FIGURE 13.6 Geometry of a conceptual three-dimensional detector.

the detector plane can be treated in the same way as a 2D image. In the data analysis of the 3D image, it is necessary to convert the (x,y,z) coordinates into diffraction parameters. Assuming the third dimension is given as the wavelength λ, the diffraction space coordinates $(2\theta,\gamma)$ for a voxel at $V(x,y,z)$ are given by

$$2\theta = \arccos \frac{x \sin\alpha + D\cos\alpha}{\sqrt{D^2 + x^2 + y^2}}, \ (0 < 2\theta < \pi) \tag{13.7}$$

$$\gamma = \frac{x\cos\alpha - D\sin\alpha}{|x\cos\alpha - D\sin\alpha|} \arccos \frac{-y}{\sqrt{y^2 + (x\cos\alpha - D\sin\alpha)^2}}, \ (-\pi < \gamma \leq \pi) \tag{13.8}$$

$$\lambda = z \tag{13.9}$$

where D is the sample-to-detector distance and α is the swing angle. Therefore a voxel $V(x,y,z)$ can be expressed by a voxel $V(2\theta,\gamma,\lambda)$. The unit diffraction vector components $\{h_1, h_2, h_3\}$ in the sample coordinates $\mathbf{S_1S_2S_3}$ corresponding to each pixel can than be calculated by

$$\begin{aligned}
h_1 &= \sin\theta(\sin\phi\sin\psi\sin\omega + \cos\phi\cos\omega) + \cos\theta\cos\gamma\sin\phi\cos\psi \\
&\quad - \cos\theta\sin\gamma(\sin\phi\sin\psi\cos\omega - \cos\phi\sin\omega) \\
h_2 &= -\sin\theta(\cos\phi\sin\psi\sin\omega - \sin\phi\cos\omega) - \cos\theta\cos\gamma\cos\phi\cos\psi \\
&\quad + \cos\theta\sin\gamma(\cos\phi\sin\psi\cos\omega + \sin\phi\sin\omega) \\
h_3 &= \sin\theta\cos\psi\sin\omega - \cos\theta\sin\gamma\cos\psi\cos\omega - \cos\theta\cos\gamma\sin\psi
\end{aligned} \tag{13.10}$$

The diffraction vectors associated with the voxels in the same voxel column have identical unit vectors with respect to the sample coordinates, but different magnitudes given by

$$\left|\frac{\mathbf{s}-\mathbf{s}_0}{\lambda}\right| = \frac{2\sin\theta}{\lambda} = \frac{1}{d} \tag{13.11}$$

where vectors $\mathbf{s_0}/\lambda$ and $\mathbf{s}/\lambda$ represent the incident beam and diffracted beam respectively. The d is the d-spacing of crystal planes satisfying the Bragg condition. It can be easily seen that all voxels in a voxel column represent the same orientation in the sample space, but each voxel represents the diffraction condition for crystallographic planes of different d-spacing.

Many advantages of 2D detectors have been discussed in previous chapters. A 3D X-ray image contains many slices of 2D images at various energy levels. Therefore a 3D detector maintains all the advantages of 2D detectors in addition to others. A 3D detector can collect diffraction patterns from a broad energy spectrum. The entire or a large range of the radiation spectrum from either a laboratory source or a synchrotron source can be used for diffraction analysis. Monochromatization is not necessary for a 3D detector. The characteristic lines from an X-ray tube, such as K_α and K_β, may be used as energy calibration references. Fluorescence from the sample does not have to be avoided. Instead, the absorption edge or fluorescence of the sample materials may either be used as energy calibration references with known materials, or be analyzed as important information of materials. This leads to the possibility that XRD and XRF (X-ray fluorescent) data can be collected by the same 3D detector.

13.3.3 Three-Dimensional Detector and Reciprocal Space

Zero-dimensional, one-dimensional, and two-dimensional detectors are called point, line, and area detectors respectively. As a natural extension, the three-dimensional detector can be called a volume detector. The comparison between the point detector (0D), line detector (1D), area detector (2D), and volume detector (3D) can be given in reciprocal space on an Ewald sphere

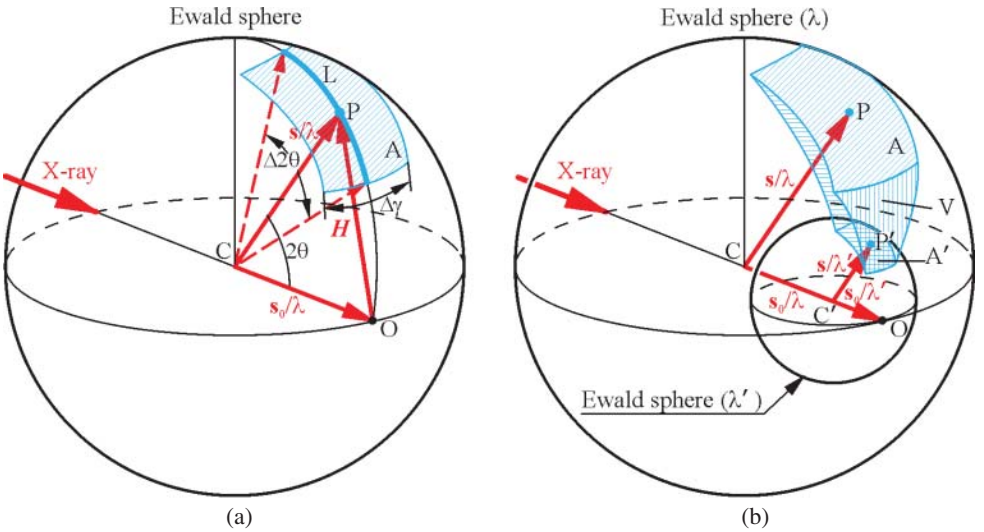


FIGURE 13.7 Comparison of detectors with Ewald sphere: (a) point, line, and area detectors, (b) three-dimensional detector.

in Figure 13.7. Figure 13.7(a) shows the point, line, and area detector. For the point detector in the Ewald sphere, both incident beam vector $\mathbf{s_0}/\lambda$ and diffracted beam vector $\mathbf{s}/\lambda$ start at point C and end at points O and P respectively. The angle between the incident beam and diffracted beam is 2θ. The vector from O to P is the diffraction vector $\boldsymbol{H}$. We can use point P to represent the point detector. For a line detector, the incident beam vector is the same $\mathbf{s_0}/\lambda$, but the ends of the diffracted vectors measured by the line detector, corresponding to a range of $\Delta 2\theta$, are distributed along a curve L on the Ewald sphere. The curve L represents the line detector. For an area detector, the diffracted vector has distributions in a two-dimensional area on the Ewald sphere surface corresponding to $\Delta 2\theta$ and $\Delta\gamma$. The area A represents the area detector. Since a single wavelength is used, the point P, line L, and area A all lie on the same Ewald sphere. Figure 13.7(b) illustrates the three-dimensional detector. The incident beam has a variable wavelength from λ to λ'. For simplicity, only two Ewald spheres corresponding to λ and λ' are shown. For the wavelength λ, the incident beam vector $\mathbf{s_0}/\lambda$ starts at point C and ends at points O. The diffracted beam vector corresponding to a pixel on the area detector $\mathbf{s}/\lambda$ starts at point C and ends at point P. The coverage of the 3D detector at the wavelength level λ is the area A on the Ewald sphere (λ). For the wavelength λ', the incident beam vector $\mathbf{s_0}/\lambda'$ starts at point C$'$ and ends at points O. The diffracted beam vector, corresponding to the same pixel on the 3D detector but with a different wavelength, $\mathbf{s}/\lambda'$ starts at point C$'$ and ends at point P$'$. The coverage of the 3D detector at the wavelength level λ' is the area A$'$ on the Ewald sphere for λ'. Both Ewald spheres meet at the origin of reciprocal space O. Considering all the wavelengths between λ and λ', the coverage of the 3D detector is the volume given between the area A and the area A$'$. The volume V represents the reciprocal space coverage of the 3D detector. By using a 3D detector as described above, it is possible to collect three-dimensional reciprocal space maps with white radiation instead of tuning the X-ray energy [7].

13.4 PIXEL DIRECT DIFFRACTION ANALYSIS

13.4.1 Concept

This section presents a new diffraction data analysis strategy – pixel direct diffraction (PDD) analysis. PDD analysis is based on diffraction vectors associated to each pixel in diffraction frames collected with area detectors. Conventionally, a 2D frame is treated as a continuous distribution of diffraction intensity, and 2D diffraction patterns are integrated to diffraction profiles as intensity distributions vs. 2θ or γ angles. In the PDD concept, the diffraction meaning of each pixel is treated independently and the final diffraction results are generated by a collective consideration of all pixel diffractions. The final crystallographic results are based on the statistical analysis of all pixels. This method results in a more accurate diffraction analysis.

Diffraction data collected with an area detector is typically in the form of two-dimensional images, also referred to as data frames or frames. A frame is treated as a continuous distribution of diffraction intensity. When data frames are used for X-ray powder diffraction analysis, a typical process is first to integrate the data frames to generate a diffraction profile and then the diffraction peak position and diffraction profile shape are analyzed on the integrated profile. For SCD spots, the data frames are typically integrated to produce a set of integrated intensities for all measured diffraction spots [8]. The integrated intensity for each spot can be calculated either from the summation of pixel counts of the pixels covered in the spot region or from a curve fitting to the intensity distribution in the spot region. These data integration processes can dramatically reduce the demand on computer storage size. The integrated data is also suitable for further analysis by the established methods. For example, the diffraction profile is typically used to perform

a "search/match" for phase identification [9]. In stress analysis, the peak shift is determined from the profile. However, data integration can also lose or distort important information in the original two-dimensional frames. For examples, the values of the integrated intensities vs. 2θ or γ angles are dependent on the integration method. The intensity variations due to texture are lost once 2D frames are integrated to diffraction profiles. The distortion of diffraction rings due to stresses will result in broadened diffraction peaks. In PDD analysis, each pixel in an area detector is treated as an independent detector unit, and the event measured by this single pixel is calibrated, corrected, and analyzed independently until the final stage when the final results are generated from the collection of all the independent events. It is expected that the PDD method requires much more computing power, which can be satisfied by fast growing computer technology today and tomorrow. In order to describe the concept of the PDD method, applications in X-ray powder diffraction will be discussed hereafter. The possible applications for SCD will not be explored here.

13.4.2 Pixel Diffraction Vector and Pixel Count

In pixel direct diffraction (PDD) analysis, it is necessary to find the diffraction vector corresponding to each pixel in the diffraction frames. The first step is to calculate diffraction space coordinates $(2\theta,\gamma)$ of each pixel. The calculation is based on the detector space parameters and the pixel position in the detector. Equations (13.7) and (13.8) can be used to calculate the diffraction space coordinates $(2\theta,\gamma)$ of each pixel. Equations (13.10) can be used to calculate the direction of the pixel diffraction vector. Pixel intensity is the total count collected by a pixel. The pixel intensity is determined by the diffraction intensity at the solid angle covered by the detector pixel. Pixel intensity should be normalized by the detector geometry, pixel size, and pixel sensitivity. The normalization can be given by

$$I_{x,y} = G_{x,y} \cdot S_{x,y} I_{x,y}^{measured} \tag{13.12}$$

where $I_{x,y}$ is the normalized intensity for $P(x, y)$, which is the pixel count collected by a pixel if all pixels have the same distance to the instrument center with the same sensitivity, $G_{x,y}$ is the geometry normalization factor, and $S_{x,y}$ is the sensitivity normalization factor for $P(x, y)$. For an ideal detector with a spherical sensitive area, $G_{x,y} = 1$. For a detector with all pixels having the same size and sensitivity, we have $S_{x,y} = 1$, otherwise $S_{x,y}$ should be generated by detector calibration. The $S_{x,y}$ value for a pixel is a constant within the linear range of the pixel counting rate, otherwise it is a function of the counting rate for a non-linear counting curve. For a flat detector, the geometry normalization factor $G_{x,y}$ is given by

$$G_{x,y} = \frac{D^2 + x^2 + y^2}{D^2} \tag{13.13}$$

For a cylinder shaped detector, the geometry normalization factor $G_{x,y}$ is given by

$$G_{x,y} = \frac{D^2 + y^2}{D^2} \tag{13.14}$$

After the normalization, all pixels will give the same count if the detector is exposed to a uniformly radiating point source.

13.4.3 PDD Analysis in Phase-ID, Texture, and Stress

The conventional way of doing phase identification with a two-dimensional diffraction pattern is to integrate the frame to generate a diffraction pattern similar to one collected with scanning point detector or linear detector. The peak positions and intensities are evaluated from the diffraction

pattern and matched to searchable database, such as ICDD PDF files. With the pixel direct diffraction (PDD) method the two-dimensional diffraction frame is directly analyzed without data integration. Since the pixels' γ values are irrelevant for phase identification, all the pixels are evaluated by their 2θ positions (optionally relative intensity) in the search-and-match algorithm. The challenge is to find the statistical merit of significance by fitting all pixels to a known PDF card and to find the best fit. Many current algorithms may be modified for this purpose [9].

The pole-figure process from 2D frames by 2θ-integration was discussed in Chapter 8. With the PDD method for texture analysis, 2θ-integration is not necessary. Instead, each pixel intensity is treated as a pole density and is mapped to the pole-figure by the following equation:

$$\alpha = \sin^{-1}|h_3| = \cos^{-1}\sqrt{h_1^2 + h_2^2} \tag{13.15}$$

$$\beta = \pm\cos^{-1}\frac{h_1}{\sqrt{h_1^2 + h_2^2}} \quad \begin{cases} \beta \geq 0^\circ & if \quad h_2 \geq 0 \\ \beta < 0^\circ & if \quad h_2 < 0 \end{cases} \tag{13.16}$$

where α takes a value between 0° to 90° ($0^\circ \leq \alpha \leq 90^\circ$) and β takes values in two ranges with the above equation ($0^\circ \leq \beta \leq 180^\circ$ when $h_2 \geq 0$ and $-180^\circ \leq \beta < 0^\circ$ when $h_2 < 0$). The unit diffraction vector components $\{h_1, h_2, h_3\}$ are calculated by equations (13.10). The pole-figure is stored and displayed as a bitmap image with pixels. We start with a so-called "non-normalized" pole-figure in which only the relative pole density is considered. The distribution of the pole density data points generated from pixels is not necessarily homogeneous on a pole-figure. Depending on the instrument configuration and data collection strategy, more data points may be available in some regions and less in other regions. In the pole-figure construction from 2D fames by the PDD method, the intensity of each pixel is mapped onto the corresponding pole-figure pixel. Since a pole-figure is only about a particular family of crystal planes, a 2θ window should be applied such that only the pixels within the window are mapped to the pole-figure. Some pole-figure pixels may be filled by pole-density values from several frame pixels so that the final value should be an average after all frames are processed. There may be some regions in the pole-figure without any measured data point. These pole-figure pixels should not be confused with pixels that simply have zero pole-density. One method to make this distinction is to store all the filled pixels with the pole-density value plus one, while the unmapped pixels possess the value 0. A linear interpolation within a defined box is sufficient to fill the unmapped pixels in the pole-figure. The pole-figure generated by the pixel mapping can then be processed by interpolation, normalization, and symmetry operation as described in Chapter 8.

Stress analysis by XRD^2 should be most benefitted by the PDD method. In the 2D method described in Chapter 9, each section of the γ range is integrated into a diffraction profile first and then the corresponding 2θ value is determined by various profile fitting methods. Since the large size frame is reduced to a set of (γ,2θ) values. The total number of linear equations in the least squares calculation is relatively small. This is an advantage only when computing power is very limited. With today's much greater computing power, this advantage gradually diminishes. Furthermore, there are many disadvantages with the integration and fitting method. For instance, different integration and fitting methods may give different 2θ values from the same raw data. This is the major source of inconsistency when the same stress data is evaluated by different fitting algorithms. A "poorly" integrated profile may appear at some γ-integration range due to texture, large screens, shadows, or weak diffraction. The profile at these γ angles may not have enough statistics to determine the peak 2θ position with reasonable accuracy. The 2θ values from those data points carry large error, which has a big impact on the least squares regression results. That means a profile with poor statistics has more weight in the stress calculation. The intensity

weighted least squares method introduced in Chapter 9 may overcome the poor statistics. The PDD direct method would be able to avoid both the discrepancy in profile fitting and the poor statistics without ambiguity.

With the PDD approach, each pixel within the selected region is treated like a peak with angular position $(2\theta,\gamma)$ and intensity. The pixel intensity weighted least squares (PIWLS) is used to fit all the pixel values to the fundamental equations for stress. The summed square of residuals is given by [10]

$$S = \sum_{i=1}^{n} I_i r_i^2 = \sum_{i=1}^{n} I_i (y_i - \hat{y}_i)^2 \tag{13.17}$$

where I_i is the pixel intensity used as weighting factors, n is the number of total pixels in the selected region for all 2D frames, and S is the sum of squares error to be minimized in the least squares regression. The selected region is given by the 2θ range ($2\theta_1$ to $2\theta_2$) and γ range (γ_1 to γ_2) as shown in Figure 9.17. The observed response value is the measured strain corresponding to each pixel.

$$y_i = \ln\left(\frac{\sin\theta_0}{\sin\theta_i}\right) \tag{13.18}$$

and the fitted response value is given by the fundamental equation as

$$\hat{y}_i = p_{11}\sigma_{11} + p_{12}\sigma_{12} + p_{22}\sigma_{22} + p_{13}\sigma_{13} + p_{23}\sigma_{23} + p_{33}\sigma_{33} + p_{ph}\sigma_{ph} \tag{13.19}$$

where stress coefficients are calculated from the goniometer angles (ω,ψ,ϕ), elastic constants, and pixel angular positions $(2\theta_i,\gamma_i)$. For programming convenience, all possible stress components are included in the linear expression, but they may not all appear as non-zero values at the same time. For instance, the pseudo-hydrostatic stress term should be set to zero for the triaxial stress state. The stress components are either set as unknown (x) or set to zero for various stress state as listed in Table 9.6.

With PIWLS for stress analysis, the integration and profile fitting can all be avoided, so that the smearing effect caused by γ-integration can be totally eliminated. All pixels in the selected region are used for stress calculation. The contribution of each pixel is determined by the pixel intensity. Since the importance of each pixel is determined by the pixel intensity, weak diffraction due to texture or poor sampling will have less impact on the stress calculation. As all the pixels in the selected region are to be fitted for the PIWLS regression, stress analysis by the PDD approach takes significantly more computing resources.

There are other advantages of PDD analysis. Since each pixel is treated independently, it is easier to handle the data from a defective detector with bad pixels, multiple detectors, or a mosaic detector with a dead seaming region. It is possible to correct each pixel based on its special characteristics, such as sensitivity or non-linear response curve. Spatial correction on the 2D frame may not be necessary. Instead of generating a new corrected frame with interpolated new pixels, all the original pixels are calibrated and assigned a calibrated pixel position (x,y) or diffraction space parameter $(2\theta,\gamma)$. Instrumental correction and Lorentz-polarization-absorption (LPA) correction can all be done independently and individually to each pixel.

13.5 HIGH RESOLUTION TWO-DIMENSIONAL X-RAY DIFFRACTOMETER

13.5.1 Background

The previous chapters have demonstrated many advantages of the two-dimensional X-ray diffraction system when used for applications such as phase identification, texture, and stress. High

resolution X-ray diffraction (HRXRD) systems are required for applications, such as interface between epitaxial film and substrate, particle size broadening, high resolution RSM, diffuse scattering, and various crystal defects [11–14]. HRXRD requires a primary X-ray beam with extremely narrow spectral width, high parallelism, and high flux density. This can be achieved by using a brilliant X-ray source with fine focus, multilayer mirror, channel cut monochromator, pinholes, and slits [11, 15]. Many optics, such as, monochromator and slits can also be used in the receiving side in front of a 0D detector for improve resolution and reduce background. Similar optics on primary side can also be used for HRXRD with a 2D detector, but no optics can be added in front of a 2D detector. Therefore, the angular resolution of a two-dimensional X-ray diffractometer is mainly determined by the pixel size or point spread function (PSF) of the 2D detector and the detector distance. One suggestion would be to reduce both the incident X-ray beam size and pixel size (assuming 1 pixel PSF) to achieve the high resolution. However, this is only feasible for fine powder or polycrystalline materials with homogenous and randomly oriented crystallites. The effective sampling volume is significantly reduced with a smaller beam size, which results in a poor sampling statistics and also reduced X-ray counts if the incident beam has the same flux density. With the advance of detector technology, the pixel size and PSF can be further reduced along with the improvement of other properties. But there is a limit determined by the nature of the sample microstructure. For most laboratory XRD^2 systems, the incident X-ray beam size is between 50 μm to 1000 μm, therefore a pixel size or PSF in the range of 50 μm to 200 μm is reasonable. Except for some special applications, further reducing the pixel size or PSF below 50 μm is not a good approach for improving the angular resolution.

Practically, with all other conditions the same, a long detector distance with large 2D detector is typically a preferred approach for achieving high resolution. This is the case for most two-dimensional small angle X-ray scattering (SAXS) systems. However, the long detector distance, especially with a large 2D detector, is not practical for a high resolution two-dimensional X-ray diffraction (HRXRD^2) system because of the challenge of moving the detector swing angle with accurate positioning. It also takes a lot of space to achieve such a swing angle in either the horizontal θ-2θ configuration or vertical θ-θ configuration. In addition, a vacuum beam path required to eliminate the air scattering for the long sample-to-detector distance causes extra burden to move the detector. The new configuration proposed in the following section is one solution for achieving high resolution for both small angle X-ray scattering (SAXS) and wide angle X-ray diffraction (WAXD).

13.5.2 HRXRD^2 in Reciprocal Space

The fundamentals and instrumentation of HRXRD^2 can be visualized by an illustration containing reciprocal space and real space elements as shown in Figure 13.8. In real space, the sample is mounted at C and the detector is located at detector distance D from the sample and swing angle α from the incident X-ray beam. The Ewald sphere (A) is centered at C. The image of 2D detector is projected onto the surface of the Ewald sphere, as given by the green region. The size of the green region is determined by the 2D detector size and the detector distance. For a given detector pixel size, a better resolution can be achieved with longer detector distance. For an arbitrary pixel P(x,y) on a 2D detector, we can have a point P projected on the Ewald sphere. Both incident beam vector $\mathbf{s_0}/\lambda$ and diffracted beam vector $\mathbf{s}/\lambda$ start at point C and end at points O and P respectively. The angle between the incident beam and diffracted beam is 2θ. The vector from O to P is the diffraction vector $\boldsymbol{H}$. The reciprocal lattice, determined by the crystal (sample) structure and orientation, has an origin at O. Except for the origin (000), each lattice point is denoted by a set of three integers (hkl), which are the number of translations of the three reciprocal lattice axes respectively to reach the lattice point. For a perfect crystal, each reciprocal lattice point has zero

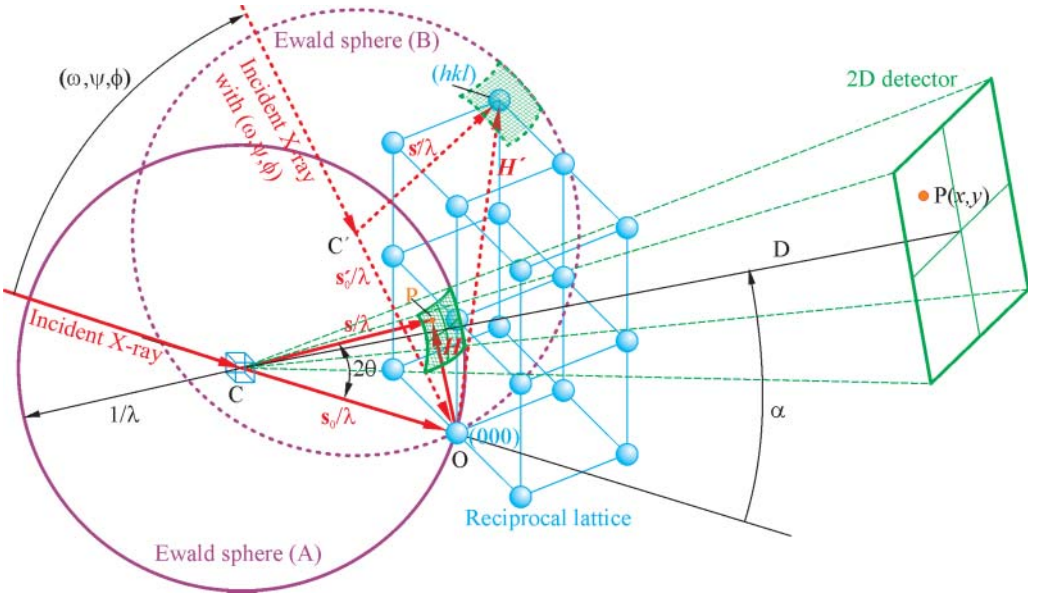


FIGURE 13.8 High resolution XRD[2] in reciprocal space and the Ewald sphere.

dimensions, or more precisely, a three-dimensional delta function. We use a reciprocal lattice from a single crystal to explain the geometry relation. The actual reciprocal space distribution is determined by the sample, such as random powder, textured polycrystalline, thin film, or single crystal.

When the detector swing angle is set to zero, or a small value so that the trajectory of incident beam hits the detector, the projected image on the Ewald sphere will cover and cross through the origin of the reciprocal lattice. This is the condition for small angle X-ray scattering (SAXS). Unlike for other reciprocal lattice points, the reciprocal lattice point at the origin (000) is always on the surface of the Ewald sphere regardless of the sample orientation. However, the sample orientation determines the cross-section surface on (000) point, as illustrated by the Ewald sphere (A) and (B). To cover any other reciprocal lattice point, the detector swing angle has to be set to the right angular range and the sample rotates to a given orientation. The sample rotation can be achieved either by rotating the sample or by rotating the incident beam relative to the sample. For instance, the reciprocal lattice point (*hkl*) is not on the surface of Ewald sphere (A) so cannot be detected by the 2D detector. In order to measure the lattice point (*hkl*) and its vicinity, the incident X-ray beam has to be changed by the sample rotations by a combination of (ω,ψ,ϕ). The center of Ewald sphere (B) is on C′. The diffraction vector $\boldsymbol{H}'$ now points to the reciprocal lattice point (*hkl*). The detector swing angle should also be set to a value based on an angle between the incident beam vector $\mathbf{s}'_0/\lambda$ and diffracted beam vector $\mathbf{s}'/\lambda$.

Assuming the instrument broadening is only from a parallel beam, the 2θ resolution associated to an arbitrary pixel in a 2D detector is given as

$$\Delta 2\theta = \frac{D\sqrt{\Delta x^2 + b^2}}{D^2 + x^2 + y^2} \tag{13.20}$$

where D is sample-to-detector distance, b is the beam size in diameter, x and y are the location of the pixel in the detector, and Δx is the pixel size assuming a square pixel (or FWHM of PSF if

it is more than the pixel size). The resolution within the Ewald sphere surface corresponding to a pixel can be given in Q space as

$$\Delta q = \frac{2\pi}{\lambda} \cdot \frac{D\sqrt{\Delta x^2 + b^2}}{D^2 + x^2 + y^2} \tag{13.21}$$

Δq is the best resolution within the Ewald sphere surface covered by a 2D detector. The equation shows that increasing detector distance is the only way to improve the resolution for a given detector (Δx) and incident X-ray beam (λ and b). For instance, a system with $\Delta x = 75\,\mu m$, $b = 50\,\mu m$, and $\lambda = 0.154059\,nm$, the best resolution for detector center ($x = y = 0$) is $\Delta q = 0.0184\,nm^{-1}$ at detector distance $D = 200\,mm$, but $\Delta q = 0.0061\,nm^{-1}$ at detector distance $D = 600\,mm$.

13.5.3 New Configuration for HRXRD[2]

In order to overcome the challenge and space requirements of achieving long detector distance with a typical two-dimensional X-ray diffractometer in the horizontal θ-2θ configuration and the vertical θ-θ configuration, an innovative configuration, referred as 2θ-β configuration, is introduced in this section. The innovative high resolution two-dimensional X-ray diffractometer is suitable for both WAXD and SAXS.

Figure 13.9 shows the configuration of a horizontal diffractometer with the 2θ-β configuration. As observed by the operator, the goniometer is mounted in the left side of the X-ray tube and primary optics, so the system is categorized as a left-hand system. The diffractometer plane is given by the primary X-ray beam ($\mathbf{X_L}$ axis) and $\mathbf{Y_L}$ axis. The diffractometer plane is in the horizontal position, so it is also referred to as a horizontal diffractometer. In this configuration, the detector is fixed on the instrument base through a long detector track. Due to its fixed position, the detector can be mounted at a long distance from the instrument center, therefore it can achieve high angular resolution. The swing angle is achieved by α rotation above the $\mathbf{Z_L}$ axis. The primary X-ray beam and optics ($\mathbf{X_L}$ axis) are mounted on a track fixed to the main axis (α) of the goniometer. When α is zero, the primary X-ray beam points to the center of the detector. The β is a left-hand rotation about the $\mathbf{Z_L}$ axis. When β is at zero, the sample surface plane is perpendicular to the detector plane. The α and β are the two main axes of the goniometer and driven by motors independently. The ω angle is defined as a right-handed rotation about $\mathbf{Z_L}$ axis. But in 2θ-β configuration, the ω axis is not an independent axis and is not driven by any motor directly. Because the $\mathbf{X_L}$ axis rotates with the primary beam and optics, ω becomes a function of α and β:

$$\omega = \alpha - \beta \tag{13.22}$$

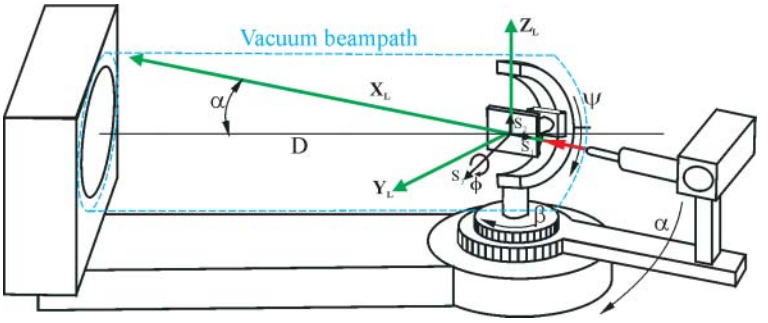


FIGURE 13.9 Two-dimensional X-ray diffractometer with left-hand goniometer in horizontal 2θ-β configuration.

The ψ and ϕ are defined in the same way as in the horizontal θ-2θ configuration in Chapter 2. For the convenience of the operator, the 2θ-β configuration may be operated as a virtual θ-2θ configuration. The ω angle is updated and displayed as a calculated value from β and α values, but changed by driving the β axis. In this case, the β angle can be hidden as long as the ω is updated and displayed accordingly. With the conversion from β to ω, the geometry convention of the new configuration is consistent with the standard XRD^2 system in the θ-2θ configuration. Similarly, the diffraction condition of the 2θ-β configuration equivalent to the θ-θ configuration can also be given by

$$\theta_1 = \alpha - \beta \tag{13.23}$$

$$\theta_2 = \beta \tag{13.24}$$

Based on the above relationship, all the data collection strategies designed for both the θ-2θ and θ-θ configurations can be implemented by the 2θ-β configuration with equivalent diffraction condition. Therefore most algorithms derived for the standard XRD^2 system are still valid.

When α is zero, the primary X-ray beam points to the center of the detector. This is a configuration analogous to a typical SAXS system. With the coverage of various α angles, the system can collect WAXD data at high resolution. Due to the long detector distance, it is also necessary to have the complete or at least the secondary beam path (between sample and detector) evacuated to eliminate air scatter.

Figure 13.10(a) is a top view of the high resolution two-dimensional X-ray diffractometer in horizontal 2θ-β configuration. A 2D detector with substantial detection area is mounted on the extreme left of the diffractometer with a long distance (D) to the instrument center (sample). The secondary beam path between the detector and sample is evacuated to eliminate air scatter. The primary X-ray beam and optics ($\mathbf{X_L}$ axis) is mounted on a track fixed to the main axis (α) of the goniometer. The swing angle is achieved by α rotation. The sample is mounted inside the sample chamber at the center of the instrument. The goniometer and the sample stage are not shown in the figure, but can be any sample stage, such as a Eulerian cradle and XYZ stage. The sample is mounted in reflection mode. The sample surface is rotated by a left-hand rotation β, which determines that the angle between the sample surface and incident beam is ω.

Figure 13.10(b) is a top view of the high resolution two-dimensional X-ray diffractometer in horizontal 2θ-β configuration with incident X-ray beam at on-axis position. The primary X-ray beam and optics ($\mathbf{X_L}$ axis) is moved to the on-axis position ($\alpha = 0$). The sample is mounted in transmission mode for SAXS and can also be mounted in reflection mode for grazing incidence small angle scattering (GISAXS). Since the transmitted direct X-ray beam points to the detector, a beamstop is used to prevent it from hitting the detector. Figure 10.13(c) is a side view of the high resolution two-dimensional X-ray diffractometer in vertical 2θ-β configuration. The primary X-ray beam and optics ($\mathbf{X_L}$ axis) are mounted on a track fixed to the main axis (α) of the goniometer. The swing angle is achieved by α rotation. The sample is mounted in reflection mode and can also be in transmission mode. The vertical configuration allows the sample to be mounted with surface normal point up or with a small tilt angle.

In Figure 13.10, the sample chamber and secondary beam path are evacuated to eliminate air scatter. The X-ray source and optics are outside the sample chamber, so the incident X-ray beam can reach the sample through an X-ray transparent window, such as a beryllium foil or Kapton film. Figure 13.11(a) illustrates such a mechanism. The sample chamber has a slot following the possible incident beam direction at all α angles. The slot is sealed with the X-ray transparent window to allow the incident beam to reach the sample. The window is made of materials with low X-ray absorption so the X-ray beam can penetrate the window with minimal attenuation.

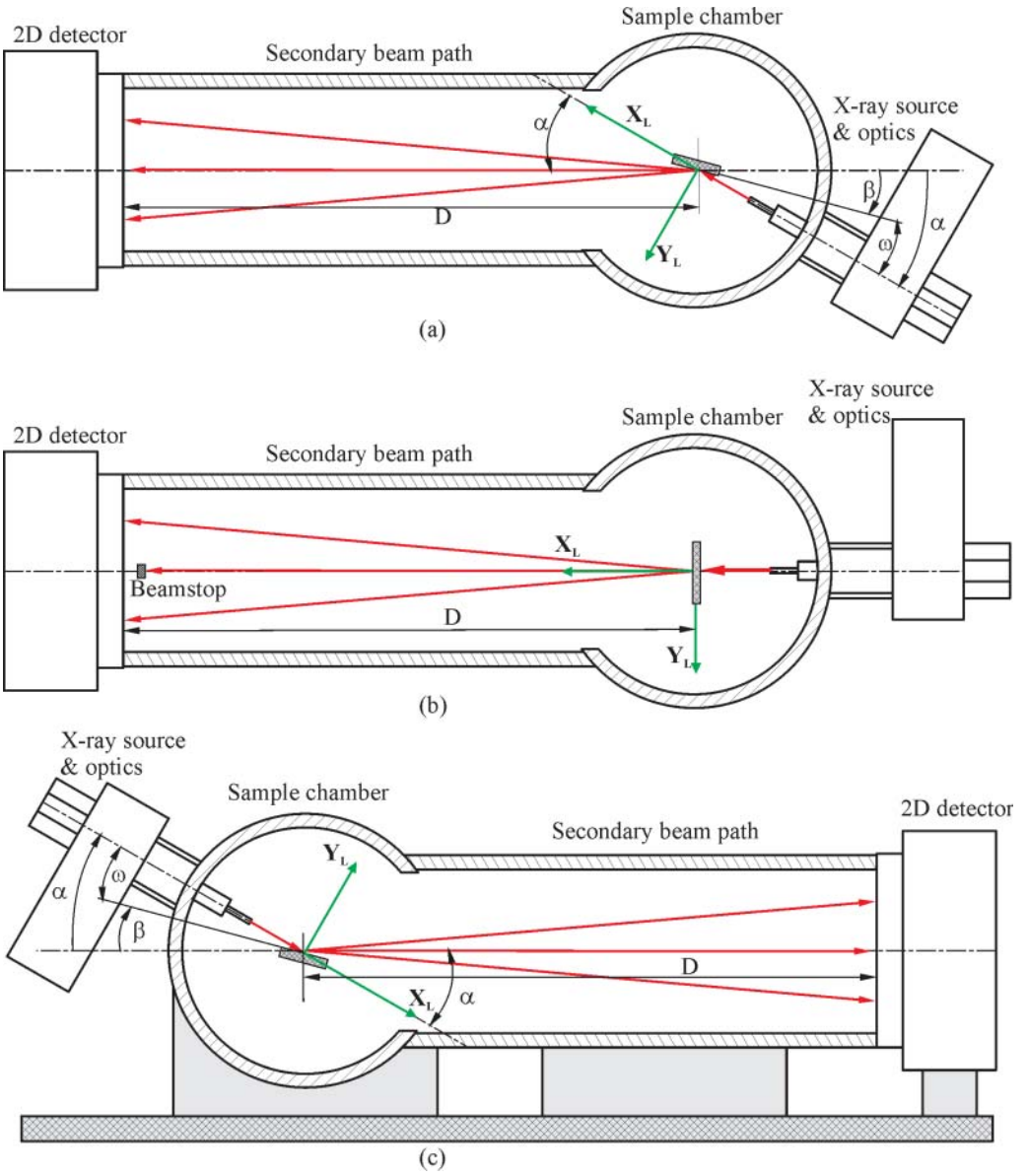


FIGURE 13.10 High resolution two-dimensional X-ray diffractometer in (a) horizontal 2θ-β configuration at off-axis position (top view), (b) horizontal 2θ-β configuration at on-axis position (top view), (c) vertical 2θ-β configuration (side view).

Since there is no air scatter inside the chamber, and the scatter from the window is minimal, there is no further collimation inside the chamber.

Figure 13.11(b) shows another alternative solution where part of the X-ray collimation is kept inside the sample chamber. This will improve the collimation and eliminate the scattered X-rays from the window material. The inside collimator may be coupled to the outside optics by mechanical connection. As shown in the figure, the inside collimator and outside optics are connected to the same rotation axis α. Apparently, there are many ways to keep the inside

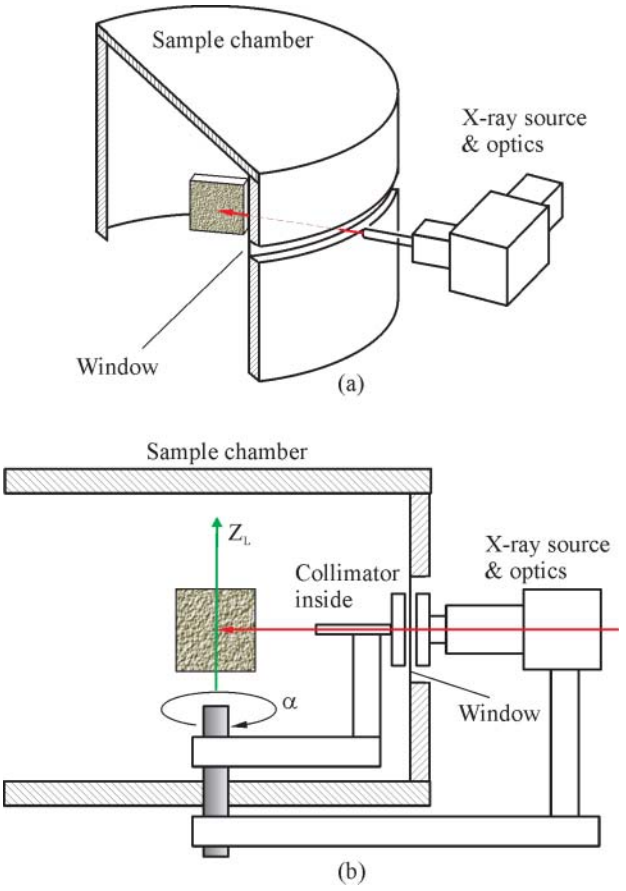


FIGURE 13.11 (a) X-ray transparent window for the incident X-ray beam, (b) coupling of the collimator inside the sample chamber and X-ray optics outside of the chamber.

collimator synchronized with the outside X-ray source and optics. For example, the inside collimator can be driven by a separate mechanism, the synchronization being achieved by computer control. In another example, the inside collimator is mounted on a rotation axis without rotation restriction, while the specific angular position is fixed by a magnetic coupling to the outside optics. The window is thin enough to have the magnetic field pass through.

The beamstop is needed when the direct X-ray beam points to the active area of the 2D detector. When the direct X-ray beam is off the detector active area, the beamstop is not only unnecessary, but may also block some of the diffraction pattern. Figure 13.12 gives some examples of the possible solutions, in which: (a) is a beamstop mounted at the center of the detector, (b) is a strip beamstop extended horizontally to cover all the area possible to be exposed to the direct X-ray beam, and (c) is a beamstop mounted on a motorized track so the beamstop can follow the direction of the direct X-ray beam and move out of the active area for WAXD applications. The beamstop (a) can only block the direct beam at on-axis position. The swing angle α has to be set either at zero or above a certain value to prevent the direct beam from striking the detection area not blocked by the beamstop. The beamstop (b) works for all swing angles, but scattered/diffracted X-rays are blocked so as to leave a blank strip on the 2D diffraction patterns. The beamstop (c) works best for all conditions. It can be seen that there are many possible solutions following the same principle.

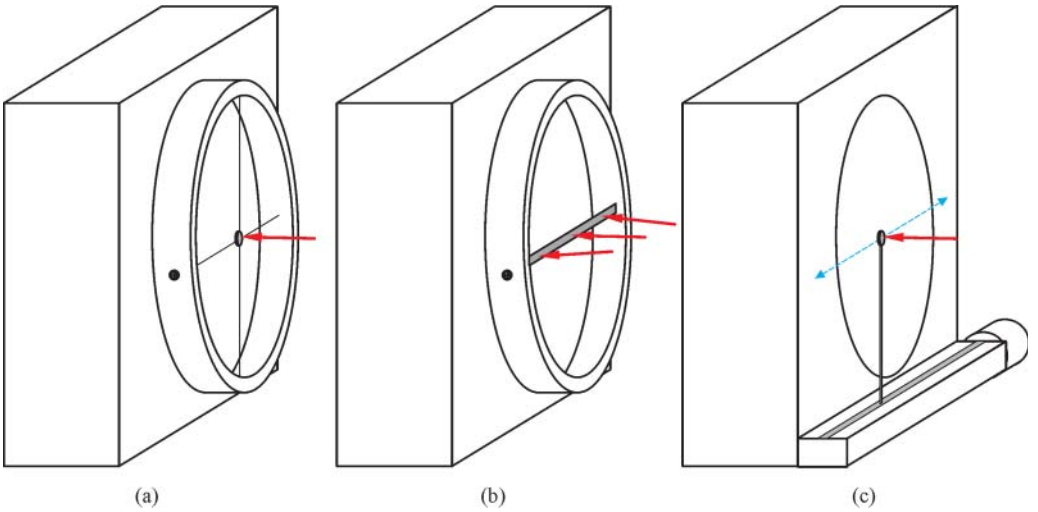


FIGURE 13.12 Various designs for the beamstop: (a) fixed to the center, (b) strip beamstop, (c) motorized beamstop.

REFERENCES

1. P. R. Rudolf and B. G. Landes, Two-dimensional X-ray diffraction and scattering of microcrystalline and polymeric materials, *Spectroscopy*, **9**(6), 22–33, 1994.
2. S. N. Sulyanov, A. N. Popov, and D. M. Kheiker, Using a two-dimensional detector for X-ray powder diffractometry, *J. Appl. Cryst.* (1994) **27**, 934–942.
3. B. B. He, "Introduction to two-dimensional X-ray diffraction", *Powder Diffraction*, 2003, **18** (2) 71–85.
4. B. B. He, Scanning line detector for two-dimensional X-ray diffractometer, US Patent No. 7,190,762, Mar. 13, 2007.
5. U. L. Olsen, S. Schmidt, and H. F. Poulsen, A high-spatial-resolution three-dimensional detector array for 30–200 keV X-rays based on structured scintillators, *J. Synchrotron Rad.* (2008). **15**, 363–370.
6. W. Leitenberger et al., Application of a pnCCD in X-ray diffraction: a three-dimensional X-ray detector, *J. Synchrotron Rad.* (2008). **15**, 449–457.
7. T. W. Cornelius, et al., Three-dimensional diffraction mapping by tuning the X-ray energy, *J. Synchrotron Rad.* (2011). **18**, 413–417.
8. D. E. McRee, *Practical Protein Crystallography*, Academic Press, San Diego, 1993, pp. 84–86.
9. R. Jenkins and R. L. Snyder, *Introduction to X-ray Powder Diffractometry*, John Wiley & Sons, New York, 1996.
10. E. Prince and P.T. Boggs, Least squares, *International Table for X-ray Crystallography*, Vol. C., edited by A. J. C. Wilson, Kluwer Academic Publishers, 594–604, (1992).
11. M. Birkholz, Thin Film Analysis by X-ray Scattering, Wiley-VCH, Weinheim, 2006, 297–341.
12. B. E. Warren. *X-ray Diffraction*, Dover Publications, Inc., New York, 1990.
13. K. Inaba et al., High resolution X-ray diffraction analyses of (La,Sr)MnO3/ZnO/Sapphire(0001) double heteroepitaxial films, *Advances in Materials Physics and Chemistry*, 2013, **3**, 72–89.
14. R. Blondé, et al., High-resolution X-ray diffraction investigation on the evolution of the substructure of individual austenite grains in TRIP steels during tensile deformation, *J. Appl. Cryst.* (2014). **47**, 965–973.
15. M. Jergel, et al., Extreme X-ray beam compression for a high resolution table-top grazing-incidence small-angle X-ray scattering setup, *J. Appl. Cryst.* (2013). **46**, 1544–1550.

APPENDIX A

VALUES OF COMMONLY USED PARAMETERS

The following table lists the most commonly used values of various parameters for X-ray diffraction. The values of the three emission lines are converted from the values of photon energy in Table 1-2 of *X-ray Data Booklet*, *3rd Edition* (A. C. Thompson, et al., Lawrence Berkeley National Laboratory, September, 2009). The relation between wavelength λ in Å and photon energy E in eV is given by $\lambda = 12398.4/E$. The rest of the values are taken from *Elements of X-Ray Diffraction*, *2nd Edition* (B. D. Cullity, Addison-Wesley, Reading, MA, 1978). The author believes the accuracy of the values is sufficient for most applications although the actual accuracy may be less than the number of significant figures. More values and their original sources can be found in the *International Table for X-ray Crystallography*, Vol. C. (edited by A. J. C. Wilson, Kluwer Academic Publishers, 1992).

Two-Dimensional X-Ray Diffraction, Second Edition. Bob Baoping He.
© 2018 John Wiley & Sons, Inc. Published 2018 by John Wiley & Sons, Inc.

Element		Atomic	Density	Mass absorption coefficient μ/ρ (cm^2/g)				Emission lines and absorption edge (Å)			
Z		weight	(g/cm^3)	Mo-K_α	Cu-K_α	Co-K_α	Cr-K_α	$K_{\alpha1}$	$K_{\alpha2}$	$K\beta$	K_{edge}
1	H	1.008	8.375×10^{-5}	0.3727	0.3912	0.3966	0.4116				
2	He	4.002	1.664×10^{-4}	0.2019	0.2835	0.3288	0.4648				
3	Li	6.941	0.533	0.1968	0.4770	0.6590	1.243	228			226.5
4	Be	9.012	1.85	0.2451	1.007	1.522	3.183	114			111
5	B	10.811	2.47	0.3451	2.142	3.357	7.232	67.6			
6	C	12.011	2.27	0.5348	4.219	6.683	14.46	44.8			43.68
7	N	14.007	1.165×10^{-3}	0.7898	7.142	11.33	24.42	31.6			30.99
8	O	15.999	1.332×10^{-3}	1.147	11.03	17.44	37.19	23.62			23.32
9	F	18.998	1.696×10^{-3}	1.584	15.95	25.12	53.14	18.32			
10	Ne	20.180	8.387×10^{-4}	2.209	22.13	34.69	72.71	14.610	14.610	14.452	14.3018
11	Na	22.990	0.966	2.939	30.30	47.34	98.48	11.9103	11.9103	11.575	11.569
12	Mg	24.305	1.74	3.979	40.88	63.54	130.8	9.8902	9.8902	9.521	9.5122
13	Al	26.982	2.70	5.043	50.23	77.54	158.0	8.3395	8.3420	7.961	7.94813
14	Si	28.086	2.33	6.533	65.32	100.4	202.7	7.12560	7.12806	6.75316	6.738
15	P	30.974	1.82	7.870	77.28	118.0	235.5	6.1570	6.1601	5.7961	5.784
16	S	32.066	2.09	9.625	92.53	141.2	281.9	5.37230	5.37509	5.03174	5.0185
17	Cl	35.452	3.214×10^{-3}	11.64	109.2	164.7	321.5	4.7279	4.7308	4.4035	4.3971
18	Ar	39.948	1.663×10^{-3}	12.62	119.5	180.9	355.5	4.1919	4.1948	3.8860	3.87090
19	K	39.098	0.862	16.20	148.4	222.0	426.8	3.7414	3.7445	3.4540	3.4365
20	Ca	40.078	1.53	19.00	171.4	257.4	499.6	3.35847	3.36174	3.08979	3.0703
21	Sc	44.956	2.99	21.04	186.0	275.5	520.9	3.03095	3.03429	2.77960	2.762
22	Ti	47.88	4.51	23.25	202.4	300.5	571.4	2.74858	2.75223	2.51397	2.49734
23	V	50.942	6.09	25.24	222.6	332.7	75.06	2.50361	2.50744	2.28446	2.2691
24	Cr	51.996	7.19	29.25	252.3	375.0	85.71	2.28975	2.29365	2.08492	2.07020
25	Mn	54.938	7.47	31.86	272.5	405.1	96.08	2.10187	2.10583	1.91025	1.89643

26	Fe	55.847	7.87	37.74	304.4	56.25	113.1	1.93631	1.94002	1.75665	1.74346
27	Co	58.933	8.8	41.02	338.6	62.86	124.6	1.78900	1.79289	1.62083	1.60815
28	Ni	58.69	8.91	47.24	48.83	73.75	145.7	1.65795	1.66179	1.50017	1.48807
29	Cu	63.546	8.93	49.34	51.54	78.11	155.2	1.54059	1.54441	1.39225	1.38059
30	Zn	65.39	7.13	55.46	59.51	88.71	171.7	1.43519	1.43903	1.29528	1.2834
31	Ga	69.723	5.91	56.90	62.13	94.15	186.9	1.34012	1.34403	1.20793	1.1958
32	Ge	72.61	5.32	60.47	67.92	102.0	199.9	1.25408	1.25804	1.12896	1.11658
33	As	74.922	5.78	65.97	75.65	114.0	224.0	1.17590	1.17990	1.05732	1.0450
34	Se	78.96	4.81	68.82	82.89	125.1	246.1	1.10479	1.10884	0.99220	0.97974
35	Br	79.904	3.12	74.68	90.29	135.8	266.2	1.03977	1.04385	0.93281	0.9204
36	Kr	83.80	3.488×10^{-3}	79.10	97.02	145.7	284.6	0.98019	0.98416	0.87857	0.86552
37	Rb	85.468	1.59	83.00	106.3	159.6	311.7	0.92558	0.92971	0.82870	0.81554
38	Sr	87.62	2.68	88.04	115.3	173.5	339.3	0.87528	0.87945	0.78294	0.76973
39	Y	88.906	4.48	97.56	127.1	190.2	368.9	0.82886	0.83306	0.74074	0.72766
40	Zr	91.224	6.51	16.10	136.8	204.9	398.6	0.78595	0.79017	0.70175	0.68883
41	Nb	92.906	8.58	16.96	148.8	222.9	431.9	0.74621	0.75046	0.66578	0.65298
42	Mo	95.94	10.22	18.44	158.3	236.6	457.4	0.70932	0.71361	0.63230	0.61978
43	Tc	98.906	11.50	19.78	167.7	250.8	485.5	0.67503	0.67933	0.60131	0.58906
44	Ru	101.07	12.36	21.33	180.8	269.4	517.9	0.64310	0.64742	0.57249	0.56051
45	Rh	102.906	12.42	23.05	194.1	289.0	555.2	0.61329	0.61764	0.54562	0.53395
46	Pd	106.42	12.00	24.42	205.0	304.3	580.9	0.58546	0.58984	0.52053	0.5092
47	Ag	107.868	10.50	26.38	218.1	323.5	617.4	0.55942	0.56381	0.49708	0.48589
48	Cd	112.411	8.68	27.73	229.3	341.8	658.8	0.53502	0.53943	0.47512	0.46407
49	In	114.82	7.29	29.13	242.1	362.7	705.8	0.51213	0.51656	0.45456	0.44371
50	Sn	118.710	7.29	31.18	253.3	374.1	708.8	0.49061	0.49506	0.43525	0.42467
51	Sb	121.75	6.69	33.01	266.5	391.3	733.4	0.47037	0.47484	0.41710	0.40668
52	Te	127.60	6.25	33.92	273.4	404.4	768.9	0.45131	0.45580	0.40000	0.38974
53	I	126.904	4.95	36.33	291.7	434.0	835.2	0.43333	0.43784	0.38391	0.37381
54	Xe	131.29	5.495×10^{-3}	38.31	309.8	459.0	755.4	0.41635	0.42088	0.36874	0.3584
55	Cs	132.905	1.91	40.44	325.4	483.8	802.7	0.40030	0.40484	0.35437	0.34451

(continued)

Element		Atomic	Density	Mass absorption coefficient μ/ρ (cm^2/g)				Emission lines and absorption edge (Å)			
Z		weight	(g/cm^3)	Mo-K_α	Cu-K_α	Co-K_α	Cr-K_α	$K_{\alpha1}$	$K_{\alpha2}$	$K\beta$	K_{edge}
56	Ba	137.327	3.59	42.37	336.1	499.0	587.3	0.38512	0.38968	0.34082	0.33104
57	La	138.906	6.17	45.34	353.5	519.0	222.9	0.37075	0.37532	0.32799	0.31844
58	Ce	140.115	6.77	48.56	378.8	559.1	240.4	0.35710	0.36169	0.31582	0.30648
59	Pr	140.908	6.78	50.78	402.2	596.2	260.5	0.34415	0.34876	0.30427	0.29518
60	Nd	144.24	7.00	53.28	417.9	531.7	271.3	0.33185	0.33648	0.29331	0.28453
61	Pm	(147)		55.52	441.1	401.4	284.7	0.32017	0.32481	0.28290	0.27431
62	Sm	150.36	7.54	57.96	453.5	411.8	295.0	0.30905	0.31371	0.27301	0.26464
63	Eu	151.965	5.25	61.18	417.9	165.2	312.7	0.29845	0.30313	0.26358	0.25553
64	Gd	157.25	7.87	62.79	426.7	169.5	318.9	0.28836	0.29304	0.25460	0.24681
65	Tb	158.925	8.27	66.77	321.9	178.7	338.9	0.27873	0.28343	0.24609	0.23841
66	Dy	162.50	8.53	68.89	336.6	184.9	351.7	0.26954	0.27425	0.23789	0.23048
67	Ho	164.930	8.80	72.14	128.4	189.8	363.3	0.26076	0.26549	0.23012	0.22291
68	Er	167.26	9.04	75.61	134.3	198.4	379.7	0.25237	0.25712	0.22267	0.21567
69	Tm	168.934	9.33	78.98	140.2	207.4	397.0	0.24434	0.24910	0.21556	0.20880
70	Yb	173.04	6.97	80.23	144.7	214.0	409.6	0.23666	0.24143	0.20883	0.20224
71	Lu	174.967	9.84	84.18	152.0	224.6	429.5	0.22930	0.23409	0.20231	0.19585
72	Hf	178.49	13.28	86.33	157.7	232.9	445.0	0.22223	0.22703	0.19607	0.18982
73	Ta	180.948	16.67	89.51	161.5	238.3	454.7	0.21550	0.22031	0.19009	0.18394
74	W	183.85	19.25	95.76	170.5	249.7	470.4	0.20901	0.21383	0.18438	0.17837
75	Re	186.207	21.02	98.74	178.3	261.8	495.5	0.20279	0.20762	0.17888	0.17302
76	Os	190.2	22.58	100.2	183.8	270.3	512.4	0.19680	0.20164	0.17362	0.16787
77	Ir	192.22	22.55	103.4	192.2	283.4	539.6	0.19105	0.19591	0.16855	0.16292
78	Pt	195.08	21.44	108.6	198.2	295.2	571.6	0.18552	0.19042	0.16368	0.15818
79	Au	196.967	19.28	111.3	207.8	303.3	568.0	0.18020	0.18508	0.15899	0.153593
80	Hg	200.59	13.55	114.7	216.2	317.0	597.9	0.17507	0.17996	0.15449	0.14918

81	Tl	204.383	11.87	119.4	222.2	326.3	616.9	0.17014	0.17504	0.15015	0.14495
82	Pb	207.2	11.34	122.8	232.1	340.8	644.5	0.16538	0.17030	0.14597	0.140880
83	Bi	208.980	9.80	125.9	242.9	355.3	667.2	0.16079	0.16572	0.14195	0.13694
84	Po	(209)	9.32					0.15637	0.16131	0.13807	
85	At	(210)						0.15209	0.15704	0.13433	
86	Rn	(222)	4.40	117.2	263.7	387.1	731.4	0.14799	0.15293	0.13069	
87	Fr	(223)						0.14400	0.14897	0.12720	
88	Ra	226.026	5					0.14014	0.14513	0.12382	
89	Ac	(227)						0.13642	0.14142	0.12055	
90	Th	232.038	11.72	99.46	306.8	449.0	844.1	0.13282	0.13783	0.11740	0.11307
91	Pa	231.036	15.37					0.12933	0.13435	0.11435	
92	U	238.028	19.05	96.68	305.7	446.3	774.0	0.12595	0.13097	0.11140	0.10723
93	Np	237.048	20.25								
94	Pu	(242)	19.81	48.84	352.9	519.6	803.2				

APPENDIX B

SYMBOLS

Most symbols used in this book are frequently referred to in the literature and commonly accepted in the X-ray diffraction field. Some symbols are defined specifically for two-dimensional X-ray diffraction. The author has attempted to keep the symbols consistent, but cannot avoid a symbol having to be assigned to several physical meanings in different parts of the book, or different symbols being used to describe virtually the same parameter. In order to avoid possible confusion being caused by the variety of different definitions of symbols, the definitions of some symbols are listed here.

α	Detector swing angle to define the angle between detector center to the laboratory axis X_L, alternatively $2\theta_D$
	Maximum angle of convergence
	Takeoff angle – the angle between exit beam and anode surface in the X-ray tube
	Radial angle defining the pole direction of a reflecting plane relative to a sample plane
	Capture angle of an X-ray optic device
	Miscut angle of single crystal wafer
α, β, γ	Lattice parameters of a unit cell: the angles between the three unit cell vectors
α_H	Angle between diffraction vector and sample surface
α_I	Exit angle – angle between diffracted X-ray beam and sample surface
α_F	Incident angle – angle between incident X-ray beam and sample surface
α_{max}	Maximum angular resolution of a SAXS system
β	Azimuthal angle between the pole direction and a reference direction
	Maximum divergency angle of the X-ray collimation
	Convergence angle of the X-ray beam from an X-ray optic device
β_1	Incident beam divergence within the diffractometer plane
β_2	Incident beam divergence perpendicular to the diffractometer plane

Two-Dimensional X-Ray Diffraction, Second Edition. Bob Baoping He.
© 2018 John Wiley & Sons, Inc. Published 2018 by John Wiley & Sons, Inc.

γ	Azimuthal angle about X_L defining the direction of the diffracted beams on the diffraction cone
γ_1	Lower γ boundary of (2θ- or γ-) integration range
γ_2	Higher γ boundary of (2θ- or γ-) integration range
$\Delta\gamma$	γ-integration range
δ	Gap between knife-edge and sample surface
ε_{ij}	Strain tensor with six components: ε_{11}, ε_{12}, ε_{22}, ε_{13}, ε_{23}, ε_{33}
ε_n	Strain in plane normal direction
$\varepsilon_{\phi\psi}$	Measured strain in the orientation given by ϕ and ψ angles
θ	Bragg angle – angle between incident X-ray beam (or reflected beam) and the reflecting crystal plane; commonly denoted as 2θ and also referred to as scattering angle
$2\theta_0$	Unstressed Bragg angle, normally used for stress measurement to represent 2θ value without stress
θ_1	Incident angle in a θ-θ diffractometer
θ_2	Diffracted angle in a θ-θ diffractometer
$2\theta_1$	Lower 2θ boundary of (2θ- or γ-) integration range
$2\theta_2$	Higher 2θ boundary of (2θ- or γ-) integration range
$2\theta_D$	Detector swing angle to define the angle between the detector center to the laboratory axis X_L, alternatively α
$2\theta_M$	Bragg angle of the monochromator crystal
Θ	Capture solid angle of an X-ray optic device, such as a mirror
λ	X-ray wavelength
λ_{SWL}	Short wavelength limit
μ	Linear absorption coefficient, typical unit: 1/cm
μ/ρ	Mass absorption coefficient, typical unit: cm^2/g
ν	Poisson ratio
σ	Normal stress Standard deviation of a Gaussian distribution
σ_ϕ	Measured normal stress in the direction given by ϕ angle
σ_{ij}	Stress tensor with six components: σ_{11}, σ_{12}, σ_{22}, σ_{13}, σ_{23}, σ_{33}
σ_I, σ_{II}, σ_{III}	Principal stress components
σ_{ph}	Pseudo-hydrostatic stress value introduced by an error in stress-free d-spacing
τ	Detector dead time X-ray penetration thickness X-ray beam path length in the sample Shear stress
τ_ϕ	Measured shear stress in the direction given by ϕ angle
ϕ	Left-handed sample rotation angle about its surface normal or axis
φ_1	One of the Eulerian angles defining crystallite orientation with respect to the sample coordinates
φ_2	One of the Eulerian angles defining crystallite orientation with respect to the sample coordinates
Φ	Convergence solid angle of the X-ray beam from the optic One of the Eulerian angles defining crystallite orientation with respect to the sample coordinates
χ_g	Sample rotation angle about a rotation axis within the X_L-Y_L plane

ψ	Sample rotation with the same rotation axis as χ_g except different starting point $\chi_g = 90° - \psi$
ψ	Tilt angle between the sample surface normal and the diffraction vector; ψ-tilt is used for stress measurement in the conventional diffractometer
$\Delta\psi$	Virtual oscillation angle for stress measurement using the 2D detector
	Angular range of the diffraction vector distribution corresponding to a range of diffraction ring
ω	Right-handed rotation of the sample about Z_L
$\Delta\Omega$	Solid angle covered by a pixel or detector region
Ω	Solid angle of the whole detector area
	Angular window of an instrument in solid angle
a, b, c	Lattice parameters of a unit cell; the lengths of the three unit cell vectors
a, b, c	Three vectors defining a unit cell
a*, b*, c*	Three vectors denoting the reciprocal lattice axes
A	Sample absorption factor or transmission coefficient
A_{BB}	Transmission coefficient in Bragg–Brentano geometry ($=1/[2\mu]$)
A_o	Cross-section area of the incident beam on the sample
A_1	Effective focal spot area of an X-ray source
A_2	Focus image area of X-ray beam from an X-ray optic
A_{nm}	Coefficients of the orientation function for fiber texture
A_{RX}	Anisotropic factor used in stress calculation
B/b	Defocusing factor given by the ratio of the sizes of diffracted beam (B) and incident beam (b)
B_L	Background intensity at the lower 2θ side of a diffraction peak
B_H	Background intensity at the higher 2θ side of a diffraction peak
C	Combined pixel intensity correction factor
C_{air}	Pixel intensity correction factor for air scatter
C_{Be}	Pixel intensity correction factor for Be-window absorption
C_{ijkl}	Elastic stiffness coefficients
C_S	Pixel intensity correction factor for Be-window absorption
C_L	Pixel intensity correction factor for the Lorentz factor
C_P	Pixel intensity correction factor for the polarization factor
C_S	Pixel intensity correction factor for sample absorption
$C_{hkl}^{nm}(\chi)$	Coefficients of crystal lattice symmetry for the ODF of fiber texture
C_l^{mn}	ODF coefficients, also referred as C-coefficients
D	Detector distance from the instrument center, also called sample-to-detector distance
d	Distance between two adjacent crystal planes, also called d-spacing
	Pinhole diameter in the collimator
	Average diameter of crystallites
d_{hkl}	d-spacing of a specific crystalline plane with index (hkl)
d_i	Diameter of crystallites of the i-th phase
d_0	Unstressed d-spacing, normally used for stress measurement to represent d-spacing value without stress
$d_{\phi\psi}$	Measured d-spacing in the orientation given by ϕ and ψ angles
DQE	Detective quantum efficiency or detector quantum efficiency
DR	Dynamic range of a detector
E	Energy of X-ray photons, typically in eV or keV
	Young's modulus

f	Size of a spot focus X-ray source, the same as S_1
	Atomic scattering factor
$f(g)$	Orientation distribution function (ODF), $f(g) = f(\varphi_1, \Phi, \varphi_2)$
f_1	Focal length from the focal spot to X-ray optic
f_2	Focal length from the X-ray optic to the focal image
f_i	Volume fraction of measuring crystallites
f_{ij}	Strain coefficient used for strain measurement with six components: $f_{11}, f_{12}, f_{22}, f_{13}, f_{23}, f_{33}$
F_{hkl}	Structure factor of the crystal plane family {hkl}
g_{hkl}	Normalized pole density distribution function
g	Combination of all three Eulerian angles $\{\varphi_1, \Phi, \varphi_2\}$ defining the crystallite orientation with respect to the sample coordinates
G_n^{hkl}	Factors in the series of normalized Legendre polynomials given by the coefficients of the ODF for fiber texture
G_t	Fraction of total diffracted intensity contributed by the surface layer thickness t
$G_{x,y}$	Geometry normalization factor for the pixel $P(x, y)$
h_1, h_2, h_3	Three components of a unit diffraction (scattering) vector in sample coordinates
$\boldsymbol{h_S}$	Unit diffraction (scattering) vector in sample coordinates
h_x, h_y, h_z	Three components of a unit diffraction (scattering) vector in laboratory coordinates
$\boldsymbol{h_L}$	Unit diffraction (scattering) vector in laboratory coordinates
$\boldsymbol{H}$	Diffraction vector in general expression
$\boldsymbol{H_{hkl}}$	Diffraction vector or reciprocal lattice vector
I	X-ray intensity or integrated X-ray intensity
$\mathrm{I_o}$	X-ray intensity of incident beam
$\boldsymbol{k_o}$	Wave vector of the incident beam
$\boldsymbol{k}$	Wave vector of the diffracted beam
$\mathrm{K}_{\alpha 1}$	One of the characteristic lines of the radiation spectrum from X-ray tube
$\mathrm{K}_{\alpha 2}$	One of the characteristic lines of the radiation spectrum from X-ray tube
K_{α}	Combined radiation of $\mathrm{K}_{\alpha 1}$ and $\mathrm{K}_{\alpha 2}$ lines
K_{β}	One of the characteristic lines of the radiation spectrum from X-ray tube; not typically used for X-ray diffraction
m_{ij}	Number of contributing subpixels in a pixel for spatial correction
L	Lorentz factor
M	Magnification ratio of an X-ray optical system
	Total counts of all pixels in the flood-field image
	Total number of subpixels in a pixel for spatial correction
$2M_t$	Attenuation factor due to lattice thermal vibration
$2M_s$	Attenuation factor due to static displacement
$\boldsymbol{n}$	Unit vector of the sample normal
N	Total number of X-ray counts measured by a detector in a given time
N_o	Total number of X-ray photons incident to a detector
N_b	Background counts due to detector noise or background scattering
N_{DL}	Detection limit of a detector
N_e	Ideal quantum yield of a CCD detector
N_i	Normalization factor for a pixel $\mathrm{P_i}$ used for non-uniform response correction
N_p	Total number of X-ray counts, including peak and background
N_S	Total number of contributing crystallites to diffraction
p_i	Counts measured by a pixel

p_{ij}	Stress coefficient used for stress measurement with six components: $p_{11}, p_{12}, p_{22}, p_{13}, p_{23}, p_{33}$
p_{hkl}	Multiplicity factor of the crystal plane family {hkl}
P	Polarization factor
$P(\alpha,\beta)$	Pole density at the pole-figure angles (α,β)
$\bar{P}_n(\cos\chi)$	Normalized Legendre polynomials for calculating fiber texture ODF
q	Modulus of the scattering vector, most frequently used in thin film analysis and small angle scattering
q_x, q_y, q_z	Three components of $\boldsymbol{Q}$ vector expressed in sample orientation
$\boldsymbol{Q}$	Scattering vector or $\boldsymbol{Q}$ vector
r	Distance from a pixel on an area detector to the sample
r_f	Radius of the focusing circle in Bragg–Brentano geometry
r_{ij}	Ratio of the contributing area to the whole pixel area used for spatial correction
	Residuals for detector calibration by the least square fitting
R	Resolution of a SAXS system defined as the theoretically largest resolvable Bragg spacing
	Radius of goniometer circle in Bragg–Brentano geometry
	Radius of a cylindrical detector
	Count rate of a detector
R_B	Noise rate of a photon counting detector
R_{DL}	Count rate at detection limit
R_i	Reflection factor used for retained austenite measurement (i stands for different phases
R_{global}	Global count rate of an area detector (in cps)
R_{local}	Local count rate of an area detector (in cps/mm^2)
R_{pixel}	Pixel count rate of an area detector (in cps/pixel)
R_m	Measured count rate with counting loss ΔR
$\mathrm{R_{BS}}$	Resolution of limit of the beamstop of a SAXS system
$\mathbf{R_x}, \mathbf{R_y}, \mathbf{R_z}$	Detector rotations about three axes, also referred to as roll, pitch and yaw
$\mathbf{s_o}$	Unit vector of the incident beam
$\mathbf{s}$	Unit vector of the diffracted beam
S	Spot size of an X-ray beam on the sample
$\mathrm{S_1}$	One of the macroscopic elastic constants used for stress measurement, also expressed as $\mathrm{S_1(hkl)}$ if the anisotropic correction for a specific crystalline plane is considered
S_1	One of the two macroscopic elastic constants
	Size of an X-ray source
$S_1^{\{hkl\}}$	One of the two X-ray elastic constants (XEC) for crystal planes $\{hkl\}$
$\frac{1}{2}S_2$	One of the two macroscopic elastic constants
$\frac{1}{2}S_2^{\{hkl\}}$	One of the two X-ray elastic constants (XEC) for crystal planes $\{hkl\}$
$S_{x,y}$	Sensitivity normalization factor for the pixel $P(x, y)$
S_{ijkl}	Elastic compliances
$\mathbf{S_1}$	One of the sample coordinates; it is in the same direction as the sample translation axis X, except the origin is fixed on the sample
	Size of an X-ray image after X-ray optic device
$\mathbf{S_2}$	One of the sample coordinates; it is in the same direction as the sample translation axis Y except that the origin is fixed on the sample

$\mathbf{S_3}$	One of the sample coordinates; it is in the same direction as the sample translation axis Z except that the origin is fixed on the sample
t	Thickness of a sample or sample layer
T	Transmission coefficient
	Sample transmission coefficient normalized by A_{BB} . $T = A/A_{BB}$
$T_l^{mn}(g)$	Generalized spherical harmonic functions, l is the order of the series, and m and n denote finite numbers of independent C-coefficient at each order
u	Pixel position in horizontal direction on a flattened cylindrical 2D image
v	Pixel position in vertical direction on a flattened cylindrical 2D image
	Volume of unit cell
v_i	Volume of individual crystallites of the i-th phase
V	Volume of the crystal unit cell
	Effective sampling volume in diffraction
	Voltage applied to the X-ray generator
w_i	Weight friction of an element in a material
	Weighting factor in least square regression
x	Pixel position in a line or area detector in the direction parallel to the diffractometer plane
x_{pc}	Percent crystallinity
$\mathbf{X}$	One of the sample translation coordinates with the origin on the instrument center; $\mathbf{X}$ is in the opposite direction of the incident X-ray beam when $\omega = \phi = 0$; $\mathbf{X}$ normally lies on the sample surface
y	Pixel position in an area detector in the direction perpendicular to the diffractometer plane
y_i	Observed response value of the i-th data point for the least square analysis
$\hat{y}_i$	Fitted response value of the i-th data point for the least square analysis
$\mathbf{Y}$	One of the sample translation coordinates with the origin on the instrument center; $\mathbf{Y}$ normally lies on the sample surface and makes a 90° right-handed angle from $\mathbf{X}$
$\mathbf{Z}$	One of the sample translation coordinates with the origin on the instrument center; $\mathbf{Z}$ is normally in the direction of the sample surface normal
$\mathbf{X_L}$	One of the laboratory coordinates; $\mathbf{X_L}$ is in the direction of the incident X-ray beam
$\mathbf{Y_L}$	One of the laboratory coordinates; $\mathbf{Y_L}$ lies in the diffractometer plane and makes up a right handed rectangular coordinate system with $\mathbf{X_L}$ and $\mathbf{Z_L}$
$\mathbf{Z_L}$	One of the laboratory coordinates; $\mathbf{Z_L}$ is up from the center of instrument and perpendicular to the diffractometer plane

INDEX

α swing angle, 36–38, 169–167, 447–449
β-filter, 71–73
γ angle, 32
γ-integration, 177–185, 291, 328
θ-θ configuration, 48–49, 142, 309, 381
θ-2θ configuration, 48–49, 142
φ angle, 46–47, 247–248, 306–307
χ_g angle, 46–47
ψ angle, 46–47
ψ-tilt, 288–289
ω angle, 46–47
0D detector *see* Point detector
1D detector *see* Line detector
2θ-β configuration, 447–449
2θ angle, 13–14, 30–32
2θ resolution, 117–118,217, 427, 446
2θ-integration, 177–185, 251–253
2D detector *see* Area detector
3D detector *see* Three-dimensional detector
4π detector *see* Ideal detector

Aberration *see also* Defocusing effect
  by flat specimen, 67
Absorption, 61–62, 201–207
  by sample, 203–207
  correction, 201–207, 255
  table, 454–457
  Be-window, 201–203
Absorption coefficient, 61–62, 454–457
Active area, 107–108, 136
Air scattering, 13–14, 66–69, 201–202, 361–364, 398, 448–449
All data point correction (ADPC), 322–325
Amorphous solid phase, 2, 13–14, 395–401
Angular accuracy and precision, 145–149
Angular coverage:
  in γ, 109–111
  by detector, 100–103, 107–111
  by pixel, 112–114
Angular resolution, 112–118
Angular sample oscillation, 225–226
Angular window, 223–225
Anisotropy factor, 278–279
Anode, detector, 119–120, 130–132
Anode wire, detector, 120
Anomalous scattering, 215
Antiscatter slit, 66–67
Archeology, 25
Area detector, 23, 107–137, 157–176
  angular coverage, 107–111
  blank margin, 111–112
  detector plane, 162–163
  flood field correction, 157–161
  maximum measurable angle, 111–112
  parallax effect, 132,163
  position accuracy, 168–176
  position calibration, 169–170
  spatial correction, 161–167

Two-Dimensional X-Ray Diffraction, Second Edition. Bob Baoping He.

© 2018 John Wiley & Sons, Inc. Published 2018 by John Wiley & Sons, Inc.

Area detector (*Continued*)
swing angle, 36–38, 169–167, 447–449
window absorption correction, 201–203
Atomic scattering, 214
Attenuation coefficient *see* Absorption coefficient
Attenuation factor, 213, 216

Background correction:
2θ-integration, 252–253, 314–315
peak evaluation for stress, 314–315
Background counts, 94
Background noise, 99
Background subtraction, 398–401
Backlash, goniometer, 149
Backward diffraction, 30–32 *see also* Diffraction cone
Be-window *see* Detector, window
Beam center, 38,167–171
Beam divergence, 63–85 *see also* Divergent beam
Beam stop, 69–70, 359–374, 450–451
Blank margin, area detector, 111–112
Bragg angle, 13–14, 30–32
Bragg–Brentano geometry, 66–67, 204–205, 212–232
Bragg's Law, 12, 33, 54
Bravais lattice, 4–9
Bremsstrahlung, 57, 73–75
Brightness, 59, 63
Brilliance, 59–60, 63–65

Calibration source, 112–113, 158–159
Capillary optics, 82–85
Capture angle, 64–65, 76–77
CCD detector, 122–125, 135–136
back illuminated, 123
back thinned, 123
demagnification, 124
direct detection, 124–125
fiber optic faceplate, 125
fiber optic taper, 124
front illuminated, 122–123
indirect detection, 123–125
potential well, 122–125
zinger noise, 125
Characteristic lines, 57–58, 97–98
Charge-coupled device (CCD) *see* CCD detector
CMOS detector, 125–126
Coherent scattering, 11
Collimator, 68–70, 80–83, 359–361
Combinatorial chemistry, 379–380
Combinatorial screening, 380–392
cross contamination, 383–387
library plate (*see* Material library)
material library, 379–383
polymorphs, 382
Raman, 390–392
reflection geometry, 380–381
retractable knife-edge, 383–387
transmission geometry, 386–390
Compton scattering, 61, 398
Conic section, of diffraction cone, 36–40
Continuous radiation *see* Bremsstrahlung
Conventional diffractometer, 67–69 *see also* Bragg-Brentano geometry
Convergence angle, 66–68
Convergent beam, 63–65, 76–82
Cooling, detector, 92, 123–125
Corrected frame, 157–167
Corundum, calibration standard, 169–176
$\cos^3\varphi$ falloff, 113, 184, 186
Count rate, 92–97, 136
Counterbalance, 149–150
Counting loss, detector, 94–97
Counting statistics, 92–94
CPAD detector, 129–130
Crossfire *see* Convergence angle
Crystal direction, 6
Crystal orientation, 257, 414–417
Crystal plane, 2, 6–8
Crystal size, 22, 402–411
γ-profile analysis, 404–411
calibration factor, 408–411
Cauchy profile, 403
Gaussian profile, 403
instrumental window, 406
line profile analysis, 402–404
Scherrer equation, 402
Crystal structure, 2–9
Crystal systems, 4–5
Crystallite(s), 17, 221–227, 235, 326–327, 398, 402–411
Crystallographic axes, 3
Cubic system, 4
Curved detector, 43–46
Cylinder projection, 188–197
Cylinder-shaped detector *see* Curved detector

d-spacing, 12, 33, 283, 300–301
for strain measurement, 281–282
of multilayer mirror, 75–78, 437
stress free, 300–301
Data collection strategy, 218–220, 242–250, 264–265, 309–313
Dead time, detector, 95–97, 120
Debye cone, 30–37 *see also* Diffraction cone
Debye ring, 30–37 *see also* Diffraction ring

Debye–Scherrer camera, 88–89
Defocusing effect, 218–220, 383, 436
Defocusing factor, 218–219
Detection area *see* Active area
Detection limit, detector, 99–100, 106–107
Detector, 35–45, 87–137
  γ-optimized mode, 110–111, 196
  2θ-optimized mode, 110–111
  charge sharing, 127, 129
  cooling, 92, 123–125
  counting loss, 94–97
  dead time, 95–97, 120
  detection limit, 99–100, 106–107
  drift time, 95–97
  dynamic range, 99–100, 136
  energy resolution, 97–98
  energy window, 97
  gain, 106
  linearity, 95–96
  noise, 99
  out of diffractometer plane, 40–45
  pixel, 38–41, 100–103, 113–118, 126–127
  point detector, 89–100
  rectangular detector, 110–111
  saturation, 96
  window, 119, 131–132, 162–163, 201–203
Detector distance *see* Sample-to-detector distance
Detector plane, 162–164
Detector quantum efficiency (DQE), 94–95, 135–136
Detector space, 35–45
  parameters, 36–42
Diffracted beam, 30–35, 66–69
Diffracted X-rays *see* Diffracted beam
Diffraction:
  cone, 19–20, 30–37, 171–176
  frame, 20–23
  pattern, 13–14, 19–23, 133
  ring, 20–23, 30–46 (*see also* Diffraction, cone)
  spots, 20
Diffraction space, 31–46
  parameters, 32
Diffraction vector, 18–19, 25–32, 52
Diffraction vector cone, 18–19, 34–35
Diffractometer, 23–24, 48–49, 66–68, 142–148
  θ-θ configuration, 48–49, 142, 309, 381
  θ-2θ configuration, 48–49, 142
  ψ-diffractometer for stress, 288–289
  ω-diffractometer for stress, 288–289
  2θ-β configuration, 447–449
  accuracy, 145–151
  automatic reflection-transmission conversion, 390–391
  Bragg–Brentano, 65–67
  counterbalance, 149–150
  environment stages, 105, 151–155
  four-circle, 29, 46–49
  horizontal, 48–49
  parallel beam geometry, 67–68
  plane, 30–32, 40–43, 48–49, 66–67, 289
  reflection mode, 68, 203–204, 380–381
  sample alignment, 150–151
  sample stages, 142–145
  transmission mode, 220–221, 248–250, 386–390
  two-circle base goniometer, 141–142
  vertical, 48–49, 381–390
Distorted image, 161–167
Divergence, 63–77, 223–225
Divergent beam, 64–65, 80–82 *see also* Divergence
Divergent slit, 67
Drift time, 95–98
Dynamic range, detector, 99–100, 136
Dynamic sample height alignment, 321–322

Effective sampling volume, 222–223, 405–407
Energy dispersive X-ray diffraction, 98
Energy range, detector, 94–95
Energy resolution, detector, 97–98, 438–439
Energy window, detector, 97
Environment stage, 151–155
Eulerian angles, 256–258
Eulerian geometry, 46–47, 143–145
Ewald sphere, 19, 52, 424–425, 440, 446

Fiber texture, 229–233, 260–264 *see also* Texture
Fiber texture plot (FTP), 232–233
Fiducial plate, 162–163
Flat 2D detector *see* Detector
Flood field correction, 159–161
Fluence, 63, 135
Fluorescence, 58, 69, 308
Flux, 63
Flux density, 63 *see also* Fluence
Focal spot, 59 *see also* Brilliance
Focusing circle, 66–67 *see also* Goniometer, circle
Forensics, 25
Forward diffraction, 30 *see also* Diffraction, cone
Frame integration, 177–185
  bin method, 182–183
  subpixel method, 183–185
Full width at half maximum (FWHM), 12
Fundamental equations:
  Bragg's Law, 12, 33, 54
  crystal size, 408–409
  Laue equation, 17, 32
  pixel to diffraction space, 38, 44

Fundamental equations (*Continued*)
reciprocal space mapping, 425–426
relationship between the fundamental equations, 53–55
stress, 293–295
texture, 239
unit diffraction vector, 34, 51

Gage repeatability and reproducibility (GRR), 347–349
Gandolfi camera, 13, 18, 89
Gas amplification, 90
Gaseous ionization detector *see* Proportional counter
Gaussian distribution, 92–93, 115
Global count rate, 104–106, 136
Göbel mirror, 77–79
Goniometer, 23, 141–150
accuracy, 145–151
alignment, 145–149
backlash, 149
circle, 66–67
counterbalance, 149–150
main axes, 141–142
sequence of axes, 144–145
sphere of confusion, 145–147
two-circle, 141–142
Goniometer center *see* Instrument center
Graphite crystal *see* Monochromator
Grazing incident, 418–422
Guinier camera, 89

Hall–Petch equation, 402
Helium beam path, 362
High resolution reciprocal space mapping, 424–429, 445–447
High resolution two-dimensional X-ray diffraction ($HRXRD^2$), 445–451
High temperature stage, 151–155
High throughput screening, 379–392
Horizontal goniometer, 48–49
HPC detector, 127–129 *see also* Pixel array detector
Hybrid photon counting pixel detector *see* HPC detector
Hydrostatic stress *see* Stress state, equitriaxial

Ideal detector, 35–36
Image focus, 64–65
size, 64–77
Image plate (IP), 121–122, 135–136
Incident angle, 12, 49, 65–67, 218–219, 332–340, 418–421
Incident beam, 32–33 *see also* Incident X-rays
path, 69
Incident X-ray, 12–21, 30–37
Instrument broadening, 117, 404, 427
Instrument center, 31–37, 47–48, 141–142
Integrated RSM, 427–429
Integrating detector, 119–135
Intensity:
γ-integration, 177–185, 291–308
2θ-integration, 177–185, 251–253
brightness, 59, 63
brilliance, 59–60, 63–65
fluence, 63, 135
flux, 59, 63
flux density, 63 (*see also* Fluence)
relative intensity, 212–213
Interplanar spacing, 12 *see also d*-spacing
Irradiated area, 65, 89, 145, 216

K absorption edge, 62, 72, 454–457
Kappa geometry, 51
Kirkpatric–Baez scheme, 78 *see also* Multilayer mirror, cross-coupled
Knife-edge, monochromator, 74

Laboratory coordinates, 32–37, 46, 50, 53
Laser video system, 150–151
Lattice constants, 4
Lattice direction, 6–8
Lattice parameters, 4
Lattice plane, 6
Laue camera, 87
Laue equation, 17, 32
Least square regression, 317–320
intensity weighted, 318–320
Legendre polynomials, 230–232
Limiting sphere, 17–18
Line detector, 100–106
curved, 100–101
straight, 100–107
Line focus, 59–60
Line source, 65–67
Line spread function (LSF), 106, 114–115
Linear absorption coefficient, 61 *see also* Absorption
Liouville's theorem, 63–65
Liquid metal jet anode, 60
Loading strain, 339
Local count rate, 104, 120, 136
Lorentz correction, 197
Lorentz polarization and absorption (LPA) factor, 197–201

Mass absorption coefficient, 61, 454–457 *see also* Absorption
Material library, 379–383
Maximum count rate, 95–97, 104, 107, 133, 136
Maximum measureable angle, 112
Merge of multiple frames, 186–196
Merge of overlapping region, 191–193
Microdiffraction, 25, 150–151, 291
Microgap detector *see* MikroGap detector
Microsource, 60
Mikrogap detector, 130–136
  amplification gap, 131–132
  delay lines, 131–132
  grid, 131
  radiation hardness, 134
  resistive anode, 131–132
Miller–Bravais indices, 6–7
Miller indices, 6
Mirror *see* Multilayer mirror
Miscut angle, 416–417
Monocapillary, 83 *see also* Capillary optics
  tapered, 83
Monochromator, 73–75
  channel cut, 75
  knife-edge, 74–75
Montel scheme *see* Multilayer mirror, side-by-side
Mosaic structure, 11
Mosaicity, 11, 74, 224
Multilayer mirror, 75–79
  cross-coupled, 78–79
  elliptical, 76–77
  magnification ratio, 77
  parabolic, 76
  scanning line detector, 436–437
  side-by-side, 78–79
Multiple frame merge, 186–196
Multiple {*hkl*} rings for stress measurement, 335–339
Multiplicity factor, 213, 408–409
Multiwire proportional counter (MWPC), 119–121, 135–136

Noise, detector, 99
Nonparalyzable dead time, detector, 96
Nonuniform response correction, detector, 159–161 *see also* Flood field correction
Normalized Legendre polynomials, 230–232
Normalized pole density function, 229–232

Optics, 63–85
  focusing optics, 76, 84
  parallel optics, 76, 84
Orientation distribution function (ODF), 256–260

Parallax effect, area detector, 132, 163
Parallel beam geometry, 67–68
Parallel plate avalanche chamber *see* MikroGap detector
Parallel-plate resistive-anode chamber *see* MikroGap detector
Paralyzable dead time, detector, 96
Peak broadening, 12, 280, 403–404
Pearson VII, 315–316
Percent crystallinity, 395–401
  external method, 398–400
  full method, 400–401
  internal method, 398–399
  rolling ball background subtraction, 400
  scatter correction, 397–398
Pharmaceutical, 26, 379–393, 405–412
Phase ID *see* Phase identification
Phase identification, 211–233
Phosphor, 91, 123–125
Photographic film, 88, 107
Photomultiplier, 91
Photon-counting detector, 92, 119–121, 126–128
Pinhole:
  antiscattering, 80
  collimation, 70, 80–81, 360
  scatterless, 360
Pinhole collimator, 80–83 *see also* Collimator, Pinhole
Pitch, detector position, 168–176
Pixel, detector, 38–41, 100–103
Pixel angular range, 112–113
Pixel array detector (PAD), 126–129
Pixel count rate, 104
Pixel direct diffraction analysis (PDD), 441–444
  pixel diffraction vector, 442
  pixel intensity weighted least squares (PIWLS), 444
  stress, 443–444
  texture, 442–443
Pixel resolution, 114–115, 426
Pixel size, 112–118, 126–127
Point detector, 89–100, 240, 250, 326, 340
Point spread function (PSF), 114–118, 127, 136
Poisson distribution, 92, 97, 221
Poisson's ratio, 216, 278, 294, 351
Polarization correction, 197–201
Pole density (distribution) function, 227–230, 236–241
Pole figure, 238–241 *see also* Texture
Polycapillary, 83–85 *see also* Capillary optics
Polychromatic radiation, 57
Polycrystalline materials, 20–21, 212, 227, 235, 271

Polymer, 264–267, 340–346, 395–401
  biaxial drawing, 265–267
  crystallinity, 395–401
  pole figure, 265–267
  stress, 344–346
Powder diffraction, 17–18, 211–226
Powder diffraction file (PDF), 212
Preferred orientation *see* Texture
Primary beam path, 69, 73, 80–81
Proportional counter, 90, 95

Raw data frame, 114
Raw frame, 163–167 *see also* Raw data frame
Real time readout, 120
Receiving slit, 65–67, 216–218
Reciprocal lattice, 14–18
  vector, 14–17
Reciprocal space, 14–16, 52–53, 424–427, 440–441, 445–446
  mapping, 424–427
Rectangular detector, 110–111
Reflection angle, 12, 218
Reflection mode diffraction, 68, 203–204, 380–387
Reflection plane, 3
Reflection sphere *see* Ewald sphere
Reflectivity, 423–424
Reflectometry, 423–424
Relative intensity, 212–213
Residual stress, 279–280 *see also* Stress
Retained austenite, 412–414
  by CCD detector, 412–413
  reflection factor, 412–414
Rocking angle, 224–225
Roll, detector position, 168–176
Rotating anode generator, 58–60

Sample absorption correction, 203–207
Sample alignment, 150–151
Sample coordinates, 46–51, 273, 425–426
Sample oscillation, 225–227
Sample space, 46–51
Sample stage, 23, 141–144
Sample-to-detector distance, 35–38, 108–117, 162, 446–447
Sampling statistics, 118, 221–226
Saturation, detector, 96
SAXS *see* Small angle X-ray scattering
Scanning 2D pattern, 194–196
Scanning line detector, 434–437
Scattering angle, 13–14, 188–190, 194 *see also* 2θ angle
Scattering pattern, 13 *see also* SAXS
Scattering vector, 18, 35, 52 *see also* Diffraction vector
Scintillation counter, 91–95
Scintillator, 91, 123, 129
Secondary beam path, 68–69, 362–373, 448–449
Seemann–Bohlin camera, 89
Semiconductor detector *see* Solid-state detector
Short wavelength limit, 57
Si(Li) detector *see* Solid-state detector
$\sin^2\psi$ and 2D method comparison, 310, 326–327, 348
$\sin^2\psi$ method, 283–288
  with area detector, 291–292
Single crystal diffraction, 2, 20
Single tilt method, 340–347 *see also* Stress
Small angle X-ray scattering, 357–374
  γ-integration, 366–367
  2θ-integration, 366–367
  beam stop, 359–362, 370–372
  helium beam path, 362
  optics, 359–361
  particles in solution, 367–368
  pinhole collimation, 360
  resolution, 359
  scanning, 367–369
  scattering vector, 358
  secondary beam path, 361–364
  silver behenate, 365
  transmission measurement, 367, 372
  vacuum beam path, 363
  vertical system, 372–374
Smearing effect, 70–71, 194–196
Solid-state detector, 91–92, 95
Soller slits, 66–68
Spatial correction, 161–167
Spatial linearity, 114
Spatial redistribution function *see* Point spread function
Specific loading, 60
Spectrum, of X-rays, 57–58
Spectrum purity, 63, 73–75
Sphere of confusion (SoC), 145–147 *see also* Goniometer
Spot focus, 59, 71, 74
Stacking sequence, 47, 145
Strain, 276–278
  engineering strain, 276
  logarithmic strain (*see* Strain, true strain)
  natural strain (*see* Strain, true strain)
  shear strain, 276–277
  strain coefficients, 294
  tensor, 276–277

true shear strain, 276
true strain, 276
Stress, 271–352
ψ-diffractometer, 288–289 (*see also* Side-inclination)
ψ-tilt, 288–289
ω-diffractometer, 288–289 (*see also* Iso-inclination)
2D fundamental equation, 292–300
all data point correction (ADPC), 322–325
anisotropic factor, 278–279
coating, 340–347
conventional and 2D theory, 295–297
data collection strategy, 309–313
data integration, 313–318
diffraction cone distortion simulation, 302–306
dynamic sample height alignment, 321–322
elastic compliances, 277
elastic stiffness coefficients, 277
elasticity, 277–279
fundamental equation, 292–300
gage repeatability and reproducibility (GRR), 347–349
Hook's law, 277–278
in-depth gradient, 333–335
iso-inclination, 288–289 (*see also* ψ-tilt)
$K_{\alpha 2}$ correction, 314
$K_{\alpha 2}$ stripping (*see* $K_{\alpha 2}$ correction)
with large grain, 319–320
layer removal, 333
macroscopic elastic constants, 278, 351–352
mapping, 329–332
multiple {hkl} rings, 335–339
normal stress, 272–276
parameters, 351–352
peak evaluation, 313–316
Pearson VII, 315–316
Poisson's ratio, 278
polymer, 340–346
principal stresses, 272, 275, 349–351
pseudo-hydrostatic stress, 298–301
residual stress, 279–280
shear, 273, 278
shear modulus, 278
side-inclination, 288–289 (*see also* ψ-tilt)
simulated diffraction ring, 302–306
$\sin^2\psi$ method, 283–288
$\sin^2\psi$ method and 2D method, 310, 326–327
$\sin^2\psi$ method with area detector, 291–292
single tilt method, 340–347
standard, 324–325
stress coefficients, 295, 302
stress-free $2\theta_0$ (*see* stress-free *d*-spacing)
stress-free *d*-spacing, 286–287, 300–301
stress-free sample, 320–324
synchrotron beam, 336–339
tensor, 273–275
tensor of second order, 277, 292
with texture, 285, 319–320
thin film, 332–346
virtual oscillation, 327–328
X-ray elastic constants (XEC), 278–279
Young's modulus, 278, 351–352
Stress-free *d*-spacing, 300–301
Stress state, 273–275
biaxial, 274
biaxial with shear, 274
equibiaxial, 274, 299, 305
equitriaxial, 275
triaxial, 274
uniaxial, 274, 305
Structure factor, 218
Subpixel, 160–165, 183–184,191
Synchrotron radiation, 62–63, 137, 338

Takeoff angle, 58–59
Target loading, 60
Target material *see* X-ray tube, anode
Temperature calibration, 153–155
Tensor of second order, 277, 292
Texture, 229–233, 235–269, 443
2θ-integration, 251–253
absorption correction, 255
calculated pole figure, 259–267
data collection strategy, 242–250
direct observation, 268–269
Eulerian angle and space, 256–258
fiber texture, 229–233, 260–264
fundamental equations, 238–241
multiple scan, 243–246
orientation distribution function (ODF), 230–232, 256–260
orientation relationship, 268
pole density, 227–230, 240–241
pole density function, 227–230, 236–241
pole figure, 236–255
pole figure interpolation, 255
pole-figure normalization, 256
pole-figure symmetry, 250
polymer, 264–267
single scan, 242–243
stereographic projection, 237–238
Thin film, 243–246, 332–339, 418–429
grazing incident, 418–422
reciprocal space mapping,424–429
reflectivity, 423–424

Thin film (*Continued*)
stress, 332–346
texture, 243–246
Three-dimensional detector, 438–441
3D image, 439
energy dispersive pixel, 438
Ewald sphere, 440–441
reciprocal space, 440–441
voxel, 438–439
Total external reflection *see* Capillary optics
Townsend avalanche, 90
Transformation matrix, 50–51
Translation axes, of sample, 46–47, 141–144
Translational sample oscillation, 225–226
Transmission coefficient, 203–207, 222
Transmission mode diffraction, 220–221, 248–250, 386–390
Two-dimensional detector *see* Area detector

Unit cell, 2–6
Unit diffraction vector, 33–35, 50–55, 199, 204–206
absorption correction, 204–206
crystal orientation, 414–417
fundamental equations for stress, 283, 293
fundamental equations for texture, 228, 239
polarization, 199
reciprocal space, 52, 425–426
transformation to sample space, 50–51
virtual oscillation, 224
Unit vector *see* Unit diffraction vector

Vacuum beam path, 362–363, 448–449
Vertical goniometer, 48–49, 381–390
Virtual oscillation, 224–226, 327–329

Wavelength, 11–12, 57–58, 438–441, 454–457
White radiation *see* Bremsstrahlung
Window absorption correction, 201–203

X-ray elastic constants (XEC), 278–279, 251–252
X-ray generation, 57–59 *see also* X-ray tube
X-ray optics, 63–85
X-ray source, 57–63
brightness, 59–63
size, 59, 64–65, 76–77
X-ray tube, 58–59
anode, 59
line focus, 59
spot focus, 59
takeoff angle, 59

Yaw, detector position, 168–176
Young's modulus, 278, 351–352